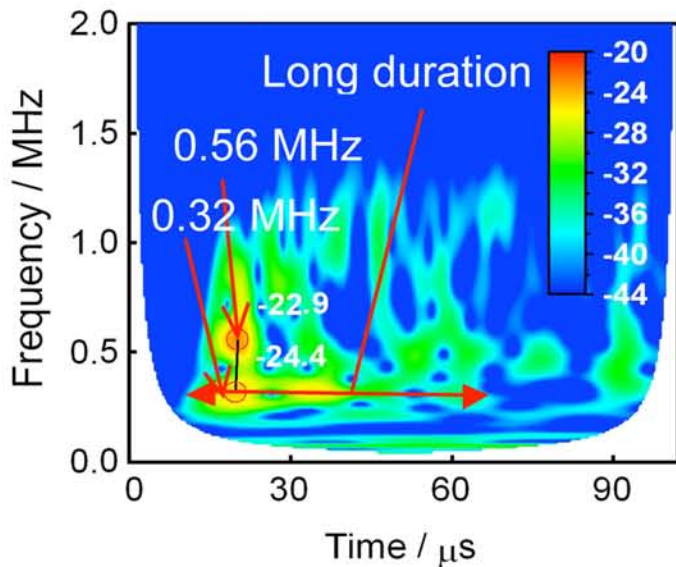


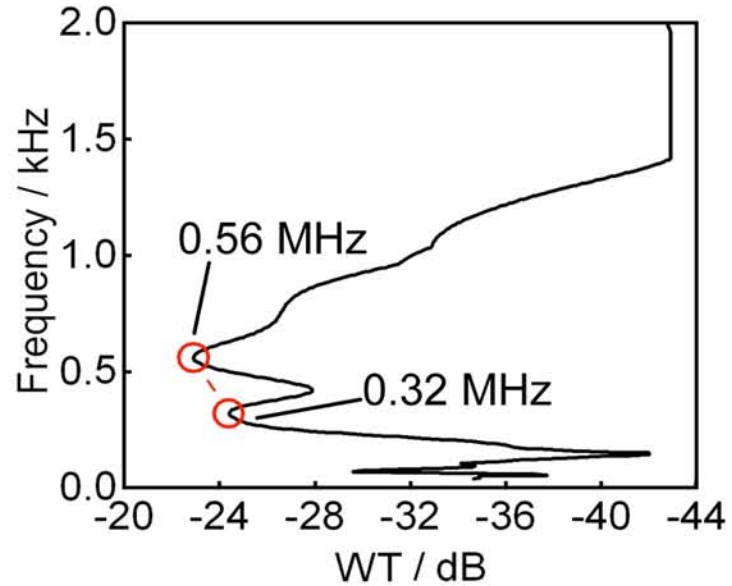
An International
Forum For
The AE Science
and Technology

JOURNAL OF ACOUSTIC EMISSION

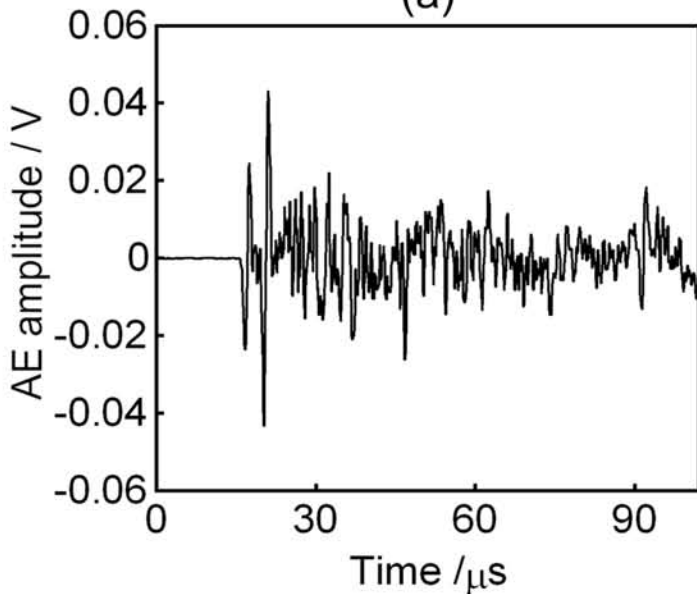
Vol.26/January-December 2008



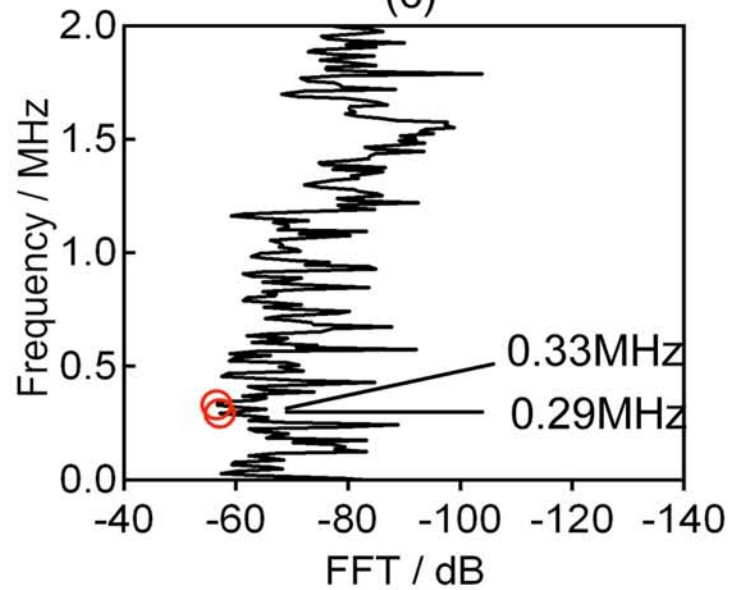
(a)



(c)



(b)



(d)

**With WT Projection TMU Study Reveals
Major Frequencies Hidden in FFT**

Endorsed by
AEWG
and
EWGAE

Published by
Acoustic Emission Group
Encino, CA USA

Journal of Acoustic Emission, Volume 26, 2008

VIEWING AN ARTICLE IN CD-ROM

You need a software that can read a pdf-file, such as Adobe Acrobat Reader®. Install one first before going further. You can download the latest version from www.adobe.com. Use of Adobe Acrobat® (not provided) allows one to utilize the Search function. This gives the power to search for a name or a word in the entire volume and is highly recommended.

PDF Files: Contents are listed below. Individual papers have file names of **26-xxx.pdf**, with xxx as their first page number.

Contents

26-001	Acoustic Emission Investigation of Coating Fracture and Delamination in Hybrid Carbon Fiber Reinforced Plastic Structures Markus G. R. Sause, Daniel Schultheiß and Siegfried Horn	1-13
26-014	Acoustic Emissions Related to the Dehydration Stress Behavior of Green Norway Spruce Wood Sabine Rosner, Bo Karlsson, Johannes Konnerth and Christian Hansmann	14-22
26-023	Investigation of the Z-Direction Strength Properties of Paper by Use of Acoustic Emission Monitoring S. Norgren, P. A. Gradin, S. Nyström and M. Gullikson	23-31
26-032	Assessment of Stress Corrosion Cracking in Prestressing Strands Using AE Technique Marianne Perrin, Laurent Gaillet, Christian Tessier and Hassane Idrissi	32-39
26-040	Comparison of Wavelet Transform and Choi-Williams Distribution to Determine Group Velocities for Different Acoustic Emission Sensors M. A. Hamstad	40-59
26-060	A Comparison of AE Sensor Calibration Methods Jiri Keprt and Petr Benes	60-71
26-072	Experimental Transfer Functions of Acoustic Emission Sensors Kanji Ono, Hideo Cho and Takuma Matsuo	72-90
26-091	Couplants and Their Influence on AE Sensor Sensitivity Pete Theobald, Bajram Zeqiri and Janine Avison	91-97
26-098	Laboratory Experiments for Assessing the Detectability of Specific Defects by Acoustic Emission Testing Franz Rauscher	98-108
26-109	Integrity Evaluation of COPVs by Means of Acoustic Emission Testing Yoshihiro Mizutani, Kouki Saiga, Hideyuki Nakamura, Nobuhito Takizawa, Takahiro Arakawa and Akira Todoroki	109-119
26-120	Structural Integrity Evaluation of CNG Composite Cylinders by Acoustic Emission Monitoring Olivier Skawinski, Patrice Hulot, Christophe Binétruy and Christian Rasche	120-131
26-132	Automated Method for Statistical Processing of AE Testing Data V. A. Barat and A. L. Alyakritskiy	132-141
26-142	Termites Detection via Spectral Kurtosis and Wavelet De-Noising of Acoustic Emission Signals Juan-José G. De La Rosa, Antolino Gallego, Rosa Piotrkowski, Enrique Castro and Antonio Moreno-Muñoz	142-151

26-152	Acousto-Ultrasonic Signal Analysis for Damage Detection in GFRP Adhesive Joints Andreas J. Brunner and Giovanni P. Terrasi	152-159
26-160	Bending Fracture Behavior of 3D-Woven SiC/SiC Composites with Transpiration Cooling Structure Characterized by AE Wavelet Analysis Toshimitsu Hayashi and Shuichi Wakayama	160-171
26-172	Acoustic Emission Monitoring of Bridge Structures in the Field and Laboratory Rhys Pullin, Karen M. Holford, Robert J. Lark and Mark J. Eaton	172-181
26-182	Arrival Time Detection in Thin Multilayer Plates on the Basis of Akaike Information Criterion Petr Sedlak, Yuichiro Hirose, Manabu Enoki and Josef Sikula	182-188
26-189	Some Possibilities of AE Signal Treatment at Contact Damage Tests of Materials and Bearings Pavel Mazal, Filip Hort, Martin Drab and Tomas Slunecko	189-198
26-199	Laser Cutting and Acoustic Emission Signals Tomaž Kek and Janez Grum	199-207
26-208	Online Monitoring of Hot Die Forging Processes Using Acoustic Emission (Part I) Islam El-Galy and Bernd-Arno Behrens	208-219
26-220	Natural Fiber Composites Monitored by Acoustic Emission Igor Maria De Rosa, Carlo Santulli and Fabrizio Sarasini	220-228
26-229	Acoustic Emission Feature for Early Failure Warning of CFRP Composites Subjected to Cyclic Fatigue Runar Unnthorsson, Thomas P. Runarsson and Magnus T. Jonsson	229-239
26-240	Identification of Damage Initiation and Development in Textile Composite Materials Using Acoustic Emission D.S. Ivanov, S.V. Lomov, I. Verpoest and M. Wevers	240-246
26-247	Wavelet Entropy and Power of AE Signals as Tools to Evaluate Damage in Coatings Submitted to Scratch Test Rosa Piotrkowski, Antolino Gallego and Enrique Castro	247-261
26-262	AE Entropy for the Condition Monitoring of CFRP Subjected to Cyclic Fatigue Runar Unnthorsson, Thomas P. Runarsson and Magnus T. Jonsson	262-269
26-270	Experimental Simulation and Dynamic Behavior of the AE due to Martensitic Transformation Using Shear Wave Transmission Sensor Takeshi Yasuda, Shinya Kondo, Hideo Nishino and Kenichi Yoshida	270-278
26-279	Implementation of Acoustic Emission Method to the Conventional NDT Structure in Oil Refinery V.P. Gomera, V.L. Sokolov and V.P. Fedorov	279-289
26-290	An Experimental Analysis of Frequency Emission and Noise Diagnosis of Commercial Aircraft on Approach S. Khardi	290-310
26-311	New Developments of Software for A-line Family AE Systems Sergey Elizarov, Anton Bukatin, Mikhail Rostovtsev and Denis Terentyev	311-317
26-317	Application of Acoustic Emission in Optimizing the Design of New Generation castings of High-Voltage Electric Devices Jan Płowiec, Wojciech L. Spychalski, Huber Matysiak and Jakub Michalski	318-325

Contents26	Contents of Volume 26 (2008)	I-1 – I-3
AUindex26	Authors Index of Volume 26	I-4
AusNotes	Policy/Author's Notes/Meeting Calendar/DVD/Subscription Information	I-5 – I-7

JAE Index Folder*	Cumulative Indices of J. of Acoustic Emission, 1982 – 2008
Contents1-26	Contents Volumes 1-26
Authors Index1-26	Authors Index Volumes 1-26

PhD Thesis of Runar Unnthorsson, University of Iceland, 2008*

* indicates the availability in CD-ROM only. Indices are also available for download from www.aewg.org.

Cover Illustration is from Paper 26-160 by Toshimitsu Hayashi and Shuichi Wakayama.

This figure shows the WT diagram, AE signal, projected WT-frequency curve and FFT spectrum. While WT identifies the first major frequency at 0.56 MHz and the second major frequency at 0.32 MHz, FFT shows the 1st and 2nd major frequencies of ~0.3 MHz as these frequency components have long duration. This clearly shows that FFT analysis failed to detect the highest characteristic frequency at 0.56 MHz.

In using FFT, it is essential to be cognizant of this shortcoming. Read further in the text.

AUTHORS INDEX, Volume 26, 2008

A. L. Alyakritskiy	26-132	Hideyuki Nakamura	26-109
Takahiro Arakawa	26-109	Hideo Nishino	26-270
Janine Avison	26-091	S. Norgren	26-023
V. A. Barat	26-132	S. Nyström	26-023
Bernd-Arno Behrens	26-208	Kanji Ono	26-072
Petr Benes	26-060	Marianne Perrin	26-032
Christophe Binétruy	26-120	Rosa Piotrkowski	26-142, 26-247
Andreas J. Brunner	26-152	Jan Płowiec	26-317
Anton Bukatin	26-311	Rhys Pullin	26-172
Enrique Castro	26-142, 26-247		
Hideo Cho	26-072	Christian Rasche	26-120
		Franz Rauscher	26-098
Igor Maria De Rosa	26-220	Sabine Rosner	26-014
Juan-José G. De La Rosa	26-142	Mikhail Rostovtsev	26-311
Martin Drab	26-189	Thomas P. Runarsson	26-229, 26-262
Mark J. Eaton	26-172		
Islam El-Galy	26-208	Kouki Saiga	26-109
Sergey Elizarov	26-311	Carlo Santulli	26-220
Manabu Enoki	26-182	Fabrizio Sarasini	26-220
V.P. Fedorov	26-279	Markus G. R. Sause	26-001
		Daniel Schultheiß	26-001
Laurent Gaillet	26-032	Petr Sedlak	26-182
Antolino Gallego	26-142, 26-247	Josef Sikula	26-182
V.P. Gomera	26-279	Olivier Skawinski	26-120
P. A. Gradin	26-023	V.L. Sokolov	26-279
Janez Grum	26-199	Wojciech L. Spychalski	26-317
M. Gullikson	26-023	Tomas Slunecko	26-189
M. A. Hamstad	26-040	Nobuhito Takizawa	26-109
Christian Hansmann	26-014	Denis Terentyev	26-311
Toshimitsu Hayashi	26-160	Giovanni P. Terrasi	26-152
Yuichiro Hirose	26-182	Christian Tessier	26-032
Karen M. Holford	26-172	Pete Theobald	26-091
Siegfried Horn	26-001	Akira Todoroki	26-109
Filip Hort	26-189		
Patrice Hulot	26-120	Runar Unnthorsson	26-229, 26-262
Hassane Idrissi	26-032	I. Verpoest	26-240
D.S. Ivanov	26-240	Shuichi Wakayama	26-160
Magnus T. Jonsson	26-229, 26-262	M. Wevers	26-240
		Takeshi Yasuda	26-270
Bo Karlsson	26-014	Kenichi Yoshida	26-270
Tomaž Kek	26-199	Bajram Zeqiri	26-091
Jiri Keprt	26-060		
S. Khardi	26-290		
Shinya Kondo	26-270		
Johannes Konnerth	26-014		
Robert J. Lark	26-172		
S.V. Lomov	26-240		
Takuma Matsuo	26-072		
Huber Matysiak	26-317		
Pavel Mazal	26-189		
Jakub Michalski	26-317		
Yoshihiro Mizutani	26-109		
Antonio Moreno-Muñoz	26-142		

JOURNAL OF ACOUSTIC EMISSION

Editor: Kanji Ono

Associate Editors: A. G. Beattie, T. F. Drouillard, M. Ohtsu and W. H. Prosser

1. Aims and Scope of the Journal

Journal of Acoustic Emission is an international journal designed to be of broad interest and use to both researcher and practitioner of acoustic emission. It will publish original contributions of all aspects of research and significant engineering advances in the sciences and applications of acoustic emission. The journal will also publish reviews, the abstracts of papers presented at meetings, technical notes, communications and summaries of reports. Current news of interest to the acoustic emission communities, announcements of future conferences and working group meetings and new products will also be included.

Journal of Acoustic Emission includes the following classes of subject matters;

A. Research Articles: Manuscripts should represent completed original work embodying the results of extensive investigation. These will be judged for scientific and technical merit.

B. Applications: Articles must present significant advances in the engineering applications of acoustic emission. Material will be subject to reviews for adequate description of procedures, substantial database and objective interpretation.

C. Technical Notes and Communications: These allow publications of short items of current interest, new or improved experimental techniques and procedures, discussion of published articles and relevant applications.

D. AE Program and Data Files: Original program files and data files that can be read by others and analyzed will be distributed in CD-ROM.

Reviews, Tutorial Articles and Special Contributions will address the subjects of general interest. Nontechnical part will cover book reviews, significant personal and technical accomplishments, current news and new products.

2. Endorsement

Acoustic Emission Working Group (AEWG), European Working Group on Acoustic Emission (EWGAE), have endorsed the publication of Journal of Acoustic Emission.

3. Governing Body

The Editor and Associate Editors will implement the editorial policies described above. The Editorial Board will advise the editors on any major change. The Editor, Professor Kanji Ono, has the general responsibility for all the matters. Associate Editors assist the review processes as lead reviewers. The members of the Editorial Board are selected for their knowledge and experience on AE and will advise and assist the editors on the publication

policies and other aspects. The Board presently includes the following members:

A. Anastasopoulos	(Greece)
F.C. Beall	(USA)
J. Bohse	(Germany)
P. Cole	(UK)
L. Golaski	(Poland)
M.A. Hamstad	(USA)
R. Hay	(Canada)
K.M. Holford	(UK)
O.Y. Kwon	(Korea)
J.C. Lenain	(France)
G. Manthei	(Germany)
P. Mazal	(Czech Republic)
C.R.L. Murthy	(India)
A.A. Pollock	(USA)
F. Rauscher	(Austria)
T. Shiotani	(Japan)
P. Tschliesnig	(Austria)
H. Vallen	(Germany)
M. Wevers	(Belgium)
B.R.A. Wood	(Australia)

4. Publication

Journal of Acoustic Emission is published annually in CD-ROM by Acoustic Emission Group, PMB 409, 4924 Balboa Blvd, Encino, CA 91316. It may also be reached at 2121H, Engr. V, University of California, Los Angeles, California 90095-1595 (USA). tel. 310-825-5233. FAX 818-990-1686. e-mail: aegroup7@gmail.com or ono@ucla.edu

5. Subscription

Subscription should be sent to Acoustic Emission Group. Annual rate for 2009 is US \$111.00 including CD-ROM delivery, by priority mail in the U.S. and by air for Canada and elsewhere. For additional print copy, add \$45. Overseas orders must be paid in US currencies with a check drawn on a US bank. PayPal payment accepted. Inquire for individual (with institutional order) and bookseller discounts. See also page I-8.

6. Advertisement

No advertisement will be accepted, but announcements for books, training courses and future meetings on AE will be included without charge.

Notes for Contributors

1. General

The Journal will publish contributions from all parts of the world and manuscripts for publication should be submitted to the Editor. Send to:

Professor Kanji Ono, Editor - JAE
Rm. 2121H, Engr. V, MSE Dept.
University of California
420 Westwood Plaza,
Los Angeles, California 90095-1595 USA
FAX (1) 818-990-1686
e-mail: ono@ucla.edu

Authors of any AE related publications are encouraged to send a copy to:

Mr. T.F. Drouillard, Associate Editor - JAE
11791 Spruce Canyon Circle
Golden, Colorado 80403 USA

Only papers not previously published will be accepted. Authors must agree to transfer the copyright to the Journal and not to publish elsewhere, the same paper submitted to and accepted by the Journal. A paper is acceptable if it is a revision of a governmental or organizational report, or if it is based on a paper published with limited distribution. Compilation of annotated data files will be accepted for inclusion in CD-ROM distribution, so that others can share in their analysis for research as well as training. ASCII or widely accepted data formats will be required.

The language of the Journal is English. All papers should be written concisely and clearly.

2. Page Charges

No page charge is levied. The contents of CD-ROM will be supplied to the authors free of charge via Internet site.

3. Manuscript for Review

Manuscripts for review need only to be typed legibly; preferably, double-spaced on only one side of the page with wide margins. The title should be brief. An abstract of 100-200 words is needed for articles. Except for short communications, descriptive heading should be used to divide the paper into its component parts. Use the International System of Units (SI).

References to published literature should be quoted in the text citing authors and the year of publication or consecutive numbers. These are to be grouped together

at the end of the paper in alphabetical and chronological order. Journal references should be arranged as below. Titles for journal or book articles are helpful for readers, but may be omitted.

H.L. Dunegan, D.O. Harris and C.A. Tatro (1968), *Eng. Fract. Mech.*, 1, 105-122.

Y. Krampfner, A. Kawamoto, K. Ono and A.T. Green (1975), "Acoustic Emission Characteristics of Cu Alloys under Low-Cycle Fatigue Conditions," NASA CR-134766, University of California, Los Angeles and Acoustic Emission Tech. Corp., Sacramento, April.

A.E. Lord, Jr. (1975), *Physical Acoustics: Principles and Methods*, vol. 11, eds. W. P. Mason and R. N. Thurston, Academic Press, New York, pp. 289-353.

Abbreviations of journal titles should follow those used in the ASM Metals Abstracts. In every case, authors' initials, appropriate volume and page numbers should be included. The title of the cited journal reference is optional.

Illustrations and tables should be planned to fit a single page width (165 mm or 6.5"). For the reviewing processes, these need not be of high quality, but submit glossy prints or equivalent electronic files with the final manuscript. Lines and letters should be legible.

4. Review

All manuscripts will be judged by qualified reviewer(s). Each paper is reviewed by one of the editors and may be sent for review by members of the Editorial Board. The Board member may seek another independent review. In case of disputes, the author may request other reviewers.

5. Electronic Media

This Journal will be primarily distributed electronically by CD-ROM. In order to expedite processing and minimize errors, the authors are requested to submit electronic files of the paper. We can read Macintosh and IBM PC formats. On the INTERNET, you can send an MS Word file and the separate figure files to "aegroup7@gmail.com".

6. Color Illustration

We can process color illustration needed to enhance the technical content of an article. With the new format, authors are encouraged to use them.

MEETING CALENDAR:

AEWG-52

52nd Meeting of AEWG will be held at Stone Harbor Resort, Sturgeon Bay, WI, USA, on October 19-21, 2009. Abstracts should be sent to Daniel R Marron, (dmarron@northwestern.edu) by May 31, 2009.

Web sites are: <http://www.aewg.org/> and <http://iti.northwestern.edu/aewg09>.

E-GLEA 6

6th Meeting of the Latin American Acoustic Emission Group will be held at Ciudad de Gramado, Brazil on September 16-18, 2009. Contact Dr. José Ruzzante for details at ruzzante@cnea.gov.ar

Web sites are: <http://www.cnea.gov.ar/cac/endye/glea.htm>; <http://eglea2009.demet.ufrgs.br>

JAE DVD: Vol. 1-24 (1982-2006)

A DVD contains all the articles from the past 25 years of Journal of Acoustic Emission. Cost is \$200 plus shipping of \$8. Send an order to Acoustic Emission Group (address below).

2009 SUBSCRIPTION RATES

Base rate (CD-ROM) for one year	\$111.00
CD-ROM + printed copy, US priority mail:	\$151.00
CD-ROM + printed copy, non-US priority mail:	\$156.00
Print copy only with priority shipping (US)	\$140.00
Print copy only with priority/air shipping (non-US)	\$145.00
For countries without Global Priority Service*,	\$160.00
* incl. Argentina, Greece, Italy, Russia, Ukraine	

Payment must be in U.S. dollars drawn on a U.S. bank. Bank transfer accepted at
California Bank and Trust, San Fernando Valley Office (Account No. 080-03416470)
16130 Ventura Blvd, Encino, CA 91436 USA (Swift code: CALBUS66)

PAYPAL payment is accepted. Inquire via e-mail.

Back issues available; Inquiry and all orders should be sent to (or Fax 1-818-990-1686):

Acoustic Emission Group
PMB 409, 4924 Balboa Blvd. Encino, CA 91316 USA

For inquiry through Internet, use the following address: aegroup7@gmail.com
Editor-Publisher Kanji Ono Tel. (818) 849-9190
Publication Date of This Issue (Volume 26): 25 April 2009.

ACOUSTIC EMISSION INVESTIGATION OF COATING FRACTURE AND DELAMINATION IN HYBRID CARBON FIBER REINFORCED PLASTIC STRUCTURES

MARKUS G. R. SAUSE¹, DANIEL SCHULTHEIß² and SIEGFRIED HORN¹

¹University of Augsburg, Institute for Physics, Experimentalphysik II, D-86135 Augsburg, Germany; ²BMW Group Forschung und Technik, D-80788 München, Germany

Abstract

Nickel-copper-coated and uncoated carbon-fiber reinforced plastic specimens were investigated by acoustic emission (AE) analysis during four-point bending tests and subsequently characterized by scanning electron microscopy. As a function of applied loading, AE originating from coating failure consisting of crack initiation, crack growth and delamination was detected. The evolution of coating failure observed by AE is consistent with the degradation detected by electron microscopy. In particular, the AE originating from coating failure turns out to be distinguishable from signals arising from failure of the carbon-fiber reinforced plastic. The combination of pattern recognition techniques and advanced frequency-spectrum analysis shows promise to distinguish between different failure mechanisms and, therefore, could be a valuable tool for the investigation of comparable hybrid materials.

1. Introduction

In recent years, the aerospace and automotive industry has developed a lively interest in lightweight applications. Reducing overall weight is the key for energy efficiency, a larger carrying capacity and, therefore, greater competitiveness. In this context, the European project StorHy (Hydrogen Storage Systems for Automotive Application) investigates a liquid-hydrogen tank system made of carbon-fiber reinforced plastic (CFRP). While the required mechanical strength of such tank systems can be achieved by usage of CFRP [StorHy, 2007], the gas permeability is remarkably higher than in conventional metallic storage systems [Schultheiß, 2007]. The most encouraging approach to decrease gas permeation through CFRP is to apply a metallic coating, a so-called liner. Recently several liner materials and methods for coating of CFRP vessels were investigated in StorHy. The best liner solution turned out to be chemically deposited copper, followed by an electroplated copper layer. A closely related liner system also investigated in StorHy is a nickel-copper coating [Schultheiß, 2007]. The characterization of adhesive strength and of maximum allowable strain during mechanical loading of such liner materials is of great importance to optimize the method of liner application and to predict the gas-tightness of a liner under real environmental conditions.

Commonly used surface-sensitive diagnostic methods like scanning electron microscopy (SEM) are insufficient tools for the detection of all possible failure sources. Due to the thickness of the metallic liner, which is in the range of 20 - 60 μm , we can only investigate the delamination between liner and CFRP substrate by SEM after completion of mechanical loading and subsequent destruction of the sample. A direct correlation between the applied strain and the first appearance of delamination and its further progress is impossible. In contrast, acoustic emission (AE) analysis provides a suitable method to obtain the strain dependence of crack formation and crack growth within the liner and liner delamination. In the following, we refer to these mechanisms as coating failure.

In the past, many papers concerning the distinction between AE signals due to different failure mechanisms were published. Based on classical methods like AE activity changes, amplitude distribution and source localization, a change in AE signals during loading of CFRP specimens was observed [Ceysson, 1995], [Sato, 1986], [Komai, 1991]. A further assignment of AE signals to at least two distinct types of failure was achieved by measurement of waveform, wave mode and frequency distribution [deGroot, 1995], [Ni, 2007]. For fiber failure a significant spectral weight was observed at frequencies above 350 kHz, whereas the spectral weight of AE signals relating to matrix failure shifts to lower frequencies (< 350 kHz) [Bohse, 2001].

Several studies investigated crack formation, crack progress and delamination of metallic coatings on metallic substrates. Here AE signals were used to determine the quality of coatings [Fu, 2000]. It was demonstrated that AE signals due to different failure mechanisms can be separated using wave-mode analysis and AE activity analysis [Lin, 1997], [Ma, 2001], [Nikulin, 2005]. In [Miguel, 2003] fatigue evolution for tungsten-carbide/cobalt-coated steel specimens was investigated and four different stages of fracture could be distinguished.

Unsupervised pattern recognition techniques provide a completely different approach to classify AE data. Here, a set of N parameters characteristic for a waveform are extracted, and in the following this set is used to represent the respective AE signal. The values of these parameters are arranged into a N -dimensional space and are scanned for accumulation points using clustering algorithms. According to [Anastassopoulos, 1995, 2000] optimization of numerical discrimination between resulting clusters can be achieved using the heuristic ratios τ and R_{ij} as a measure. R_{ij} is the mean value of the ratios, calculated from average within-cluster-distance to distance between any pair of clusters, whereas τ is defined by the ratio of the minimum distance between any pair of clusters to the maximum of the average within-cluster distances. If the separation between the clusters is large enough the respective AE is likely to be of different origin.

Numerical optimization (minimizing R_{ij} , maximizing τ) of these heuristic ratios as a function of cluster numbers can be used to estimate the number of associated failure mechanisms recorded within the dataset [Anastassopoulos, 1995]. In Ativitavas [2006] and Anastassopoulos [2000], it is also shown that clustering techniques using neuronal network algorithms can successfully distinguish between failure mechanisms in complex CFRP structures and, therefore, are the most promising algorithms for pattern recognition in CFRP materials.

In the present investigation we want to establish the potential of AE analysis as a method for quality assurance and health monitoring of coated CFRP tank systems. Based on advanced AE analysis techniques like pattern recognition, the long-term objective is to distinguish between AE signals arising from liner material failure and those due to failure of structural integrity of CFRP. In this report, we focus on failure mechanisms in the metallic liner. In our special case, we were able to distinguish AE signals originating from liner and CFRP by comparison of coated and uncoated specimens.

2. Experimental

The present investigations were performed on rectangular CFRP-specimens according to DIN-EN-ISO 14125 (class IV type), i.e. specimen dimensions are (100 ± 10) mm \times (15 ± 0.5) mm \times (2 ± 0.2) mm ($l \times w \times h$) [DIN14125]. The matrix consists of a polyurethane-based epoxy resin (Araldite: LY 564/HY 2954). Carbon fibers of type SIGRATEx KDK 8054/120 are arranged in

six plies (0° - 90° textured) of woven fabric. The CFRP substrates were coated by subsequent chemical deposition of a $10\text{-}\mu\text{m}$ electroless Ni-layer and an electroplated $50\text{-}\mu\text{m}$ Cu-layer. The position of the coating was slightly asymmetric with respect to the midpoint of the sample (coating offset, see Fig. 1) with dimensions of $(25\pm 1)\text{ mm} \times (15\pm 0.5)\text{ mm}$ ($l \times w$). This coating dimension avoids contact between the lower supports and coating during four-point bending. Bending tests were also performed according to DIN-EN-ISO 14125 with an inner distance between supports of $(27\pm 1)\text{ mm}$ and an outer distance of $(81\pm 2)\text{ mm}$, respectively (see Fig. 1).

An Instron machine (Type 8502) was used for loading of the specimens. For all measurements the specimen was oriented with the coating on the tensile loading side (specimen bottom), which corresponds to the outer side of a pressurized vessel. To ensure a statistically representative result, five coated and five uncoated samples were investigated using AE analysis. Another eight coated specimens were subjected to different strain levels for investigation in an environmental SEM (Type XL30, FEI Company) to compare microscopic observations with results derived from AE-analysis.

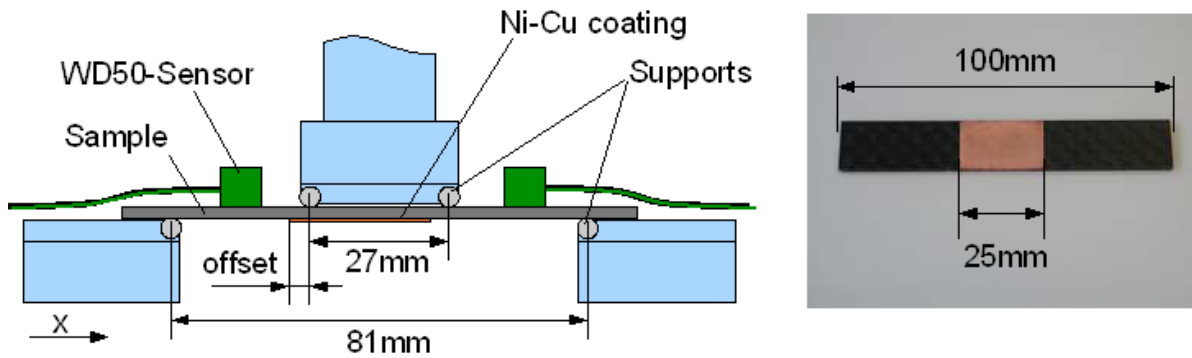


Fig. 1: Schematic drawing of experimental setup (left) and photograph of specimen including dimensions (right).

Acoustic emission was detected by two PAC-WD50 wideband sensors in linear geometry. For acoustic coupling Baysilone silicone grease (Bayer Material Science) of medium viscosity was used, the mechanical contact being provided by two clamps. To suppress detection of friction noise a band-pass ranging from 20 kHz up to 3 MHz was used. In addition, hard rubber plates were positioned below the lower supports, to minimize hydraulic noise arising from the bending machine. The hard rubber plates had no significant influence on the mechanical loading properties due to their hardness in comparison to the maximum load level. The AE waveforms were recorded using a PAC PCI-2 data acquisition system with AEwin software at a sampling rate of 10 MS/s. Data reduction was performed using the software Noesis (Enviroacoustics). To analyze AE, the AE signals were localized in linear geometry and only the events within a distance of 40 mm around the specimen center were considered in the investigation. As the exact phase and group velocities depend on the propagating medium and propagation direction [Lee, 2005], the sound velocity used for localization was calculated from automatic sensor tests (AST) [AEwin, 2002]. The so determined velocity varied between 5000 m/s and 6000 m/s. Based on the sensors diameter of 10 mm, a time window for delay-time determination was calculated, which corresponds to an uncertainty in sound velocity of the order of 1000 m/s. This uncertainty also includes an error assumption for delay-time determination. In total, the error estimation for linear location resulted in $\pm 2.5\text{ mm}$.

The remaining AE signals were analyzed following a classical approach based on waveform parameters, signal location and activity changes. Following references [Anastassopoulos, 1995,

2000], [Noesis, 2006] and [Philippidis, 1998], the same waveform parameters were also investigated using unsupervised pattern recognition techniques to separate the AE of different failure mechanisms. For this purpose the heuristic discrimination of the AE signals dependent on cluster numbers was investigated. The heuristic ratios R_{ij} and τ used for the determination of discrimination efficiency during unsupervised pattern recognition are automatically calculated by Noesis for each partitioning applied to a dataset [Noesis, 2006]. Both values are heuristic criteria based on the ratio of average within-cluster distances to the distance between clusters. R_{ij} is the mean value of the ratios, calculated from average within-cluster distance to the distance between any pair of clusters, whereas τ is defined by the ratio of the minimum distance between any pair of clusters to the maximum of the average within-cluster distances. Therefore, minimization of R_{ij} and maximization of τ results in better discrimination of the resulting data partition. The 12 AE parameters were chosen to provide a correlation level between 16% and 80%. Eliminating waveform parameters like threshold (constant), channels and runtime parameters, the remaining parameters were projected on their principal component axis using a covariance analysis. K-means and Kohonen liquid vector quantizers (LVQ) were used as clustering algorithms with several weighting options for normalization procedures. Finally, using frequency power spectrum analysis a comparison between signal clusters obtained from pattern recognition was performed. For this purpose, a Fourier transform on each waveform with a rectangular window function and 0.1- μ s resolution using the Danielson-Lanczos algorithm was performed. This yielded defined frequency power spectra. Subsequently the arithmetic average, standard deviation, maximum and minimum values were calculated for each cluster using self-written software.

3. Results and Discussion

3.1 Scanning Electron Microscopy

Five coated and three uncoated samples were loaded to different strain levels. Their AE was recorded and afterwards the structural damage was assessed by scanning electron microscopy. The SEM investigations were used to correlate AE signals and the corresponding failure mechanism. An overview of the maximum load levels (ϵ_{\max}) and the respective damage as found by SEM in top view is given in Table 1.

At low strain levels ($\epsilon = 0.33\%$), microcracks develop in the nickel layer (Fig. 2a). With increased loading ($\epsilon = 0.65\%$), the cracks grow beneath the copper layer and cause extensive delamination at the interface region between copper and nickel (Fig. 2b). At even higher strain levels ($\epsilon = 1.23\%$), macroscopic cracks evolve in the maximum strain region of the coating and propagate over the whole specimen width (Fig. 2c). For a strain level of $\epsilon \geq 1.40\%$, matrix cracks, fiber-matrix debonding and fiber breakage are observed (Fig. 2d). In uncoated CFRP specimens, similar evolution of matrix and fiber failure is observed, but, remarkably, the onset of such failures in coated CFRPs shifts to strain values below $\epsilon = 0.65\%$. This could be due to an additional tension caused by the coating or by CFRP degradation during the liner application process. In the following, the results of the microscopic investigation will be used to correlate the AE signal and the observed failure mechanisms of the coating. To this end, we use the strain level and the location, at which cracks and delamination develop, as well as their frequency of occurrence.

3.2 Classical Approach

To compare AE signals between coated and uncoated specimens loaded to $\epsilon = 1.73\%$, the classical approach of AE-energy and amplitude distribution analysis was chosen. The waveform parameters discussed in this investigation are defined according to [AEwin, 2002] as maximum

Table 1: Overview of specimens prepared for SEM, their loading stages and associated damage assessment.

Material	ϵ_{max}	Results of SEM investigation
CFRP-NiCu	0.33 %	Microcracks start in Ni-Layer (Fig. 2a).
CFRP-NiCu	0.65 %	Microcracks increase in size, delamination at Ni-Cu interface, matrix cracks start to evolve in CFRP-specimen (Fig. 2b).
CFRP-NiCu	1.15 %	Cracks appear at the area of strain maximum of the Cu-Layer, matrix cracks increase in number and size, fiber failure is observed at specimen edges.
CFRP-NiCu	1.23 %	Macroscopic cracks (size ≥ 1 mm) evolve inside the Cu-Layer (Fig. 2c).
CFRP-NiCu	1.40 %	Coating failure progresses, large matrix cracks and fiber breakages occur (Fig. 2d).
CFRP	0.65 %	No damage detected.
CFRP	1.23 %	Minor matrix cracks evolve along fiber directions (0° and 90°).
CFRP	1.40 %	Macroscopic matrix cracks appear, fiber breakages and interlaminar fracture is observed.

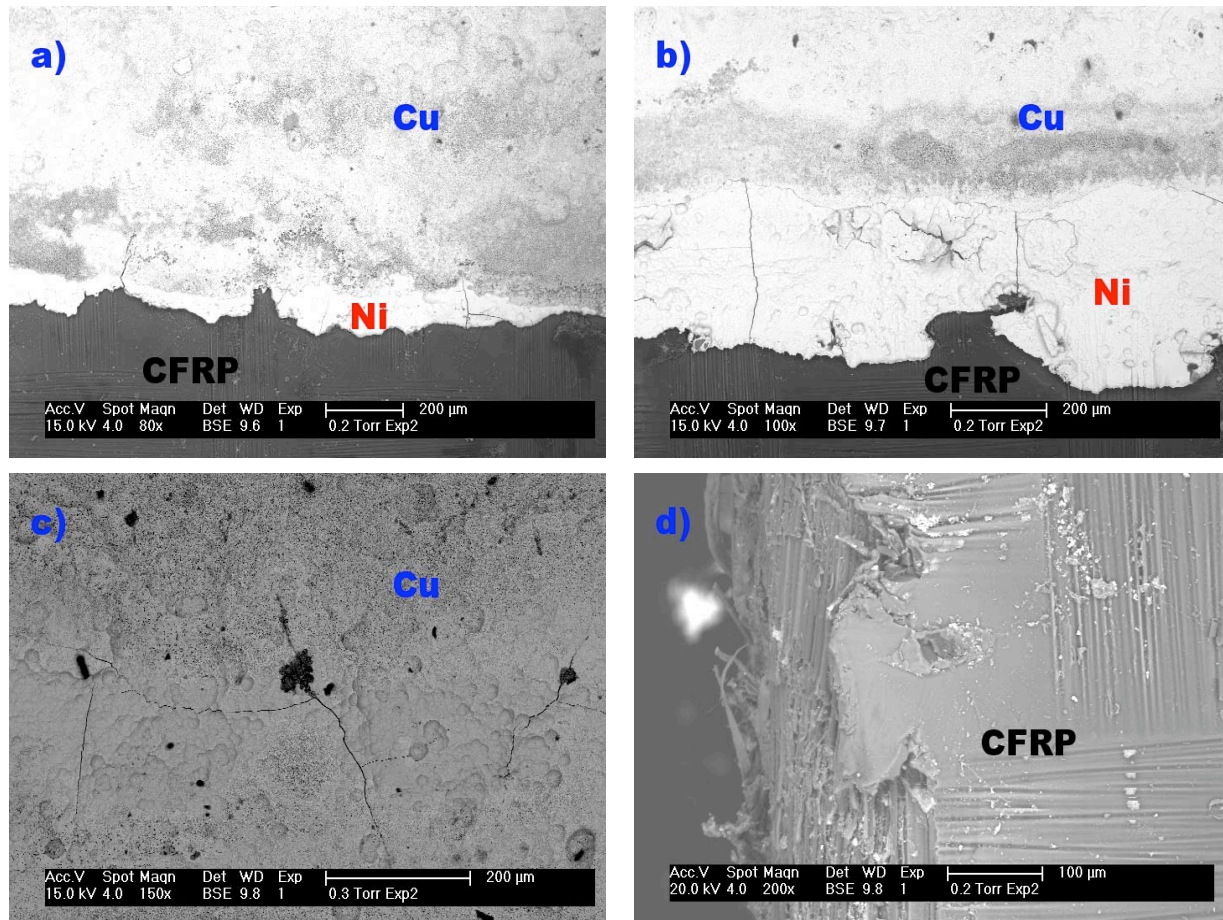


Fig. 2: Top view SEM images of Ni-Cu-coated CFRP specimens at different strain levels. (a) Fringe of coating at $\epsilon = 0.33\%$, (b) fringe of coating at $\epsilon = 0.65\%$, (c) center of coating at $\epsilon = 1.23\%$ and (d) CFRP edge at $\epsilon = 1.40\%$.

signal amplitude, absolute signal energy and root mean square (RMS) value of the waveform. Both the stress-strain curve (Fig. 3a) and the onset of AE activity indicate the start of failure in the uncoated CFRP substrates to occur at a strain level of $\varepsilon = 1.0 - 1.2\%$. In contrast, a large number of additional AE signals arise for coated samples at $\varepsilon \leq 1.0\%$ (see Fig. 3b). Since the CFRP samples are identical for both specimen series, these additional signals are attributed solely to coating failure. This is supported by the fact that the additional AE signals do not correspond to significant changes in the stress-strain curve (Fig. 3b) in contrast to CFRP failure (Fig. 3a). This is expected since the liner should have a negligible influence on the specimens' mechanical properties, which are dominated by the matrix-fiber interaction. Although AE signals from coating and CFRP failure are clearly distinguishable by the strain range of their occurrence, the distribution range of amplitude and energy is comparable (Figs. 3 and 4). For $\varepsilon \geq 1.0\%$, the highest amplitude and highest energy AE signals arise in both coated and uncoated samples, which go along with distinct dips in the stress-strain curve. Therefore, these correspond to severe failures inside the CFRP substrate like single or multiple fiber breakages. Comparable amplitudes and energies are also observed at strain levels $\varepsilon \leq 1.0\%$ in coated CFRP specimens. Consequently, no clear distinction between liner and CFRP failure can be achieved based on the range of energy or amplitude distribution alone.

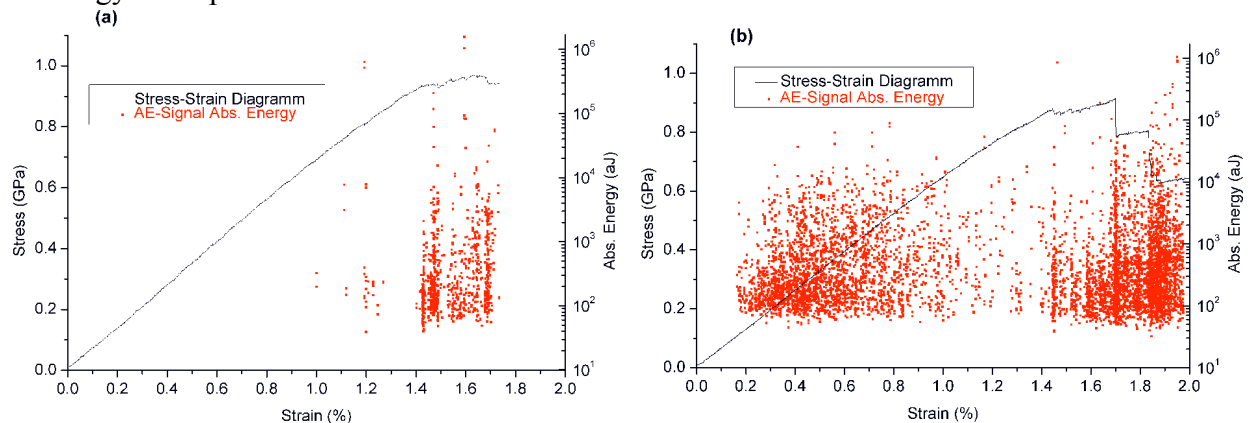


Fig. 3: Absolute energy of AE signal vs. strain (dots) and stress-strain diagram (line) in (a) uncoated and (b) coated CFRP specimen.

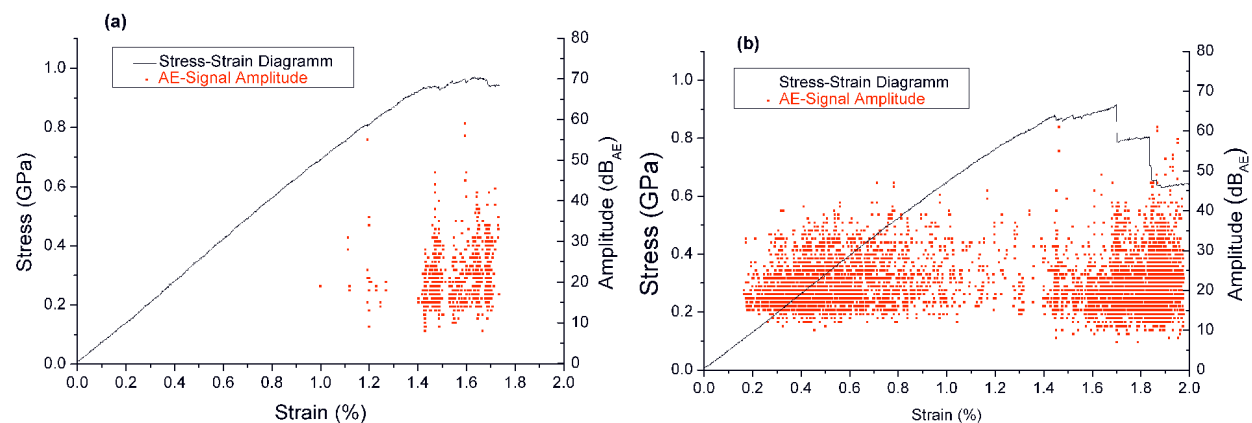


Fig. 4: Amplitude of AE signal vs. strain (dots) and stress-strain diagram (line) in (a) uncoated and (b) coated CFRP specimen.

In the following we want to correlate the failure positions found by SEM to locations calculated from the arrival time of the AE signals. In Fig. 5, a comparison between the x-location of the AE signals of coated and uncoated CFRPs is shown. For uncoated CFRP specimens, most

AE sources are located at two distinct positions, which correspond to the contact positions of the inner supports. At these positions, where the maximum stress level occurs, the highest damage level is observed in electron microscopy. In contrast, the locations of AE sources of the coated specimens are broadly distributed over the coated area (see Fig. 5b). SEM images as a function of loading show that cracks occur over the coated area with preferred direction perpendicular to the sensor alignment. In addition, at $\varepsilon \geq 0.65\%$, extensive delamination is observed. The delamination starts at the fringe of the coating and causes a large amount of AE signals from the coated area. Additionally, the distribution of the AE sources reflects the slightly asymmetric position of the coated area, with respect to the midpoint of the sample (coating offset). At the position of the inner supports, peaks with higher energies arise. These peaks also occur in uncoated CFRP specimens at equal stress levels and, consequently, are attributed to structural damage at the inner supports (see Fig. 5b).

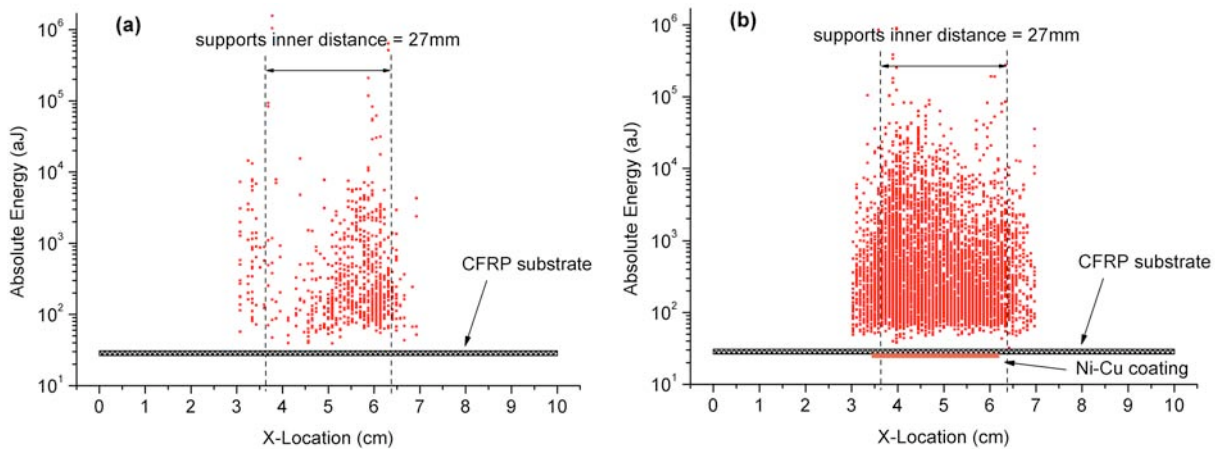


Fig. 5: Absolute energy of AE signal vs. calculated x-position in (a) uncoated and (b) coated CFRP specimen.

The previous discussion suggests that the AE signals detected below $\varepsilon \leq 0.8\%$ arise solely from coating failure, and are therefore denoted “Coating AE signals” in the following. Further, AE signals recorded at bending tests of uncoated CFRP specimens are denoted “CFRP AE signals”. In Fig. 6a, the absolute energy of the Coating AE signals ($\varepsilon \leq 0.80\%$) and CFRP AE signals ($\varepsilon \leq 1.73\%$) of two representative datasets are plotted against their RMS-values. While for all Coating AE signal datasets, a well defined maximal RMS-threshold between 0.04 mV and 0.06 mV was found, the energy value range of the Coating AE signal and CFRP AE signal are not significantly different. All AE signals above this RMS threshold level are attributed to CFRP AE signals and arise at defined strain values, at which the stress-strain curve indicates partial or total structural failure of the CFRP specimen. CFRP AE signals with an RMS value below the threshold level are attributed to minor failures, like crack propagation through epoxy resin in fiber directions or between ply layers (Mode I and Mode II) [Bohse, 2001, 2004]. In summary, we attribute RMS-values above threshold level to structural failure, whereas signals due to coating failure stay below the RMS-threshold.

For other classical waveform parameters (durations, counts or calculated features like frequencies), no obvious distinction between AE signals of coating and CFRP failure was found. For both datasets discussed above (Coating AE signal and CFRP AE signal), all of the investigated waveform parameters are within the same range of values. This is exemplarily shown in Fig. 6b, in which the absolute energy is plotted against amplitude. All the conclusions discussed above apply to the complete set of specimens.

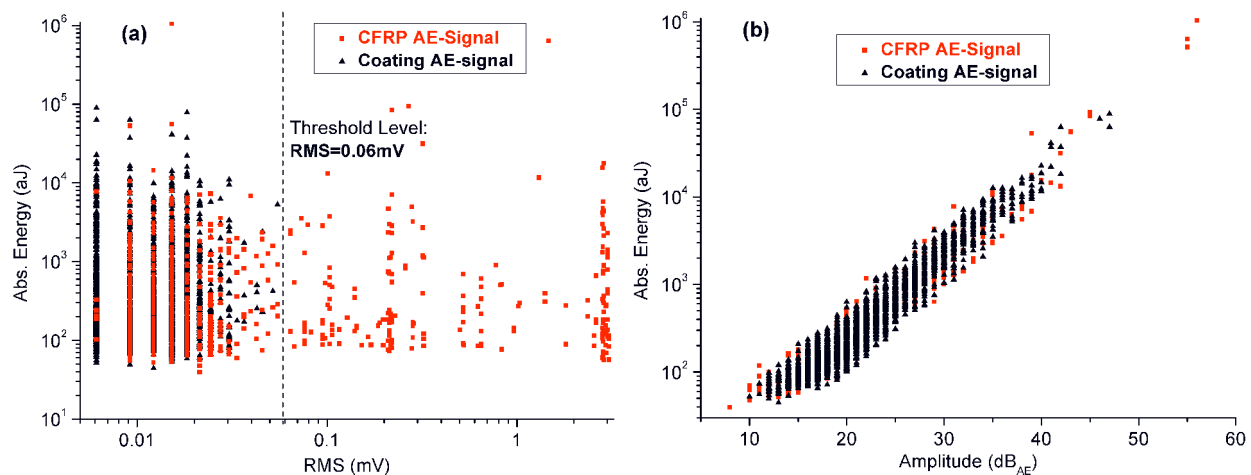


Fig. 6: (a) Absolute energy vs. RMS-value, including threshold value as discussed in text and (b) absolute energy vs. amplitude plot for two datasets.

3.3 Pattern Recognition

Based on the conclusion that AE signals at low strain levels (up to $\varepsilon = 0.8\%$) originate from coating failure, a sufficient number of AE signals is available to investigate the coating degradation. In particular we will focus on the involved failure mechanisms of the coating. For this purpose, several datasets of Coating AE signals were investigated by unsupervised clustering algorithms, after manually eliminating AE signals arising from friction and electrical discharges. For all investigations an amount $\geq 98\%$ of raw data was used.

Following references [Anastassopoulos, 1995, 2000], [Noesis, 2006], [Philippidis, 1998], we investigated the discrimination behavior of each dataset by optimizing R_{ij} and τ values. The respective dataset was partitioned into clusters using k-means and Kohonen LVQ algorithms available in Noesis 5.1 [Noesis, 2006]. In the following, one representative dataset will be discussed.

In Fig. 7a, the values of R_{ij} and τ of this dataset obtained from both k-means and Kohonen LVQ algorithms are plotted against cluster numbers. In this investigation, a maximum of ten clusters was chosen, since saturation of R_{ij} and τ values was already observed within this limit. Best numerical discrimination with a distinct minimum in R_{ij} and a corresponding maximum in τ was achieved using Kohonen LVQ at four clusters (see Fig. 7a). For comparison, an analysis on the same dataset using k-means yielded no obvious discrimination optimum. An accompanying investigation of other datasets yielded similar results for R_{ij} and τ , which are listed in Table 2. Figure 7b shows the partitioning based on the Kohonen LVQ in a suitable principal component covariance projection. The figure suggests that this procedure is suited to discriminate between recorded AE signals. In the following, AE signals belonging to the four clusters are marked by different colors.

To further discuss the correlation between the obtained clusters and failure mechanisms we plot the absolute energy of AE signals vs. amplitude in Fig. 8a and the absolute energy vs. the strain, at which they occur in Fig. 8b. Additionally, the calculated x-location for each AE signal is plotted against its corresponding cluster number (marked by its designated color) in Fig. 9.

AE signals belonging to cluster 1, which are only detected above $\varepsilon = 0.3\%$, show the highest amplitudes and energies. As demonstrated in [Miguel, 2003], the highest signal amplitudes arise during rapid crack propagation and usually appear at medium stages of coating failure. The AE

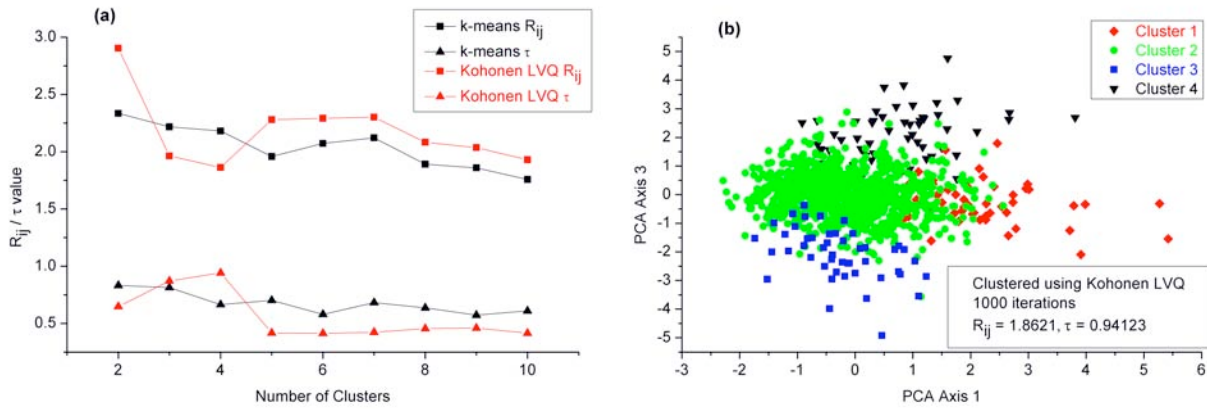


Fig. 7: Optimization of R_{ij} and τ values using k-means and Kohonen-LVQ algorithms (a) and dataset partitioning after clustering with Kohonen-LVQ in principal component projection (b).

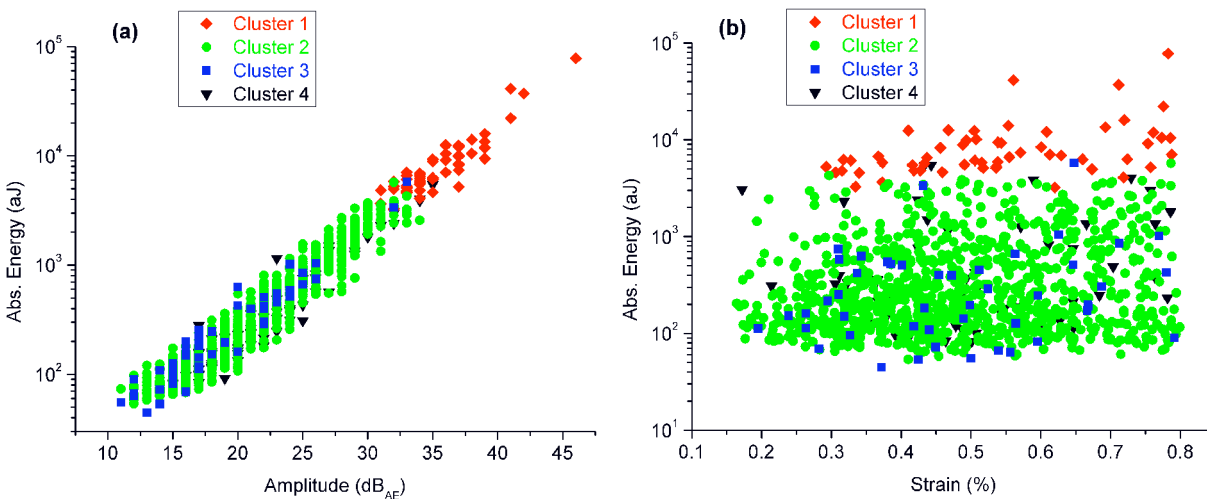


Fig. 8: Optimal dataset partitioning in classical amplitude versus energy plot (a) and strain versus energy diagram (b).

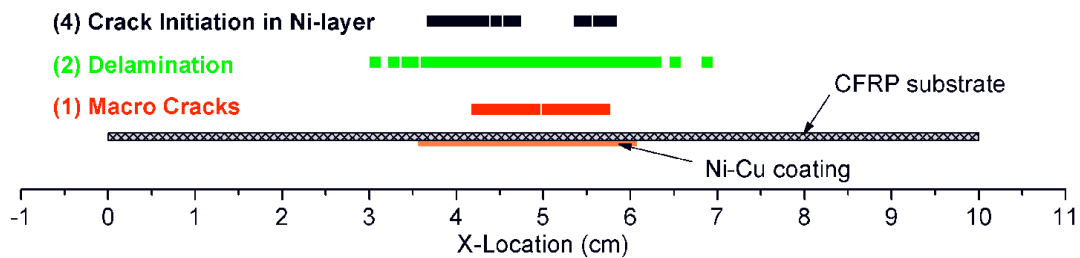


Fig. 9: AE signal x-Location versus cluster number together with specimen dimensions.

sources of cluster 1 are located around the maximum stress region of a specimen and, therefore, the signals of this cluster can be associated with macroscopic crack propagation within the Cu-layer, consistent with SEM observations.

In contrast, AE signals belonging to cluster 2 are broadly distributed in energy and amplitude. This cluster contains the largest number of AE signals. Based upon the micro-mechanical fracture model, it was shown in [Bohse, 2000] that energy release rate of Mode-I delamination is proportional to the crack velocity times specimen width. This corresponds to the delaminated coating area per time in our case. Due to the extensive delamination observed during loading this damage mechanism will produce a considerably higher amount of AE signals than crack propa-

gation. Because of the weak adhesion between coating and CFRP-substrate most specimens investigated showed delamination in large areas. Even full-scale delamination was observed. The location of the corresponding AE sources shows a broad spatial distribution covering the whole coated area in agreement with SEM observations (see also 3.2). We, therefore, attribute AE signals belonging to cluster 2 to coating delamination.

An inspection of the recorded AE signals belonging to cluster 3 shows that they exhibit multiple reflections or originate from transient noise. Reflections and transient noise strongly influence the range of amplitude, energy and duration of AE signals. This can cause a large scattering of the values of these waveform parameters. Therefore, signals of this cluster are declared undefined and are ignored for further investigations. In fact applying the Kohonen LVQ algorithm to the different datasets resulted in either four or three distinguishable clusters as numerical optimum (see Table 2) depending on the quality of the respective dataset.

The investigation of AE signals of cluster 4 also shows a large scattering of all classical waveform parameters. In contrast to cluster 3, AE signals of cluster 4 show a characteristic frequency composition and well-defined AE sources location. All signals belonging to cluster 4 originate from fringes of the coated area, and therefore can be correlated with a failure mechanism different from cluster 1 and 2. This correlation could not be achieved using waveform parameters, but instead by investigating the AE power spectrum (see 3.4).

Table 2: Parameters for dataset partitioning using Kohonen LVQ at numerical optimum and corresponding number of clusters.

Specimen Number	R_{ij}	τ	Achieved Clusters
1	1.8454	0.72821	4
2	1.8577	0.81497	3
3	1.8621	0.94123	4
4	1.3941	0.95336	3
5	1.5313	0.91335	3

3.4 Power Spectrum Analysis

The measured power spectrum is determined by the characteristics of the AE source and the transmitting medium. Due to anisotropic dispersion, anisotropic attenuation and frequency dependent attenuation in CFRP specimens [Bohse, 2004], the frequency distribution of the AE signals is strongly dependent on its propagation path. To minimize this effect, our experimental setup ensures that the distance between AE source and sensor does not exceed 30 mm. At the same time, the used transducers provide a broad range of sensitivity. Based on these two measures we can assume that both transducers are able to detect all frequency contributions to the AE signal within the used range of 20 kHz – 1 MHz. Hence we think that the influence of propagation path length and frequency dependent dispersion and attenuation can be neglected. In the following an investigation of the averaged frequency power spectra was performed for each cluster derived from pattern recognition techniques. The respective power spectrum of each cluster averaged over all cluster members is shown in Fig. 10a for one representative dataset. In order to compare the power spectra of all clusters the intensity of the spectra was normalized to a major peak occurring at 267 kHz, which is common to all clusters. These normalized frequency power spectra are presented in Fig. 10b. Normalization procedure using the total area below the power spectrum yields the same result.

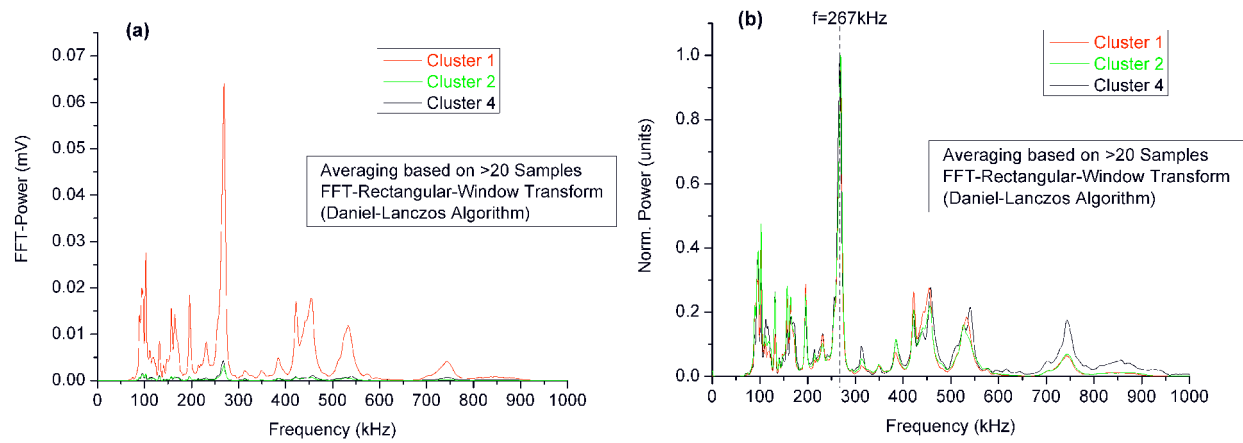


Fig. 10: Averaged power spectra for each cluster derived from pattern recognition (a) and after normalization (b).

Due to its radiation direction, cracking (in-plane direction) is expected to cause more spectral weight at higher frequencies than delamination between coating and substrate (out-of-plane direction) [Bohse, 2004]. The average power spectrum of cluster 4 shows more weight at frequencies above 500 kHz, compared to both other clusters. As already discussed in 3.3, AE signals contributing to cluster 4 are located at the fringes of the applied coating. In this area the chemically deposited nickel layer is not completely covered by copper and cracks in the nickel layer were observed in SEM imaging immediately at the onset of mechanical loading (see Figs. 2a and 2b). The fact that cracks appear immediately upon mechanical loading reflects the strain dependent evolution of AE signals contributing to cluster 4. These are also observed immediately at the onset and during mechanical loading. The fact that both sensors detected AE signals from both fringes of coating confirms our assumption that the effects of dispersion and frequency dependent attenuation are negligible in our experimental setup. Therefore we attribute cluster 4 to crack initiation and growth in the nickel-starting layer.

The power spectra of clusters 1 and 2 behave similarly for frequencies above 500 kHz, but are distinctly different for frequencies below 140 kHz. Here cluster 2 shows more spectral weight than cluster 1. This difference in the power spectra reflects the difference of the corresponding failure mechanism as already discussed in 3.3.

4. Conclusions

For metal-coated CFRP substrates investigated here, crack initiation and delamination between coating and CFRP substrate could not be inferred from signatures in stress-strain curves and, therefore, could not be predicted solely from investigations of mechanical properties. Instead, the onset of acoustic emission provides stress-dependent information about failure initiation in coatings applied to CFRP and can hence be used to determine its load limit. In addition, AE shows the ability to monitor the evolution of failure mechanisms in functional coatings as demonstrated by comparing SEM imaging and AE analysis as a function of loading. Based on RMS-values and localization of AE signals it appears to be possible to distinguish between structural failure of the CFRP substrate and coating.

An application of pattern recognition techniques to investigate the involved failure mechanisms of the coating yielded three distinct clusters of AE signals for all specimens investigated. A correlation of failure mechanisms (crack initiation, crack growth and delamination) observed in SEM investigations with AE signals could be obtained. This correlation shows good agree-

ment in location, time of origin and frequency of occurrence. AE signals corresponding to crack initiation and coating delamination are within the same range for most of the common waveform parameters. In contrast, the average power spectra calculated for each cluster were clearly distinguishable, i.e., signals from coating cracks and delamination could be distinguished.

In summary, we have shown that the combination of pattern recognition techniques and power spectrum analysis could be a powerful tool to identify failure mechanisms in hybrid materials. This suggests that AE analysis is generally applicable for health monitoring and quality assurance of hybrid materials, as shown here in case of coated CFRP structures. Therefore, further investigations will focus on the determination of quality criteria of hybrid materials, e.g., to discriminate between failure mechanisms at the interface and in the bulk, respectively.

References

- [AEwin, 2002] “*AEwin Software*”, User’s Manual, Physical Acoustics Corporation (2002).
- [Anastassopoulos, 1995] A. A. Anastassopoulos and T. P. Philippidis, “Clustering Methodology for the Evaluation of Acoustic Emission from Composites”, *Journal of Acoustic Emission*, **13**, 11–21 (1995).
- [Anastassopoulos, 2000] A. Anastassopoulos, A. Tsimogiannis and D. Kouroussis, “Unsupervised Classification of Acoustic Emission Sources from Aerial Man Lift Devices”, *World Conference on NDT -15th WCNDT*, Roma, Italy (2000).
- [Ativitavas, 2006] N. Ativitavas, T. Pothisiri and T. J. Fowler, “Identification of Fiber-reinforced Plastic Failure Mechanisms from Acoustic Emission Data using Neural Networks”, *Journal of Composite Materials*, **40** (3), 193–226 (2006).
- [Bohse, 2000] J. Bohse, J. Chen and A. Brunner, “Acoustic Emission Analysis And Micro-Mechanical Interpretation of Mode I Fracture Toughness Tests On Composite Materials”, *Fracture of Polymers and Composites and Adhesives*, ESIS publication 27, pp. 15–26 (2000).
- [Bohse, 2001] J. Bohse and J. Chen, “Acoustic Emission Examination Of Mode I, Mode II and Mixed-Mode I/II Interlaminar Fracture Of Unidirectional Fiber-Reinforced Polymers”, *Journal of Acoustic Emission*, **19**, 01–10 (2001).
- [Bohse, 2004] J. Bohse. “Acoustic Emission Examination Of Polymer-Matrix Composites”, *Journal of Acoustic Emission*, **22**, 208–223 (2004).
- [Ceysson, 1995] O. Ceysson, M. Salvia and L. Vincent, “Damage Mechanisms Characterisation Of Carbon Fibre/Epoxy Composite Laminates By Both Electrical Resistance Measurements And Acoustic Emission Analysis”, *Scripta Materialia*, **34**, 1273–1280 (1996).
- [deGroot, 1995] P. deGroot, P. Wijnen and R. Janssen. “Real-Time Frequency Determination Of Acoustic Emission For different Fracture Mechanisms In Carbon/Epoxy Composites”, *Composites Science and Technology*, **55**, 405–412 (1995).
- [DIN14125] DIN-EN-ISO 14125, “*Bestimmung der Biegeeigenschaften*“ (1998).

- [Fu, 2000] L. Fu, K. Khor, H. Ng and T. Teo, “Non-destructive evaluation of plasma sprayed functionally graded thermal barrier coatings”, *Surface and Coatings Technology*, **130**, 233–239 (2000).
- [Komai, 1991] K. Komai, K. Minoshima and T. Shibutani, “*Investigations of the Fracture Mechanism of Carbon/Epoxy Composites by AE Signal Analyses*”, *JSME International Journal*, **34**, 381–388 (1991).
- [Lee, 2005] J. Lee, Y. Kim and H. Kim, “Group Velocity of Lamb Wave S_0 Mode in Laminated Unidirectional CFRP Plates”, *Key Engineering Materials*, **297-300**, 2213–2218 (2005).
- [Lin, 1997] C. Lin, S. Leigh and C. Berndt, “Acoustic emission responses of plasma-sprayed alumina-3% deposits”. *Thin Solid Films*, **310**, 108–114 (1997).
- [Ma, 2001] X. Q. Ma, H. Cho and M. Takemoto, “Acoustic emission source analysis of plasma sprayed thermal barrier coatings during four-point bend tests”, *Surface and Coatings Technology*, **139**, 55–62 (2001).
- [Miguel, 2003] J. Miguel, J. Guilemany, B. Mellor and Y. Xu, “*Acoustic emission study on WC/Co thermal sprayed coatings*”, *Materials Science and Engineering A*, Vol. 352, pp. 55–63 (2003).
- [Ni, 2007] Q. Q. Ni and E. Jinen. “Fracture Behavior And Acoustic Emission In Bending Tests On Single-Fiber Composites”, *Engineering Fracture Mechanics*, **56**, 779–796 (1997).
- [Nikulin, 2005] S. Nikulin, V. Khanzhin, A. Rozhnov, A. Babukin and V. Belov, “Analysis Of Crack Resistance And Quality Of Thin Coatings By Acoustic Emission”, *Proc. The 8th International Conference of the Slovenian Society for Non-Destructive Testing*, Portoroz, Slovenia (2005).
- [Noesis, 2006] “*NOESIS Advanced Acoustic Emission Data Analysis and Pattern Recognition & Neural Networks Software for Acoustic Emission Applications*”, User’s Manual, Enviroacoustics S.E. (2006).
- [Philippidis, 1998] T. Philippidis, V. Nikolaidis and A. Anastassopoulos, “Damage Characterisation of C/C laminates using Neural Network Techniques on AE signals”, *NDT&E International*, **31**, 329–340 (1998).
- [Sato, 1986] N. Sato, T. Kurauchi and O. Kamigaito, “Fracture mechanism of unidirectional carbon-fibre reinforced epoxy resin composite”, *Journal of Material Science*, **21**, 1005–1010 (1986).
- [Schultheiß, 2007] D. Schultheiß, “*Permeation Barrier for Lightweight Liquid Hydrogen Tanks*”, PhD-thesis, University of Augsburg (2007).
- [StorHy, 2007] “*StorHy - Hydrogen Storage Systems for Automotive Application*”, 3rd Periodic Activity Report (2007).

ACOUSTIC EMISSIONS RELATED TO THE DEHYDRATION STRESS BEHAVIOR OF GREEN NORWAY SPRUCE WOOD

SABINE ROSNER¹, BO KARLSSON², JOHANNES KONNERTH³
and CHRISTIAN HANSMANN⁴

¹ Institute of Botany, Department of Integrative Biology, University of Natural Resources and Applied Life Sciences, BOKU Vienna, Gregor Mendel-Str. 33, A-1180 Vienna, Austria; ² The Forestry Research Institute of Sweden (Skogforsk), Ekebo, S-26890 Svalöv, Sweden; ³ Institute of Wood Science and Technology, Department of Material Sciences and Process Engineering, University of Natural Resources and Applied Life Sciences, BOKU Vienna, Peter Jordanstr. 82, A-1180 Vienna, Austria; ⁴ Competence Centre for Wood Composites and Wood Chemistry, St.-Peter-Str. 25, A-4021 Linz, Austria

Keywords: AE feature extraction, vulnerability to cavitation, wood shrinkage

Abstract

Waveform features of acoustic emission (AE) signals emitted from cavitation events in water-conducting elements of dehydrating wood bear a lot of information about both wood structure and the behavior under dehydration stress. We present two applications of AE feature extraction on wood; first, the prognosis of the survival prospects of trees under drought stress by constructing vulnerability curves and second, monitoring of the shrinkage behavior during lumber drying. AE testing was performed with resonant 150 kHz transducers on Norway spruce wood with different structural characteristics. Radial wood shrinkage was calculated from changes in the contact pressure between the AE transducer and the wood specimen. The reference method to assess the vulnerability to cavitation was the hydraulic method, where vulnerability curves were constructed by plotting the percent loss of conductivity vs. an overpressure of compressed air. Vulnerability curves were also constructed by relating the cumulated amount of AE energy to the applied overpressure. Samples with smaller conduit diameters showed lower mean AE energies and were less sensitive to cavitation and thus to drought stress. Two shrinkage processes can be observed during wood dehydration; the initial process, induced by tensile stresses, and the final shrinkage process, which started when most of the tracheids reach relative water contents below the fiber saturation point. Wood less sensitive to cavitation showed lower shrinkage and mean AE energy /min but higher total AE activity than wood with higher sensitivity to cavitation. The negative relationship between maximum AE energy and total AE activity and the positive relationship between maximum AE energy and radial lumen diameters reveals that more elastic energy is stored in bigger conduits when under tension. AE testing in combination with feature extraction offers an interesting alternative to the labor-intensive conventional methods to assess the vulnerability to cavitation and can be used to monitor the shrinkage behavior and crack development during lumber drying.

Introduction

Waveform features of AE signals from dehydrating wood bear a lot of information about both wood structure and the behavior of wood under dehydration stress. We present two applications of AE feature extraction on wood; first, a method to assess the vulnerability to cavitation of trunk wood and second, the monitoring of the wood structure-dependent shrinkage behavior during lumber drying processes.

Norway spruce wood consists to 90% of small water-conducting elements with a diameter of about 10-40 μm and a length of 1-4 mm (tracheids, Fig. 1). One annual ring, which consists of earlywood and latewood tracheids, is formed every year. Water in tracheids exists in three states, (1) as “free” liquid water, (2) as water vapor and within the tracheids, and (3) as chemically “bound” water in the cell wall matrix [1]. Water transport from the roots to the crown is achieved under tension, requiring high mechanical strength of the cell walls in order to avoid implosion, and hydraulic safety against the breakage of the water column in the conducting elements (cavitation). Cavitation is induced when the water tension increases above a certain threshold. Once cavitated, the conduit does not conduct water any longer and the hydraulic conductivity of the plant is reduced, leading to impairment of water supply of the transpiring needles [2]. Hydraulic safety depends on wood structure and can be assessed by the construction of vulnerability curves. A vulnerability curve is a plot of the percent loss in hydraulic conductivity (PLC) vs. the pressure potential in the solution of the tracheids. The most widely used drought-stress parameter is the pressure potential that causes 50% PLC. The common approach to quantify 50% PLC is to relate actual hydraulic conductivity to the hydraulic conductivity at full saturation (hydraulic method). The hydraulic method is very time consuming and demands practical experience. A more direct way to detect cavitation events is to record AE in the high-frequency range of 50 kHz to 1 MHz [3]. AE with the strongest frequencies in the range of 100-300 kHz are supposed to be induced by rapid tension release in the tracheid lumen as liquid water at negative pressure is replaced by water vapor very near vacuum pressure.

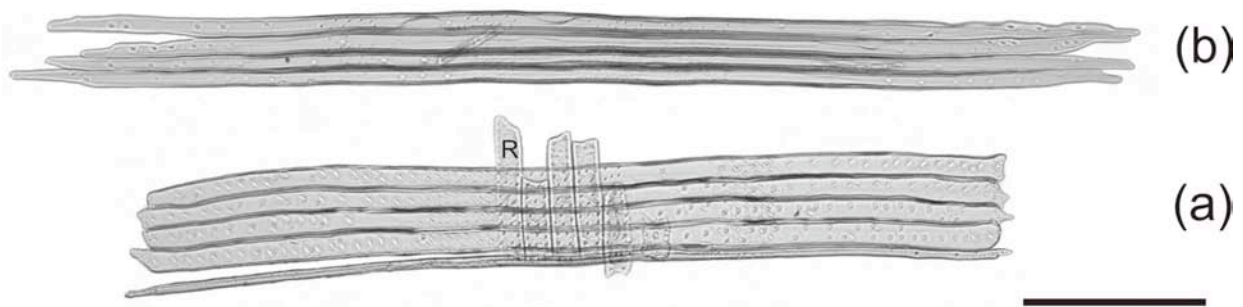


Fig. 1 (a) Macerated Norway spruce tracheids of the last latewood cell row (below) and the adjacent first earlywood cell rows formed in the following growing season and (b) tracheids of the earlywood formed later in the growing season. “R” marks a ray cell, which achieve the radial transport in wood. The reference bar represents 200 μm .

During periods of drought stress, decreases in the stem diameter of living trees can be observed [4]. This tensile strain is a consequence of adhesive forces between the water molecules and the inner conduit walls when “free” water in the tracheids comes under tension [5]. It has been hypothesized by many authors that the elastic behavior induced by water tension is strongly related to the elastic properties of the swelling tissues [5, 6] and thus to wood structure. When the moisture content of the tracheids drops below the fiber saturation point (FSP), that is when lumina contain no “free” water but cell walls are fully saturated with liquid, further dehydration leads to cell wall shrinkage processes. Checking during lumber drying occurs because wood is an anisotropic material concerning cell-wall shrinkage (radial:tangential = 1:2) and the FSP is reached far earlier in the shell than in the core of a specimen. Some authors suggest, however, that internal checks can even be induced by water tension because checking occurs long before most of the cells reach the FSP [e.g., 7]. AE testing is an established method for optimizing lumber drying conditions, where the analysis of the amplitude or energy distribution of AE signals

has been successfully used to pinpoint checking [8, 9]. Combined shrinkage- and AE tests are, however, scarce in AE literature on wood [10] and on live stems such investigation are performed at moisture contents well above the FSP [4]. Lumber shrinkage assessment starts either at moisture contents around the FSP or at “green” moisture content [11], defined as the moisture content at the time of harvesting [1]. “Green” moisture content will not correspond to the moisture content at 100% saturation when trees suffered at the time of harvesting from drought stress or when water was lost by evaporation during harvesting, transport or storage. In the present study we relate AE of dehydrating Norway spruce (*Picea abies* (L.) Karst.) sapwood with different structural characteristics to radial wood shrinkage processes from the totally saturated state till the end of all shrinkage processes.

Hydraulic Method to Assess the Vulnerability to Cavitation

Vulnerability curves were obtained on fully saturated juvenile (age = 1-2 years) and mature (age = 17-19) Norway spruce (*Picea abies* [L. Karst.]) wood beams (0.6 cm tangential, 0.6 cm radial, 10.0 cm longitudinal). After determination of the conductivity at full saturation, a positive pressure was applied to the lateral sides of the samples, while the transverse ends protruded from a double-ended pressure chamber (PMS Instruments Co., Corvallis, OR), to induce cavitation. After pressure treatment samples were weighed and hydraulic conductivity was measured again. The continuous pressure treatment leads to a decrease in hydraulic conductivity. Initially, the pressure chamber was pressurized to 0.5 MPa, and the pressure was subsequently increased after each conductivity measurement in steps of 0.5 MPa till more than 95% loss of conductivity was reached. The whole measuring procedure is described in [12]. Dry weight of the wood beams was obtained by drying wood samples at 103°C to constant weight in order to calculate the relative water loss (RWL). The pressure application was related to RWL by cubic functions [12].

AE Testing Procedure and Data Analysis

AE testing was performed with the μ DiSP™ Digital AE system from Physical Acoustics Corporation (PAC, Princeton Jct, USA). Preamplifiers (40 dB) were used in connection with R15 resonant transducers (50 to 200 kHz). AE signals were recorded with a detection threshold of 30 dB (0 dB = 1 μ V input). Extraction of AE energy (pVs) was carried out with AEWin® software (PAC). AE energy (also referred to as “PAC-Energy”) is defined as the area of the rectified voltage signal over the duration of the AE signal.

AE transducers were positioned on the tangential face of the wood beams using an acrylic resin clamp. The whole measuring procedure, where coupling pressure during the dehydration process was recorded with a DMS load cell (Type 8416-5500, range 0 - 500 N; amplification with an inline amplifier for DMS, Type 9235; Burster, Gernsbach, Germany) and water loss was measured with a balance, is described in [12]. Percent radial shrinkage (given in negative values) was calculated for 10 min time steps by relating the total radial shrinkage (digital gauge, accuracy 1 μ m) to the total coupling pressure decrease. Percent radial shrinkage was referred to the nearest 5% RWL step.

AE data filtering was done with Vallen VisualAET™ software (Vallen Systeme GmbH, Munich, Germany). Mean AE energy values were calculated for 1 minute and 10 minute time steps. Relative cumulated AE energy data were obtained by relating the stepwise cumulated mean AE energy values/10 minutes to the sum of all mean AE energy values/10 minutes. AE data were

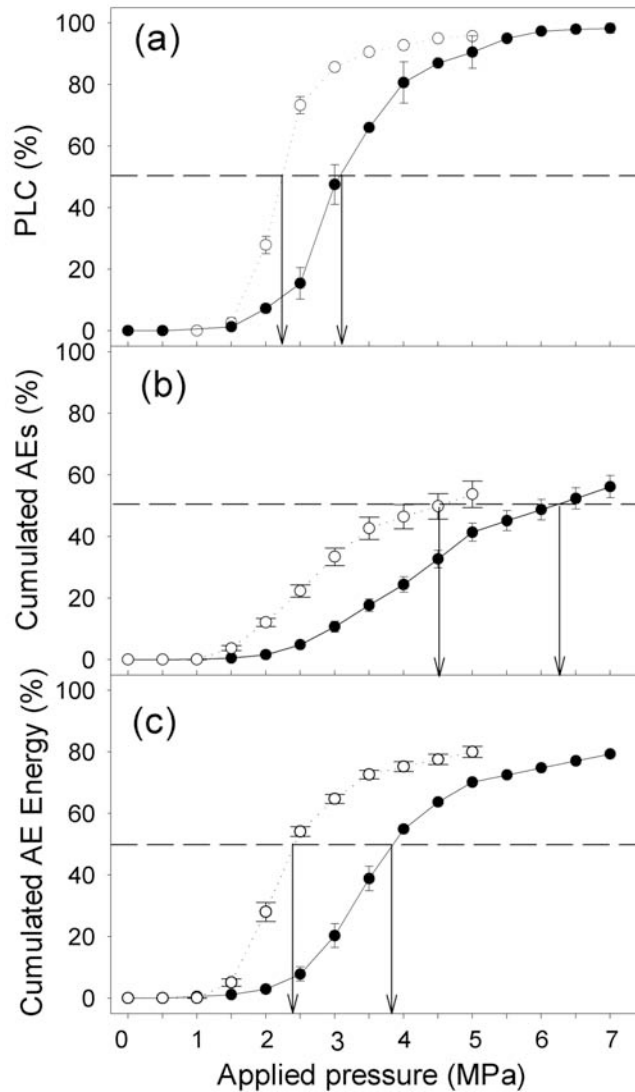


Fig. 2. (a) Percent loss of hydraulic conductivity (PLC), (b) cumulated AE signals and (c) cumulated AE energy/10 min plotted against positive pressure. Open symbols represent mature wood ($n = 12$), closed circles juvenile wood ($n = 6$).

referred to the nearest 5% RWL and thereafter to 0.5 MPa steps in order to construct vulnerability curves. Values are given as mean values \pm standard error. Differences between mean values were tested for significance by Student's *t*-test. Associations between two variables were examined using linear or quadratic regression analysis.

Anatomical investigations

Tangential double wall thickness of adjacent tracheids and lumen diameters were measured by means of a Leica DM4000M microscope interfaced with a digital camera and Leica image analysis software (Leica Microsystems Wetzlar GmbH, Germany). Tracheid dimensions of the first formed cell rows (earlywood) were measured on microtomed transverse cut faces of juvenile and mature Norway spruce wood (Fig. 5). Mean values of anatomical parameters were derived from 40 single measurements per standard beam, respectively.

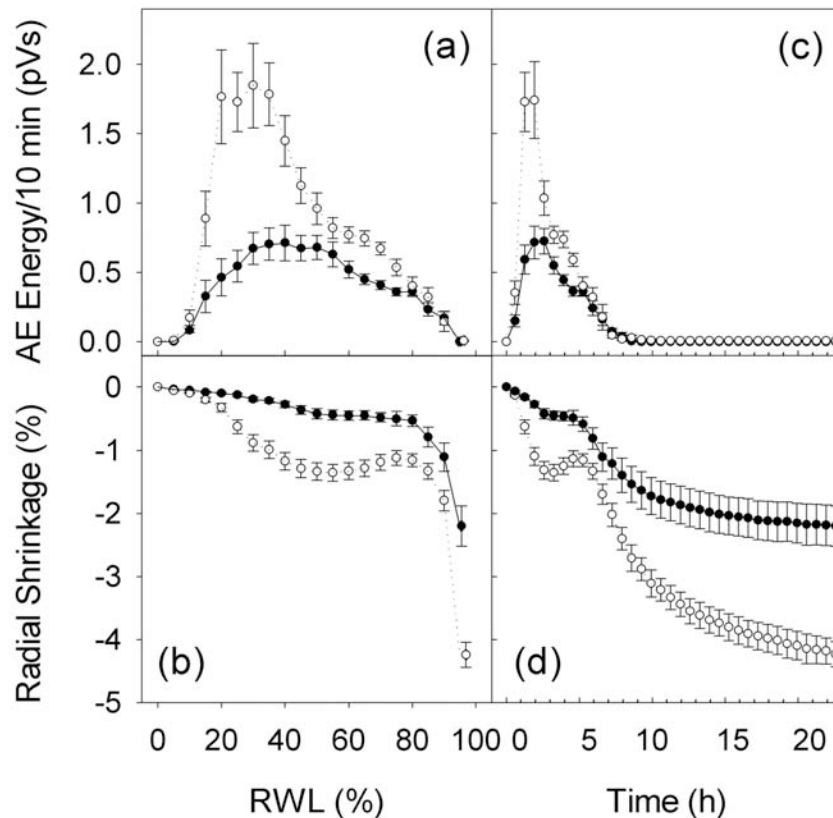


Fig. 3. (a) Changes of the mean AE energy/10 min and (b) radial shrinkage against relative water loss (RWL). (c) and (d): same AE energy and radial shrinkage against time. Open circles represent mature wood, closed circles juvenile wood ($n = 12$, respectively).

Results and Discussion

Assessment of vulnerability to cavitation

Juvenile wood had a lower vulnerability to cavitation than mature wood: For juvenile wood from the tree top much more pressure was necessary to result in 50% loss of conductivity (PLC) than for mature wood from the tree base ($3.20 \pm 0.16\%$, 2.26 ± 0.04 MPa, respectively, $P < 0.001$, Fig. 2a). The cumulated number of AE signals was not a good predictive for the PLC, because 50% cumulated AE signals were reached at much higher pressures (Fig. 2b). 50% of the cumulated AE energy was induced at 3.73 ± 0.11 MPa in juvenile and at 2.31 ± 0.05 MPa in mature wood ($P < 0.001$, Fig. 2c). We assume that the cumulated AE energy is a more reliable measure for PLC than the AE number *per se*, because the hydraulic conductivity is proportional to the 4th power of the radius of a capillary (Hagen-Poiseuille equation) and tracheid diameters are variable within a wood specimen. High mean AE energies detected at moderate water losses or pressures resemble cavitation events of more vulnerable large diameter tracheids [12].

Relationship between shrinkage processes and AE

The AE and radial shrinkage data are given in Fig. 3. Two different radial shrinkage processes were observed (Fig. 3d). First is a shrinkage period at moderate water losses, which was termed “tension shrinkage”, and second is the cell-wall shrinkage period. Prior to cavitation, dehydration stress generates tensile strains inside the most vulnerable tracheids and in tracheids near the specimen surface. Tension shrinkage started therefore right from the beginning of dehydration, before any AE signals were detected (Figs. 3a-b) and ceased in mature wood at

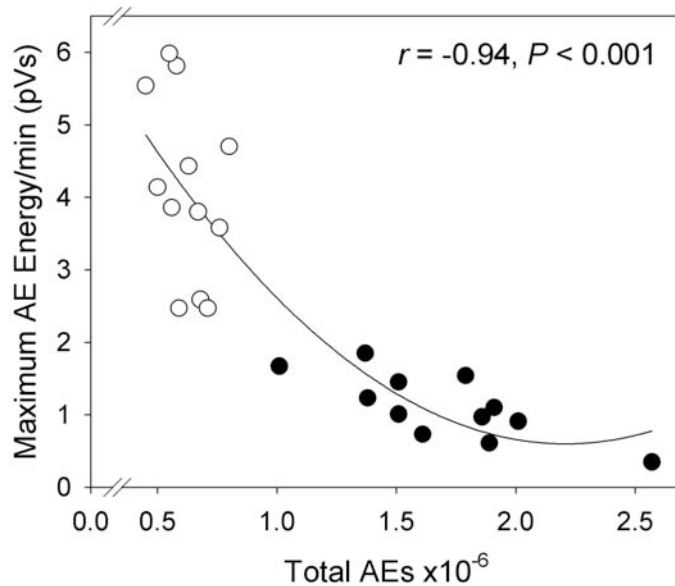


Fig. 4. Maximum mean AE energy/min related to the number of AE signals by a quadratic regression model. Open symbols represent mature wood, closed circles juvenile wood beams (6 mm x 6 mm x 100 mm).

53.99 ± 1.91% RWL and in juvenile wood at 58.94 ± 2.48% RWL. Maximum tension shrinkage was more than three times higher in mature than in juvenile wood ($-1.44 \pm 0.11\%$, $-0.42 \pm 0.01\%$, respectively, $P < 0.001$). Maximum AE energies were detected at moderate water losses, when already more than 50% of the tension shrinkage had taken place (Figs. 3a-b). Tension shrinkage ceased when mean AE energies reached constantly lower values, and was even reversible to some extent (Figs. 3c-d). Recovery from shrinkage induced by cavitation seems to occur also in live stems [4], where it can either occur as a result of cavitation, or because of a decrease in crown transpiration. In debarked sapwood specimens, shrinkage can only be reversed by a local tension stress release after cavitation, when water is pulled out of the conduit into the surrounding wood. Recovery from tension shrinkage due to cavitation occurred at higher relative water losses than one would expect, being probably masked by continuous shrinkage in wood parts, which still contained “free” water. Shrinkage and regeneration from shrinkage should therefore occur at different locations at the same time in the numerous tracheids within a standard size wood specimen, which might be the reason why there is almost no time lag between periods of stem diameter decrease and increases in cumulated AE [4].

During late dehydration stages, the reversibility of tension shrinkage was additionally overlaid by cell-wall shrinkage [10]. The fiber saturation point (FSP) refers to the moisture content of a conduit and not to a whole piece of wood and it should be therefore not the same throughout a whole wood specimen [1]. During late dehydration stages, when the drier shell of the specimen had already reached moisture contents below the FSP, cell wall contraction could therefore additionally mask recovery from tension. The partial reversibility of tension shrinkage indicates however that the first shrinkage process at moderate water losses in standard size wood specimens was not entirely induced by cell wall shrinkage of the shell at water contents below the fiber saturation point but by tensile stresses due to water tension.

The final shrinkage process started after the shrinkage recovery peak, at about 80% RWL, corresponding to moisture contents given for the FSP of spruce species 35 – 37% [13]. Mature

wood showed higher total shrinkage than juvenile wood ($-3.86 \pm 0.13\%$, $-2.31 \pm 0.23\%$, respectively, $P < 0.001$, Fig. 3d). AE ceased when only 50% of shrinkage had taken place, giving strong evidence that no crack formation occurred at moisture contents below the FSP [7].

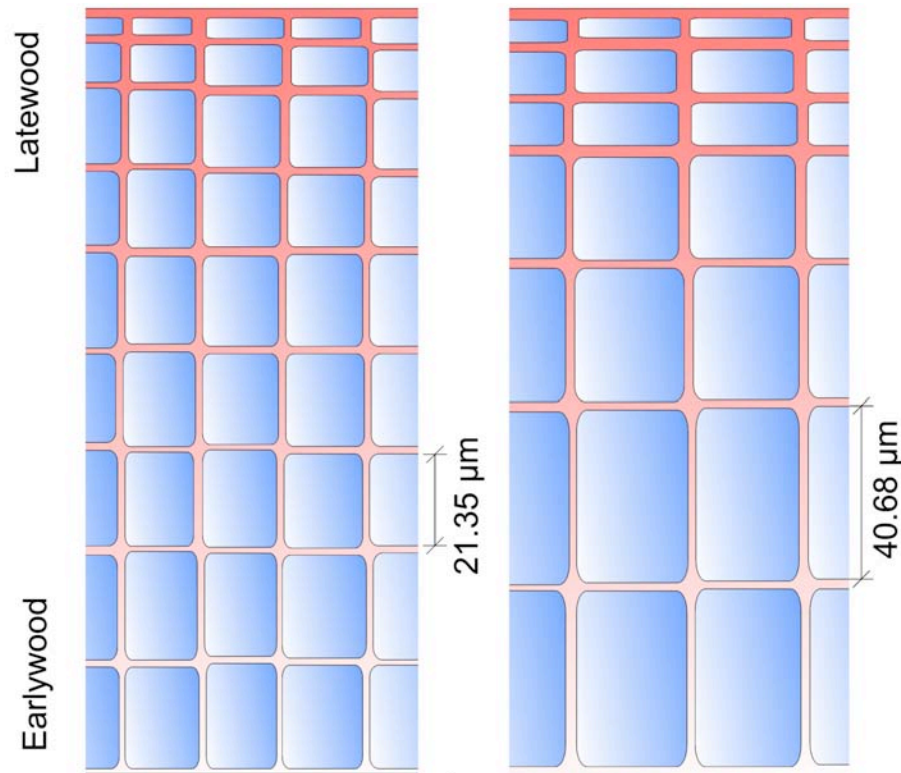


Fig. 5. Simplified model of the transverse view of one annual ring of juvenile (left side) and mature Norway spruce wood (right side). Each annual ring consists of earlywood and latewood. Juvenile wood has smaller radial and tangential lumen diameters and thinner double cell walls than mature spruce wood.

Juvenile wood beams emitted significantly more AE (numbers in 10^6 counts) than mature wood beams (1.70 ± 0.11 , 0.62 ± 0.03 , $P < 0.001$) and maximum AE energy/min was lower in juvenile than in mature wood beams (1.17 ± 0.12 pVs, 4.21 ± 0.32 pVs, $P < 0.001$). The maximum AE energy/min was strongly related to the total number of AEs (Fig. 4), total shrinkage ($r = -0.80$, $P < 0.001$) and maximum tension shrinkage ($r = -0.88$, $P < 0.001$). The total number of AE signals was higher in samples with lower total shrinkage ($r = 0.80$, $P < 0.001$) and tension shrinkage ($r = 0.83$, $P < 0.001$). The higher total number of AE signals and lower mean AE energies measured in juvenile than in mature wood indicate that lower vulnerability to cavitation was associated with a higher number of tracheids/volume with smaller lumen diameters [12]. Anatomical investigations showed that juvenile wood had significantly thinner double cell walls ($3.34 \pm 0.06 \mu\text{m}$, $4.41 \pm 0.11 \mu\text{m}$, $P < 0.001$) and radial lumen dimensions ($21.35 \pm 0.60 \mu\text{m}$, $39.68 \pm 1.57 \mu\text{m}$, $P < 0.001$) than mature wood (Fig. 5). The maximum AE energy/min increased therefore linearly with the radial lumen diameters (Fig. 6).

Norway spruce trees mainly vary cell size to optimize water transport and mechanical stability whereas modification of the cell wall organization plays a minor role [14]. Mature wood, which was more vulnerable to cavitation showed higher tension shrinkage and total shrinkage (Fig. 3d). Mature wood was thus more prone to deformation due to the same tension than

juvenile wood, indicating that the latter seems to be designed to resist implosion under high tension. High hydraulic vulnerability seems to be related to high AE energy signals, but what is the reason for this relationship? Hydraulically less vulnerable juvenile wood showed much lower radial lumen diameters than mature wood. Wall thickness increases as well with tree ring age, however to a much lower extent than the lumen diameters. The reinforcement against collapse from bending due to tension forces increases when the thickness of the double cell wall increases relatively to its span [15]. Juvenile wood showed thus a higher wall/lumen ratio than mature wood, which results in lower susceptibility to elastic deformation due to the same tension stress. Therefore, more elastic energy is stored in bigger tracheids when under the same tension. This energy is suddenly released when the water column breaks and liquid water at negative pressure is replaced by water vapor very near vacuum pressure and later by air. Conduits, which show higher deformation under tensile stress, will therefore release AE signals with higher energy when the cell wall relaxes due to cavitation. AE signals from more hydraulically vulnerable mature wood are therefore characterized by higher mean AE energies than those from less hydraulically vulnerable juvenile wood (Fig. 6).

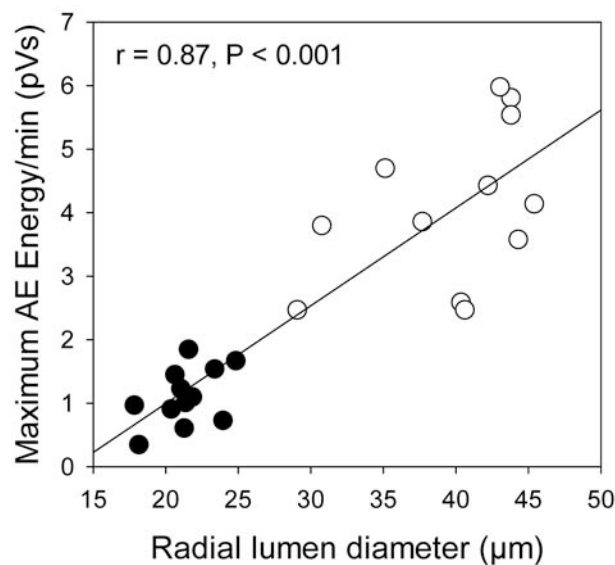


Fig. 6. Radial lumen diameter related to maximum mean AE energy/min by a linear regression model. Open symbols represent mature wood, closed circles juvenile wood beams (6 mm x 6 mm x 100 mm).

Conclusion

Analysis of the spectrum features of AE signals during wood dehydration offered an interesting alternative to the hydraulic method for assessing the hydraulic vulnerability of spruce trunkwood. Vulnerability curves were constructed by relating the relative cumulated amount of AE energy during dehydration of standard beams under defined conditions to the xylem tension. Xylem tension of the dehydrating specimens was calculated with a parallel sample set, where air overpressures were related to the relative moisture loss by cubic functions. The xylem tension corresponding to 50% of the cumulated AE energy can be a useful parameter to quantify hydraulic vulnerability. The major advantage of the AE method presented is that it is readily automated and easier in handling compared to the labor-intensive hydraulic method.

Combined AE and shrinkage testing gave strong evidence that the relationship between changes in xylem tension and tensile strains measured at the surface of a tree trunk are strongly dependent on wood structure. Diurnal stem-diameter changes caused by tensile strain are used to pinpoint periods of drought stress in trees. Our results underline that the relationship between water potential and tensile strain is not constant, but requires time-consuming calibrations for each single tree if different trees should be compared [15]. Another source of error, which might underestimate actual drought stress, is that tension shrinkage is not only reversible due to an increase in water potential and refilling of cavitated water conducting elements in the night, but also due to tension release by cavitation. Combined AE and shrinkage testing could be also a useful tool to monitor the shrinkage behavior leading to crack development during industrial lumber drying.

Acknowledgements

This study was financed by the Austrian Science Fund FWF (Project T304-B16).

References

1. C. Skaar, *Wood-Water Relations*, Springer-Verlag, 1988, 283 p.
2. M.H. Zimmermann, *Xylem structure and the ascent of sap*, Springer-Verlag, 1983, 143 p.
3. M.T. Tyree, J.S. Sperry, *Plant, Cell and Environment* **12**, 1989, 371-382.
4. T. Hölttä, T. Vesala, E. Nikinmaa, M. Perämäki, E. Siivola, M. Mencuccini, *Tree Physiology* **25**, 2005, 237-243.
5. T.T. Kozlowski. Shrinking and Swelling of Plant Tissues. In: T.T. Kozlowski, ed. *Water deficits and plant growth. Vol. III, Plant Responses and Control of Water Balance*, Academic Press, 1972, 1-64.
6. J. Irvine, J. Grace, *Planta* **202**, 1997, 455-461.
7. R.E. Booker, *Proceedings of the 4th IUFRO Wood Drying Conference: Improving Wood Drying Technology*, 1994, pp. 133-140.
8. F.C. Beall, *Wood Science and Technology* **36**, 2002, 197-212.
9. S. Kawamoto, R.S. Williams, *Acoustic emission and acousto-ultrasonic techniques for wood and wood-based composites A Review*, U.S. Department of Agriculture, Forest Service, Forest Products Laboratory, Gen. Techn. Rep. FPL-GTR-134, 2002, 16 p.
10. S. Rosner, *Journal of Acoustic Emission* **25**, 2007, 149-156.
11. H. Sakagami, J. Matsumura, K. Oda, *IAWA Journal* **28**, 2007, 29-37.
12. S. Rosner, A. Klein, R. Wimmer, B. Karlsson, *New Phytologist* **171**, 2006, 105-116.
13. A. Bernhart, *Forstwirtschaftliches Zentralblatt* **84**, 1965, 347-356.
14. M. Eder, K. Jungnikl, I. Burgert, *Trees* **23**, 2009: 79-84.
15. U.G. Hacke, J.S. Sperry, W.T. Pockman, S.D. Davis, K. McCulloh, *Oecologia* **126**, 2001, 457-461.
16. T. Alméras, J. Gril, *Tree Physiology* **27**, 2007, 1505-1516.

INVESTIGATION OF THE Z-DIRECTION STRENGTH PROPERTIES OF PAPER BY USE OF ACOUSTIC EMISSION MONITORING

S. NORGRÉN, P. A. GRADIN, S. NYSTRÖM and M. GULLIKSON

Mid Sweden University, FSCN, SE-851 70 Sundsvall, Sweden

Keywords: Z-test, Z-direction strength, cohesive zone, fiber/fiber bonds

Abstract

In the quality assessment of paper, a standard test referred to as the Z-test is often utilised. It consists in gluing a piece of paper between two circular metallic grips and loading it with a tensile load in the thickness direction of the paper. The fracture load or rather the maximum load the paper specimen can withstand is then taken as a measure of the Z-direction strength of the paper tested. The interpretation of the results and how to use the results has been and still is a question of some controversy. To shed some light over the deformation or damage processes active when a paper is loaded in the thickness direction, specially designed grips were developed and manufactured. The grips are designed in such a way that they admit that acoustic emission (AE) sensors are mounted in the grips.

In this paper, the method is presented together with a simple analytical model, relevant for the Z-test. Also, some experimental results are given and it is concluded that the analytical model can, at least in a qualitative way, predict not only the load versus displacement behaviour but also the total number of AE events versus displacement relation.

Introduction

In the papermaking society, there exist a number of testing methods, the results from which are believed to say something about the quality of the paper. In for instance a situation where the paper is to be printed on, or when the paper is coated with some coating color, it might happen that the paper delaminates due to that coating color or printing ink sticks simultaneously to the paper and a roller in a roller nip, causing out of plane loading of the paper. One testing method, which is believed to give a measure of the sensitivity to delamination is the Z-strength test [1]. In essence, the test consists in that a quadratic paper specimen is glued in between two grips with a circular cross section (with a diameter less than the side length of the paper specimen) and loaded in the thickness direction. The maximum force divided by the grip area is defined as the Z-strength. This test is not free from criticism since it is obvious that the stress field in the paper specimen is far from being homogenous and for instance, the stresses in the thickness direction will take on comparatively large values in a region close to the circular boundary of the grips. Since paper is not a homogeneous material, the paper will start to degrade in some weak point, affected by the high stresses. After a while, the damage will have reached such a level that a real crack initiates and starts to grow across the grip area. The maximum load and the start of crack growth probably coincide. Since there are local conditions that are responsible for the fracture of the specimen, it is questionable to define an average measure of the strength. To gain some further insight into the delamination process, it would be of particular interest to be able to determine at which load the damage growth starts to initiate and also to study how the damage progresses up to the point and after, where a crack is formed. Therefore, in an attempt to extract more information from a traditional Z-strength test, acoustic emission (AE) monitoring was used to record the elastic stress waves, emitted due to the breaking of fiber/fiber bonds.

AE Monitoring

When some internal event happens fast enough in a structure, the emitted elastic stress wave can be recorded (provided the amplitude is high enough) by e.g. a piezoelectric resonance frequency sensor. One example of such an internal event can be the breaking of a fiber/fiber bond and in fact, AE monitoring has been used on paper before (c.f. [2-5]) but then only in connection with ordinary tensile tests. To use AE in a Z-strength test is not as simple since the AE sensors cannot be attached directly to the paper specimen. To this end, the grips used in the Z-strength test were modified so that one AE sensor could be attached to each of the two grips. This is of course not ideal, since there is a metallic layer between the sensor and the paper specimen and hence there is a possibility of wave reflection at the paper – grip interface due to acoustic impedance mismatch. In spite of this, it was possible to detect signals from the loaded paper specimen even though the number of events recorded might not be entirely representative for the true number of broken fiber/fiber bonds.

Experimental

In the experiments, the AE – unit: Vallen Systeme AMSY 4 was used together with the sensors: Vallen Systeme AMSY 4 PROTO 410 and the preamplifiers: Vallen Systeme AEP 4H- 10k with an amplification of 34 dB. A threshold value of 40 dB was used in all tests.

A paper sample was first covered with a double side tape on both sides. The paper sample was attached to the first sample holder as seen in Fig. 1a. The second upper sample holder must be placed precisely over the first sample holder. A position fixture was used to attain that. The second sample holder was put on the paper sample as seen in Fig. 1b. The sample holders are made of steel and have a radius of 17.5 mm. The sample holders are sliced out so the AE sensors can be placed as close to the paper surfaces as possible. The thickness of the steel layer was about 2 mm at that position.

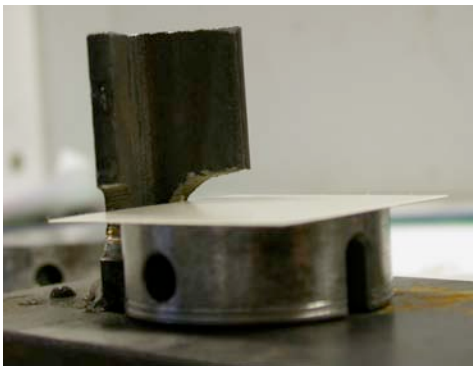


Fig. 1a: Sample holder with a paper sample in position.



Fig. 1b: The upper grip aligned in position over the lower grip.

The paper sample was compressed with a pressure that during testing forces the paper to delaminate in a “perfect breakage”, i.e., the paper divides into two halves when the MTS machine pulls the sample holders apart and the whole fracture surface are within the paper structure. Pressure levels between 3 to 7 MPa were applied in the L&W sheet press (see Fig. 2a) to receive clean breakage. As it was of interest to detect the real elongation in Z- direction an extensometer (MTS model 632, 110-210) was attached to the sample holder by rubber bands as shown in Fig. 2b.



Fig. 2a: Paper sample in holder placed in a L&W sheet press.



Fig. 2b: A MTS extensometer attached to the sample holder.



Fig. 3a: View of one of the AE sensors used in the experiments.

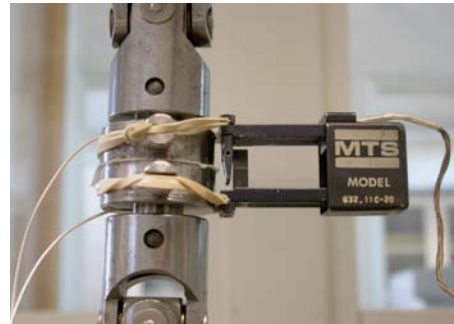


Fig. 3b: Sample holder with extensometer and AE sensor attached in position to measurement between moment free hinges in the MTS machine.

Figure 3a shows an AE sensor of model PROTO 410. This sensor is specially designed with magnetic capability so it can be attached to steel surfaces. Two sensors were used, one in the upper and one in the lower sample holder. The last step before pulling in Z-direction is to fasten sample holders between two moment free hinges, which are in turn attached to the MTS machine. This is done simultaneously with the placement of the AE sensors. The setup is shown in Fig. 3b. The pulling speed is 0.1 mm/min.



Fig. 4a: An unwanted type of fracture. The sample breaks not only in the paper layer but also between the paper and the tape.



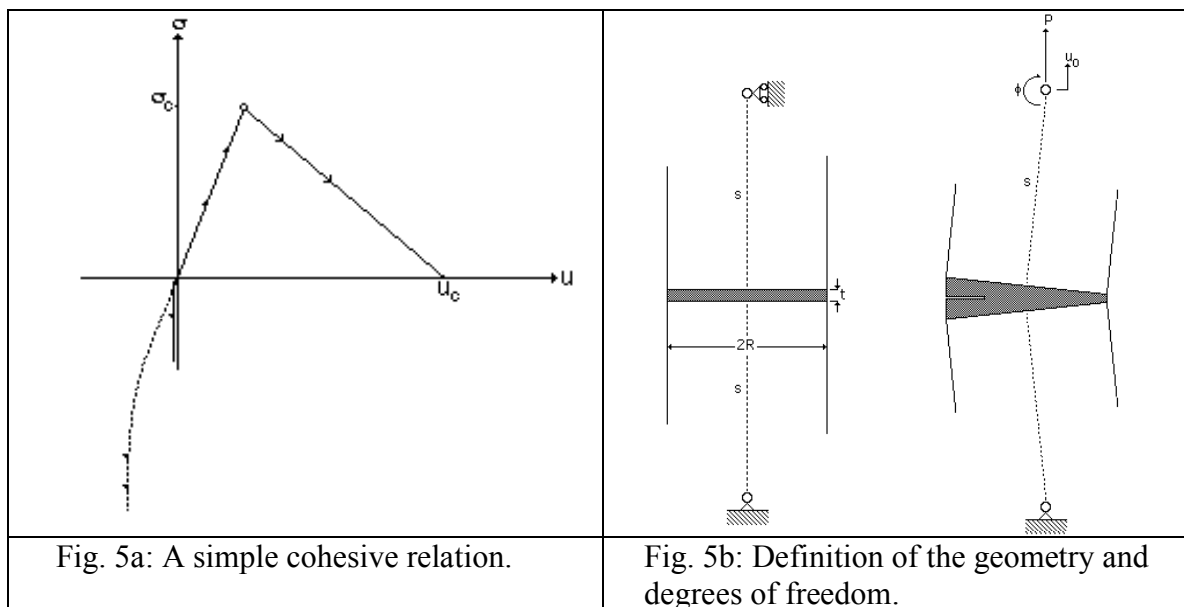
Fig. 4b: Perfectly delaminated samples collected after testing.

As seen in Fig. 4a, a test can go wrong. Here, the paper partly breaks in the middle, which it should (to the right in the picture), but also shows an unwanted incident. Half the paper has come loose from the metal surface (left in the picture). This leads to an irrelevant maximum load at breakage and also incorrect breaking AE events are recorded. Such results are rejected. At least 8 correct samples (Fig. 3b) from each paper sample have been tested to reach relevant data at acceptably low standard deviation.

The paper qualities considered were: Light weight coated (LWC) paper with sw of 60 g/m² and paper board with sw of 281 g/m²

Cohesive Zone Model

In order to connect the AE output to the state of the paper specimen, a simple analytical model will be employed. During the tests, it was observed that a crack in the paper initiated in a point on the boundary and propagated over the cross section of the paper sample. For simplicity the crack front is assumed to be straight and further on, the stress state in the sample is assumed to be uniaxial and described by a simple cohesive relation according to Fig. 5.



In Fig. 5a, σ denotes stress and u displacement in the thickness direction of the paper sample. On the compression side the material can be assumed to behave according to the dotted line since the grips are very stiff. For simplicity, the stiffness is assumed to be infinite as soon as u becomes negative. When σ becomes equal to σ_c , the cohesive zone starts to develop and transfers load up to the point where $u = u_c$. At this point it should be noted that in small region around the (weak) point where the cohesive zone starts to develop initially, the cohesive relation will most likely be different from the relation for the rest of the material in that for example σ_c will be lower. In Fig. 5b are shown the degrees of freedom used to describe the deformations.

The loading of the paper sample can be divided into three cases shown in Fig. 6. With reference to this figure, depending on the load level, the material can be entirely elastic (I), a cohesive zone can have started to develop (II) or the cohesive zone can be fully developed and a crack has formed (III). The variables used to define a general situation are shown in Fig. 7.

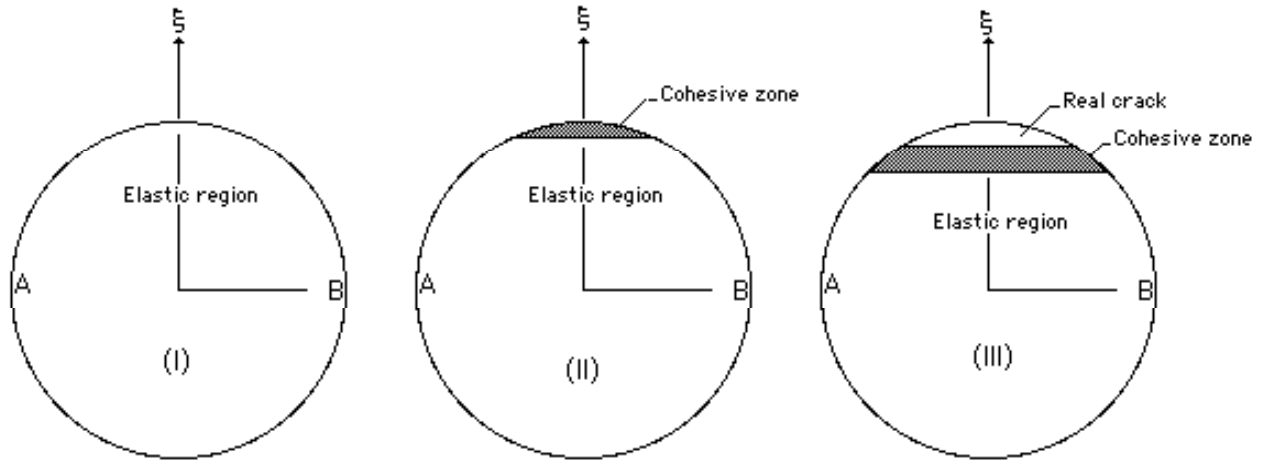


Fig. 6: Three consecutive loading cases.

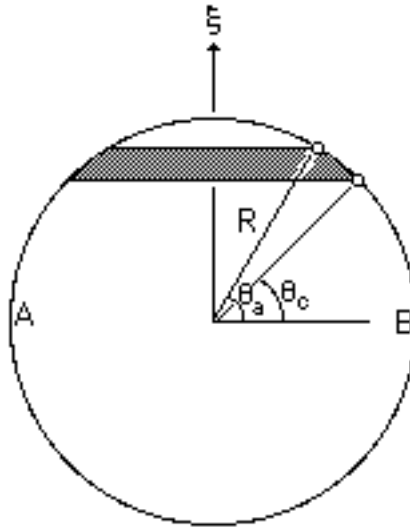


Fig. 7: Angles θ_a and θ_c used to describe a general situation.

The elastic case (case I in Fig. 6) is obtained when $\theta_a = \theta_c = \pi/2$. Case II is defined by $\theta_a = \pi/2$ and $\theta_c < \pi/2$. Case III finally is given by $\theta_c < \theta_a \leq \pi/2$. R denotes the radius of the grips. Letting σ denote the stress in the thickness direction of the paper sample, the following two relations must be satisfied for reasons of equilibrium (see Fig. 5b):

$$\int_A \sigma dA = P; \quad \int_A \sigma \xi dA = -Ps\phi \quad (1)$$

where ξ is defined in Fig. 8 and it has been assumed that ϕ is a small angle. The displacement $u(\xi)$ in the thickness direction can be expressed in the degrees of freedom u_0 and ϕ according to:

$$u(\xi) = u_0 + \xi\phi \quad (2)$$

This is because the grips can be assumed to be rigid. Dividing by the paper thickness t , the strain ε in the thickness direction is obtained as:

$$\varepsilon(\xi) = (u_0 + \xi\phi)/t \quad (3)$$

In the elastic region, the stress is (since a uniaxial stress state is assumed) given by:

$$\sigma(\xi) = E\varepsilon(\xi) \quad (4)$$

Introducing the following transformation:

$$\xi = R\sin\theta \quad (5)$$

will turn (1) in to:

$$2R^2 \int_{-\pi/2}^{\theta} \sigma \cos^2\theta d\theta = P; \quad 2R^3 \int_{-\pi/2}^{\theta} \sigma \cos^2\theta \sin\theta d\theta = -Ps\phi \quad (6a, b)$$

Putting $\theta_a = \theta_c = \pi/2$ will give the elastic case (I) and the value of u_0 , which will give $\sigma = \sigma_c$, can be determined. Remember the note made previously about the initial value of σ_c .

For reasons of simplicity, the analysis will start when the displacement in $\theta = \pi/2$ equals u_c . Then a real crack is forming and one enters case III. Over the part of the cross section where a real crack is propagating, the stress is of course equal to zero. Over the cohesive zone, i.e. when $\theta_c \leq \theta \leq \theta_a$, one will have for σ :

$$\sigma = \sigma_c(\sin\theta_a - \sin\theta)/(\sin\theta_a - \sin\theta_c) \quad (7)$$

In addition to equations (6a, b), one must have that for $\theta = \theta_a$, $u = u_c$, which condition with equations (2) and (5), will give:

$$u_c = u_0 + R\phi\sin\theta_a \quad (8)$$

Also, for $\theta = \theta_c$, $u = \sigma_c t/E$, which (again with (2) and (5)) will give:

$$\sigma_c t/E = u_0 + R\phi\sin\theta_c \quad (9)$$

Equations (6a, b), (8) and (9) will give four equations for the four unknowns P , θ_a , θ_c and ϕ (choosing u_0 to be the independent parameter in this case). If, during the analysis, the displacement at $\theta = -\pi/2$ becomes equal to zero one has to proceed in a different manner. Putting the displacement at $\theta = -\pi/2$ equal to zero will give with (2) and (5) that:

$$u_0 - R\phi = 0 \quad (10)$$

Now, consider Fig. 8:

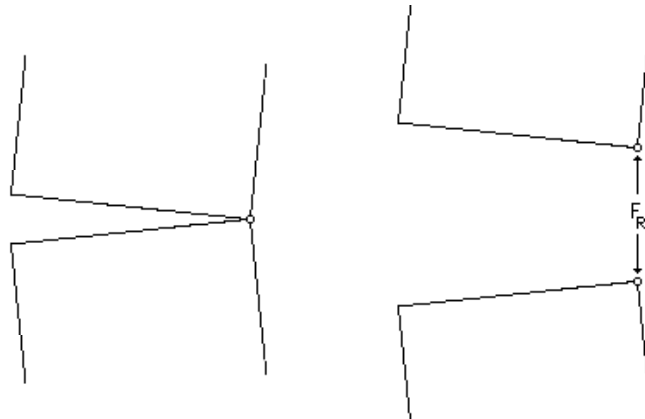


Fig. 8: Contacting points.

The reaction force F_R will affect equations (6a, b) such that:

$$2R^2 \int_{-\pi/2}^{\theta} \sigma \cos^2 \theta d\theta = P + F_R; \quad 2R^3 \int_{-\pi/2}^{\theta} \sigma \cos^2 \theta \sin \theta d\theta = -Ps\phi - F_R R \quad (6'a, b)$$

One extra equation is gained, i.e. equation (10) but at the price of another unknown; F_R . However five unknowns; F , F_R , ϕ , θ_a and θ_c are determined by equations (6'a, b), (8), (9), and (10). If, at some instant, the reaction force F_R goes from a positive value to zero, then F_R is put equal to zero, equation (10) becomes invalid and the analysis proceed as before.

It should be pointed out that all results are based on the assumption that unloading over the cohesive zone never occurs.

In order to relate the results from the analytical model to the AE output, it is reasonable to assume that to create one unit stress free area, in average N_0 fiber bonds have to be broken. This means that for a given value of θ_a , one contribution to the number of broken bonds is:

$$N_0 \int_{\theta_a}^{\pi/2} dA(\theta) = 2N_0 R^2 \int_{\theta_a}^{\pi/2} \cos^2 \theta d\theta.$$

In the cohesive zone the material has failed completely at $\theta = \theta_a$ while at $\theta = \theta_c$, the material is intact. If it is assumed that the number of broken bonds per unit area varies linearly over the cohesive zone, this will give another contribution to the total number of broken bonds according to:

$$2N_0 R^2 \int_{\theta_c}^{\theta} ((\sin \theta - \sin \theta_c) \cos^2 \theta / (\sin \theta_a - \sin \theta_c)) d\theta$$

such that the total number of broken bonds will be proportional to Ψ given by:

$$\Psi = \int_{\theta_a}^{\pi/2} \cos^2 \theta d\theta + \int_{\theta_c}^{\theta} ((\sin \theta - \sin \theta_c) \cos^2 \theta / (\sin \theta_a - \sin \theta_c)) d\theta \quad (11)$$

If there is a direct proportionality between the total number of broken bonds and total number of AE events $\sum ev$ one will have the form of the AE curve given by:

$$\sum ev = \alpha \Psi \quad (12)$$

where α is a constant.

Results

Numerical example

To solve the equations, MATLAB [6] was utilized. The following input data were used:

$$R = 17.5 \text{ mm}, s = 50 \text{ mm}, t = 0.042 \text{ mm}.$$

$$\sigma_c = 50 \text{ MPa}, E = 500 \text{ MPa}, G_c = \sigma_c u_0 / 2 = 0.14 \text{ N/mm}$$

In Fig. 9a is shown the applied load P versus the load point displacement u_0 . while Fig. 9b shows Ψ versus the load point displacement u_0 .

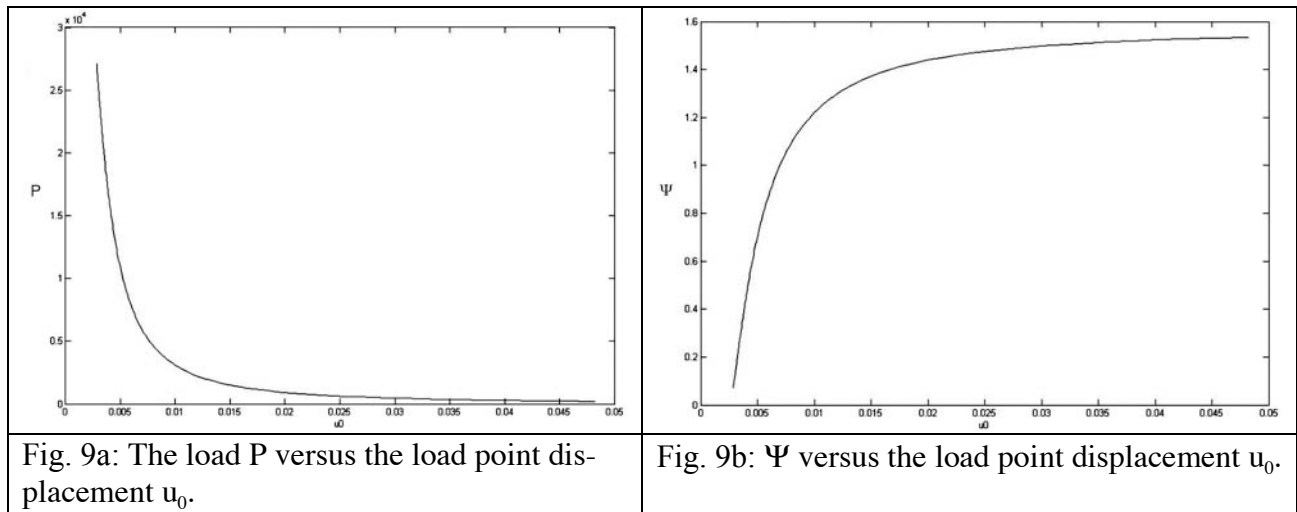


Fig. 9a: The load P versus the load point displacement u_0 .

Fig. 9b: Ψ versus the load point displacement u_0 .

It should be pointed out that the results given in Figs. 9a and 9b are at best qualitative. However, the experimental P vs. u_0 curves shows the same behavior as is shown in Fig. 9b. Also, the experimental AE curves exhibit a steep slope just after load maximum and another observation is that as the load point displacement u_0 is increased, the AE curve levels out.

One thing that must be remembered is that the model does not account for the initiation of damage, i.e. for phase II but only for the propagation of a real crack across the cross section of the grips.

Experimental Results

The load – displacement curves and corresponding AE curves are shown in Fig. 10 for the two paper qualities. These were as mentioned before; light-weight coated (LWC) paper and paper board. The curves represent average values for at least 8 specimens. Note that on the horizontal axis in Fig. 10, time in seconds is the parameter. With a given deformation rate, this can easily be converted to displacement.

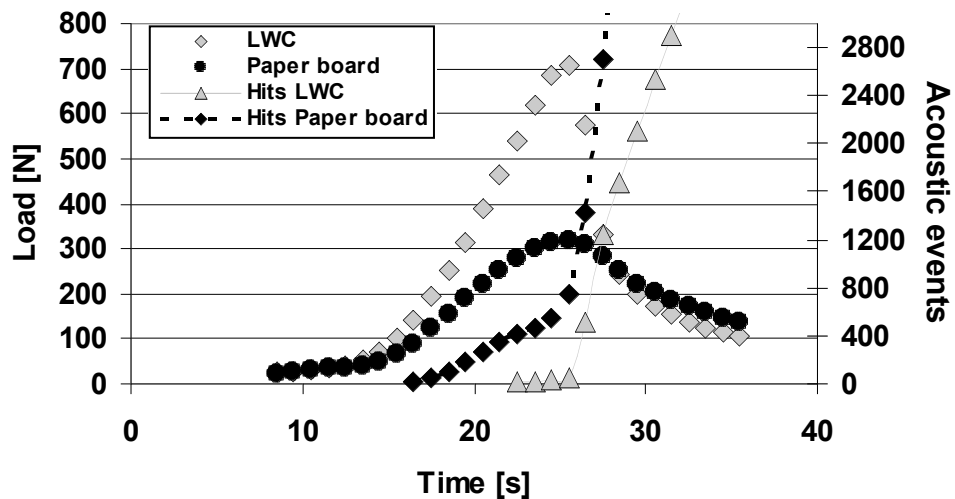


Fig. 10: Curves for load and cumulative AE events for a paperboard and LWC versus time.

As can be observed from Fig. 10, there was a big difference between the behavior of LWC and paper board. The most obvious difference is the peak load level in that the paper board load curve peaked at about 320 N while the LWC load curve peaked at about 700 N. Also, the shapes of the curves show differences. For example, LWC seems to be quite brittle since the load decreases rapidly after the load peak and there are also very few AE events before the peak load is reached. As the load decreases after the load peak, the AE events increased dramatically (in agreement with the results from the analytical model). The paper board, on the other hand, had a more non-brittle behavior in that damage (AE) started well before the peak load was reached. Also, the drop in load after the peak load was not as dramatic as for LWC.

Discussion

An experimental device for studying the damage evolution in paper when loaded in the thickness (Z) direction has been presented. The method, when applied to two different paper qualities, shows promising results in that it is possible to get some information regarding the toughness of the paper material. It is also possible to determine the load or deformation when damage initiates. This together with for example the finite element method, can give information about stress and strain fields at the onset of damage. An analytical model is also developed which in spite of its simplicity seems to be able to predict, at least in a qualitative sense, both the load – displacement and AE relations. With a more refined model it might be possible to perform parameter estimation, i.e. to estimate from experimental data, the cohesive strength and fracture energy.

Acknowledgements

We would like to take this opportunity to thank the companies that have supplied us with paper samples (too many to mention here). In addition, the Swedish Energy Agency, the Foundation for Knowledge and Competence, EU Objective 1 Programme (Region of South Forest Counties), and the Bo Rydin Foundation are greatly acknowledged for their financial support.

References

- [1] SCAN-P 80:98; Z-directional tensile strength.
- [2] Gradin PA, Nyström S, Flink P, Forsberg S, Stollmaier F., Acoustic Emission Monitoring of Light Weight Coated Paper. *J of Pulp and Paper Science*, **23**, (3), March 1997.
- [3] Isaksson P., Hägglund R., Gradin P. A., Continuum Damage Mechanics Applied to Paper. *International Journal of Solids and Structures*, **41** (2004) pp 4731 – 4735.
- [4] Isaksson P., Gradin P.A. and Kulachenko A., The onset and progression of damage in isotropic paper sheets. *Int. J. Solids Struct.* **43**, 713-726. (2006).
- [5] Gradin, P A., Graham, D., Nygård, P. and Vallen, H., The Use of Acoustic Emission Monitoring to Rank Paper Materials With Respect to their Fracture Toughness. *Experimental Mechanics*, **48**, (1), February 2008.
- [6] MatLab version 6.5., The MathWorks Inc., Natick, MA, USA; 2002.

ASSESSMENT OF STRESS CORROSION CRACKING IN PRESTRESSING STRANDS USING AE TECHNIQUE

MARIANNE PERRIN^{1,2}, LAURENT GAILLET¹, CHRISTIAN TESSIER¹
and HASSANE IDRISSE²

¹Laboratoire Central des Ponts et Chaussées, Centre de Nantes, Div. MACOA, route de Bouaye, BP 4129, 44341 Bouguenais cedex, France; ²Laboratoire MATEIS-CNRS UMR-5510, Equipe RI₂S, INSA-Lyon, Bât. L. de Vinci, 21 ave. J. Capelle, 69621 Villeurbanne cedex, France

Keywords: Corrosion AE monitoring, prestressing steel

Abstract

Detecting corrosion of prestressing strands in concrete structures requires non-destructive techniques like acoustic emission (AE), which allows the monitoring of active defects of the structures. The aim of this work is to adapt AE to structural characteristics of bridges, to detect and localize stress corrosion cracking (hydrogen embrittlement, HE) of tendons. Accelerated corrosion tests with ammonium thiocyanate on tensioned cables have permitted to validate AE system capacity to detect signals coming from hydrogen embrittlement mechanism. Distinction by AE of the different stages of the mechanism (crack initiation, crack propagation, etc.) occurring on prestressing strands is observed. Limited accessibility to strands on bridges has also been taken into account by placing AE sensors on strand anchorage. Results show effects of wave dispersion but the discrimination of AE hits is possible. This work presents the potential of AE monitoring to detect, in their earliest stage, damages to prestressing strands, but the limitations of AE technique is also pointed out.

Introduction

Non-destructive testing is multi-faceted and diversified. Most of them allow no real-time control of structural damage evolution, in contrast to acoustic emission (AE). Due to the collection by sensors placed on the structure of acoustic waves emitted by active defects, the detection and localization of damages can be done [1, 2]. Naturally, a non-destructive method has to be adapted to the degradation characteristics but also to the monitored structure.

Bridges studied in this work are prestressed concrete bridges. In addition to many bridges, which benefit from this technology (48% of new structures use this construction technique), this method is also used for nuclear power-plant construction or for energy production units. It is based on concrete compression maintained by the way of tensioned strands (at 80% of the guaranteed ultimate tensile strength, GUTS) of high mechanical strength [3]. Strands are maintained in ducts placed inside concrete walls of post-tensioned prestressed concrete bridges. A grout is injected inside the duct to protect strands from corrosion. Concrete compression is realized by the way of anchorage systems at each side of the concrete unit [4]. Despite the use of protection, metallic strands can suffer from corrosion, notably stress corrosion cracking [5]. It can be initiated by material surface defects or by ionic species in the interstitial liquid of concrete, near strands. In these initiation zones, the presence of high strain conditions associated with an appreciable hydrogen concentration cause the metallic embrittlement [6]. When stresses in the crack tip reach a critical value, then the crack propagates until rapid wire failure.

AE has shown its capacity to detect corrosion phenomenon [7-14]. Besides, it is used on bridges to detect different damage types [15-18], but also in other areas, especially on metallic structures suffering from corrosion like storage tanks.

This work offers to validate the capacity of AE technique to detect stress corrosion cracking (hydrogen embrittlement), and the final aim is to be able to characterize the different degradation stages of prestressing tendons. Characteristic parameters coming from AE analysis are attributed to each corrosion mechanism. At the same time, a comparison of results obtained on sensors attached at different places on the structure is done to observe the acoustic waves propagation.

Testing Device and Experimental Procedure

Specimens are prestressing strands of T15.7 type. It is a cable including a straight central wire with six other wires surrounding it helicoidally (Fig. 1). The steel used to manufacture these strands is obtained after cold drawing process. This process results in a microstructure composed of fine pearlitic grains fully oriented in the wire axis. This microstructure offers to the strand important mechanical characteristics, notably concerning the ultimate tensile strength (UTS) about 1900 MPa (the force of 285 kN for T15.7 unit).



Fig. 1. T15.7 strand geometry: composed by a central wire and 6 helical wires.

Table 1. Chemical composition and mechanical properties of cold-drawn steel for T15.7.

Chemical composition [wt%]	
C	0.8
Si	0.25
Mn	0.50
P	0.02
S	0.02
Mechanical properties	
$F_{0,1}$ [kN]	275
F_m [kN]	295
Elongation [%]	5.3
Sectional area [mm ²]	150
Pitch [mm]	240

The testing device used to apply a constant elongation to specimens is presented on Fig. 2. Basically, it is composed of a rigid frame and a hydraulic jack allowing tensioning a cable at 80% of its GUTS (≈ 220 kN).

The corrosion cell permits to apply a corrosive environment to the strand. The corrosive solution chosen is ammonium thiocyanate (NH_4SCN) with a concentration of 250 g.l^{-1} , following EN-ISO Standard 15630-3. The ammonium thiocyanate is known to make steel prone to

hydrogen embrittlement by inhibition of recombination reaction of hydrogen atoms. During the test, the corrosive solution is kept at a constant temperature (50°C).

Some selection tests of the sensors have permitted to choose the sensor presenting the best detection/easy use ratio. The sensor having the best results is a resonant type micro-80 (EPA). For the strand monitoring in laboratory, four sensors have been used (Fig. 2). Sensors 1 and 2 are located on each side of the corrosion cell to have reference signals. Sensors 3 and 4 are attached on the anchorage system: sensor 3 is placed on the wedge system and sensor 4 on the wire end. The sensor coupling with the structure is done with a rigid paste (HBMX60 paste). Received signals are amplified and then processed by the AE system. The sampling frequency used for the data acquisition is 1 MHz. The acquisition threshold used is 26 dB.

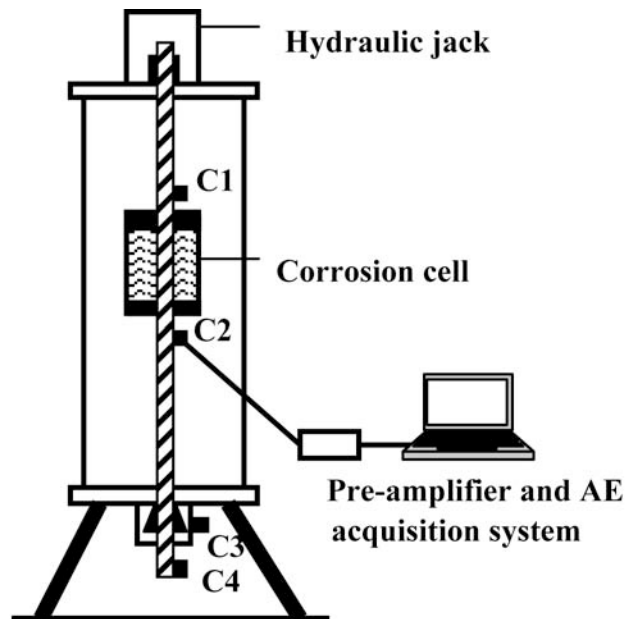


Fig. 2. Strand loading system and AE sensor positions.

Results and Discussion

Metallographic observations of the specimen:

The fracture surface of broken wire is of brittle type and shows three propagation stages (Fig. 3a). The primary crack meets several smaller cracks on the surface of the wire. The propagation depth of the primary crack is relatively shallow, about 370 μm . The second stage of the crack progress is mode II propagation (Fig. 3b). This propagation process is typical of cold-drawn steel SCC due to the microstructure, which can be assimilating to an orthotropic material [19-21]. The last stage of the fracture surface is a shear failure with some radial marks oriented toward the primary crack (Fig. 3d).

Despite the crack propagation is not a pure mode I, a first approximation of the threshold stress intensity factor K_{SCC} can be made with the Valiente method [22]. The wire is considered as a bar with a 5.2 mm diameter. The guaranteed ultimate tensile strength of the wire is 1860 MPa. The K_{SCC} factor obtained is 56 $\text{MPa}\sqrt{\text{m}}$. This value is lower than classical stress intensity factor of cold-drawn steel [23]. It is also lower than Toribio [19] values obtained with a hydrogen embrittlement. It can be explained by the important quantity of hydrogen, which has penetrated in steel in this case by comparison to other works.

The hydrogen effect on strand damages is also present on the specimen surface. Lots of small cracks are visible on the wire surface due to the important introduction of hydrogen inside the metallic matrix. Some longitudinal secondary cracks are also present (Fig. 3c).

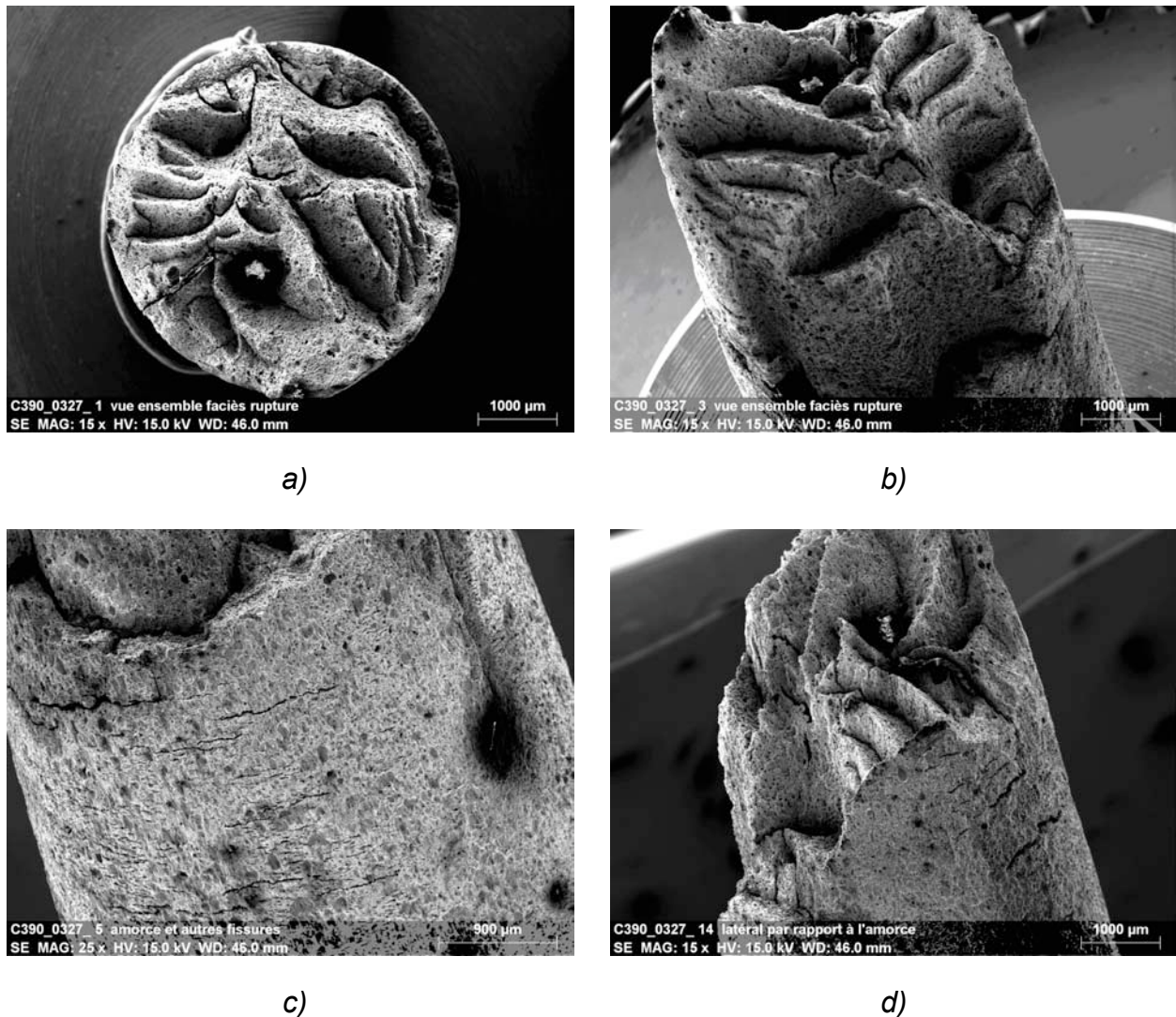


Fig. 3. a) Fracture surface with mode I crack propagation, b) fracture surface with radial marks, c) microcracks and longitudinal secondary cracks, d) shear failure and surface cracks.

Hydrogen embrittlement detection:

Sensor having collected the most AE hits is sensor 2 (Fig. 4). Collection ratio differences between all sensors can be explained:

- For sensors 3 and 4, separated from corrosion cell (signal dispersion coming from wave propagation and multiple impedance crossings).
- For sensor 1, by a less efficient coupling than for sensor 2.

All analysis will be based on results obtained on sensor 2. Figure 5 present cumulative AE number and cumulative energy evolutions with time. We can see four different stages:

Stage 1: from 0 to 15-20 hours. We observe a low number of hits, whose energy is also low. This stage corresponds to the homogenization and chemical stabilization of specimen in the corrosive solution after the filling up of the corrosion cell. This stage is then inherent to the test procedure.

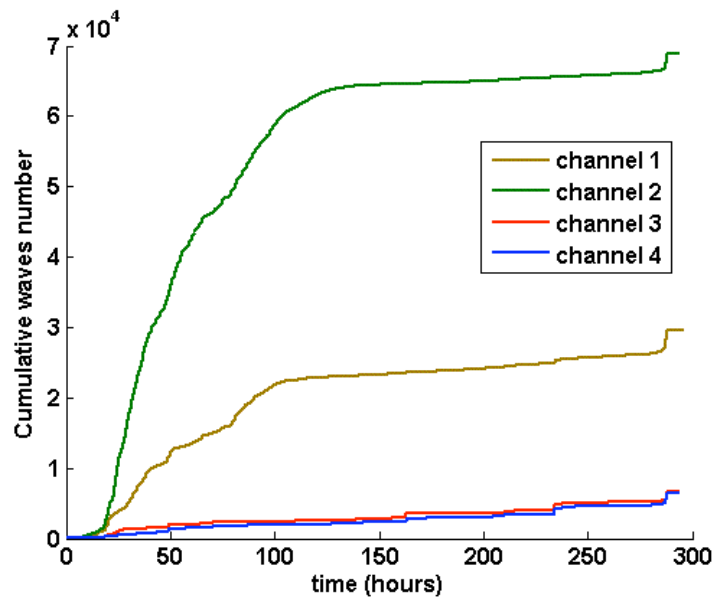


Fig. 4. AE hits evolution on each channel.

Stage 2: from 15-20 hours to 110-120 hours. For this period, AE behavior is characterized by a substantial increase of AE hits, but AE energy evolves differently. From the literature, we can attribute this behavior to hydrogen formation and bubble bursting at the specimen surface [12, 24-26]. Besides, Jomdecha et al. [27] showed that for stress corrosion cracking mechanism, a strong AE activity appears to come from hydrogen. These mechanisms involve the pseudo-passive layer breakdown and the beginning of hydrogen diffusion inside metal matrix.

Stage 3: from 110-120 hours to 275 hours. It can be characterized like a steady state where the increase of AE hits is very low, so as cumulative energy. It is an initiation stage concerning hydrogen embrittlement and general corrosion occurs. A post-mortem analysis has shown general corrosion near fracture area. At the end of this stage when hydrogen uptake is sufficient for the steel to exceed the threshold stress intensity factor (K_{SCC+HE}), rapid crack propagation takes place.

Stage 4: after 275 hours. It is pure crack propagation phenomenon affecting a large volume of metal characterized by low AE hits of high energies. This stage is very brief until final strand failure (<12 hours).

Characteristics of AE hits coming from each damage stage have been analyzed. First stage has been omitted from this study because its length is very limited and its detection on bridges is of little interest. Four AE parameters (amplitude, duration, counts, cumulative hits) characterizing evolution during stages 2, 3 and 4 (Table 2) have been selected. All hits have been considered including hits near strand breakage. Best discriminating parameters for each stage are duration and counts. Although high cumulative hits characterize phase 2, this parameter does not allow clear distinction between phase 3 and phase 4. Amplitude is also unable to distinguish between phases 2 and 3.

AE monitoring on the anchorage system:

For all tests, sensors 3 and 4 (placed on anchorage and on strand end, respectively) have detected strand corrosion degradation. The evolution for both sensor locations are quite similar and when we compare with results obtained for channel 2, the four damage stages are not so clearly

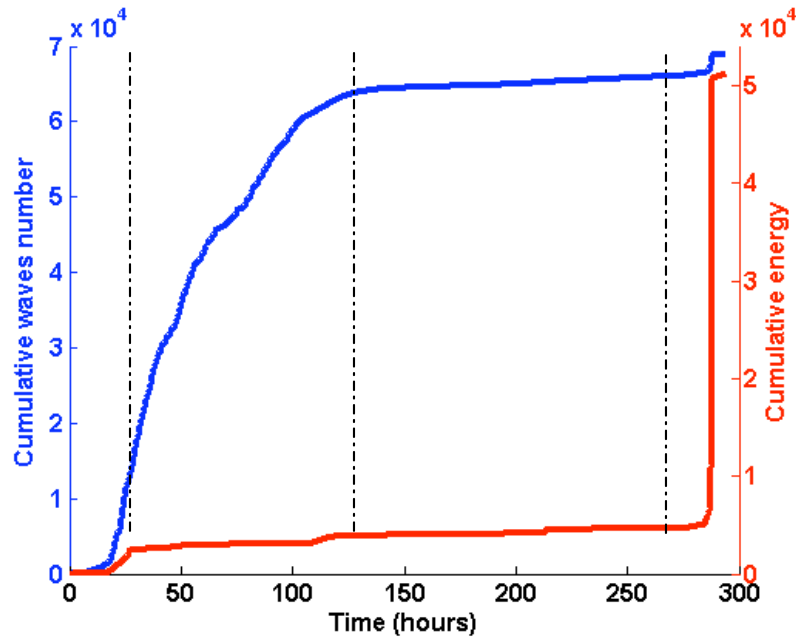


Fig. 5. AE hits and energy evolutions with time on channel 2.

Table 2. Means values of AE parameters and cumulative hits for damage stages 2, 3 and 4 (channel 2).

AE on channel 2	Stage 2	Stage 3	Stage 4
Amplitude (dB)	33	33	39
Duration (μ s)	182	384	664
Counts	8	22	67
Σ AE hits	62138	2627	2793

recognized. Nevertheless, we can identify stages 1 and 4 limits. When we apply now the same data processing as above (Table 3) we observe that amplitude parameter has nearly the same value for sensors 2 to 4 (channels 2 to 4).

Concerning AE hits, their cumulative number is clearly lower for channel 3 and 4 (notably for stage 2) than for channel 2. Despite a reversal of lower duration value for sensor 4, duration and counts seem to be also valid discrimination parameters for sensors attached on the anchorage system.

Conclusion

Although SCC mechanisms induced by hydrogen are complex, AE has permitted to distinguish different damage stages. By a rather simple approach using classical AE parameters, AE monitoring is able to differentiate four stages of the evolution of corrosion damage. Most emitting mechanisms are bursting of hydrogen bubbles or fast crack propagation that can easily be determined with these parameters.

A comparison of AE signals collected near the damage zone (sensor 2) and behind anchorage system (sensor 3 and 4) permits us to conclude that a discrimination of the different damage mechanisms by usual AE parameters is possible placing sensors on anchorage area. This is in many cases the only accessible zone on structures.

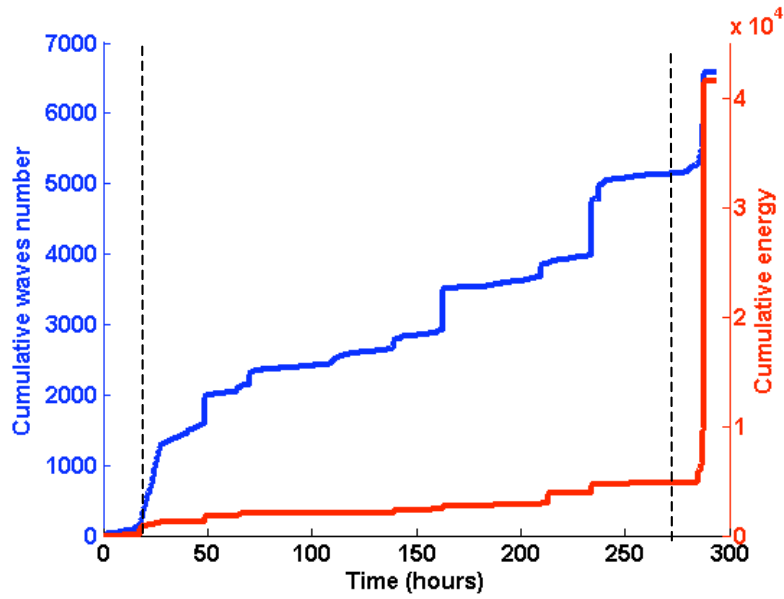


Fig. 6. Hits and energy evolutions with time on sensor 3 (channel 3).

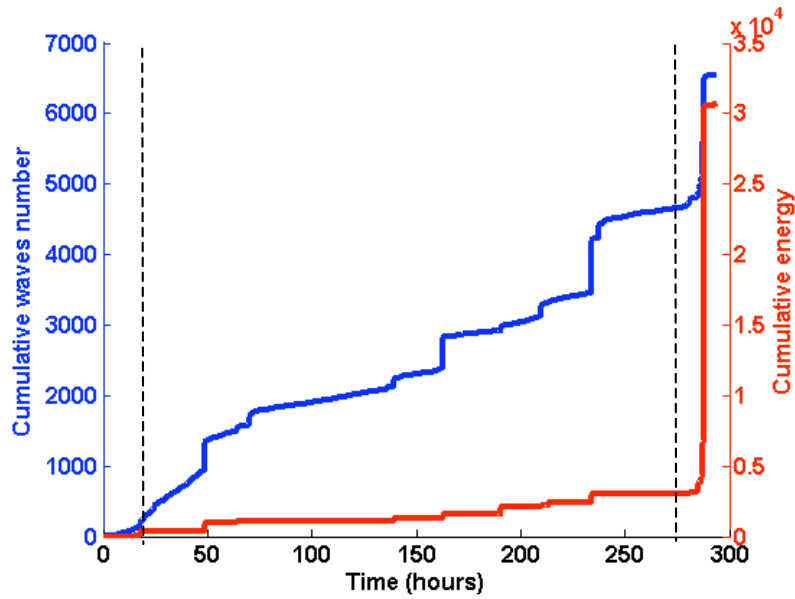


Fig. 7 Hits and energy evolutions with time on sensor 4 (channel 4).

Table 3. Mean values of AE parameters and cumulative hits for damage stages 2, 3 and 4.

AE on channel 3	Stage 2	Stage 3	Stage 4
Amplitude (dB)	33	34	39
Duration (μ s)	790	1138	1303
Counts	34	68	89
CumulativeAE hits	2470	2553	1437
AE on channel 4	Stage 2	Stage 3	Stage 4
Amplitude (dB)	34	34	39
Duration (μ s)	543	1115	757
Counts	41	58	72
CumulativeAE hits	1902	2640	1864

Results obtained are promising and show interesting capacities of AE for the early detection of stress-corrosion cracking damages in prestressing strands tensioned in bridge configurations.

Acknowledgement

This work has been realized as a part of ACTENA French project. Authors thank EDF (French Electricity) and ANR (National Research Agency) for their financial support.

References

1. Roget J.: Essais non destructifs : l'émission acoustique, mise en œuvre et applications, éditions AFNOR CETIM.
2. Roget J.: Techniques de l'ingénieur, traité Mesures et Contrôles, R 3200, pp. 1-10.
3. Chaussin R.: Techniques de l'ingénieur, traité Construction, C2360, 1990, pp. 1-77.
4. Jartoux P., Fargeot B., Tourneur C.: Techniques de l'ingénieur, traité construction, C2372, 1996, pp. 1-34.
5. Nürnberger U.: Otto Graf Journal, N°13, 2002, pp. 9-25.
6. Schroeder R.M.: Corrosion Science, **45**, 2003, 1969-1983.
7. Idrissi H., Liman A.: NDT&E International, **36**, 2003, 563-569.
8. Darowicki K., Mirakowski A., Krakowiak S.: Corrosion Science, **45**, 2003, 1747-1756.
9. Kovac J., Leban M., Legat A.: Electrochemica Acta, **52**, 2007, 7607-7616.
10. Idrissi H., Derenne J., Mazille H.: Journal of Acoustic Emission, **18**, 2000, 409-416.
11. Idrissi H., Limam A.: Journal of Acoustic Emission, **18**, 2000, 417-423.
12. Fregonese M., Idrissi H., Mazille H., Cetre Y., Renaud L.: Corrosion Science, **43**, 2001, 627-641.
13. Bellenger F., Mazille H., Idrissi H.: NDT&E International, **35**, 2002, 385-392.
14. Ramadan S., Gaillet L., Tessier C., Idrissi H.: Applied Surface Science, **254**, 2008, 2255-2261.
15. Matsuyama K., Fujiwara T., Ashibashi A., Ohtsu M.: *National conference on subsurface and civil engineering acoustic emission*, n°5, Kumamoto, Japan, 1993.
16. Zejli H., Lacksimi A., Tessier C., Gaillet L., Benmedakhene S.: Advanced Materials Research, **13-14**, 2006, 345-350.
17. Brevet P., Robert J.L., Gaillet L.: *Proceedings of the EWGAE 2002 European Working Group on Acoustic Emission*, Prague, Czech Republic, 2002, pp. 11-13.
18. Gaillet L., Tessier C., Bruhat B., Michel R.: Bulletin des laboratoires des ponts et chaussées, **250-251**, 2004, 55-63.
19. Toribio J., Ovejero E., Corrosion Science, **49**, 2007, 3539-3556.
20. Toribio J., Valiente A., Engineering Failure Analysis, **13**, 2006, 301-311.
21. Toribio J., Ovejero E., Engineering Failure Analysis, **12**, 2005, 654-661.
22. Valiente A., Ph.D. thesis, Polytechnic University of Madrid, 1980.
23. Brevet P., Raharinaivo A., Siegert D., Bulletin des laboratoires des ponts et chaussées, **250-251**, 2004, 75-92.
24. Ramadan S., Idrissi H.: Desalination, **219**, 2008, 358-366.
25. Didier-Laurent S., Idrissi H., Roue L.: Journal of Power Sources, **179**, 2008, 412-416.
26. Yuyama S., Hisamatsu Y., Kishi T., Nakasa H.: *Proceedings of the Fifth International Conference on Acoustic Emission*, Tokyo, 1980, pp. 115.
27. Jomdecha C., Prateepasen A., Kaewtrakulpong P.: NDT&E International, **40**, 2007, 584-593.

COMPARISON OF WAVELET TRANSFORM AND CHOI-WILLIAMS DISTRIBUTION TO DETERMINE GROUP VELOCITIES FOR DIFFERENT ACOUSTIC EMISSION SENSORS^{#*}

M. A. HAMSTAD

University of Denver, Department of Mechanical and Materials Engineering, Denver, CO 80208
and National Institute of Standards and Technology, Boulder, CO 80305, USA

Keywords: AE arrival times, AE sensors, Choi-Williams distribution, group velocities, Lamb modes, thin plate, wavelet transform

Abstract

Acoustic emission (AE) sources in a plate generate dispersive Lamb waves. In this research, pencil lead breaks (PLBs) were made on an edge of a 3.1 mm thick aluminum alloy plate to generate such AE waves. The PLBs were made near the plate mid-plane and near the bottom of the edge. The waves were sensed by pairs of AE sensors (both resonant or both non-resonant wide-band). Each sensor of each pair was located at a different distance from the plate edge PLB position. The signals from the different sensors and source positions were analyzed and contrasted. The recorded signals were processed by a wavelet transform (WT), and the group velocity curves for the appropriate Lamb modes were superimposed to clearly identify the modes in the signal. The threshold-independent mode arrival times at specific intense signal frequencies were determined by the time of the peak WT magnitude at the intense frequency. Since the two sensors were located at different known distances from the PLB position, an experimental group velocity was calculated based on the difference in arrival times and the difference in distance. This velocity was then compared to the theoretical group velocity for the relevant mode and frequency. In addition, an alternate frequency/time analysis method was used. This was the Choi-Williams distribution (CWD). The same procedures used for the WT results were followed for the CWD distribution. In addition the experimental results were compared to finite element calculated results for plate-edge monopoles both near the mid-plane and near the top plate edge. Group velocities within 6.5 % of the theoretical values were obtained with all the sensor types when certain intense resonant frequencies were ignored for two of the three resonant sensor types.

Introduction

The author and his co-workers have published a number of papers on the analysis of finite-element modeled (FEM) acoustic emission (AE) signals in a 4.7 mm thick aluminum plate [1- 6]. One focus of this work has been to demonstrate the use of a wavelet transform (WT) to obtain accurate and threshold-independent arrival times from the peak WT magnitude of certain intense frequencies of the Lamb modes. Since these arrival times were associated with specific known group velocities, very accurate source locations could be calculated for the dispersive AE waves

[#] Contribution of the U.S. National Institute of Standards and Technology; not subject to copyright in the United States

^{*} Trade and company names are included only for complete scientific/technical description; endorsement is neither intended nor implied.

even in the presence of significant electronic preamplifier noise [6]. This result was due to the fact that the WT spreads out the noise in frequency, while the arrival of a mode in an AE signal concentrates the signal energy at specific frequencies and specific times. In addition, since WT-based arrival times are obtained from regions of the AE signal that have significant amplitude, the above approach is also much more robust in the presence of preamplifier noise than AE analysis techniques that seek to obtain the arrival time from the very first arrival of an AE signal. This result is due to the fact that the first arrival region of an AE signal is often considerably lower in amplitude than the peak region of the signal. Thus, the very first arrival may be “lost” in the noise.

Due to the small spatial resolution of the FEM results (typically a 0.3 mm cell size), the WT-based arrival times were in essence obtained from the signal from a perfectly flat-with-frequency point-contact “pseudo” displacement sensor. Thus, a question remains with respect to the above research. What is the accuracy of arrival times obtained in a similar fashion from the signals from real AE sensors?

The purpose of the research reported here was to examine with signals from real AE sensors whether experimentally obtained mode arrival times from pencil lead break (PLB) generated waves accurately corresponded to theoretical group velocities in a thin aluminum plate. These experiments were done using a variety of AE sensor types, and the arrival times were determined from frequency/time analysis, as was done with the FEM-generated results. The sensors included both wideband (with response approximately flat with frequency over certain frequency ranges) and resonant sensors (this characterization of the sensors was based on information available from sensor suppliers). Both a WT and the Choi-Williams distribution (CWD) were compared relative to their use for determination of accurate mode arrival times as measured by the closeness of the experimental group velocities to theory. These comparisons were made from the arrival times of the more intense modal regions in the frequency/time magnitude results.

Experiment

Previous finite element modeled results as well as experimental results demonstrated that PLBs applied to the edge of a plate generated AE waves that were much more similar to the AE from modeled results from interior buried dipole AE sources than PLBs applied to the plate top or bottom surface [7,8]. Hence, PLBs (0.3 mm diameter, 2H hardness, length of about 2 mm) were applied to the edge of an aluminum alloy plate having a thickness of 3.1 mm. Two sensors of each type were mounted at a time on the upper plate surface by use of vacuum grease as the couplant. They were mounted on a line perpendicular to the plate-edge PLB position (located at the midpoint along the long edge of the plate). One sensor was mounted at 127 mm (5 in.) from the edge, and the other at 305 mm (12 in.). Based on the results of previous modeling that showed the modal distribution of energy in an AE signal strongly depended on the source depth in a plate [1], the pencil lead was broken in contact with the plate edge near the mid-plane and also near the bottom of the edge. A third AE sensor located on the plate top surface near the PLB point was used to provide a consistent trigger signal for a 12-bit transient digital recorder. A passive four-pole Butterworth filter was used to high-pass the signals at 50 kHz before the signals were recorded with a time step of 0.1 μ s. A total of six different models of AE sensors were used, including two commercially available wideband sensors (designated WB #1 and WB #2) and three commercially available resonant sensors (designated Res #1, Res #2 and Res #3). In addition, a high sensitivity wideband sensor developed at NIST Boulder was used (designated FHWA) [9, 10]. Some information about the sensors is shown in Table 1. No special purchase

Table 1 Listing of sensors used.

Sensor names	Expected response character	Freq. [kHz] of peak response
FHWA	Wideband	Not applicable
WB #1	Wideband	Not applicable
WB #2	Wideband	Not applicable
Res #1	Resonant	125
Res #2	Resonant	500
Res #3	Resonant	150

of sensors was made; instead available sensors from other projects were used. Appropriate pre-amplifiers and preamplifier gains were used with each sensor. In all cases the high-pass frequency of the preamplifiers was either 1 kHz or 5 kHz, and the low-pass frequency was at least 1 MHz. A total of at least three PLBs was made for each source position for each set of sensors to make sure that representative results were obtained. In the analysis, only the representative signals from one PLB (per source position) were used for each set of sensors. The transverse dimensions of the plate (1220 mm by 1525 mm) were large enough to preclude reflections from the plate edges arriving during the duration of the waves propagating directly from the PLB position to the sensors.

In addition, finite element modeled results were also obtained for a 3.1 mm thick aluminum plate. These results were “converted” from existing results for a 4.7 mm thick aluminum plate by use of a technique previously demonstrated [11]. Because the “converted” 3.1 mm thick results were generated from the existing results for a different plate thickness and propagation distance, the in-plane monopole source depths (below the top surface of the plate) and the propagation distance were directly determined by the “conversion” process applied to the original data. Thus, the propagation distance to the “pseudo” sensor position was 120 mm from the monopole source applied to the plate edge. In addition, the two source depths were 0.52 mm (near the plate top edge) and 1.35 mm (near the plate mid-plane) below the top plate surface. After the conversion process was applied to the unfiltered FEM data, the signal that represented the out-of-plane top surface displacement versus time was digitally filtered with a four-pole 50 kHz high-pass Butterworth filter and then resampled in time from 29.6 ns to 0.1 μ s per point. The resultant data corresponded to the sampling interval of the experimental data. The domain of the plate for the finite element modeled (FEM) data was smaller in size (530 mm on the source side by 330 mm in the propagation direction) than the experimental plate. The plate was still of sufficient size that edge reflections did not occur during the full arrival of the signal that propagated directly from the source to the “pseudo” sensor position.

Group Velocity Curves for a Thin Aluminum Plate and Frequency/Time Analysis Procedures

Group velocity curves [12] of the fundamental symmetric and the first two antisymmetric Lamb modes for the 3.1 mm thick plate are shown in Fig. 1. Additional group velocity modes were not considered because their frequencies were beyond those normally used in AE for the current plate thickness. WTs [12] of the signals from the PLBs and FEM results were calculated. Group velocity curves were superimposed on the WT results by use of the known propagation distances. To correctly superimpose the group velocity curves (after the effect of propagation distance was accounted for), the curves were offset in time to match (by eye) the WT experimental results for the FHWA sensor. Then this same time offset was used for all the other

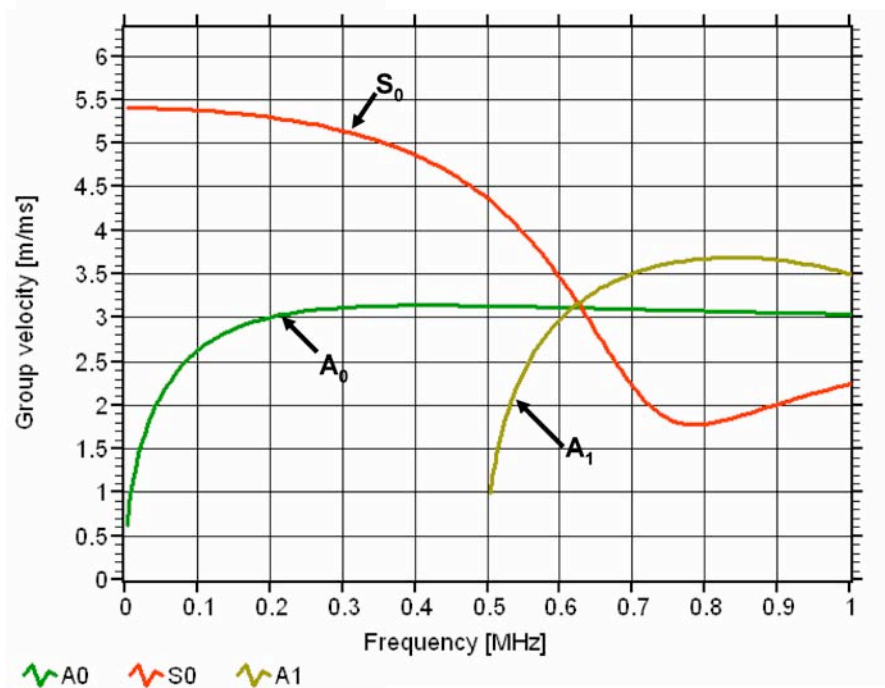


Fig. 1. Relevant group velocities vs. frequency for an aluminum plate of 3.1 mm thickness [12].

sensor results. This time adjustment was not necessary for the FEM results, because the displacement versus time data started at the time of the AE source initiation. The key parameters chosen for the WT calculation were a frequency resolution of 3 kHz (frequency band) and a wavelet size of 600 samples. In addition, a feature of the WT software was used to determine the frequencies, arrival times (at the peak magnitude of the frequency band) and the peak magnitude of the more intense mode arrivals.

An alternate frequency/time analysis was also applied to each experimental signal and to the FEM results. This approach was the CWD. This computation was made using the LabVIEW implementation (Easy CWD) [13]. Other than the default parameters, the following settings were used: (i) 2048 frequency bins, (ii) time resolution of 0.1 μ s, (iii) analytic signal and (iv) $\alpha = 0.1$ (this parameter controls the balance between resolution and cross-term interference). The CWD implementation did not allow for the superposition of the group velocity curves, but it was easy to pick out the modes by eye by use of the insight from the WT results for the same signals. Again the frequency, arrival times (at the peak of the frequency band) and the peak magnitude of the more intense mode arrivals were obtained from the CWD results by use of custom additions to the LabVIEW programming.

The frequencies of the intense mode arrivals were reported as the frequency at the high end of the WT and CWD frequency bands. Because the CWD bands were 2.44 kHz wide, the reported frequency was the largest number without decimal values in each band.

Typical Time Domain Results for Signals from Experimental PLBs and the FEM Data

Because the spread in time between the modes increased as the propagation distance increased, the signals at the farther distance (305 mm) were initially selected for more detailed examination. Thus, mode identification was enhanced. For an edge in-plane PLB near the mid-plane of the plate, Fig. 2 illustrates typical experimental time domains of the signals from all

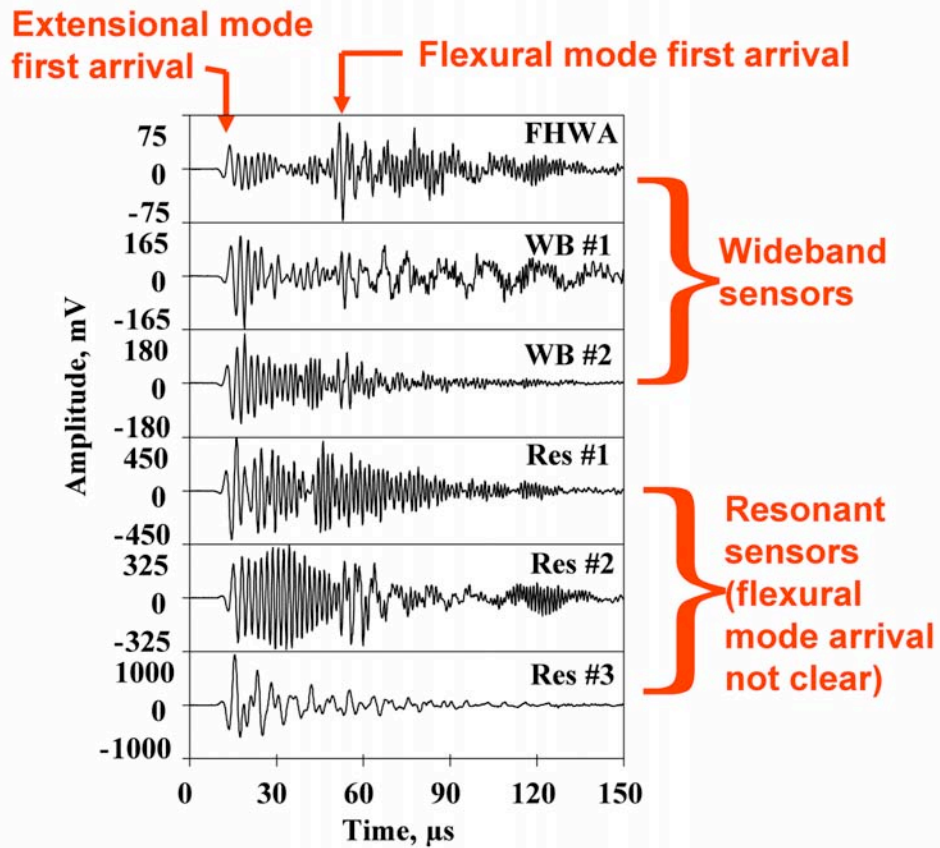


Fig. 2. Time domains for the different sensors at 305 mm propagation distance from PLB near the mid-plane of plate.

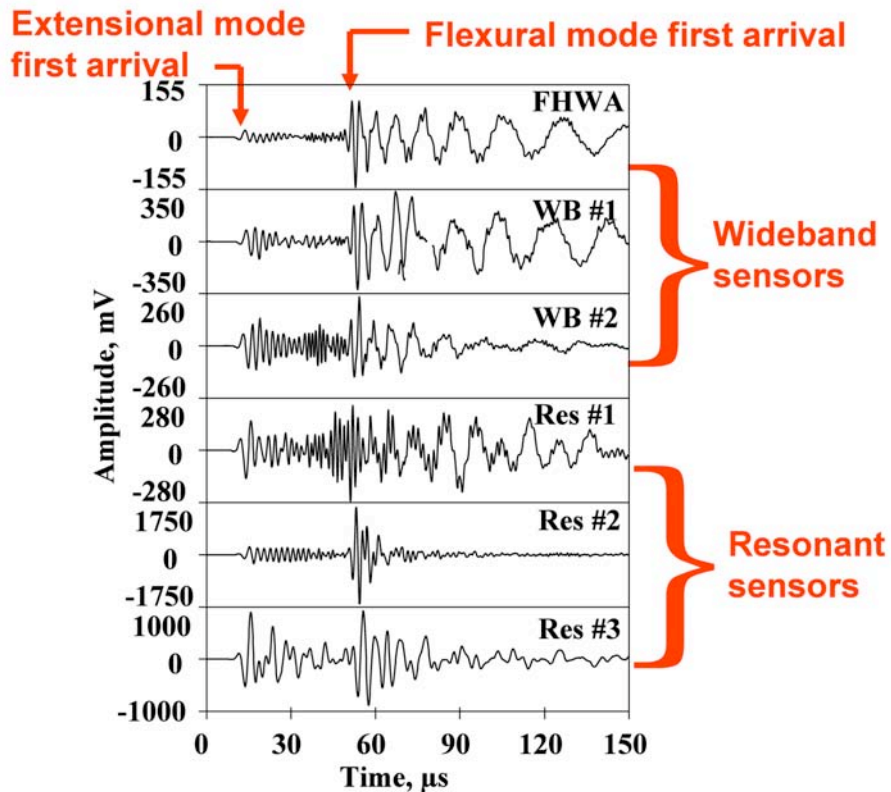


Fig. 3. Time domains for the different sensors at 305 mm propagation distance from PLB near the bottom edge of plate.

the sensor types. Figure 3 shows the typical time domain results for an in-plane edge PLB near the bottom of the plate.

Figure 2 demonstrates that for nominally the same displacement wave passing beneath the sensors, there was a wide variety of waveforms from the different sensors for the near mid-plane PLB. Only the wideband FHWA and WB #1 sensor signals were reasonably similar. As expected from the group velocity curves, the S_0 (extensional) mode first arrival was clearly observed at the beginning of all the signals. From the wideband sensor signals, the first arrival of the A_0 (flexural) mode can also be identified by eye, as indicated by the arrow in Fig. 2. In contrast, the first arrival of the flexural mode cannot be easily identified in the resonant sensor signals. Close examination by use of an expanded time scale of the signal from the Res #2 sensor does show the first arrival of the A_0 mode, but it was a little later than with the wideband sensors.

For the PLB source near the bottom edge, Fig. 3 shows the first arrival of the extensional mode for all the sensor signals. Also, with the exception of the Res #1 sensor, the first arrival region of the flexural mode can be identified by eye, as indicated by the arrow in Fig. 3. For this source position, the time domain signals were still quite different from each other, but they were more similar to each other than for the near mid-plane source. The signals from all three wideband sensors were the most like each other for the near bottom edge source.

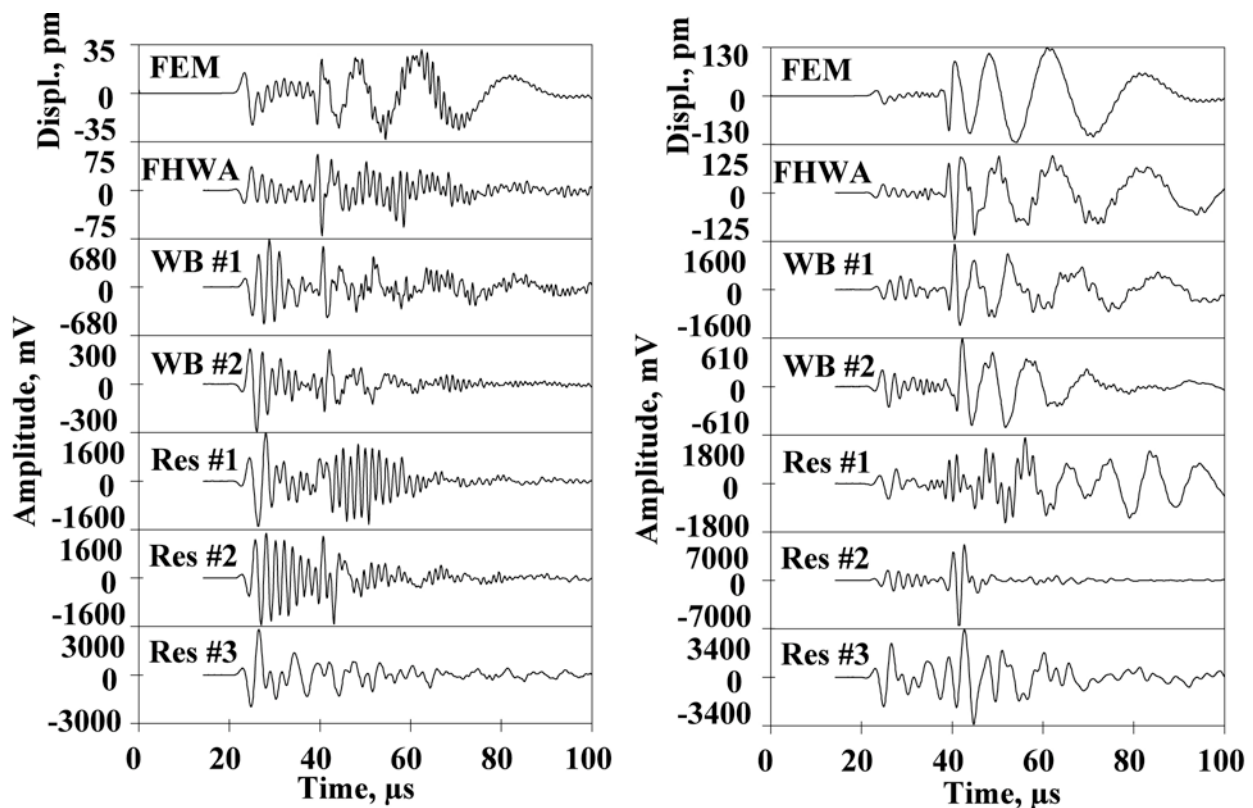


Fig. 4. FEM displacement at 120 mm propagation distance and sensor signals at 127 mm for in-plane source. Left column source near mid-plane and right column source near a plate surface.

It is of interest to compare the PLB results with the FEM results. Figure 4 shows the FEM out-of-plane displacement versus time for the in-plane edge monopole source located at two depths. These results are shown as the top waveforms in part (a) at 1.35 mm depth (near the mid-plane) and in part (b) at 0.52 mm depth (near the top edge). Figure 4 also shows the PLB waveforms for the different sensors at the 127 mm propagation distance. Although the

propagation distance of the FEM result was a little less at 120 mm, it is clear that both the extensional and flexural mode signals show clear first arrival regions in the FEM signals, while the PLB signals in general show mode arrival characteristics similar to those discussed above for the larger propagation distance. In addition, it is worthwhile to note that the wideband sensor signals were much closer to those from the FEM computation. The resonant sensor signals were not nearly as close to the FEM-based signals. In closing this paragraph, we point out that the only significant difference between a source near the top edge (FEM data) and one near the bottom edge (PLB data) is a change in phase of the anti-symmetric modes.

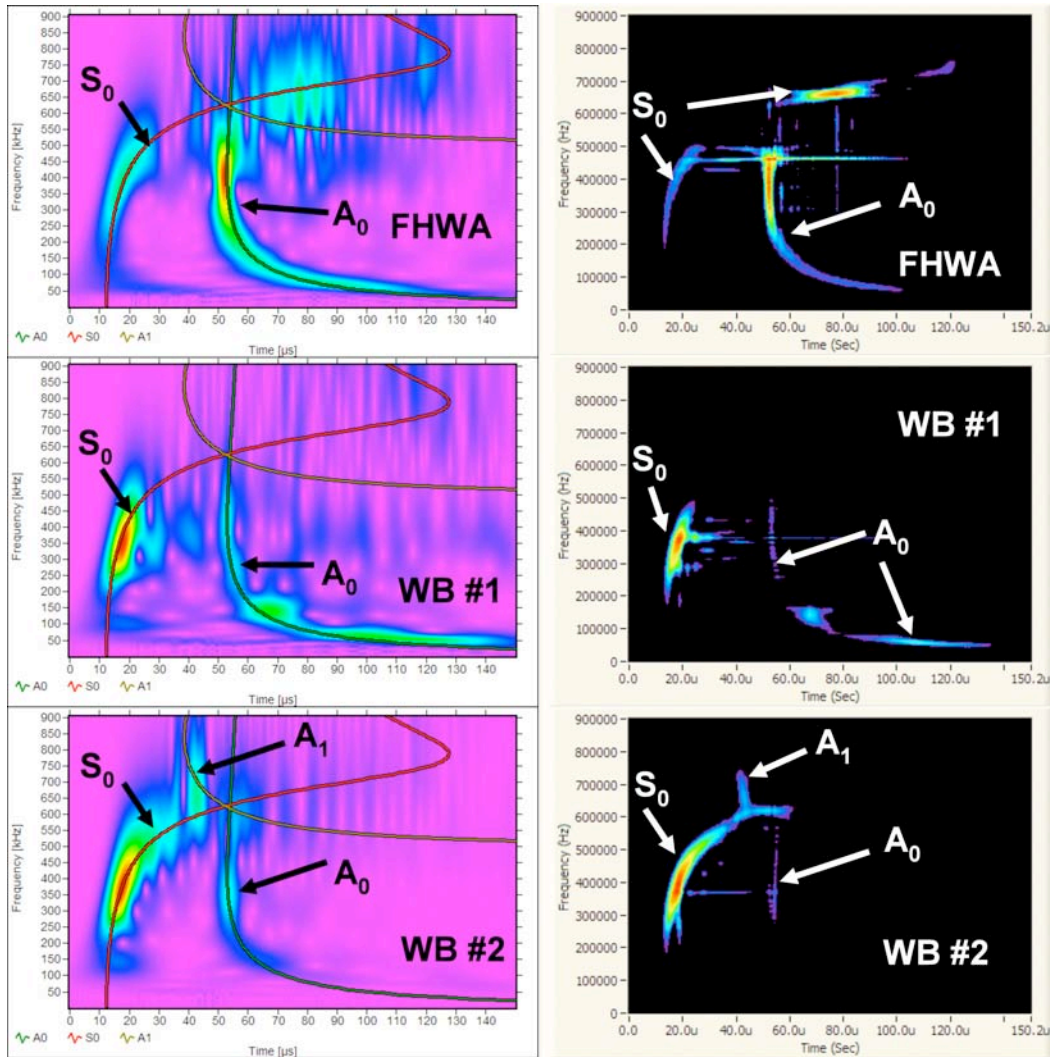


Fig. 5. WT (left column) and CWD (right column) of signals (Fig. 2) resulting from PLB near the mid-plane of the plate sensed by wideband sensors at a propagation distance of 305 mm.

Typical Frequency/Time Results for Signals from Experimental PLBs and the FEM Results

The left columns of Figs. 5 through 8 show the results after the WT was applied to the sensor signals. The A_0 and S_0 modes are labeled in all the figures, and the A_1 mode is labeled in figures where it was relevant. Figures 5 and 7 respectively show the wideband sensor results for the near mid-plane and near bottom edge PLBs. Figures 6 and 8 respectively show the resonant sensor results for the near mid-plane and near bottom edge PLBs. With the help of the group velocity

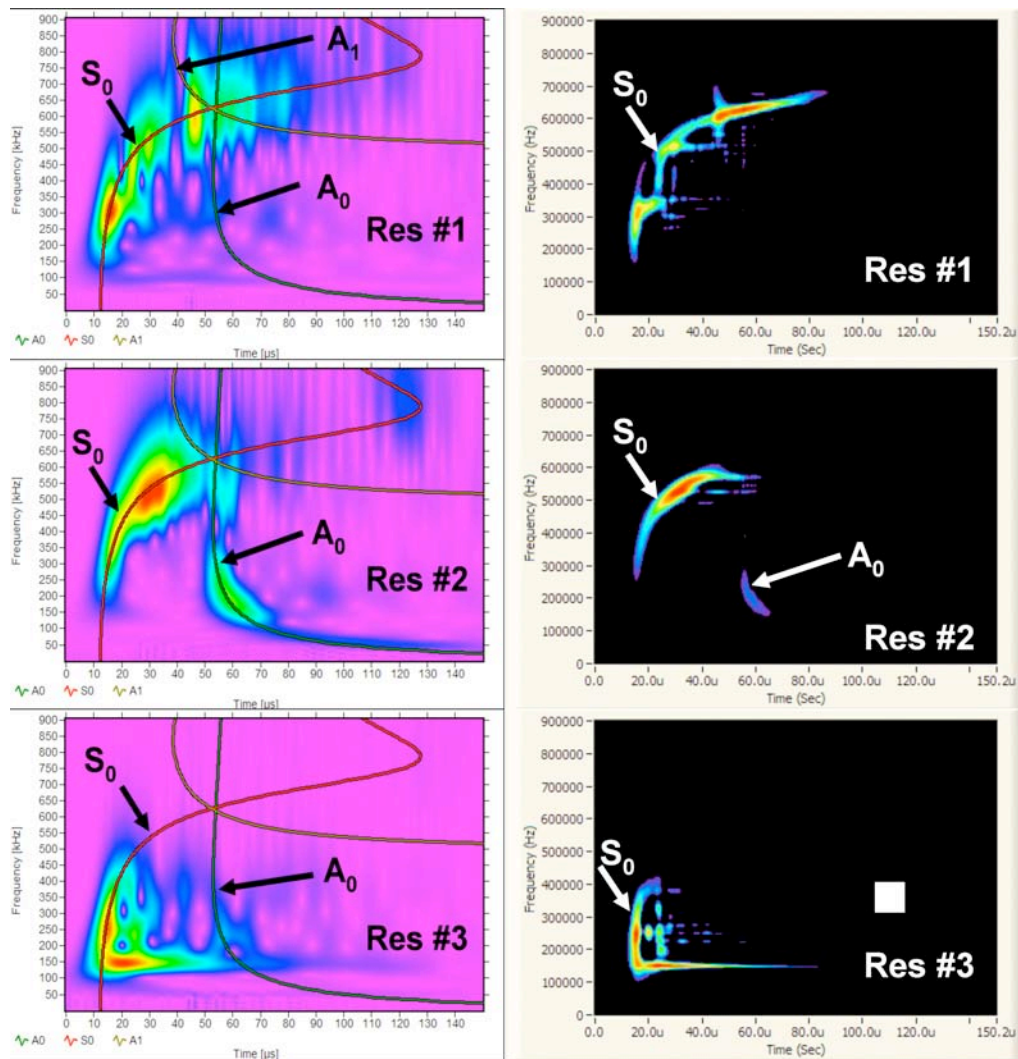


Fig. 6. WT (left column) and CWD (right column) of signals (Fig. 2) resulting from PLB near the mid-plane of the plate sensed by resonant sensors at a propagation distance of 305 mm.

curves at the known propagations distances, it was easy to identify the modes that were intense for all the sensors at both source depths. Thus the WT results provide a clearer picture of the modes and their arrivals than do the original amplitude versus time results. This result is particularly the case for the resonant sensors. Of even more importance, the WT results also identified the frequencies within the modes that were most intense for the different sensors at the two different source depths.

Because the waves that the sensors responded to were very similar for each PLB position, the WT results demonstrate significant distinctions between the response characteristics of the different sensors. First, considering the wideband sensor data for the near mid-plane source, the FHWA sensor responded most strongly in the A_0 mode, while the other two wideband sensors responded most strongly in the S_0 mode (see Fig. 5). Second, with these same three wideband sensors for the near bottom edge source, the signals responded most strongly in the A_0 mode. For this source depth, Fig. 7 shows that there were two regions of most intensity in the A_0 mode for the signals from the WB #1 and WB #2 sensors, and only one lower frequency region for the signals from the FHWA sensor.

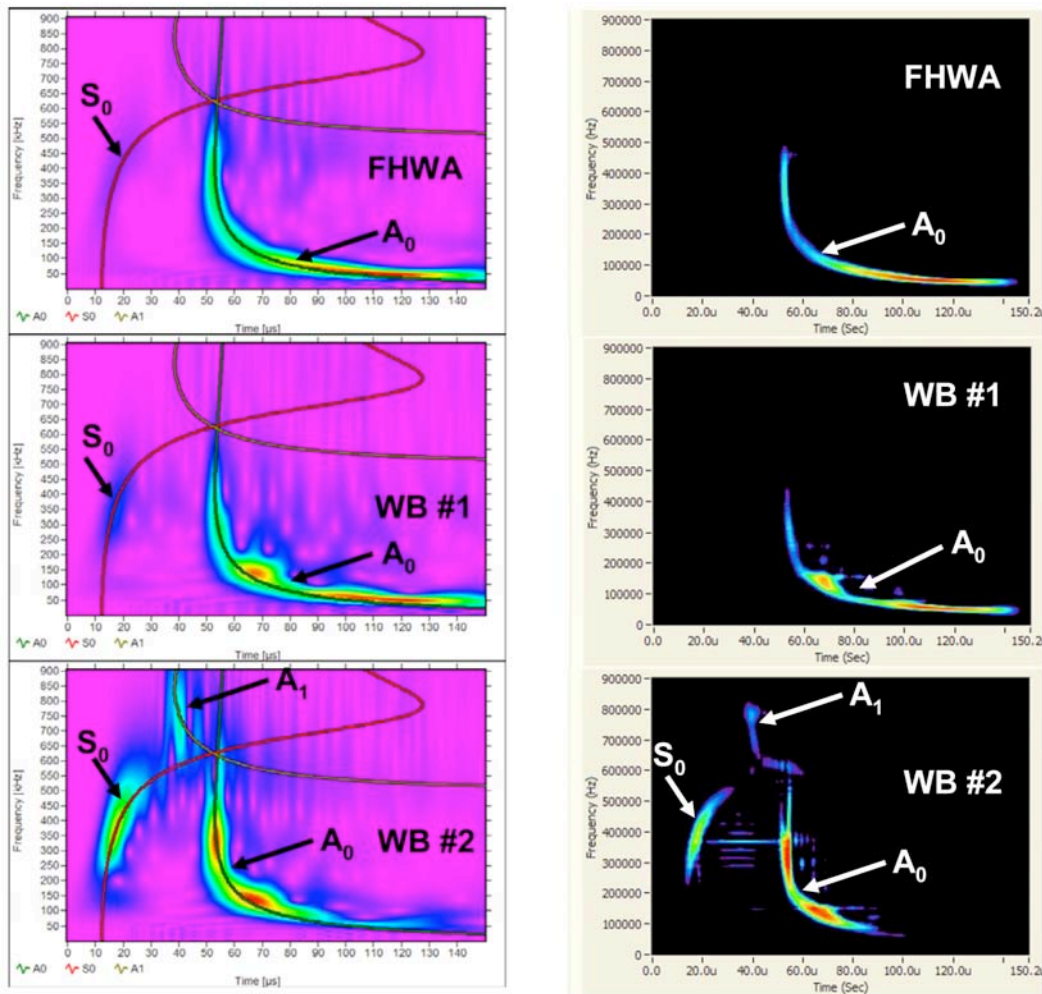


Fig. 7. WT (left column) and CWD (right column) of signals (Fig. 3) resulting from PLB near the bottom edge of the plate sensed by wideband sensors at a propagation distance of 305 mm.

Examination of the resonant sensors WT results shown in Fig. 6 for the near mid-plane source position showed that the S_0 mode was dominant in the signals from each sensor. In addition the figure showed that there was a considerable difference in the dominant frequency within that mode for the different sensors. For the source position near the bottom edge, the A_0 mode dominated for all the resonant sensors, as can be observed in Fig. 8. Again there was a wide range in the most dominant frequency within the mode. When the WT results for the different resonant sensors were examined in more depth, it was found that not only are there different frequencies within the modes more intense than those that were intense for the wideband sensors, but there is evidence that points to resonances within the signals from these sensors. For example for the near mid-plane source, the Res #3 sensor result shows a time-extended high intensity region of the S_0 mode at about 150 kHz (see Fig. 6). This resonance was expected based on the characteristics of this sensor. Another example of such behavior was present in the WT results of the Res #1 sensor signal for the source near the bottom edge. In this case, there was an extended intense region at about 100 kHz, where the intense region starts at the A_0 mode curve and then continues with intensity (as time increases) at this same frequency (see Fig. 8). These examples of resonant behavior were not present in the wideband sensor results. For example in contrast to the Res #1 result, for the same near bottom edge source position, the FHWA sensor's intense region closely follows the A_0 mode curve (see Fig. 7).

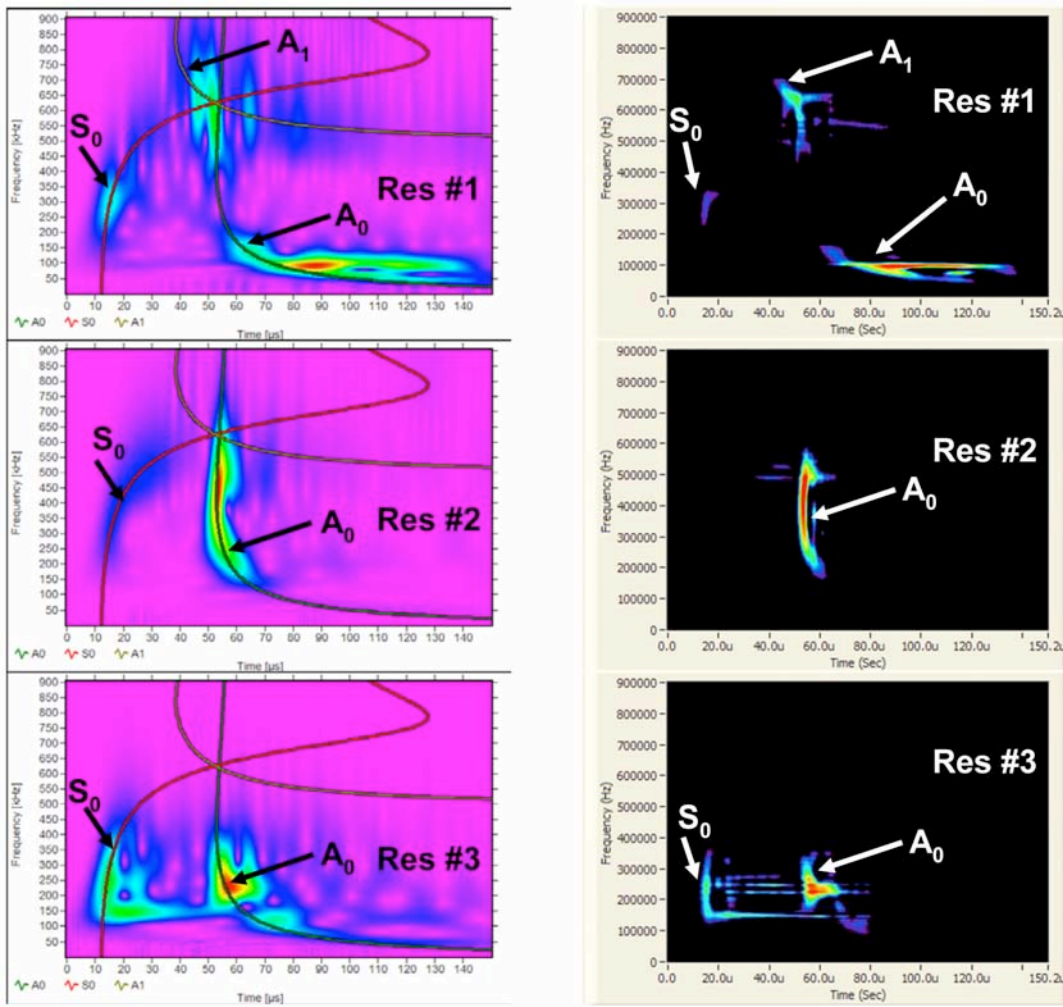


Fig. 8. WT (left column) and CWD (right column) of signals (Fig. 3) resulting from PLB near the bottom edge of the plate sensed by resonant sensors at a propagation distance of 305 mm.

Corresponding to the WTs of the signals from the different sensors for the two source positions, the CWD results from the sensor signals are shown in the right columns of Figs. 5 through 8 for the 305 mm propagation distance. Based on the adjacent WT results, the intense modes in the CWD were labeled as shown. The most intense regions for each sensor at each depth were similar to the WT results except for a slight difference in the CWD for the FHWA sensor for the in-plane source. In this case, there is an additional intense region within the S_0 mode at approximately 650 kHz in the CWD result. This region does not show as strongly in the WT result for this signal. Further contrasts between the CWD and the WT results will be discussed later in this paper.

The WT and CWD results were also obtained from the FEM-generated signals at the two depths. Figure 9 shows these results in the left column for the near mid-plane source results and in the right column for the near top surface results. Due to the fact that the FEM results represent those from a perfect wideband sensor, it makes the most sense to compare them with the experimental results from the wideband sensors. In this comparison, there was a significant difference for the near mid-plane result. For the FEM signals, the WT and CWD (respectively Figs. 9(a) and (c)) results show that the most intense region was in the low frequency region (centered around 60 kHz) of the A_0 mode. In the experimental case for the near mid-plane PLB, the most intense region, except for the FHWA sensor, was in the S_0 mode at both propagation distances

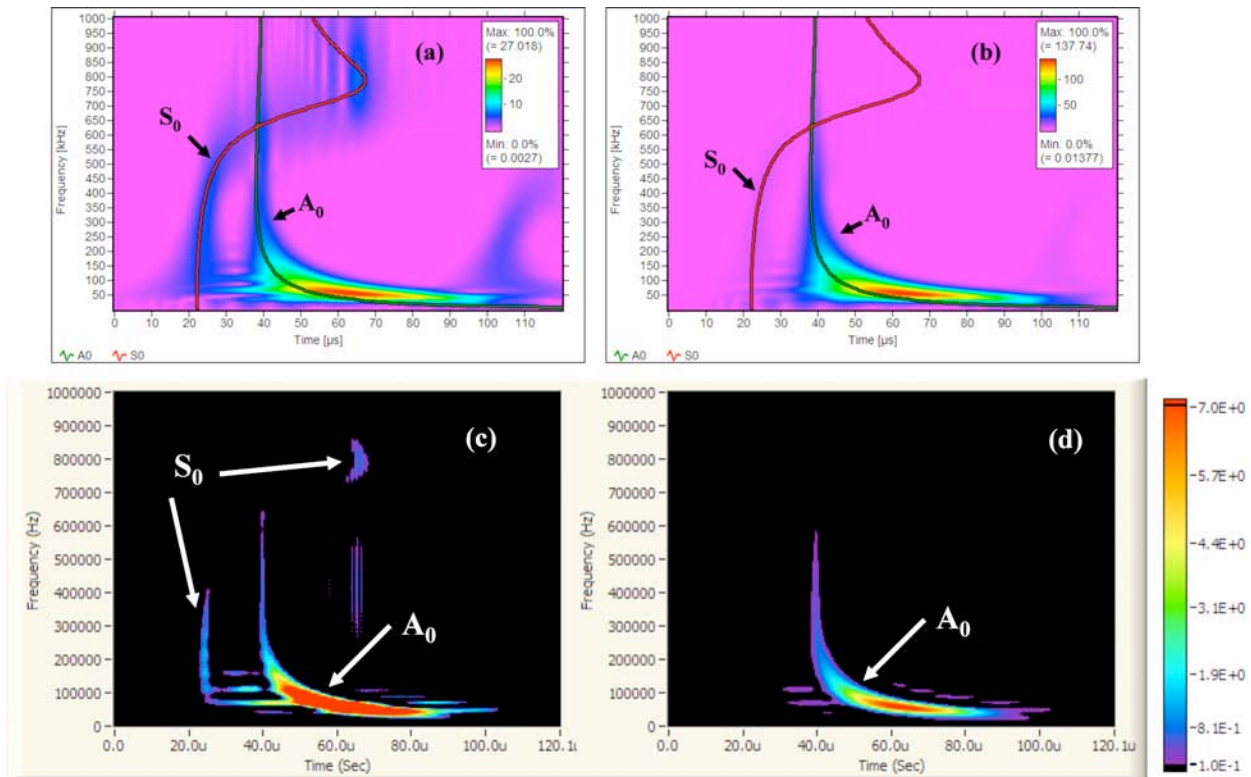


Fig. 9. WTs of finite element modeled signals shown in top row of Fig. 4; (a) near mid-plane source and (b) near top edge. CWD for the same two modeled signals; (c) and (d) correspond respectively to the signals resulting in the WTs in (a) and (b).

(results at 127 mm are not shown). For the FHWA sensor the most intense mode was the A_0 mode, but the intense frequency regions were at higher frequencies than with those from the FEM results. Specifically the FHWA signal had two nearly identical magnitude WT peaks at 291 kHz and 513 kHz at the 127 mm distance, and at the 305 mm distance the most intense WT peak was at 405 kHz. For the source position nearer a plate surface, the FEM result (Figs. 9(b) and (d)) was quite similar to the experimental wideband sensor results at both distances (results for the 127 mm distance are not shown) for the FHWA and WB #1 sensors, as shown in Fig. 7 at the 305 mm distance, with the most intense region being in the low frequency region centered around 60 kHz (at the 127 mm distance the results were similar, but are not shown). The WB #2 sensor had its most intense region at a higher frequency of the A_0 mode centered at about 138 kHz in the WT result. This observation indicates the WB #2 sensor has a poorer low frequency response compared to that of the other two wideband sensors.

Group Velocity Results for PLBs near the Mid-plane and Bottom-edge of the Plate

Because, as previously noted, the individual mode/frequency combinations with significant intensity are most easily characterized at the further propagation distance, the WTs and CWDs for the 305 mm propagation distance were used to define the intense mode/frequency combinations (i.e., the regions in the frequency versus time plane where the magnitudes of the WT or CWD were large at mode arrivals) to be used to determine mode arrival times at both propagation distances. It is worth noting that the frequency at the peak within the modes was not exactly the same for the WT and CWD for a particularly intense modal region. The process of determining of arrival times is demonstrated in Fig. 10 for a signal from the FHWA sensor for a near mid-

Table 2 Mode/Frequency combinations and group velocities for PLB near mid-plane.

Sensor	Mode/Frequency [kHz]	Magnitude as a percentage of maximum	Experimental group velocity [mm/ μ s]	Theory group velocity [mm/ μ s]	Signed percentage difference in velocity
FHWA	A ₀ /405	100	3.16	3.14	0.6
	A ₀ /463	100	3.03	3.14	-3.4
	S ₀ /627	55	2.78	2.91	-4.7
	S ₀ /661	93	2.56	2.46	4.1
WB #1	S ₀ /351	100	5.08	4.99	1.8
	S ₀ /371	100	4.91	4.93	-0.4
	A ₀ /141	62	2.80	2.85	-1.7
	A ₀ /146	36	2.80	2.87	-2.5
	A ₀ /60	61	2.34	2.26	3.6
	A ₀ /61	36	2.26	2.30	-1.9
WB #2	S ₀ /375	100	4.95	4.92	0.7
	S ₀ /397	100	4.89	4.84	0.9
Res #1	S ₀ /306	100	5.37	5.12	5.0
	S ₀ /307	83	5.44	5.11	6.5
	S ₀ /441	77	4.49	4.63	-3.0
	S ₀ /517	71	4.32	4.13	4.5
Res #2	S ₀ /510	100	4.04	4.18	-3.3
	S ₀ /527	100	4.03	4.05	-0.4
	A ₀ /195	66	2.99	3.00	-0.5
	A ₀ /222	22	3.09	3.05	1.8
Res #3	S ₀ /147	100	5.40	5.35	1.1
	S ₀ /153	100	5.37	5.34	0.6
	S ₀ /252	94	5.25	5.22	0.5
	S ₀ /251	98	5.26	5.22	0.5

plane PLB. This figure shows the signal, the CWD and WT, and the magnitude versus time of both the CWD and the WT coefficients for the 405 kHz frequency band. The time of the maximum magnitude peak was used to define the arrival time of the A₀ mode in this case. Using the differences in the arrival times (since the signals from the two sensors had a common trigger) an experimental group velocity was calculated based on the difference in propagation distance of 178 mm. Table 2 summarizes the more intense mode/frequency combinations and their relative magnitude (from the 305 mm results) at the mode arrival along with the calculated experimental group velocity. The relative magnitude was calculated based on the maximum frequency/time intensity for the whole signal. In addition, the table shows the theoretical group velocities (from the data shown in Fig. 1) and a sign-based percentage difference of the experimental velocity relative to the theoretical one. In the table, there are two lines for each mode/frequency case. The first line gives the WT results, and the second line gives the associated CWD results for each sensor and mode/frequency case. When the local maximum of an intense frequency was near the 50 kHz filter's high-pass frequency, a frequency of 60 kHz was used for the WT and 61 kHz for the CWD. Only the intense mode/frequency combinations that had magnitude maxima for the same mode at both propagation distances at the frequency determined from the 305 mm distance data were considered. Also, the table does not include intense frequencies where the mode could not be clearly identified.

Following the same procedures used to create Table 2, Table 3 was created for the PLB source near the bottom edge of the plate. In both tables, only the fundamental modes appear.

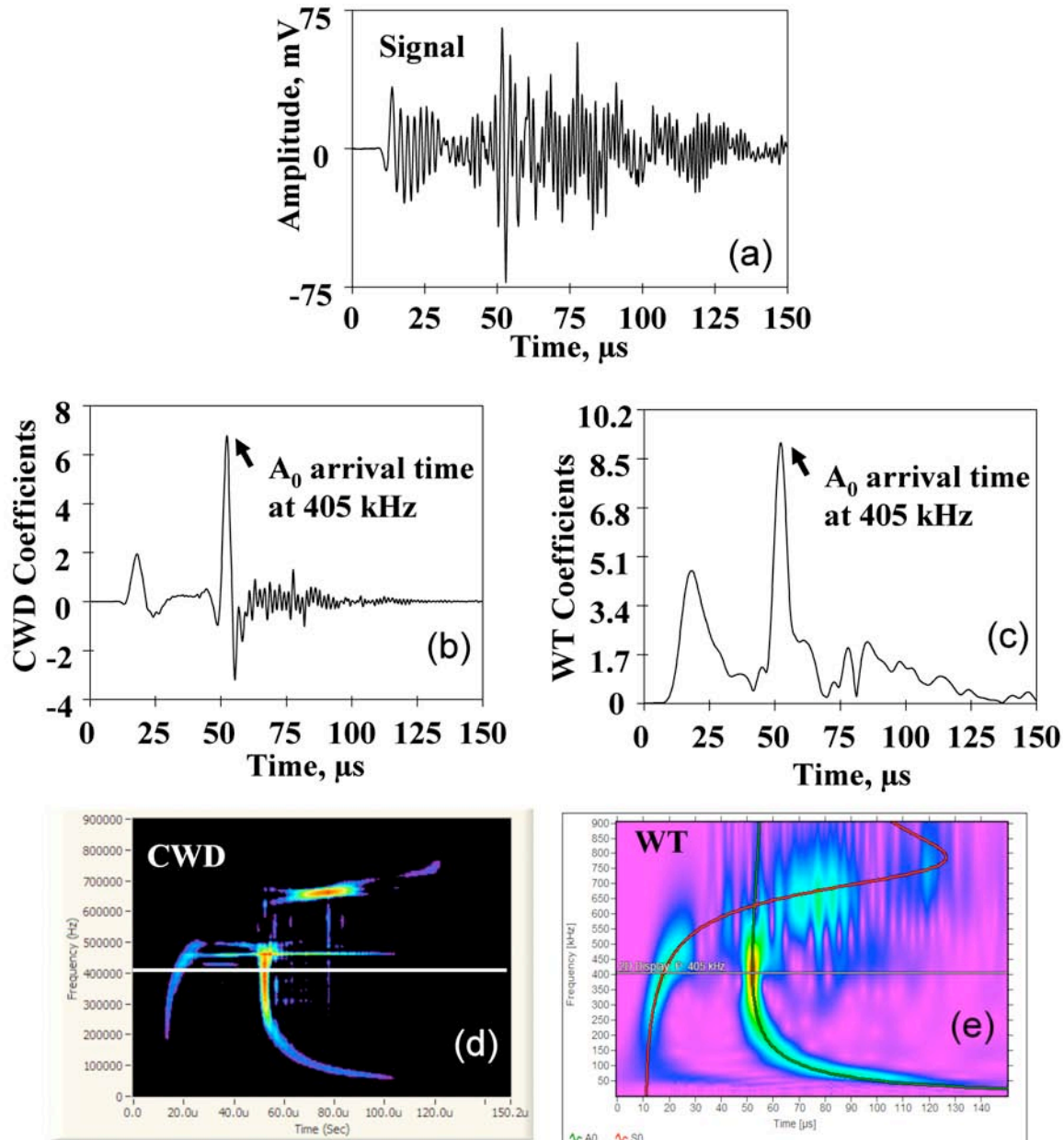


Fig. 10. Illustration of determination of the A_0 mode arrival times for the signal (FHWA sensor for near mid-plane PLB; propagation distance 305 mm) shown in (a). The CWD and WT coefficients at 405 kHz are shown respectively in (b) and (c). The full CWD and WT are shown respectively in (d) and (e) with a line at 405 kHz.

Observations Based on Tables 2 and 3

In spite of the dominance of a particular mode for each of the two source positions, Tables 2 and 3 show that the frequencies that were intense within each mode varied widely over the six different sensors. Interestingly, this was the case even for the wideband sensors (for the near mid-plane source and the S_0 mode, the minimum and maximum intense frequencies were 60 kHz and 661 kHz; for the source near the bottom edge and the A_0 mode these maximum and minimum frequency values were respectively at 60 kHz and 384 kHz). With the resonant sensors, the range of intense S_0 mode frequencies varied from 147 kHz to 527 kHz for the near mid-plane source, and the range of A_0 mode frequencies varied from 93 kHz to 466 kHz for the

near bottom edge source. It seems most likely that these wide variations in the intense frequencies within the modes were due to both the intense mode/frequency combinations in the generated Lamb waves and the details of the different sensor's response sensitivity as a function of frequency. Thus, the observed intense mode frequencies do not in general directly correlate with the sensor resonant frequencies.

Table 3 Mode/Frequency combinations and group velocities for PLB near bottom edge.

Sensor	Mode/Frequency [kHz]	Magnitude as a percentage of maximum	Experimental group velocity [mm/ μ s]	Theory group velocity [mm/ μ s]	Signed percentage difference in velocity
FHWA	A ₀ /60	100	2.23	2.26	-1.6
	A ₀ /61	100	2.25	2.30	-2.2
	A ₀ /384	64	3.16	3.14	0.6
	A ₀ /346	45	3.15	3.13	0.6
WB #1	A ₀ /60	100	2.32	2.26	2.4
	A ₀ /61	100	2.27	2.30	-1.3
	A ₀ /141	96	2.80	2.85	-1.7
	A ₀ /146	88	2.78	2.87	-3.1
	A ₀ /288	58	3.09	3.11	-0.7
	A ₀ /317	38	3.11	3.12	-0.5
WB #2	A ₀ /138	100	2.88	2.83	1.6
	A ₀ /151	100	2.87	2.88	-0.2
	A ₀ /330	99	3.21	3.13	2.6
	A ₀ /349	100	3.17	3.13	1.2
Res #1	A ₀ /93	100	3.77	2.59	45
	A ₀ /100	100	3.41	2.64	29
	S ₀ /300	43	5.39	5.14	4.8
	----	----	----	----	----
Res #2	A ₀ /441	100	3.16	3.14	0.9
	A ₀ /466	100	3.16	3.16	0.7
Res #3	A ₀ /231	100	3.08	3.06	0.8
	A ₀ /239	100	3.07	3.07	0.3

Since the time domain signals processed by both the CWD and the WT were identical, it was not surprising that there were related pairs (except for one case) of intense regions as shown in Tables 2 and 3. In the single case in Table 3 for the Res #1 sensor, the CWD did not have the same peak modal location at both propagation distances; hence no result is included in the table in this case. Examination of these pairs shows that generally the CWD gives a higher frequency for the frequency of the intense regions of the modes (ignoring the cases of the arbitrarily selected frequencies of 60 and 61 kHz). This result seems to be consistent with those of the following experiment. Three sine waves of frequencies 60 kHz, 270 kHz and 522 kHz (all with the same amplitude, with a 0.1 μ s time step) were superimposed, and then the WT and CWD were applied. For the results shown in Fig. 11, the CWD band magnitudes (that included the sine wave frequencies) expressed as a percentage from low to high frequency were 100, 100 and 67. On the other hand, the WT magnitudes show an increasingly greater reduction at the higher frequencies, since their respective values were 100, 48 and 36. Thus the magnitude reduction of higher frequencies does not appear in the CWD result to the same large degree as with the WT. Also as can be clearly seen in Fig. 11, the WT results show that the single frequency input signal has intensity that increasingly spreads over a wider frequency range in the WT result as the

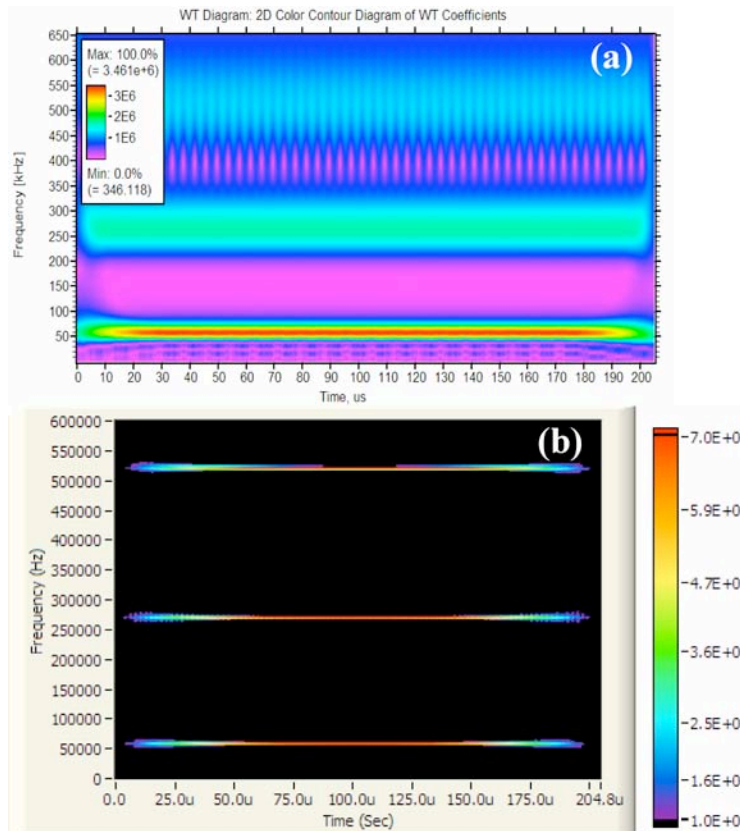


Fig. 11. Results for WT (a) and CWD (b) both applied to signal comprised of superposition of sine waves of equal amplitude at frequencies of 60 kHz, 270 kHz and 522 kHz.

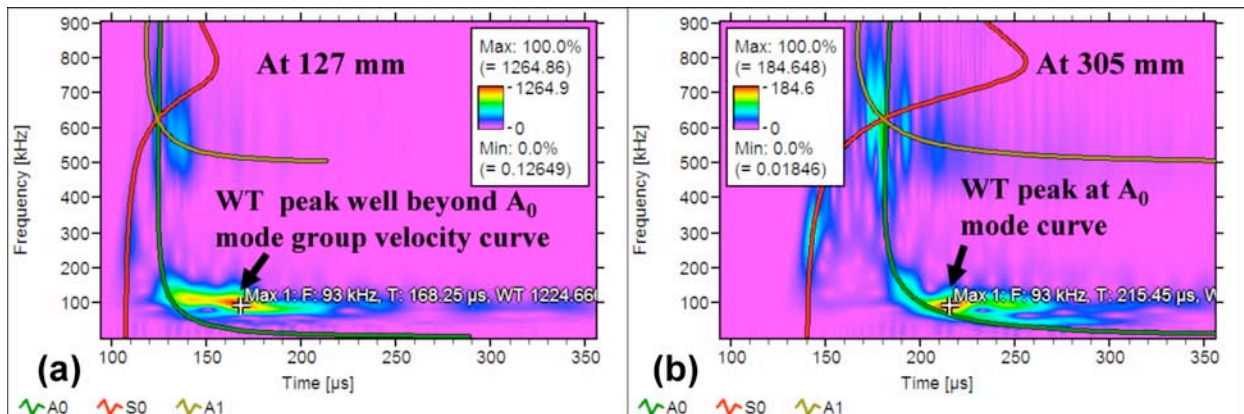


Fig. 12. Illustration of cause of group velocity error with resonant Res #1 sensor at 93 kHz for PLB source near bottom edge. Shows in (a) the peak is not in the same relation to the A₀ group velocity curve as shown in (b).

signal frequency increases. In summary, this contrast between the CWD and the WT results can be expected to result in the CWD frequency of the pair being higher at higher frequency intense modal regions.

The group velocity results in Tables 2 and 3 show that with the wideband sensors, the difference between the experimental velocity and the theoretical values was less than 5%. For the resonant sensors, the difference between experiment and theory was less than 6.5%, with one exception. In this case (Res #1 sensor for the near bottom edge source), the most intense region of

the A_0 mode had large differences from the theoretical group velocity (WT – 45 % and CWD – 29 %). Using the WT result, Fig. 12 illustrates the cause of this large difference. This figure shows that at the farther distance the WT peak at 93 kHz was quite close to the A_0 curve, but due to a resonance at the shorter distance, the WT peak was well beyond the A_0 curve even though the intensity began just beyond the A_0 curve. It should be noted that the error with the CWD was still large, but it was considerably less. This result may be due to sharper peaks in time in lower frequency bands with the CWD compared to the WT, as will be demonstrated later in this paper. Such large differences in the experimental versus theoretical group velocities, implies that if arrival times were used from this intense region, poor results would be obtained for calculated source locations.

The results in the tables contribute to a false impression relative to the use of resonant sensors. The reason is that a number of intense regions for these sensors were not included in the table. They were not included due to several facts: (i) the mode associated with the frequency of the intense region changed between the 305 propagation distance and the 127 mm distance; (ii) there was an intensity peak near the intersection of all three modes (at about 625 kHz), and the location of the peak magnitude changed in time relative to this intersection at the two distances; and (iii) the mode of the intense frequency peak could not be determined. These three characteristics were not observed with the wideband sensors. Figures 13 through 15 illustrate some of these aspects with the WT results shown at the two propagation distances. Figure 13 demonstrates a case where the mode corresponding to the peak WT coefficient at a resonant frequency changed when the propagation distance changed. At the 127 mm distance, the peak at 147 kHz was near the A_0 mode. While at the 305 mm distance, the peak was near the S_0 mode. Thus, the signals from the Res #3 sensor at this intense frequency did not provide arrival times at a fixed group velocity for the PLB source near the bottom edge.

Another example with the resonant Res #1 sensor is shown in Fig. 14 for a PLB near the mid-plane. In this case, the WT coefficient peak at 594 kHz changed its relationship in time relative to the intersection of the three modes (A_0 , A_1 and S_0) at the two different propagation distances. This change again would yield arrival times from the intense region that did not correspond to a single group velocity at different propagation distances.

A final example to demonstrate the potential issues is shown in Fig. 15. In this case for the Res #1 sensor, the mode of the WT coefficient peak at 573 kHz changed from the A_1 mode at 127 mm to the A_0 mode at 305 mm. This change for a PLB near the bottom edge would not result in peak-determined arrival times at this frequency for the same mode and group velocity when the propagation distance changed. We note that the CWD results were similar for these three examples.

Since the intense mode/frequency combinations generated by AE sources in plates vary as a function of source depth [1] and plate thickness [11], it is not possible to predict ahead of time when a resonant sensor will yield poor results in the determination of accurate arrival times at a particular intense frequency. One resonant sensor (Res #2) yielded accurate group velocity results for the sources at both source depths. This result was likely due to the fact that the intense frequencies were located at points where there was a significant difference in the group velocities of the two fundamental modes, and these frequencies were away from the intersection of all three modes. Thus, the results of the current experiment imply that if one is planning to use time/frequency analysis to obtain accurate mode arrival times, it does not make sense to use resonant sensors unless some significant experimental effort is expended to determine the

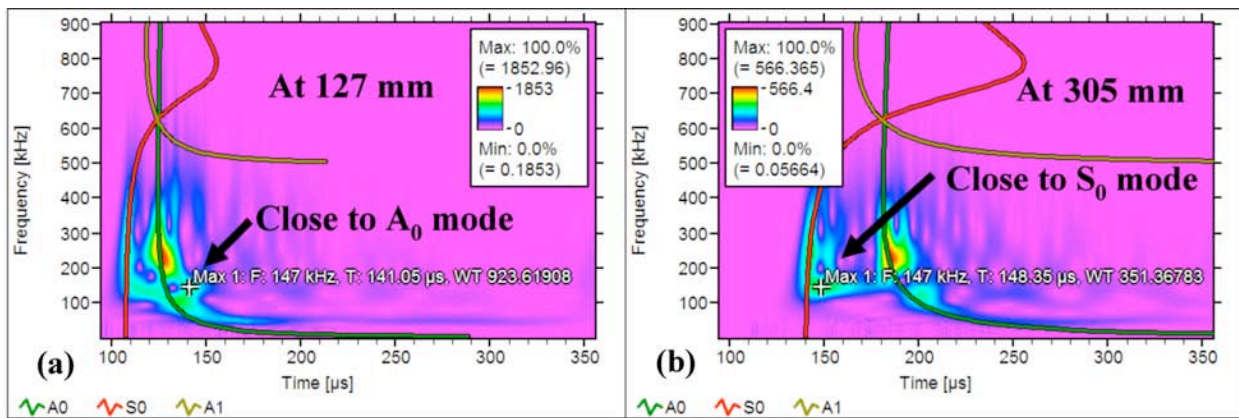


Fig. 13. Example of nearest mode at 147 kHz peak changing with propagation distance for resonant Res #3 sensor for PLB near bottom edge.

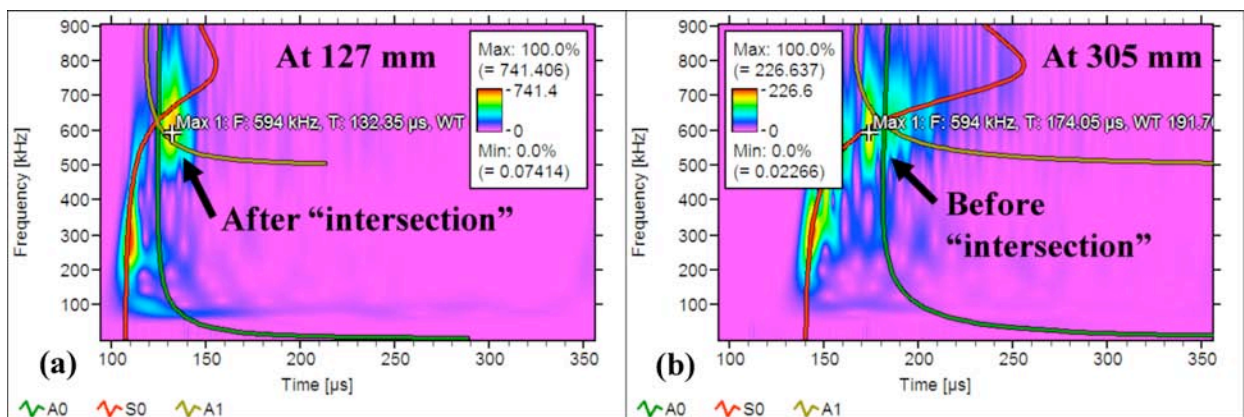


Fig. 14. Example of mode changing relationship in time to intersection of three modes at 594 kHz peak for resonant Res #1 sensor for PLB near mid-plane.

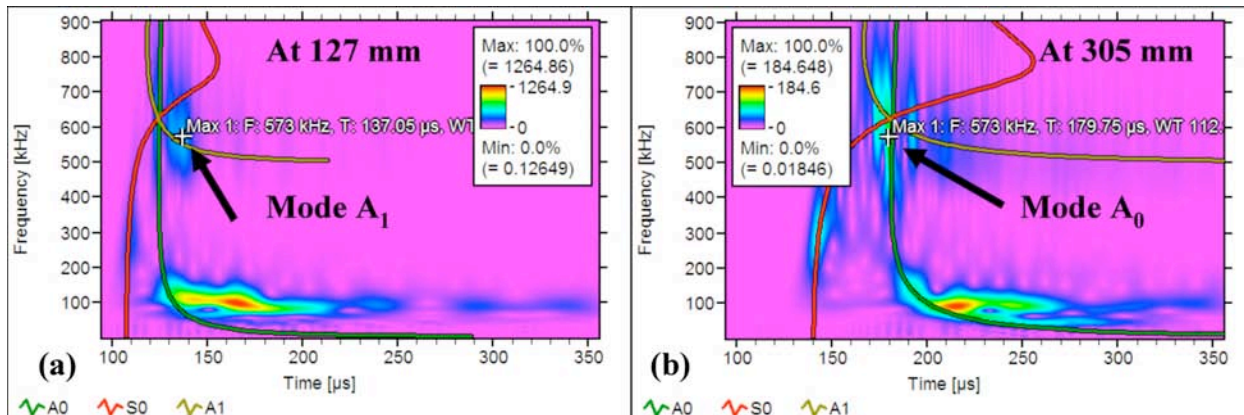


Fig. 15. Example of mode of peak changing with propagation distance at 573 kHz with resonant Res #1 sensor for PLB near bottom edge.

frequencies that should not be used. But, if such effort is invested, then the results from resonant sensors can be used to obtain accurate arrival times that correspond to a single group velocity. Thus, accurate source locations could be calculated by use of resonant sensors with their typical advantage in sensitivity. This situation would enhance AE nondestructive examinations that depend on identifying clusters of events originating from a flaw in a structure that does not have edge reflections (for example a large diameter sphere).

Potential Frequencies for the Sensors for the 3.1 mm Thick Plate

Based on the results in Tables 2 and 3 and the discussion relative to the frequencies that were not included in the table, Table 4 provides potential frequencies (really the high-end frequency of a frequency band) to use with the WT or CWD to obtain accurate arrival times from real AE signals with the different sensors in a 3.1 mm thick aluminum plate. For each sensor, the first line in the table provides a frequency for WT analysis and the second line gives one for CWD analysis. The suggested frequencies are those that were the most intense in the case of the wideband sensors. In the case of the resonant sensors, as can be seen from Tables 2 and 3 the suggested frequencies were not always the most intense for the Res #1 and Res #3 sensors. This table also suggests the frequencies to avoid to prevent obtaining inaccurate arrival times that do not correspond to the same mode arrivals at different propagation distances. Since there are two frequencies (except for one CWD case) associated with each sensor (for the two different depth regions), for real AE testing it will be necessary to select the best frequency for each AE event and to verify that the mode of the peak magnitude arrival time corresponds to the expected one at that frequency. Previous modeling work [14] has shown that the ratio of the peak magnitudes at the two frequencies can be used to choose which frequency will provide the best signal-to-noise ratio. In addition as shown in previous work [15], the group velocities from the two modes at that frequency can be used to verify the mode when source location calculations are made with each group velocity (for the different source depths) using the determined arrival times. The velocity that provides the smallest “Lucy” value [15] identifies the mode and results in the most accurate source location. It is interesting to note in Table 4, that the two resonant sensors, which have frequencies to avoid, result in the frequencies from the intense signal region of the WT and CWD being relatively close to each other, whereas, with the wideband sensors, the paired intense frequencies always resulted in the CWD frequency being significantly larger than the WT frequency.

Table 4 Suggested frequencies for arrival times from the WT and/or CWD.

Sensor	Frequency [kHz], mode for near mid-plane source	Frequency [kHz], mode for near plate surface source	Frequency [kHz] to avoid for near mid-plane source	Frequency [kHz] to avoid for near plate surface source
FHWA	405, A ₀	60, A ₀	----	----
	463, A ₀	61, A ₀	----	----
WB #1	351, S ₀	60, A ₀	----	----
	371, S ₀	61, A ₀	----	----
WB #2	375, S ₀	138, A ₀	----	----
	397, S ₀	151, A ₀	----	----
Res #1	306, S ₀	300, S ₀	594	93, 573
	307, S ₀	----	610	100, 581
Res #2	510, S ₀	441, A ₀	----	----
	527, S ₀	466, A ₀	----	----
Res #3	252, S ₀	231, A ₀	----	147
	251, S ₀	239, A ₀	----	151

On the Use of the WT and CWD to Determine Arrival Times for Thicker Plates

If one considers the situation for thicker plates where more modes will be present (in the normal frequency range used in AE) and will be in closer proximity in time and frequency, the

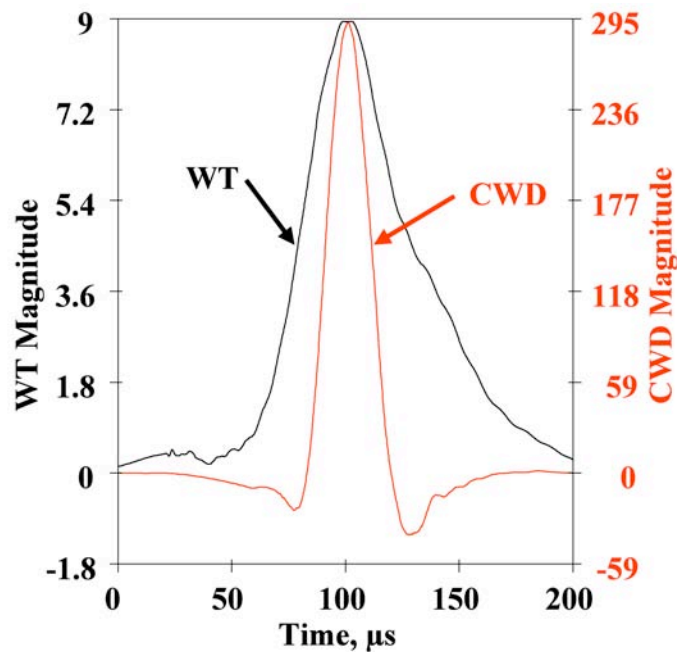


Fig. 16. Magnitude of CWD and WT coefficients versus time for nominal 60 kHz band, FHWA sensor and near bottom edge source for propagation distance of 305 mm.

accuracy of the mode arrival-time results determined with the WT versus those determined with the CWD may be different. In these thicker plates in the typical frequency range for AE monitoring, it may be expected that the CWD will be more likely to provide results not determined by a combination of modes. This result is likely to be due to the sharper peaks of mode arrivals with CWD as a function of time at lower frequencies, as shown in Fig. 16. In this case for a near bottom edge PLB source with the signal from the FHWA sensor, the CWD peak corresponding to the arrival of the A_0 mode is sharper than that from the WT for the same signal. Thus there would be less opportunity for adjacent mode arrivals at this frequency to result in a peak magnitude from more than one mode when the CWD is used.

Further, the potential superiority of the CWD in this plate may be due to sharper peaks at a fixed signal time as a function of frequency at higher frequencies. As an example one can consider the related pair of intense arrivals from a near mid-plane PLB source and the FHWA sensor data at a propagation distance of 305 mm. In this case, the WT magnitudes from the same arrival time at 10 % above and 10 % below the peak frequency of 627 kHz (S_0 mode) were respectively 90 % and 88 % of the peak magnitude at the peak frequency. In contrast, the CWD respective magnitudes from the same arrival time at 10 % above and 10% below the peak frequency of 661 kHz (S_0 mode) were respectively 4 % and 21 % of the peak magnitude at the peak frequency.

Finally, based on the current thin-plate results, it may be expected with resonant sensors that there will be a set of frequencies to avoid in thick plates.

Conclusions

In the case of a relatively thin and large plate:

- Use of either the WT or the CWD allows easy determination of the arrivals of the two fundamental modes with both the resonant and wideband sensors used in this study.

- Even though the different sensor models responded to nearly the same waves, there was a wide range of intense frequencies for the signals from PLBs at each of the two source depths.
- The experimental group velocities as determined with all the sensors (with one exception) were close to the theoretical values (less than 6.5 % difference) when certain intense frequencies of the resonant sensors were not used to obtain arrival times and group velocities.
- Cases that were ignored with the resonant sensors primarily dealt with an inability to identify any precise and/or consistent mode arrival at each propagation distance.
- Typically the high intensity regions determined with the CWD occurred at a higher frequency compared with the WT-determined frequencies for each intense modal region. This result is consistent with the fact that at higher frequencies the WT (in contrast to the CWD) spreads the intensity from a single frequency signal into adjacent frequency regions.
- At lower signal frequencies, the CWD magnitude results had sharper peaks (as a function of time) at mode arrivals than the WT. In addition, it also had sharper peaks (as a function of frequency) than the WT at higher frequencies.
- It might be expected that the CWD will provide more accurate arrival time results than the WT for thicker plates when more modes will be present and will be closer in time to each other.

Acknowledgement

The loan of the Res #1 sensors from Prof. K. Ono was much appreciated.

References

1. M. A. Hamstad, A. O’Gallagher and J. Gary, J. of Acoustic Emission, **20**, 2002, 39-61.
2. M.A. Hamstad, J. Gary and A. O’Gallagher, J. of Acoustic Emission, **20**, 2002, 62-82.
3. K. S. Downs, M. A. Hamstad and A. O’Gallagher, J. of Acoustic Emission, **21**, 2003, 52-69.
4. M.A. Hamstad, K.S. Downs and A. O’Gallagher, J. of Acoustic Emission, **21**, 2003, 70-94 and A1-A7
5. M. A. Hamstad and A. O’Gallagher, J. of Acoustic Emission, **22**, 1-21, A1-A7, 2004.
6. M.A. Hamstad and A. O’Gallagher, J. of Acoustic Emission, **23**, 2005, 1- 24.
7. M.A. Hamstad, *Advanced Materials Research*, **13-14**, 2006, 61-67.
8. M.A. Hamstad, J. Acoustic Emission, **25**, 2007, 92-106.
9. M.A. Hamstad and C.M. Fortunko, *Nondestructive Evaluation of Aging Bridges and Highways*, Steve Chase, Editor, Proc. SPIE 2456, pp. 281-288, 1995.
10. M.A. Hamstad, Wood and Fiber Science, **29** (3), 1997, 239-248.
11. M. A. Hamstad, J. Gary and A. O’Gallagher, J. of Acoustic Emission, **16**, (1-4), 1998, S251 to S259.
12. Vallen, J., *AGU-Vallen Wavelet transform software* version R2007.0309 and *Vallen Dispersion software* version R2006.1024, Vallen-Systeme GmbH, Icking, Germany (2007).
13. LabVIEW, *Signal Processing Toolkit*, Version 7.5, National Instruments, Austin, TX.
14. M.A. Hamstad, ICAE-6, *Advances in Acoustic Emission*, 2007, pp. 247-252
15. M.A. Hamstad, J. Acoustic Emission, **25**, 2007, 194-214.

A COMPARISON OF AE SENSOR CALIBRATION METHODS

JIRI KEPRT and PETR BENES

Brno University of Technology, Department of Control and Instrumentation, Kolejní 2906/4,
Brno, 612 00, Czech Republic

Keywords: AE sensor calibration, Reciprocity calibration, Step force calibration, Uncertainty

Abstract

The paper reviews the background of the primary calibration of acoustic emission (AE) sensors and the determination of uncertainty in the calibration. The main sources of uncertainty in practical usage of calibration results are discussed. The comparison of the results of the reciprocity primary calibration, step-force and reciprocity calibration with broadband-pulse excitation method is presented. The shape of calibration characteristics corresponds well up to 300 kHz. The calculation of the uncertainty in all the calibration methods is described. The problem of propagation of uncertainty in the fast Fourier algorithm was solved. Uncertainty of measurement by primary calibration is determined and the influence of selected sources of uncertainty for each used method of calibration is presented and practically measured results are discussed. Piezoelectric AE sensor PAC UT1000 was used as the sensor under test. The big influence on uncertainty in calibrations was the influence of remounting sensors and influence of precision of measuring device. This influence is possible to suppress by correct and precise mounting of the sensors and using of more accurate measuring device with high resolution.

AE Sensors

Transducers used for AE measurement are in general sensitive to motion normal to the surface, to which they are attached. Typically, AE transducers are sensitive to frequencies above 100 kHz. Resonant transducers are highly sensitive to a narrow frequency range, which must be carefully selected depending on the application. Resonant transducers in the range of 150 to 300 kHz are probably the most widely used. The highest frequencies likely to be of interest to users of AE transducers are in the range from 800 kHz to 1 MHz.

There are several ways how this transduction can be achieved. The piezoelectric effect, capacitance methods and optical interferometry are common techniques used for the detection of AE signals. Piezoelectric devices offer the greatest sensitivity and thus they are the most widely used type of transducer in AE applications. Interferometers and capacitance transducers are often used as reference sensors in the calibration of piezoelectric AE transducers.

AE Sensor Calibration

A main problem of the calibration is to find the characteristic of the transducer. A frequency response of a specific sensor in the mechanical input quantity (velocity, displacement) is the most common result of calibration. Output quantity of calibration is voltage relate to unit of mechanical input. The absolute value of input quantity and its shape has to be known for primary calibration. Good metrology of the AE calibration method is necessary to be able to compare the results of calibration made by other laboratories or to compare the effects of aging, thermal cycling and so on.

Step-function calibration

ASTM E1106 [1] and ISO 12713 [2] outline a step-force method for primary calibration of AE sensors. The basis for the step function force calibration is that known, well-characterized displacements can be generated on a plane surface of a test block. A step function force applied to a point on one surface of the test block initiates an elastic disturbance that travels through the block. In general it is possible to use configuration of sensor for surface calibration and for through-pulse calibration.

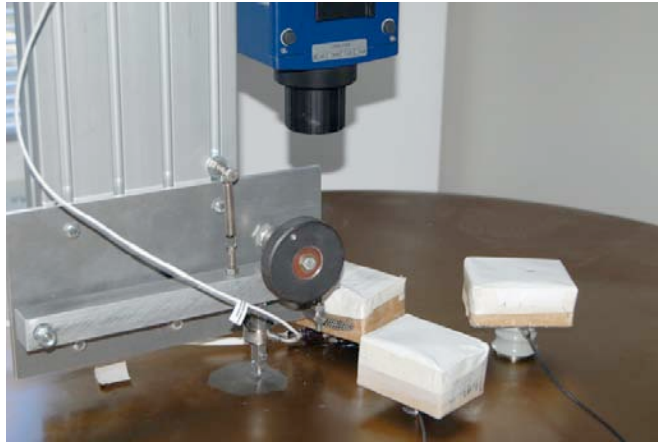


Fig. 1 Setup for step-function calibration.

It uses a standard reference capacitance transducer and the step-force is generated by the fracture of a glass capillary. The response of the sensor being calibrated to the step-force source is then compared with the reference transducer, which measures the surface displacement due to the elastic surface waves. The displacement at the position of the reference transducer can also be calculated using elastic theory – Pekeris’s solution of Lamb’s problem. The surface motion on the transfer block, determined using either technique, is the free motion of the surface and not the loaded surface displacement, under the transducer being calibrated. The loading effect of the sensor being calibrated, therefore, affects the measurement being made and thus becomes part of the calibration.



Fig. 2 Workspace for primary calibration.

The measured data are used to calculate a fast Fourier transform to determine values of the spectra from unknown and reference sensor. The response of the transducer under test is as follows:

$$D(f_m) = \frac{U(f_m)}{S(f_m)} \quad (1)$$

where $U(f_m)$ is spectrum from unknown sensor and $S(f_m)$ is spectrum from standard sensor or from solution of Lamb's problem.

It is generally assumed that a transducer has only normal sensitivity because of its axial symmetry (an assumption that may not be justified). Calibration by the surface pulse technique for a transducer having significant sensitivity to tangential displacement will be in error, because the surface pulse from the step force contains a tangential component approximately as large as the normal component [3].

Reciprocity calibration

NDIS 2109 [4] outlines reciprocity calibration. Reciprocity calibration works on reciprocity theorem that is known from electrical circuits. This principal can be use for electromechanical system and makes relation between transition of the sensor acting as source and later as receiver. Reciprocity applies to a category of passive electromechanical transducers that have two important characteristics - they are purely electrostatic or purely electromagnetic in nature and they are reversible – can be used as either a source or a receiver of mechanical energy. This category includes all known commercial AE transducer without preamplifiers [3].

The input current and reception signal voltage for tone bursts of varying frequency are established for each pair together with the reciprocity parameter, allowing each transducer to be calibrated by measuring electrical signals only. The transducer characteristics are defined as the transmission voltage response in the transmitter configuration and the free-field voltage sensitivity in the receiver configuration.

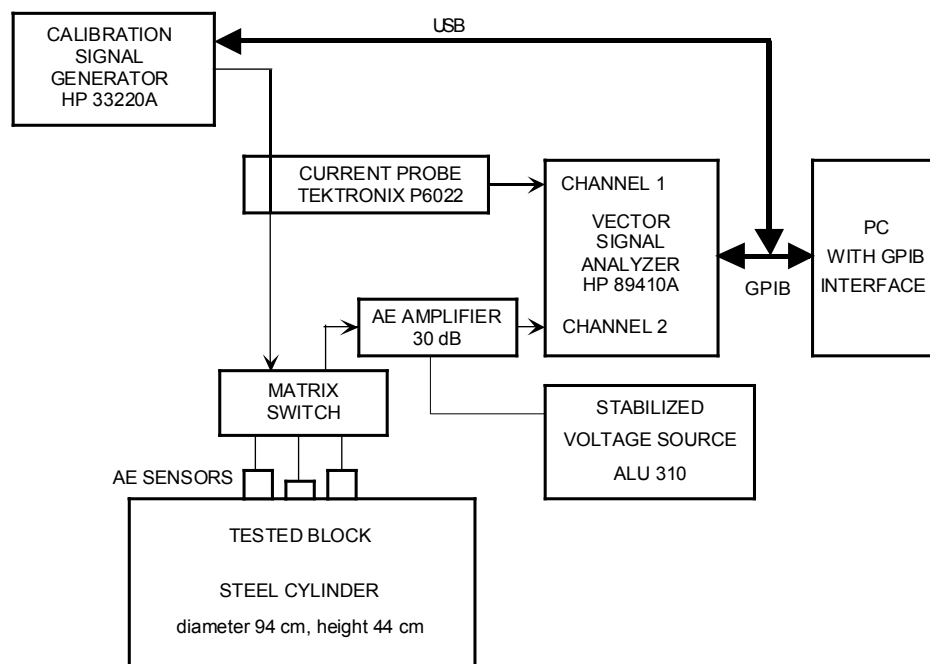


Fig. 3 Schema of workspace for reciprocity calibration with HP 89410A.

The primary advantage of the reciprocity calibration technique is that it avoids the necessity of measuring or producing a known mechanical displacement or force. All of the basic measurements made during the calibration are electrical. It is important to note that the mechanical transfer function or Green function for the transmission of signals from the source location to receiver location must be known. This function is equivalent to the reciprocity parameter, that describes a transfer function of a Rayleigh-wave and it takes into account the frequency of the Rayleigh wave and the material properties of the propagating medium. It is the frequency domain representation of the elasticity theory solution [3]. Equation 2 shows the calculation of frequency response for sensor 2.

$$|F_2(f)| = \sqrt{\frac{1}{|H(f)|} \frac{|U_{12}(f)| |U_{23}(f)| |I_{31}(f)|}{|I_{12}(f)| |I_{23}(f)| |U_{31}(f)|}} \quad (2)$$

U : voltage [V], I : current [A], H : reciprocity parameter [$\text{m}\cdot\text{s}^{-1}\cdot\text{N}^{-1}$] according to Hatano [5].

Reciprocity calibration with broadband impulses

This method is based on a method of reciprocity calibration, modified by Goujon and Baboux [6]. Their method was supplemented by using more than one excitation and final characteristics were calculated from multiple measured characteristics.

The experimental setup is similar to usual reciprocity calibration. When the sensors are working as transmitters, the transducers are driven with a short-pulse excitation (single-period sinusoid or single period Gaussian). The excitation of sensor is provided for example at 100 kHz, 200 kHz ... 1 MHz. The voltages and currents required for reciprocity calibration by Hatano [5] are then calculated from the fast Fourier transforms of the signals recorded with high sampling frequency. Sensitivities of the sensor are calculated for each excitation. The final characteristics for each sensor is calculated point to point by weighted mean of sensitivities of the two nearest excitation frequency to the calculated point. For example the final point of sensitivity at 110 kHz was calculated as $0.1 * 110 \text{ kHz (200 kHz excitation)} + 0.9 * 110 \text{ kHz (100 kHz excitation)}$.

This broadband excitation allows a better discrimination between the direct signal and the echoes against the borders [6]. This method of the calibration is much faster than method according to standard reciprocity calibration and can be used to proof quality of sensor's mounting on the surface before usual standard reciprocity calibration measurement.

Comparison of the results for different calibration methods is shown on Fig. 4. This figure shows three measured characteristics for an AE sensor, PAC UT1000, mounted on the surface of a steel block. The orange curve shows results from step-function calibration, the black from reciprocity calibration and the blue from reciprocity calibration with broadband-pulse excitation.

Analysis of Uncertainty in AE Sensor Calibration

Analysis of uncertainty in step function calibration

Calculations of determination of uncertainty for the step function calibration result from following basic equation for calculation of sensitivity of sensor:

$$U = \frac{FFT(U_{cal})}{FFT(U_{ref})} \quad (3)$$

U_{cal} is voltage of calibrated sensor [V], U_{ref} is voltage on reference sensor [V], or determined by calculation.

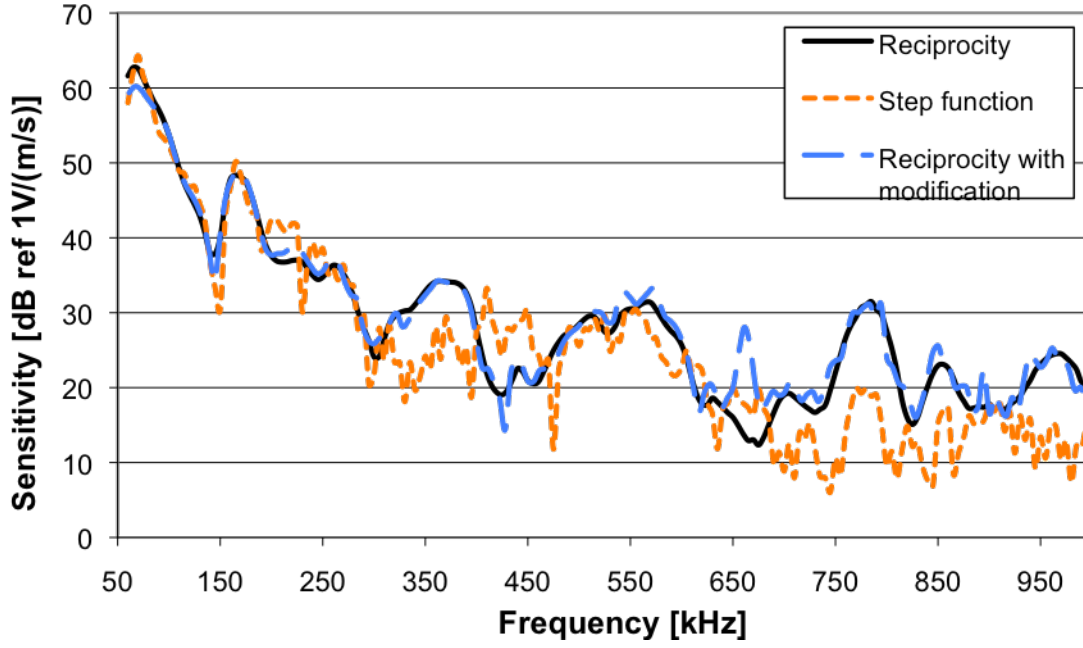


Fig. 4 Results of three methods of calibration of PAC UT1000.

Main problem was to determine the propagation of uncertainty in Discrete Fast Fourier Transform algorithm (FFT). The calculations follow [7]. Equation for FFT is

$$X(k) = \sum_{n=0}^{N-1} x(n) \cdot e^{-j\frac{2\pi}{N}nk} \quad (4)$$

General complex sequence $X(k)$ can be described as $X(k) = R(k) + j I(k)$. Spectrum modulus is calculated as:

$$M(k) = |X(k)| = \sqrt{R^2(k) + I^2(k)} \quad (5)$$

Amplitude of first frequency point

$$V_0 = M(0)/N \quad (6)$$

and subsequent points

$$V_{im} = 2M(i)/N \quad (7)$$

Uncertainty of modulus M can be determined [7] as:

$$U^2_{M(k)} = \begin{cases} N \cdot U_q^2 & \text{for } k = 0 \\ \frac{N}{2} \cdot U_q^2 & \text{for } k \neq 0 \end{cases} \quad (8)$$

The partial derivatives according all variable were calculated

$$\frac{\partial U}{\partial FFT(U_{cal})} = \frac{1}{FFT(U_{ref})} \quad (9)$$

$$\frac{\partial U}{\partial FFT(U_{ref})} = -\frac{FFT(U_{cal})}{FFT(U_{ref})^2} \quad (10)$$

The uncertainty of type A and B was calculated for calibrated sensor and following combined uncertainty

$$u_c^2(y) = \left(\frac{2}{N} u_{ref}^2 \right) \cdot \left(\frac{1}{FFT(U_{ref})} \right)^2 + \left(\frac{2}{N} u_{cal}^2 \right) \cdot \left(-\frac{FFT(U_{cal})}{FFT(U_{ref})^2} \right)^2 \quad (11)$$

Finally the expanded uncertainty with coverage factor 2 was calculated.

Analysis of uncertainty in reciprocity calibration

Calculations for the uncertainty of the reciprocity calibration are explained for second sensor. The equation (2) shows calculation of frequency response for second sensor.

The partial derivatives according all variable were calculated. For example for variable U_{12} Eq. (12) and I_{12} Eq. (13):

$$\frac{\partial F_2(f)}{\partial U_{12}(f)} = \sqrt{\frac{U_{23}(f)I_{31}(f)}{H(f)I_{12}(f)I_{23}(f)U_{31}(f)}}} \cdot \frac{1}{2\sqrt{U_{12}(f)}} \quad (12)$$

$$\frac{\partial F_2(f)}{\partial I_{12}(f)} = \sqrt{\frac{U_{12}(f)U_{23}(f)I_{31}(f)}{H(f)I_{23}(f)U_{31}(f)}}} \cdot \frac{1}{2\sqrt{U_{12}(f)}^3} \quad (13)$$

Evaluation of the uncertainty type A is based on a series at least of 10 measurements. Experimental standard deviation was used as an uncertainty of type A for measurements of voltage and current. Uncertainty of current probe was determined from measurements of probe characteristics and from manual.

Main source of uncertainty of type B was vector signal analyzer HP 89410A. Its absolute amplitude full-scale accuracy is ± 0.5 dB from full-scale [8]. Also the uncertainty of current probe was included and uncertainty of AE signal amplifier was included. For measuring devices PXI 5122 by National Instruments and Handy Scope 3 by TeePee the uncertainty of type B was determined according to manual of producer.

Because of simultaneous measurements of voltage and current for each pair it was assumed that at least two input quantities are interdependent. So the correlation for each combination of variables was calculated according to [9]. The assumption that the variables are correlated was not confirmed and from calculations followed, that the calculated covariance was negligible. Expanded uncertainty was calculated with the value of coverage factor 2.

Analysis of uncertainty in reciprocity calibration with broadband pulse excitation

The main problem was to determine uncertainty of calculated currents and voltages. Because these variables were calculated from FFT, so the determination of uncertainty of modulus was the same as in equation (8) according to [7]. These values were supplement to calculations as the uncertainties of voltages and currents and following calculations were the same as for standard reciprocity calibration.

Influence of Sources of Uncertainty on Step-function Calibration

Measuring device was driven by a trigger of 0.05 V and 200 μ s of input signal was sampled. Signal of the capillary break was calculated by MatLab with the same length and sampling parameters as real signal and validated by the noisy signal from interferometer. Signal generated from MatLab was recalculated from displacement to velocity. Final characteristics are calculated according to equation 1. Calculations of uncertainty for the step-function calibration result were determined. Main problem was to determine the propagation of uncertainty in discrete fast Fourier transform algorithm (FFT). The calculations follow [7].

Third column shows the mean of uncertainties [%] in range from 60 to 300 kHz and the fourth column for range 300 kHz to 1 MHz. The first row shows the influence of thickness of

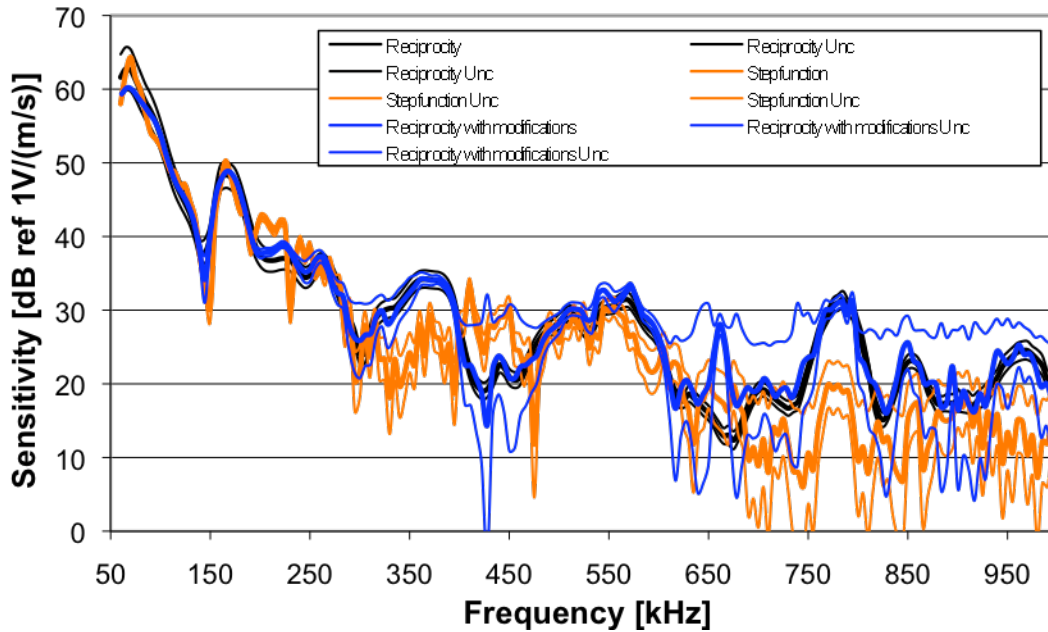


Fig. 5 Results of three methods of calibration of PAC UT1000 with uncertainties.

Table 1. Comparison influences on uncertainty of various sources in step function calibration.

	Source of uncertainty	Median uncer. type A (region 1)	Median uncer. type A (region 2)	Max uncer. type A
1	thickness of capillary	6.7	10.3	17.0
2	speed of capillary break	4.2	7.1	11.0
3	rotating with UT1000	5.1	8.0	25.2

used capillary from 0.11 to 0.32 mm. The second row shows the influence of speed of breaking capillary. It varies from slow to fast and the third shows the influence of slewing with reference sensor.

Influence of Sources of Uncertainty on Reciprocity Calibration

The analysis of influence of sources of uncertainty on measured characteristics was done. To be able to compare the impact of the sources to the final characteristics the uncertainty type A was calculated from the experimental standard deviation of final calculated sensitivities. Calibration of UT1000 (PAC) was measured many times on the same conditions and with the same equipment and only the one condition was change to determine uncertainty of this source. The results were summarized to following Table 2.

Evaluation of the uncertainty type A is based on a series at least of 10 measurements. Experimental standard deviation was used as an uncertainty of type A for measurements of voltage and current. Uncertainty of current probe was determined from measurements of probe characteristics and from manual. Main source of uncertainty of type B was the vector signal analyzer, HP 89410A. Its absolute accuracy in amplitude is ± 0.5 dB at full-scale [8]. Also the uncertainty of current probe was included and uncertainty of AE signal amplifier was included. For measuring devices PXI 5122 by National Instruments and Handy Scope 3 by TeePee the uncertainty of type B was determined according to manual of producer.

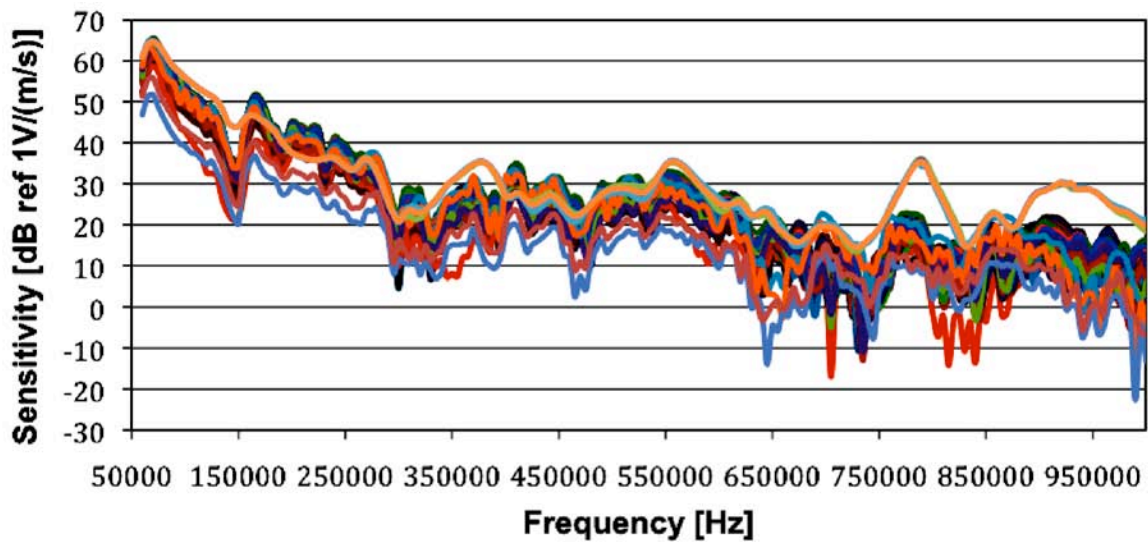


Fig. 6 Influence of slewing with UT1000 sensor on step function calibration.

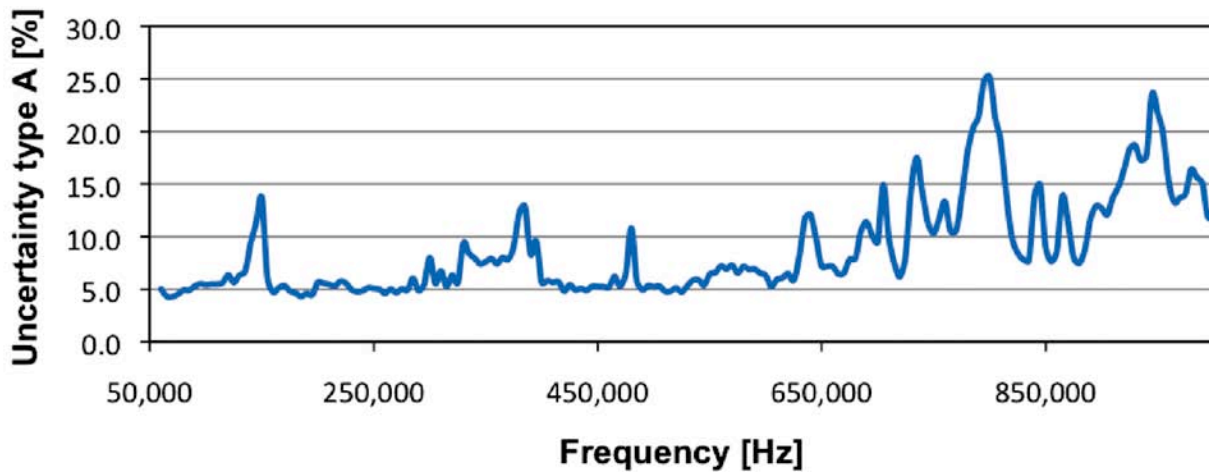


Fig. 7 Uncertainty of slewing with UT1000 sensor on step-function calibration.

Third column of the following Table 2 shows the mean of uncertainties [%] in region 1 (60 - 300 kHz) and the fourth column for region 2 (0.3 - 1 MHz). Step of the measurement was 5 kHz. The duration of the driving signal was 100 μ s according to the size of the testing block. The first row shows the influence of used channel on matrix switch. Second was measured with and without weight (normal force 10 N). Third shows influence of temperature. The case of sensor was raised from 25 to 60°C and the temperature was measured by surface temperature sensor. Fourth shows the influence of setting time of couplant, the value being calculated from more than a hundred measurements during two days.

Fifth row in Table 2 shows the influence of amount of couplant from none to excessive. The sixth row shows influence of remounting reference sensor, UT1000. The other sensor lies for a few days. Seventh shows the influence of remounting pair sensors (K2G (s.n. 58507-00797 by Krautkramer) and Aura (s.n. SV416-416004 by Aura Milevsko). The reference sensor lies for a few days. Eighth shows the influence of slewing with reference sensor. Ninth shows the influence of moving with weight on the top of the mounted sensor. Tenth shows the influence of incorrect positioning on the surface. The reference sensor was positioned from 2 to 10 cm from the correct position to the direction opposite to direction to the center of triangle of sensor and

reciprocity parameter was calculated for correct position. One of the largest influences was the remounting of the pair sensor.

Table 2 Comparison influences on uncertainty of various sources in reciprocity calibration.

	Source of uncertainty	Median uncer. type A (region 1)	Median uncer. type A (region 2)	Max uncer. type A
1	used channel on matrix switcher	0.4	0.3	0.7
2	with and without normal force	0.1	0.3	1.7
3	temperature	0.7	2.4	8.1
4	time stability of couplant	0.1	0.2	1.6
5	amount of binding paste	13.8	9.3	16.7
6	remounting of UT1000 sensor	5.1	5.4	17.1
7	remounting of pair sensors	8.3	13.7	31.0
8	slewing with sensor	1.6	4.9	11.2
9	moving with weight	2.9	3.5	11.9
10	incorrect position of pair sensors	6.1	9.2	21.7

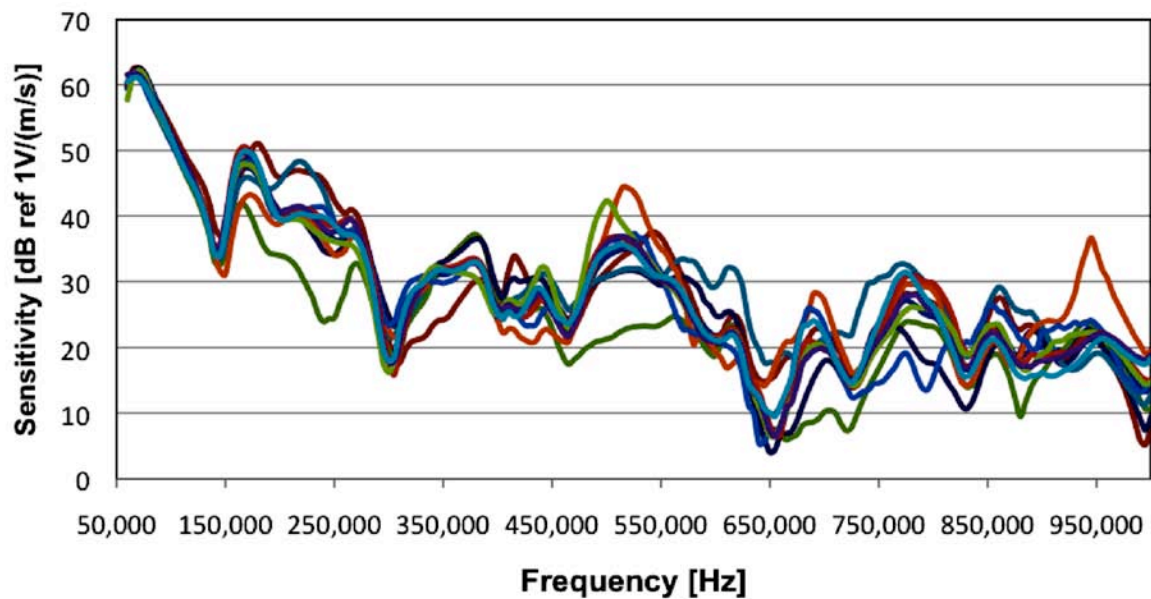


Fig. 8 Influence of remounting of pair sensor on reciprocity calibration.

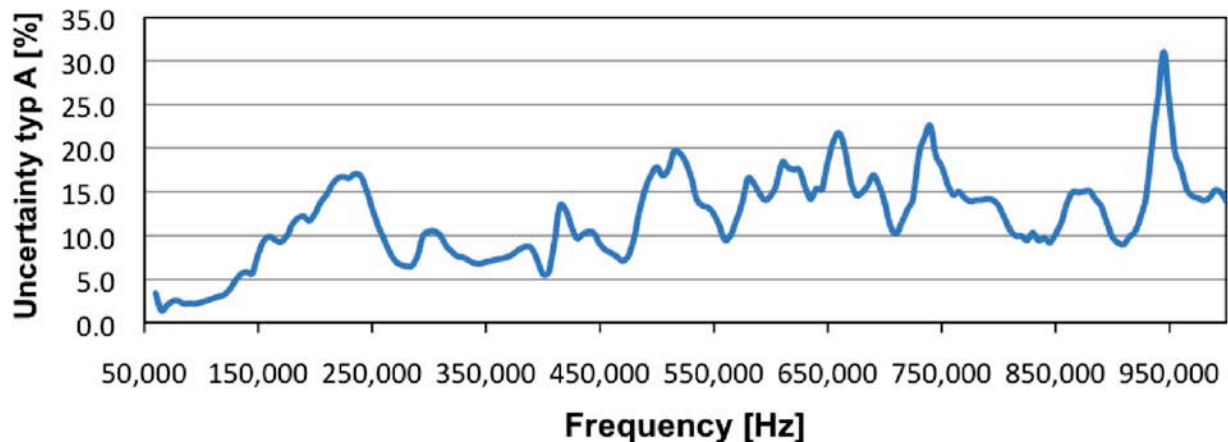


Fig. 9 Uncertainty of remounting of pair sensor on reciprocity calibration.

Comparison of Uncertainties with Error Requirements in ASTM 1106

Figure 10 shows the results of combined uncertainties for all the methods of calibration related to final characteristics of each method. So the results are presented in percent of final characteristics. The orange curve shows errors from step-function calibration, the black from reciprocity calibration and the blue from reciprocity calibration with broadband-pulse excitation.

The error for step-function measurement and reciprocity measurement with broadband-pulse excitation is low up to 300 kHz and then it grows. The main peaks in error are on defined frequencies caused by aperture effect of finite length of sensor surface of PAC UT1000 having the radius of 0.775 cm. Zero points calculated according to [1] are 237, 433, 628 and 823 kHz for Rayleigh wave speed $3006 \text{ m}\cdot\text{s}^{-1}$ for our testing block.

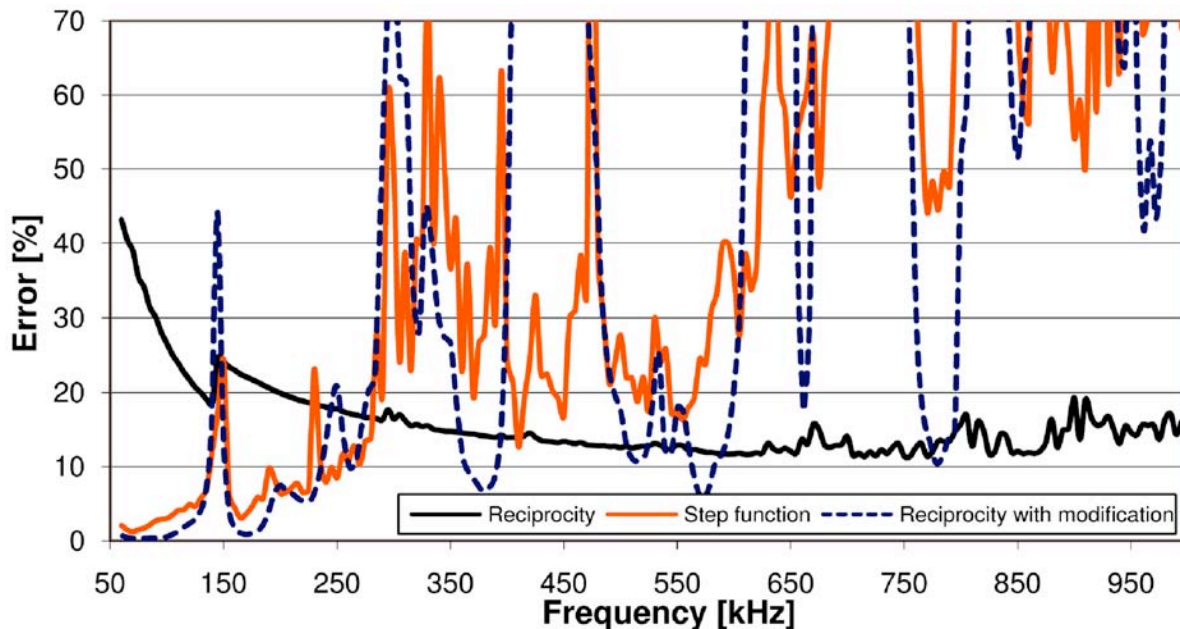


Fig. 10 Combined uncertainties for different calibration methods.

ASTM 1106 [1] and ISO 13713 [2] present that the error of measurements between 100 kHz and 1 MHz should be up to $\pm 10\%$. The data from repeated calibration with remounting sensor should be collected and the overall system should produce calibration with precision of $\pm 15\%$.

From Fig. 10 follows that previous assertion is valid for range 60 kHz to 300 kHz. On higher frequencies the sensitivity of the sensor is too low and uncertainty grows. For example, at 70 kHz the sensitivity is 62.5 dB ref. 1 V/(m/s) and at 300 kHz the sensitivity is 24.1 dB ref. 1 V/(m/s). So the difference is 38.4 dB ref. 1 V/(m/s). The final uncertainty of step-function calibration and reciprocity calibration with broadband-pulse excitation is in fact dependent on value of sensitivity of sensor on a certain frequency.

Conclusions

The paper reviews the background, the methodology and the standardization of the primary calibration of AE sensors. The reciprocity calibration, reciprocity calibration with broadband pulse excitation and step-function method of absolute calibration were practically realized in laboratory of vibro-diagnostics at Brno University of Technology. The whole experiment was

managed by PC with LabVIEW 8.5. The software and measuring apparatus enables primary calibration of AE sensors by reciprocity method according to NDIS 2109 [4] and by step-function method according to ASTM 1106 [1]. Approximately 1600 calibrations and 100 different sensors were measured.

The comparison of the results of all of the method is presented on Figs. 4 and 5. The shape corresponds well up to 300 kHz. The method of reciprocity calibration with broadband-pulse excitation was based on the modification of reciprocity calibration by Goujon and Baboux [6]. Their method was supplemented by using more than one excitation on different frequencies and final characteristics were calculated from more than one measured characteristics. The experimental setup is similar to usual reciprocity calibration. This method of the calibration is much faster than usual reciprocity method.

The results correspond well with results from basic reciprocity calibration, but the uncertainty is worse especially on higher frequencies where the sensitivity of UT1000 is lower. So the method can be used to verify the quality of sensor's mounting on the surface before usual reciprocity calibration measurement.

The uncertainty of all methods was determined. PAC UT1000 (s.n. 169) was used as the sensor-under-test. The problem of the propagation of uncertainty in discrete fast Fourier transform algorithm was solved. For measurements we used more accurate measuring devices than HP 89410A – PXI 5122 by NI and Handy Scope 3 by TeePee. PXI – 5122 by National Instruments was most cost-effective. It has the sampling frequency up to 100 MHz, good dynamic range and accuracy better than HP. Handy Scope 3 is unsuitable for measurements of reciprocity method with broadband-pulse excitation and step-function calibration due to its poor dynamic range and lower sampling frequency and resolution.

The main sources of the uncertainty were described and its influence to uncertainty is presented. The big influence on uncertainty in reciprocity calibration was the influence of remounting reference sensor and pair sensors. By correct and precise mounting of the sensors, this influence can be reduced. The repeatability of the step function calibration is in general worse than in reciprocity calibration for high frequency range up to 300 kHz. Noise is crucial, so we recommend using of digitizers with high resolution. For example NI 5922 with 24-bit flexible resolution.

Acknowledgment

This research has been supported by Grand Agency of the Czech Republic under the contract GACR 101/06/1689 and by the Czech Ministry for Education in frame of the Research Intention JC MSM 0021630529: Intelligent systems in automation.

References

1. ASTM Standard E1106-86: Standard Method for Primary Calibration of Acoustic Emission sensors, 1986, ASTM, Philadelphia.
2. ISO 12713: 1998(E) Non-destructive testing - Acoustic emission inspection - Primary calibration of transducers.
3. Miller, R. K., McIntre, P.: *Acoustic Emission Testing (Nondestructive Testing Handbook, Volume 5)*, American Society for Nondestructive Testing, 1987.

4. NDIS 2109-91: Method for Absolute Calibration of Acoustic Emission Transducers by Reciprocity Technique, The Japanese Society for Non-Destructive Inspection, 1991.
5. Hatano, H., Chaya, T., Watanabe, S., Jinbo, K.: Reciprocity Calibration of Impulse Responses of Acoustic Emission Transducers, IEEE Transactions UFFC, **5** (45), September 1998, 1221 – 1228.
6. Goujon L., Baboux J. C.: Behaviour of acoustic emission sensors using broadband calibration techniques, Measurement Science Technology, **14**, 2003, 903 – 908.
7. Betta G., Liguori C., Pietrosanto A.: Propagation of uncertainty in a discrete Fourier transform algorithm, Elsevier Measurement **27**, 2000, 231 – 239.
8. HP 89410A/HP 89441A Operator's Guide, Hewlett-Packard Company, 1998.
9. Laaneots R., Mathiesen O.: *An introduction to metrology*, TUT Press, 2006.

TRANSFER FUNCTIONS OF ACOUSTIC EMISSION SENSORS

KANJI ONO¹, HIDEO CHO² and TAKUMA MATSUO²

¹University of California, Los Angeles, Los Angeles, CA 90095, USA;

²Aoyama Gakuin University, Sagamihara, Kanagawa, Japan

Keywords: AE sensors, transfer functions, plane waves, spherical waves, pulse-laser excitation, deconvolution, interferometer

Abstract

We have obtained the transfer functions of a wide range of AE sensors commonly available and utilized. These were determined by the excitation of input waves using an ultrasonic transmitter or pulse-laser in conjunction with a transfer block, a laser interferometer and a deconvolution procedure typically in the frequency domain. Sensor responses depend on the wave types; i.e., plane waves, and spherical waves with different radius of curvature. Using typical source waveforms and a convolution procedure, one can then visualize waveforms expected out of these AE sensors. Some sensors showed displacement response, while another gave velocity response. These response types also depended on incident wave types, requiring additional characterization steps in sensor calibration procedures.

Introduction

Acoustic emission (AE) sensors play a crucial part in determining AE behavior of materials and structures. The characteristics of AE sensors control the waveforms of AE signals detected. Manufacturers usually provide the sensitivity and frequency response of an AE sensor in terms of velocity response in reference to 1 V/ μ bar or 1 V/m/s. Here, 1 V/ μ bar can be converted (using aluminum dilatational wave velocity of 6.15 mm/ μ s) to 1.1×10^8 V/m/s. Typical peak sensitivity values are about -65 dB in reference to 1 V/ μ bar for normally incident waves and correspond to 6×10^4 V/m/s. Some sensors produce the output proportional to acceleration, while others respond to displacement. These are calibrated differently and reported in mV/Gal or in reference to 1 V/ μ m, for example [1]. Such information is useful in sensor selection for laboratory work and for field applications, but is inadequate to characterize the input since a sensor response depends on frequency and other conditions. Thus, in order to understand mechanical incident waves that generated AE waveforms, we need the transfer function of an AE sensor.

Let us consider mechanical input, $x(t)$, to a sensor and assume x represents displacement as a function of time, t . $x(t)$ is normal surface motion at the epicenter and is generated on the sensing surface of a transfer block by a laser or a piezoelectric transmitter source on the opposite face (at $-X_0$). See Fig. 1. Voltage output from the sensor, $y(t)$, is given by the convolution of the input $x(t)$ and the impulse response of the sensor, $h(t)$, as

$$y(t) = \int_{-\infty}^{\infty} h(\lambda)x(t - \lambda)d\lambda \quad (1)$$

The Fourier transform of $h(t)$, or $H(j\omega)$ where $j^2 = -1$ and ω is angular frequency, $2\pi f$, is known as the transfer function or system function and relates the input and output in the frequency domain. Here, we use the time domain representation, $h(t)$, with displacement input as the transfer function. This allows us to simulate expected waveforms corresponding to arbitrary input functions. Furthermore, we limit the input to be displacement of normal incidence to the sensor face.

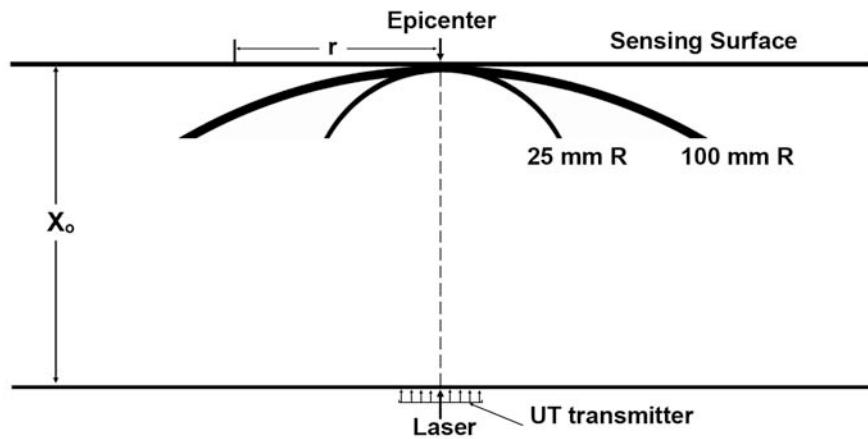


Fig. 1 Experimental schema. Wave excitation from the bottom surface of transfer block, thickness X_0 (100-mm and 25-mm plates used). Sensor placed at the epicenter on the sensing surface side. Relative changes in the radius of curvature for the two plates shown.

Dependence on incident angle is expected and will be examined in the future. It is also possible to define a similar function for velocity or acceleration applied to the sensor face. However, it is not feasible to consider surface-wave input or sensor response at this time even though surface waves are important in AE signal detection and analysis.

In the above definition of the transfer function, $x(t)$ was treated as scalar. In reality, any sensor face has a finite area, typically circular with radius, r_0 . We must consider spatial dependence and define the surface displacement as $x(r, t)$, where r is the distance from the epicenter assuming circular symmetry (cf. Fig. 1). In turn, $x(r, t)$ is given by the convolution of the impulse response (Green's function) of the transfer block (of thickness, X_0) and forces applied at the opposite face. The forces are dynamic and can be applied at a point (focused laser sources) or distributed over an area (piezoelectric sources). When a point source is used, the waves spread spherically to radius of X_0 or larger as they reach the calibration surface where the sensor is located. The thickness of the transfer block is a parameter we need to consider since it defines the radius of spherical waves exciting a sensor. Using a suitable distributed source, plane waves of limited size can be produced in the so-called near-field region, as is well known in ultrasonic testing. It would be convenient to use if a single universal transfer function is obtained for a sensor. At this stage, this is not feasible and we will consider below specific transfer functions for three input wave types, one for plane wave condition and two for spherical wave conditions. The latter two apply to AE signals that travel distances of X_0 from source to sensor.

The transfer function concept was utilized in fundamental studies of AE source functions and provided valuable insight to the nature of the origins of AE. A well-characterized sensor, such as a NIST capacitive or conical sensor was used, and sensor outputs were analyzed by a deconvolution procedure, and the AE source functions were deduced. In these studies, the breakage of glass capillary usually provided the calibration source of a step force of a short rise time of $\sim 1 \mu\text{s}$, generating stress waves with a known theoretical basis. See ASTM E-1106, which serves as the primary standard for all AE sensor calibration (for the surface waves) in the US [1]. Some efforts to get the transfer functions via frequency domain procedures were reported [2], but no systematic study is known. Manthei [3] used a procedure similar to one at NIST and obtained experimental calibration response to glass capillary breaks for lab-built sensors and a reference sensor (Panametrics V103). The results were in the form of output peak voltage per unit force for the body waves of normal incidence due to glass capillary breaks. By comparing the predicted

epicentral velocity signal for a glass capillary break with the observed, he concluded these sensors to be of velocity-sensitive type. At this stage, the velocity was not measured, so the result is useful mainly for relative calibration. It is noted that the initial single-sided peak has the half-height width of 1.9 μs (Fig. 5 in Ref. 3). This is comparable to the width expected from the resonance frequency (1 MHz) and a typical glass capillary break of 1 μs [4], though the pulse length may be extended by the use of plexiglas as the transfer block that attenuates the high frequency components. His finding is consistent with the expected velocity response near sensor resonance.

Some AE sensors are referred to have velocity response or resistance controlled. Others may be of displacement response or mass controlled. The third type is acceleration response or stiffness controlled. Such characterization is based on a simple one-dimensional analysis of a damped oscillator, which is used to represent a piezoelectric sensor [5, 6]. In this most simplistic model, a sensor is considered as a mass (m) connected to a Voigt model (a spring (k) and a dash-pot (η) in parallel connection). Taking sensor frame displacement as x and frame-mass relative displacement as y , we obtain (with a super-dot indicating a time derivative)

$$m(\ddot{x} + \ddot{y}) + \eta \dot{y} + ky = 0 \quad (2)$$

Applying sinusoidal vibration at f , we obtain the following:

$$y = \frac{(f / f_o)^2}{1 - (f / f_o)^2 + j(f / f_o) / Q} x \quad (3)$$

where $f_o = (1/2\pi)(k/m)^{1/2}$ is the natural frequency and quality factor $Q = (mk/\eta)^{1/2}$. In approximation, we have

$$\begin{aligned} f \ll f_o &\rightarrow y \approx (f / f_o)^2 x = -\ddot{x} / \omega_o^2 \\ f \approx f_o &\rightarrow y \approx -jQ(f / f_o)x = -(Q / \omega_o)\dot{x} \\ f \gg f_o &\rightarrow y \approx -x \end{aligned} \quad (4)$$

Equation (4) then predicts an acceleration response (stiffness controlled vibration) at lower frequencies, a velocity response (resistance controlled vibration) near the natural frequency, while displacement response (mass controlled vibration) is expected at higher frequencies. Note that this analysis was initially applied for a mass-loaded spring seismometer and is useful for a single-mode vibration sensor. We need caution in applying this analysis or results in typical AE sensors, in which cross-coupled modes are commonly exploited for improved sensitivity. Besides, AE signals are transients and the above analysis is for steady state oscillations.

More advanced transducer analyses are given in Mason [7], where equivalent circuit models are developed for various boundary conditions. The simplest case is for a free resonator and is represented by a series of capacitor, inductor and resistor in parallel to a capacitor. This is equivalent to the above mechanical model.

Once the transfer function of an AE sensor is known, a convolution procedure (Eq. (1)) allows one to simulate the sensor output signals using different input signals. This in turn provides the insight to original source mechanisms of AE. In order to obtain the transfer function, one needs a repeatable wave source and a transfer block of adequate size. It is also essential to determine the displacement (or velocity) of the surface on which to install a sensor under test. A classic setup was used at NIST using a glass capillary break and a capacitive transducer [1, 4]. A steel cylinder of 90-cm diameter and 43-cm high was the transfer block. In our initial work previously reported [8], we used a setup, consisting of a pulse laser, an aluminum plate (25-mm thickness) and a laser interferometer. In this work, we added a larger cylindrical aluminum block

(100-mm thickness x 300-mm diameter) and also used a piezoelectric ultrasonic sensor as a transmitter. Despite the block size limitation, this still provides information useful in understanding AE waveforms encountered in many AE studies. Another significant development is the consideration of plane waves and spherical waves from a point source as input. These required separate approach to get the transfer function of AE sensors specific to an input wave type. It was also found that various vibration modes of a sensor are activated over time and depending on the excitation wave types. This necessitates serious reconsideration of sensor calibration methods in the future.

Experimental

The initial source of impulse was a pulsed YAG laser and the output was ~ 2 mJ, focused on 0.5~1-mm-diameter area. Unfocused laser pulses were also used and a 4~5-mm diameter ring-like zone had high beam intensity. In the previous work, laser pulse impinged on an aluminum plate of 25 mm thickness. This resulted in a sharp displacement pulse on the opposite side, having the peak width of 50 ns at half height and the peak displacement amplitude of 1.4~1.9 nm (Fig. 2a) depending on the laser output. Three additional reflected pulses follow, but these are 11, 20 and 24 dB below the initial pulse height. Two larger blocks were added in this study. These are 300-mm diameter cylindrical shapes of 100-mm or 500-mm thickness. The largest block turned out to be a wrong geometry and produced extended echo-trains almost submerging the primary signals. Thus, the present work mainly utilized the 100-mm thick block. Displacement waveform on the opposite surface is given in Fig. 2b for the focused laser beam. The half-height peak width was 25 ns and was a half that of the 25-mm plate case. The extrapolated base width was 48 ns and the main motion of the waveform can be represented by a symmetrical triangular pulse of 48-ns duration. This shape has wide frequency content, well beyond 10 MHz and frequency at -3 dB point is 13 MHz. Unfocused beam produced similar pulse widths.

Effects of beam spread are examined. Relative changes in the radius of curvature are shown in Fig. 1. From a point source to a typical 13-mm diameter sensor, one expects 35 or 140 ns delay for 100 or 25 mm plate, causing significant changes in the displacements on the sensor surface. Figure 3 shows displacement measured on the 100-mm block from unfocused laser source. Despite the spread at the source, the peak amplitude decreased and arrival time was delayed. At 12 mm off-center, the peak amplitude was $\sim 1/3$ and the peak delay was 200 ns. Assuming a circular symmetry, one can simulate the averaged displacement response over aperture area of different diameter. Using the data of the epicenter (marked 0 mm in Fig. 3), 2-, 4- or 6-mm off-center, area-averaged displacement was calculated for 2-mm, 6-mm, 10-mm, or 14-mm diameter aperture. Here, the displacements were summed in proportion to the areas of circular zones of 1-3, 3-5 and 5-7 mm radii. Results are shown in Fig. 4. The peak amplitude increased with larger aperture and resulted in 25-times higher peak value for 14-mm size over the peak value of 2-mm size. Peak width at base also broadened from 50 ns to over 250 ns. While displacement sequence or locations were ignored, the results can approximate averaged displacement response. Thus, capacitance sensors with a given area should produce outputs similar to those in Fig. 4. In piezoelectric sensors, however, arrival phases are expected to affect the sensor output substantially.

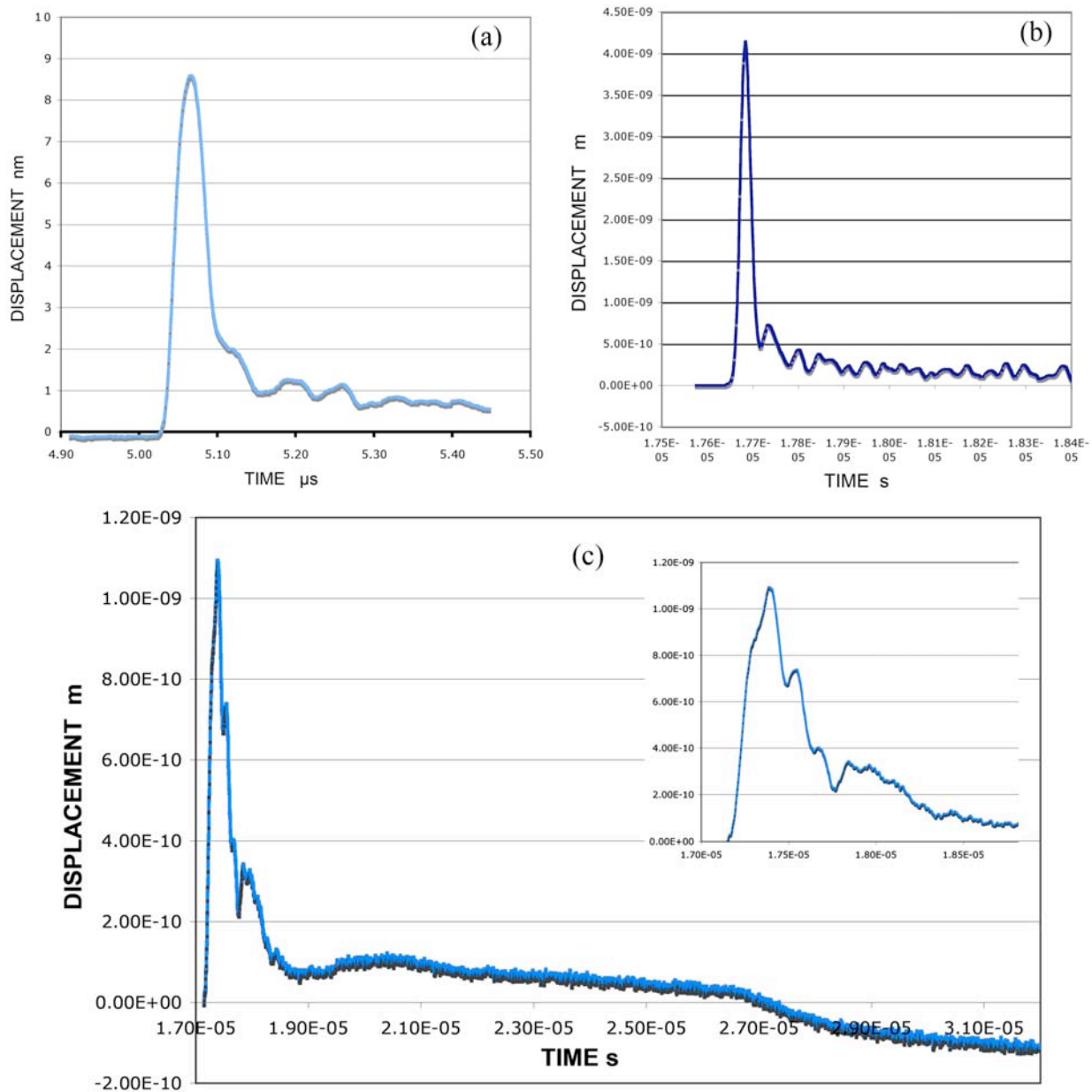


Fig. 2 (a) Epicentral displacement pulse from a focused laser, 25-mm plate. (b) From a focused laser, 100-mm plate. (c) From FC500 piezoelectric transducer (2.25 MHz, 19 mm aperture). See insert for the initial 1.8- μ s portion. FC500 excitation is about ten times broader than laser.

In order to enlarge the size of source and to obtain plane waves on the sensing surface, a piezoelectric ultrasonic sensor was used as a transmitter. We used AET FC500, which has nominal resonance frequency of 2.25 MHz and 19-mm aperture size. It was driven by a negative-going step of 1- μ s duration (430 V/ μ s peak slope over 0.7 μ s). This produced a displacement waveform on the opposite surface as shown in Fig. 2c. This waveform is much broader than the laser-induced waves. The main motion is a triangular pulse of 240-ns rise and 360-ns trailing times as shown in the insert of Fig. 2c and is limited in its bandwidth. Frequency at -3 dB point is 1.2 MHz. The uniformity of the surface displacement can be seen in Fig. 5, where a PAC Pico sensor was placed at the epicenter (0 mm), 4-mm or 6-mm off-center. Amplitude was within ± 1 dB and the phase was essentially identical. 2-mm off-center data was identical to the epicentral one and

not shown. Thus, this source can be utilized for plane-wave input to a sensor of 13-mm diameter or less.

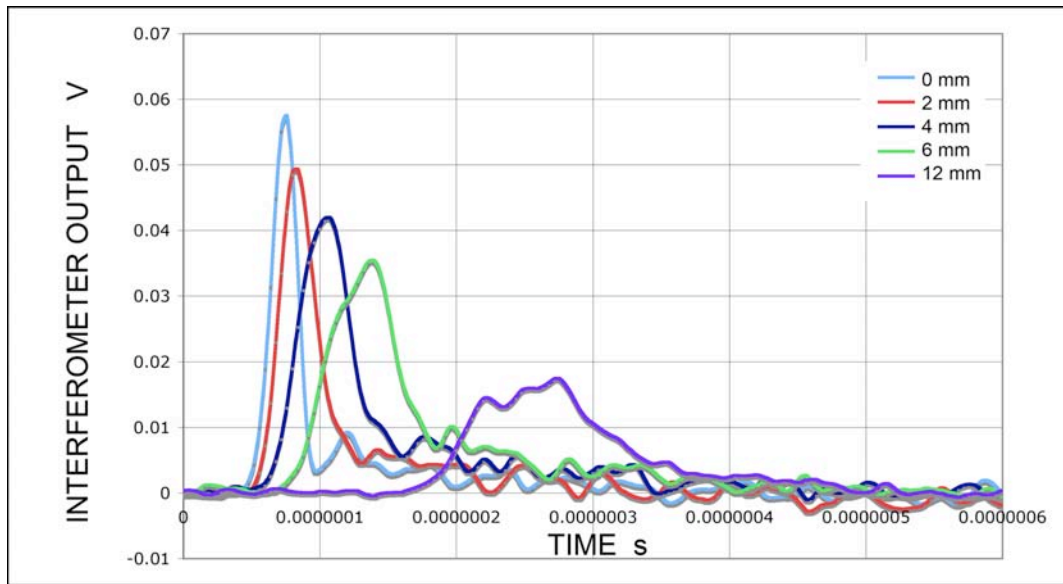


Fig. 3 Displacement measured on the 100-mm block from unfocused laser source. At epicenter (0 mm) the peak is the sharpest and highest, broadening and lowering with offset of 2, 4, 6 and 12 mm. With larger offset, peak arrival was also delayed. (x-axis length: 0.6 μ s)

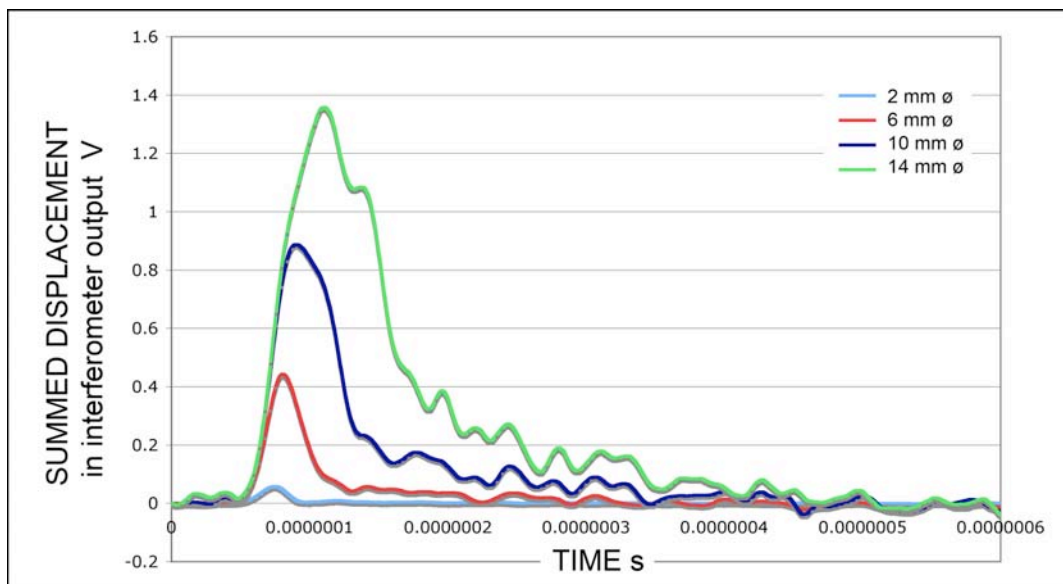


Fig. 4 The averaging of displacement response for larger aperture-size receivers. The epicentral response is used for 2-mm aperture, while displacements measured at larger offset were proportionately summed. (x-axis length: 0.6 μ s)

The normal displacement was detected by a laser interferometer (Thales Laser S.A., SH-140; dc-20 MHz). A sensor under test was placed opposite the laser impingement or FC500 transmitter and its output recorded by a digitizer with 100x signal averaging. Typical sampling frequency was 250 MHz, but was also at 100 MHz or 1 GHz. Acoustic couplant was silicone grease (HIVAC-G, Shin-etsu).

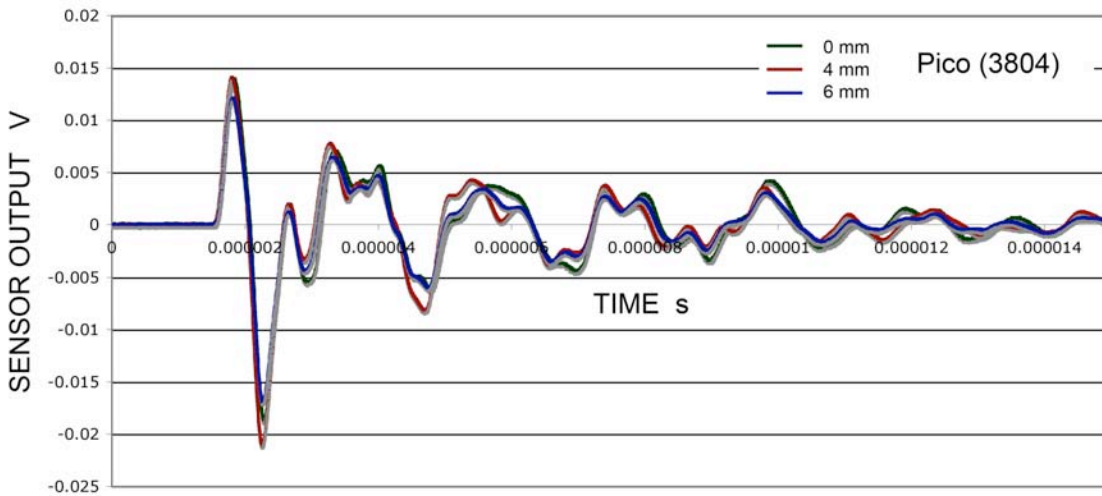


Fig. 5 Similarity of surface displacements produced by AET FC500 on 100-mm block and detected by a PAC Pico sensor placed at the epicenter (0 mm), 4-mm or 6-mm off-center.

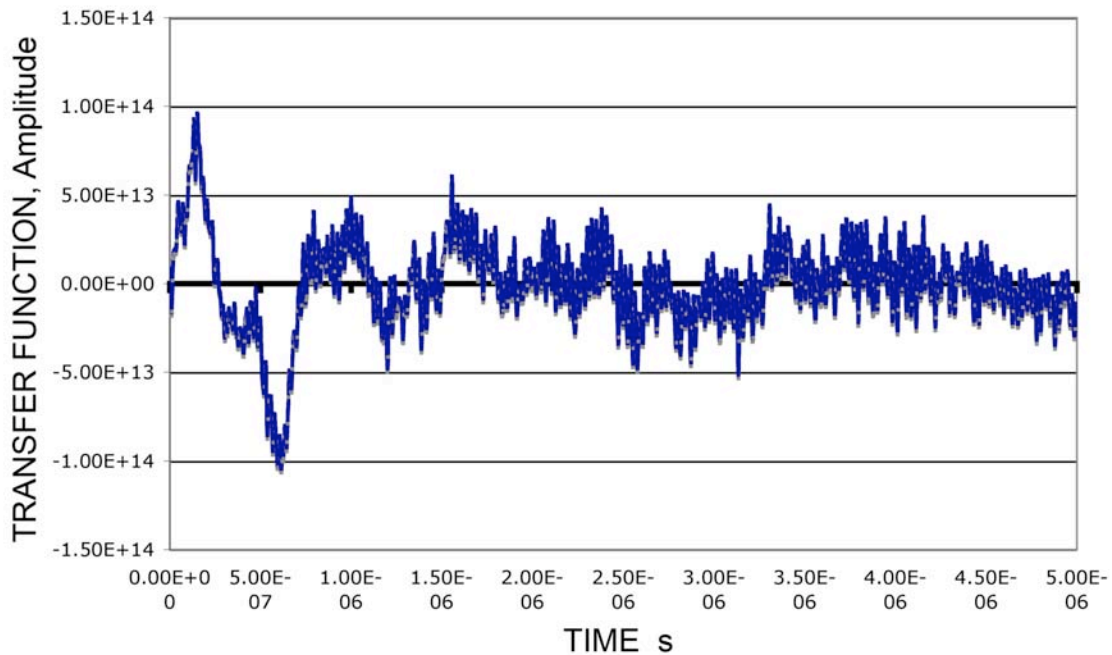


Fig. 6 The transfer function of a PAC Pico sensor (s/n 3804) calculated from the epicentral data of Fig. 5 and surface displacement produced by AET FC500 on 100-mm block (Fig. 2c).

Results

1. Transfer functions

The transfer function of a sensor was obtained from its response to excitation and the corresponding displacement waveform using a frequency-domain deconvolution procedure. Noise in the sensor response before the arrival of excitation signals was eliminated and cosine taper window was applied first. Note also that digital data was 5-MHz low-pass filtered before the deconvolution was applied. A Butterworth low-pass filter (<30 MHz) was applied on the deconvoluted transfer function. Some high-frequency noise still remained in some results, making several of them irrelevant. The amplitude of transfer functions is in the unit of V/ m·s. The results given in various figures in this work are in terms of V/m·(time step), with 10-ns time step. In taking the

convolution integral, this time step is multiplied; thus, the values given here must be reduced by 10^8 in using them with the standard unit of V/m.s.

a. Pico sensor: The waveform due to FC500 excitation taken by a Pico sensor (PAC, ser. 3804) given in Fig. 5 indicates initial oscillations of $0.7 \mu\text{s}$ duration (1.4 MHz) followed by 5 cycles at $\sim 2.2 \mu\text{s}$ period. The latter corresponds to the main resonance of this sensor at 450 kHz. Shown in Fig. 6 is the transfer function of this sensor, which shows a bipolar pulse of $0.74 \mu\text{s}$ duration. Two additional cycles can be discerned in noise. Thus, both the sensor output and the transfer function exhibit velocity response to unipolar displacement input at 1.4 MHz. The main 450-kHz resonance of this sensor is, however, difficult to recognize in the transfer function, partly because of large high-frequency noise remaining after low-pass filtering. It is also impossible to assign response type at 450 kHz.

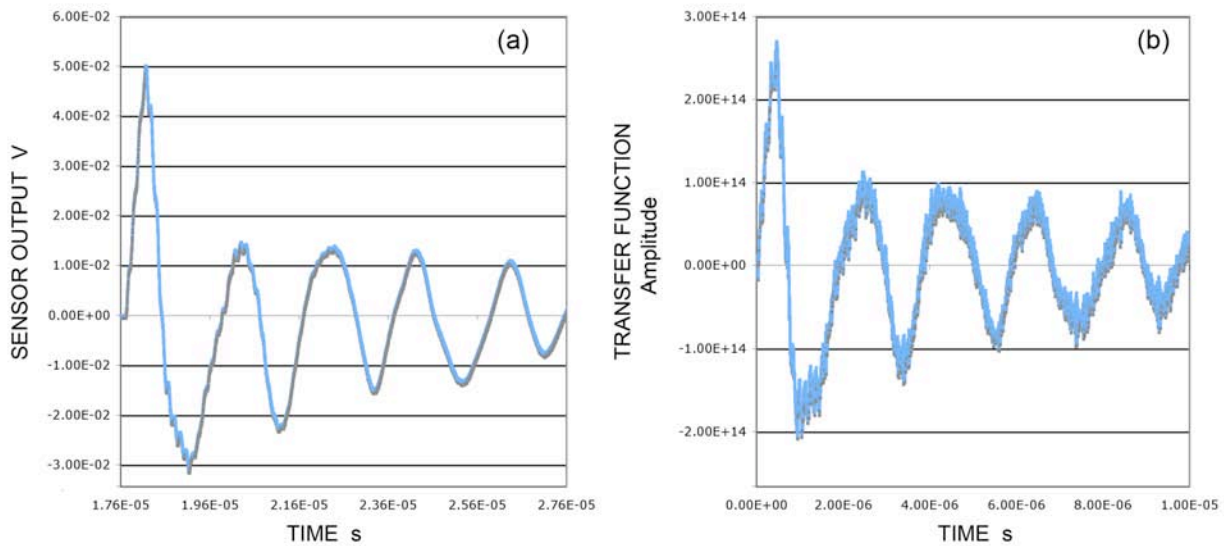


Fig. 7 (a) Waveform and (b) transfer function of a Pico sensor (s/n 3804) obtained using focused laser and 100-mm transfer block. (x-axis length: $10 \mu\text{s}$)

It is also possible to define a transfer function even when the acoustic input waves are spherical. Figure 7 shows the waveform and transfer function obtained using 100-mm transfer block. Since the displacement input (Fig. 2b) has a narrow pulse width (25 ns at half height), the waveform and transfer function resemble each other well except for higher noise in the transfer function. The shape is closer to the velocity response with the first negative peak being $3/4$ height of the first positive peak. The main 450-kHz resonance of this sensor is also clearly visible. Since this was obscure in the plane-wave input case above, this may be due to the spherical nature of incident waves. This may also cause the broadened first peak ($0.45 \mu\text{s}$) that has 4~5 times the half height peak width shown in Fig. 6b. These two effects are difficult to rationalize on the basis of spherical waves, however.

Effects of the radius of curvature of spherical incident waves are substantial. Previously, we reported a transfer function using 25-mm thick block [8]. This is shown in Fig. 8. The highest peak is the third one and it is obvious that multiple incident modes contributed to this complex transfer function. The main 450-kHz resonance of this sensor is most evident and the first bipolar pulse can be considered to exhibit velocity response.

From the three transfer functions of a single Pico sensor, it is evident that the nature of incident waves strongly affects the sensor response. It also shows that the type of sensor response, velocity or displacement, for example, must identify the input condition.

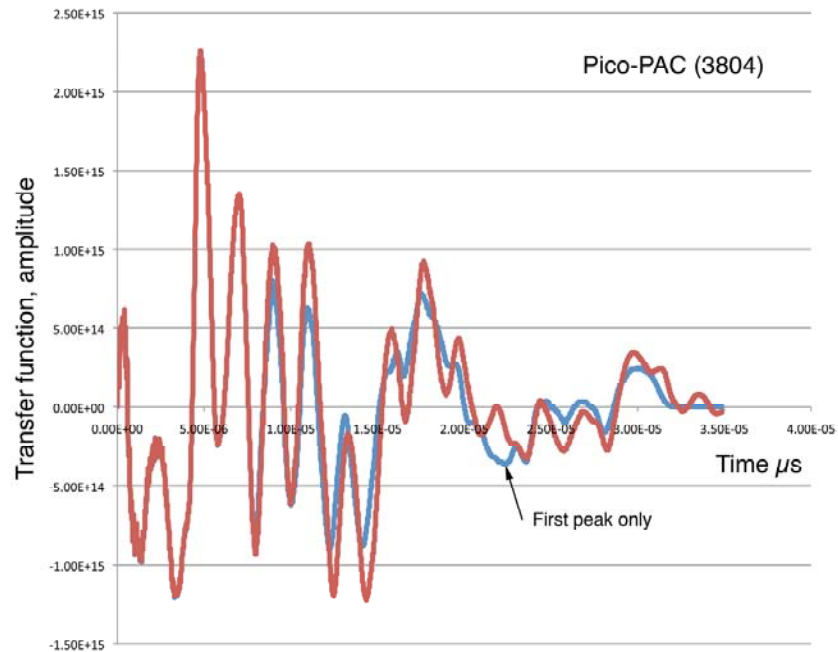


Fig. 8 Transfer function of a Pico sensor (red), which accounted for three reflected laser pulses. First-peak only (blue) curve is essentially same as measured waveform for $t < 30 \mu\text{s}$. [8]

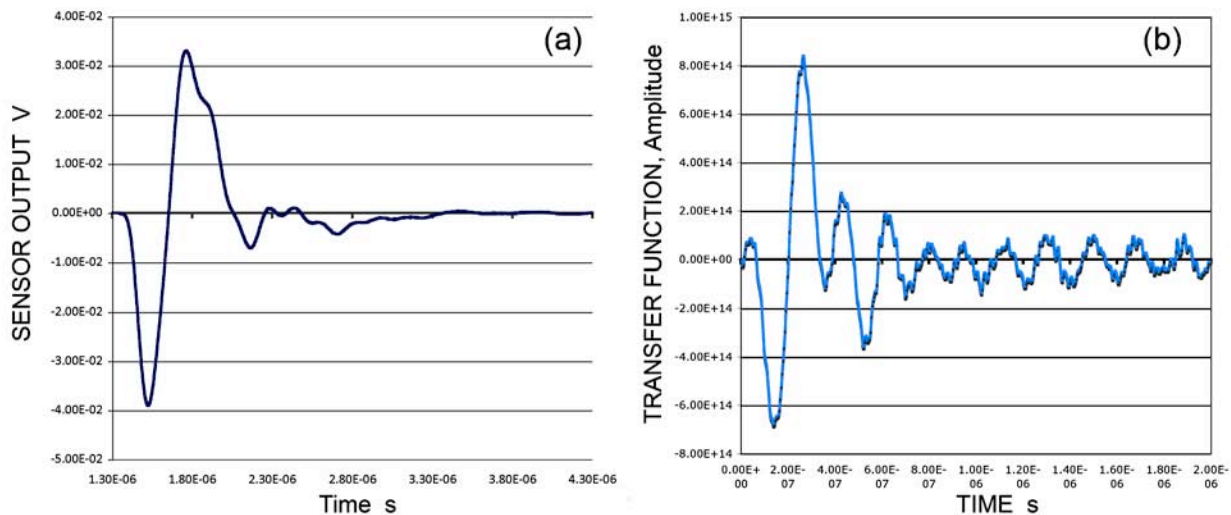


Fig. 9 (a) Waveform and (b) transfer function of a V1030 sensor (10 MHz) obtained using FC500 transmitter and 100-mm transfer block.

b. V1030 sensor: This sensor from Panametrics is a damped ultrasonic transducer and we misidentified it previously as V103 [8]. Current Panametrics V103 has nominal resonance frequency of 1 MHz, while our V1030 has 10 MHz/0.5" inscription. Using the plane-wave input with FC500 transmitter through 100-mm block, we obtained the waveform and transfer function as shown in Fig. 9. The waveform is a typical bipolar pulse, indicative of the velocity response with $0.68 \mu\text{s}$ duration. This is much longer than the 10-MHz inscription implies, but the rise time was faster than $0.15 \mu\text{s}$ (which is shorter than the incident wave rise time of $0.24 \mu\text{s}$). The transfer

function also shows the main feature to be a bipolar pulse of 0.27 μs duration, i.e., the velocity response. However, it is followed by a 5.5-MHz wave train. The origin of this trailing vibration is still obscure.

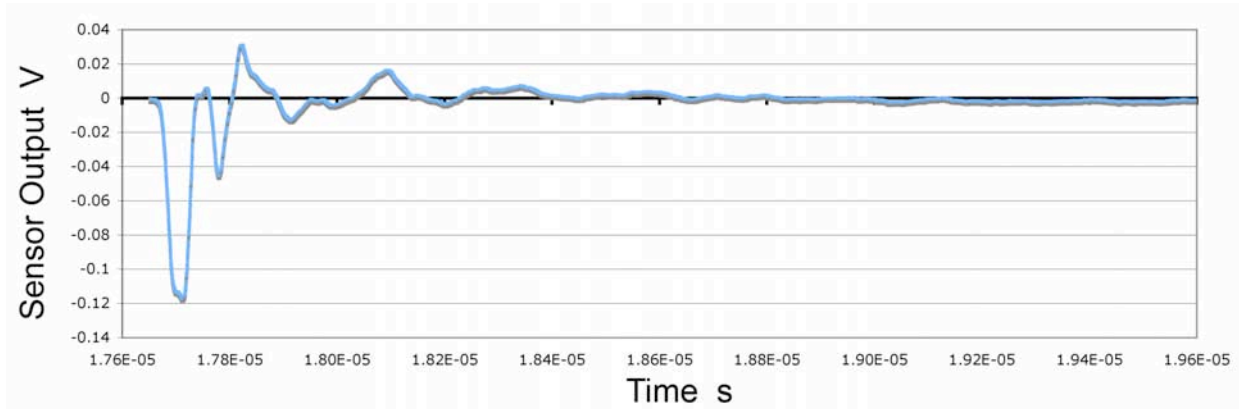


Fig. 10 Waveform of V1030 sensor obtained using focused laser and 100-mm transfer block.

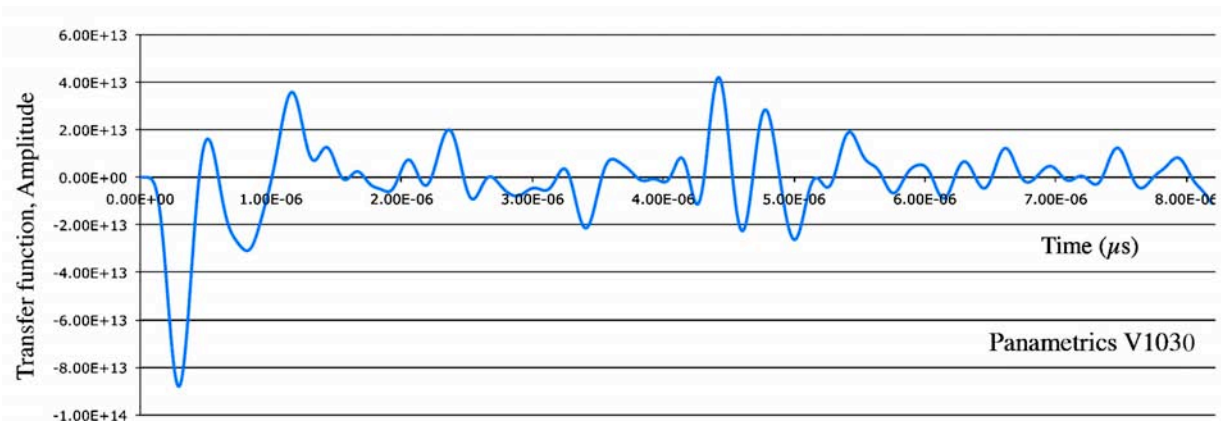


Fig. 11 Waveform of V1030 sensor obtained using focused laser and 25-mm transfer block. [8]

Using spherical incident waves and 100-mm block, V1030 sensor produced the output shown in Fig. 10. The main pulse is a negative-going narrow peak having half-height duration of 0.25 μs . It is followed by lower amplitude oscillations. The transfer function contained strong noise at 35 MHz and meaningful features could not be deduced. The previous result of transfer function obtained using 25-mm radius spherical waves also showed the main peak to be a unipolar pulse, followed by numerous oscillations (see Fig. 11 [8]). For this large aperture sensor, both spherical incident waves resulted in apparent displacement response. In spite of a simple structure of averaged displacement for larger aperture shown in Fig. 4, real sensors must be sensitive to the phase distribution of incident waves. The averaged displacements may be applicable for capacitive sensors only.

From the present results, the conventional wisdom of using well-damped sensors for high-fidelity waveform acquisition needs to be reexamined carefully. Depending on the types of waves being detected, appropriate sensor calibration has to be conducted considering the source types and propagation distances.

c. B-1080 sensor: This is a broadband sensor from Digital Wave. This is twice more sensitive compared to V1030, in part due to the addition of FET input stage on the sensor. This sensor

output indicates the acceleration response to a displacement pulse input, although the two positive-going pulses are not quite symmetric in shape. However, the peak heights are almost identical and the peak positions were symmetric. The transfer function calculation was not successful, again with strong high-frequency noise that could not be eliminated.

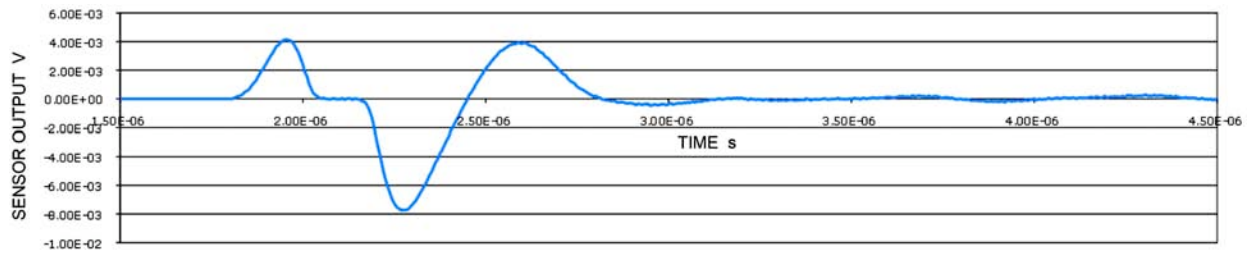


Fig. 12 Waveform of a Digital Wave B-1080 sensor excited by FC500-generated plane waves.

d. WD sensor: This is a popular wide-band sensor from PAC with multiple resonances having multi-element sensing design. Its sensitivity is higher than broadband sensors (V1030 and B-1080). Because it has a disc and two ring elements, its response is expected to be complex.

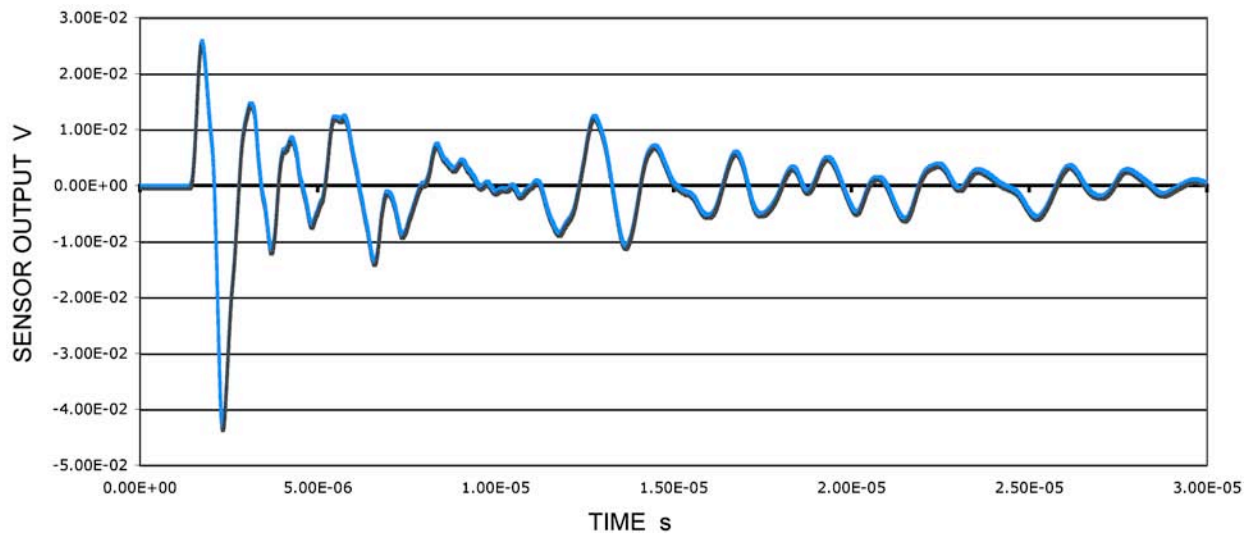


Fig. 13 Waveform of a PAC WD sensor excited by FC500-generated plane waves.

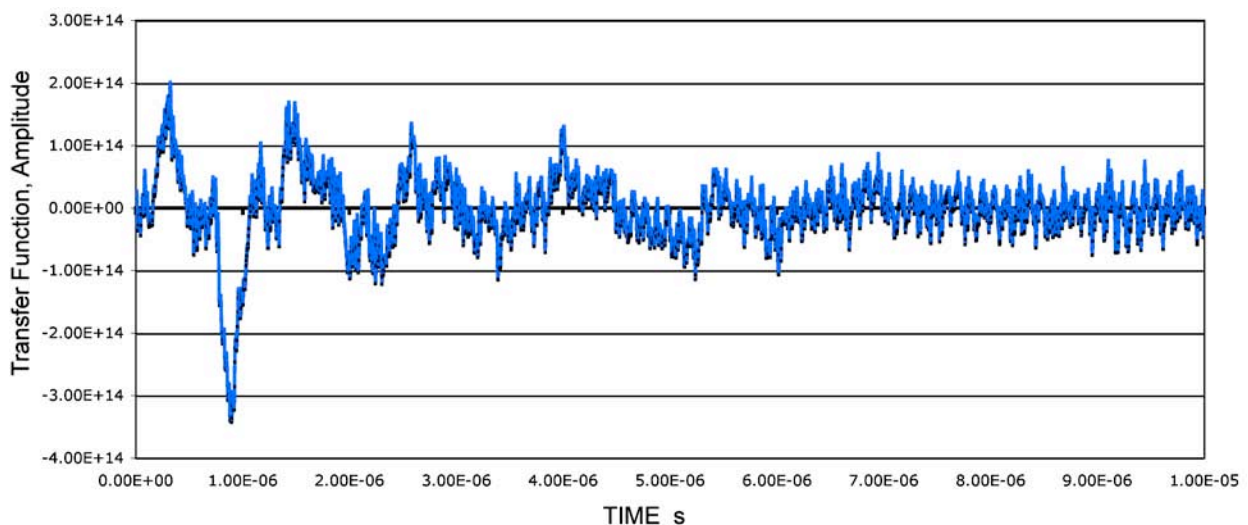


Fig. 14 Transfer function of a PAC WD sensor excited by FC500-generated plane waves.

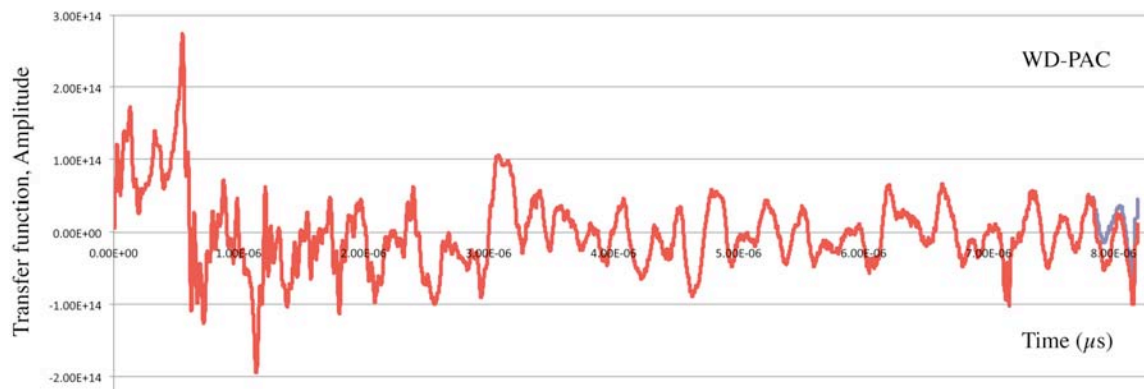


Fig. 15 Transfer function of a PAC WD sensor excited by a laser pulse on 25-mm plate. [8]

Under the plane-wave excitation with 100-mm block, the waveform and transfer function were obtained as shown in Figs. 13 and 14. The first three peaks of the waveform are indicative of the acceleration response (also for transfer function plot albeit with strong high-frequency noise) as in B1080 above. In this case, many oscillations follow without any definitive pattern. The two initial positive peaks have a 1.4- μ s period while many pairs of peaks have 1 to 1.8 μ s duration. However, the main resonances of WD sensor are at 200 to 500 kHz range and 2 to 5 μ s periods are not discernible in Fig. 13. Periods corresponding to 1 to 1.6 MHz are present for the transfer function plot, but again no indication of low-frequency resonances can be found.

The present result differs drastically from the transfer function obtained using 25-mm radius spherical waves [8]. The previously obtained function is shown in Fig. 15, where two strongest peaks of opposite signs seem to imply the velocity response. (The velocity response is confirmed on the basis of source wave convolution, as discussed later.) The origin of many oscillations observed in Fig. 15 was not elucidated. Again, the type of incident waves affected the basic character of the transfer function.

e. R15 sensor: This utilitarian sensor from PAC and others of similar designs with 140-175 kHz resonance have been used widely during the past four decades. This is usually not intended for waveform acquisition, but its waveform and transfer function are obtained as the representative of widely used resonant sensors. See Figs. 16 and 17 for the plane-wave input case. The observed waveform shows well-separated pulses corresponding to the front-face arrival of the incident wave (marked A), the back-face arrival (B), the return of reflected wave at the front face (C) and the second arrival to the back face (D). These are spaced at 1.40 μ s and the amplitude of B-pulse is 1.7 times that of A-pulse. Other peaks are more irregularly spaced and it is hard to identify its main resonance frequency of 150 kHz from period observation. Broad peaks at \sim 12, \sim 20 and \sim 28 μ s may possibly correspond to the main resonance. On the other hand, the first 10 μ s (see Fig. 16 insert) contains 13-14 peaks, implying that this sensor has a high-frequency sensitivity and can be used in the same way as a WD sensor above to detect AE activities at different frequency ranges. The transfer function shown in Fig. 17 has a similar pulse sequence, with a – d peaks corresponding to A – D peaks in Fig. 16. The pulse sequence A-B-C with the strongest B suggests acceleration response. However, these three peaks are separated by two-cycle oscillation and the transfer function sequence a-b-c has a large positive peak following b-pulse, making acceleration designation tenuous.

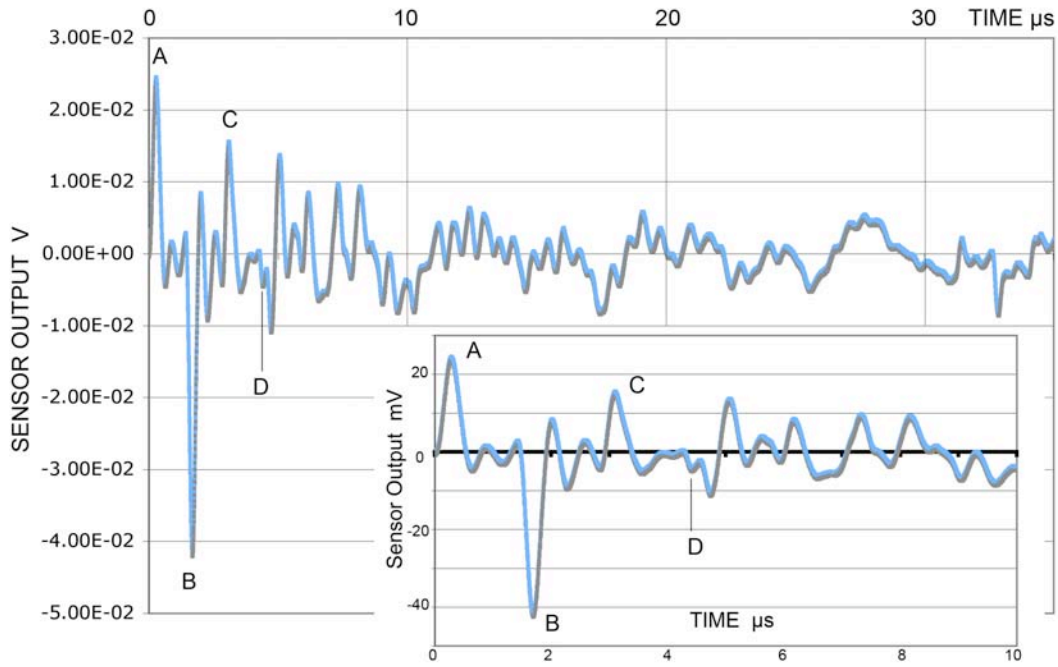


Fig. 16 Waveform of a PAC R15 (s/n 89) sensor excited by FC500-generated plane waves.

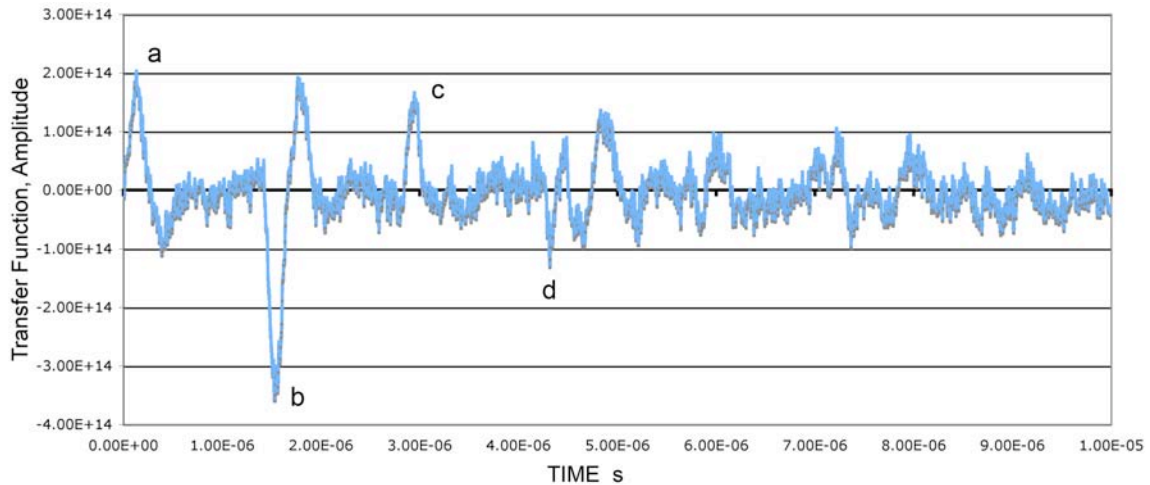


Fig. 17 Transfer function of a PAC R15 sensor excited by FC500-generated plane waves.

The transfer function calculated from 25-mm radius spherical wave input is given in Fig. 18 and has less discernible structures under $10 \mu\text{s}$, but $\sim 7\text{-}\mu\text{s}$ period becomes visible at longer duration. Its FFT is shown in the lower plot and clearly shows the presence of expected resonance structures at 155, 250 and 366 kHz, as indicated in the figure. However, two higher resonance frequencies had no corresponding peaks with a usual face-to-face testing method. The resonance oscillation in the transfer function appears to need spherical incident waves since it was invisible in the case of plane-wave input (in both the time and frequency domains).

f. PZT elements: Three PZT discs were similarly excited by plane or spherical waves. These are PZT-5 elements of 11.0-mm ϕ (diameter) x 5.4-mm thickness (designated as 175), 18-mm ϕ x 5.35 (400) and 10-mm ϕ x 14.4 mm (100), respectively. Disc 175 was taken out of AET AC175 sensor with nominal 175-kHz resonance. Disc 400 and 100 were ordered as 400-kHz or 100-kHz element. The waveform (left plot) and transfer function (right plot) of Disc 175 with plane-wave input are shown in Fig. 19. Those of Disc 400 were very similar, while we failed to get the trans-

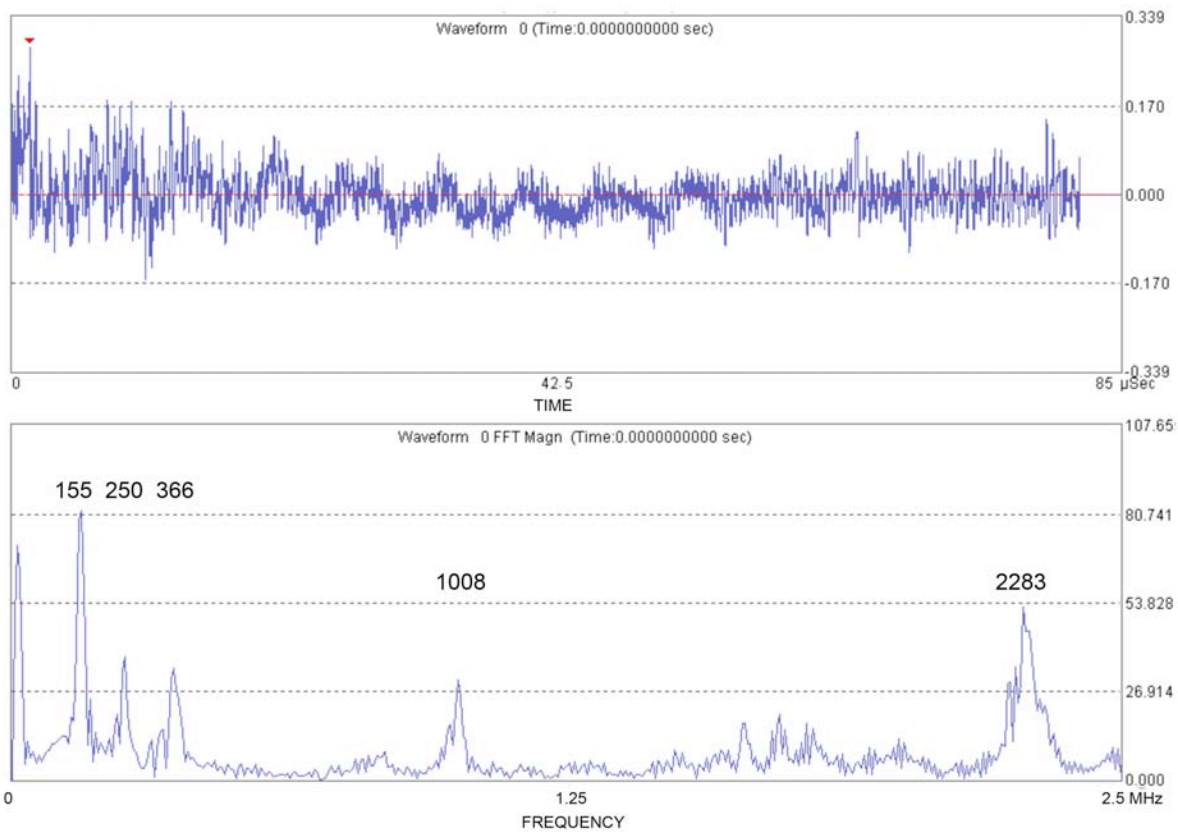


Fig. 18 Transfer function of a PAC R15 sensor (top) and its FFT (bottom) with peak frequencies in kHz. FFT used Noesis software.

fer function of Disc 100. Thus, these will be omitted from further discussion. Figure 19 shows similar features of the waveform and transfer function observed for R15 sensor in the beginning (cf. Figs. 16, 17). For Disc 175, the initial pulse spacing of $1.11 \mu\text{s}$ continues with regularity. One distinction is that here each pulse is bipolar, especially for the transfer function plot. This makes the disc to resonate at 900 kHz rather than the intended frequency of 450-kHz thickness resonance. The bipolar shapes may be construed as the velocity response, but it is a weak argument and further study must follow.

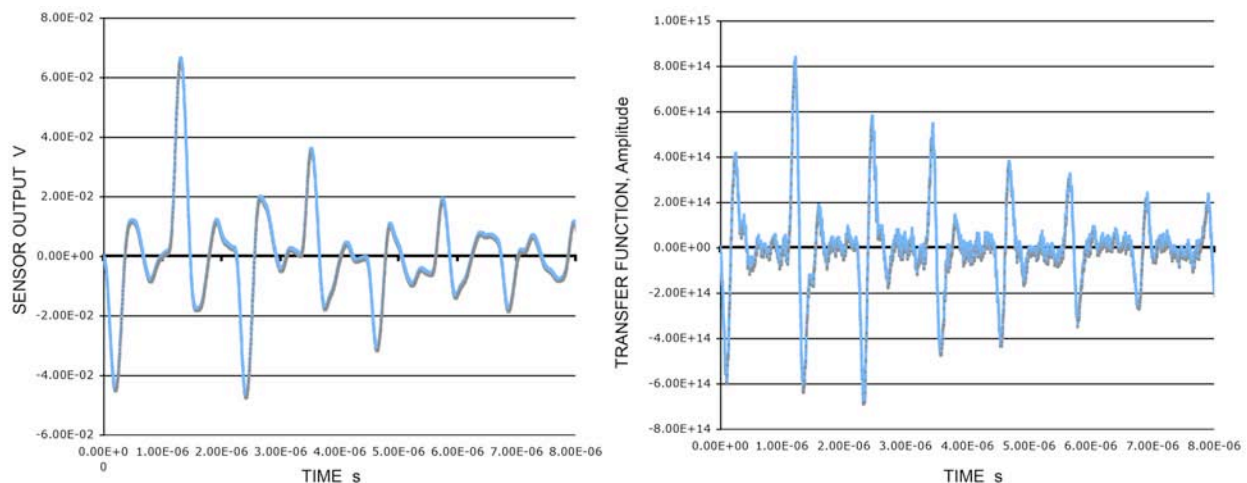


Fig. 19 Waveform and transfer function of Disc 175 PZT-5 element excited by plane waves using FC500 and 100-mm block. (x-axis length: $8 \mu\text{s}$)

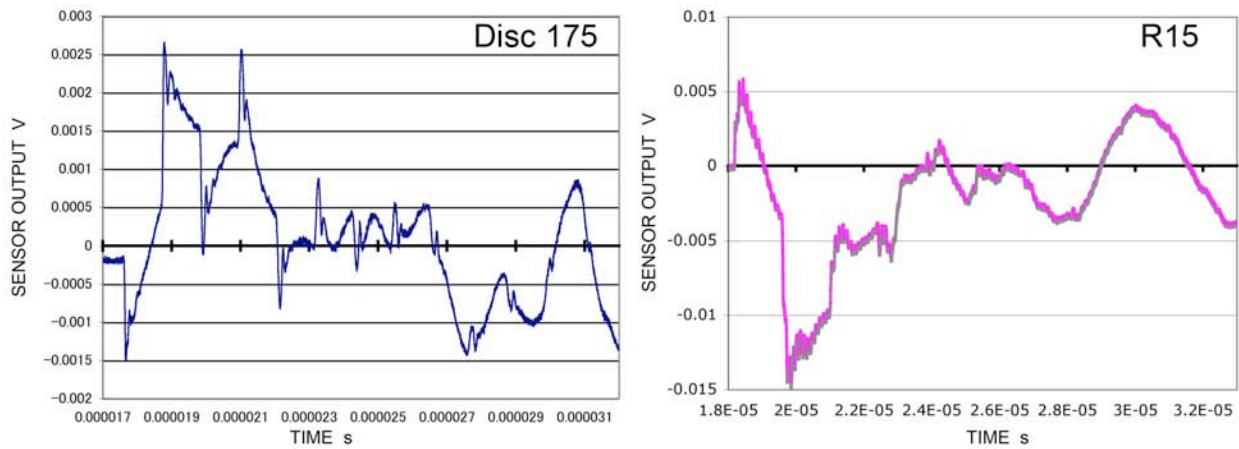


Fig. 20 Waveforms of Disc 175 PZT-5 element and R15 sensor excited by spherical waves using a pulse laser and 100-mm block. (x-axis length: 15 μ s)

When these same discs were excited by spherical waves, the response was quite different as shown in Fig. 20. Here, 100-mm block and a laser source were used. Left plot is for Disc 175, while right plot is for R15. In both cases, sharp spikes are followed by decaying output corresponding to the arrival of incident waves at the front or back surface. After a few cycles, these are replaced by smoother oscillations of respective resonance frequency. In the un-damped Disc 175, sudden rise-and-fall cycles lasted longer and these can be seen even after 12 μ s. In R15 with backing material in the sensor construction, these disappeared after the third cycles. When sharp steps are smoothed out (by filtering), this response gives rise to velocity-response at the thickness resonance as expected. However, when the main resonance frequency develops from cross-coupling effects (e.g., between thickness and radial modes), it is not possible to interpret the response mode.

2. Source wave convolution

When the transfer function of a sensor is known, we can construct the output signals from input displacement waveforms by performing convolution operation [8]. In order to show the utility of this procedure, we conducted a series of model computation. The transfer functions used were those obtained using 25-mm radius spherical waves.

We used three types of displacement waveforms to represent a source function. Type 1 is a single full-cycle sinewave, Type 2 a half-cycle sinewave from -90° to $+90^\circ$ (a smoothed step-function) and Type 3 a half-cycle sinewave from 0 to $+180^\circ$, respectively. The frequency of the waves was chosen at 100, 200, 500 kHz, 1 or 2 MHz. Zero-padding was applied as needed to avoid edge effects. Down-slope was also added for Type 2. For Types 1 and 3, the displacement waveforms are continuous, but their derivatives or velocity waveforms had discontinuities at the beginning and end. The velocity waveforms for Type 2 are of a half-cycle sinewave.

a. Pico sensor: The convolved waveforms are given in Fig. 21. For Type 2, a half-cycle sinewave is the prominent feature indicative of possible velocity response, but Types 1 and 3 waveforms indicate oscillations at input frequency. These Pico waveforms thus give no clear correspondence to displacement or velocity input. Considering the findings reported earlier in this work, this is not surprising. This sensor responds initially at a higher frequency (Fig. 8), followed by the main resonance frequency of 450 to 500 kHz. In the plane-wave excitation case, a velocity response is expected at 1.4 MHz at the beginning according to Fig. 5. Thus, we cannot assign

response type for the slowly developed vibration mode. Amplitude of convoluted waves is given in arbitrary unit, although the output values are given as obtained. When a sinewave of unity amplitude is given as source input, it represents ± 1 -m displacement. However, the output is not necessarily proportional to displacement and further evaluation is needed to establish a proper unit to use.

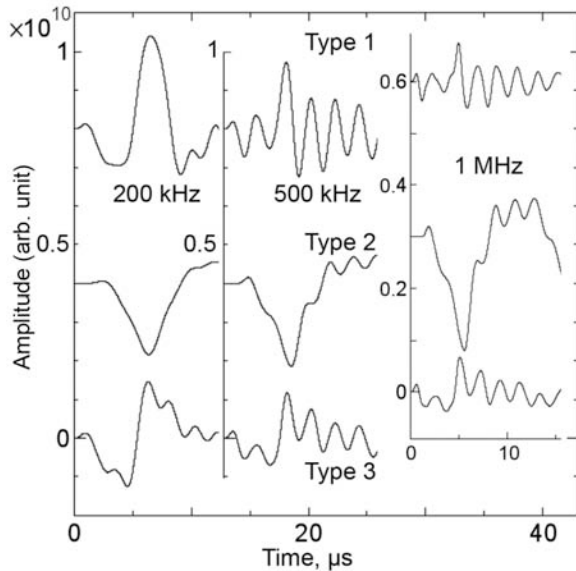


Fig. 21 Pico-sensor responses to 3 input types.

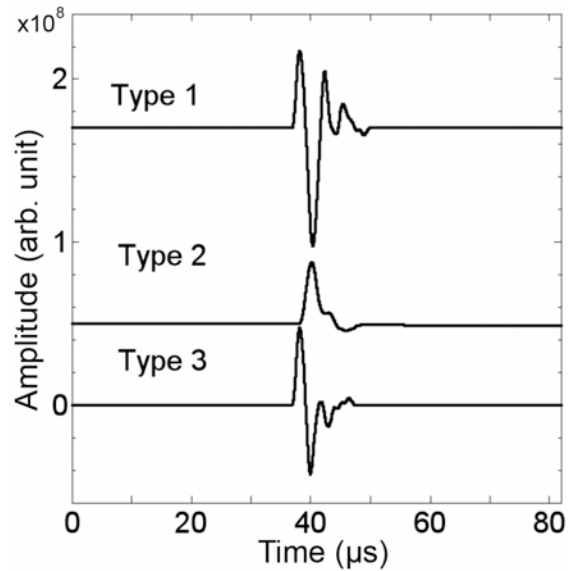


Fig. 22 WD-sensor responses at 200 kHz.

Pico sensors have been used to evaluate crack-induced AE through source simulation analysis [9-11], where the signal rise time is an important parameter. Thus, we examined the linearity with respect to the source-function rise time. For Type 2 signals, nominal displacement input rise times are 0.25, 0.5 and 1 μ s for 2, 1 and 0.5 MHz; the corresponding rise times of the convoluted waveforms were 4.60, 4.71 and 4.91 μ s, indicating proportional increments with a delay. Similar relations are observed for Types 1 and 3 signals. This implies that Pico sensors can be used for comparative rise time studies. However, this sensor appears to have a mixed response to input displacement and velocity and may cause difficulties in characterizing the nature of source events. We also need to clarify the origin of the rise time stretching of about 4 μ s.

b. *WD sensor*: The convoluted waveforms for 200-kHz sources are given in Fig. 22. Type 1 shows a large dip between two sharp peaks. This waveform resembles the velocity source wave of Type 1 or the derivative of a full-cycle sinewave displacement. The base duration is extended to 6.64 μ s compared to 5- μ s input. Type 2 corresponds to a half-cycle sinewave, with an extrapolated base width of 4.0 μ s (1.5 μ s longer than 2.5 μ s input width). Again, this corresponds to the derivative of Type 2 displacement input. Type 3 is the initial part of Type 1, with the base width shortened to 4.48 μ s (still ~ 2 μ s longer than the input width). The rise time to the first peak was 1.28, 2.30 and 1.28 μ s for the three types. Here, the rise time of 1.28 μ s for Types 1 and 3 results from 10 ns effective rise time, while 2.30 μ s for Type 2 is due to the smoothed step rise time of 1.25 μ s duration. Thus, the WD sensor contributed 1~1.3 μ s to the observed rise time at 200 kHz.

Type-2 waveforms using five different source frequencies are shown in Fig. 23. The lower frequency signals are closer to a half-cycle sinewave, while effects of additional peaks are more visible at 2 MHz, especially at the trailing part beyond the main peak having minor oscillations.

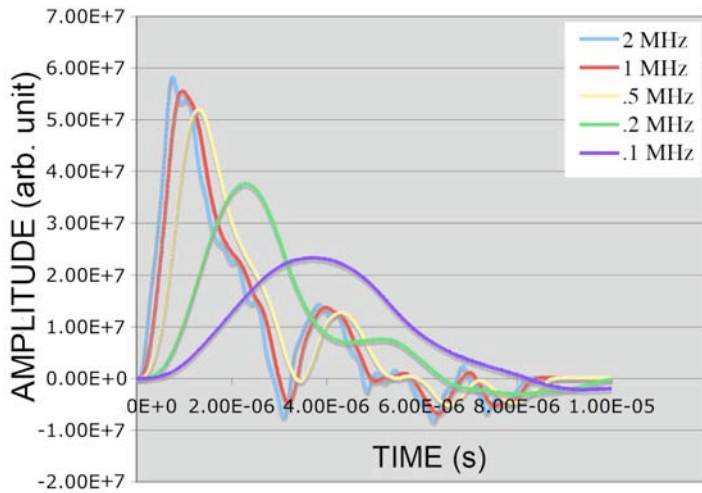


Fig. 23 WD waveforms for Type-2 input.

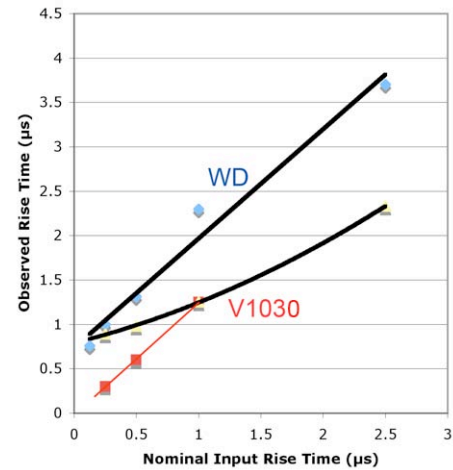


Fig. 24 Rise time for WD and V1030.

The main features of Fig. 22 were also observed at 100 kHz to 2 MHz. In all cases, the WD sensor gives consistent velocity response in the three types of source waves. This finding needs further tests at more frequencies that differ from the sensor resonances (100, 230, 480 kHz) [12], but WD responds basically to velocity signals of spherical wave input. Note that it is difficult to reach this conclusion from visual inspection of the transfer function (Fig. 15).

The observed rise time decreased smoothly with frequency, as shown in Fig. 24, where its values for Type 2 are plotted against nominal (velocity) input rise time. The observed rise time is always larger than the nominal value and the difference ranges from 1.20 μs (100 kHz) to 0.63 μs (2 MHz). Because of multiple resonance characteristics of this sensor, this finding is unexpected and surprising, but WD sensor is useful even for rise time studies.

c. *V1030 sensor*: The convolved waveforms for 500-kHz sources are given in Fig. 25. For spherical wave input, this sensor gives displacement response, with full or half sinewave output for Types 1 and 3 and a step-down waveform for Type 2. This reflects the nature of its transfer function with the negative-going main peak when excited by 25-mm radius spherical waves. This behavior is expected from its heavily damped construction for ultrasonic testing applications. The waveforms were similar at 200 kHz, but at 1 MHz, an additional peak overlapped and response became a mixed one. The observed width of the first full cycle was 4.91, 2.30, 1.51 and 0.53 μs for 0.2, 0.5, 1 and 2 MHz source, showing anomaly at 1 MHz.

Type-2 response of V1030 sensor is shown in Fig. 25. The anticipated step-down behavior was seen at 0.2 and 0.5 MHz with the “rise” time of 2.33 and 1.25 μs . These compare well with the nominal values of 2.5 and 1.25 μs . At 1 and 2 MHz, a faster rising component (at 0.30 and ~ 0.6 μs) appears before the main peaks at 0.98 and 0.89 μs (see Fig. 24). The main peak rise times follow a smooth curve, ending at 0.85 μs for zero nominal source rise time. The origin of the fast component is apparently due to the main peak (at 0.30 μs) in the transfer function, whereas the main peak in the convolved waves combines the first two large peaks (at 0.30 and 0.83 μs) in the transfer function. While the overall behavior of V1030 sensor is primarily displacement response, these additional deviations complicate the interpretation and careful waveform evaluation is needed. We obviously cannot assume a heavily damped sensor to be always well behaving.

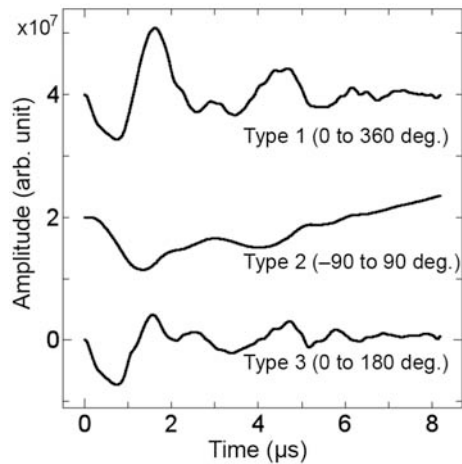


Fig. 25 V1030-sensor responses at 500 kHz.

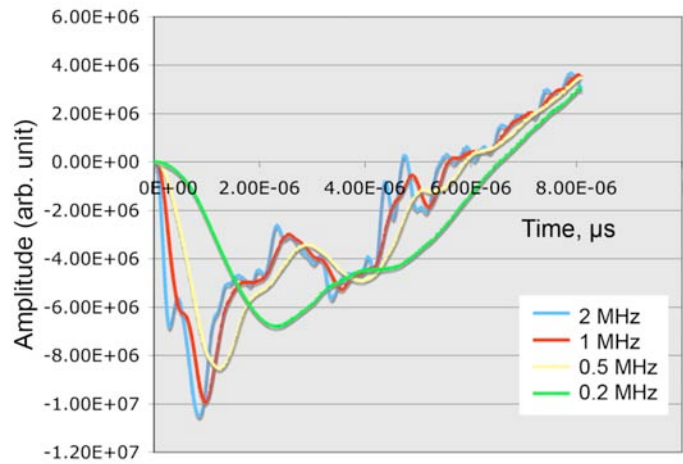


Fig. 26 V1030 waveforms for Type-2 input.

Discussion

The calibration procedure described here is a straightforward application of current laser-sensing technology in measuring the displacement of elastic waves. In combination with piezoelectric or laser generation of planar or spherical waves, we can characterize AE sensors in a new way; that is, the transfer function of a sensor, which should be available in addition to the customary frequency response characteristics per ASTM E-1106. It also became evident that the transfer function of a sensor depends on the incident wave types as different vibration modes of a sensing element are excited in non-unique manners. This resulted in sensor response characteristics (i.e., acceleration, velocity, or displacement) that are dependent on the incident wave modes.

In light of the present study, we must reevaluate the NIST-developed calibration standard (ASTM E-1106 and ISO equivalent) since it relies on circular waves propagating on a steel block. Depending on the distance from the central glass-capillary break, the wave front changes producing distance- and aperture size-dependent calibration standard. Through-transmission calibration method also faces difficulty of spherical wave propagation.

Because most AE sources can be regarded as a point source, AE sensors must detect spherical waves. We have used two thicknesses for the transfer block. Systematic study of effects of the radius of curvature is needed. Also required is the understanding of how various vibration modes are excited within the sensing element. In this connection, the results reported here on PZT elements must be further examined as to how electrical signals are generated in relation to the position of elastic wave front. Rouby [13] examined long ago how each component of a signal waveform is generated. However, the comparison of R15 and Disc 175 results (cf. Figs. 16, 19 and 20) immediately shows vastly different behavior (input: plane or spherical incident waves; output: bipolar vs. unipolar). Thus, careful model experiments must be conducted to elucidate mechanisms of signal generation as functions of the radius of curvature of incident waves and the degree and types of cross-coupled vibration modes.

Conclusions

The transfer functions of representative AE sensors were obtained using the excitation by an ultrasonic transmitter or pulse laser and displacement measurement using a laser interferometer. Types of incident waves are critically important in defining the transfer functions as different

vibration modes were excited. These also affected the sensor response characteristics (i.e., acceleration, velocity, or displacement). The transfer functions and typical source waveforms were combined by convolution. Results demonstrate the nature of sensor responses and the utility of the approach used here. This study points to the need of reexamining the standard calibration method in terms of wave front radius effects. Wider uses of transfer functions can improve our understanding of various AE sources.

Acknowledgement

The authors are grateful to Drs. Al Beattie, G. Manthei and M. Ohtsu for helpful comments and to Messrs. Allen Green and Hal Dunegan for valuable discussion on sensor calibration.

References

1. *NDT Handbook, vol. 6, Acoustic Emission Testing*, ASNT, Columbus, OH, 2005, pp. 54-60.
2. B. Allemann, L. Gauckler, W. Hundt and F. Rehsteiner, *J. Acoustic Emission*, **14**, (1996) 119-126.
3. G. Manthei, *Bull. Seismological Society of America*, **95** (5), (2005), 1674-1700.
4. F.R. Breckenridge, C.E. Tschiegg and M. Greenspan, *J. Acoust. Soc. Am.*, **57** (3), (1975), 626-631.
5. T. F. Heuter and R.H. Bolt, *Sonics, techniques for the use of sound and ultrasound in engineering and science*, J. Wiley, New York, 1955, pp. 9-28.
6. *Acoustic Emission*, JSNDI, Tokyo, Japan, 1990, p. 14.
7. W.P. Mason, *Physical Acoustics and the Properties of Solids*. Van Nostrand, 1958, pp. 51-86.
8. K. Ono and H. Cho, *Proc. 28th European Conf. AE Testing*, Krakow, 2008, pp. 25-30.
9. Y. Mizutani, H. Nishino, M. Takemoto and K. Ono, *J. Acoustic Emission*, **18**, (2000) 286-292.
10. S. Fujimoto, M. Takemoto and K. Ono, *J. Acoustic Emission*, **19**, (2001) 69-74.
11. K. Kagayama, T. Ogawa, A. Yonezu, H. Cho and M. Takemoto, *J. Acoustic Emission*, **24**, (2006), 127-138.
12. M. Eaton, K. Holford, C. Featherston and R. Pullin, *J. Acoustic Emission*, **25**, (2007) 140-148.
13. D. Rouby, *Proc. 3rd International Symp. on AE from Composite Materials*, AEEM-3, Paris, ASNT, 1989, pp. 313-322.

COUPLANTS AND THEIR INFLUENCE ON AE SENSOR SENSITIVITY

PETE THEOBALD, BAJRAM ZEQRIRI and JANINE AVISON

National Physical Laboratory, Teddington, Middlesex, TW11 0LW, United Kingdom

Keywords: Acoustic couplant, sensor sensitivity

Abstract

The removal of air from the interface between a measurement surface and an AE sensor is crucial to the transmission of ultrasonic energy. The acoustic impedance of air is around 5 orders of magnitude lower than that of the two contacting surfaces, allowing for very little transmission of acoustic energy at the frequencies typical of acoustic emission (AE). The use of a couplant can greatly improve this transmission by around 2 times at 100 kHz and more than 10 times at 500 kHz; a typical gel-based couplant having a high acoustic impedance around 4 orders of magnitude higher than that of air. The effectiveness of a given couplant is dependent on its acoustic impedance, acoustic absorption, application thickness and viscosity. Each of these can have a strong influence on the sensitivity response of the sensor and can ultimately change the way the sensor responds to different wave modes. This paper considers a number of ultrasonic/AE couplants and compares the sensor response for each couplant to longitudinal and shear waves, demonstrating that a high-performance ultrasonic couplant can improve sensor sensitivity significantly above 400 kHz compared with a grease-type couplant.

Introduction

When attaching an AE sensor to a measurement surface, a couplant material is used to remove any air from the interface, introduced due to the microstructure and surface roughness of the two contacting surfaces. The reason for doing this is that the acoustic impedance of air is much lower than that of the sensor face or material surface and will cause considerable loss in transmission. Piezo-ceramic has relatively high acoustic impedance, as does steel (a typical measurement surface) making them a relatively good match. However, the acoustic impedance of air is around 5 orders of magnitude lower than that of piezo-ceramic or steel and so introducing a couplant layer with an acoustic impedance higher than that of air, which displaces the air between the two surfaces, can increase transmission substantially [1]. For AE applications, there is a range of couplants to choose from depending on the requirements dictated by the application. The properties of the chosen couplant can have a significant effect on the output generated by the sensor and thus the quality of the measurement. Couplants with high acoustic impedance have been shown to produce substantially better ultrasonic transmission than standard couplants [2] and are used in ultrasonic applications to improve the signal-to-noise ratio. For AE and vibration applications, studies have compared the properties of common couplants and have made recommendations based on transmission and ease of use etc. [3].

Whilst couplants no doubt improve the transmission between the contact surface and the sensor, they do introduce a certain amount of variability [4] and different couplants can provide different transmission properties as a function of frequency [5]. During calibration, this can have an effect not only on the apparent sensitivity of the sensor but also its frequency response. For the calibration of an AE sensor, a single couplant is usually selected and the sensitivity of the sensor as a function of frequency is usually stated using the selected couplant [6-13]. This paper considers the effect of couplant choice on the stated sensitivity of the sensor during calibration.

Couplant Requirements

When selecting a couplant for use during an AE measurement or monitoring application, a number of factors need to be considered, of which acoustic transmission is just one. The most important factors might be long-term stability depending upon length of measurement, removal and reapplication of the sensor, the mounting surface condition or shape, sources of vibration which could displace the sensor, mounting surface temperature, etc. There are a number of couplant types to choose from, typically liquid, gel or grease. Other types of couplants based on compounds or adhesives can be used, which provide bonding of the sensor to the surface.

Generally, the acoustic performance of a couplant is dictated by the acoustic impedance, acoustic absorption and the couplant thickness. In addition to these, the ability of the couplant to force air bubbles from the contacting layer is extremely important and this often requires a relatively low viscosity. Equally important is the wetting ability of the couplant. This is related to the surface tension of the couplant and describes the level of molecular contact between a couplant and the compressing surfaces. This is often related to viscosity and good wetting fluids, like water, can often result in less air between the couplant and the two compressing surfaces.

Acoustic emission sensors have a dominant response to particle motion normal to the surface and for this type of measurement the properties described above are most applicable. However, if detecting particle motion is parallel to the sensor face (shear motion), which is a common requirement in plate structures, the viscosity of the couplant will become a more important transmission property. A high-viscosity couplant or a rigid bond will provide greater transmission of these in-plane particle motions than couplants with the conventional properties described above.

Measurements and Results

A number of couplants were selected for testing. Glycerin, propylene glycol, ultrasound gel and silicone grease are compared in this paper. Glycerin and propylene glycol were selected as these are considered high-performance ultrasonic couplants, particularly glycerin, which provides a layer of relatively 'high-impedance' couplant. Ultrasound gel was also used as this couplant is routinely used for AE sensor calibration at the National Physical Laboratory [9, 10], providing good transmission but only suitable for relatively short measurement periods. The main advantage of this type of gel is its extremely good wetting properties, which combined with a relatively low viscosity, result in very low air content in the coupling layer. Silicone grease was also used in the comparison as this and other similar performing greases are widely used in practical AE applications due to their stability with time and their non-drip consistency. A dry contact was also used for reference purposes to demonstrate the effect of using no couplant. Two sets of measurements were performed. Firstly, a longitudinal sensor calibration was performed against a velocity interferometer to obtain the sensor sensitivity in V/mm/s as a function of frequency. This calibration was performed for each couplant on the same sensor to show the effect of the couplant on the sensitivity response of the sensor. Secondly, a relative comparison was performed between each couplant showing how the sensor's response to a normal incidence shear wave is affected by the couplant. For the shear-wave measurements, a couplant designed specifically for shear wave transmission (Panametrics shear-wave couplant) was used in place of the glycerin.

The measurements were performed on a 410-mm diameter hemi-spherical aluminium block with a flat top of approximate diameter of 50 mm, for mounting the sensor under test. The flat

top is also polished flat to provide a suitable optical reflection for calibration of the sensor against a laser interferometer. In this case, the polished surface also acts as an idealised coupling surface and resulted in reduced variability between couplings. A Panametrics V189-RB 0.5 MHz, 1.5-inch diameter NDT source transducer was bonded with cyanoacrylate to the base of the hemisphere as shown in Fig. 1. The interferometer was aligned with its optical beam normal to the surface of the flat top along the central axis of the block. The Panametrics V189-RB transducer was excited with a 1- μ s pulse generated by an Agilent 33220A function generator. Following propagation through the block, the out-of-plane displacement component of the longitudinal wave was measured using the interferometer. The output from the interferometer was captured at a sample rate of 25 mega-samples per second using a TDS 5054 oscilloscope with the trigger synchronised with the function generator. A total of 3000 time averages were used to measure the interferometer output to improve the signal-to-noise ratio. Once the velocity history of the surface had been established using the interferometer, a PAC S9208 sensor (with 40 dB pre-amplification and a 20 kHz high-pass filter) was then coupled to the flat top of the hemisphere, with the selected couplant, in place of the interferometer laser beam. The sensor was chosen due to its broadband response up to 1 MHz. The same procedure was then followed to capture the voltage output from the sensor with 100 time averages being used. This process was repeated for each couplant. To improve repeatability and allow comparison between the different couplants, the position of the sensor on the surface was fixed using a three-point guide and held in place with a constant mass of approximately 6 N. Using a constant force does mean that a more viscous couplant might result in a thicker layer and less air removal. To counter this, an increasing force was applied during installation of the sensor, whilst simultaneously monitoring the sensor output. Once the apparent maximum output was achieved, the force was reduced to the holding force of 6 N, ensuring that the sensor output did not drop during this reduction. This approach ensures that the maximum acoustic performance is established for each couplant and reduces variability between re-couplings. It is however acknowledged by the authors, that this may not represent a realistic scenario for *in-situ* use.

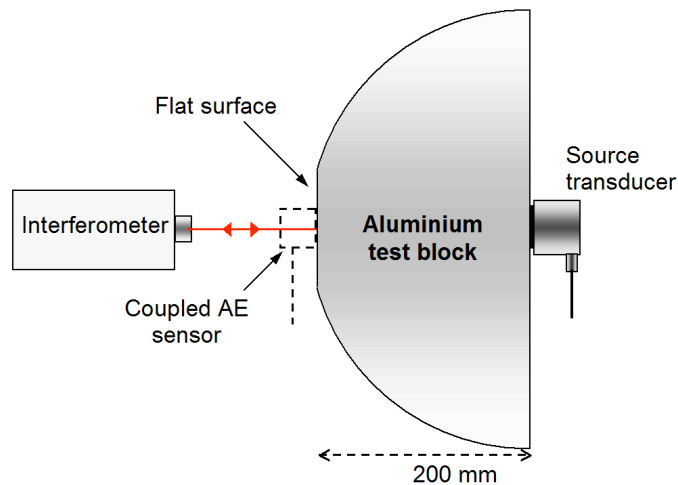


Fig. 1. Measurement configuration for out-of-plane motion.

For the shear-wave measurements, a Panametrics V152-RB 0.5 MHz, 1.0-inch normal incidence shear-wave transducer was used to generate a shear wave at the sensor after propagation through the block shown in Fig. 1, with a velocity or displacement component parallel to the surface. This transducer was also bonded to the transmission surface using cyanoacrylate to provide a rigid bond for optimum shear-wave transmission. For these measurements, only the sensor outputs were measured. In this configuration it was not possible to calibrate the response of the

sensor to the velocity component parallel to the surface as the interferometer measures only the normal velocity component of the surface, although calibration to this in-plane component using optical interferometry has been reported in the literature [10-11].

For both the longitudinal and shear wave measurements, the sensor was coupled a number of times using each couplant. This was done to establish both the overall variability of re-coupling the sensor and to establish the maximum peak-to-peak signal level achievable with each couplant.

The sensor measurement in Fig. 2 shows the longitudinal-wave arrival following a 32- μs propagation time through the aluminium block. At around 64 μs , a direct shear wave arrives, which is generated from the edges of the transducer. Although this is difficult to identify from the sensor output, it is identifiable from the interferometer measurements (not shown). The direct echo does not arrive until around 96 μs and is just visible at the end of the time waveform shown in Fig. 2. To obtain the magnitude sensitivity, the quotient of the spectra of the sensor-output voltage and the interferometer velocity output is calculated. However, to ensure that the sensitivity is calculated for only the longitudinal-wave arrival, the time waveforms are time-gated before the shear-wave arrival as indicated in Fig. 2.

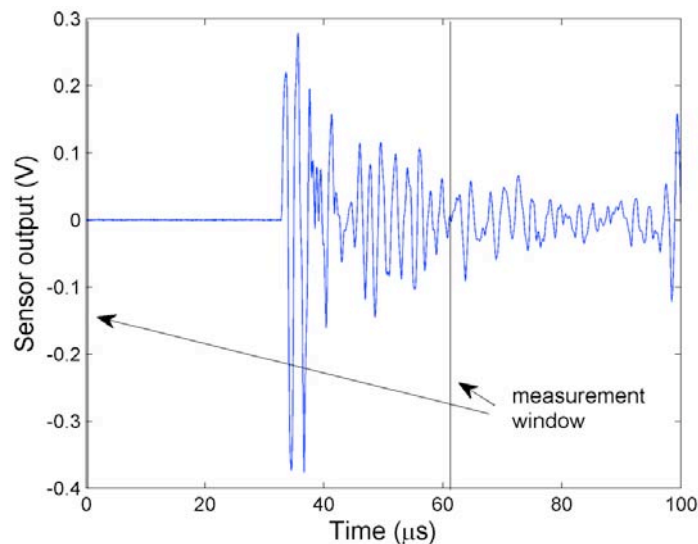


Fig. 2. Sensor output time waveform for longitudinal wave measurements.

Figure 3 shows the calibration results of the S9208 AE sensor for its velocity sensitivity to the longitudinal wave when coupled using the high-impedance glycerin, propylene glycol, ultrasound gel, silicone grease and a dry contact with no couplant. In each case, the sensitivity is derived from the maximum signal level achievable with each couplant. At lower frequencies, below 400 kHz, the couplant appears to have very little effect on the sensitivity of the sensor, with the variability observed between 200 kHz and 400 kHz being almost within the variability due to re-coupling which was around 5% to 15% depending on the couplant. However, above 400 kHz there is greater difference in sensitivity, particularly at frequencies where the sensor exhibits resonance behaviour, which cannot be explained by re-coupling variability. This shows that the glycerin, propylene glycol and particularly the ultrasound gel do provide the greatest sensitivity. Conversely, silicone grease provides poorer sensitivity at the higher frequencies, up to as much as 65% less than the ultrasound gel, for the best coupling achievable with each couplant. This indicates that ultrasound gel has a lower attenuation coefficient at the higher frequencies than

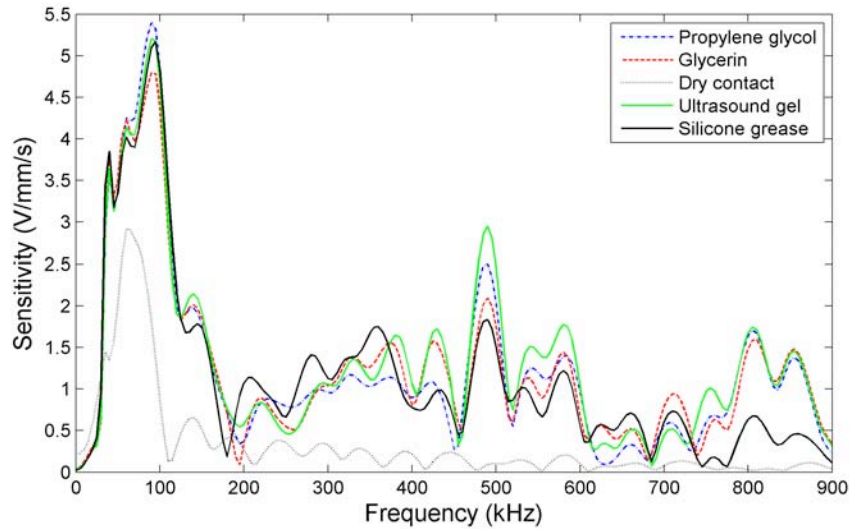


Fig. 3. Calibration of S9208 velocity sensitivity for longitudinal wave using different couplants.

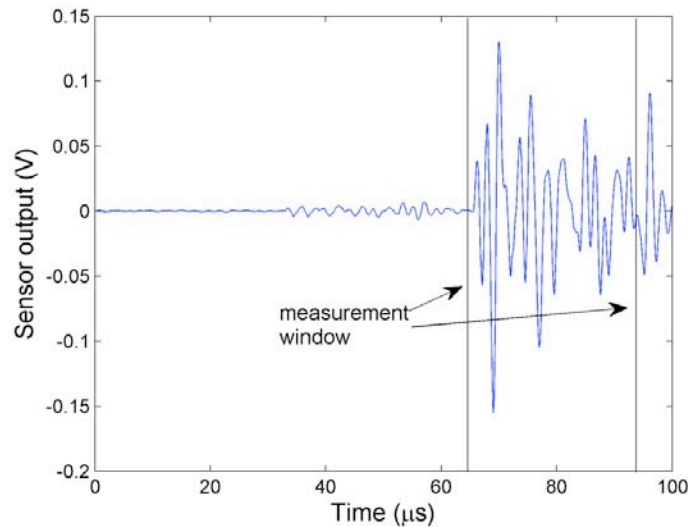


Fig. 4. Sensor output time waveform for shear-wave measurements.

silicone grease as both have comparable acoustic impedance. The ultrasound gel could also benefit from good wetting, good air removal properties and a thinner coupling layer. These differences do have implications for couplant choice when providing the calibration sensitivity of the sensor and even more so when performing broadband or high-frequency AE measurements. A poor choice of couplant could not only have a negative impact on the signal-to-noise ratio, but could ultimately change the shape of the AE-event waveform being investigated. The dry contact also shows a large reduction in sensitivity as expected - around a 50% reduction at 100 kHz and substantially more at higher frequencies. This is to be expected due to the high acoustic absorption in air (which effectively fills the gaps in the sensor-surface contact) at ultrasonic frequencies and the very high impedance mismatch. The sensor measurement in Fig. 4 shows a shear-wave arrival following a 64- μs propagation time through the aluminium block. This wave mode is generated at the source transducer such that it arrives with its particle velocity parallel to the sensor surface. A small longitudinal-wave arrival can also be seen arriving after a delay of 32 μs . Although small, it is assumed that a direct echo of the longitudinal wave arrives at around 96 μs and so the time waveforms are time-gated between 64 μs and 96 μs as shown in Fig. 4.

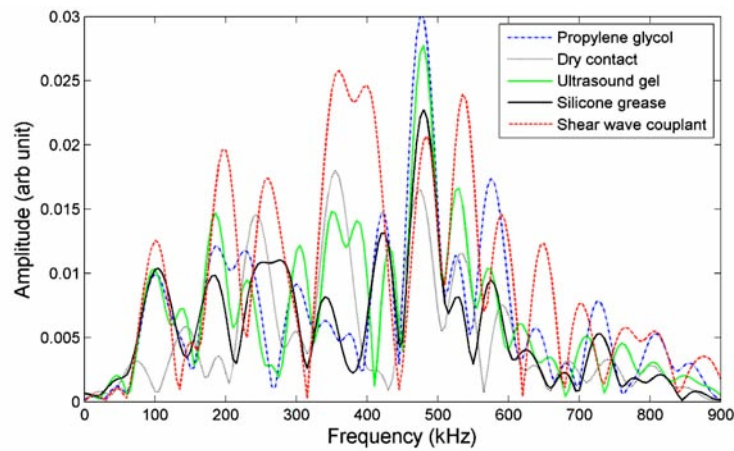


Fig. 5. Response of S9208 to shear wave using different couplants.

Figure 5 shows the response of the S9208 AE sensor to the 1- μ s pulse generated by the V152-RD normal-incidence shear-wave transducer when coupled using the propylene glycol, ultrasound gel, silicone grease and a dry contact with no couplant. In addition to these, a Panametrics shear-wave couplant, which is specifically designed to have a very high viscosity to maximise shear-wave transmission, was included in the comparison. It should be noted that Fig. 5 cannot be compared with Fig. 3 to assess the sensors longitudinal and shear wave response as Fig. 3 is a sensitivity derived from the quotient of the spectra of the sensor and interferometer signals, whereas Fig. 5 only considers the direct output spectrum of the sensor.

The shear-wave couplant clearly provides the greatest transmission of the shear wave in this case, but, more interestingly, the dry contact is now not so poor when compared to the use of a couplant. The dry contact is in fact comparable to the silicone grease. The most probable reason for this is that for good shear-wave transmission acoustic impedance and absorption are no longer the dominant factors. The transfer of shear forces between atoms is likely to dominate and for this to be most effective, a rigid contact is necessary. Although the effective contact area for the dry contact would be significantly reduced by the microstructure of the two surfaces, the small contacting area is sufficiently rigid to provide transmission comparable to a low rigidity/viscosity couplant, which provides a full area contact in this case. However, the measurements were performed on a polished metal surface, which should allow for a good dry contact. The type of measurement surfaces encountered in practice would likely perform very poorly for a dry contact. For the shear-wave measurements however, the couplant effect on frequency response is less clear. The ultrasound gel and propylene glycol provided surprisingly good transmission of the shear wave given their very low viscosity. The silicone grease performed less effectively but has the benefit that it does not drip or dry up with time, which can be a problem with liquid-based couplants. The silicone grease also had the lowest re-coupling variability of less than 8% in both sets of measurements. The performance of couplants for shear waves with particle motion parallel to the surface also represents their performance to symmetric Lamb waves. Similarly the longitudinal wave results presented with particle motion normal to the surface will be representative of couplant performance for anti-symmetric Lamb waves, which propagate in plate structures [14].

Conclusions

The effect of couplant on the calibration of the velocity sensitivity response of an AE sensor to a longitudinal wave (out-of-plane) has been considered and shows the effect of the couplant to

be broadly unnoticeable within the re-coupling variations. However, at higher AE frequencies above 400 kHz, the properties of the couplant become more important. At these higher frequencies, silicone grease reduced the sensitivity of the sensor by up to 65% compared with a high-performance ultrasonic couplant such as propylene glycol. Although this has implications for the accuracy of the sensitivity calibrations for AE sensors, it will also have an impact on AE measurements. A poor choice of couplant could significantly reduce signal-to-noise ratio in broadband or high-frequency AE measurements and could lead to distortion of the waveform being measured.

In addition to this, shear-wave measurements have shown that for the measurement of wave modes with particle motion parallel to the surface, such as symmetric Lamb waves, there is no real benefit in using couplants conventionally considered to be 'high-performance' ultrasonic couplants. Given that both planes of particle motion would be encountered in typical AE applications, a balanced choice should be made between the requirement for out-of-plane and in-plane particle motion and required mechanical/material/chemical properties.

Acknowledgements

We gratefully acknowledge the financial support of the UK Department of Innovation, Universities and Skills (National Measurement System Programmes Unit).

© Crown copyright 2008. Reproduced by permission of the Controller of HMSO and the Queen's printer for Scotland.

References

1. ASTM E650-97 *Standard Guide for Mounting Piezoelectric Acoustic Emission Sensors*, 2007.
2. Culjat M. O., Singh R. S., White S. N., Neurgaonkar R. R., Brown E. R.: *Acoustics Research Letters Online*, **6**(3), (2006), 125-129.
3. Colombo S., Giannopoulos A., Forde, M. C., Hasson R., Mulholland J.: *NDT&E International*, **38**, (2005), 187-193.
4. Dugmore K., Jonson D., Walker M.: *Composite Structures*, **58**, (2002), 601-603.
5. Sun L., Kulkarni S. S., Achenbach J. D., Krishnaswamy S.: *J. Acoust. Soc. Am.*, **120** (5), (2006), 2500-2505.
6. Hsu N. N., Breckenridge F. R.: *Mat. Eval.* **39** (1), (1981), 60-68.
7. American National Standard, ASTM E 1106-07 *Standard method for primary calibration of acoustic emission sensors*.
8. Miller R. K., McIntire P. (eds.), *Nondestructive Testing Handbook*, 2nd ed. Vol. 5, *Acoustic Emission Testing*, American Society for Non-destructive Testing, 1987, pp. 120-134.
9. Theobald P. D, Esward T. J., Dowson S. P., Preston R. C.: *Ultrasonics* **43**, 2005, 343-350.
10. Theobald P., Dar F.: *Key Engineering Materials*, **13-14**, (2006), 91-97.
11. Theobald P.: *Ultrasonics*, 10.1016/j.ultras.2009.03.004, (2009).
12. Goujon L., Baboux J. C.: *Meas. Sci. Technol.*, **14**, (2003), 903-908.
13. Hatano H., Chaya T., Watanabe S., Jinbo K.: *IEEE Trans. Ultrason. Ferr. Freq. Contr.*, **45** (5), (1998), 1221-1228.
14. Viktorov I. A.: *Rayleigh and Lamb Waves*, Translated from Russian, Plenum Press N.Y, 1967.

LABORATORY EXPERIMENTS FOR ASSESSING THE DETECTABILITY OF SPECIFIC DEFECTS BY ACOUSTIC EMISSION TESTING

FRANZ RAUSCHER

Vienna University of Technology, Institute for Engineering Design and Logistics Engineering,
Research Group for Pressure Vessel and Plant Technology, Gusshausstrasse 30, 1040 Vienna,
Austria

Keywords: pressure vessel, experiments, detectability

Abstract

For acoustic emission (AE) testing of pressure vessels during in-service inspection, special experiments must be performed to get the appropriate information in some cases. Design of such experiments, especially the loading history, is the focus of this paper. Limitations on the experimental load history, which result from the Kaiser-effect and the goal of the test, are given. Another important point is the generation of an appropriate defect. An example with an initial artificial weld defect and defect growth by pressure cycling is given. The measured low AE activity during this test shows that experimental verification for AE testing may be necessary, even if standard procedures are used.

Introduction

In the last decades acoustic emission (AE) testing was developed further [1], and many dangerous defects were found [e.g., 2-4], and probably accidents have been prevented. Frequently, economic reasons are the determining factor of whether or not AE testing is used during in-service inspection. To get an optimum on safety, the question whether or not defects and failure modes, which are probable in the specific case, can be detected by AE testing should dominate the decision. Of course, AE is an integral testing method and able to detect unforeseeable defects, which is a favorable property for inspection strategy.

Finding experimental evidence that a specific type of defect is detectable is difficult. One of the reasons why the transfer of results from experiments to AE testing is difficult is the complicated load history, which is applied to pressure vessels prior to AE testing. Therefore, this paper focuses on experimental loading histories for studying the AE characteristics of defects during AE testing of pressure vessels.

Here, AE testing during in-service inspection, not during pressure testing after fabrication, is mainly considered. The focus lies on local defects, like welding defects, cracks, pitting, etc., and global wall thinning and design failures are outside of the scope of this paper.

Loading History

Loading histories of pressure vessels (Fig. 1) start with the pressure tests after fabrication. AE testing during the first pressure test is not the focus of this paper. During service, the vessel is usually pressurized with more or less pressure variations, but pressure has to be below maximum allowable pressure p_S , which is the relief pressure of the safety valve. Because of limited tightness of safety valves near the relief pressure, operating pressures are usually below p_S . When the safety valve opens, according to the European Pressure Equipment Directive (PED), the pressure

is allowed to exceed p_s by 10%. For AE testing the pressure should be raised to a value higher than the maximum value reached during the operating period before the test, but the maximum pressure of the first pressure test is usually not exceeded.

Initial defects may be present after fabrication. If they are not detected before the vessel goes into service, they may grow during the service period. Other defects may be initiated and grow during service. The goal of the in-service inspection is to detect all dangerous defects before they lead to catastrophic failure.

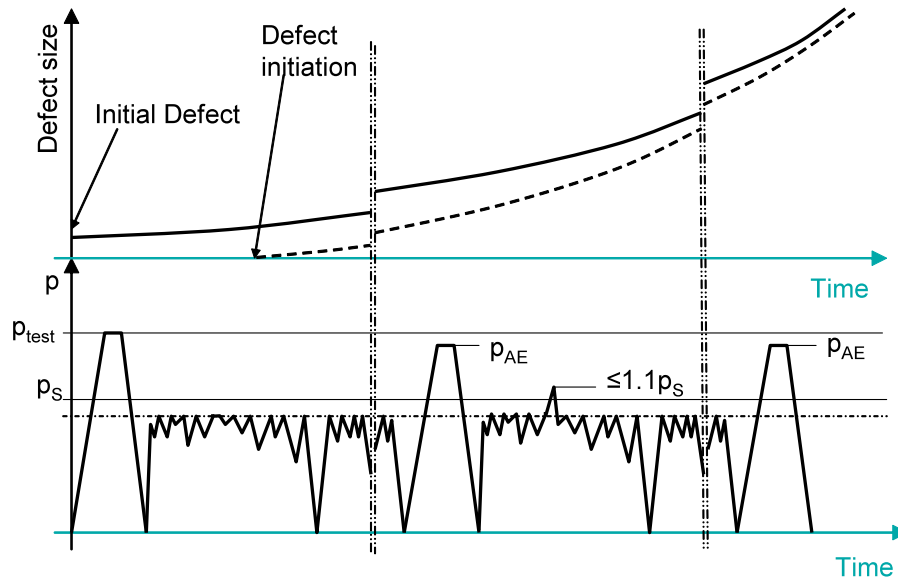


Fig. 1. Typical loading history of pressure vessel; p , pressure; p_s , maximum allowable pressure; p_{test} , test pressure; p_{AE} , maximum pressure at AE testing.

Plastic Deformation

For the AE generation, plastic deformation is important. First yielding produces AE itself, and the resulting large deformations activate many secondary AE sources. To see the possible plastic deformations of vessels, in [5] a finite-element (FE) simulation was performed for an example vessel HSD01 (Fig. 2a). For this vessel, stress-strain curves for the base materials as well as for the welding materials were available because it was investigated during a European research project. It is a vessel made of high strength steel, and for the allowable pressure, the largest allowable one was evaluated. For details about the analysis see [5].

At the beginning of the simulation, some artificial shrinkage was introduced into the welding material to simulate residual stresses from the welding process. Afterwards the first pressure test up to the test pressure $p_{test} = 419$ bar (Fig. 2b 1-2) was simulated. The simulation continued with one operating cycle up to $p_s = 293$ bar (Fig. 2b 4-5) and a second pressure test (Fig. 2b 6). After reaching the maximum pressure of the pressure test the pressure was further increased to 486 bar (Fig. 2b 7). Figure 2c shows the von Mises equivalent stress vs. the circumferential strain at the Point A (Fig. 2a): Due to shrinkage of weld material, large stresses and some initial strain are present at the beginning (Fig. 2c 1). At the first pressurization, plastic deformation starts at the beginning (Fig. 2c 1-2). During unloading and the operating cycle, practically no plastic strain is accumulated (Fig. 2c 2-5). Also in the second pressure test, almost no plastic deformation occurs, as long as the maximum pressure of the first pressure test is not exceeded (Fig. 2c 5-6). Only if

the maximum pressure of the first pressure test is exceeded plastic deformation starts again (Fig. 2c 6-7).

Due to yielding the residual stresses are changed in a way that the subsequent unloading and reloading can take place without (or with very small) plastic deformation. Exceeding the first maximum pressure leads to considerable new plastic deformations. Like plastic deformation, AE activity is totally different whether or not the first load limit is exceeded (Kaiser effect - compare to Fig. 6). This has to be considered when specifying the loading history for verification experiments.

Experimental Load History

When designing experiments for studying AE testing, one has to consider that during AE testing for in-service inspection the maximum loading of the first pressure test is usually not exceeded. Only the maximum of the operating load, at which defect initiation and/or growth took place, should be exceeded during the AE testing.

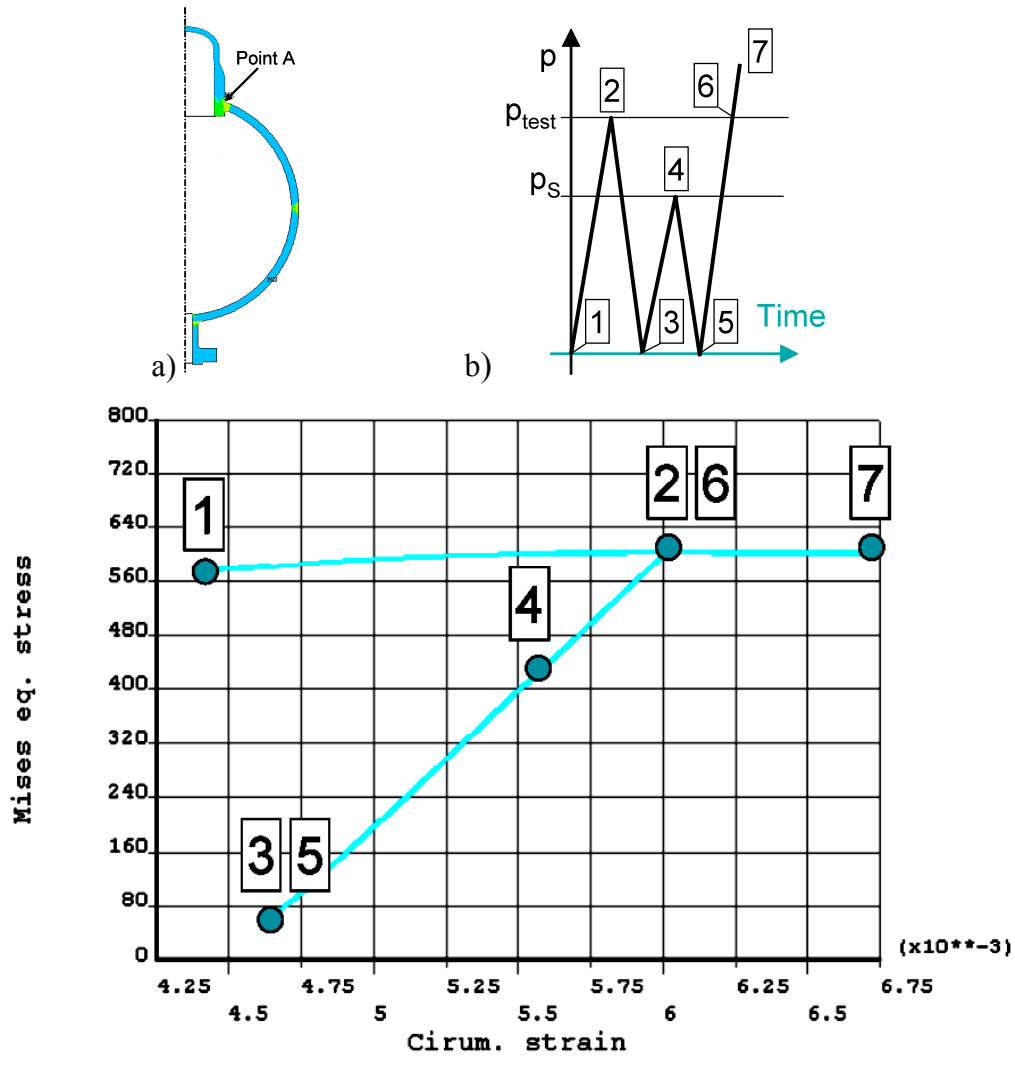


Fig. 2. Example HSD01, plastic strain in spherical vessel with residual stress [5]; a) FE model with point A shown, b) simulated cycles; c) circumferential strain vs. von Mises equivalent stress at point A.

Therefore, for finding an appropriate experimental loading history, the following procedure (Fig. 3) is proposed:

At first a load L_S , which corresponds to the load of the vessel at the maximum admissible pressure p_S , has to be specified. This can be a pressure, if a vessel is tested, or a force resulting in an appropriate stress level, if simple tension specimens are used. At this point the usual safety factors in pressure vessel design have to be considered (usually a safety factor of at least 1.5 to the appropriate proof or yield stress is applied at operating conditions). Starting from this load the following procedure can be applied:

- a) If an initial defect from fabrication should be simulated, a sample with an initial defect can be used, or an initial defect can be introduced at the beginning (Defect introduction 1 at Fig. 3).
- b) The test itself should start with a loading cycle, which simulates the first pressure test. The appropriate load L_{test} can be evaluated by multiplying the load corresponding to p_S (L_S) with the appropriate pressure test factor.
- c) After this loading cycle, an optional reference cycle up to the load L_{test} can be applied. This cycle gives some reference for the AE of the sample without defect or with the initial defect after the first pressure test.
- d) If defect initiation during operation should be simulated, a defect can be introduced after the first pressure test (Defect introduction 2 at Fig. 3).
- e) Now load variations should be applied. In this phase, the load has to be smaller than the maximum load, which will be reached at the vessel during operation. At least a few load cycles up to the maximum load, which can be reached at this phase, should be applied. Simulating defect growth by the investigated mechanism (fatigue, corrosion, etc.) would be optimal in this phase.
- f) Now a loading cycle simulating the AE test can be applied. Here, it is clear that the load should only be increased up to a value L_{AE} reached during the planned test. If the load is raised to a larger value, may be up to burst or fracture, AE above the load L_{AE} would not arise at a comparable AE test. At least AE above the load L_{test} is not comparable to AE during AE testing during in-service inspection.
- g) Simulation of further defect growth and further AE tests are of course possible.

Fatigue Cracks Starting from an Artificial Notch as Examples of Defects

Saw cuts (Fig. 4a), which cause U-shaped notches, have been used in connection with gas cylinders made of high strength steel [5, 7]. These U-shaped notches cause fatigue cracks growing from both sides of the notch into the ligament. Frequently during crack opening, shear cracks are formed, which connect these two cracks. Increased friction at the crack surface may result. V-shaped notches (Fig. 4b) cause crack initiation nearly in one plane, but the fabrication may be more complicated.

Introduction of welding defects in a defined way is difficult. In [6] a special procedure was used (Fig. 5c) to introduce a welding defect inside of an existing vessel. Here a notch was cut through the whole wall thickness. Afterwards a strip was pressed into the bottom of the notch. Onto this strip the weld was placed. The resulting crack-like notches are somewhat similar to welding defects like lack of fusion at the weld root.

The introduced notches have to be relatively deep to get fatigue crack growth within a practicable number of cycles, and with the usual nominal stresses in pressure vessels. Notches of 1/3 to 1/2 of the wall thickness in connection with cycle numbers of 10,000 full pressure cycles may be

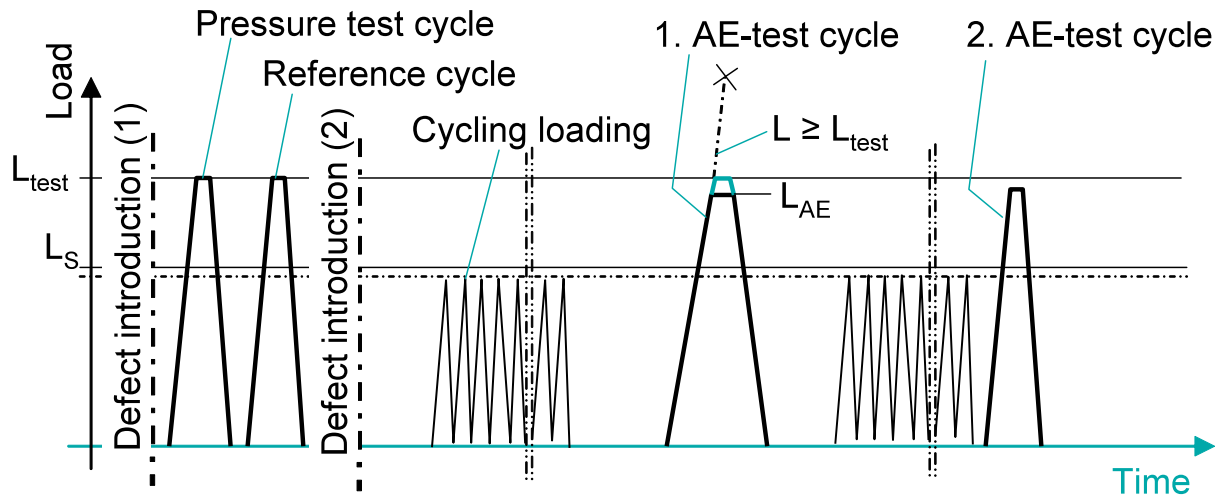


Fig. 3. Load history for experimental testing; L_s , load according to load at allowable pressure, L_{test} , load according to load at pressure test.

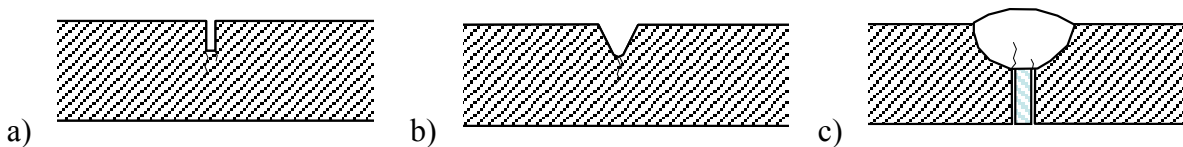


Fig. 4. Examples of artificial defects: a) saw cut (U-notch), b) V-notch, c) artificial weld defect.

necessary. Careful monitoring of defect growth during cycling is needed to do the AE tests at appropriate time. In [6] online crack growth measurement based on strain gauge measurements was used.

The pressure cycling with pressure variations as large as possible and with the large defects (both necessary to get crack initiation and growth with a practicable number of cycles) causes large cyclic plastic deformation in the ligament, which causes brittle material components to break. Therefore, AE activity during pressure tests after this cycling may be low. This was seen in a test with a defect in ferritic weld material as described in the following:

Example

Within the following experiment [6] an old vessel ST6599 (Fig. 5a) was tested by means of pressure tests and cyclic pressurization. The vessel was made of St41KT (0.17%C, 0.018%P, 0.022%S), a material according to ÖNORM M3121. This material corresponds to P265GH of EN 10028-2. The vessel diameter was 800 mm and the wall thickness 15 mm.

As an initial defect, before the first pressure test, an artificial weld defect of the type given in Fig. 4c was introduced on the vessel. Therefore, a saw cut was introduced in the original longitudinal weld, a steel strip was placed into this cut, and the weld was placed on the strip (Fig. 5b). For reference, a second weld with the intention of having no defect (marked “New Weld” in Fig 5a) was placed on the vessel. In this case only a V-notch, which partially penetrated the wall thickness was introduced and filled up by welding.

The testing procedure started with a pressure test, consisting of three pressure cycles (Fig. 6) up to a pressure of $1.43p_S$ ($p_S = 32$ bar). After the pressure test, the vessel was cycled with sinusoidal pressure variation between 2 bar and p_S until crack initiation was indicated (strain gauge measurements). Afterwards a pressure test and the next cycling followed. The procedure was repeated until the vessel failed at the 6th pressure test through leakage at the artificial weld defect (Table 1).

AE was measured with 5 SE150 sensors with a resonance frequency of 150 kHz and threshold settings between 31.2 and 35 dB_{AE} (Table 2) were used. A 0.5-mm pencil-lead break results in an AE event of about 84 dB_{AE} at 30 cm distance (distance of the artificial weld defect to the first hit sensor). Strain gauges were used for online crack growth detection (Fig. 5a). The indication was based on stiffness changes.

The micrograph (cross section a short distance from the leak) of the defect after the test (Fig. 7a) shows the crack starting at one side of the steel strip, almost in a single plane, and clear crack blunting at the 5th and 6th pressure tests. At the fracture surface (Fig. 7b) at least the crack tip at the last three pressure tests can clearly be seen.

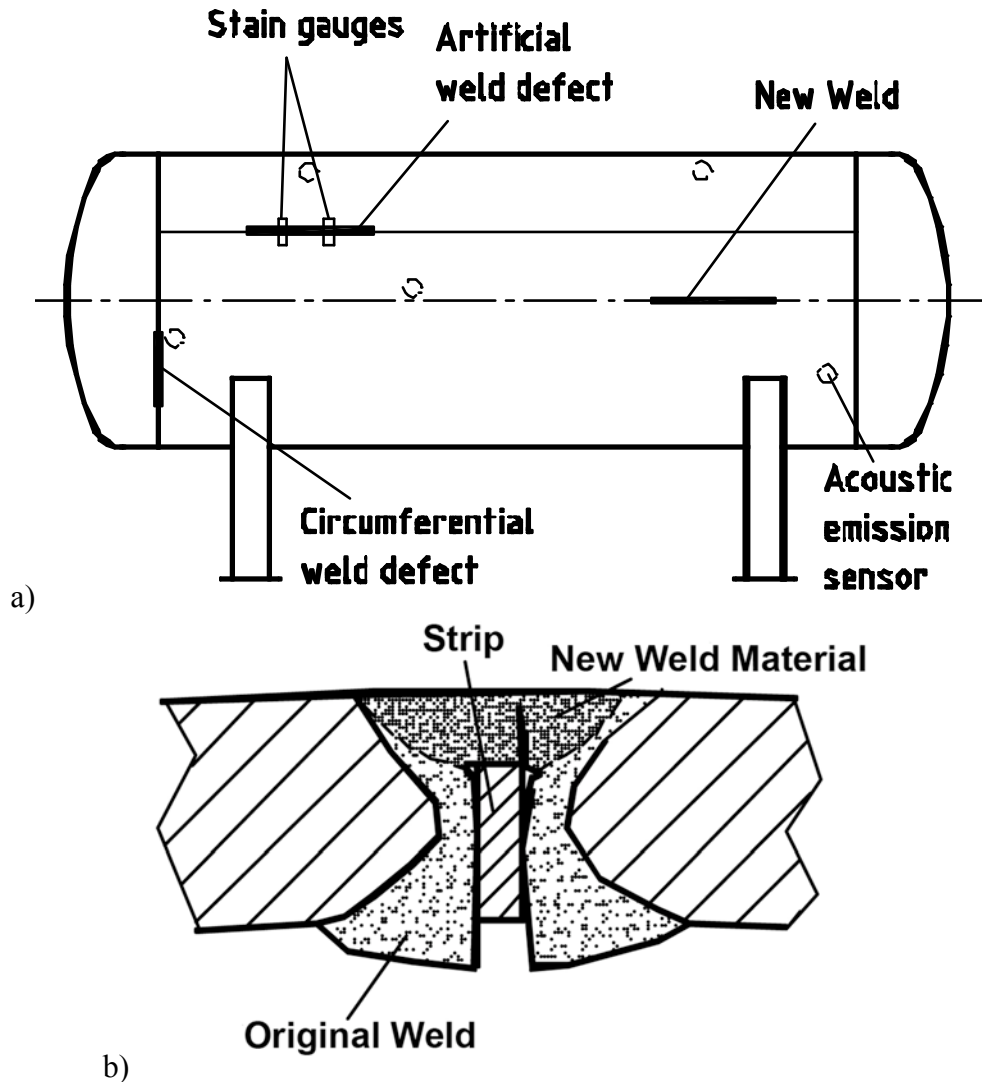


Fig. 5. Experiment ST6599 [6]: a) Test vessel, b) sketch of artificial weld defect,

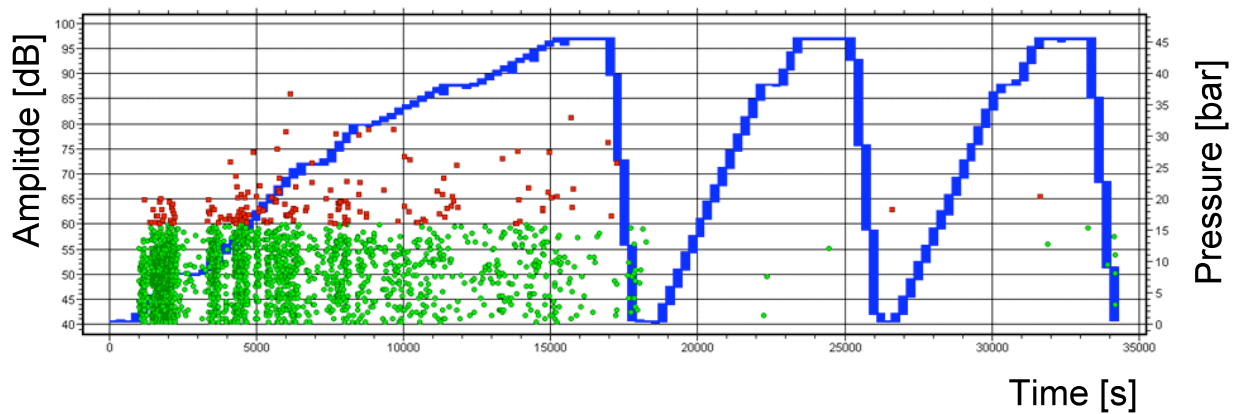


Fig. 6. First pressure test with three pressure cycles of experiment ST6599 - events located at defect region (longitudinal weld defect).

Table 1: Experimental procedure.

Experimental Step	Pressure	Cycles
1 st pressure test	$p_t = 45,8$ bar	3 Cycles
1 st cyclic pressurisation	2 – 30 bar	5064 cycles
2 nd pressure test	$p_t = 45,8$ bar	3 Cycles
2 nd cyclic pressurisation	2 – 30 bar	4397 cycles
3 rd pressure test	$p_t = 45,8$ bar	3 Cycles
3 rd cyclic pressurisation	2 – 30 bar	1850 cycles
4 th pressure test	$p_t = 45,8$ bar	3 Cycles
4 th cyclic pressurisation	2 – 30 bar	1222 cycles
5 th pressure test	$p_t = 45,8$ bar	3 Cycles
5 th cyclic pressurisation	2 – 30 bar	809 cycles
6 th pressure test	Leakage at 39,9 bar	Leakage at first pressurization

Table 2: Threshold settings.

	Threshold [dB]	Waveform recorded for $A > [dB]$
1 st pressure test until 8 bar	31.2	43
1 st pressure test after 8 bar	35.6	49.8
Cyclic pressurisation	35.6	49.8
2 nd pressure test	31.2	49.8
3 rd to 5 th pressure test	31.2	33.7
6 th pressure test	31.2	31.2

During the pressure tests and cycling considerable acoustic emission activity was acquired from the investigated weld defect, the “New Weld” and from a position called “Circumferential weld defect” (Fig. 5a). With radiography in the “New Weld” and “Circumferential weld defect” also considerable defects were found. Micrographs at the locations with the largest indications showed insufficient penetration at “Circumferential weld defect” and bad bounding at “New Weld”. Details of this can be found in [6]; here only signals from the investigated weld defect are further discussed:

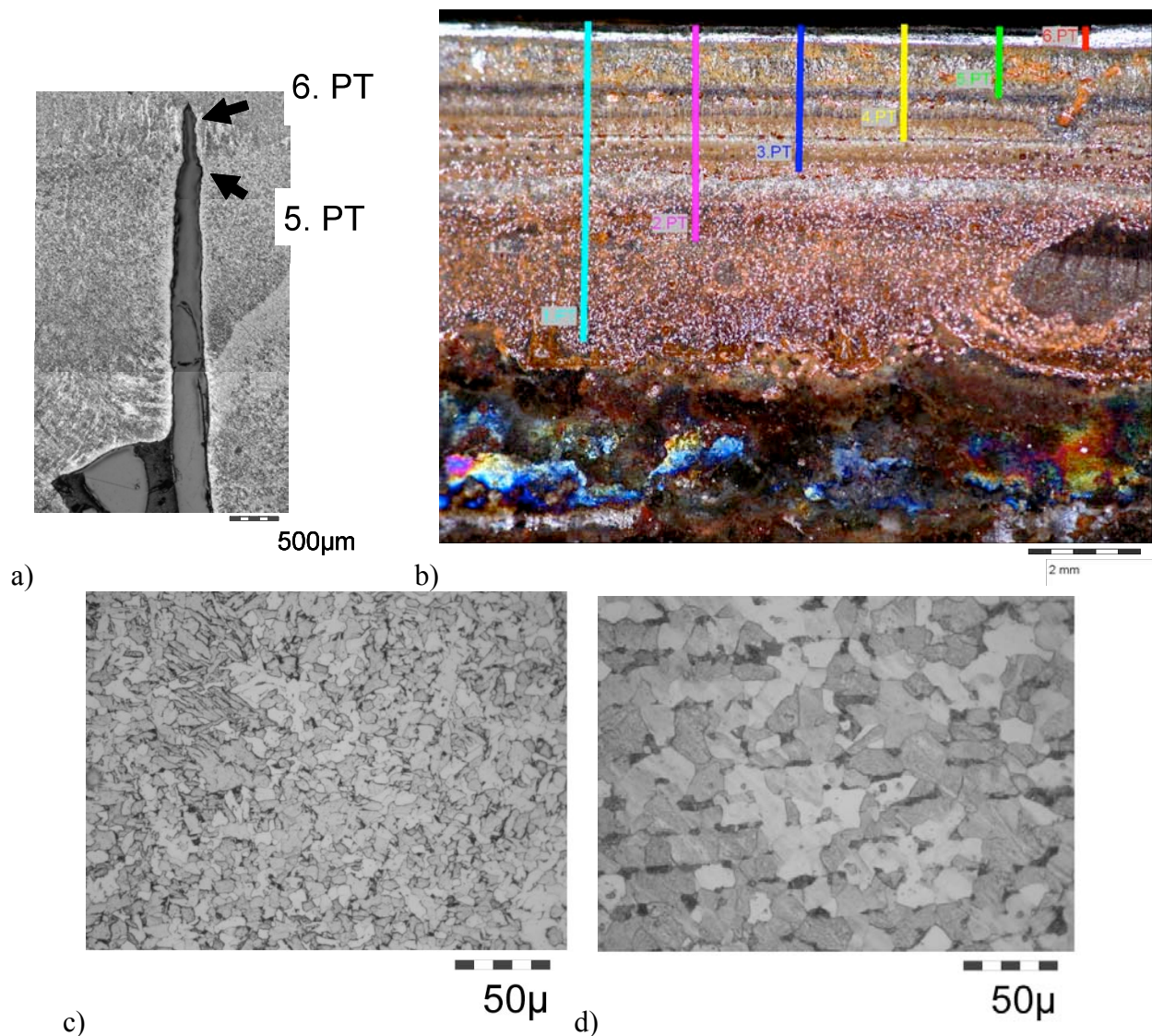


Fig. 7: artificial weld defect (after cycling and pressure tests); a) micrograph; b) fracture surface; c) microstructure of ligament; d) microstructure of base material ST41KT

The most important phase during AE examination is the phase of increasing pressure, including the hold periods, of the first pressure cycle of a pressure test – this is the period from start of the pressure test until start of pressure release. For this phase of the pressure tests 1 – 6, the numbers of AE events within the investigated region, i.e. the longitudinal weld defect, are given in Table 3. For comparison also the sum for the whole vessel is given. Figure 8 summarises the acquired events from the investigated defect during the last pressure test until leakage.

Description of the values in Table 3:

≥80 dB, located: Here the number of located events with amplitudes larger than 80 dB at the first hit sensor is given. The numbers of events that are located within the considered regions are given. Hsu-Nielson sources (0.5 mm) at the investigated regions reach at the first hit sensor amplitudes between 80 and 85 dB, therefore, amplitudes larger than 80 dB have intensities similar or larger than the Hsu-Nielson source (0.5 mm).

60 dB, located: Here the number of located events with amplitudes larger than 60 dB at the first hit sensor are given. The amplitude of 60 dB is 20 dB smaller than the one reached by Hsu-

Nielson sources. Above this amplitude, with the arrangement used, location processing with good reliability is possible.

TR-page available: Here the number of events is given for which at least for the 1st hit sensor the waveform data was acquired. Only the events, which are assigned to the considered region according to the channel sequence criteria, are considered. This number is important for further evaluation, because more sophisticated data evaluation is only possible if the waveform is acquired.

40 dB, according to channel sequence: Here the number of events is given which reach at the 1st hit sensor an amplitude of 40 dB. Only the events, which are assigned to the considered region according to the channel sequence criteria, are considered here. The considered amplitude of 40 dB is about 40 dB smaller than the one which would be reached by the Hsu-Nielson source (0.5 mm).

Table 3: Pressure tests 1 - 6, first pressure cycle, increasing pressure: Number of events at the considered regions.

	At whole vessel				Longitudinal weld defect			
	>=80db, located	>=60db, located	TR-Pages available	>=40db, all events	>=80db, located	>=60db, located	TR-Pages available, channel sequence	>=40db, according channel sequence
1. PT	3	383	5300	19900	2	160	4020	12300
2. PT	0	6	25	73	0	2	15	47
3. PT	0	3	143	54	0	0	51	22
4. PT	1	2	92	36	1	1	43	16
5. PT	0	2	115	37	0	0	68	30
6. PT	0	2	111	47	0	1	82	39

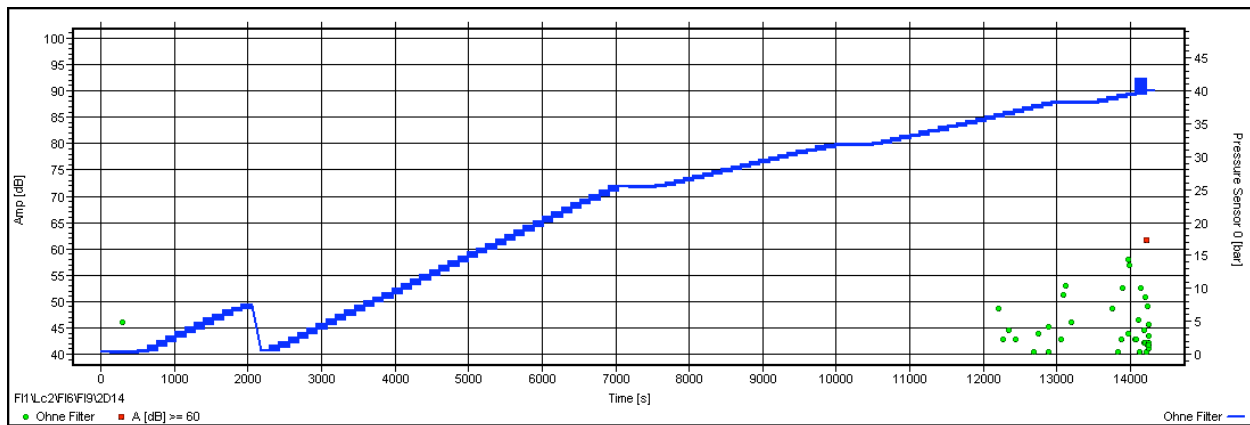


Fig. 8: Longitudinal weld defect; 6th pressure test; channel sequence filter at the top; location filter at the bottom.

During the first pressure test, large AE activity was measured. The acoustic emission during the pressure tests two to six can be characterised in the following way: There were very few signals with large amplitudes. Only at the 4th pressure test, in the region of the longitudinal weld defect, one event with amplitude near to the one of a pencil lead break was acquired. In two pressure tests, in the region of the longitudinal weld defect, no events with amplitudes larger than 60 dB were acquired. When considering low amplitude signals the activity decreased until the 4th pressure test, and increased in the 5th and the 6th pressure test again. This increase of the activity with low amplitudes correlates with crack propagation at these last two pressure tests.

For the base material, comparable small AE activities can also be found in the literature [e.g. 8]. Here the weld material, which forms the ligament for the considered crack, has a fine-grained microstructure (Fig. 7 c and d), which may be one of the reasons for the small AE activity.

The applied procedure may possibly not detect the applied type of fatigue crack (pure fatigue, without corrosion) in weld metal of low carbon steel. Most pressure vessels have only a small number of fatigue cycles and failure modes due to corrosion and interaction between corrosion and mechanical action dominate. When doing experimental verification for AE testing, which focuses on these failure modes, the corrosion effects have to be included in the experimental testing.

Conclusion

Limitations on the loading history for experiments in connection with AE testing were demonstrated. One experiment following the guidelines was conducted with an initial artificial weld defect in connection with fatigue crack growth. AE activity during the simulated AE tests was small. This shows that standard procedures of AE testing are not always appropriate. Analysis of probable defects and the possibility to detect these defects by AE testing is necessary. For some types of defects experimental verification is necessary. In the experiments the investigated defects have to be reconstructed in a proper way. Using fatigue cracks instead of cracks from stress corrosion or corrosion fatigue interaction may not be sufficient. Procedures of verification experiments, which include corrosion in an appropriate manner, are not established.

References

1. Ono K.: Structural Integrity Evaluation Using Acoustic Emission. *Journal of Acoustic Emission*, **25**, 2007, 1-20.
2. Lackner G. Tscheliesnig P.: Detection of Corrosion Damage on Pressure Equipment with Acoustic Emission. *Proceedings of 27th European Conference on Acoustic Emission Testing (EWGAE 2006)*, September 20 – 22, 2006, Cardiff, Wales, UK.
3. Kabanov B. S., Gomera V. P., Sokolov V. L., Fedorov V. P., Okhotnikov A. A.: Use of AE Method Abilities for Petrochemical Equipment Inspection. *Proc. 26th European Conference on Acoustic Emission Testing*, September 15-17, 2004, Berlin, Germany.
4. Kabanov B. S., Gomera V. P., Sokolov V. L., Okhotnikov A. A. Fedorov V. P.: AE Technology as a Key Element of the Safe Operation System at Refinery. *Proc. 25th European Conference on Acoustic Emission Testing*, September 11-13, 2002, Prague, Czech Republic.
5. Rauscher F.: *Pressure Test and Acoustic Emission Examination*; Shaker Verlag GmbH, Aachen, 2005.

6. Rauscher F., Bayray M.: Weld Defect in a Pressure Vessel Investigation of Acoustic Emission during Pressure Tests and Pressure Cycling. Bericht Nr. 26, Institut f. Apparate- u. Anlagenbau, Technische Universität Wien, 2005.
7. Rauscher F.: Gas Cylinders with Longitudinal Cracks – Cyclic Fatigue Life Time after a Pressure Test. *Proceedings ICPVT-10*, July 7-10, 2003, Vienna, Austria.
8. Wadley H.N.G., Simmons J.A.: Microscopic Origins of Acoustic Emission. In: *Nondestructive Testing Handbook, Vol. 5, Acoustic Emission Testing*. American Society for Nondestructive Testing, 1987.

INTEGRITY EVALUATION OF COPVS BY MEANS OF ACOUSTIC EMISSION TESTING

YOSHIHIRO MIZUTANI¹, KOUKI SAIGA², HIDEYUKI NAKAMURA³, NOBUHITO
TAKIZAWA³, TAKAHIRO ARAKAWA³ and AKIRA TODOROKI¹

¹ Tokyo Institute of Technology, Department of Mechanical Sciences and Engineering,
2-12-1-II-70, Ookayama, Meguro, Tokyo 152-8552, Japan; ² Japan Aerospace Exploration
Agency, Safety and Mission Assurance Department, 1-1, Sengen 2, Tsukuba, Ibaraki 305-8505,
Japan; ³ IHI Inspection & Instrumentation Co., Ltd. 1, Shin-nakahara, Isogo, Yokohama
235-8501, Japan

Keywords: COPVs, CFRP, impact damage, pressure proof test, integrity evaluation

Abstract

It is important to evaluate the integrity of composite overwrapped pressure vessels (COPVs) used for space applications. In order to examine applicability of acoustic emission testing (AT) for the evaluation, AE signals were monitored during the pressurization test of a COPV before and after an impact test. The impact test of 17-J energy was conducted by using a drop-weight impact tester to simulate machine-tool drop. A large number of emissions were monitored by the AE channel nearest the impact point. In addition, the characteristics of AE signals detected nearest the impact point were different from those by other channels. From these results, it is assumed that AT can be used for the qualitative integrity evaluation of COPVs. On the other hand, to realize the quantitative integrity evaluation, it is essential to make data-base of AE parameters.

Introduction

Composite overwrapped pressure vessels (COPVs) are widely used for space applications, such as accumulators for a space satellite and propellant tanks for a rocket. It is known that COPVs are likely to suffer complicated internal damages by being dropped or by impacts of dropped machine-tools. Even when such internal damages occurred, only small damages are caused on the impact surface in many cases. Therefore, it is difficult to find the impact damages from outer surface by visual testing (VT). Since the internal damages may reduce strength of the vessels, a reliable nondestructive testing (NDT) for the damages is desired. Applicability of various NDT methods for COPVs was evaluated by several investigators [1-3], although, the optimal inspection technique is not yet found.

Acoustic emission testing (AT) is one of the candidates for the NDT method of COPVs. Several standards on AT, such as ASME section V, article 11 [4] for evaluating the integrity of fiber-reinforced plastic vessels are available. Only a few papers [5-7] or reports [8], however, appeared in public domain for applying AT to COPVs.

In our previous study [9], the applicability of AT to the integrity evaluation of COPVs was evaluated by using coupon-level specimens. It was found that Kaiser effect and Felicity effect observed during a cyclic loading test can be used for evaluating previously induced damages such as impact damages. The detectable minimum damage size by AT was same or better than that by ultrasonic testing (UT).

In this study, as a collaborative research between Tokyo Institute of Technology and Japan Aerospace Exploration Agency, AE monitoring is conducted during the pressurization test of a real COPV before and after the impact test. IHI Inspection & Instrumentation Co., Ltd. joined this study in the measurement under the guidance of Tokyo Institute of Technology. Suitable AE parameters for the integrity evaluation are investigated and the applicability of AT is evaluated.

Experimental Setup and Procedure

A thin metal-lined composite overwrapped spherical pressure vessel of 600-mm diameter was prepared for this study. Reinforcement fibers of the vessel were carbon fibers. The vessel was fabricated by filament-winding (FW) method. Prior to this study, the vessel was pressurized to MEOP (maximum expected operating pressure) 52 times, proof pressure (1.25MEOP) 6 times and nominal burst pressure (1.5MEOP) once. Thus, it is assumed that several damages were already inflicted on the COPV before the start of this study.

Four AE sensors (Vallen-Systeme GmbH, Type VS150-RIC, nominal resonant frequency 150 kHz) were mounted on the outer surface of the vessel at quadrant locations on the equator (see Fig. 1). The programmed hydrostatic pressure cycles were applied to the vessel. The maximum pressure was set as the MEOP and was held for 30 minutes. Outputs of the AE sensors were amplified 34 dB by preamplifiers and filtered by band-pass filters of 95 to 850 kHz. The extracted signals were digitized at an interval of 200 ns with 4096 points by A/D converter.

After the first pressurization test, an impact test was conducted with a drop-weight impact tester. A hemispherical tip of 12.7-mm in diameter was used for the impactor per ISO14623. Before the impact test, AE sensors were removed from the vessel to avoid sensor damages. The impactor was dropped to the vessel along guide rails and the impact load was applied at the position 22.5° from the Ch.-4 sensor on the equator of the vessel as shown in Fig. 1. The weight of the impactor and the impact energy were 2.5 kg and 17 J, respectively. The surface damage caused by the impact was not evident by VT. After the impact test, the damage evaluation was conducted by using an ultrasonic flaw detector and UT located an elliptically shaped internal damage of about 40 mm in long axis and about 20 mm in short axis. Following the impact test, AE sensors were remounted on the same positions as before. AE activities were again monitored during the pressurization test by the same programmed pressure cycles.

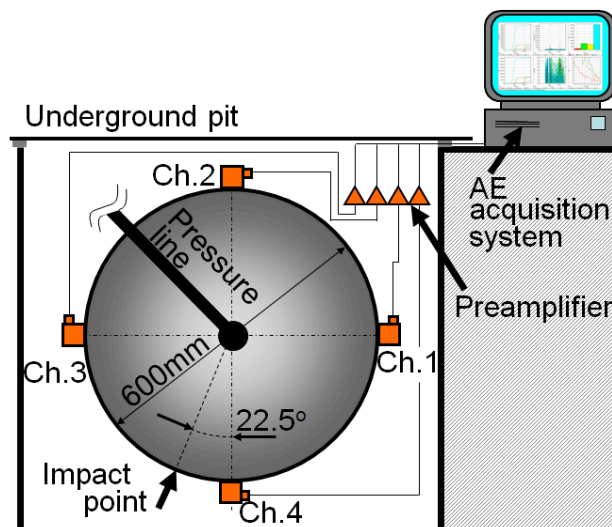


Fig. 1 Schematic representation of the pressurization test and the sensor positions.

Results and Discussion

Figure 2 shows the total number of AE hits for each channel during the pressurization test before and after the impact test. Before the impact test, the total number was almost identical among each channel. After the impact test, the total number of Ch. 4, which was the nearest to the impact point was more than twice those by other three channels. The result shows that by comparing the total number of AE hits by each channel, previously induced damages such as impact damages can be evaluated.

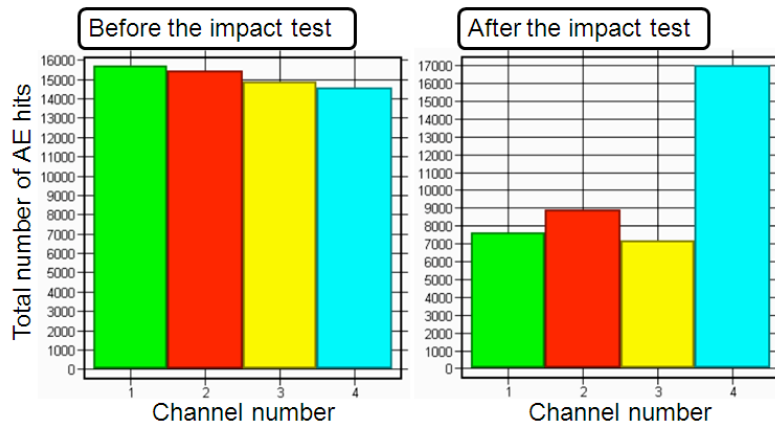


Fig. 2 The total number of AE hits for each channel during the pressurization test, before and after the impact test.

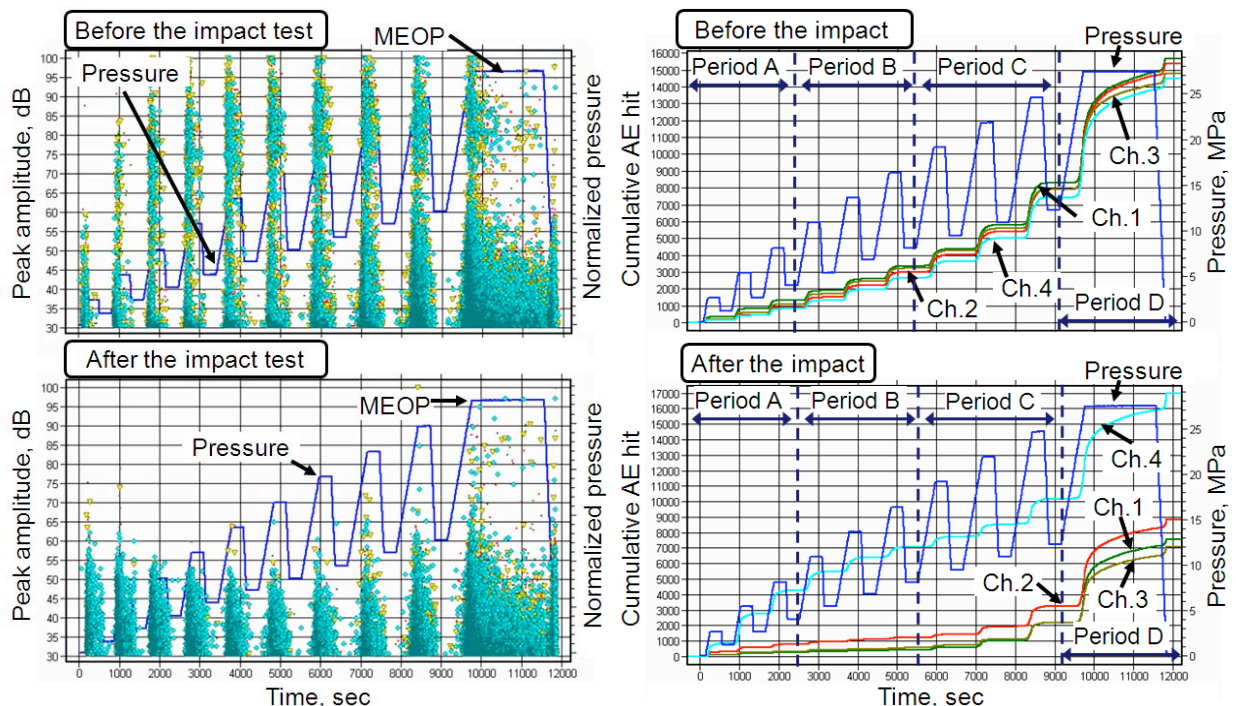


Fig. 3 AE signal peak amplitude (left) and cumulative AE hits (right) with respect to the elapsed time. The normalized pressure history is superimposed on the graphs.

Figure 3 shows peak amplitude of AE signal (left) and cumulative AE hits (right) with the elapsed time. The normalized pressure history is overlapped with these graphs. Periods A-D defined in the right are used later in detailed analysis. A large number of significant AE signals

(>65dB) were monitored by all channels throughout the first pressurization test, which was conducted before the impact test (see upper left of Fig. 3). The result reveals that the large damages occurred all over the vessel at the first pressurization test. During the pressure-hold periods of the first (before impact) and the second (after impact) pressurization tests, emissions were continuously detected. Since emissions that continue during pressure-hold generally indicate structurally significant defects, the COPV appears to have significant defects from the beginning as we mentioned in the previous section. By monitoring the AE peak amplitude and the cumulative AE hits, a newly induced damage and a damage progression can be monitored. In addition, there is a possibility to evaluate the existence of significant defects by monitoring AE during the pressure-hold.

Figure 4 shows the relationship between AE signal peak amplitudes and durations. In general, an AE event with high amplitude and long duration reveals the occurrence or progression of large-scale damage. Since a large number of such kinds of events were detected during the first pressurization test, large-scale damages or progressions occurred during the first test.

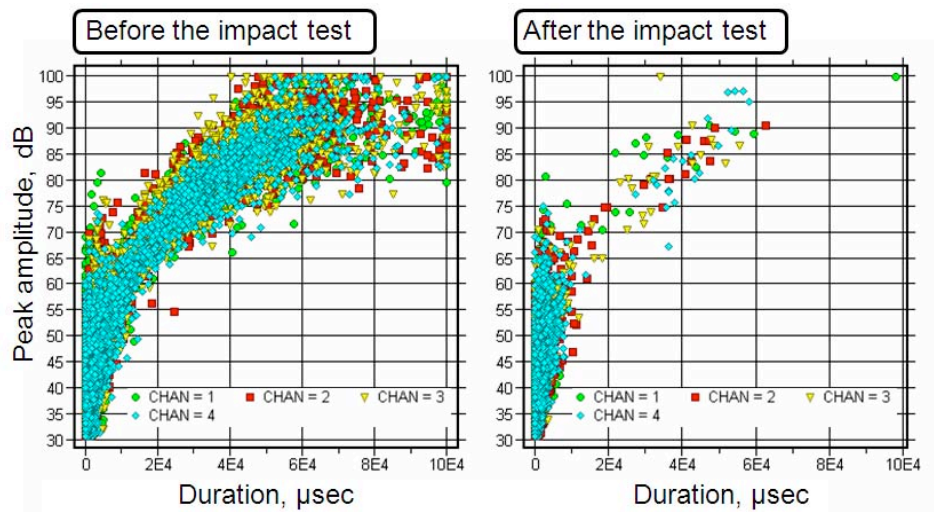


Fig. 4 Relationship between AE signal peak amplitude and duration.

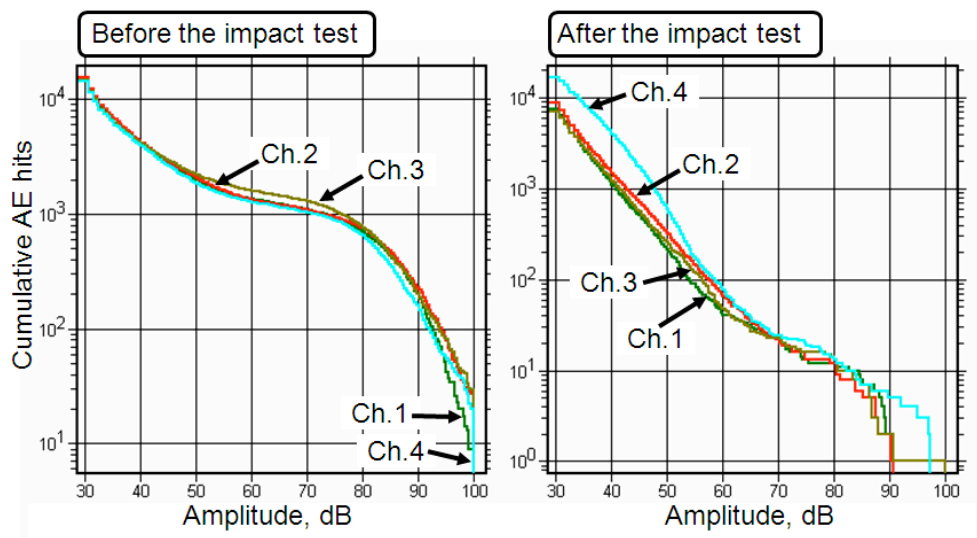


Fig. 5 Relationship between cumulative AE hits and AE peak amplitude.

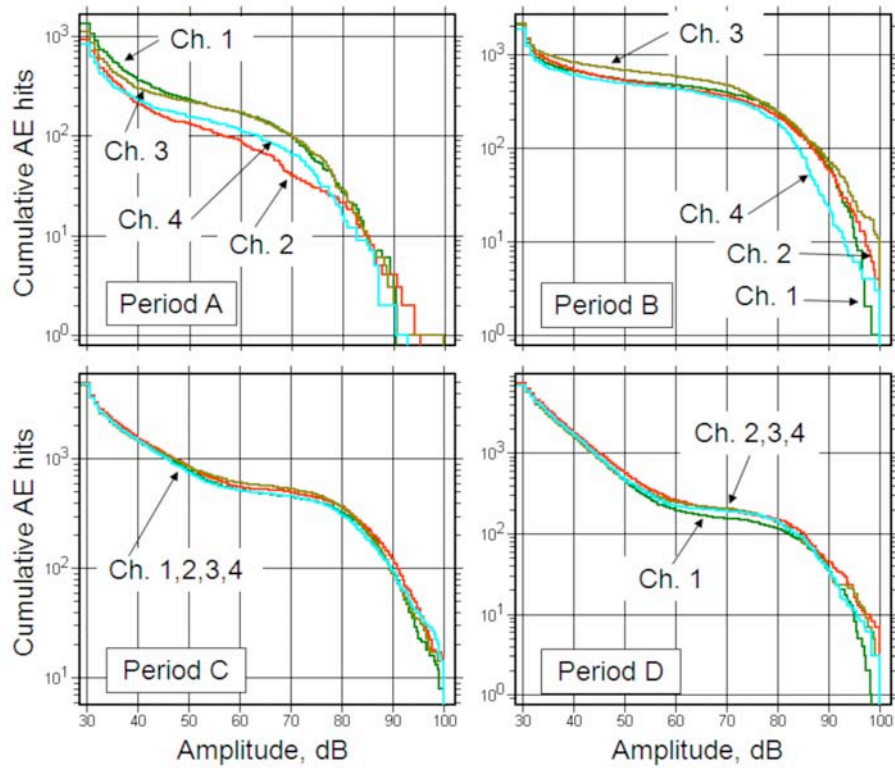


Fig. 6 Relationship between cumulative AE hits and AE peak amplitude of Period A to D for AE signals detected before the impact test. (Periods A to D are defined in right of Fig. 3.)

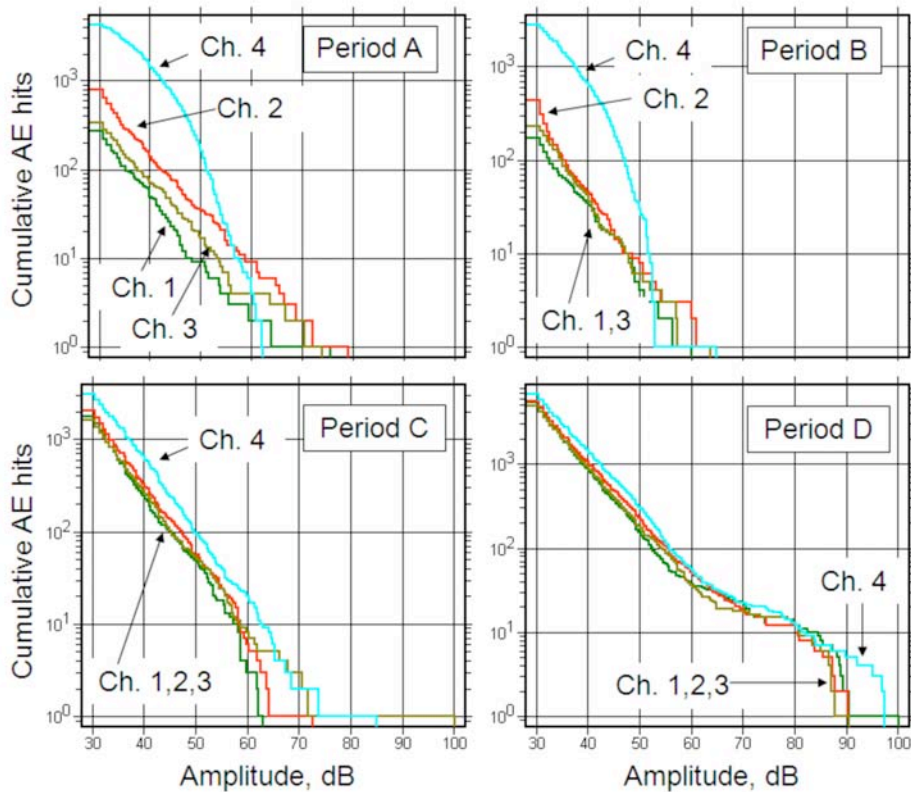


Fig. 7 Relationship between cumulative AE hits and AE peak amplitude of Periods A to D for AE signals detected after the impact test.

Figure 5 shows the relationship between cumulative AE hits and AE peak amplitude in dB before and after the impact test. The scale of the vertical axis is logarithmic. When a fracture mode is limited to one, cumulative AE hits in the graph tends to be monotonically decreased with increasing the amplitude. Therefore, the relationship of Ch. 1 to 3 monitored during the second pressurization test after impact (right of Fig. 5) reveals that fractures with limited fracture-mode occurred. On the other hand, the relationship monitored during the first pressurization test before impact (left) and Ch. 4 of the second test reveals that fractures with several fracture-modes occurred. Since there was a possibility that the fracture-modes change with elapsed time, we investigated the transition of the relationship with the elapsed time. Figure 6 and 7 show the results. As strong non-linear relationship was observed for the first pressurization test, we had assumed the relationship changed with the elapsed time. However, as shown in Fig. 6, the relationship was almost the same throughout the pressurization test. Therefore, it can be stated that fractures with several fracture-modes occurred throughout the first pressurization test. On the other hand, as shown in Fig. 7, the relationship of Ch. 4 changed with the elapsed time and quite different from those of Ch. 1 to 3 at periods A and B. This reveals that AE related to the impact damage occurred from early stage (periods A and B) of the pressurization test.

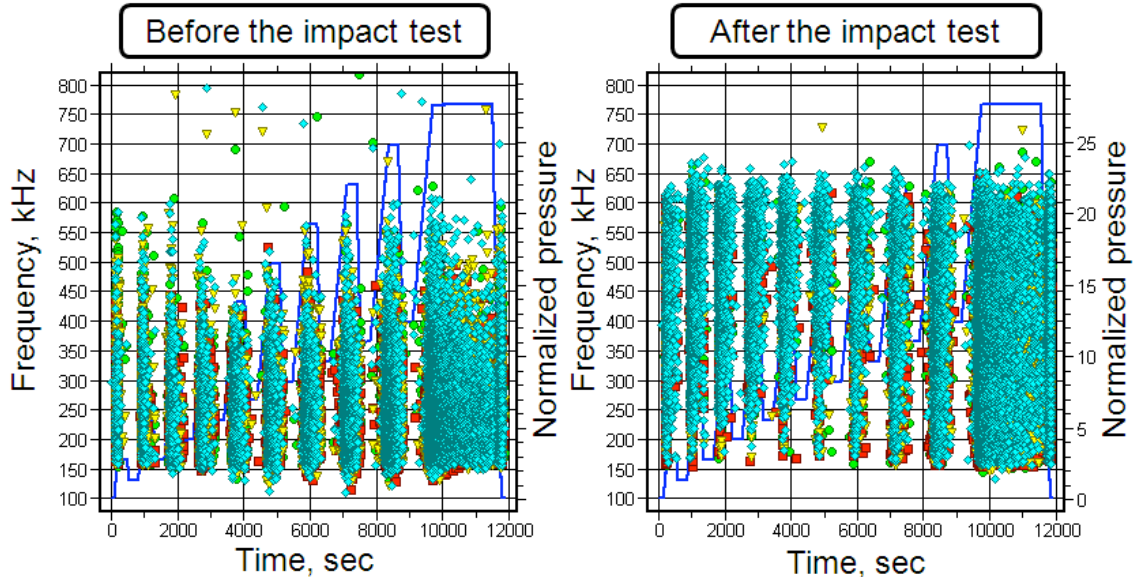


Fig. 8 Centroid frequency of detected AE signals with respect to the elapsed time. The normalized pressure history is superimposed on the graphs.

Figure 8 shows the centroid frequency of detected AE signals with the elapsed time. The distributions of the first test (before impact) and the second test (after impact) appear to be different from each other. In order to examine details of the distributions, centroid frequency's histograms for each channel were investigated. The results are shown in Fig. 9. While AE signals below 400 kHz are dominant for the first test (before impact), AE signals above 400 kHz are observed for the second test (after impact). It is assumed that the origins of AE signals are different for first and second tests. It is also important that in the second test, AE signals with high frequency components (above 500 kHz) are frequently detected by Ch. 4, which is located closest to the impact point. AE signals, which are related to impact damage are likely to generate high-frequency components. Since there was a possibility that the distributions change with elapsed time, we investigated the transition of the histogram with the elapsed time. Figure 10 to 13 show histogram of centroid frequency of periods A to D.

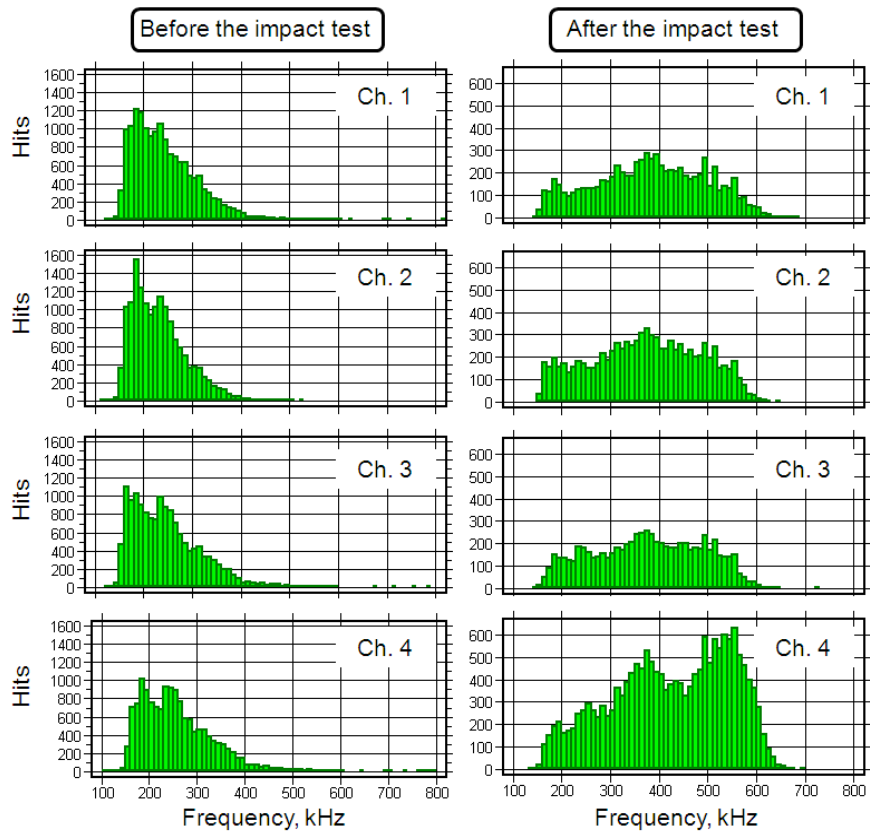


Fig. 9 Centroid frequency histograms for each channel.

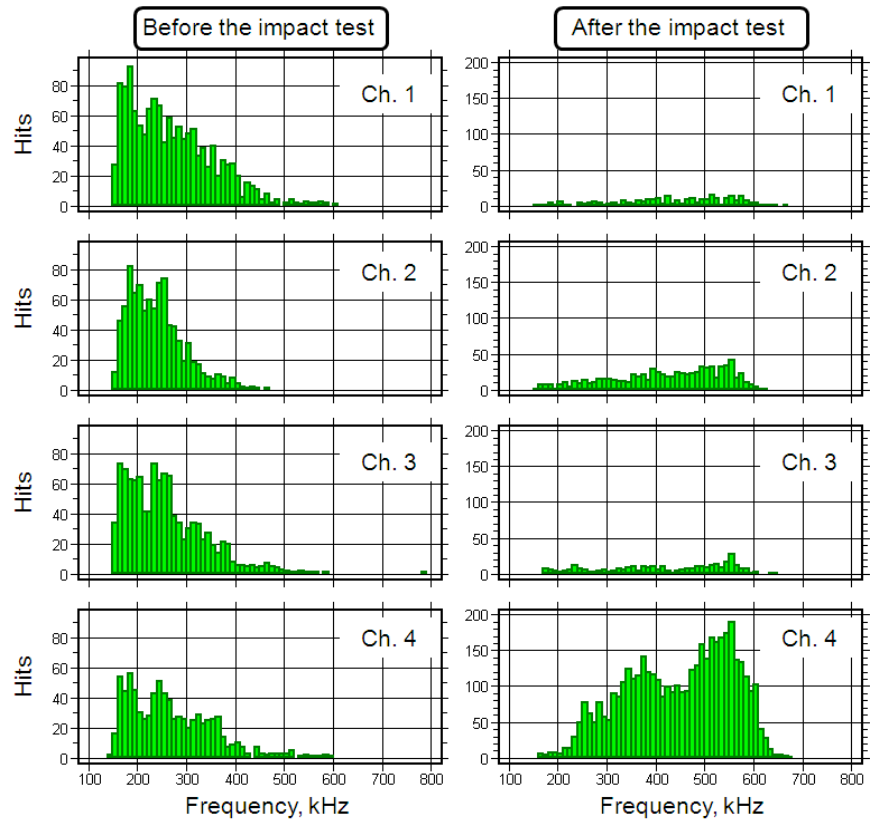


Fig. 10 Centroid frequency histograms for each channel in period A.

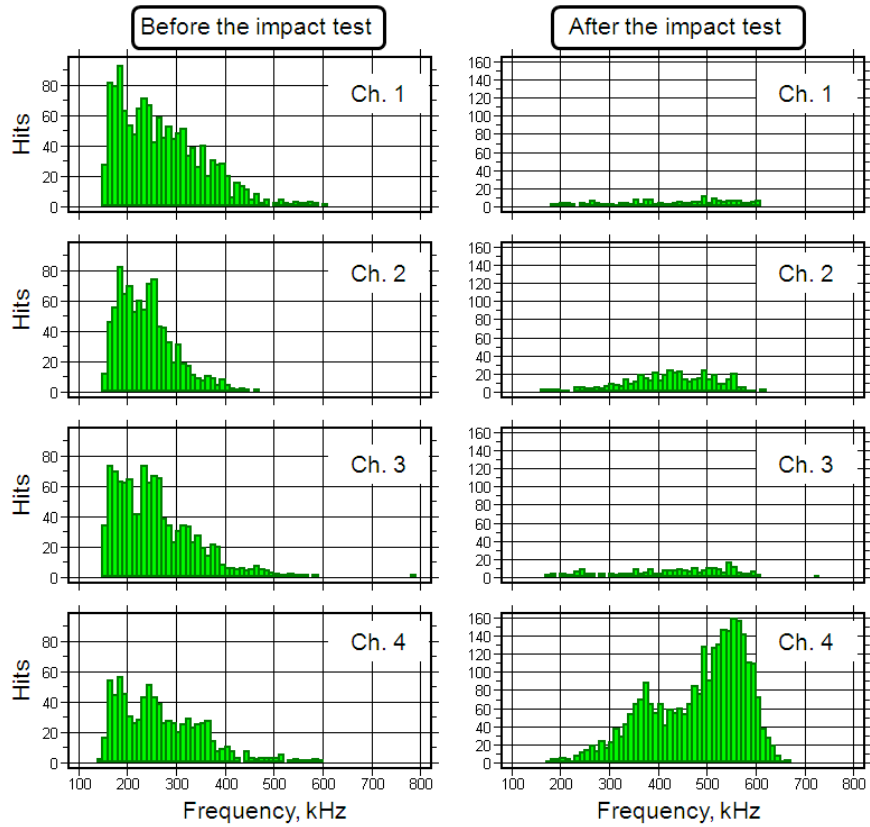


Fig. 11 Centroid frequency histograms for each channel in period B.

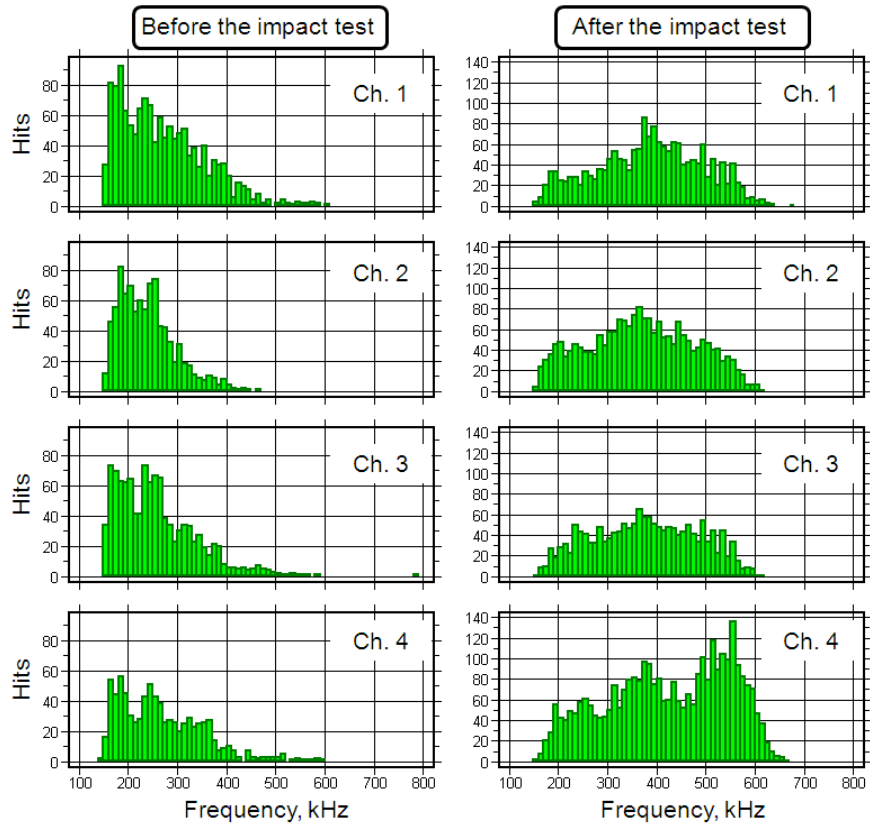


Fig. 12 Centroid frequency histograms for each channel in period C.

Distributions of the histogram for the first test are almost identical. This indicates that the origins of the AE sources did not change with the elapsed time. On the other hand, distributions for Ch. 4 of the second test changed with the elapsed time. It is also noted that the distributions are quite different from those of other channels at periods A and B and also different from those of Ch. 1 to 3 at periods A and B. This reveals that AE related to the impact damage occurred from early stages (periods A and B) and this AE consists of high-frequency components.

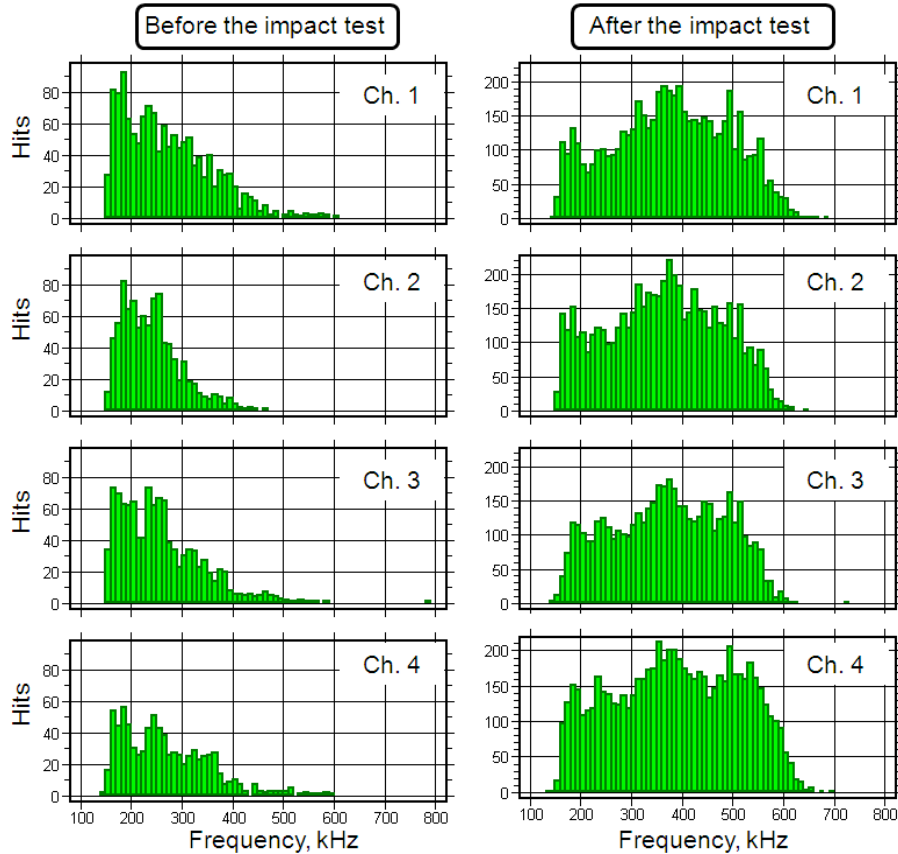


Fig. 13 Centroid frequency histograms for each channel in period D.

Figures 14 and 15 show the relationship between cumulative AE hits and load histories before and after the impact test. All AE hits were plotted in Fig. 14, while AE hits with above 40 dB peak amplitude were plotted in Fig. 15. If a perfect Kaiser effect is established, cumulative AE hits should monotonically increase with the load. As shown in the upper plot of Fig. 14, perfect Kaiser effect was not observed even during the first pressurization test, which was conducted before the impact test. This is due to the vessel may have prior internal damages from earlier testing. Felicity effect was clearly observed for both the first and the second tests (indicated by arrows). Contrary to Fig. 14, almost perfect Kaiser effects were observed below 30% of the MEOP in Fig. 15. This result indicates that the adequate threshold should be set for an appropriate damage evaluation. Focusing on Ch. 4 data of Figs. 14 and 15, Felicity ratio seems reduced after the impact test. This indicates that the damage severity of COPVs can be evaluated qualitatively by Felicity ratio.

In the first part of this paper, we found that AE signals related to impact damage were observed at early stages (periods A and B) and involved high-frequency components (from Figs. 10 and 11) with low peak amplitude (from upper plot of Fig. 7). On the other hand, in the last

part of the paper, we found that Felicity effects are observed clearly when the AE signals with small peak amplitude are eliminated. These results indicate that the effect of the impact damage appeared throughout the experiment, although adequate AE parameters should be extracted for observing the effect of the impact damage. When the quantitative evaluation is needed, it is essential to make database of AE parameters and select appropriate ranges.

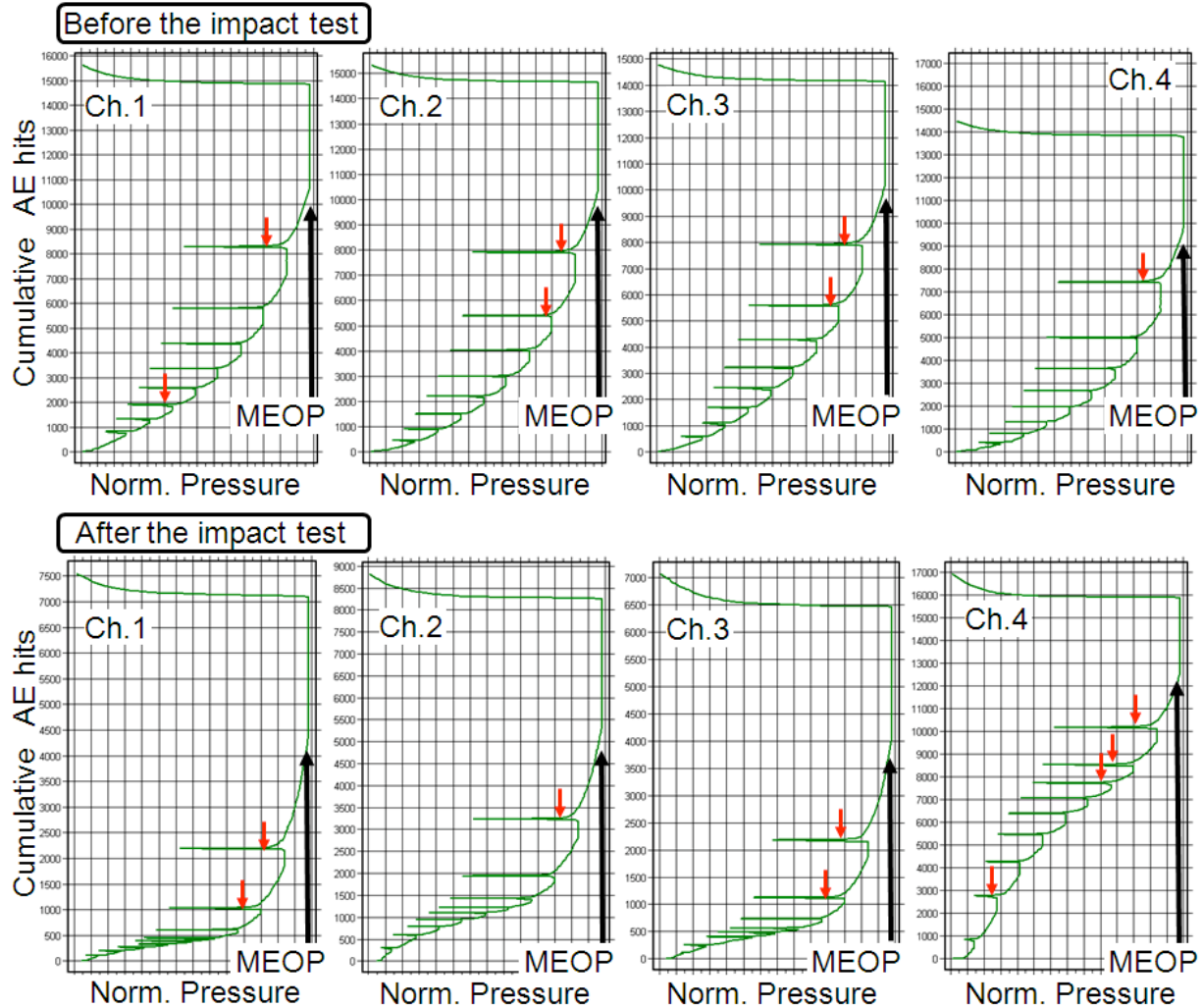


Fig. 14 Relationship between cumulative AE hits and normalized pressure. (Upper: The first pressurization test before the impact test. Lower: The second test after the impact test.)

Conclusion

In this study, the applicability of AT to the integrity evaluation of COPVs was evaluated. To simulate machine-tool drop, the impact of 17-J energy was applied to the vessel by using drop-weight impact tester. The programmed cyclic load by hydrostatic pressure was applied to the vessel before and after the impact test and AE activities were monitored during the test. In the pressurization test after the impact, the channel nearest the impact point detected a large number of AE hits. In addition, characteristics of AE signals detected nearest the impact point were different from those by other channels. From these results, it is concluded that AT can qualitatively make the integrity evaluation of COPVs. On the other hand, to realize the quantitative integrity evaluation, it is essential to make the database of AE parameters.

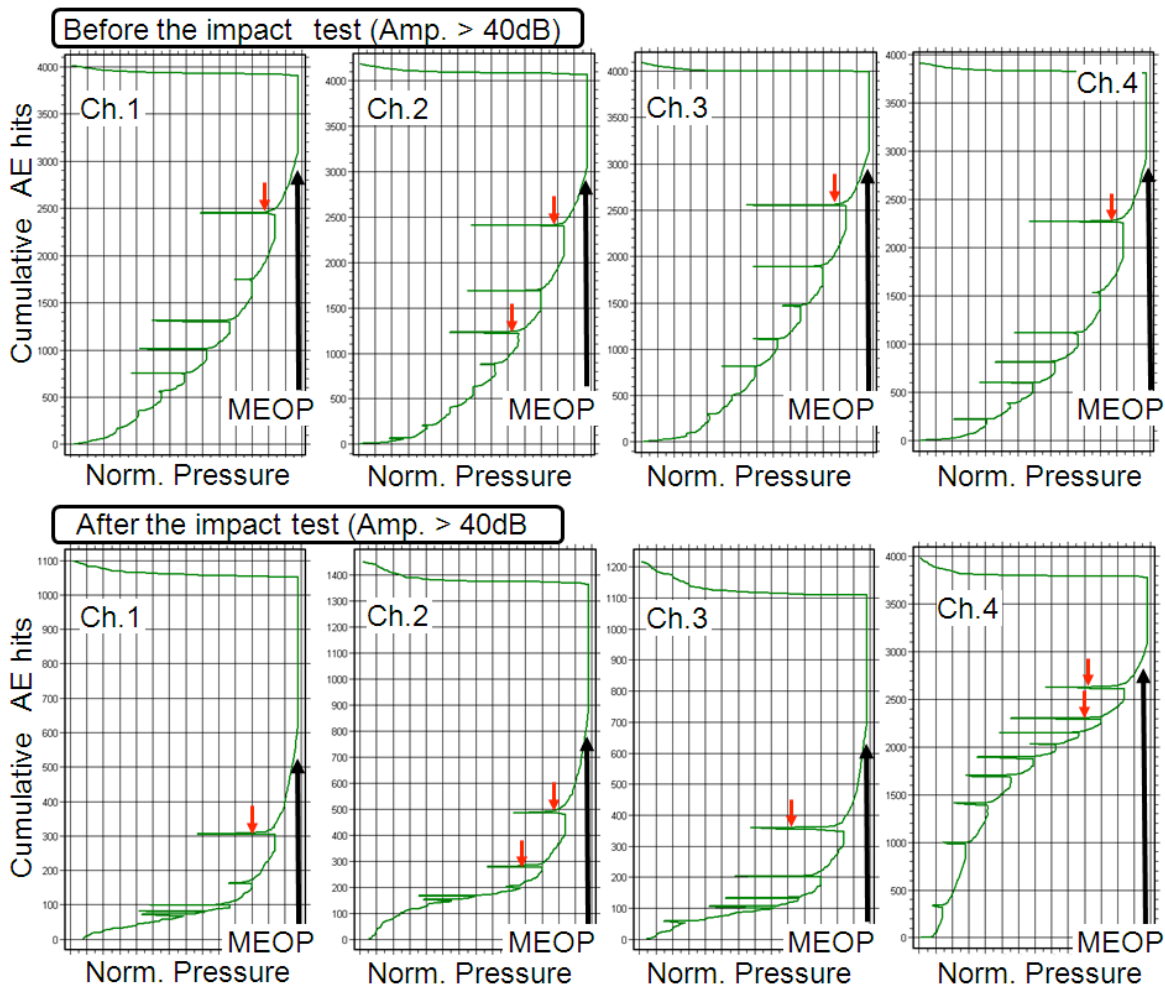


Fig. 15 Relationship between cumulative AE hits above 40 dB of AE signal amplitude and normalized pressure. (Upper: The first pressurization test. Lower: The second test.)

References

1. N. Greene et. al.: *Proc. 9th Joint FAA/DoD/NASA Conf. on Aging Aircraft*, March 6-9, 2006, Hyatt Regency, Atlanta, GA, USA.
2. R. Saulsberry: *Proc. 9th Joint FAA/DoD/NASA Conf. on Aging Aircraft*, March 6-9, 2006, Hyatt Regency, Atlanta, GA, USA
3. Examination of the Nondestructive Evaluation of Composite Gas Cylinders, Final report, USDOT, Nondestructive Testing Information Analysis Center, 2002.
4. Acoustic Emission Examination of Fiber-Reinforced Plastic Vessels, ASME Boiler and Pressure Vessel Code, Section V, Subsection A, article 11 (1983 and later editions).
5. D. J. McNally: *Materials Evaluation*, **43**, (1985), 728-732.
6. Y. Mizutani, Y. Morino, T. Takahashi, *Proc. of 44th AIAA/ASME/ASCE/AHS Structures, Structural Dynamics, and Materials Conf.*, April 7-10, 2003, Norfolk, Virginia, USA.
7. Eric v. K. Hill, S.T. Dion, J.O. Karl, N.S. Spivey and J.L. Walker II: *Proc. Sixth International Conference on Acoustic Emission*, Oct. 29-Nov. 2, 2007, Lake Tahoe, Nevada, USA.
8. C. Wilkerson: NASA Technical Memorandum 108520, 1996.
9. Y. Mizutani, R. Matsuzaki, A. Todoroki: *Proc. 19th International AE Symposium*, Dec. 9-12, 2008, Kyoto, Japan.

STRUCTURAL INTEGRITY EVALUATION OF CNG COMPOSITE CYLINDERS BY ACOUSTIC EMISSION MONITORING

OLIVIER SKAWINSKI¹, PATRICE HULOT¹, CHRISTOPHE BINÉTRUY¹
and CHRISTIAN RASCHE²

¹ Department of Polymers and Composites Technology & Mechanical Engineering, Ecole des Mines de Douai, 941 rue Charles Bourseul, B.P. 838, 59508 Douai Cedex, France;

² Dynetek Industries Ltd., 4410-46th Avenue SE, Calgary, AB, Canada T2B 3N7

Keywords: AE damage detection, composite materials, CNG cylinders

Abstract

Over the past decades, the increasing use of compressed natural gas (CNG) as an alternative fuel for vehicles has led to the design of attractive lightweight cylinders by the use of fiber-reinforced polymers. Nevertheless, the traditional inspection techniques used for steel cylinders are generally not well adapted to the composite materials. In order to ensure the safety of the users, new inspection techniques has been investigated to give an accurate evaluation of the structural integrity of composite cylinders.

The present work investigates the ability of the acoustic emission (AE) technique to detect serious damages in CNG composite cylinders. Internal pressure tests with AE monitoring were performed on CNG Type-3 cylinders (per ISO 11439 and ECE R110), made of an aluminum-liner reinforced with a carbon-fiber composite. The experiments were conducted on cylinders submitted to drop tests from different heights, cylinders submitted to ballistic impact at different energies and cylinders with longitudinal and transverse notches with different depth. Results of the AE as a function of the damage type and severity are discussed.

Introduction

In recent years, compressed natural gas (CNG) has become an attractive alternative as a fuel for vehicles, such as public buses. Compared to oil based fuels, the use of CNG reduces carbon dioxide and nitrogen oxides emission. Furthermore, the use of fiber-reinforced polymers in the design of CNG cylinders has led to attractive lightweight solutions. For the safety of the users, structural integrity of such composite cylinders must be accurately checked. Nevertheless, the actual inspection techniques, derived from the techniques used for steel cylinders, may not be well adapted to the composite materials (Bunsell, 2006).

For several years now, acoustic emission (AE) technique has been successfully applied for composite materials. By comparison with classical methods, such as hydraulic proof test or visual inspection, acoustic emission technique allows the detection of damages which are not visible at the surface of the material. Various studies performed on composite coupons with a polymer matrix have shown that the AE amplitude distribution can be used to clearly identify the main damage mechanisms (Barré *et al.*, 1994; Hamstad, 1982; Kotsikos *et al.*, 1999). The development of this non-destructive testing method has also led to successful industrial applications for periodic inspection of glass-fiber reinforced plastic storage tanks (ASTM E1067) and of composite bucket trucks, used for inspecting the high-voltage transmission lines (ASTM F914) (Wevers *et al.*, 2000).

Furthermore, recent works have shown the potential of AE technique for inspection of composite pipes and pressure vessels (Dong *et al.*, 1998, Gebiski *et al.*, 2001, Webster, 1999, Wood *et al.*, 2000). The AE technique presents a great potential for the inspection of CNG composite cylinders, as it should not require the removal of the cylinders from the vehicles. This technique could be used as an on-board inspection method and structural integrity of the composite part could be checked by AE monitoring during the filling of the cylinder to its service pressure, for example.

In the present work, the AE technique has been used during a hydraulic pressure test in order to check CNG composite cylinders with typical critical defects:

- Damages from low velocity impact (drop test),
- Damages from ballistic impact (high velocity),
- Longitudinal and transverse notches inside the composite overwrap.

After the pressure test with AE monitoring, each cylinder was submitted to a fatigue test to increase their mechanical ageing, in order to estimate the severity of each defect.

Experimental

Specimens: This study concerning AE analysis of fully wrapped aluminum liners was performed on DyneCell[®] composite cylinders, manufactured by Dynetek (cf. Fig. 1).



- ECE approval n°: E1 110R-000039
- Working pressure: 200 bar @ 15°C
- Nominal internal volume: 76 liter
- Nominal dimension: 402 x 864 mm
- Nominal weight: 28 kg

Fig. 1. Characteristics of the tested composites cylinders, Dynecell[®].

Ten cylinders (1 reference specimen with no defect + 3 specimens submitted to drop test + 3 specimens submitted to ballistic impact + 3 specimens with notches) were tested. Three cylinders, each completely filled with water, were dropped once at a 45° angle onto a concrete surface, impacting one of the dome end (cf. Fig. 2). These three cylinders, referenced J3386, J3416 and J2105, were respectively dropped from a height of 0.472 m, 0.944 m and 1.888 m (corresponding approximately to impact energies of 500 J, 1000 J and 2000 J). After drop test, each cylinder presented two impacted areas: the first one, the main impact area, corresponds to the main impact, while the second one, the rebound impact area, occurred on the opposite dome after the rebound of the structure (cf. Fig. 4a).

Ballistic tests were performed on the cylindrical part of three cylinders, referenced J3462, J2041 and J2043, which were respectively impacted at an energy level of 137 J (velocity = 158 m/s), 280 J (velocity = 226 m/s) and 419 J (velocity = 276 m/s) with a steel projectile with a conical head and a weight of 11 g. The ballistic tests were performed by the French Defense Research Agency in Paris (DGA) with a gas gun facility, developed to fire a projectile up to 600

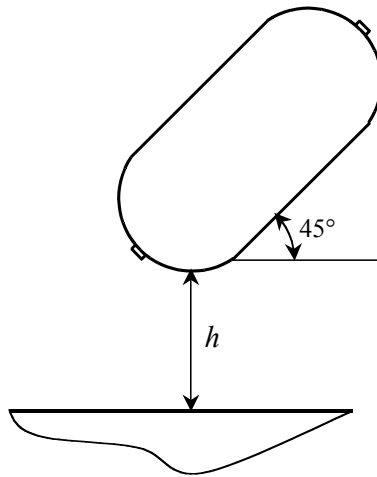


Fig. 2. Drop test on cylinders.

m/s. Preliminary tests were carried out in order to adapt the velocity of the projectile in order to generate a non perforating damage.

Two notches, one longitudinal and the other transverse, were made with a Dremel[®] tool on three cylinders in the central part along two planes forming an angle of approximately 120°. The two notches were made with a 1-mm-thick cutter to a length in the bottom of the notch of 50 mm (equal to approximately five times the composite thickness). The notches for the three cylinders, referenced J2112, J2144 and J3419, are respectively 1.25-mm, 2.5-mm and 5-mm deep.

Pressure test: The pressure required to perform the hydraulic test is supplied by a servo-hydraulic intensifier system. This system is able to control the rate of pressurization accurately by means of a programmable automatic device. The equipment used for this test is depicted in Fig. 3; it includes:

- an 11-kW mono-pump producing a maximum pressure of 250 bars,
- an accumulator,
- a multiplying unit used to pressurize the specimen by quadruplicating the pressure of the pump. This transfer booster enables to transfer the pressure from oil to water, the pipes being pressurized with water,
- a servo-valve allowing the control of the applied pressure.

The loading procedure for pressure test on the composite cylinders at ambient temperature is composed of a pressure cycle described as followed:

- Pressure ramp at a pressurization rate of 1 bar/s up to $P_{\text{Test}} = 300$ bar,
- Hold period of 4 min at 300 bar,
- Unload at a depressurization rate of 1 bar/s down to atmospheric pressure.

After the pressure test with AE monitoring, the cylinders were subjected to a hydraulic fatigue test (5000 cycles between 30 and 300 bar at 5 cycles/minute and room temperature) in order to investigate the evolution of each defect and to estimate its severity.

AE equipment: The Euro Physical Acoustics (EPA) DISP[®] system was used to monitor the AE signals during the tests, based on two PCI-4 boards, with the following characteristics:

- 8 AE channels,
- Frequency bandwidth: 10 kHz-2 MHz,
- Minimum threshold: 18 dB,
- 8 parametric input channels.

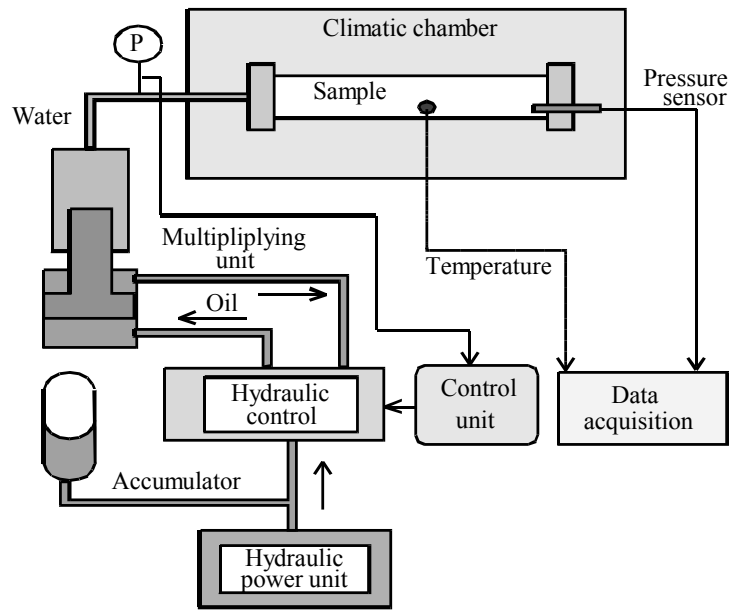


Fig. 3. Schematic illustration of the pressure test facility.

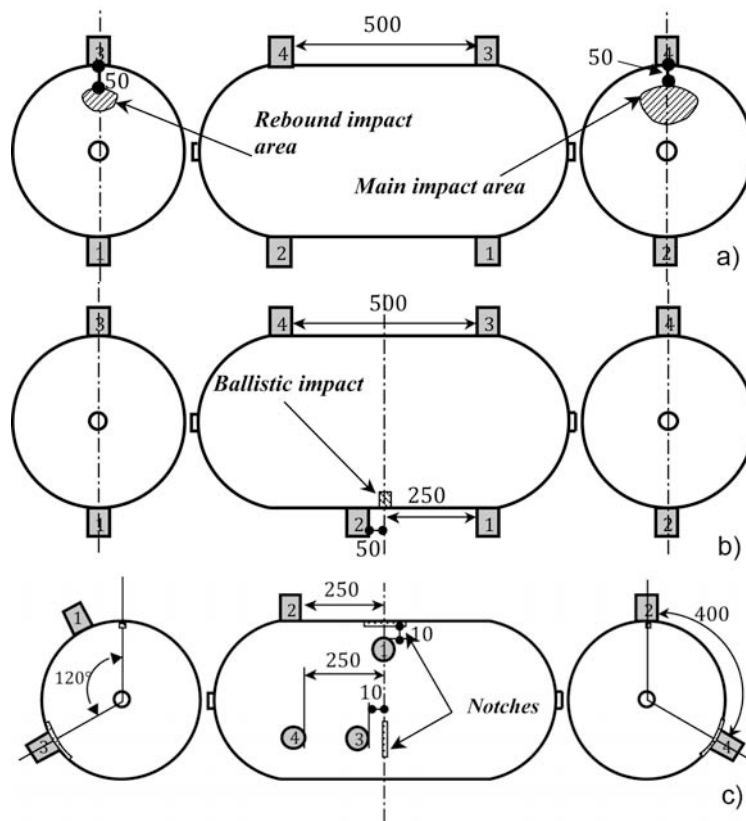


Fig. 4. Sensors location: a. for cylinders without defect and after drop test. b. for cylinders after ballistic impact. c. for cylinders with notches (all dimension in mm).

During the pressure tests, four R15 AE sensors, supplied by EPA, (150 kHz resonant frequency, operating frequency range: 50-200 kHz) were used with 2/4/6 preamplifiers. The gain of preamplifiers was 40 dB while fixed 40-dB threshold level was applied for the tests. Silicone

grease 500 was used as a couplant at the structure-to-sensor interface. Figure 4 presents the sensors location for the different pressure tests with AE monitoring.

Before the pressure test with AE monitoring, calibration of the sensors is realized through Hsu-Nielsen test in order to simulate an acoustic event using the fracture of a brittle pencil lead. This generates an intense acoustic signal, quite similar to a natural AE source, such that the sensors detect it as a strong burst. It also allows to check whether the transducers are in good contact with the cylinder.

Results

In this work, the considered approach aims to relate basic AE parameters (the cumulative number of hits and counts) to the damage type and severity in order to investigate the structural integrity of the composite cylinders. Table 1 presents the AE activity recorded during the pressure test on the ten cylinders. By comparison to the damaged cylinders, the cylinder without defect shows a low AE activity and could be then clearly identified by this technique.

Table 1. Results of the AE monitoring.

Cylinder reference	Defect	AE test results
J2045	None	Σ Hits = 769, Σ Counts = 3,666
J3386	Drop test, 500 J	Σ Hits = 9,780, Σ Counts = 61,690
J3416	Drop test, 1000 J	Σ Hits = 25,688, Σ Counts = 160,053
J2105	Drop test, 2000 J	Σ Hits = 44,232, Σ Counts = 366,804
J3462	Ballistic impact, 137 J	Σ Hits = 9,784, Σ Counts = 322,891
J2041	Ballistic impact, 280 J	Σ Hits = 34,729, Σ Counts = 1,184,880
J2043	Ballistic impact, 419 J	Σ Hits = 79,719, Σ Counts = 2,736,485
J2112	Flaws, 1.25 mm deep	Σ Hits = 173,772, Σ Counts = 6,668,306
J2144	Flaws, 2.5 mm deep	Σ Hits = 141,975, Σ Counts = 6,542,613
J3419	Flaws, 5 mm deep	Σ Hits = 160,280, Σ Counts = 6,423,255

Table 2. Results of the fatigue test.

Cylinder reference	Defect	Fatigue test results
J2045	None	No failure after 5000 cycles
J3386	Drop test, 500 J	No failure after 5000 cycles
J3416	Drop test, 1000 J	No failure after 5000 cycles
J2105	Drop test, 2000 J	Failure after 2924 cycles
J3462	Ballistic impact, 137 J	Failure after 4376 cycles
J2041	Ballistic impact, 280 J	Failure after 3216 cycles
J2043	Ballistic impact, 419 J	Failure after 892 cycles
J2112	Flaws, 1.25 mm deep	No failure after 5000 cycles
J2144	Flaws, 2.5 mm deep	No failure after 5000 cycles
J3419	Flaws, 5 mm deep	No failure after 5000 cycles

AE activity recorded during the pressurization of the cylinders with drop impact damages is plotted in Fig. 5. The total number of hits and counts increases almost linearly with the impact

energy. Most hits were recorded by the sensor N°4, placed close to the main impact area (for the three different impact energies, about 80 % of the total hits were recorded by sensor N°4).

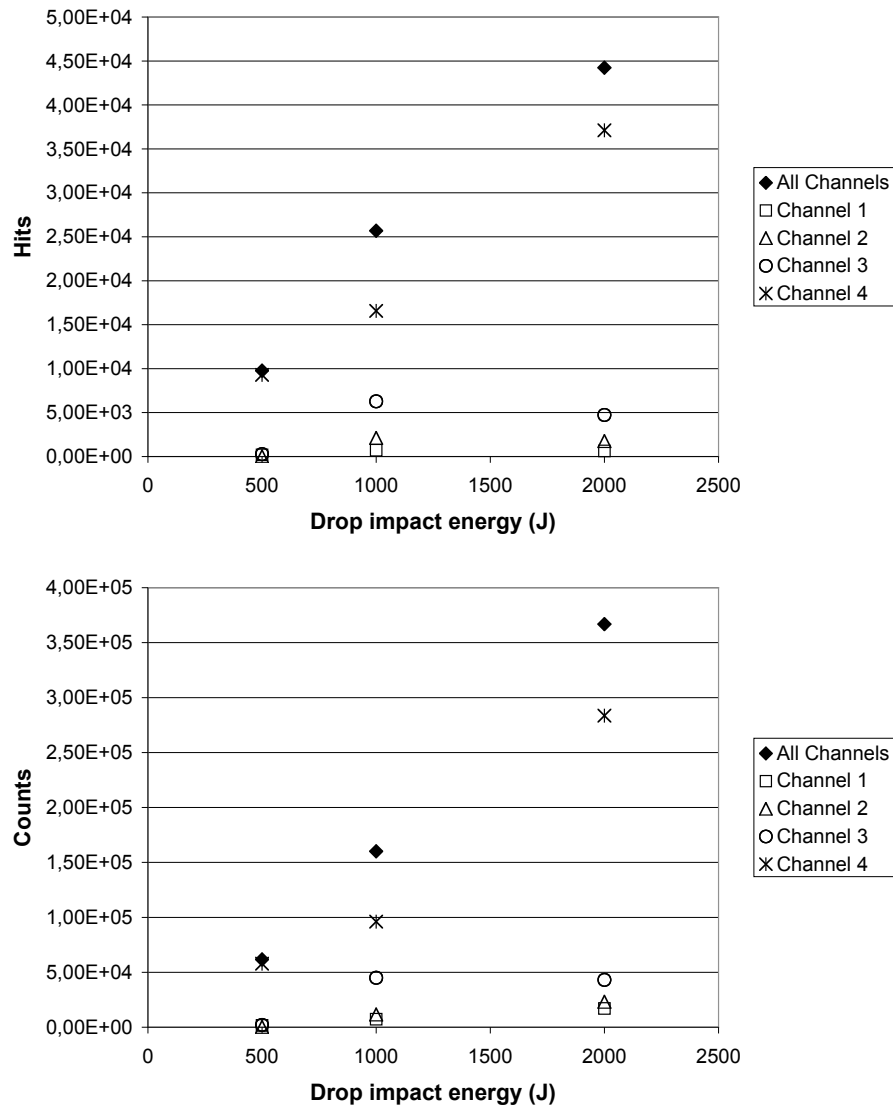


Fig. 5. Evolutions of AE hits and counts as a function of the drop impact energy.

AE activity recorded during the hydraulic pressure tests on cylinders with ballistic impact damages is plotted in Fig. 6a and b. As in the previous case, AE activity increased almost linearly with the impact energy. Most hits (around 70 % of total hits number for the different impact energies) were recorded by sensor N°2, placed at 50 mm far from the impact point; see Fig. 6a.

Figure 7 shows the evolution of AE hits and counts recorded during the pressure test as a function of notch depth. As confirmed by these 2 graphs, the severity of the damage (in our case the notch depth) seems to have no influence on the AE activity. Among all the tested cylinders, the total number of hits and counts is the highest for the specimens with notches. The highest number of recorded AE hits or counts was obtained for the cylinder with 1.25-mm deep flaws. The sensor N°1, close to the longitudinal notch, recorded around 60 % of all the hits.

The cylinders were finally submitted to a fatigue test (5000 cycles between 30 and 300 bar) in order to have an estimation of the defect influence on the structure integrity. Results of these

tests are presented in Table 2. Most of the cylinders withstood the fatigue test without failure. The cylinder, impacted at low velocity and with an energy of 2000 J, failed approximately after 3000 cycles with a leak before break, a safety issue as required by the standards. All the ballistic impacted cylinders failed also by leakage during the fatigue test and the number of cycles to failure decreases when the impact energy increases.

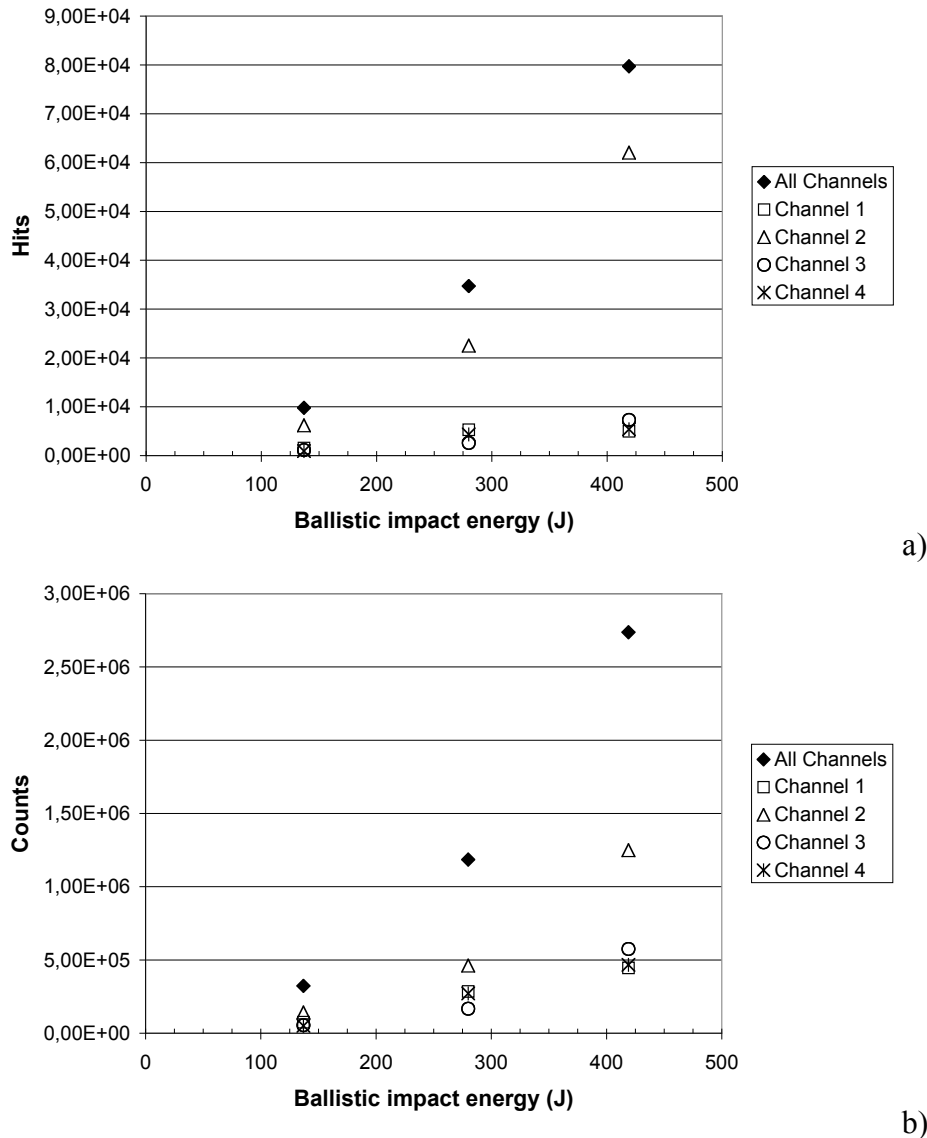


Fig. 6. Evolutions of a) AE counts and b) hits as a function of the ballistic impact energy.

After the cycling test, significant delamination of a circumferential composite strip was observed on both side of the longitudinal notch for each cylinder with notch defect (cf. Fig. 8).

Discussion

In this work, the severity of the investigated defects can be related to the impact energy for the drop and ballistic tests and to the depth for the notched cylinders. The experimental results show that, for the adopted AE sensor location, the acoustic activity increases almost linearly with the damage severity for the cylinders submitted to drop test and ballistic impact, unlike the cylinders with notches. In the case of impact defects, the severity of the damages may be estimated by the AE method. For the cylinders with notches, considering the results in terms of AE activity

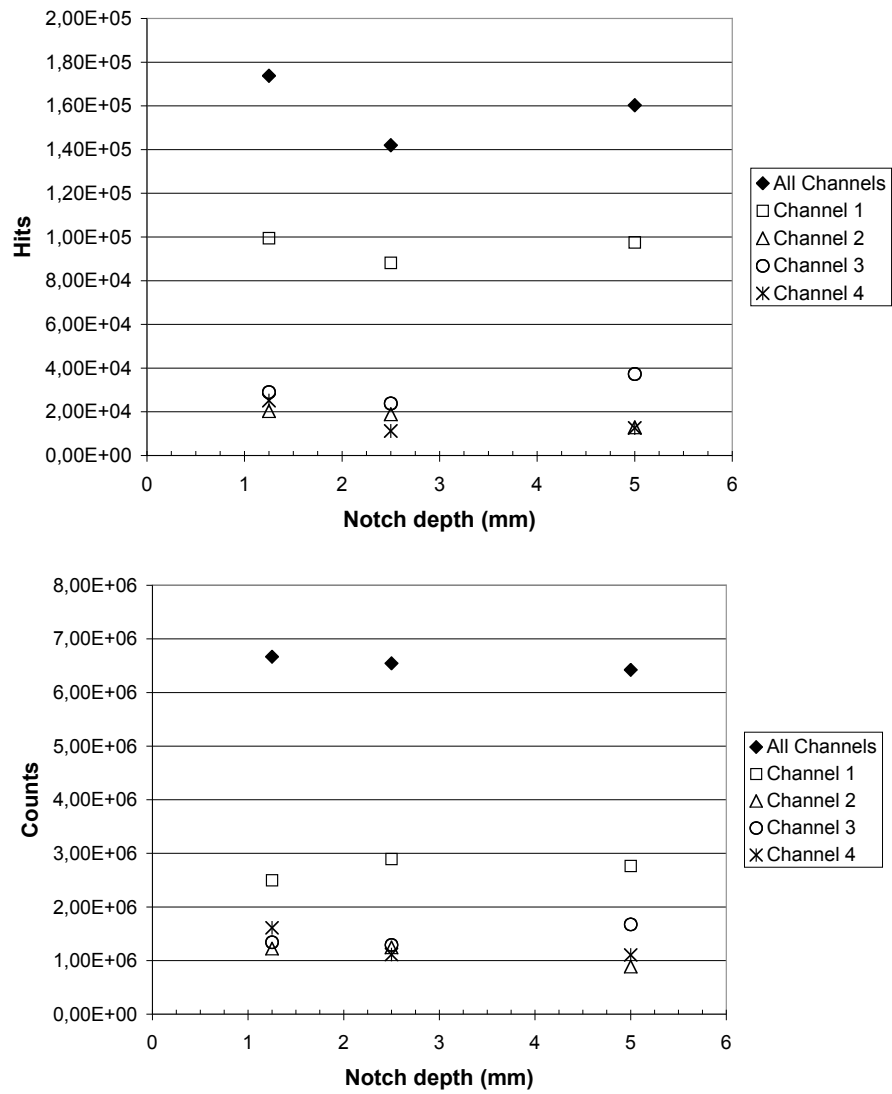


Fig. 7. Evolutions of AE hits and counts as a function of the notch depth.

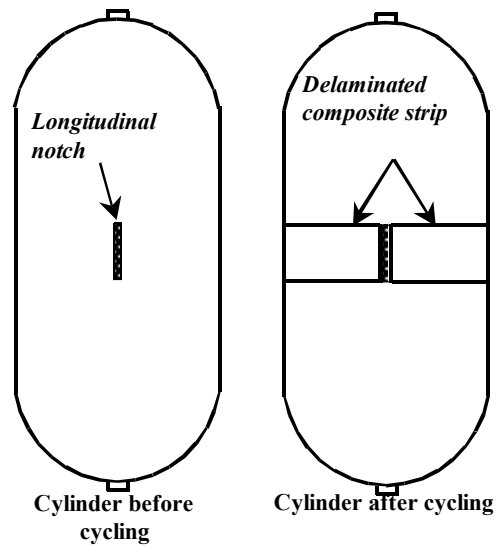


Fig. 8. Delamination of the cylinders with notches after fatigue.

(no significant difference regarding the notch depth) and damages, observed after cycling, it seems that the delamination was the main source of AE during the pressure test with AE monitoring. The fact that delamination propagation occurred in a similar way for the three different notch depths could explain why no significant difference in AE activity was recorded and why the number of AE hits or counts could not be representative of the defect severity for the range of notch depth considered in this study. The loading of the structures during the pressure test does not cause the propagation of the matched notch but mostly delamination that is induced by the longitudinal notch but not influenced by its depth.

The influence of each type of defect on the structural integrity of the cylinders seems difficult to estimate regarding the results of the AE activity in terms of total number of hits and counts. In comparison with the cylinders with notches, the AE activity due to ballistic impact damages is lower. Nevertheless, regarding the failure of these cylinders during the fatigue test, the impact ballistic defects are found to be more critical. The difficulty to estimate the gravity of the defects by considering the total number of hits or counts may also be related to the failure mode, that was observed during the fatigue tests. For the cylinders which did not pass the 5000 cycles at 300 bar, the failure occurred by leakage, this kind of failure is induced by liner cracking and may occur even if the composite shell keeps good load bearing properties, which could ensure a sufficient burst pressure if the structure was tight. For this reason, it seems that AE monitoring may give a good assessment of the composite shell damage level, but may not give sufficient information for predicting the leakage risk.

Table 3. Results of high amplitude AE (80-100 dB).

Cylinder reference	Defect	AE between 80 and 100 dB
J2045	None	Σ Hits = 0, Σ Counts = 0
J3386	Drop test, 500 J	Σ Hits = 0, Σ Counts = 0
J3416	Drop test, 1000 J	Σ Hits = 2, Σ Counts = 977
J2105	Drop test, 2000 J	Σ Hits = 13, Σ Counts = 14,423
J3462	Ballistic impact, 137 J	Σ Hits = 58, Σ Counts = 110,987
J2041	Ballistic impact, 280 J	Σ Hits = 238, Σ Counts = 481,985
J2043	Ballistic impact, 419 J	Σ Hits = 495, Σ Counts = 1,192,418
J2112	Flaws, 1.25 mm deep	Σ Hits = 2014, Σ Counts = 2,265,270
J2144	Flaws, 2.5 mm deep	Σ Hits = 1990, Σ Counts = 3,003,495
J3419	Flaws, 5 mm deep	Σ Hits = 1803, Σ Counts = 2,643,058

The defect effect on the structural integrity could also be evaluated by the high amplitude AE events. Several works, performed on fiber-reinforced polymer (composite) coupons, have shown that AE amplitude distribution can be used to identify the main damage mechanisms (matrix cracking, interface fracture, fiber pull-out, fiber fracture) in composite materials (Barré *et al.*, 1994; Kotsikos *et al.*, 1999). High amplitude signals, over 80 dB, are generally associated to fiber fractures, which can be considered as the most critical damage mechanism regarding the structural integrity of the cylinders. Nevertheless, this correlation between the AE amplitude distribution and the damage mechanisms is generally difficult to apply to large composite structures due to significant attenuation of acoustic waves in the heterogeneous materials. Table 3 presents the high amplitude AE activity (amplitude between 80 and 100 dB), recorded by the four AE sensors during the pressure tests. For the cylinders after drop test and ballistic impact, the

number of high amplitude hits increases with the impact energy. Only a few hits between 80 and 100 dB were recorded for the cylinders after drop test. The highest numbers of high amplitude hits were obtained for the cylinders with notches and the high amplitude activity does not seem to be influenced by the notch depth. Considering the results of the high amplitude activity, the notches should be considered as the most critical defect for the structural integrity of the cylinders.

In this study, the results also show that the number of AE events recorded by the sensor placed close to the defects (i.e., the main source of AE signals) is significantly higher than for the other sensors (60 to 80 % of the total number of hits was recorded by the sensor close to the damage). Furthermore, from the Hsu-Nielsen tests performed on the reference cylinder, the attenuation coefficient, β , and the wave speed, v , was determined for different directions (cf. Fig. 9). These results show an anisotropic behavior and a significant attenuation of the acoustic signals. Considering this significant attenuation effect for the composite materials and the fact that a critical damage might not be clearly localized before placing the sensors on the structure (which was not the case in this study for the created defects), measurements show that the number of sensors and their position will have an influence on the recorded AE events.

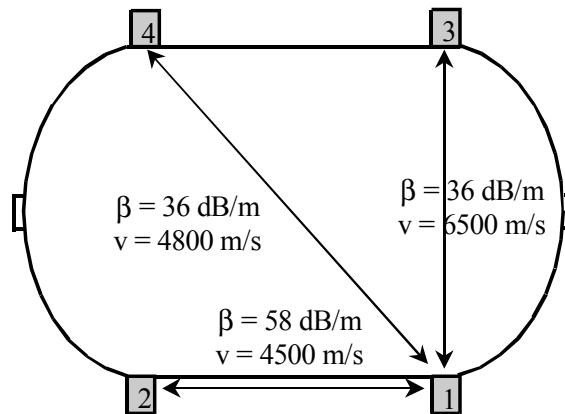


Fig. 9. Attenuation coefficient, β , and acoustic wave speed, v .

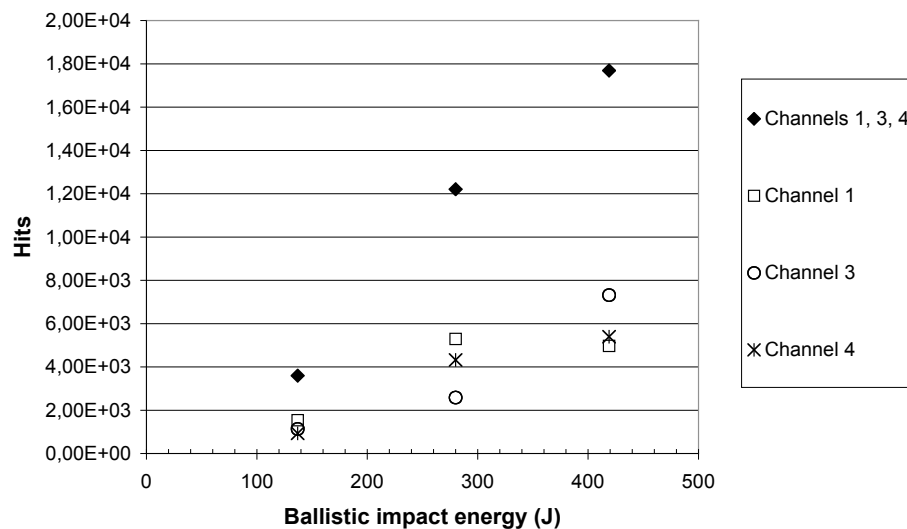


Fig. 10. Evolution of AE hits as a function of the ballistic impact energy without results from the AE sensor close to the damage.

Furthermore, the influence of the sensor in the vicinity of the damaged area may be estimated by considering the previous results without taking into account the hits recorded by this sensor. Figure 10 shows the number of hits, recorded by all the AE sensors except the one close to the impact point, versus the impact energy for the cylinders after ballistic impact. The total number of hits increases almost linearly with the impact energy and the defect severity may still be estimated without taking into account the sensor close to the defect. On the contrary, for the cylinders after drop test (cf. Fig. 11), no linear relationship between hits and energy can be established when the hits, which were recorded by the sensor close to the main impact area, are not taken into account. For the ballistic impact, the damaged area is mainly restricted to a limited zone around the impact point. After a drop test, two damaged areas may be identified (cf. Fig. 4a): the main impact area under the impact point, and the rebound impact area on the opposite dome. Without the hits from the sensor close to the main impact area, the evaluation by AE monitoring mainly concerns the second damaged area, as shown by the significant number of hits, recorded by the sensor N°3, close to the rebound impact area, for impact energies of 1000 and 2000 J.

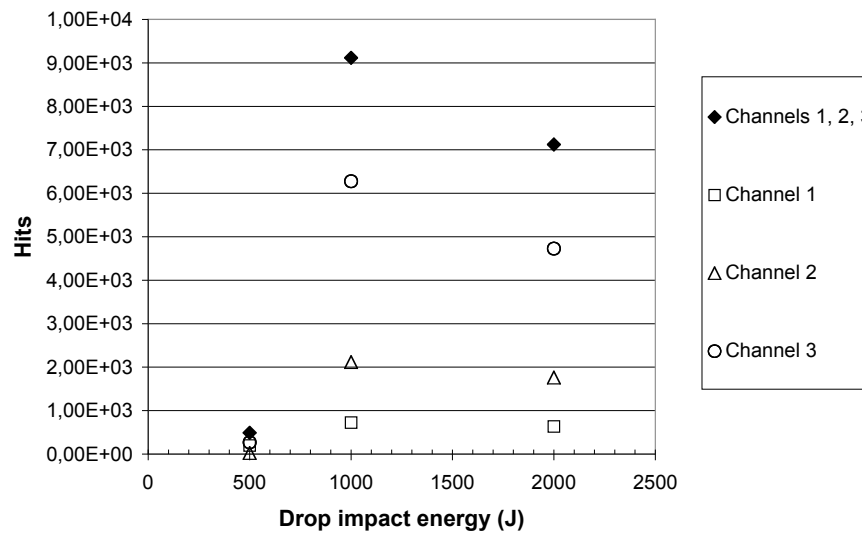


Fig. 11. Evolution of AE hits as a function of the drop impact energy without results from the AE sensor close to the damage.

Conclusions

This work shows the influence of critical defects (flaws, ballistic impact, drop test) on the AE activity of composite cylinders.

For the ballistic and drop test impact, AE activity increases almost linearly with the impact energy, and in this case, the damage severity may therefore be estimated by the number of AE hits and/or counts monitored during the AE test. For notches, the damage severity has no influence on the AE activity. It seems that delamination, induced whatever the notch depth is, is the main source of acoustic emission.

For the different investigated damages, considering the total number of hits and counts, and particularly considering the high amplitude acoustic signals, appears insufficient to estimate the structural integrity: the highest AE activity was obtained for cylinders with notches, and these structures did not fail during the fatigue test. But, this difficulty to determine a basic AE criterion in order to evaluate the cylinder integrity may also be related to the failure mode. Failure by

leakage is not acceptable for the integrity of a pressure vessel, but this kind of failure, related to the liner tightness, can happen even if the composite shell keeps good mechanical properties. For this reason, even if the proposed AE analysis may give a good evaluation of the damage level for the composite material, it seems insufficient for the leakage risk prediction.

This work also confirmed the significant attenuation of acoustic signals in composite materials. This result underlines that the number and the position of AE sensors may be a critical point for large composite structures.

References

- S. Barré, M. Benzeggagh (1994), "On the use of acoustic emission to investigate damage mechanisms in glass-fibre-reinforced polypropylene", *Composite Science and Technology*, **52**, 369-376.
- A. R. Bunsell (2006), "Composite pressure vessels supply an answer to transport problems", *Reinforced Plastics*, **50** (2), 38-41.
- L. Dong, J. Mistry (1998), "Acoustic emission monitoring of composite cylinders", *Composite Structures*, **40** (2), 149-158.
- P. Gebiski, L. Golaski, K. Ono (2001), "Acoustic emission monitoring of fatigue of glass-fiber wound pipes under biaxial loading", *Journal of Acoustic Emission*, **19**, 285-314.
- M. Hamstad (1982), "Testing fiber composites with acoustic emission monitoring", *Journal of Acoustic Emission*, **1**, 151-164.
- G. Kotsikos, J. T. Evans, A. G. Gibson, J. Hale (1999), "Use of acoustic emission to characterize corrosion fatigue damage accumulation in glass fibre reinforced polyester laminates", *Polymer Composites*, **20** (5), 689-696.
- M. Wevers, M. Surgeon (2000), "5.14 Acoustic emission and composites", *Comprehensive Composite Materials Book*, vol. 5, eds. A. Kelly, C. Zweben, R. Talreja, J.E. Manson, Pergamon, pp. 345-357.
- C. Webster (1999), "Assessment of the use of acoustic emission as an inspection method for FRP wrapped cylinders", *Transport Canada Publication N° TP 13505E*, Powertech Labs Inc.
- B. Wood, R. Harris (2000), "Structural integrity and remnant life evaluation of pressure equipment from acoustic emission monitoring", *International Journal of Pressure Vessels and Piping*, **77**, 125-132.

AUTOMATED METHOD FOR STATISTIC PROCESSING OF AE TESTING DATA

V. A. BARAT and A. L. ALYAKRITSKIY

Research Dept, Interunis Ltd., bld. 24, corp 3-4, Myasnitskaya str., Moscow, 101000, Russia

Keywords: signal processing, AE data classification

Abstract

Acoustic emission (AE) as a nondestructive testing method allows estimating the condition of sophisticated industrial objects, detecting defects at their initiation, and preventing development of such defects. The reliability of detection and the accuracy of determination of AE source location depend on the correct interpretation of the AE testing results. Testing procedures of different industrial equipment are intended for estimating condition of the objects on the basis of AE parameters, while the AE signals proper are not used in analysis as the primary diagnostic data.

We have developed the statistical method of analysis to study the whole complex of measured data, both the AE parameters and signal waveforms. This method is based on the two-level clustering of data, such as AE signals from separate channels, and "groups of signals" formed on the basis of the primary clustering. The algorithm allows the determination of the quantity of AE sources, and estimates the degree of their danger without resorting to the preliminary location. The zonal location is carried out after the determination of AE sources. It avoids the so-called false locations, which considerably complicate the location map. On the basis of classification results, one can correct the AE signal arrival time, and such correction makes it possible to improve the accuracy of the AE source location.

The characteristic property of the developed method is data processing in an automatic mode, with minimal operator intervention. In this case there is no need to employ a high-skilled operator. Since the AE signals themselves are used for analysis, the obtained results prove to be more reliable than those obtained when working with the AE parameters. The algorithm built on the developed method has been successfully applied for processing data obtained as a result of laboratory research of the corrosion development, for studying reinforced concrete structures, and also as an additional instrument for processing data of the industrial AE testing.

Introduction

Each AE event defines a unique process occurring at a certain point of the test object. When AE signals propagate from the point of emission to a sensor, the waveforms are complicated due to conversions to different modes of waves, multiplicity of distribution paths, and due to wave velocity dispersion by frequency. AE signals contain information not only about the AE source event for this signal, but in the highest degree about parameters of acoustic and electric path. In this connection construction of the analytical or even numerical diagnosis model for interpretation of AE signals appears to be an intricate and nontrivial problem, the solution of which cannot be generalized for the test equipment of different types.

While the data interpretation based on accurate diagnostic models appears to be difficult, the statistical analysis is a reasonable choice for carrying out the data interpretation and classifica-

tion with the high certainty. At present the statistical methods of data analysis are widely applied both in industrial AE systems and in laboratory research and the applications are varied: data clustering, correlation analysis, and check of different statistical hypotheses.

In this paper the statistical method of analysis enabling the automatic clustering of AE testing data is presented. This method makes it possible to process bulk data obtained as a result of the AE testing or during the laboratory research in the absence of *a priori* information. As a consequence of processing, the data are structured and organized; each cluster formed as a result of analysis characterizes an AE source at a definite stage of development.

Method Description

Statistical analysis of AE data is used rather frequently. However, different methods of data processing pursue different aims, and have special features of implementation [4, 5, 7, 8]. Our approach is based on the idea that the signals generated by the same AE source have a similar waveform. This similarity may be explained by the similar way of AE wave generation and by the same acoustic path for AE wave propagation. AE waves from the growing defect propagate in all directions. At the sensor location point these waves are registered and transformed into AE signals. With the help of signal analysis we simulate the reverse process – signals grouping and unifying.

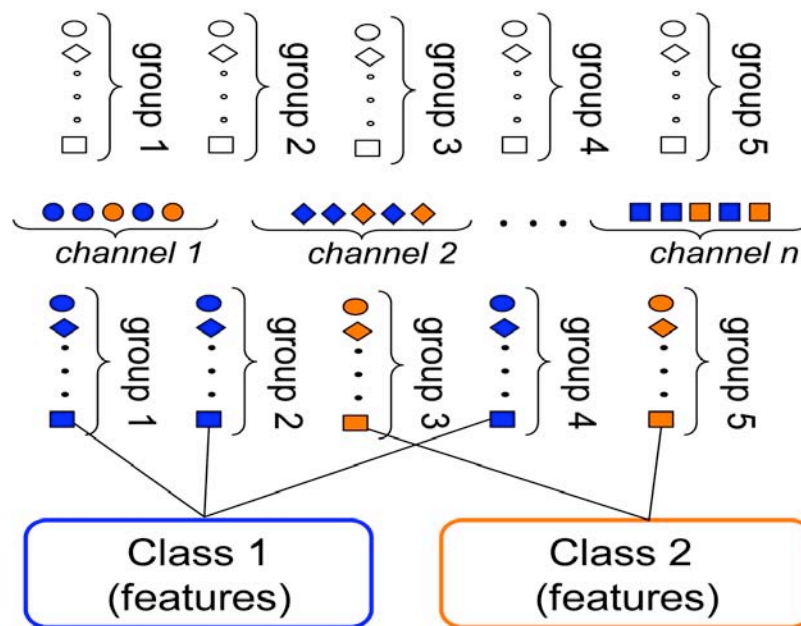


Fig. 1. Flowchart of automated method of AE data analysis.

The initial data for algorithm, which realizes this method, can be both the AE signals and their parameters computed under data acquisition in on-line mode. When the processing begins, the initial data represent a bulk of different diagnostic data, and at each step of algorithm the data consecutive structuring takes place. At the first step the signals generated by the same AE event are grouped together. For that purpose we compare the differences in the signals arrival time with the distances between sensors. This group of AE signals is designated in Fig. 1 with small figures (circles, rhombs and squares) joined by a brace. Different shapes of these figures represent different measuring channels, by which the signals are registered. Each group characterizes one AE event.

At the second step the groups obtained are classified. Algorithm designed for this purpose has a hierarchical structure. At the first stage AE signals are classified in accordance with the signal waveform similarity. In the diagram different classes of signals are marked with different colors. The groups of signals are classified according to the result of previous classification. The groups, wherein the signals recorded by the same channel have a similar waveform, are assigned to the same class. The classes of groups obtained in this way correspond with a high degree of probability to the potential AE sources.

When a part of AE signals is defined only by parameters, and waveforms are absent, the “classes of signals” and “classes of groups” are formed on the basis of incomplete diagnosis information. For classification of AE signals specified only by their parameters, each “class of groups” is characterized with a feature set included into the list of impulse parameters to be defined. In this case the classification of AE impulses for which there are no primary diagnosis data is accomplished on the basis of multidimensional empirical distribution function built for the calculated features.

Clustering of Acoustic Emission Signals

Estimation of similarity

For AE signal clustering, it is necessary to determine a distance measure [3]. In order that an estimation error of AE parameters does not influence on the classification result, the correlation coefficient r was used as a measure of similarity of two signals; see Eq. (1). The preliminary analysis has shown that signals relevant to the same AE source and recorded by the same measuring channel have a high correlation coefficient, whose value varies from 0.70 to 0.99 depending on the nature of the AE generating process.

$$r = \frac{\sum_{i=1}^N (x_i - \bar{x})(y_i - \bar{y})}{\sqrt{\sum_{i=1}^N (x_i - \bar{x})^2} \sqrt{\sum_{i=1}^N (y_i - \bar{y})^2}} \quad (1)$$

Using the correlation coefficient as the distance measure of AE signals, an automatic correction of arrival times of signals, which belong to the same cluster, can be carried out, because the cross-correlation function reaches its peak at the time corresponding to a difference of arrival times of AE signals.

Wavelet analysis

When processing bulk data, the calculation of correlation coefficients for all pairs of signals requires a long time; to speed up the data processing, a wavelet decomposition may be used, namely, a signal decomposition by wavelet packets [2].

The decomposition by wavelet packets is one of variety of the multi-resolution analysis, and it is the signal decomposition on the basis of wavelets (in a general case by the Riss basis) specified for a sequence of subspaces embedded to each other.

$$w_{2n}(x) = \sqrt{2} \sum_k h(k) w_n(2t - k) \quad w_{2n+1}(x) = \sqrt{2} \sum_k g(k) w_n(2t - k), \quad (2)$$

where $g(k) = (-1)^k h(1 - k)$ is defined by the type of wavelet function.

Under a discrete wavelet transform the signal is decomposed into a low-frequency component - approximation and a high-frequency component - detailing. At the next level both the approximation and the detailing are subject to further decomposition. So, at j -level of decomposition the 2^j coefficients are calculated. In this case the coefficient (j, k) localizes energy within the frequency range (Eq. 3), where Ω_0 is the frequency corresponding to a half of the sampling rate frequency (Fig. 2)

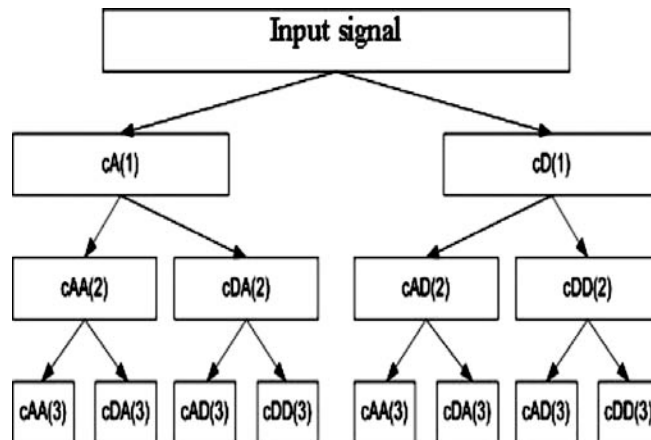


Fig. 2 Wavelet-packed decomposition

$$\Delta\Omega = \left(\frac{\Omega_0}{2^j} k, \frac{\Omega_0}{2^j} (k+1) \right) \quad (3)$$

As a rule, the AE signal energy is non-uniformly distributed on the spectrum, and often 3 or 5 coefficients of cluster decomposition are sufficient for location of 95-99% of the energy. Moreover, the dimension of informational components, as a rule, is at least four times smaller than the original signal dimension.

This paper offers the assessment method of signal shape similarity on the basis of weighted sum of correlation coefficient of significant approximations and detailings of signal wavelet-decomposition. The research has shown that the accuracy of this estimation is about 85%.

$$r = \sum \alpha \cdot r_{ij} \quad (4)$$

Figure 3 illustrates the estimation method offered. Figures 3a and 3b show the input signals x and y . Instead of direct calculation by Eq. 1 we calculate the cross-correlation function between significant wavelet decomposition coefficients. In this example we have taken only two significant wavelet-decomposition coefficients, C42 (Figs. 3c, e) and C54 (Figs. 3d, f), duration of which is more than one order lower than the duration of the initial signals. Because the calculation rate of cross-correlation function is proportional to the square of signal duration, the use of Eq. (4) allows the significant reduction in the time of computation of the degree of signals similarity.

Clustering scheme selection

With the clustering of AE signals, the quantity of clusters is to correspond to the quantity of the assumed AE events. In designing the clustering algorithm, a particular attention was given to the true determination of cluster quantity. For illustrating this aim, we suggested a two-stage

clustering diagram, as shown in Fig. 4; that is, the flowchart of clustering algorithm. At the first stage, a hierarchical agglomerative algorithm with complete link clustering is applied. Complete link clustering provides the maximum distance between elements of each cluster. This clustering method allows for avoiding an undesirable merging of clusters. At the second step, the iterative method providing the controllable merging of clusters is applied.

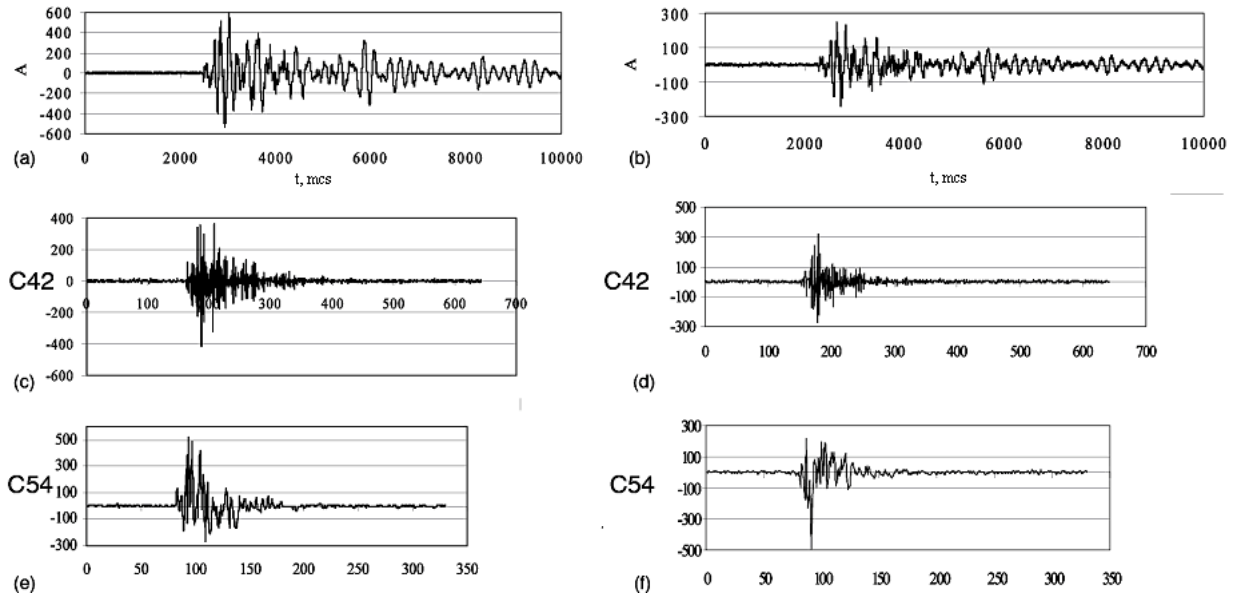


Fig. 3a and b - Initial signals for correlation coefficient calculation; c and e – significant coefficients, C42 and C54, of wavelet-decomposition for signal 3a; d and f - significant coefficients, C42 and C54, of wavelet-decomposition for signal 3b.

The distances between centers of mass of the clusters formed are calculated, and two clusters having the maximum and above-threshold distance between the clusters centers are merged. Thereafter, the re-clustering is accomplished by the method of k-averages.

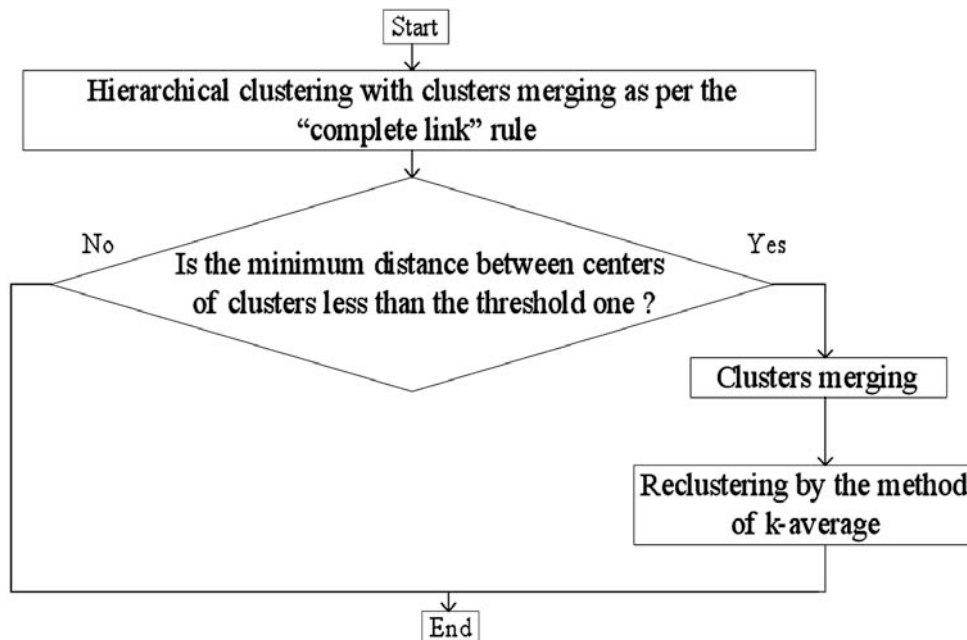


Fig. 4. Flowchart of two-stage clustering algorithm of AE signals.

When using this flowchart of clustering algorithm, the clustering is flexible and controllable; it uses two settings – the threshold value for signal addition to the cluster (at hierarchical clustering) and the threshold value for the inter-cluster distance. The setting values are selected on the basis of information about the test object and the testing conditions.

Clustering of Groups of Acoustic Emission Signals

At the next stage of algorithm, the groups of signals relevant to the same AE event are analyzed. For formation of such groups, we analyzed the arrival times of AE signals and the difference of recording time of the first and last signals in the group. The latter should not exceed the specified value, which is determined by the ratio of its maximum overall dimension and minimum velocity of acoustic wave propagation experimentally measured for the given test object. An AE signal beyond the time window is initial AE signal for the next group.

To the same “class of groups” assigned are the groups wherein the signals recorded by the same measuring channels corresponding to the same classes of signals. The study of algorithm has shown that for assigning the group of signals to one or another class it is sufficient that the classes of signals coincide at least for two channels in the group.

The membership of “classes of groups” can be also defined for AE signals, even with no information about the AE signal waveform. For this purpose, each “class of groups” obtained is characterized by the values of features listed below representing a median of distribution for each class.

- Numbers of three channels with minimum time of signal arrival $\{n_{t_1}, n_{t_2}, n_{t_3}\}$
- Numbers of three channels with maximum signal amplitude $\{n_{a_1}, n_{a_2}, n_{a_3}\}$
- Maximum value of signal amplitude in the group A_{max}
- Ratio of amplitudes of signals recorded by channels n_{t_2} and n_{t_1} , and also n_{t_3} and n_{t_1} $\{A_{21}$ & $A_{31}\}$

The signal group belonging to one or another class is defined similarly to the k-averages method, by the minimum distance between the features, characterizing each “class of groups” and the group of features to be analyzed.

The “classes of groups” obtained by such a manner characterize the potential AE sources with a high degree of probability. The quantity of “classes of groups” corresponds to the quantity of AE sources; the numbers of channels, by which the signals with the minimum arrival time are recorded, define the number of location zone. The quantity of groups in each class and the energy of AE signals included into the group can define the degree of danger of AE source.

Results and Discussion

The practical examples can visually confirm the effectiveness of the present method. To research regularities of AE in concrete, a series of experiments was carried out. On a concrete cube with a 1-m side length, eight AE sensors were placed, one at each vertex. The AE sensors were used both for AE measurement mode and as a pulser for the simulation of AE sources.

To illustrate advantages of the present method, two of the experiments were selected. Experiment 1 illustrates the case when the AE sources are not found because of mechanical noise and impacts. There are two AE sources, a pulser that simulates a growing defect, and a hammer

that simulates mechanical noise of equipment. Figure 3a shows the result of volume location of the AE sources. Indications distributed over the whole field of location are generated by the mechanical noise source or hammer blows. As the hammer impacts are made manually, the relevant signals have different waveforms. In this case, determination of the arrival time by the threshold method entails the difference in arrival time errors. The errors of arrival time determination differ in their meaning and sign for the signals with different waveforms. This is one of the possible reasons for the distribution of source locations.

Application of the statistical method of data analysis allows not only forming “the class of groups” of AE impulses emitted by the simulator, but also pointing out as an independent class the signals relevant to the hammer blows. Table on Fig. 5 shows the results of operation; the attributes given in this table conform to the list of “class of group” features. The names of features in this table comply with the previous list of features. Each line of the table characterizes one “class of groups”

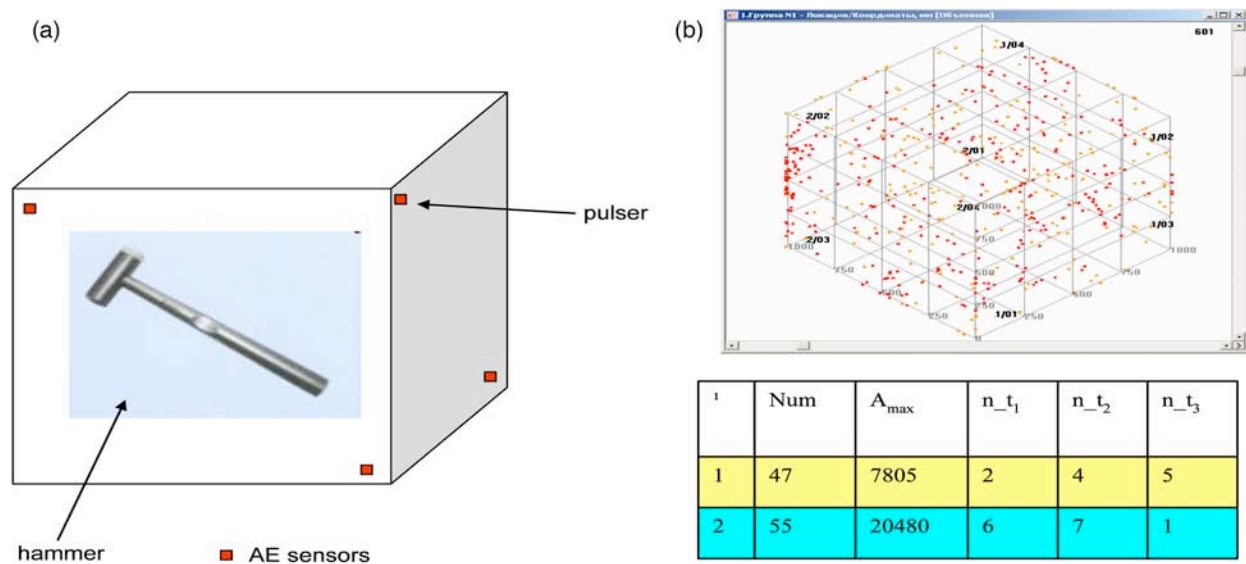


Fig. 5 Diagram of experiment 1, results of volume location and signal analysis statistics.

In Experiment 2, there are six AE sources in all. Two types of acoustic waves were generated at three positions on the concrete cube surface by means of a pulser and a Hsu-Nielsen source. Figure 6b shows the three locations of the AE sources. During the statistical processing of data, application of the present method can give six classes of events corresponding to two different sources of AE at three points on the test object surface, as shown in the table on Fig. 6. There are two “classes of groups” in each location zone, which is defined by the channels number {n_{t1}, n_{t2}, n_{t3}}.

One more useful implementation of the present method is structuring and data compression. The data structuring is realized due to replacement of the AE signals being analyzed by the “classes of signals” and “classes of groups”. Thus, the quantity of the information under analysis is reduced considerably. For example, during experimental AE studies from pitting corrosion growth, several hundred thousand signals were recorded; after the statistical analysis of data in an auto-mode without preprocessing about 20 representative classes of “groups of pulses” describing different stages of corrosion damage development were defined [6].

In practical AE applications, it is effective to use automated method of statistical analysis for processing of the AE monitoring data, especially when it is necessary to analyze changes in the structure of AE signals recorded for any length of time, and also in the case of testing sophisticated industrial facilities, for which the construction of an acceptable location scheme appears to be difficult.

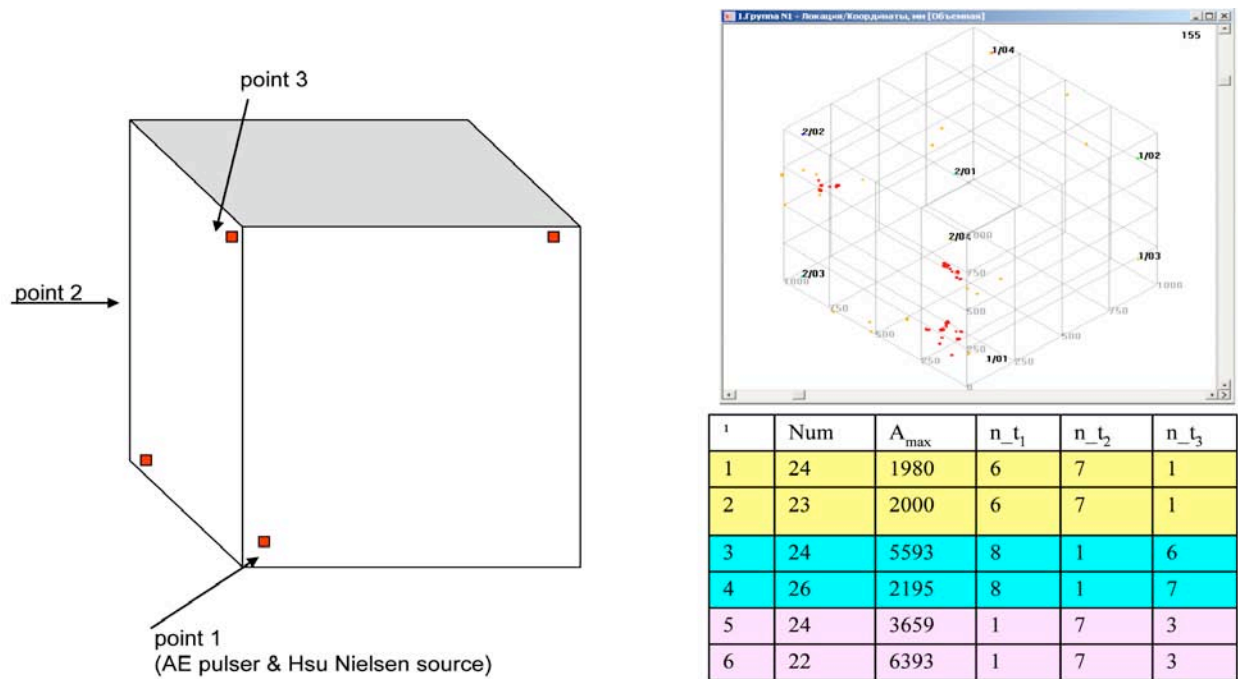


Fig. 6 Diagram of experiment 2, results of volume location and signal analysis statistics.

Additional Possibilities of the Method

The offered statistical method gives comprehensive possibilities to the user, such as AE data structuring, AE source detection and estimation of their quantity. Besides that our method has two additional possibilities, which are not directly connected with the final results. They are arrival time correction and some kind of noise filtration.

The arrival time correction is a very important problem. Precision of the arrival time estimation ensures the precise location. As it was mentioned above, the similarity of AE signals is measured with the help of correlation coefficient.

To calculate the correlation coefficient, it is necessary to calculate at first the cross-correlation function. The cross-correlation function reaches its peak at the time corresponding to the difference of arrival times of AE signals. So, we can correct the difference of arrival times of any two signals belonging to the same class.

At such approach the class of “AE signals groups” is located at one point. For correct location it is necessary only to specify the arrival times of impulses for a single element of the class. Figures 7a and b shows two signals of acoustic emission. These signals have the similar shape, but because of different amplitude the signals reach a threshold value at different times. As is evident from Fig. 7c, the error of determination of these signals arrival time difference makes about 200 μs.

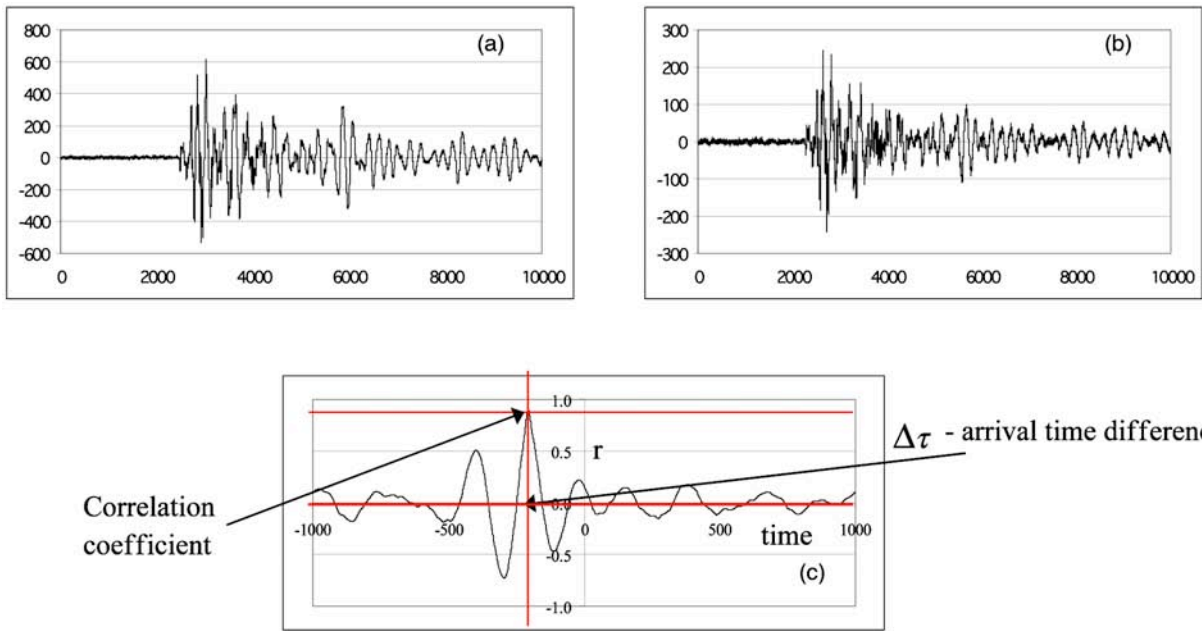


Fig. 7 a and b – AE signals; c – cross-correlation function of signals of 7a and 7b above.

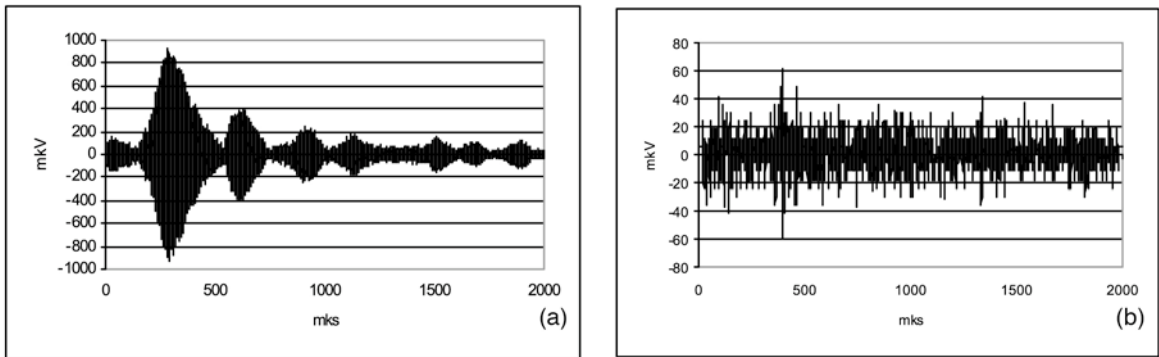


Fig. 8 Types of noise removed under data structuring: a) band noise; b) stochastic noise.

Additional possibility is filtration of some types of noise. An uncorrelated stochastic noise is removed automatically because according to the accepted mode of classification it cannot be referred to any class. Some types of the correlated noise, for example, harmonic ones, form their own classes, and may be excluded from consideration under an expert analysis of the results obtained.

Conclusion

In this paper described is an automated statistical analysis method of AE data, which makes it possible to structure the AE test data through partitioning into different clusters or the groups of signals, characterizing the different AE sources. The key features of the given method are, firstly, the possibility to process data in an automatic mode with minimum involvement of operator and a minimum number of settings, and, secondly, the possibility to carry out the analysis of the heterogeneous diagnosis information. Based on the results of statistical analysis, it is possible to specify the quantity of AE sources, to carry out its zone location, and to get additional evaluation of the danger criterion without resorting to the preliminary location.

When using the correlation coefficient as a measure of proximity under cluster analysis of AE signals, we can carry out an automatic correction of signal arrival times belonging to the same clusters, because the cross-correlation function reaches its peak at the point of time corresponding to the difference of arrival times of AE signals.

References

1. V.A. Barat, A.L. Alyakritskiy. Statistical method for processing of AE signals and their parameters for increasing of reliability of the testing results. *Proceeding of the 17th Russian-International Scientific-Technological Conference on Non-Destructive Testing and Diagnostics*. Ekaterinburg, 2005. (on the CD-ROM)
2. Ingrid Daubechies, *Ten lectures on wavelets*, SIAM, Philadelphia, 1992.
3. Ajvazyan S.A., Buhstaber V.M., Enjukov I.S., Meshalkin L.D., *Applied statistics in 3 parts*, 1989. (in Russian)
4. L.N. Stepanova, A.E. Kareev. Development of a method for the dynamic clustering of AE signals for increase of accuracy of their localization, *Control Diagnostika*, 2003, № 6, pp. 15-20. (in Russian)
5. A. A. Anastassopoulos, T. P. Philippidis. Clustering Methodologies for the evaluation of AE from Composites, *Journal of Acoustic Emission*, **13**, (1/2), 1995, 11-21.
6. Yu.S. Popkov, A.L. Alyakritskiy, E.Yu. Sorokin, D.A. Terentyev. AE method for determination of pitting corrosion depth and monitoring of defect propagation rate. *the Proceeding of EW-GAE 2008*.
7. Vallen VisualAE™. The standard in Acoustic Emission software. Vallen-Systeme GmbH. <http://www.vallen.de>
8. AE-Studio. NPF Diaton. http://www.diatontest.ru/ae_studio.htm

TERMITES DETECTION VIA SPECTRAL KURTOSIS AND WAVELET DE-NOISING OF ACOUSTIC EMISSION SIGNALS

JUAN-JOSÉ G. DE LA ROSA¹, ANTOLINO GALLEGOS², ROSA PIOTRKOWSKI³,
ENRIQUE CASTRO² and ANTONIO MORENO-MUÑOZ⁴

¹University of Cádiz, Electronics Area, Research Group PAIDI-TIC-168. Algeciras Polytechnic School, 11202 Algeciras-Cádiz, Spain; ²Univ. of Granada, Dept. of Applied Physics, 18071 Granada, Spain; ³Escuela de Ciencia y Tecnología, Universidad Nacional San Martín, Buenos Aires, Argentina, ⁴University of Córdoba, Electronics Area, Research Group PAIDI-TIC-168. Campus Rabanales. Edificio Albert Einstein, 14071 Córdoba, Spain

Keywords: Higher-Order Statistics, Insect detection, Spectral Kurtosis.

Abstract

In this paper we present the operation results of a portable computer-based measurement equipment conceived to perform non-destructive testing of suspicious termite infestations. Its signal processing module is based in the Spectral Kurtosis (SK), with the de-noising complement of the discrete wavelet transform (DWT). The SK pattern allows the targeting of alarms and activity signals. The DWT complements the SK, by keeping the successive approximations of the termite emissions, supposed more non-Gaussian (less noisy) and with less entropy than the detail approximations. For a given mother wavelet, the maximum acceptable level, in the wavelet decomposition tree, which preserves the insects' emissions features, depends on the comparative evolution of the approximations details' entropies, and the value of the global spectral kurtosis associated to the approximation of the separated signals. The paper explains the detection criterion by showing different types of real-life recordings (alarms, activity, and background).

Introduction

Biological transients gather all the natural complexity of their associated sources, and the media through which they propagate. As a consequence, finding the most adequate method to get a complete characterization of the emission implies the selection of the appropriate model, which better explains the processes of generation, propagation and capture of the emitted signals. This description matches the issue of measurement termite activity.

This paper presents the improved equipment over previous prototype's performance, based in the time-frequency domain analysis of the kurtosis, described in [1-2]. The measurement method is based in the interpretation of the spectral kurtosis (SK) graph, along with the wavelet analysis, which is thought as an aid. At the same time, we use a simple data acquisition unit, the sound card (maximum speed at 44.1 kHz), which simplifies the hardware unit and the criterion of detection. The instruments for plague detection are thought with the objective of decreasing subjectivity of the field operator [1-5]. On-site monitoring implies reproducing the natural phenomenon of insect emissions with high accuracy. As a consequence it is imperative the use of a deep storage device, and high sensitive probes with a selective frequency response. These features make the price paid high, and do not guarantee the success of the detection.

Regarding the procedures, the prior detection methods are very much dependent on the detection of the excess of power in the signals; these are the so-called second-order methods. For

example, the RMS calculation can only characterize the intensity, and does not provide information regarding the envelope of the signal nor the amplitude fluctuations. Another handicap of the second-order principle, e.g. the power spectrum, attends to the preservation of the energy during data processing. Consequently, the eradication of additive noise lies in filter design and sub-band decomposition, like wavelets and wavelet packets.

As an alternative to improve noise rejection and complete characterization of the signals, in the past ten years, a myriad of higher-order statistics (HOS) methods are being applied in different fields of science and technology, in scenarios involving signal separation and characterization of non-Gaussian measurements [6]. Concretely, the area of diagnostics-monitoring of rotating machines is also under our interest due to the similarities of the signals to be monitored with the transients from termites. Many time-series of faulty rotating machines consist of more-or-less repetitive short transients of random amplitudes and random occurrences of the impulses [7].

This paper describes a method based in the SK (related to the fourth-order cumulant at zero lags) to detect infestations of subterranean termites in a real-life scenario (southern Spain). Wavelet decomposition is used as an extra tool to aid detection from the preservation of the approximation of the signal, which is thought to be more Gaussian than the details.

The interpretation of the results is focused on the peakedness of the statistical probability distribution associated to each frequency component of the signal, to get a measure of the distance from the Gaussian distribution. The SK serves as a twofold tool. First, it enhances non-Gaussian signals over the background. Secondly, it offers a more complete characterization of the transients emitted by the insects, providing the user with the probability associated to each frequency component.

The paper is structured as follows: in the following section a review on termite detection and relevant HOS experiences sets the foundations. Then we make a brief report on the definition of kurtosis; we use an unbiased estimator of the SK, successfully used in [1-2]. Results are presented thereafter. Finally, conclusions are drawn.

Subterranean Termites: Detection project towards HOS

Termite detection has been gaining importance within the research community in the last two decades, mainly due to the urgency of avoiding the use of harming termiticides, and to the joint use of new emerging techniques of detection and hormonal treatments, with the aim of performing an early treatment of the infestation. A localized partial infestation can be exterminated after two or three generations of the colony's members with the aid of these hormones, which stop chitin synthesis. A chitin synthesis inhibitor kills termites by inhibiting formation of a new exoskeleton when they shed their old one. As a direct consequence, the weakened unprotected workers stop feeding the queen termite, which dies of starvation.

The primary method of termite detection consists of looking for evidence of activity. But only about 25 % of the building structure is accessible, and the conclusions depend very much on the level of expertise and the criteria of the inspector [1-5]. As a consequence, new techniques have been developed to remove subjectivity and gain accessibility.

User-friendly equipment is currently used in targeting subterranean infestations by means of temporal analysis of the vibratory data sequences. An acoustic-emission (AE) sensor or an accelerometer is fixed to the suspicious structure. This class of instruments is based on the calculation of the RMS value of the vibratory waveform. The RMS value comprises information of the AE raw signal power during each time-interval of measurement (averaging time). This measurement strategy conveys a loss of potentially valuable information both in the time and in the frequency domain [1-5]. A more sophisticated family of instruments makes use of spectral analysis and digital filtering to detect and characterize vibratory signals [4]. Other second-order tools, like wavelets and wavelet packets (time-dependent technique) concentrate on transients and non-stationary movements, making possible the detection of singularities and sharp transitions, by means of sub-band decomposition.

Higher-order statistics are being widely used in several fields. The spectral kurtosis has been successfully described and applied to the vibratory surveillance and diagnostics of rotating machines [7]. In the field of insect detection, the work presented in [2] set the foundations of the present paper. The combined use of the SK and the time-domain sliding kurtosis showed marked features associated to termite emissions. In the frequency domain (sample frequency 64.0 kHz), three frequency zones were identified in the spectral kurtosis graph as evidence of infestation; two in the audio band (which will be also checked in the present paper) and one in the near ultrasound (roughly equal to 22 kHz). In the present paper the sample frequency was fixed to 44.1 kHz and the sound card was directly driven by MATLAB. Results are presented in the user interface, which is shown in Fig. 1; in this measurement situation, the time-raw data contains alarms and activity signals from termites. This is a clear example of positive detection.

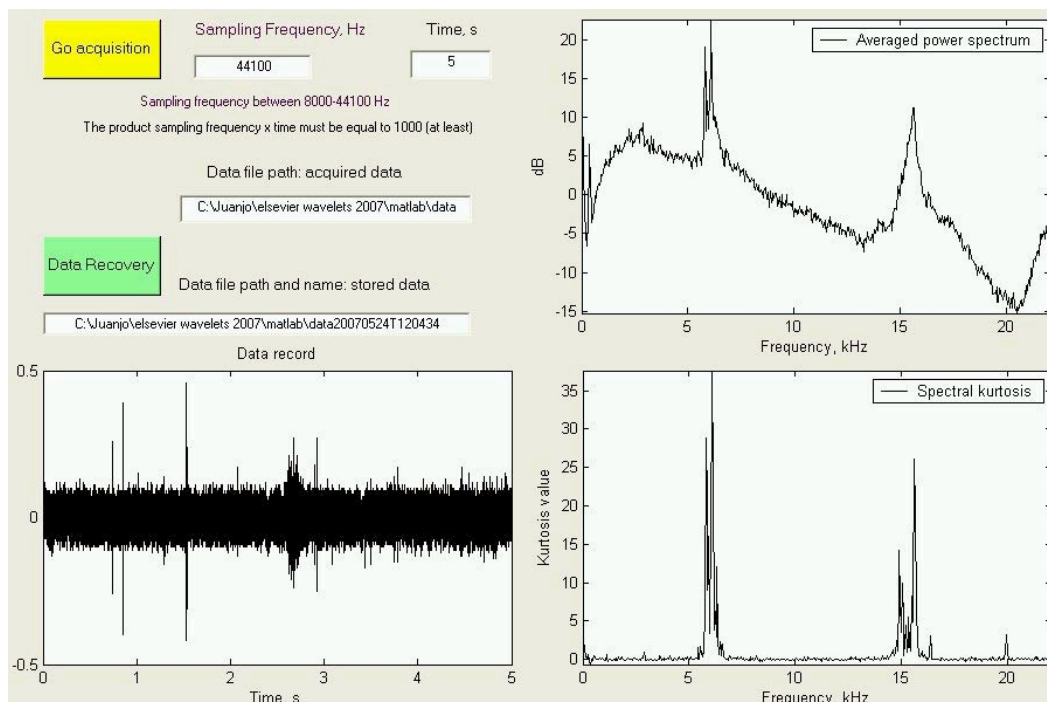


Fig. 1. The graphical user interface, which presents the results to the field operator. The SK graph is in the bottom-right corner.

The developed virtual instrument also calculates and presents the spectrum (upper-right) and the raw data (bottom-left). The field operator adds therefore visual information to the classical audio-based criterion, which was by the way very subjective and very expertise-dependent.

Kurtosis and the SK Estimator

Kurtosis is a measure of the "peakedness" of the probability distribution of a real-valued random variable. Higher kurtosis means more of the variance is due to infrequent extreme deviations, as opposed to frequent modestly-sized deviations. This fact is used in this paper to detect termite AE in an urban background. Kurtosis is more commonly defined as the fourth central cumulant divided by the square of the variance of the probability distribution, which is the so-called excess kurtosis, i.e. [2, 8-9]:

$$\gamma_{4,x} = E\{x^4(t)\} - 3(\gamma_{2,x})^2 = C_{4,x}(0,0,0) \quad (1)$$

Ideally, the SK is a representation of the kurtosis of each frequency component of a process (or data from a measurement instrument, X_i). For estimation issues, we will consider M realizations of the process; each containing N points; i.e. we consider M measurement sweeps, each sweep with N points. The time spacing between points is the sampling period T_s .

A biased estimator for the spectral kurtosis and for a number M of N -point realizations at the frequency index m , is given by [2]:

$$\hat{G}_{2,X}^{N,M}(m) = \frac{M}{M-1} \left[\frac{(M+1) \sum_{i=1}^M |X_N^i(m)|^4}{\left(\sum_{i=1}^M |X_N^i(m)|^2 \right)^2} - 2 \right]. \quad (2)$$

This estimator is the one we have implemented in the program code in order to perform the data computation and it was also used successfully in [2].

Regarding the experimental signals, we expect to detect positive peaks in the kurtosis's spectrum, which may be associated to termite AE, characterized by random-amplitude impulse-like events. This non-Gaussian behavior should be enhanced over the symmetrically distributed electronic noise, introduced in the measurement system. Speech is perhaps also reflected in the SK, but not in the frequencies where termite emissions manifest. Besides, we assume, as a starting point, that non-Gaussian behavior of termite emissions is more acute than in speech. As a consequence, these emissions would be clearly outlined in the kurtosis spectrum. As a final remark, we expect that constant amplitude interferences are clearly differentiated due to their negative peaks in the SK.

To show the ideal performance of the estimator, which has been described in these lines, and also described in [1-2], we show an example based in synthetics. A mixture of six different signals has been designed. Each mixture is the sum of a constant-amplitude sine wave of 2 kHz, a constant-amplitude sine wave at 9 kHz, a Gaussian-distributed-amplitude sine wave at 5 kHz, a Gaussian-distributed-amplitude sine wave at 18 kHz, a Gaussian white noise, and a colored Gaussian noise between 12 and 13 kHz. Each mixture (realization or sample register) contains 1324 points. Negative kurtosis is expected for constant-amplitude processes, positive kurtosis should be associated to random-amplitudes and zero kurtosis will characterize both Gaussian-noise processes.

A simulation has been made in order to show the influence of the number of sample registers (M) in the averaged results for the SK graph, and to test its performance. Figure 2 shows a good performance because enough registers have been averaged ($M=500$).

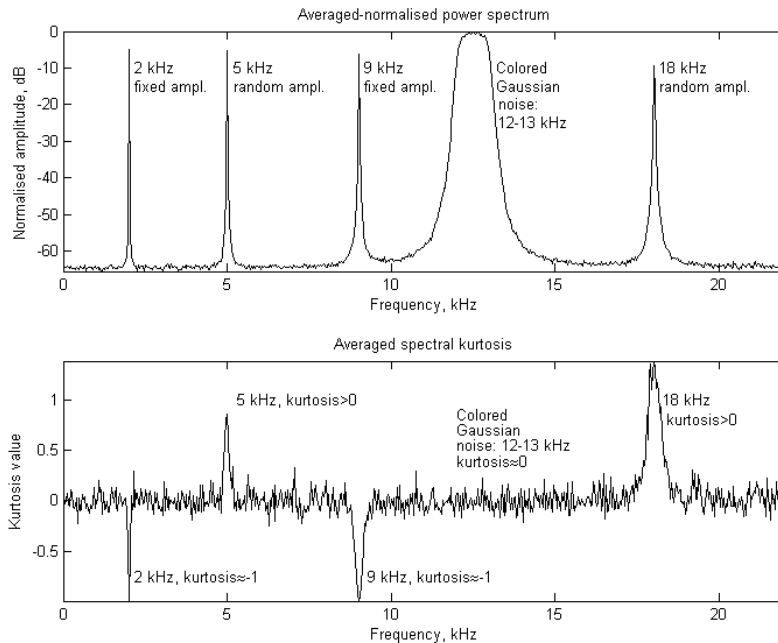


Fig. 2. Performance of the SK estimator over a set, mixed of synthetics.

De-noising strategy via wavelets. Selecting the optimum decomposition level

The mother wavelet *Daubechies 5* has been selected as the most similar mother wavelet, because of the highest coefficients in the decomposition tree. Given the mother wavelet, to show the process of selecting the maximum decomposition level in the wavelet tree, we have adopted a criterion based on the calculation of *Shannon's* entropy (information entropy), which is a measure of the uncertainty associated with a random variable, X ; this entropy denoted by $H(X)$, and defined by Eq. (3):

$$H(X) = - \sum_{i=1}^N p(x_i) \log_{10} [p(x_i)], \quad (3)$$

where X is an N -outcome measurement process $\{x_i = 1 \dots N\}$, and $p(x_i)$ is the probability density function of the outcome x_i .

We show the strategy via the following example, based on real-life data, like the recordings of Fig. 1, Fig. 4(a) and (b). The entropy of the approximations and the details are compared for each level of comparison as shown in Fig. 3. By looking at the entropy evolution graph of Fig. 3, we see that at level 4, the entropy of the approximations is less than the entropy of the details. So, level 3 is in a sense, a point of entropy inversion. On the other hand, level 4 exhibits the lowest entropy being at the same time lower than the details' entropy. No improvement is obtained for level 5, where these entropies are very similar (approximations and details' entropies are almost the same). We can also see that the global difference of entropies increases towards zero, at level 5, as a complementary indication that further decomposition will not suppose progress in de-noising. This decomposition strategy is satisfied for the 98 % of the data registers, collected at the same place.

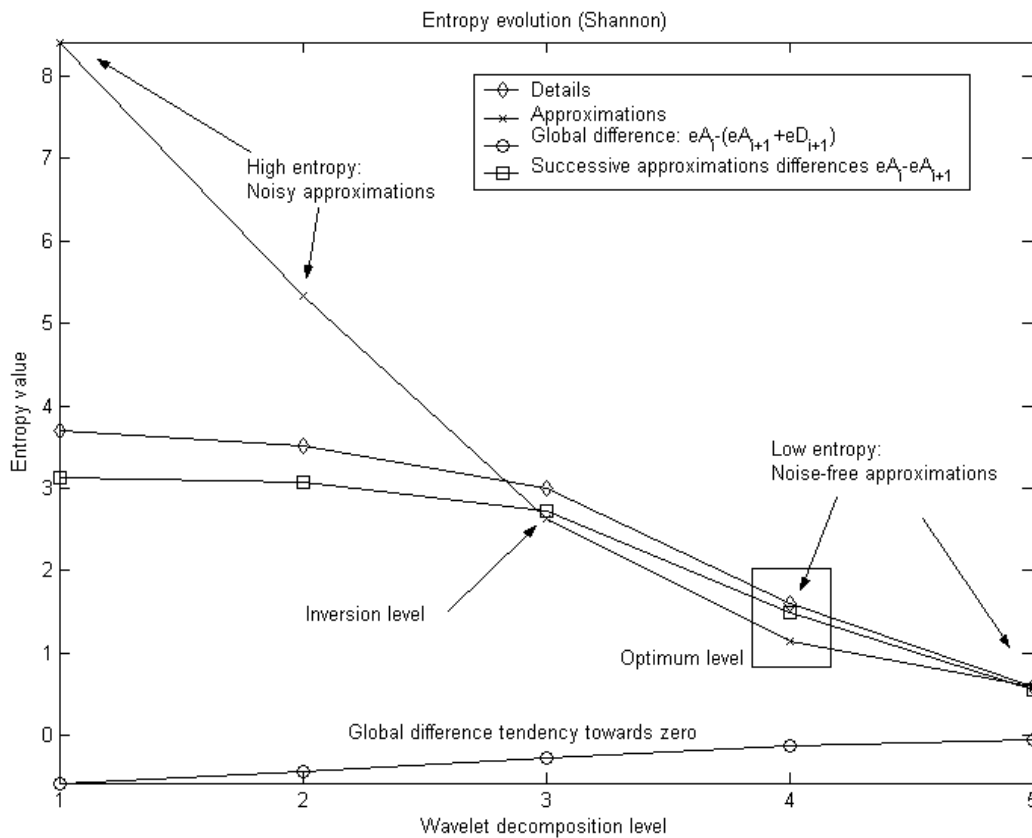


Fig. 3. Entropy evolution showing the optimum level (4). Level 3 is an inversion point and level 4 exhibits the lowest entropy being at the same time lower than the details' entropy.

Experiment and Results

In this section we describe the experiment and measurement situations. A piezoelectric probe (model SP-1L, Acoustic Emission Consulting) is used in the final version of the instrument, and was described in detail in [2]. The sensor is connected to the sound card of a lap-top computer and the acquisition is driven by MATLAB, via the Graphical User Interface (GUI). The user interface was presented in Fig. 1. The operator can select the acquisition time and the sample frequency (maximum 44.1 kHz). In the bottom-right corner of Fig. 1, the SK graph is presented. The user can also examine the raw data and the spectrum. Automatically, the instrument saves the acquired data (labeling the file with the date). Additionally, the operator can recall the stored files.

The electronic transducer is presented in Fig. 4, along with its charge-to-volt conversion modulus (Integrated Circuit Piezoelectric; ICP interface), and the accessory to fix it in the wood that we used to test the sensor's performance in the lab. A bare waveguide has been used for insertion into soil. With the aim to have a frequency characterization of the sensor we test its impulsive response in the lab by emulating a fiber breaking in a piece of wood, where the sensor was attached via the drill bit. The witness instrument was a high-performance digital storage oscilloscope (Agilent-54622A). In Fig. 5, we show a photo of the calibration session, where the instrument's display shows a single capture (and its associated power spectrum) of the vibratory and AE signal once it has propagated through the wood. We can appreciate two differentiated frequency bands. The first 30 kHz resonant band offer the possibility of sensing AE signals from

termites (feeding and excavating). Then we find a resonant bump around 100 kHz (only for the sensor SP1-H), which by the way has been useful for ultrasonic purposes by the research team.

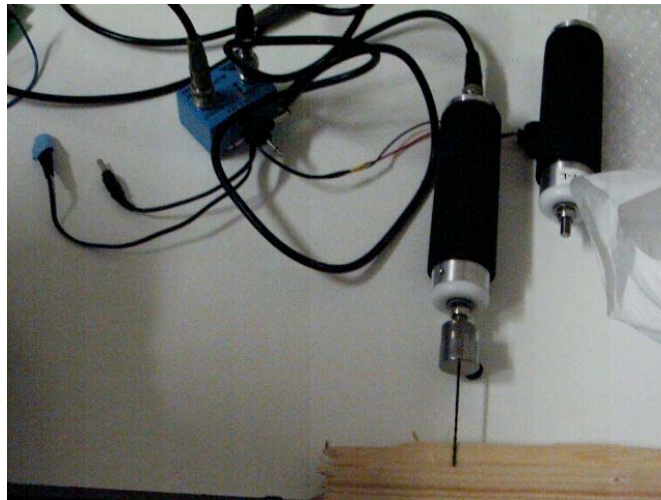


Fig. 4. A photograph of the sensors SP1-L and SP1-H, with the mounted accessories (drill bit) prepared to couple it into the a test-piece of wood, in our lab. On the left, the charge-to-volt converter according to the Integrated Circuit Piezoelectric (ICP) protocol.

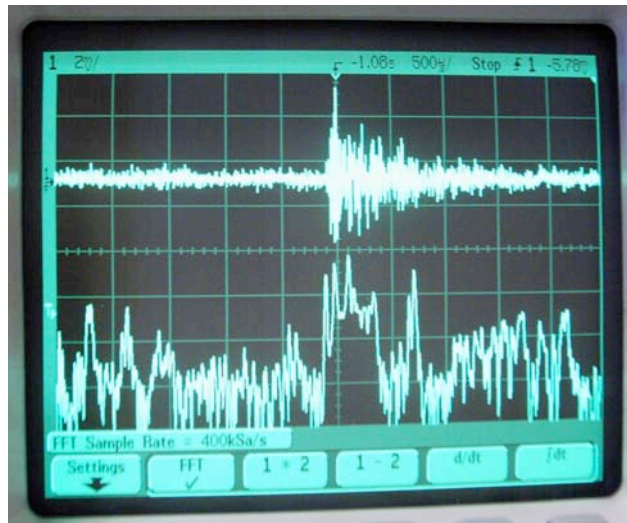


Fig. 5. A photograph of the testing lab session with the sensor SP1-H (a high frequency version of the SP1-L) and a deep memory digital-storage oscilloscope. The acoustic emission event has been sampled at 400 kHz. Horizontal division = 20 kHz.

Termite sounds from feeding are like sharp pops and crackles in the audio output [1-2]. Hit rates of 25-100 /s are common in infestation. The key of the SK detection strategy used in this work lies in the potential enhancement of the non-Gaussian behavior of these emissions. If this happens, i.e. if an increase of the non-Gaussian activity (increase in the kurtosis, peakedness of the probability distribution) is observed in the SK graph, there may be infestation in the surrounding subterranean perimeter, where the transducer is attached.

An additional remark (justifying the use of the SK graph) lies in the fact that the kurtosis as a global indicator, considered as the average of the kurtosis computed for each individual frequency component, is not a valid tool to target termite activity. This is due to the fact that no

discrimination is made among the frequency bands of the emissions, which may be originated by different agents.

Hereinafter, in addition to the detection measurement situation presented in Fig. 1, where the detection is clear, other situations are outlined. In Fig. 6(a) a doubtful measurement case is presented. Activity evidence (low-level alarms) is outlined only near 6 kHz. Once, the wavelets have been applied, shown in Fig. 6(b), the enhancement near 6 kHz and 16 kHz confirms the detection.

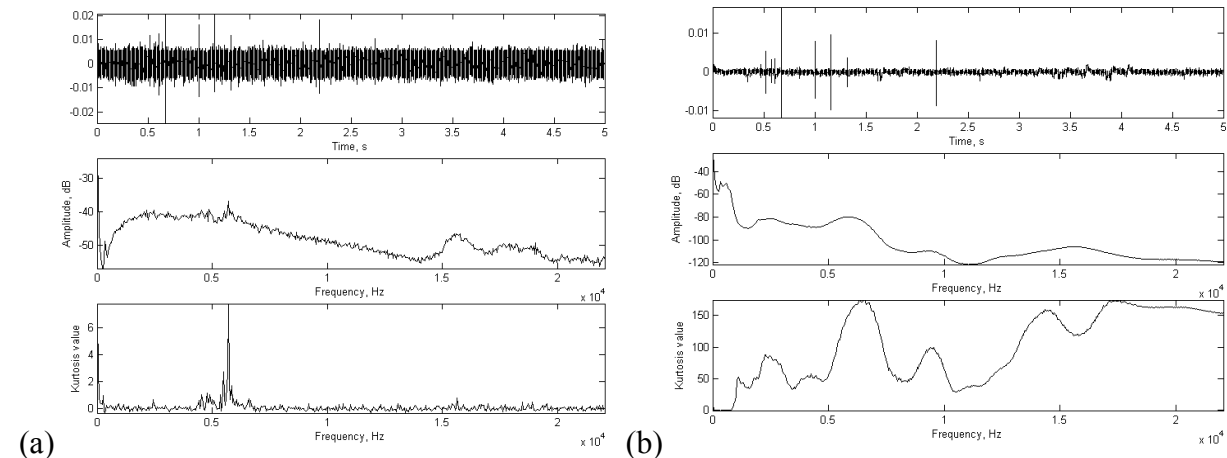


Fig. 6. (a) A doubtful measurement situation without de-noising, where probably low-level alarm signals predominate. (b) De-noising confirms activity, eliciting the bump near 6 kHz and the enhanced zone near 16 kHz.

The next figures, Fig. 7 (a) and (b), show the measurement's performance over a background. In the time-domain, the impulses that are similar to Dirac's deltas are associated to cracks or little movements of the sensor while attached in the ground. So it is important to distinguish these false positives from the impulses induced by termites. De-noising neither add new information nor reveal termite infestation. The impulses in the time domain are the classical artificial cracks resulting for the movement of the sensor in the soil.

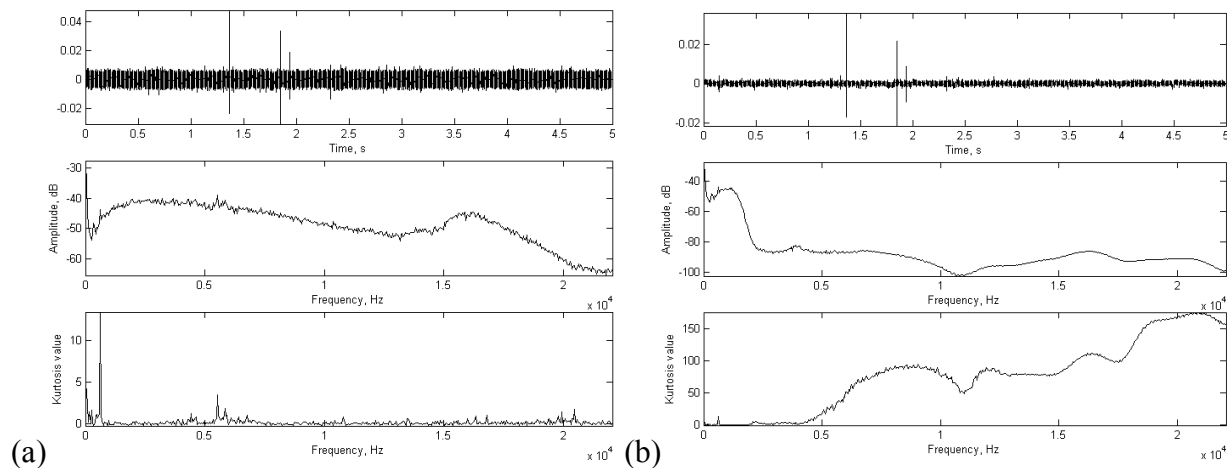


Fig. 7. (a) SK calculation over a background sample register. No activity is seen in the surroundings of the characteristic frequencies. (b) De-noising does not reveal infestation.

The final figures, Fig. 8 (a) and (b), represent another case of detection. This time detection is very clear and again, we can observe the clear bumps near the characteristic frequencies. The bump at the left of 6 kHz reflects the presence of alarms but probably far from the termites whose activity produces the bumps at the right of 6 kHz and 16 kHz. The spectral kurtosis of the de-noised register exhibits several frequency bumps, not only for the frequencies in the interest zones (6 kHz and 16 kHz), but also for the rest of the audio signals. These figures have shown that, despite the fact that audio signals can exhibit non-Gaussian behavior, the non-Gaussian degree of termite activity is higher.

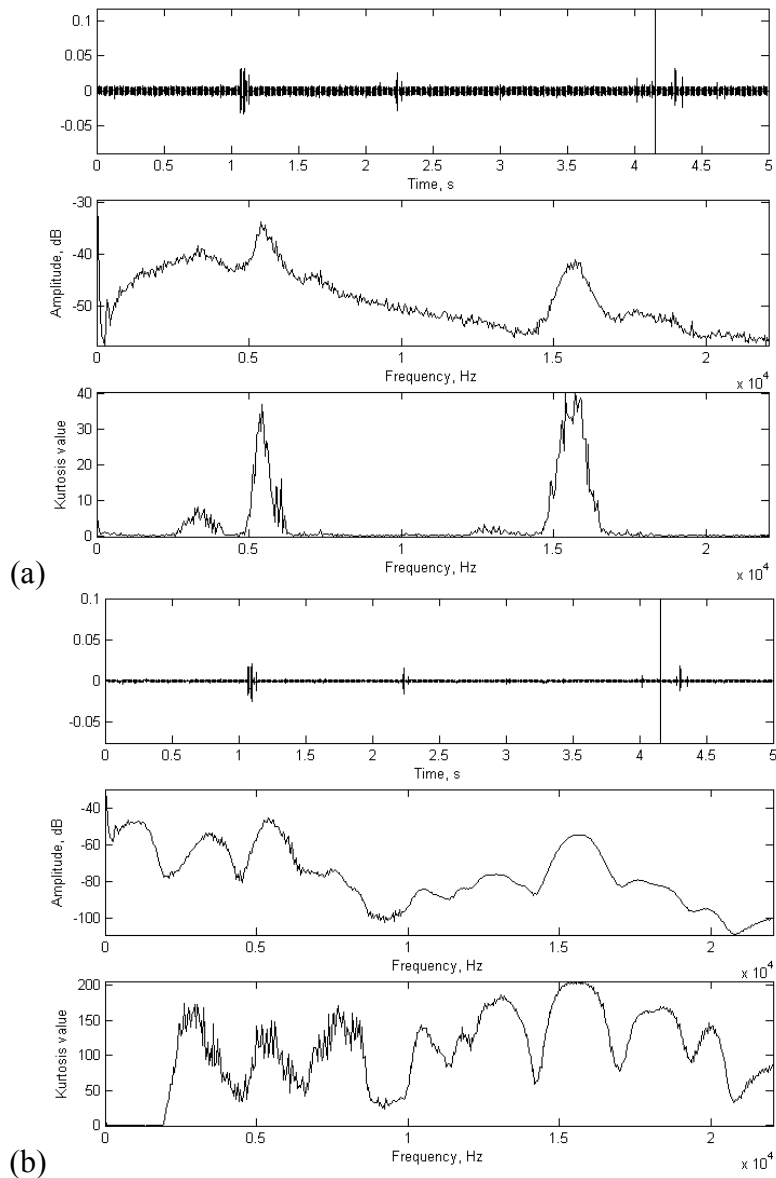


Fig. 8. (a) A clear targeting case with a higher degree of activity. (b) De-noising confirms infestation.

Conclusion

Assuming the starting hypothesis that the insect emissions may have a more peaked probability distribution than any other simultaneous source of emission in the measurement perimeter, we have design a termite detection strategy and a virtual instrument based in the calculation of the 4th-order cumulants for zero time lags, which are indicative of the signals'

kurtosis. The instrument is actually in use by a Spanish company. An estimator of the spectral kurtosis has been used to perform a selective analysis of the peakedness of the signal. It has been shown that new frequency components gain in relevance in the spectral SK graphs. The main goal of this signal-processing method is to reduce subjectivity due to visual or listening inspection of the registers. This means that in a noisy environment, it may be possible to ignore termite feeding activity even with an *ad hoc* sensor because, despite the fact that the sensor is capable of registering these low-level emissions, the human ear can easily ignore them [2]. The SK signal processing modulus complements human's ear, adding higher-order statistical features, which improve detection, thanks to the noise rejection action, enhancing non-Gaussian features.

Acknowledgments

The authors would like to thank the Spanish Ministry of Science and Education for funding the PETRI project PTR95-0824-OP dealing with plague detection using higher-order statistics. Our unforgettable thanks to the trust we have from the Andalusian Government for funding the excellence project PAI2005-TIC00155.

References

1. De la Rosa, J. J. G., Gallego, A., Piotrkowski, R., Castro, E. and Moreno, A. (2008). Spectral kurtosis-based virtual instrument for non-destructive acoustic emission targeting of termites. Proceedings of The 28-th European Conference on Acoustic Emission Testing, September 17-19, Kraków, Poland, pp. 94-99.
2. De la Rosa, J. J. G. and Muñoz, A. M. (2008). Higher-order cumulants and spectral kurtosis for early detection of subterranean termites. *Mechanical Systems and Signal Processing (Ed. Elsevier)*, **22** (1): 279–294. Available online 1 September 2007.
3. De la Rosa, J. J. G., Lloret, I., Moreno, A., Puntonet, C. G., and Górriz, J. M. (2006). Wavelets and wavelet packets applied to detect and characterize transient alarm signals from termites. *Measurement (Ed. Elsevier)*, **39**(6): 553–564. Available online 10 January 2006.
4. Mankin, R. W. and Fisher, J. R. (2002). Current and potential uses of acoustic systems for detection of soil insects infestations. In *Proceedings of the Fourth Symposium on Agroacoustic*, pages 152–158.
5. Robbins, W. P., Mueller, R. K., Schaal, T., and Ebeling, T. (1991). Characteristics of acoustic emission signals generated by termite activity in wood. In *Proceedings of the IEEE Ultrasonic Symposium*, pages 1047–1051.
6. De la Rosa, J. J. G., Piotrkowski, R., and Ruzzante, J. (2007b). Third-order spectral characterization of acoustic emission signals in ring-type samples from steel pipes for the oil industry. *Mechanical Systems and Signal Processing (Ed. Elsevier)*, **21**(4): 1917–1926. Available online 10 October 2006.
7. Antoni, J. (2006b). The spectral kurtosis: application to the vibratory surveillance and diagnostics of rotating machines. *Mechanical Systems and Signal Processing (Ed. Elsevier)*, **20**(2): 308–331.
8. Mendel, J. M. (1991). Tutorial on higher-order statistics (spectra) in signal processing and system theory: Theoretical results and some applications. *Proceedings of the IEEE*, **79**(3): 278–305.
9. Nikias, C. L. and Mendel, J. M. (1993). Signal processing with higher-order spectra. *IEEE Signal Processing Magazine*, pages 10–37.

ACOUSTO-ULTRASONIC SIGNAL ANALYSIS FOR DAMAGE DETECTION IN GFRP ADHESIVE JOINTS

ANDREAS J. BRUNNER and GIOVANNI P. TERRASI

Empa, Swiss Federal Laboratories for Materials Testing and Research, Laboratory for Mechanical Systems Engineering, Ueberlandstrasse 129, CH-8600 Dübendorf, Switzerland

Keywords: Adhesive joints, GFRP, tensile load, damage accumulation

Abstract

Selected tensile tests on balanced, adhesively bonded double-lap joints (DLJ) made from pultruded glass-fiber-reinforced, polymer-matrix (GFRP) flat profiles have been monitored with acoustic emission (AE) for an assessment of damage initiation and accumulation. The thickness was 10 mm for the inner and 5 mm for the two outer profiles. Three different bond-line thicknesses of the adhesive bond (nominally 0.3, 0.5 and 1.0 mm), all with an overlap length of 100 mm, were tested. The usual AE signal parameter set was recorded with four AE sensors (either of type SE-45H or SE-150M) from three tests each per DLJ type. AE sensors were mounted above and below the adhesive bond with duct tape using a silicone-free coupling agent. Sensor coupling was checked before and after the tensile tests to stress levels around 60% to 97% of the effective ultimate tensile strength (proof-load of 140 kN). The auto-calibration function of the AE equipment (type AMS-3 from Vallen Systeme) was used for checking sensor coupling before and after the proof-load tests. Transient AE waveforms were recorded during the auto-calibration with 5 MHz sampling rate. This effectively constitutes acousto-ultrasonic (AU) testing of the DLJ before and after loading. Preliminary signal classification of the AU waveforms with VisualClass® (from Vallen Systeme GmbH) had indicated that they differed when recorded before and after proof-load testing. The present paper attempts to identify the AU signal parameters responsible for this, as case study in AU waveform analysis.

Introduction

Previous experiments on the strength of adhesively bonded joints composed of glass-fiber reinforced polymer-matrix (GFRP) pultruded adherends [1-3] indicated that, even using enhanced mathematical methods on the basis of a fully linear mechanical model, a gap of around 10% between predicted and experimentally determined joint strengths remained. Reasons for this, invoked in [3], were either possible damage occurring by microscopic defect accumulation (e.g., micro-crack formation) and/or the resulting nonlinear behavior of the GFRP material at higher stresses (beyond those obtained on the samples of limited size, i.e., 40 mm x 40 mm).

Acoustic emission (AE) monitoring is, in principle, capable of detecting microscopic damage accumulation in GFRP composites. AE was hence used to monitor the area of the adhesive bond during tensile tests on a series of nine full-size adhesively bonded double-lap joints (DLJ) up to a load of 140 kN, including subsequent unloading. The DLJ were then loaded to their ultimate tensile strength, i.e., to tensile failure without AE. AE sensor coupling was checked with the auto-calibration function of the AE equipment. This constitutes an acousto-ultrasonics (AU) examination [4]. The present paper investigates whether AU analysis can yield indications of damage accumulation due to tensile loading of the DLJ.

Experimental

The balanced double-lap joints (DLJ) consisted of pultruded glass-fiber reinforced polymer-matrix (GFRP) flat profiles of 500-mm length, 100-mm width, and 5-mm and 10-mm thickness for the inner and outer DLJ profiles, respectively. A polyester resin and E-glass fibers were used for the profiles, with mainly unidirectional rovings towards the center and one and two combined mats towards the outside for the 5-mm and 10-mm thick profiles, respectively. The combined mats consisted of chopped strand mats and $0^\circ/90^\circ$ woven fabrics, which were stitched together. For the adhesive bond, a two-component polyurethane adhesive (Sika S-Force 7851) was used, and the nominal bond line thicknesses were 0.3, 0.5 and 1.0 mm. The specimens were cured under ambient laboratory conditions ($23\pm 1^\circ\text{C}$, $50\pm 5\%$ relative humidity) for one week, and then stored under comparable conditions before testing.

The tensile tests have been performed on a servo-hydraulic test machine (Instron 1346) under displacement control (0.5 mm/min). A metal plate has been inserted between the outer two profiles inside the hydraulic grips at the bottom.

For AE monitoring equipment and software from Vallen Systeme GmbH (AMS-3 and VisualAE™) have been used. At least one DLJ for each bond-line thickness has been equipped with four multi-purpose AE sensors (type SE-45H from Dunegan Engineering Corp.) while the remaining DLJ have been tested with 150-kHz resonant AE sensors (type SE-150M from the same supplier). Preamplifier gain was set at 34 dB, AE signal acquisition threshold at $50 \text{ dB}_{\text{AE}}$ (except for two DLJ with 52 and $65 \text{ dB}_{\text{AE}}$ in order to eliminate excess noise from the hydraulic grips). The AE signals were band-pass filtered between 30 and 1000 kHz. Rearm time was set to 1.38 ms. AU waveforms excited with the autocalibration function of the AE equipment (roughly $60 V_{\text{pp}}$, 800 ns duration applied to each AE sensor) have been recorded with transient recorders at a sampling rate of 5 MHz (200 pre-trigger samples, total 4096 samples).

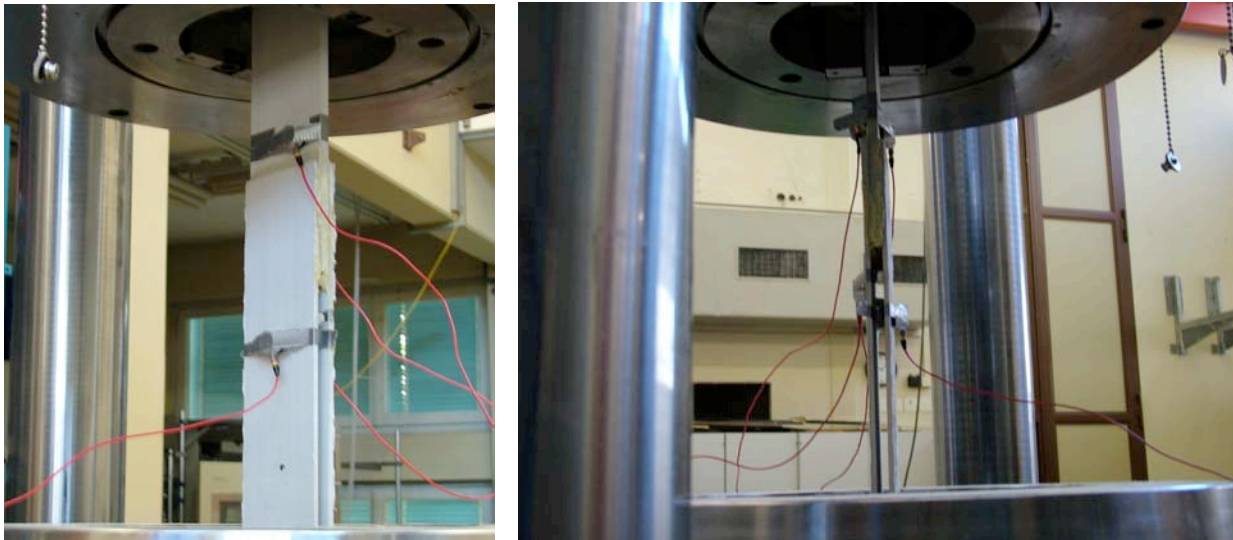


Fig. 1. Photograph of (left) a double lap joint in the test machine with two AE sensors (above and below the adhesive bond) on either side of the joint; (right) side view of the joint with the thicker inner profile on top and the thinner outer profiles on the bottom.

Results

Table 1 summarizes the applied and observed tensile failure loads of the DLJ and the type of AE sensor use for monitoring the proof load. The average tensile failure load for all DLJ, irrespective of their bond-line thickness is 182.4 ± 28 kN, and 199.1 ± 42 kN, 169.9 ± 23 kN and 178.5 ± 11 kN for 0.3, 0.5 and 1.0 mm bond-line thickness, respectively. Plotting machine load data versus time (not shown) indicated an overall non-linear behavior of the DLJ, typically starting at tensile loads below 50% of the failure load. Figure 2 shows examples of recorded AU waveforms from the auto-calibration procedure for checking on sensor coupling. It is evident that these signals contain contributions from different wave modes or (multiple) reflections due to the structure of the adhesive joints. In a preliminary analysis using a waveform classification program (VisualClass® from Vallen Systeme GmbH) such AU waveforms could be separated into those taken before and after proof loading in most cases (see [5, 6] for sample results and details on the procedure). A visual comparison of the AU waveforms in Fig. 2 shows some differences between waveforms recorded before and after the proof load, but also between comparable states of the two joints (DLJ031 and DLJ101). Qualitatively, the differences among the joints with different thickness of the adhesive layer (DLJ031 with nominally 0.3 mm, DLJ101 with nominally 1.0 mm) seem more prominent than those for each joint taken before and after proof loading (for each emitter-sensor pair considered).

Table 1: Tensile load cycles, failure load (kN) and proof-load fraction for DLJ with different bond-line thickness and AE sensor type

DLJ No.	Load cycle(s) [kN] *	Tensile failure load [kN]	Proof-load (140 kN) fraction of failure load [%]	AE sensor type
031	0-141-0, 0 to failure	155.2	90.2	SE-45H
032	0 to failure	239.2	58.5	SE-45H
033	0-140-0, 0 to failure	202.2	69.2	SE-150M
051	0-140-0, 0 to failure	143.7	97.4	SE-45H
052	0-140-0, 0-100-0, 0 to failure	188.7	74.2	SE-150M
053	0-139-0, 0 to failure	177.4	78.9	SE-150M
101	0-140-0, 0 to failure	190.8	73.4	SE-45H
102	0-140-0, 0 to failure	170.8	82.0	SE-150M
103	0-140-0, 0 to failure	174.0	80.5	SE-150M

* except for DLJ 032, the loading to failure was not monitored with AE sensors

In the following, it will be investigated whether the changes in AU waveforms recorded before and after proof-loading (visible in Fig.2 and also evident from the waveform classification [5, 6]) can be traced to specific AU signal parameters. Specifically, signal amplitude, duration, ring-down counts, (true) energy, and rise-time are investigated and compared. All data presented are averages of usually four AU waveforms, in a few cases of three or five. There are four sensor combinations that will pass guided waves through the adhesive bond and, hence through the

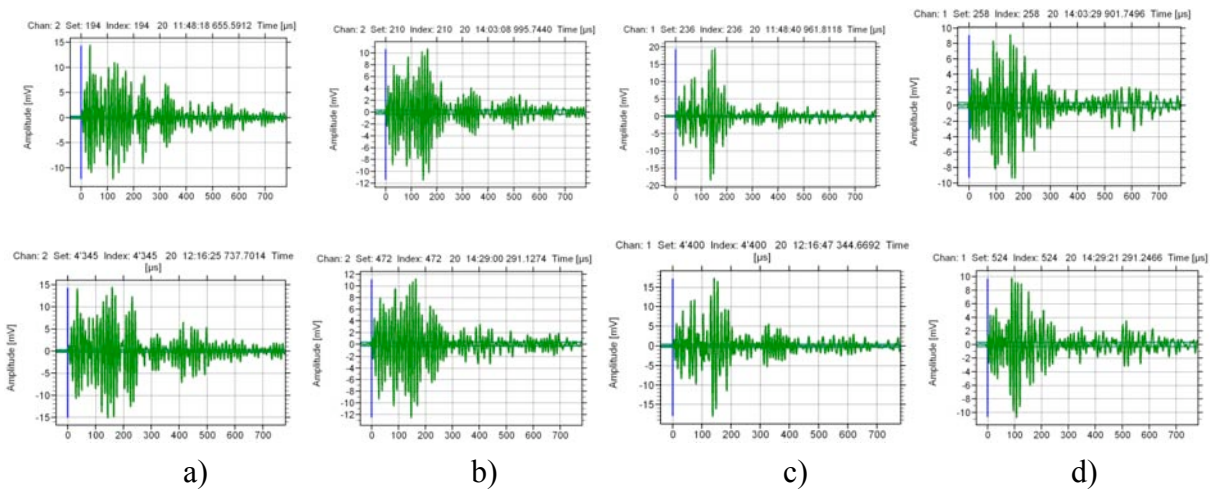


Fig. 2. Examples of AU waveforms recorded with a multifunctional AE sensor (type SE-45H) before (on top) and after (bottom) tensile proof-loading of the joints to 140 kN, waves propagating along the side of a) DLJ 031 and b) DLJ101, and from one side across to the other of c) DLJ 031 and d) DLJ101, respectively.

volume of the joint where damage accumulation occurs. The center GFRP-plate close to the top of the adhesive bond had been identified as damage initiation location from AE analysis (AE source location) and visual observation of the fracture surface after the test [7]. The sensor combinations are from top to bottom (or vice-versa) on each side of the joint (compare Fig. 1) and from top left/right hand side to bottom right/left hand side (or vice-versa).

The graphs in Fig. 3 show a clear difference between the two types of sensors (SE-45H and SE-150M). All AU signal parameters recorded before proof loading to 140 kN yielded lower values when recorded with the 150 kHz resonant sensor (SE-150M) compared with the mass-loaded multi-purpose sensor (SE-45H, displacement sensor below 45 kHz, velocity sensor above 70 kHz). AU signal amplitudes (Fig. 3 top) recorded with the 150 kHz resonant sensor seem to decrease more rapidly with increasing thickness of the adhesive than with the other sensor (SE-45H). When plotted against the nominal thickness of the adhesive layer of the double lap joints (0.3, 0.5 or 1.0 mm), AU signal parameters typically decreased with increasing thickness of the adhesive, with a few exceptions e.g., in rise time. This was observed for both sensor types, even though there was considerable scatter in some cases, which made identification of the trends with adhesive thickness difficult. Figure 3 also indicates the scatter in the data between the different emitter-sensor configurations. Note that square symbols indicate propagation along the side, triangular symbols across the joint, filled and open symbols indicate different directions of wave propagation (top-to-bottom or bottom-to-top).

AU signal parameters after proof loading the joints to 140 kN are compared with those from the as-prepared state. If plotted against thickness of the adhesive (Fig. 4), it is difficult to identify clear trends in most cases. This holds for both types of sensors (SE-45H and SE-150M). AU signal energy seems to show the most consistent change after proof loading. For sensor type SE-45H, this parameter is increasing after proof loading, while for sensor SE-150M it is decreasing in most cases (compared with the value before proof loading). AU signal energy is hence plotted against the percentage of failure load represented by the proof loading to 140 kN as well (Fig. 5).

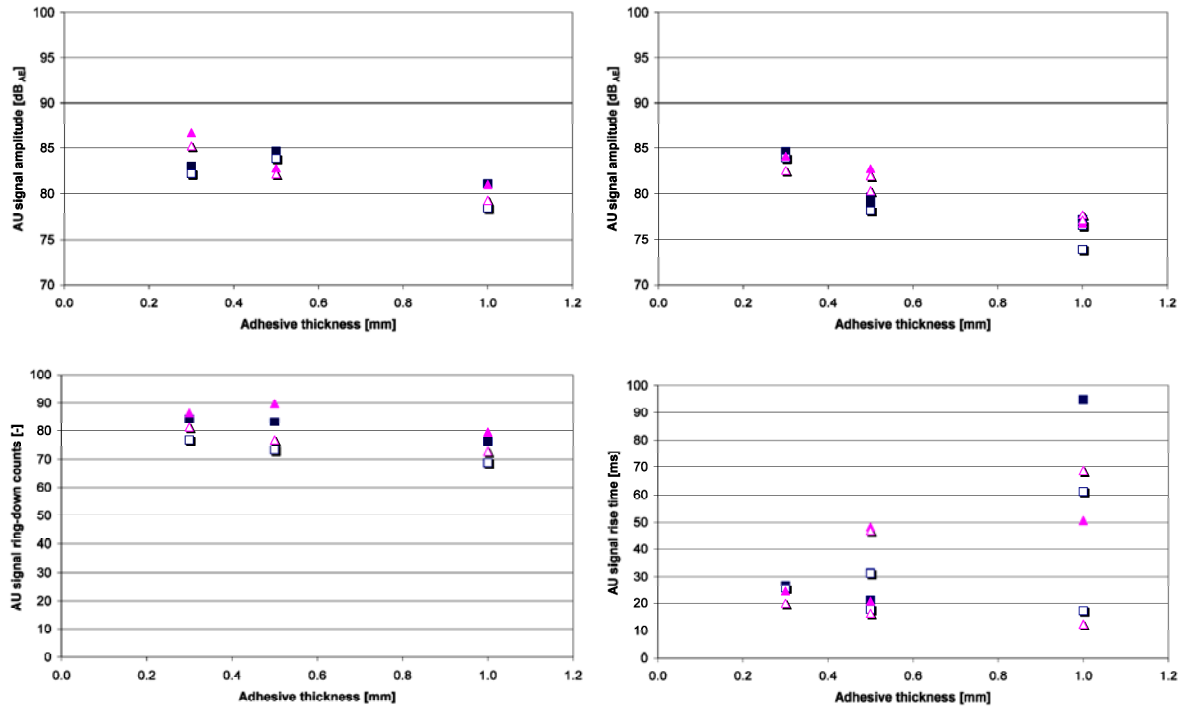


Fig. 3. Selected AU signal-parameters recorded before proof loading to 140 kN with (left) sensor type SE-45H and (right) with sensor type SE-150M plotted versus thickness of the adhesive (see text for more details).

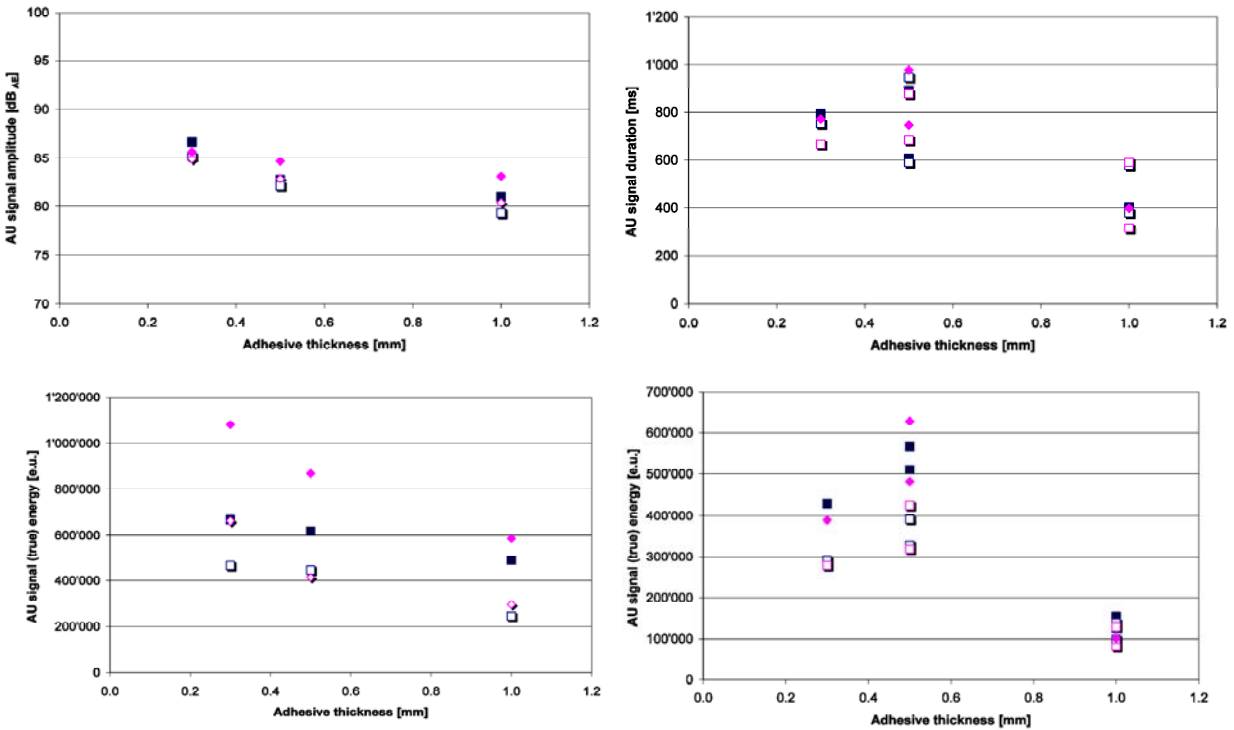


Fig. 4. Selected AU signal-parameters after proof loading to 140 kN compared with those recorded before proof loading with (left) sensor type SE-45H and (right) with sensor type SE-150M plotted versus thickness of the adhesive; square symbols indicate values before, diamond-shaped symbols values after proof loading (see text for more details).

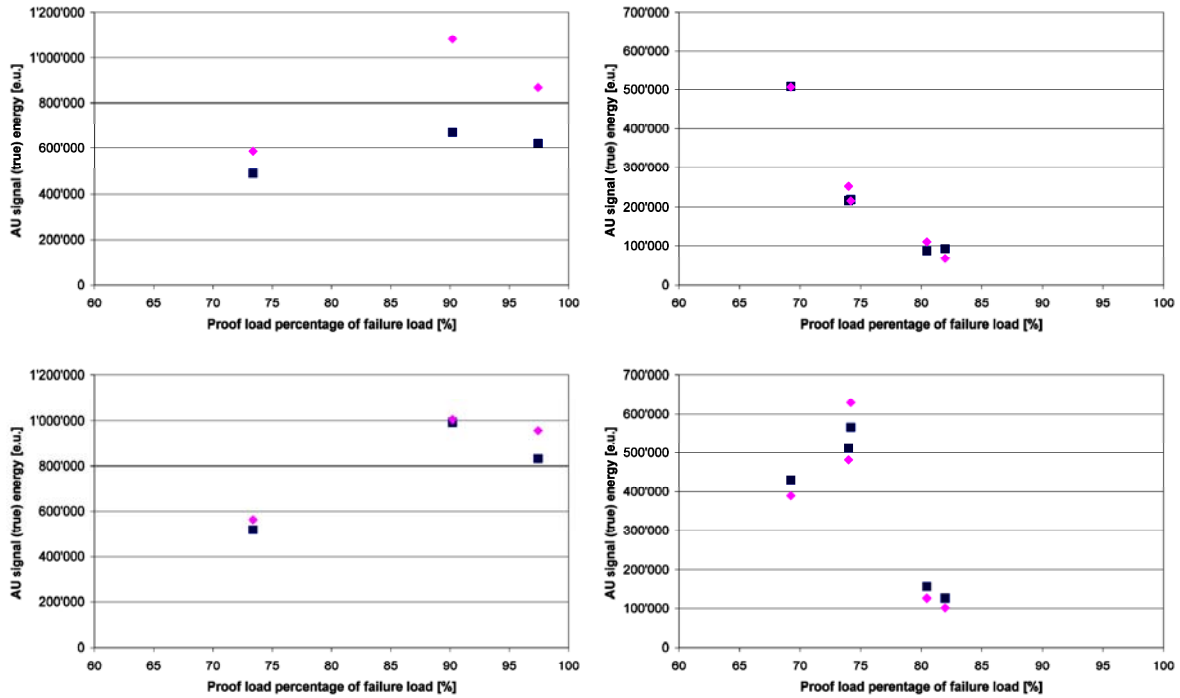


Fig. 5. AU signal-energy after proof loading to 140 kN compared with values recorded before proof loading (left) sensor type SE-45H and (right) SE-150M, (top) AU signal propagation along side of joint, (bottom) AU signal propagation across joint; square symbols indicate values before, diamond-shaped symbols values after proof loading (see text for more details).

Discussion

Due to the fairly large scatter in failure loads for each group of joints with the same thickness of the adhesive (coefficient of variation between about 6% and 20%), it is difficult to decide whether there is a dependence of the failure load on the thickness of the adhesive layer. Even the reasons for this scatter are not clear. Of course, the sample size (three joints per thickness) is too small for reliable statistics. Manufacturing effects (e.g., variation in adhesive thickness) and maybe variability in the lay-up of the GFRP plates are tentative explanations.

Nevertheless, there are indications of a dependence of the AU signal parameters on the thickness of the adhesive layer of the joints. Essentially, but sometimes with relatively large scatter, the AU signal parameter values tend to decrease with increasing thickness of the adhesive layer. This would be consistent with the assumption that increasing thickness of the adhesive layer yields increasing signal attenuation.

The observed lower values of AU signal parameters recorded with sensor type SE-150M compared with SE-45H quite likely relates to the difference in frequency response. Sensor type SE-45H has a higher sensitivity in the frequency range between 50 and 100 kHz than SE-150M (about 5-10 dB_{AE}). Fast Fourier transforms of the AU waveforms (not shown here) recorded with the different types of sensor clearly show higher contributions to the power spectra for the SE-45H in the frequency range below 100 kHz than for the 150 kHz resonant sensor.

The proof load of 140 kN amounted to between 58% and 97% of the observed failure load. This indicates that damage accumulation due to the proof load ranges from low (e.g., DLJ032) to

severe (e.g., DLJ051). That damage induced by the proof load does affect the AU waves is shown by the examples in Fig. 2. Such an effect had also been suggested by the comparative waveform classification reported in [5]. This can be interpreted as evidence that damage accumulation does affect AU waveforms, as expected [4]. However, the results presented here indicate that it is difficult to identify a single AU signal parameter as suitable damage indicator. AU signal energy yields increasing values after proof loading, if sensor type SE-45H is being used. For the 150 kHz resonant sensor (SE-150M), AU signal energy values after proof loading are decreasing, however with one exception, and the changes are comparatively small. Most of the other AU signal parameters (amplitude, duration, ring-down counts) yield partly increasing and partly decreasing values after proof loading for both types of sensors, i.e., no clear trend, while rise time does not seem to change significantly.

As an empirical observation, it can be noted that compressive damage inducing local delaminations in a GFRP-laminate made from woven reinforcement in an epoxy matrix had also shown increasing AU signal energy transmission with increasing extent of damage [6]. The mechanism(s) responsible for that, however, have not been clarified yet. These experiments were performed with special piezoelectric composite sensor elements with considerable sensitivity in the frequency range between about 30 and 100 kHz (analogous to the multipurpose sensor type used in the present investigation). The fact that the 150 kHz resonant sensor used in the present investigation noted a decrease in transmitted AU signal energy after proof loading (except in one case) and that an increase is observed, if sensors with sensitivity at lower frequencies are being used indicates that frequency-dependent wave propagation effects may play an essential role. Damage on one hand seems to produce increasing attenuation at higher frequencies (e.g., above 100 kHz), and simultaneously increasing wave energy transfer at lower frequencies. Whether this can be explained by wave mode changes, by changes in wave interference (the recorded waveforms clearly contain contributions from different wave modes or reflections, see Fig. 2), by non-linear or resonance effects or a combination of these, is not clear. Whether modeling of wave propagation would succeed in shedding light on this, is also unclear, due to the rather complex composition of the GFRP-plates and the lack of materials data as a function of damage accumulation.

In principle, it can be hypothesized that the amount of damage in the propagation path of the AU waves should also be reflected in the signal arriving at the sensor (as long as the geometry of the test piece and sensor arrangement was kept constant to exclude propagation distance dependent effects). The AU signal parameter analysis presented in this paper does seem to indicate that the change of a single parameter will not directly correlate with the amount of damage. It has to be noted, however, that the only indicator of the amount of damage available here was the ratio between proof load and failure load. It will be interesting to see whether more detailed and sophisticated methods of analysis, e.g., based on waveform classification or pattern recognition will, in the future, be able to establish a clear correlation between AU waveform changes and amount of damage. Tentatively, the observation of increasing transmitted AU signal energy (when monitoring test pieces with an AE sensor with sufficient sensitivity in the frequency range below about 100 kHz) can be taken as an indication of potential damage accumulation that may need attention and eventually follow-up inspection.

Conclusions

As a case study, acousto-ultrasonic (AU) waveforms recorded during autocalibration for checking on acoustic emission (AE) sensor coupling before and after tensile proof-tests on adhesively bonded double-lap joints made from glass-fiber reinforced polymer-matrix pultruded

plates have been analyzed by comparing selected AU signal parameters. It was noted that AU signal parameters tended to decrease with increasing (nominal) thickness of the adhesive bond (from 0.3 mm to 0.5 mm and finally to 1.0 mm). There was also a clear difference between AU signals recorded with 150 kHz resonant AE sensors compared with those recorded with multipurpose AE sensor (type SE-45H) with comparatively higher sensitivity in the frequency range between about 50 and 100 kHz. In spite of indications that waveform classification (with VisualClass® from Vallen Systeme GmbH) succeeded in distinguishing AU waveforms recorded before and after proof loading, it proved difficult to unambiguously identify a single AU signal parameter responsible for this. While for most AU signal parameters investigated, no clear trends with damage were observed, AU signal energy at least yielded distinctly increasing values when recorded with the multipurpose sensor, and simultaneously mainly decreasing values when recorded with resonant sensor after proof loading. The changes in the signal energy, however, did not seem to quantitatively correlate with the expected amount of damage. It will hence be interesting to further investigate the feasibility of advanced waveform classification and pattern recognition methods for this.

Acknowledgment

The technical support of Mr. D. Völki for performing the tensile load test at Empa is gratefully acknowledged.

References

1. Vallée T., Correia J.R., Keller Th, *Composites Science and Technology*, **66** (13), 2006, 1903-1914.
2. Vallée T, Correia J.R., Keller Th., *Composites Science and Technology*, **66** (13), 2006, 1915-1930.
3. Vallée T., Keller Th., Fourestey G., Fournier B., *Proceedings 13th International Conference on Experimental Mechanics (ICEM13)*, Alexandroupolis, 2007, Greece.
4. ASTM Standard E1495, Standard Guide for Acousto-Ultrasonic Assessment of Composites, Laminates, and Bonded Joints, ASTM International, 2002 (2007).
5. Brunner A.J., Terrasi G.P., Vallée T., Keller T, *Proceedings 28th European Conference on Acoustic Emission (EWGAE-28)*, Krakow, 2008, Poland, pp. 100-105.
6. Barbezat M., Brunner A.J., Huber Ch., Flüeler P., *Journal of Intelligent Material Systems and Structures*, **18** (5), 2007, 515-525.
7. Bohse J., Brunner A.J., Chapter 9 in: *Delamination Behaviour of Composites*, ed. S. Sridharan, Woodhead Publishing, 217-277 (2008).

BENDING FRACTURE BEHAVIOR OF 3D-WOVEN SiC/SiC COMPOSITES WITH TRANSPIRATION COOLING STRUCTURE CHARACTERIZED BY AE WAVELET ANALYSIS

TOSHIMITSU HAYASHI and SHUICHI WAKAYAMA

Tokyo Metropolitan University, 1-1 Minami-Ohsawa, Hachioji, Tokyo, 192-0397 Japan

Keywords: SiC/SiC composites, AE wavelet analysis, Bending, Porosity, FFT

Abstract

The fracture behavior of the SiC/SiC composites was examined by 4-point bending tests. The AE signals detected during the tests were processed by AE wavelet analysis, which extracted the first and second major frequencies from continuous wavelet transform (CWT) diagram. Consequently, the two-frequency combination analysis can detect local frequency components and characterize a wavelet diagram well. A history of these major frequencies was correlated to initiation and propagation of micro-damages, such as cracks in SiC matrix, crack propagation along thickness and fiber buckling. Although other micro-damages, such as fiber breaks and pull-out of fiber, have not been correlated to the AE signals, the results suggest that the two-frequency combination analysis based on CWT has great potential to characterize the micro-damages of the composites.

Introduction

SiC/SiC composites have been studied in order to increase the temperature capability of jet engine components [1, 2]. An increase in the temperature capability would raise the gas temperature and reduce the need of air cooling, both of which would improve the efficiency of a jet engine. However, active cooling is still needed for the composites to preserve structural strength, since the temperature capability of the composites is lower than the gas temperature (e.g., 1600°C at turbine inlet). In order to develop a simple cooling structure with high efficiency, a transpiration-cooling structure was created in the composites by decreasing a volume fraction of SiC matrix, which was fabricated by four cycles of matrix densification process, “polymer impregnation and pyrolysis (PIP)” [3]. In order to investigate the PIP-cycle effect on the fracture mechanism, flexural loading and unloading test was carried out in a previous study [4]. However, the observed fracture behavior could not be correlated to the captured AE signals by examining AE parameters, such as amplitude and energy. In order to fully understand the bending fracture behavior and monitor micro-damage evolution under long-term evaluation (e.g., thermal cycling test, fatigue test), better correlations between captured AE signals and micro-damages are needed.

Many authors have studied frequency analysis based on frequency domain (FT) or time-frequency domain (WT) in order to investigate correlations between micro-damages and AE signals [5-9]. Many publications on the frequency analysis dealt with CFRPs or GFRPs, which were fabricated by materials of quite different properties. As the SiC/SiC composites are fabricated by materials with similar properties (e.g., chemical compositions and mechanical property), the frequency analysis with a capability to detect minor differences in AE waveforms is required. In recent studies, the discrete wavelet transform (DWT) has often been applied to characterize the AE waveform. The DWT decomposes a signal to several scale levels that correspond to frequency range. However, it appears that the scale level of the DWT may give only a rough estimation for characterizing the AE waveforms emitted from the SiC/SiC composites. Thus, this

study applied the continuous wavelet transform (CWT), which can analyze frequency at a finer scale, for the analysis of the AE waveforms of the composites.

The purpose of this study is to correlate the micro-damages of the SiC/SiC composites to the AE waveforms by analyzing the first and second major frequencies utilizing the continuous wavelet transform (CWT).

Materials and Experimental Procedures

Materials and Specimens

The SiC/SiC composites used in this study were made of Tyranno™ ZMI SiC (Si-C-O-Zr) fiber of Ube Industries, Ltd. and SiC matrix. The composites have the 3D-orthogonally woven structure as schematically shown in Fig. 1. The 3D-woven architecture consists of three layers of X bundles, four layers of Y bundles and Z bundles. Figure 2 shows a cross-sectional view of YZ plane along “aa”. The material composition near surface is also depicted in the figure. Tensile side is not flat because of the woven structure, which results in a notch-like geometry with stress concentration. The location of the notch-like geometry indicated by a gray arrow is called a “corner” in this paper.

First, a carbon interface layer derived from the chemical vapor infiltration (CVI) process was coated on the fibers, then the SiC matrix was infiltrated using methyl-trichlorosilane by a CVI process and from polycarbosilane by several cycles of PIP process. The porosity was controlled by varying the number of PIP cycles. The specimens were fabricated with 4 cycles of PIP. After the PIP treatments, the specimens were cut and coated with a thin layer of CVI-SiC. The volume fraction of fiber, matrix and porosity are 41%, 34% and 25%, respectively. The dimensions of the specimen were 50 mm length x 4 mm (approx.) width x 2 mm (approx.) thickness. The width corresponds to the size of two pitches of the textures.

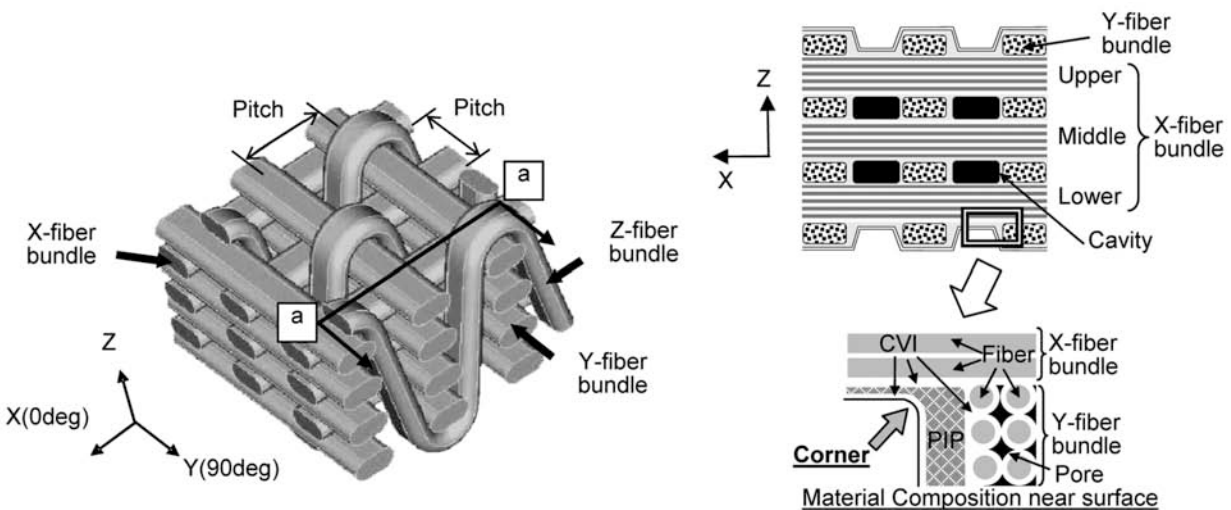


Fig. 1. Schematic diagram of SiC/SiC weave (Fiber volume ratio; X:Y:Z=1:1:0.2, pitch=2 mm).

Fig. 2. Composite cross section along “a-a”.

Experimental Procedures

Four-point bending tests were carried out with inner span of 10 mm and outer span of 30 mm at room temperature in air. Loading was applied by a universal testing machine (Instron, 5505) in Z-direction under a constant crosshead speed of 0.5 mm/min so that the tensile stress was applied

along X-direction. Deformation of the sample was measured parallel to the Z-axis by the displacement transducer and recorded by a PC-based data recorder (Kyowa, UCAM-500A).

During the test, AE signals were monitored by two wide-band AE sensors (Fuji Ceramics, M5W), which were attached on both ends of the sample. The AE signals were amplified 20 dB and the threshold level was set to the value of 3.16 mV at the input of the preamplifiers. The AE signals were processed by an AE analyzer (PAC, PCI-2 AE system) with AEWin™ operating software. Recorded AE waveforms were post-processed by the CWT using a commercial software (Weisang, Flex Pro Professional with an option of spectral analysis). *Morlet* function was chosen as the mother wavelet with non-dimensional frequency $\omega = 8$ [10].

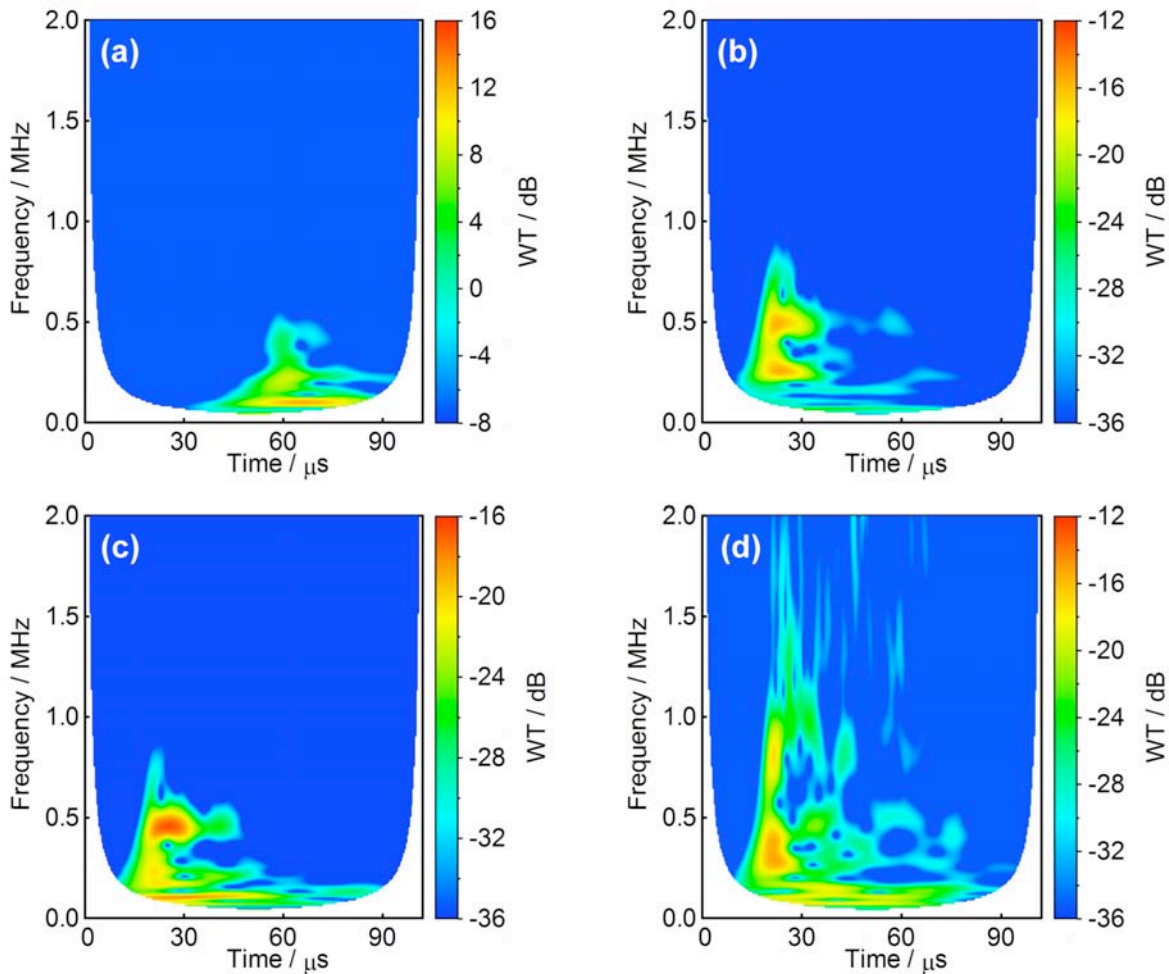


Fig. 3. CWT diagrams of AE waveforms detected during flexural loading, showing characteristic contour patterns in time-frequency domain.

Results and Discussion

The First and Second Major Frequencies in CWT Diagram

AE waveforms acquired in this study showed characteristic CWT diagrams in the time-frequency domain. As an example, some characteristic CWT diagrams obtained from the bending test are shown in Fig. 3. Each diagram has two or more characteristic peak frequencies. The sensor used has a slightly higher response between 0.2 and 0.3 MHz and flat frequency response beyond 0.5 MHz. Thus, a frequency near 0.3 MHz is detected as the dominant frequency in

most of the diagrams. Second characteristic peak frequency of the CWT diagrams often appears below or above the dominant frequency of ~ 0.3 MHz. It appears that a combination of several peak frequencies can possibly characterize and classify the CWT diagram. In this study, the 1st and 2nd major frequencies were utilized for this attempt.

Figure 4 shows the CWT diagram of an AE waveform, including cross-sectional views taken along “aa” and “bb” on the CWT diagram. In the CWT diagram, a pair of the frequencies, “FRQ1” and “FRQ2” (white arrows) are the two characteristic frequencies of this WT coefficient contour. The cross-sectional view along line “aa” is a time history of WT coefficient at the frequency “FRQ1”. Ni and Iwamoto [9] proposed that a WT-time curve at a specified frequency can identify the occurrence time and duration of the micro-fracture mode of single carbon-fiber composites. The specified frequency was selected from the peak on FFT plot of the examined AE signal. However, the WT-curve cannot fully characterize the CWT diagram, because the WT-curve contains information about only one frequency component. The WT-frequency curve taken from “bb” line of the CWT diagram exhibits a distribution of WT coefficient indicating “FRQ1” to be the major frequency. This curve does show that the frequency peak is also located near “FRQ2”, but it fails to properly account for the intensity at “FRQ2”, even though this is shown clearly in the CWT diagram. Thus, either WT-time or WT-frequency curve cannot fully characterize the CWT diagram.

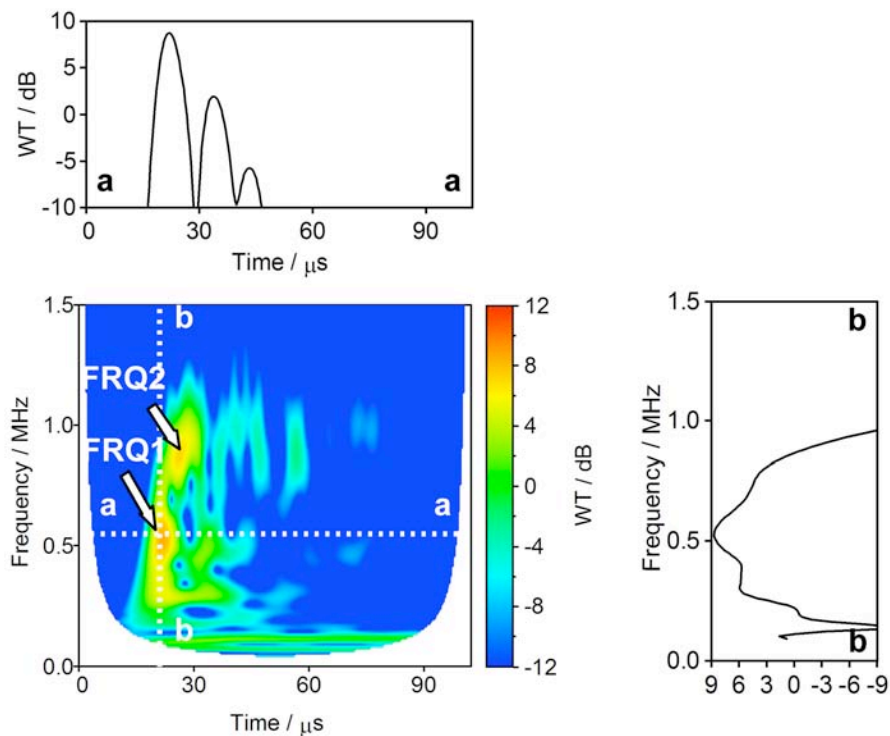


Fig. 4. Wavelet diagram with cross sectional views, taken along lines “aa” and “bb”.

Figure 5(a) shows a CWT diagram projected into WT-frequency plots of the same AE waveform (Fig. 4) for a comparison. The projected WT-frequency curves lost time information, but the frequency and intensity information of two major peaks are preserved. Figure 5(b) shows FFT of the same signal where the first major frequency in the projected WT-frequency curve is recognized only as a minor frequency in the FFT envelope due to the time averaging effect. Thus, FFT analysis fails to detect important frequency information. FFT results also indicate the

highest peak at 0.11 MHz. This can easily be mistaken as a characteristic major frequency of the AE waveform and implies that FFT-based methods must be used with caution.

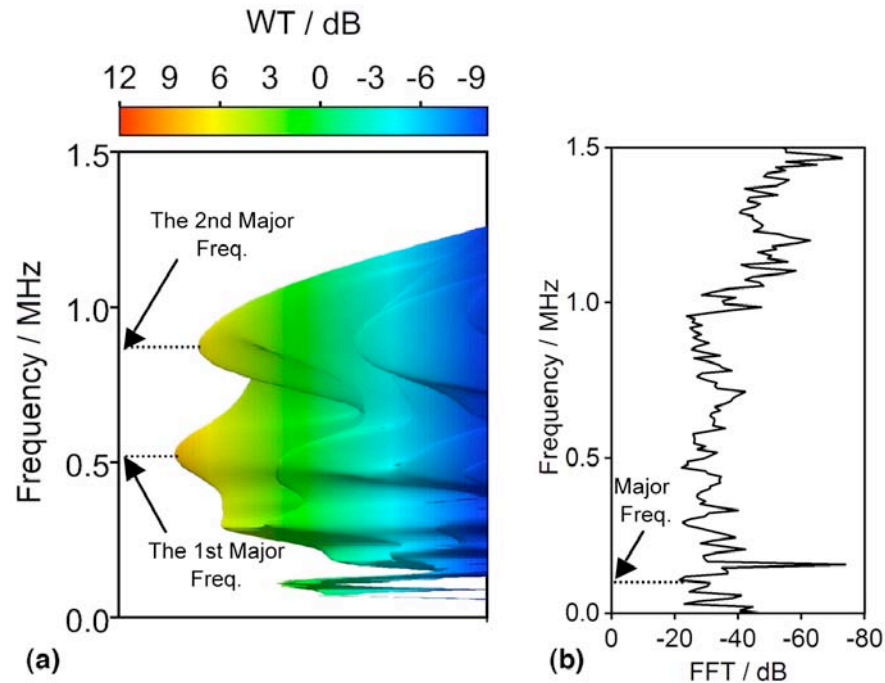


Fig. 5. The major and second major frequencies in projected WT-frequency curve of the waveform shown in Fig. 4 (WT-frequency curve not time-averaged.) (a) Projected WT-frequency curve, (b) FFT spectrum.

Comparison between Projected WT Curve and FFT Spectrum

Figure 6 shows another example where FFT fails to detect the highest peak of the AE signal. Figure 6(a), (b), (c) and (d) show the WT diagram, AE signal, projected WT-frequency curve and FFT spectrum, respectively. The 1st and 2nd major frequencies are indicated by red circles and connected by a solid line in Fig. 6(a), (c) and (d). Figure 6(a) and (b) show that a wavefront of the AE signal has the first major frequency at 0.56 MHz and the second major frequency at 0.32 MHz, and that the frequency component of ~ 0.3 MHz has long duration. It appears that these two frequencies of the wavefront are the characteristic frequencies of the AE signal. The two frequencies can be clearly recognized by the projected WT frequency curve in Fig. 6(c). On the other hand, the two peak frequencies of the FFT spectrum in Fig. 6(d) were 0.33 and 0.29 MHz.

Thus, FFT analysis failed to detect the highest characteristic frequency at 0.56 MHz. Since the frequency component of ~ 0.3 MHz showed long duration, the frequency component of ~ 0.3 MHz was estimated to have high intensity due to the time-averaging effect of FFT analysis. This example again indicated that FFT analysis is likely to fail to detect the higher frequency component of AE waveforms, because high frequency components often exhibit very short duration due to attenuation.

Figure 7 shows one more example, in which FFT failed to detect the characteristic frequency of the AE waveform, even though FFT analysis detected a relatively high frequency component. Figure 7(c) indicates that the AE waveform has the first major frequency at 0.34 MHz and the second major frequency at 0.81 MHz. Since the second major frequency component of ~ 0.8

MHz shows relatively long duration, the FFT recognizes the frequency component of 0.79 MHz as a major frequency. Thus, FFT analysis failed to detect the major characteristic frequency of 0.34 MHz.

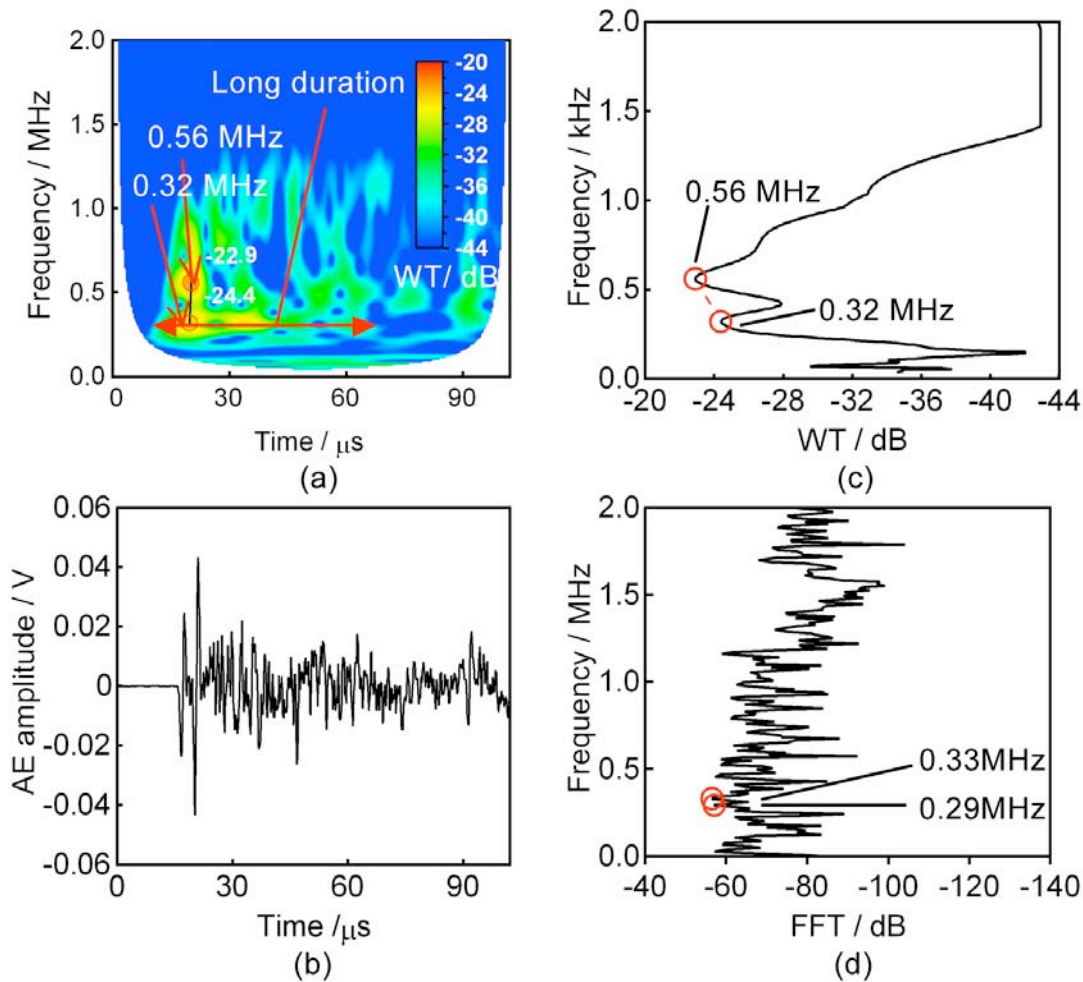


Fig. 6. Comparison between projected WT-frequency curve and FFT spectrum, showing that FFT fails to detect the highest peak of AE signal. (a) WT diagram, (b) AE signal, (c) projected WT-frequency curve, (d) FFT spectrum.

Mechanical Behavior and Microscopic Damages Observed after Bending Test

Figure 8 shows the stress-displacement curve during the bending test. The curve showed several small fluctuations before the stress reached the maximum value and a drop of stress afterward. The final bending fracture as indicated by white arrow in Fig. 8 was followed by a sharp decrease in stress.

Figure 9(a) shows SEM micrographs of the most damaged cross section of the specimen used in the bending test. The horizontal direction is the longitudinal (X-) direction of the specimen, and the tension side is at the bottom. It can be seen in Fig. 9(a) that fiber buckling was observed in the upper and lower X-fiber bundles. Fiber buckling in the upper bundle was accompanied with interlaminar cracks between X- and Y- fiber bundles. Figure 9 (a) also indicates that the upper pore is significantly larger with almost no infiltration of PIP-SiC matrix. Thus, the upper X-fiber bundle was not supported rigidly enough to sustain the compressive stress during bending. As a result, the fiber buckled in the upper fiber bundle adjacent to the large pore. The fiber

buckling in the lower fiber bundle can possibly be attributed to the severely damaged upper fiber bundle. Unfortunately, the complexities of the fiber buckling on the lower side make it difficult to interpret.

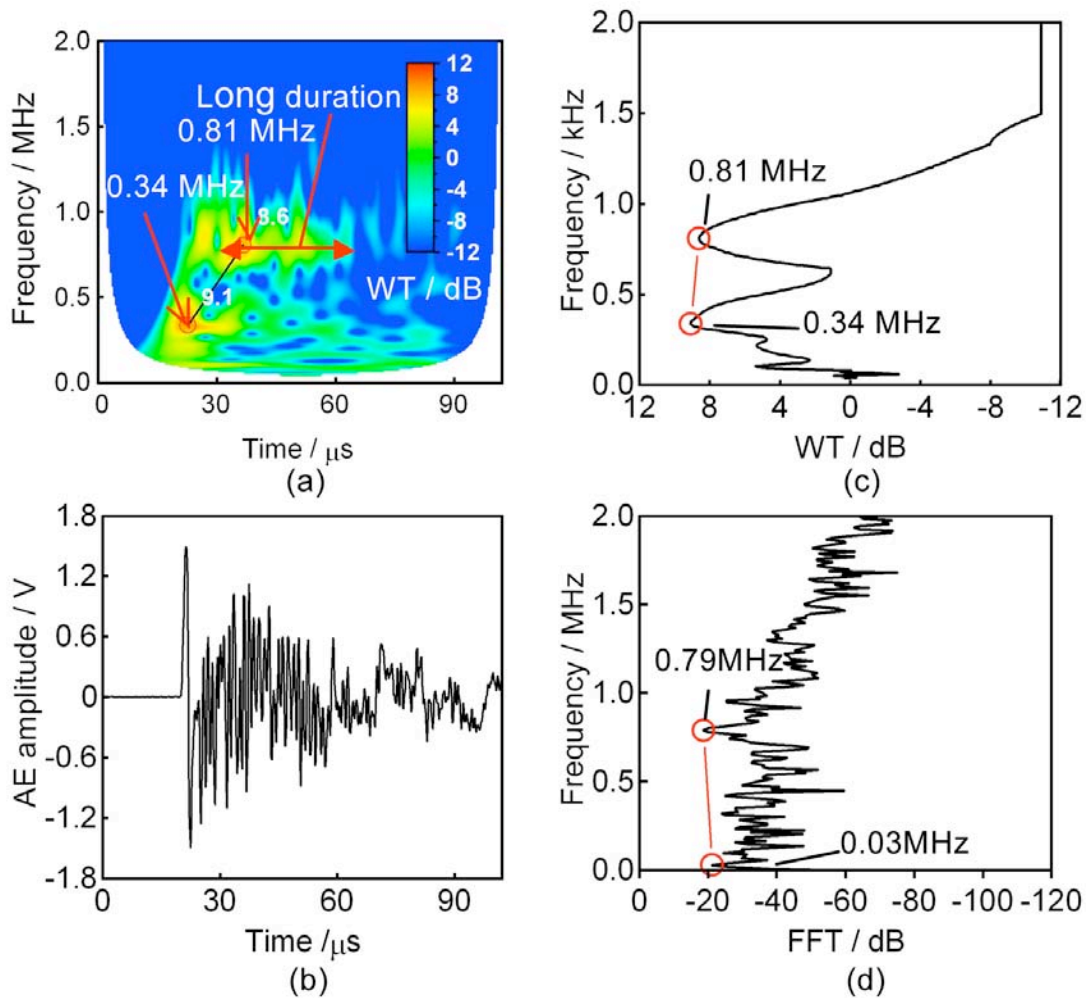


Fig. 7. Comparison between projected WT-frequency curve and FFT spectrum, showing that FFT fails to detect the highest peak of AE signal. (a) WT diagram, (b) AE signal, (c) projected WT-frequency curve, (d) FFT spectrum.

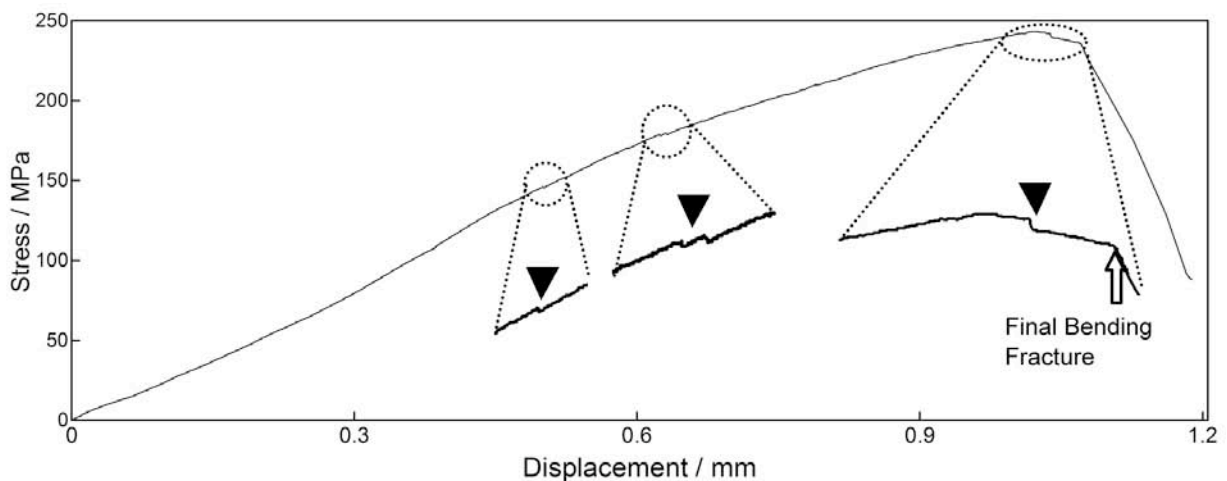


Fig. 8. Stress-displacement curve during the bending test.

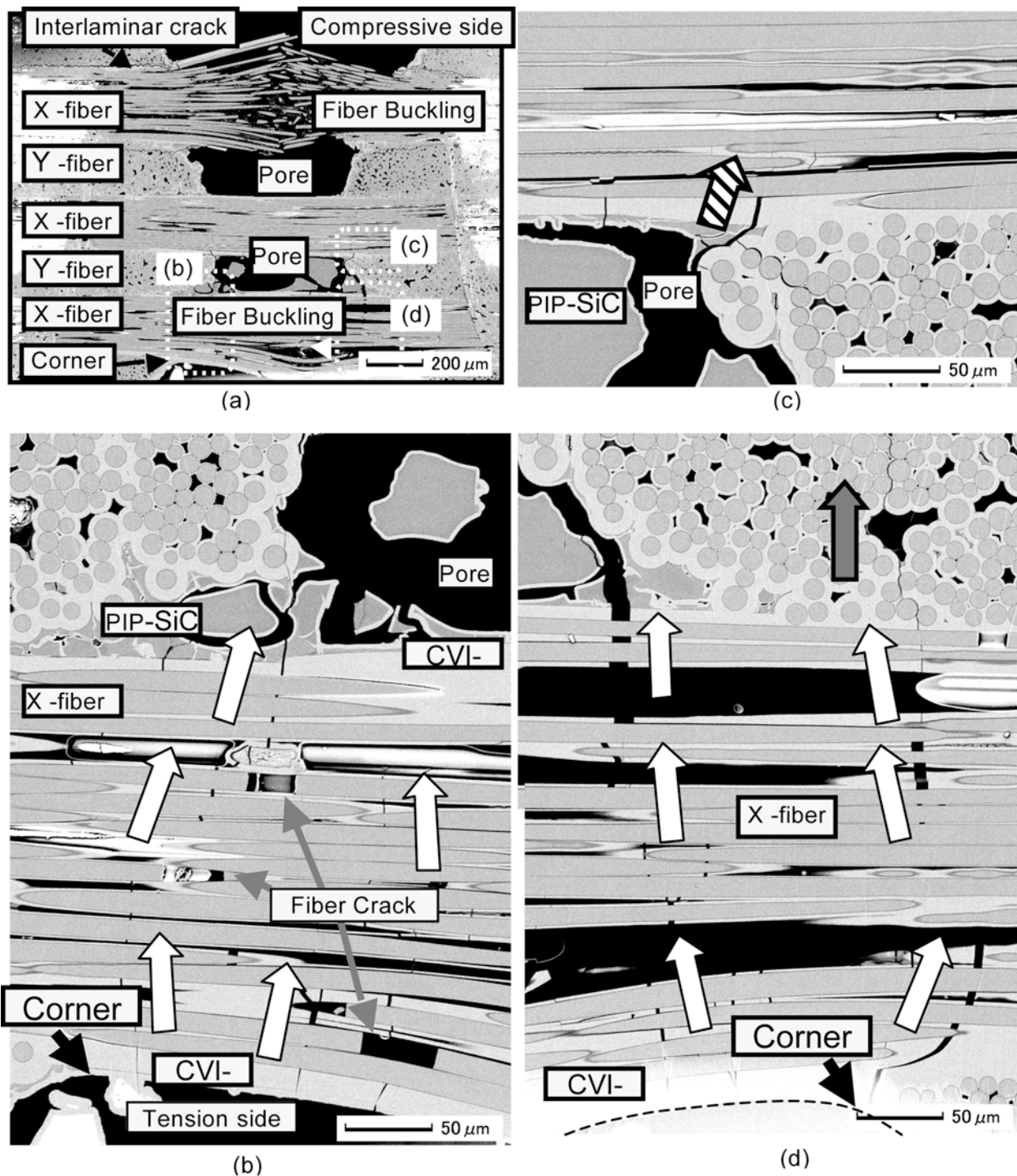


Fig. 9. SEM micrographs of cross section of the specimen subjected to the bending test.

Figure 9(b) and (d) show the 2 corners where the two fiber bundles intersect. It appears that several cracks near corner in Fig. 9(b) were propagated along thickness direction and reached the pore. A crack shown by white arrows in Fig. 9 (d) was propagated into Y-fiber bundle shown by the gray arrow. A crack initiated from the pore is also observed at the corner as shown by slashed arrow in Fig. 9(c).

AE Wavelet Analysis

Figure 10(a) and (b) show the history of the first and second major frequencies, respectively, of the first hit AE signals obtained during the bending test. Relative values of the WT coefficients of the major frequency components are indicated by the circle diameter. In Fig. 10(a), the 1st major frequency components are distributed in a limited frequency band of 250 to 500 kHz. This range corresponds to the high sensitivity range of the AE sensor-specimen combination, identified by the through-transmission experiment using a pair of M5W sensors with tone-bursts. The 2nd major frequencies, shown in Fig. 10(b), are more widely distributed and frequency components over 500 kHz and below 250 kHz were also observed.

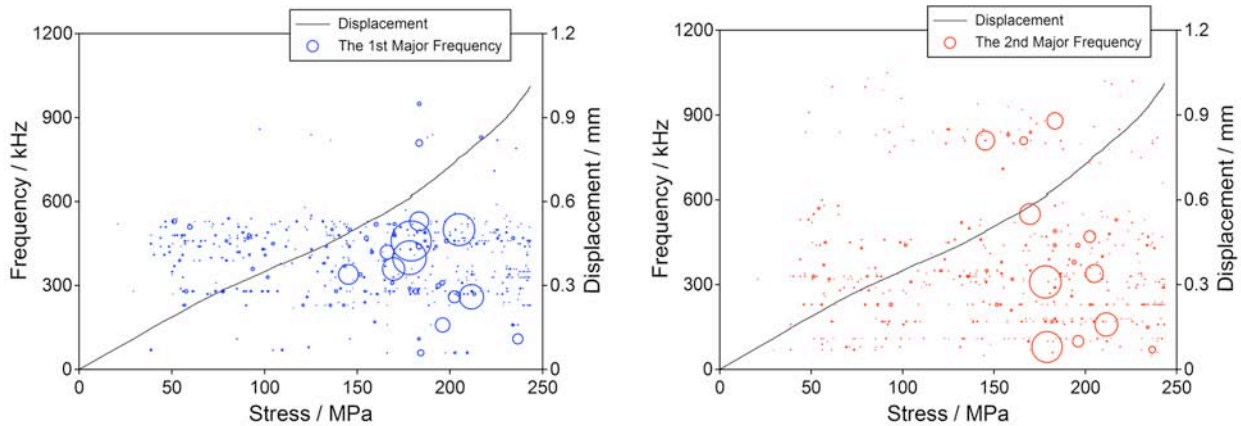


Fig. 10. Frequencies in CWT diagrams. (a) The 1st major frequency. (b) The 2nd major frequency.

The 1st and 2nd major frequency components are shown together in Fig. 11 with connecting link between the two frequencies, since a combination of the two major frequencies can be considered to represent a contour pattern shown in Fig. 3. A caption above the figure described the bending fracture process, which had been observed in the loading/unloading test [4]. The corner crack was generated in the CVI-SiC and PIP-SiC matrices on the tension-side surface in a stress range between 50 MPa and 100 MPa, which grew along thickness direction above 100 MPa and resulted in the bending fracture. The PIP-SiC crack was observed above 100 MPa in the matrix-rich region near cavity and on compressive-side surface. Accordingly, in a stress range from 50 to 100 MPa, the cracks in the both CVI-SiC and PIP-SiC matrices were only observed.

The two frequency components of low WT coefficient with widely distributed frequency range in 50-1050 kHz were observed throughout the test. The signature of the AE signal can be considered to correlate with the initiation and propagation of the crack in both CVI-SiC and PIP-SiC matrices, since only the AE signals with the signature were observed in the stress range of 50 - 100 MPa while these micro-damages were developed. In the stress range above 100 MPa, the AE signals with relatively large WT coefficient were detected.

Figure 12 shows the detailed plot of two peak frequencies against time with the axis extended to the final bending fracture, which shows the AE signals obtained over a stress of about 100 MPa. In order to focus on the characteristics of the damage process, only the combinations of frequency components with relatively large WT were enhanced by linking two frequency symbols by a thick solid line. Black arrows indicate the stress fluctuations that were observed. The

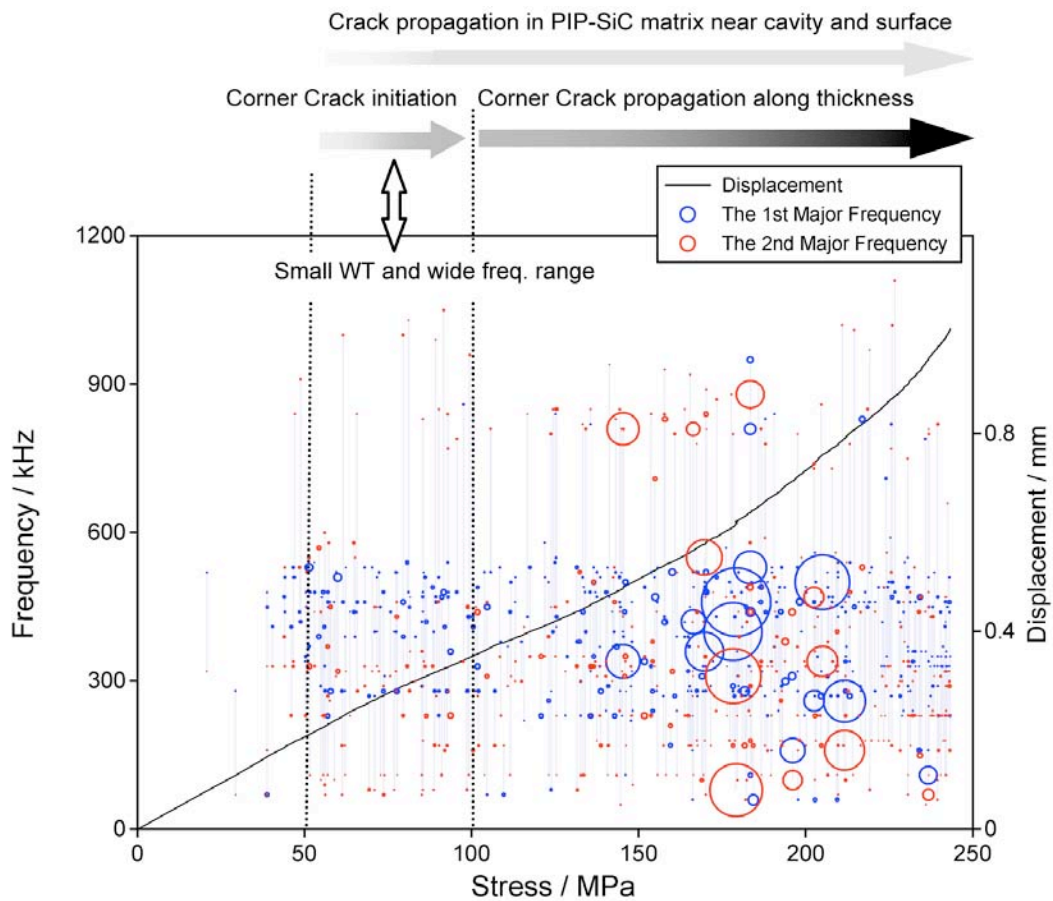


Fig. 11. Two-frequency combination and displacement during the bending test. The description above the figure showed the fracture process obtained by loading and unloading test using a same-lot specimen in the previous study [4].

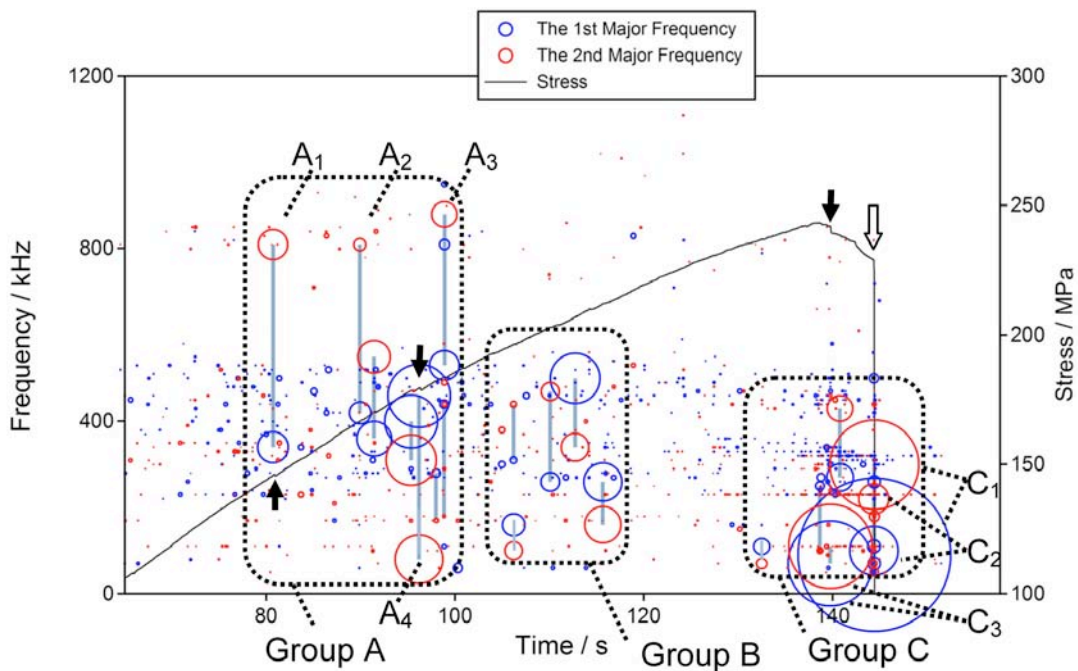


Fig. 12. Detailed plot of the two-frequency combination and stress vs. time during the bending test over a stress level of about 100 MPa.

open arrows shows where the large drop in stress occurred. It appears that the two peak frequency combinations with large WT formed several characteristic groups, which are indicated by dotted line, called group A, B and C. The AE signals, which were detected above 100 MPa, should correlate to the damages, such as the corner-crack propagation along thickness, fiber buckling and interlaminar crack, while exempting matrix cracks near surface or around pores.

The group A contains frequency components with widely distributed and large WT coefficients. The frequency combination A_1 has the 1st major frequency of 340 kHz and the 2nd major frequency of 810 kHz. The frequency combination A_1 may correspond to the initial severe damage in the tensile-side X-fiber bundle due to the corner crack propagation. The micro-damage corresponding to the A_1 was accompanied with a stress fluctuation indicated by a black arrow. It appears that the stress fluctuation can be caused by micro-damages that permit deformation of composites to relax the stress, for example, a rapid propagation of CVI-SiC matrix crack along thickness or width direction, pull-out of fiber and fiber breakage. Since the pull-out of fiber and fiber breakage can possibly occur after well developed CVI-SiC matrix crack in the fiber bundle, the A_1 may correspond to the rapid propagation of CVI-SiC matrix crack along thickness or width direction. Although the combinations $A_1\sim A_3$ contains relatively high frequency component near 800 kHz, the 1st major frequencies of A_1 , A_2 and A_3 were different. This may suggest that the $A_1\sim A_3$ correlate to different micro-damages. From the microscopic observation as shown in Fig. 9(b) and (d), the corner crack in the fiber bundle finally reached upper Y-fiber bundle or pore, which would enhance fiber pullout in the X-fiber bundle, and then result in the stress fluctuation. Since the frequency combination A_4 with low frequency component of 79 kHz accompanied by the stress fluctuation, the frequency combination of A_4 may correlate to the fiber pull-out.

After the corner crack reached a pore or Y-fiber bundle, the crack then developed into Y-fiber bundle shown by gray arrow in Fig. 9(d) or another crack may be initiated at a corner in the pore as indicated by slashed arrow in Fig. 9(c). Since these crack propagation did not accompany fiber cracks, the AE signals corresponding to these crack propagation may contain few high frequency components. Thus, "Group B" with few high frequency components indicated in Fig. 12 may correlate to the crack propagation into Y-fiber bundle and the crack initiation at a pore corner.

"Group C" in Fig. 12 contains very low frequency combinations with significantly large WT. The AE signals of C_1 and C_2 were detected at the final bending fracture with the sharp drop in stress indicated by the white arrow. It appears that the final bending fracture was accompanied with the fiber buckling, because stress cannot be held any further if such fiber buckling occurred. Thus, the AE signals of C_1 and C_2 , which were detected at the final bending fracture, can correlate to the fiber buckling. The common signature of C_1 and C_2 is that the 1st major frequencies were detected at significantly low value of 69 or 89 kHz. Another AE signal C_3 , of which the 1st major frequency was 69 kHz, was observed in advance of final bending fracture at 140 s accompanying a little drop in stress indicated by the black arrow. This may indicate that the fiber buckling was initiated then. The pattern recognition of the combination will further lead to correlate the AE signals to more microscopic damages, such as SiC fiber breakage and pull-out of fiber. Further study will be carried out to find the correlation by the two-frequency combination analysis extracted from CWT.

Conclusions

The wavelet analysis of AE signals based on the two-frequency combination extracted from CWT diagram was applied to investigate the correlation between AE signals and micro-damages in the SiC/SiC composites with transpiration structure and the following conclusions were obtained.

- 1) Major frequency components that characterize the contour pattern of the CWT diagram are extracted with a projected WT-frequency curve and used in two-frequency combination analysis.
- 2) The AE signal with low WT coefficient with widely distributed frequency corresponds to the crack in the CVI- and PIP-SiC matrices.
- 3) The crack propagation in longitudinal fiber bundle along thickness direction may be correlated to a group of two-frequency combinations, which has high, middle and low frequency components.
- 4) The fiber buckling damage was correlated to two-frequency combination, which contains low frequency component.

References

- [1] Naslain R.: *Journal of Applied Ceramic Technology*, **2** (2), 2005, 75-84.
- [2] Ohnabe H., Masaki S., Onozuka M., Miyahara K. and Sasa T.: *Composites, Part A*, **30**, 1999, 489-496.
- [3] Hayashi T., Wakayama S.: *Advanced Composite Materials*, **18**(1), 2009, 61-75.
- [4] Hayashi T., Wakayama S.: *Journal of the Japan Society for Composite Materials*, in press.
- [5] Ageorges C.; *Composites Science and Technology*, **59**, 1999, 2101-2113.
- [6] Mizutani Y., Nagashima K., Takemoto M., Ono K.: *NDT&E International*, **33**, 2000, 101-110.
- [7] Qi G., Barhorst A., Hashemi J., Kamala G.: *Composites Science and Technology*, **57**, 1997, 389-403.
- [8] Loutas T.H., Kostopoulos V., Ramirez-Jimenez C., Pharaoh M.: *Composites Science and Technology*, **66**, 2006, 1366-1375
- [9] Ni Q-Q, Iwamoto M., *Engineering Fracture Mechanics*, **69**, 2002, 717-728.
- [10] Torrence C. Compo G.: *Bulletin of the American Meteorological Society*, **79** (1), 1998, 61-78.

ACOUSTIC EMISSION MONITORING OF BRIDGE STRUCTURES IN THE FIELD AND LABORATORY

RHYS PULLIN, KAREN M. HOLFORD, ROBERT J. LARK and MARK J. EATON
Cardiff School of Engineering, The Parade, Newport Road, Cardiff, CF24 3AA, UK

Keywords: Bridge inspection, laboratory and field investigations

Abstract

Cardiff University, in association with Physical Acoustics Limited, has been actively promoting the use of acoustic emission (AE) to monitor bridge structures as part of any bridge maintenance procedure since the early 1990's, both in concrete and steel bridge structures. Scepticism of the capabilities of AE by bridge authorities has led to a large number of laboratory research projects being completed to demonstrate and validate the technique and support field results.

This paper presents the findings of two field investigations with extensive laboratory support. One is a box-girder bridge structure where a fatigue fracture was located on an internal diaphragm both on a real structure and a scale model and of the second is a steel-reinforced concrete structure where regions of possible concrete micro-fracture around steel reinforcing bars was detected. Both investigations demonstrate the capabilities of AE as a diagnostic tool as part of any bridge maintenance programme.

Introduction

Bridge structures throughout the UK are being used past their life expectancy and well beyond their original design loads. Furthermore, there is an increasing monetary pressure on bridge authorities to extend the life whilst ensuring public safety. A large aspect of increasing life expectancy is completed by periodic visual inspection and based on findings appropriate repairs or maintenance can be completed. However, visual inspection can be exceedingly difficult; in the case of steel box girder bridges special breathing apparatus and lighting equipment is required and in steel-reinforced concrete structures internal corrosion cannot, in many examples, be visualised externally.

AE monitoring offers a real and practical alternative to visual inspection with the monitoring of steel box-girder structures becoming increasingly accepted [1 - 4] but scepticism still exists across a large number of bridge authorities even though the UK Highways Agency has produced an advice note on testing structures with AE [5].

The case of steel-reinforced concrete structures is even more problematic. Fractures identified in box girders can be verified through other NDT techniques but verification of fractures in steel reinforcement is more complex and can require the removal of structural concrete, which naturally is undesirable. Examples of monitoring steel-reinforced concrete structures can be found in [6 - 9].

One method of promoting AE and demonstrating its capabilities is through laboratory testing. Verification of results is far less problematic and a greater level of confidence in field results can be gained. This paper presents the findings of two field investigations, one on a steel box girder and the other on a steel-reinforced concrete bridge - both tests had extensive laboratory support.

Experimental Procedure

Box-Girder Bridge: Cardiff University was appointed to monitor a box-girder bridge in South Wales. It has a total span of approximately 300 m and is of composite construction, with a concrete road deck supported by four steel box-girder beams. Each box-girder is approximately 1.2 m square and has a maximum span of 31 m. Welded inside the girder at various positions are 10-mm thick steel diaphragms of two types. One type provides cross sectional stiffness and maintains torsional rigidity, while the second type also transfers the shear forces carried by the girders through to the support bearings; it is the former that this study focuses on.

Initially a global approach to AE monitoring of the bridge was completed and several diaphragms emitting high activity were identified. A more detailed description of the global approach can be found in [2]; subsequently a local approach of the most emissive diaphragms was then completed [3].

Four PAC WDI sensors were mounted around the outside perimeter of the diaphragm (Fig. 1) so that the sensor face was aligned with the internal edge of the diaphragm. The painted surface was lightly sanded to remove any peaks. Sensors were mounted into position using magnetic clamps. Grease was used as an acoustic couplant. The installed sensitivity of the system was then verified using the H-N source. AE feature data was recorded for a period of 90 minutes under service loading at an acquisition threshold of 30 dB.

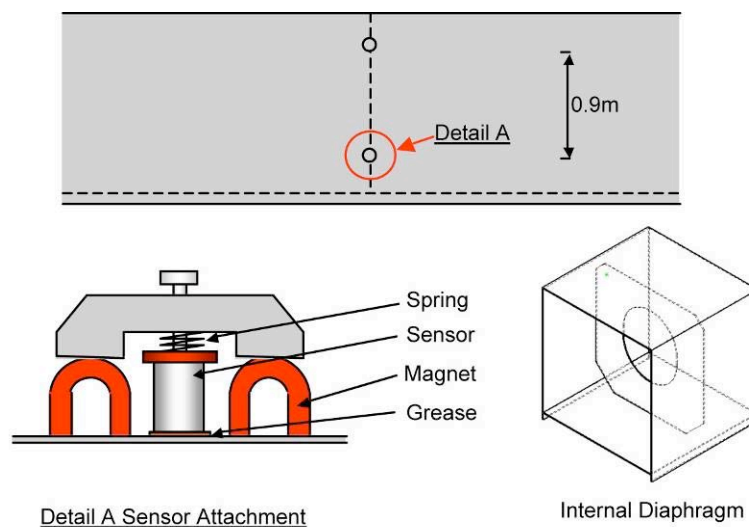


Fig. 1 Box Girder beam showing sensor attachment and internal diaphragm.

Steel-Reinforced Concrete Bridges : Cardiff University was given the opportunity to demonstrate the AE technique on a steel-reinforced concrete hinge joints (Fig. 2). Concrete hinge joints are present in over 100 bridges in England and a further 12 over-bridges, each containing two hinge joints, in Wales. They were introduced into bridge decks as a means of simplifying the design, and standardising details on bridges having a range of span and functional requirements. It is thought that the hinge joints transfer shear and accommodate small angular movements but restrict longitudinal movement [10]. It was also assumed the hinges were provided to enable the bridges to cope with possible differential settlement. The disadvantages with hinged joints are that they are not easily accessible for inspection or maintenance due to their form, and their location over or under live traffic lanes.

Previous attempts to investigate the deterioration of hinge joints by visual inspection, which involves the removal of structural concrete around the joint to expose the reinforcement bars, have noted particular defects; the majority have cracks running through the throat and a loss of waterproofing. Waterproofing failure can lead to chloride rich seepage through the joint that can cause reinforcement bar corrosion leading to eventual failure by yielding.

The joint monitored was of joint was of slab construction. The bridge is an over-bridge on the M4 in South Wales. The exact positioning of the internal reinforcement bars across the joint was unknown; however, they were believed to be at 308-mm centres. Grease was used as an acoustic couplant. An H-N source was used as a source to assess the sensitivity of the sensors.

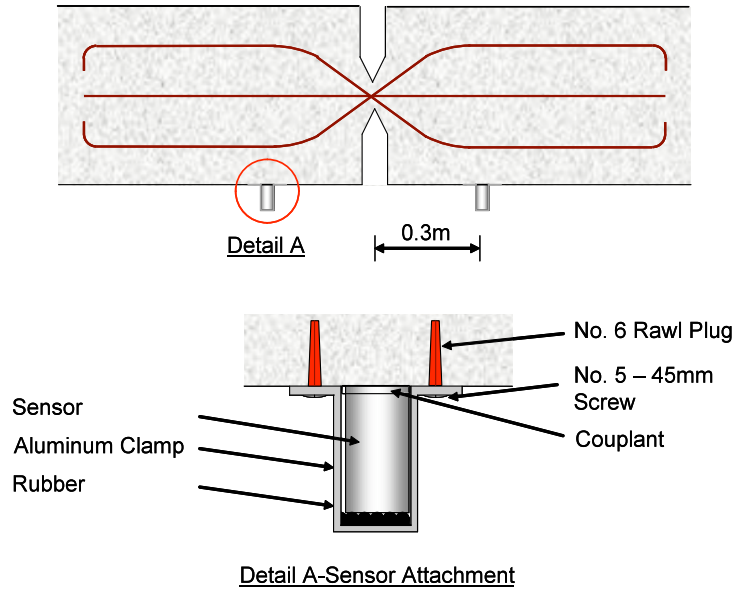


Fig. 2: Section of a typical hinge-joint assembly, sensor attachment and installed system.

Monitoring was completed for a period of 12hours (7am-7pm) for three days. Heavy vehicles crossing the joint were logged using time marks for a period of five hours during the initial day of monitoring. AE feature data was recorded at a threshold of 35 dB.

Supporting Laboratory Studies: The laboratory model of the diaphragm was fabricated to half scale. The upper section of the box section was bolted to a test frame whilst load was applied to the end section (Fig. 3a) to recreate the torsional loading associated with damage on the bridge structure. The specimen was cyclically loaded until a substantial fatigue fracture was observed. AE instrumentation was kept consistent for both the field and laboratory investigation.

Construction of a realistic hinge-joint model containing all internal reinforcing in the laboratory would have been too complex to fabricate, restrain and load so a specimen that demonstrated the capabilities of AE to detect fatigue fractures in concrete and steel-reinforcement bars was created (Fig. 3b). A circular notch smaller than the inner diameter of the threaded section was machined at the centre of the bar to initiate a fatigue crack. Two PAC R15I sensors were connected to the steel reinforcement bar using waveguides and four PAC R3I sensors were then added to the concrete faces as shown in Fig. 3. In both cases grease was used as an acoustic couplant. Specimens were loaded cyclically until failure.

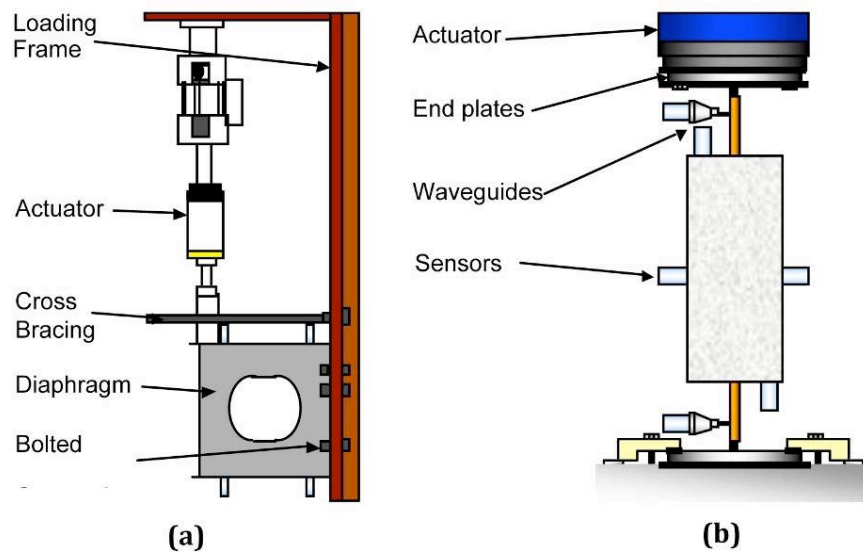


Fig. 3: Laboratory testing.

Results and Discussion

Figures 4a and b show two location plots from the field and laboratory investigation on the steel girder. The most obvious difference is the number of events detected, which is considerably less in the field investigation due to the limited period of monitoring. However, both plots show regions of high activity in the region of the cut-out. A red line representing the actual fatigue fracture has been added to Fig. 4b. Other regions of high activity are present in this plot but were being emitted from the bolted joint. This was validated using pencil-lead fractures at the bolt sites and comparing the location with these regions of high activity. Experience of bridge and laboratory testing has consistently shown that noise is a greater problem in the laboratory due to hydraulic noise and frictional noises between test-rig components.

With limited or no access to the inside of the box girder in the field, it is difficult to quantify these types of result. However, with the added result from the laboratory work, a greater confidence in identifying the source as a fracture can be made. Furthermore, results from laboratory studies can be used to aid source characterisation. In simple cases this could entail examining

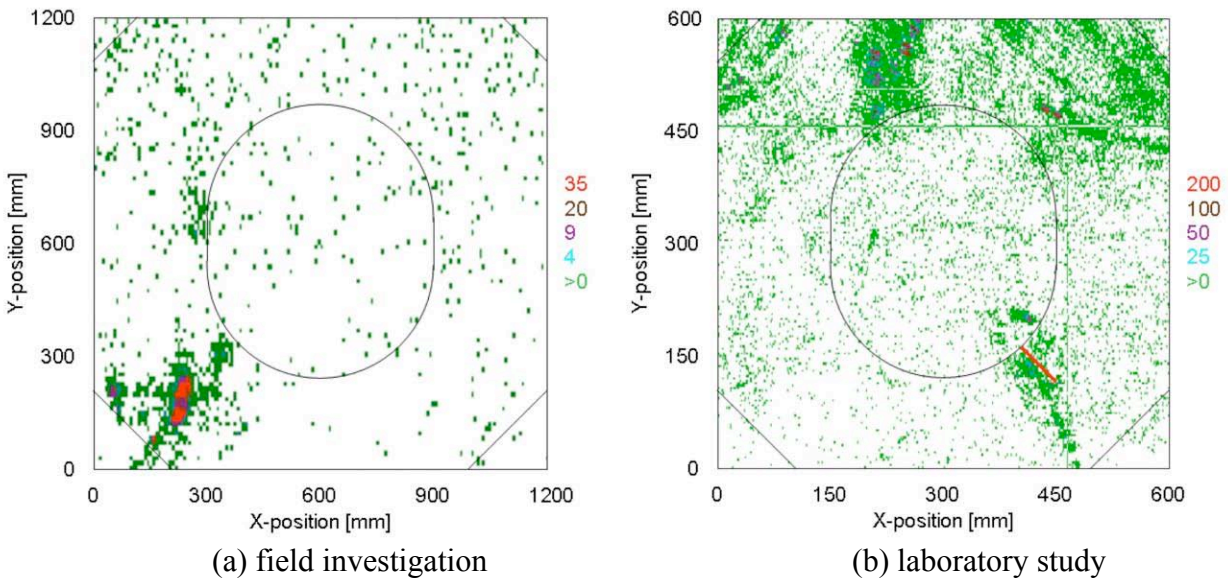


Fig. 4: Comparison of field and laboratory results from box-girder testing.

amplitude and energy trends, sometimes a more advanced technique such as neural networks may be appropriate.

The case of box girders is relatively simple, with plate geometries and non-complex propagation paths, a greater level of complexity occurs in steel-reinforced concrete bridge structures. Varying wave speeds, due to multiple materials, complex propagation paths due to aggregate and multiple damage mechanisms such as steel fatigue fracture, concrete fracture and corrosion make monitoring reinforced concrete structures difficult and the collected data difficult to interpret.

Table 1 presents the number of hits within specific amplitude ranges from each day of monitoring the slab hinge joint. The results indicate that there is not a significant difference between the number of hits on each day of monitoring suggesting that at this site one day of monitoring is sufficient to provide the necessary data.

Table 1: Summary of monitoring results.

Amplitude of Hits (dB)	No. of Hits Day 1 (x 10³)	No. of Hits Day 2 (x 10³)	No. of Hits Day 3 (x 10³)
35-45	1500	1500	1200
45-55	226	187	152
55-65	58.8	40.2	37.3
65-75	12.9	8.4	7.3
75-85	2.09	1.28	1.09
85-100	0.23	0.16	0.15

Figure 5 shows the period of logging heavy vehicles, the highest energy emissions from the joint can be associated with heavy vehicles crossing the joint, however not all heavy vehicles produced large energy emissions. During monitoring it was visually observed that all vehicles caused some emissions, these however may be associated with the normal stress loading of the joint and that vehicles travelling at higher speeds across the joint produced greater energy emissions.

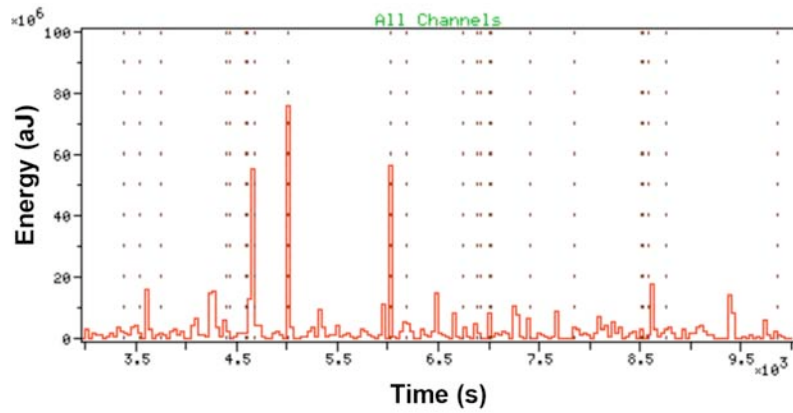


Fig. 5: Activity of joint with logged vehicles.

Figure 6 shows a planar location plot from three days of monitoring the steel-reinforced concrete hinge joint. The numbered circles represent sensor positions whilst a dashed line shows the hinge position. The plot shows several bands of emission located to the south of the joint and indicate regions of possible damage, likely to be centred around reinforcing bars. These bands occur at larger intervals than the 308-mm spacing of the bars. This implies that the AE is detecting sources at some bars but not every bar.

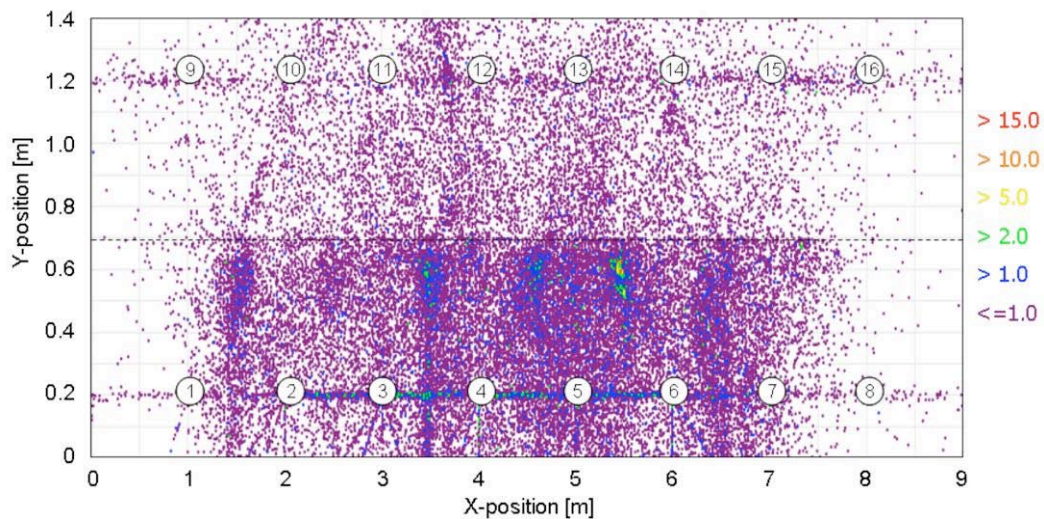


Fig. 6: Field testing location results.

After the test data was collected, three new methods of data interpretation were developed. A method utilising the kernel probability density estimation (KPDE) function [11] was created that enabled not only the density of signals, but the density of the energy of the signals to be visualised. This is currently not possible using commercial software.

Another technique was developed that expanded on the commercial technique of location cluster analysis and employed k-means analysis [12] to aid source characterisation, a summary of which is shown in Fig. 7.

The purpose of source location clustering is to automatically identify and associate groups of events, based on user controlled spatial criteria and a number of signal threshold. In commercial software, clusters can be organised in terms of their total energy, but there is a limit imposed on the total number of clusters (100), which was removed in the developed script. A k-means

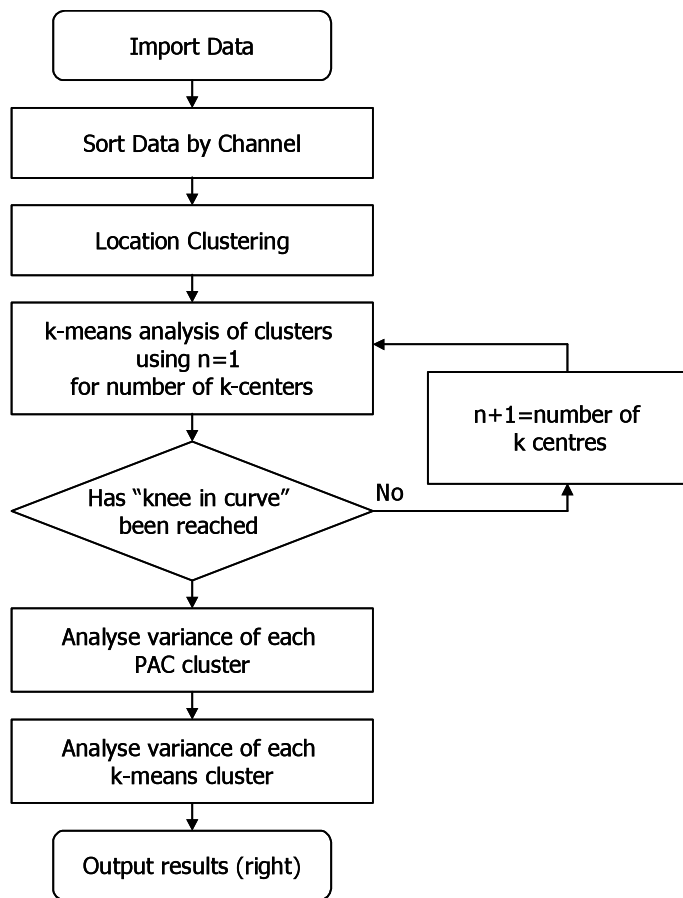


Fig. 7: Flow chart of designed script used to further analyse the recorded data.

analysis of the feature data from the location clusters can then be completed. A k-means analysis assigns a set of data points to k-centres, or means. The algorithm is popular due to its fast convergence and simplicity. The algorithm is initiated in a random state: each data point is assigned as a member of one of the k-groups. The set of centres is calculated by taking the mean of the members of each group, then each data point is re-assigned to a new group according to its nearest center. The process is repeated until no points change groups. The algorithm works exceptionally well on well-spaced groups of Gaussian-distributed data points. In order to make the AE feature data resemble this, the data is normalised, such as to have unit variance in each feature. The variance of each group in the feature space, compared with the entire data set can then be calculated. In theory any regions of high activity that are identified via source location clustering and have very similar signals, as identified via the level of variance in the feature space, are likely to be from a repetitive damage mechanism such as fatigue fracture or concrete microcracking.

The resulting plots of the KPDE analysis are presented in Figs. 8a and b. The region of high activity at approximately (5.5 m, 0.6 m) is clearly visible in Fig. 8a, whilst the remaining bands that are associated with the internal reinforcing bar are clearly visible. However of more interest is the region of densely populated energy in Fig. 8b, which using the commercial software could not be visualised. This is a region of low density in terms of events but high energy and it is very close to the centre line of the hinge section. This suggests that this region is made up of a small number of high-energy events that could be attributed to concrete fractures. Fatigue fractures of the reinforcing bar would be likely to occur more frequently and with greater consistency in

energy release under normal traffic loading. Therefore the region is attributed to concrete fractures near to the throat of the hinge.

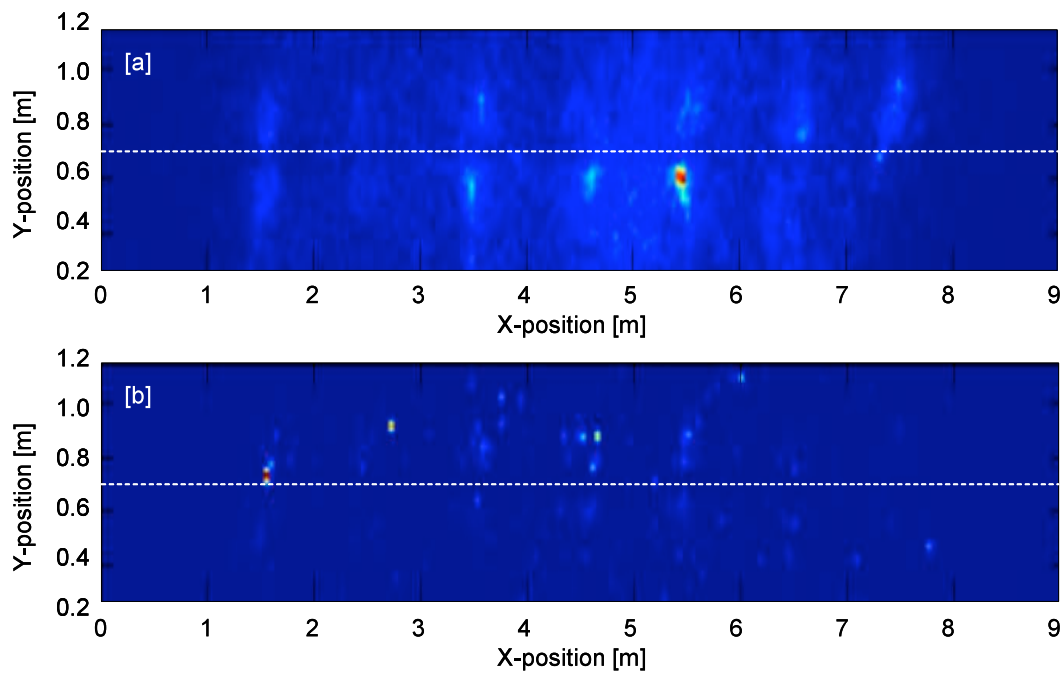


Fig. 8: Kernel probability density estimation plot (a) hits (b) energy.

To further analyse the regions of high event density on the south side of the joint in Fig. 6, feature data, including location, from channels 3, 4, 5 and 6 was processed by the developed k-means analysis based script (Fig. 9). A source cluster area, based on a circle with diameter of 30 mm, and threshold of 30 events, was used to analyse the data. A graphical representation of the script results is shown in Fig. 9, together with a key to the level of variance of the feature data. Three regions of grouped, low variance clusters are clearly visible and are in close proximity to the joint. Although the definite position of the reinforcing bars is unknown the distance between the bars is believed to be 308 mm, and the possible positions of the bars based on the lowest variance clusters are superimposed. It can be seen that the other grouped regions would also appear to be in close proximity to reinforcing bars, whilst several bars appear to have no active damage in their vicinity.

Feature data of the cluster with the highest number of events (242) in the low variance group, which is centred on a reinforcing bar, were compared with that of regions at a similar distance from the same sensor, that were not associated with a reinforcing bar position; this revealed little difference in features. This suggests that the detected signals are associated with damage in the concrete structure rather than the steel reinforcing bar, which would have distinctly different features. This suggests that the regions detected are due to microcracking of the concrete.

However, further evidence was needed to show that AE was capable of detecting damage in these complex structures, and thus a laboratory model was fabricated and tested. Figures 10a, b and c show the results of the laboratory testing of the steel-reinforced concrete specimen. Under the initial loading, a small amount of concrete fracture occurred around the region of the rebar notch, and these fractures increased through the duration of its life and further emissions are caused by localised crushing of loose aggregate. This is evident in Fig. 10a, which shows all located signals using the surface-mounted concrete sensors from the duration of the whole test.

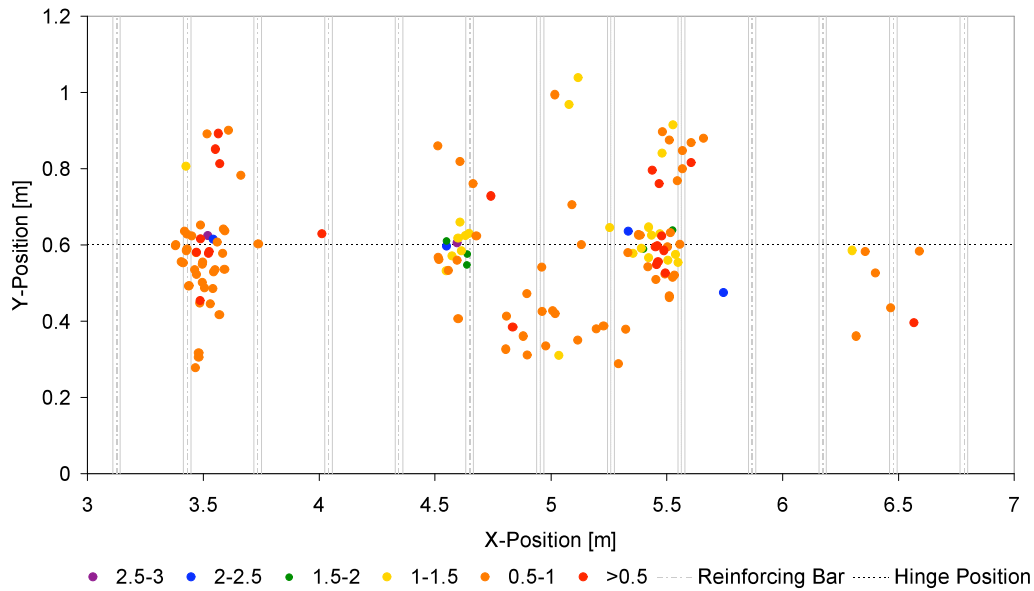


Fig. 9: Graphical display of results from k-means analysis based script.

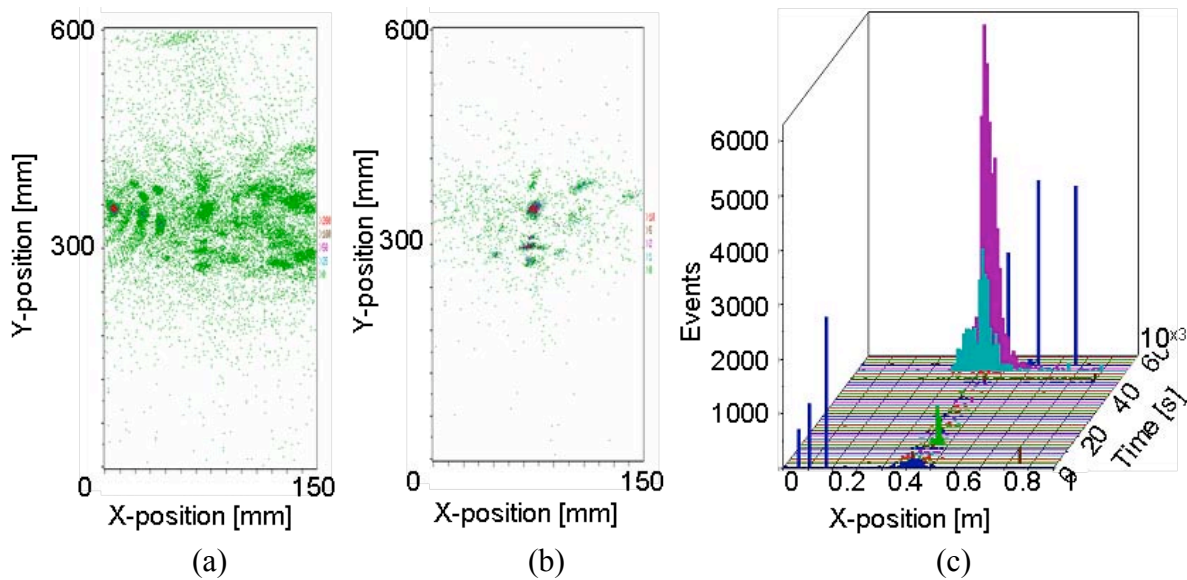


Fig. 10: Laboratory testing of concrete encased steel reinforcement bar.

Figure 10b shows the location of signals from the final 7000 cycles. It was known, based on load history, that this is when the rebar started to fatigue. The plot clearly shows that AE can detect and locate steel fatigue fractures from surface-mounted sensors, again providing confidence to bridge authorities of the capability of AE. Figure 6c shows a linear location plot against time using the sensors attached to the waveguides. The plot clearly demonstrates that the sensors detected the concrete fractures early in the investigation and detected the steel fatigue fractures at the end of the investigation. Furthermore, results of the laboratory investigations could be used to help identify fracture sources or train neural networks.

As discussed previously, monitoring of steel box-girder bridges by AE is less complex than monitoring concrete reinforced joints. Current techniques for locating and identifying damage in box girders are sufficient. However, further validation of field results, using visual inspection or

other NDT techniques, is required to convince bridge authorities of the capabilities of AE. It is more difficult to promote the use of AE in steel-reinforced concrete structures. AE has been used previously, but validation of results is often impossible as other NDT techniques cannot be used and visual inspection requires the removal of structural concrete, which is undesirable as it can cause extensive damage to the structure.

Conclusions

Results presented in this paper have demonstrated the capabilities of AE to detect damage in bridge structures. Results have been complemented by laboratory testing that has been required to support and demonstrate findings to bridge authorities.

References

- [1] D. C. Carter, R. Pullin and K. M. Holford, Acoustic Emission Studies of a Steel Box Girder Bridge, *23rd European Conference on Acoustic Emission Testing*, (1998) pp. 225-229.
- [2] K. M. Holford, D. C. Carter, R. Pullin and A. W. Davies, Bridge Integrity Assessment by Acoustic Emission – Global Monitoring, *2nd International Conference on Identification in Engineering Systems*, (1999) pp. 392-400.
- [3] R. Pullin, D. C. Carter, K. M. Holford and A. W. Davies, Bridge Integrity Assessment by Acoustic Emission – Local Monitoring, *2nd International Conference on Identification in Engineering Systems*, (1999) pp. 400-405
- [4] A. W. Davies, K. M. Holford, R. Pullin, J. Watson., P. T. Cole and S. N. Gautney, Acoustic emission monitoring trial, Report for The Highways Agency: Maintenance Agency Area 12: Midlands Links Motorway Viaducts, Cardiff University and Physical Acoustics Ltd. (1999).
- [5] Highways Agency Advice Note on NDT (BA86) (2005).
- [6] J. R. Watson, S. Yuyama, R. Pullin and M. Ing, Acoustic Emission Monitoring Applications for Civil Structures, Surrey University's International Bridge Management Conference (2005).
- [7] M. Ohtsu, A Review of AE in Civil Engineering with Emphasis on Concrete, *Journal of Acoustic Emission*, **8**, No. 4, (1989) 93-98.
- [8] M. Ohtsu, The History and Development of Acoustic Emission in Concrete Engineering, *Magazine of Concrete Research*, **48**, No. 177 (1996) 321-330.
- [9] M. J. Ing, R. Lyons and S. A. Austin, Risk-Based Investigation of Steel Reinforcement Corrosion Using the AeCorr Technique, *Proceedings of 3rd International Conference on Emerging Technologies in Non Destructive Testing*, Thessaloniki, Greece (2003), pp. 410-418.
- [10] J. R. Watson, P. T. Cole, I. Kennedy-Reid and J. Halliday, Condition Assessment of Concrete Half Joints, *First International Conference on Bridge Maintenance, Safety and Management*, Barcelona, July 14-17, 2002.
- [11] C. B. Wilson, Assessment of the reinforced concrete hinges on five M6 overbridges in Staffordshire, *Proceedings Institution Civil Engineers*, **110**, (1995) 4-10.
- [12] B. W. Silverman and B. S. Silverman, *Density Estimation for Statistics and Data Analysis*, CRC Press (1986).
- [13] C. M. Bishop, *Pattern Recognition and Machine Learning*, Springer, ISBN-10: 0387310738, (2006).

ARRIVAL TIME DETECTION IN THIN MULTILAYER PLATES ON THE BASIS OF AKAIKE INFORMATION CRITERION

PETR SEDLAK^{1,2}, YUICHIRO HIROSE¹, MANABU ENOKI¹ and JOSEF SIKULA²

¹ Department of Materials Engineering, Graduate School of Engineering, The University of Tokyo, 7-3-1 Hongo, Bunkyo, Tokyo, 113-8656, Japan; ² Czech Noise Research Laboratory, Department of Physics, FEEC, Brno University of Technology, 616 00 Brno, Czech Republic

Keywords: arrival time detection, Akaike information criterion, multi-layer plate

Abstract

The information of first-arrival time of acoustic emission (AE) signal is important in event location, event identification and source mechanism analysis. Manual picks are time-consuming and sometimes subjective. Several approaches are used in practice. New first arrival automatic determination technique of AE signals in thin metal plates is presented. Based on Akaike information criterion (AIC), proposed algorithm of the first-arrival detection uses the specific characteristic function, which is sensitive to change of frequency in contrast to others such as envelope of the signal. The approach was tested on real AE data recorded by a four-channel recording system. The results were compared to manual picks and to other AIC approach. It is shown that our two-step AIC picker is a reliable tool to identify the arrival time for AE signals.

Introduction

The precise determination of the arrival time of transient signals like AE, seismograms or ultrasound signals is one of the fundamental problems in non-destructive testing and geophysics. The information of this time is important in event location, event identification and source mechanism analysis. Manual picks are time-consuming and sometimes subjective, especially in the case of large volumes of digital data. Various techniques have been presented in the literature and are routinely used in practice, such as a passing the threshold level, analysis of the LTA/STA (long term average/short term average), high order statistics or artificial neural networks.

Modeling the signal as an autoregressive process (AR) is another approach for onset time determination. It is based on the assumption that the signal can be divided into locally stationary segments and the intervals before and after onset are two different stationary processes [1]. On the basis of this assumption, an autoregressive Akaike information criterion (AR-AIC) has been used to detect *P* and *S* phases [1-3] in seismology. For AR-AIC picker, the order of the AR process must be specified by trial and error and the AR coefficients have to be calculated for both intervals. In contrast, Maeda [4] calculated the AIC function directly from seismogram without using the AR coefficients. For time series *x* of length *N*, the AIC is defined as

$$AIC(k) = k \log(\text{var}(x[1, k])) + (N - k - 1) \log(\text{var}(x[k + 1, N])) \quad (1)$$

where *k* is range through all time of time series. However, the AIC picker does not perform well, if the signal to noise ratio is low and the arrival is not evident. Further, for AIC picker to identify the proper arrival, a limited time window of the data must be chosen [3].

Although AE and seismograms are similar to each other for first view, there also exist several differences. In seismology the signal and noise are usually located in different frequency range. AE signal and noise are often in the same frequency range and also signal-to-noise ratio is gener-

ally not constant during experiment. Kurz et al. [5] successfully applied an adapted automatic AIC picker based on Maeda's relation to AE from concrete and used the complex wavelet transform and Hilbert transform as characteristic function instead of the signal. Both these transforms lead to a certain envelope of the signal. The advantage of the envelope by wavelet transformation is that it can be calculated only for one frequency, while most of the noise of the signal is found in different frequencies. However, if two or more signals of different amplitude and frequency superpose each other, the envelope calculated by the Hilbert transform should be used.

In our case, the signal is described by the specific characteristic function, which is used as input data for AIC. This characteristic function is sensitive to change of frequency in contrast to others such as envelope of the signal, which indicates only change in amplitude of signal. The approach was tested on real AE data and compared to manual picks as well as to Kurz's AIC approach.

Two-step AIC Picker

The performance of the picker depends strongly on characteristic function. The arrival time is indicated by a change in the frequency, or amplitude, or both, in the time series, and characteristic function must respond to this change as rapidly as possible and, ideally, should enhance the change [6]. The absolute value function $CF(i) = |x(i)|$ is easy to compute and the most widely used (amplitude threshold picker). The square function $CF(i) = x(i)^2$ enhances the amplitude changes but not frequency changes. For seismogram threshold picker, Allen [6] used a function,

$$CF(i) = x(i)^2 + K (x(i) - x(i-1))^2 \quad (2)$$

where K is a weighting constant that varies with sample rate and stationary noise characteristics. Unfortunately, we discovered that these characteristic functions are not so effective for our case. We found that our AIC picker succeeds with following function,

$$CF(i) = |x(i)| + R |x(i) - x(i-1)| \quad (3)$$

where R is a constant specified by trial and error; for our case $R = 4$. This characteristic function is sensitive to change of frequency in contrast to others such as envelope of the signal.

During one experiment, an AE measurement system can recognize and record up to several thousand AE signals. The length of one AE signal and threshold level is defined by researcher in advance. If we consider the facts mentioned above about AIC pickers, the choice of correct time window is a crucial factor for the identification of proper arrival. Ideally, the time window starts in non-informative part of AE signal (noise) and ends in informative part of AE signal (real signal).

Our proposal of the first-arrival detection solves this problem. Figure 1 presents visual description of individual stages of our algorithm. The algorithm shortens the time interval of the original time window in Fig. 1a. The beginning of signal is presumed as non-informative part and it is not changed. The global maximum of the original signal in absolute value is found, t_{MAX} . This time plus time delay Δt_{AM} is considered the end of informative part of AE signal. We set the $\Delta t_{AM} = 20 \mu s$, which is reasonable for material of our interest. Mathematically, this can be defined for signal x of length N with time step $\Delta t = 0.1 \mu s$ as

$$\begin{aligned}
 i_{\max} &= i: |x(i)| = \max(x) \text{ where } x = \{x(i) | i = 1, \dots, N\} \\
 x_{NEW} &= \{x_{NEW}(i) | i = 1, \dots, (i_{\max} + 200)\}
 \end{aligned}
 \tag{4}$$

where x_{NEW} is results of shortening of time window.

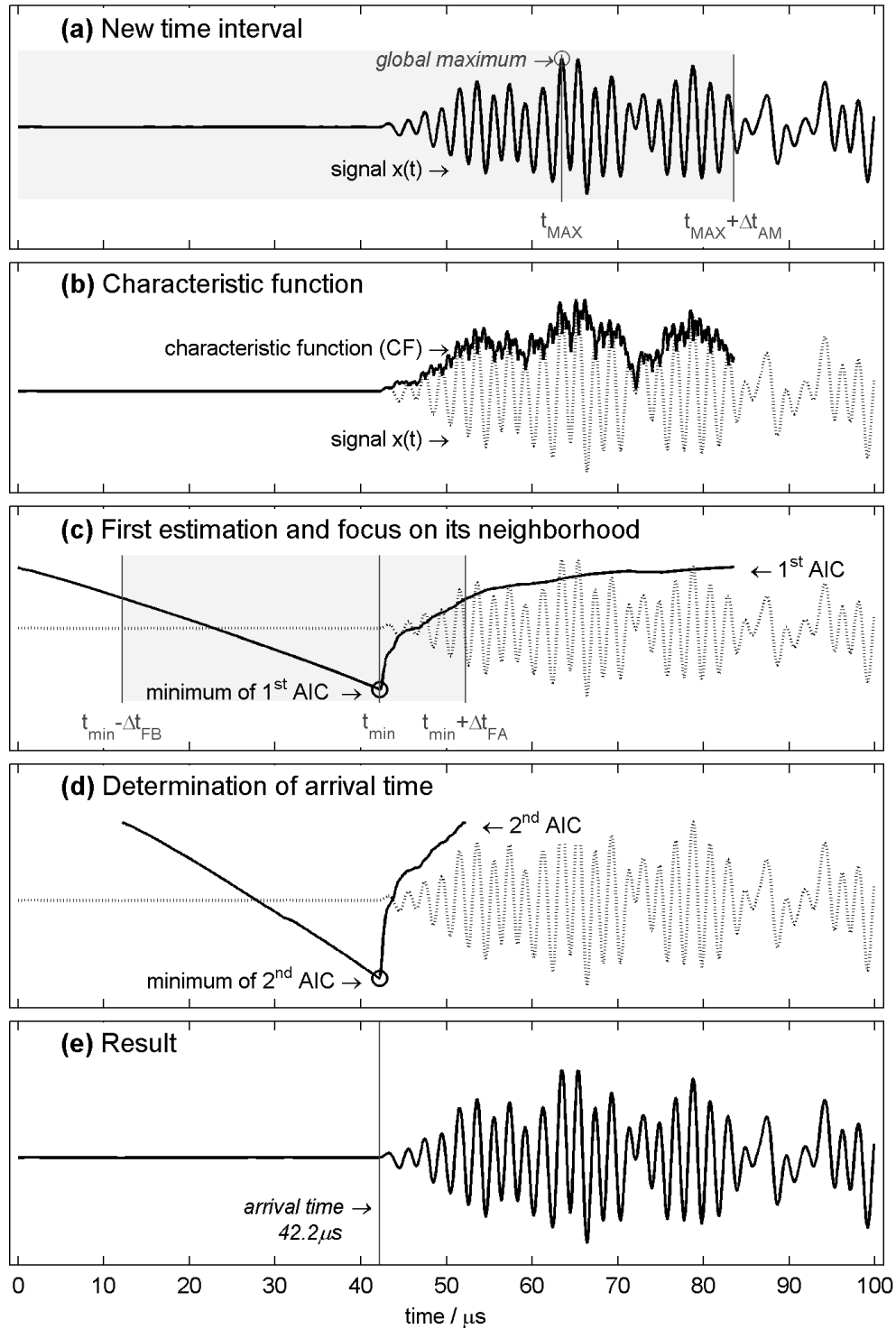


Fig. 1. Visual description of our two-step AIC picker. (a) Definition of new time interval, (b) Characteristic function, (c) Determination of first estimation of arrival time and focus on its neighborhood, (d) Determination of final arrival time, (e) Result.

Our algorithm is two-step process. First, the characteristic function Eq. 3 is computed on shortened signal (Fig. 1b) and AIC picker based on Maeda's relation Eq. 1 is applied on this CF. The global minimum of AIC function determines the first estimation of the arrival time (Fig. 1c). In second step, we focus on neighborhood of first estimation (Fig. 1c). The time interval is changed to start at Δt_{FB} before first estimation and to end at Δt_{FA} after first estimation. For our case, $\Delta t_{FA} = 10 \mu\text{s}$ and $\Delta t_{FB} = 30 \mu\text{s}$ were found by trial and error. The AIC picker is applied once again on CF in this shortened time interval (Fig. 1d). The global minimum of recalculated AIC function defines the arrival time of AE event, as can be seen in Fig. 1e.

Experiment

Acoustic emission is one of methods describing behavior and properties of materials under various conditions. Considering the nature of AE, many spurious events can occur during an experiment and represent potential errors in final conclusions. In our case, the localization is used to eliminate this possible error.

The approach was tested on real AE data. Figure 2 presents measurement set-up of this tensile test of 25-layered SPCC/SUS420J2 thin plate with four sensors, which were located in one line. The location of AE event is estimated by one-dimensional hyperbolic localization by times of first arrival. AE measurement system called Continuous Wave Memory [7] was used to recognize AE events by 15-mV threshold and to store every event in 100 μs time length. Continuous Wave Memory sampled data at a rate of 10 MHz by 12-bit A/D converter. The data were filtered numerically by a 4th-order Butterworth high-pass filter with cut-off frequency of 100 kHz.

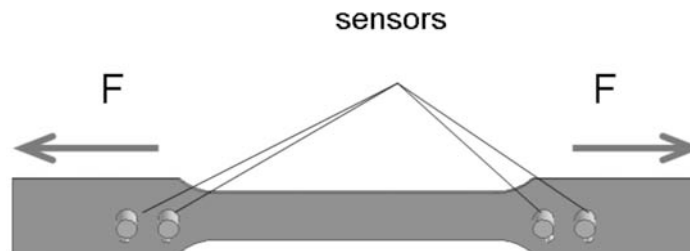


Fig. 2. Measurement set-up of tensile test.

Results and Discussion

In the test, the 25 AE events from center region of a specimen were chosen for comparative investigation. It represents 100 AE signals. Arrival times of these chosen events were determined manually as well as automatically using our approach and Kurz's approach with envelope calculated by Hilbert transform [5]. The signal-to-noise ratio (SNR) of the chosen event varied according to the test stage the individual event occurred.

Figure 3 shows that the localized events obtained with arrival times of our two-step AIC picker are all situated relatively close to the events localized with the arrival times determined manually. The events localized using arrival times determined by Kurz's AIC picker are not in such proximity to manually picked events. The explanation is within reach. The mean of differences between manual picks and Kurz's AIC picker is 2.7 μs , but maximal difference is 18 μs

(Fig. 5). In case of two-step AIC picker (Fig. 4), the mean is $0.2 \mu\text{s}$ and the maximum is $2.4 \mu\text{s}$ only.

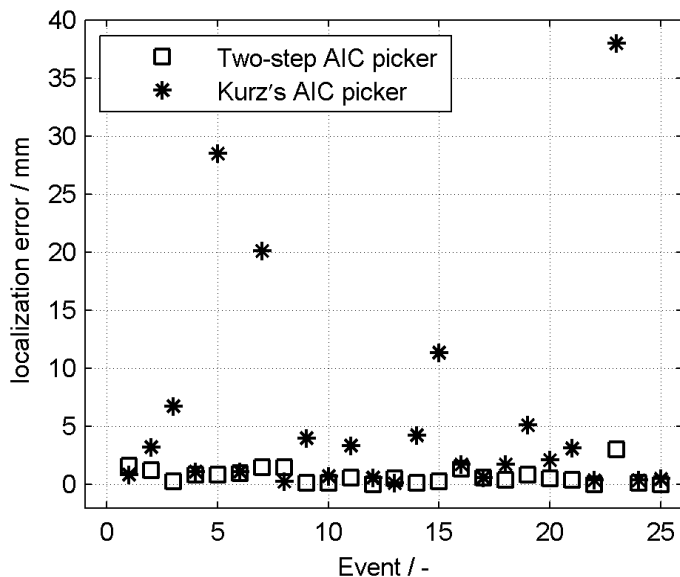


Fig. 3. Localization error: comparison of two-step AIC picker with Kurz AIC picker.

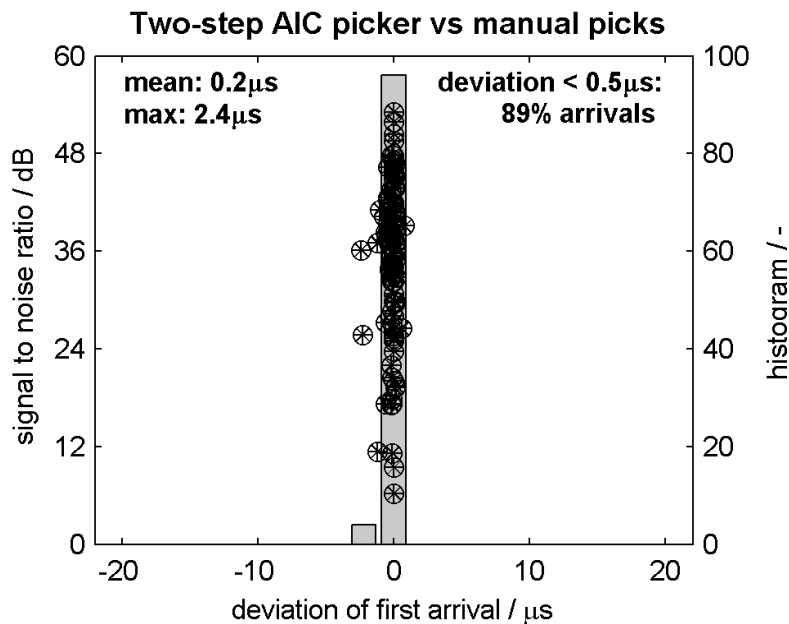


Fig. 4. Histogram of differences between manual picks and automatic picks by two-step AIC picker and its corresponding signal-to-noise ratios (circles).

We found that 89% of arrival times were determined by our approach with deviation less than $0.5 \mu\text{s}$, whereas in case of Kurz's AIC picker it was 41%. The examples of the first-arrival determination for varying signal-to-noise ratios are shown in Fig. 6.

Conclusion

A new automatic determination technique of the first-arrival times of AE signals is presented for thin metal plates. Based on Maeda's relation, the proposed algorithm of the first-arrival

detection uses the specific characteristic function. This characteristic function CF is sensitive to change of frequency in contrast to others such as envelope of the signal.

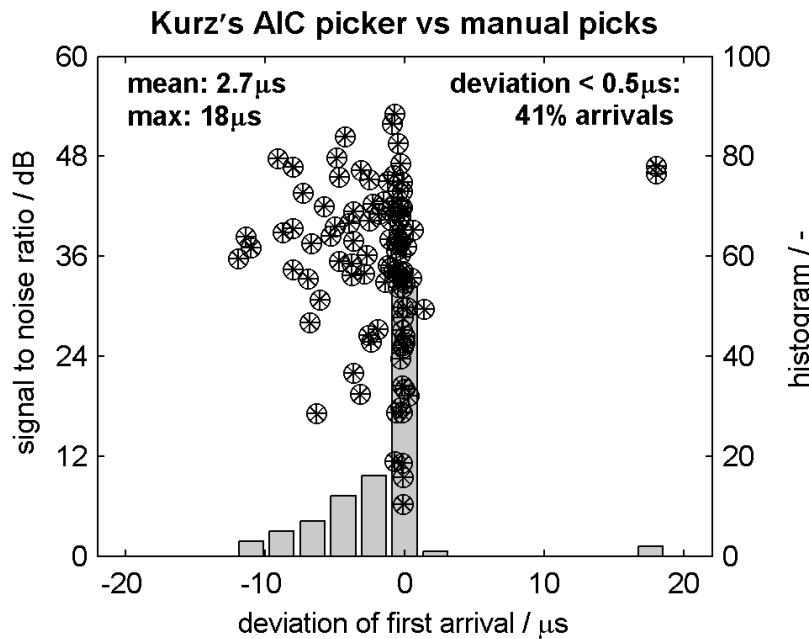


Fig. 5. Histogram of differences between manual picks and automatic picks by Kurz's AIC picker and its corresponding signal-to-noise ratios (circles).

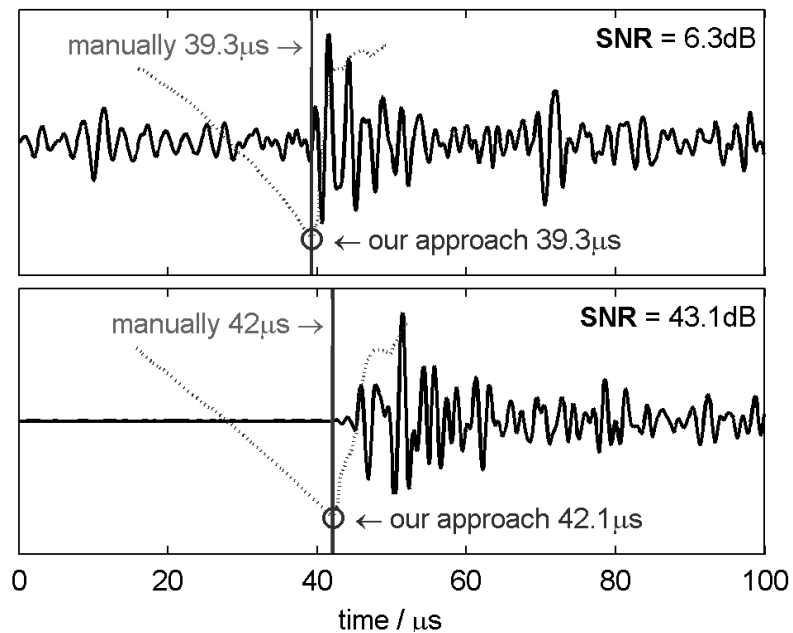


Fig. 6. Examples of first-arrival detection for varying signal-to-noise ratios in first test.

The proposed algorithm shortens the time window of an AE signal so that it ends in the informative part of the signal. The characteristic function is computed on the shortened signal and AIC picker is applied. The global minimum of AIC function determines the first estimation of the arrival time. The time window is shortened again and focused on the neighborhood of first estimation. The AIC picker is applied once again on CF in this shorter time interval. The global minimum of recalculated AIC function defines the arrival time of the AE event.

The approach was tested on a tensile test of a 25-layered SPCC/SUS420J2 thin plate. From the test, 25 AE events were chosen. Arrival times of these AE events were determined manually as well as automatically using our approach and Kurz's approach. Although we and Kurz et al. use the same Maeda's equation, the approaches differ in characteristic function. The choice of characteristic function is a crucial factor for the first-arrival detection.

The comparative investigation shows that 89% of arrival times were determined by our two-step AIC picker with deviation less than 0.5 μ s and 96% of arrival times were determined by our two-step AIC picker with deviation less than 1 μ s. It shows that the two-step AIC picker is a reliable tool for automatic identification of the arrival times for AE signals of varying signal-to-noise ratios.

Acknowledgement

The present research is conducted in LISM (Layer-Integrated Steels and Metals) Project funded by Ministry of Education, Culture, Sports, Science and Technology of Japan. Also, this research has been supported by Japan Society for the Promotion of Sciences (JSPS).

References

1. Sleemen R. van Eck T.: *Phys Earth Planet. Interiors* **113**, (1999) 265-275.
2. Leonard M. Kennett B. L. N.: *Phys. Earth Planet. Interiors* **113**, (1999) 247–264.
3. Zhang H. et al., *Bulletin of the Seismological Society of America* **93** (5), (2003) 1904–1912.
4. Maeda N.: *Zisin = Jishin* **38**, (1985) 365–379.
5. Kurz J. H. et al., *Ultrasonic* **43**, (2005) 538-546.
6. Allen R.: *Bulletin of the Seismological Society of America* **72**, (1982) 225-242.
7. Ito K. Enoki M.: *Mater. Trans.* **48**, (2007) 1221–1226.

SOME POSSIBILITIES OF AE SIGNAL TREATMENT AT CONTACT DAMAGE TESTS OF MATERIALS AND BEARINGS

PAVEL MAZAL¹, FILIP HORT¹, MARTIN DRAB² and TOMAS SLUNECKO²

¹Brno University of Technology, Technická 2, 616 69 Brno, Czech Republic;

²ZD Rpety – Dakel, Ohrobecká 408, 142 00 Prague, Czech Republic

Keywords: contact fatigue, bearing, AE signal, pitting

Abstract

This article compares recent application possibilities of the acoustic emission (AE) method for more specific identification of the stages of contact fatigue of materials. It focuses also on examples of results obtained by a new AE analyzer, which allows for continuous AE signal sensing. The results proved that AE techniques enable reliable recognition of running-in period, stabilized run and exact definition of initiation stage of surface damage, leading to pitting. First results obtained during AE signal sensing in the course of durability tests of axial and radial bearings in the contact fatigue laboratories of the Brno University of Technology are also presented.

1. Introduction

Endurance of materials against contact fatigue damage is one of the most important parameters for long-term reliable function of all types of bearings, gears and many other movable machine parts. The tests of contact fatigue of materials and bearing durability are conducted using equipments with test specimens of different form or real test bearing. In most cases the actual degree of damage is detected by sensing vibrations of the whole testing mechanism. After reaching a predefined level of vibrations, the machine is switched off and the sample or bearing is examined in detail. Although these testing machines are equipped with sensitive sensors, the results are not fully satisfactory yet. One potential improvement in the identification of damage degree is the application of acoustic emission (AE) method. This method can provide detailed information about periods of changes of damage mechanism. So far, it is difficult to precisely assign the observed changes of AE signal to the processes in material. One of the reasons is of course the limited knowledge about mechanisms of contact damage, and another one is the range of information available in AE signal.

An important reason of the loss of decisive properties of all types of bearings is the inception of point contact damage, so-called pitting, on some of its elements. Contact damage is caused by cyclically repeating processes in surface layer of material by mutual dynamic load of two bodies. Damage of surface layers causes the inception of microcracks in places of maximum sheer stress, by progressive separation of damaged surface layers and by inception of holes on the surface (Fig. 1). In the beginning, this fatigue damage results in decrease of functional properties of damaged part; however, emerged surface hole may gradually create a center of fatigue crack, which successively enlarges to the whole section of the part.

In frame of the project of Ministry of Industry and Trade of the Czech Republic, “Research of new methods of measuring and evaluation of acoustic emission signal”, a new type of analyzer has been developed that is capable of registering the whole AE signal. In this paper the

information about the processes of contact damage of materials obtained by standard methods and by this new analyzer are compared.

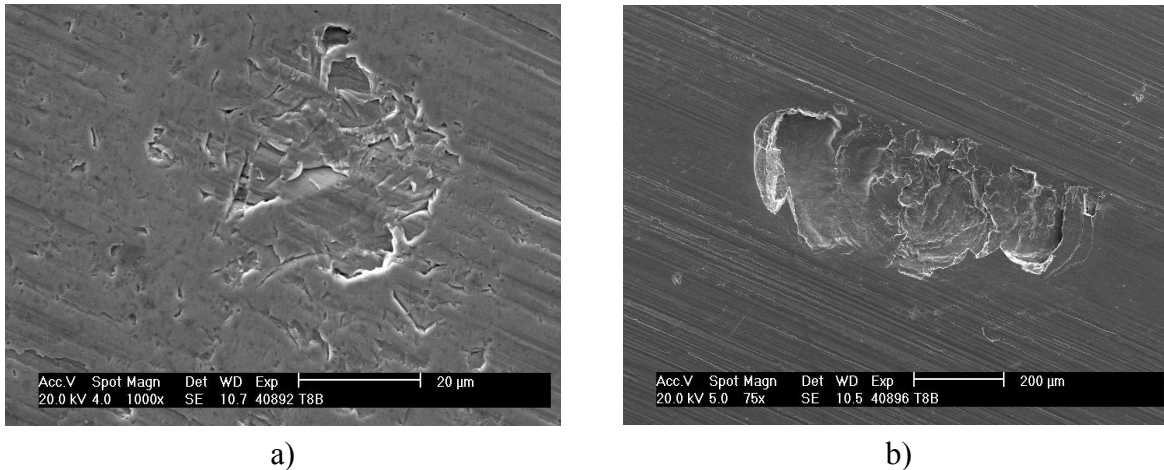


Fig. 1. Example of contact fatigue microcracks (a) and pitting damage (b) on the surface of the specimen from bearing steel (100Cr6) loaded in Axmat testing device.

Compared with classical material testing, contact fatigue is more complicated, as there is always mutual contact of at least two bodies. In case of development of contact damage, AE signal contains not only “standard information” about the activity of the defect itself, but, taking into account the change of quality of contact surface, the vibrations of the system grow and noise in the testing equipment grows as well; all this is reflected in the detected signals. We also cannot forget the important influence of the lubrication of the whole system. With respect to the sensitivity of AE method, the importance of quality of setting is apparent – choice of parameters, sensors, signal amplification, sensor locations, quality of contact between sensor and surface, etc. [1-3].

2. Experimental equipment

Three basic appliances are used for contact fatigue tests of materials and for tests of bearing life (principle of all these stations were described in other contributions [4, 5]):

- a) Axmat station – in this case, 21 balls are placed in guiding ring; they roll away on the surface of firmly fixed disc-shaped sample from tested material. This device was modified also for axial bearing tests. In this case, ring, balls and material sample are replaced by the tested axial bearing (Fig. 2a).
- b) R-mat station (Fig. 2b) – two rotating discs roll away on the surface of cylindrical sample.
- c) SA 64 testing equipment (Fig. 2c) is devoted for tests of radial bearings durability.

Sensed AE signals are amplified in preamplifier and subsequently processed in AE analyzers. Our standard AE analyzers (Dakel Xedo®) enable dividing detected signals into 16 elective energetic classes, so-called levels. In order to highlight the AE signal change, it is possible to choose only suitable levels. The sensing software Daemon® was used for sensing and evaluation of AE signal. After completion of the tests, the signal was processed by software DaeShow®. The examples of AE signal treatment are presented on Figs. 4, 5, 9 and 11.

In a part of experiments, we had the possibility to use the newly developed AE analyzer named DAKEL IPL®. It is a new state-of-the-art system for continuously recording and process-

ing data from the AE sensors. Compared to the commonly used AE analyzers, the major advantage of the DAKEL IPL is the capability of continuously sampling and storing the whole AE signals for as long as there is a disk space to store them. With the biggest currently available fast disks on the market having the limit of about 1 TB, we can store as long as 17 hours of 5-channel recording and when using RAID arrays of such disks it can be much more.

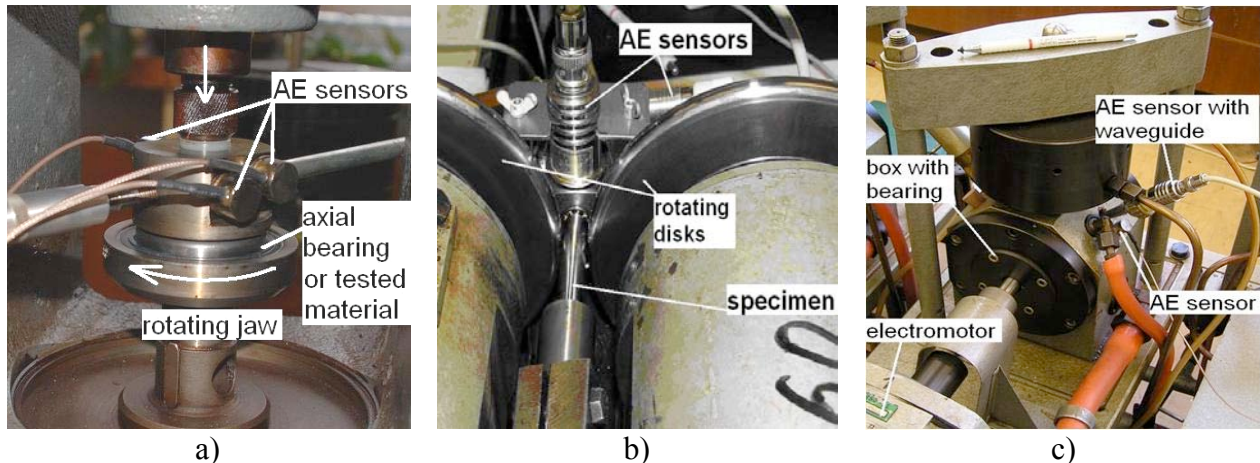


Fig. 2 a) device Axmat with axial bearing, b) detail of working part of R-mat device, c) testing station SE 64 for radial bearings durability tests.

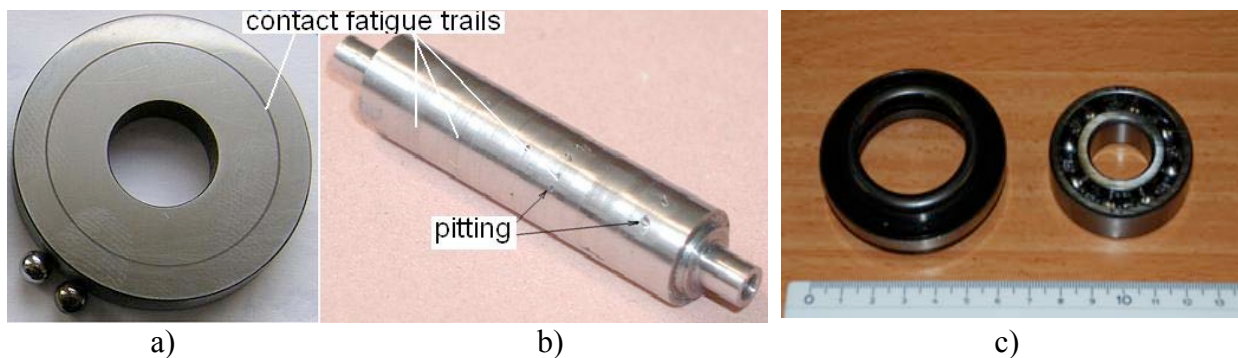


Fig. 3 Typical shapes of the tested specimens a) for Axmat device (diameter app. 40 mm), b) R-mat (diameter 10 mm) and c) tested axial and radial bearings.

The device has a total of 5 synchronous analog input channels, simultaneously and continuously sampling at 2 MHz. Out of these, 4 channels are generally used to sample the AE signals and the last channel is used for synchronous monitoring of any external physical parameter that is used to excite the testing object (such as the loading force, pressure, temperature, etc.). This comes handy when you need to correlate the AE signals to some external events in time.

The results obtained from DAKEL IPL device are commented later in the text. Some examples of the processed data from contact loading of material (on Axmat testing device) will be shown in Figs. 6-8. First results obtained on radial bearings are collected on Figs. 13 and 14.

3. Experimental results

3.1 Contact fatigue of materials:

Observed changes of the number of overshoots over adjusted levels of the signal during a test on Axmat and R-mat stations are shown in Figs. 4 and 5 [5].

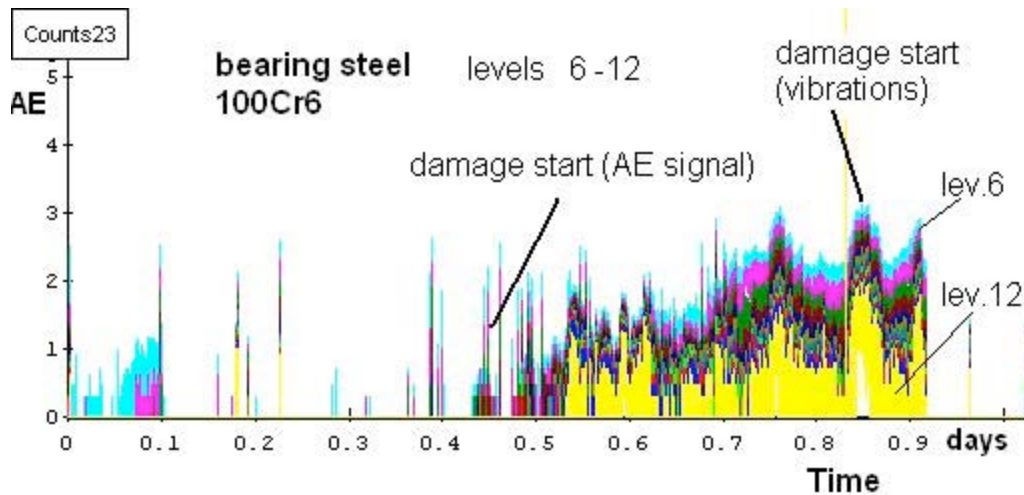


Fig. 4. Example of observed changes in the number of overshoots over adjusted levels of the signal during a test on Axmat station (bearing steel 100 Cr6).

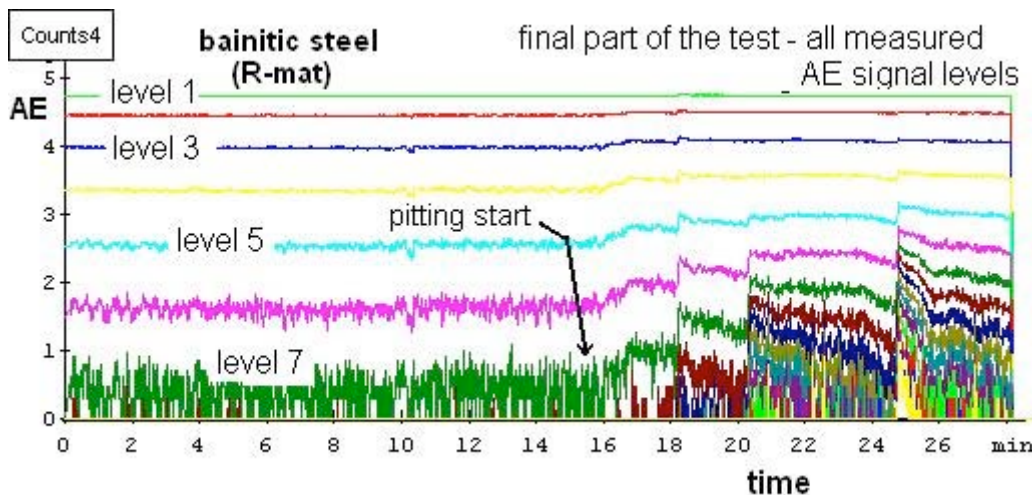


Fig. 5. Record of the final part of contact damage test of a bainitic steel on R-mat testing station.

These “simple” and basic records of AE signals enable us to obtain detailed description of the character of the damage, which emerges either as gradual breaking of the surface layer of the material and “leap” extending of pitting or possibly by widening of number of damaged places in monitored contact trace. When the test is finished, it is possible to determine the type of damage by visual observation.

Figures 6, 7 and 8 show the examples of latest records, which were obtained by DAKEL IPL, which is capable of continuously sampling and storing the whole AE signals. Changes of spectral amplitude (Fig. 6) should be a very important parameter for differentiation of damage stages. The possibility of displaying the progress of the amplitudes on selected frequencies in time is also useful (Figs. 7 and 8). In the present case, it is clear that for the identification of contact damage initiation in steel, it is suitable to observe the change of higher frequencies (in this case above ~180 kHz) in time. For comparison, the record obtained during grey cast iron contact fatigue test is also shown (Fig. 8). In this case the mechanism of damage is considerably different from steel. As a result being a relatively soft material, a deep trail with a plenty of small damages appears. Gradually the contact pressure decreases and the period of stable damage appears.

Records on levels 50 to 70 kHz correspond to this. However, unlike the case of steel, the higher frequencies do not provide any information about damage propagation.

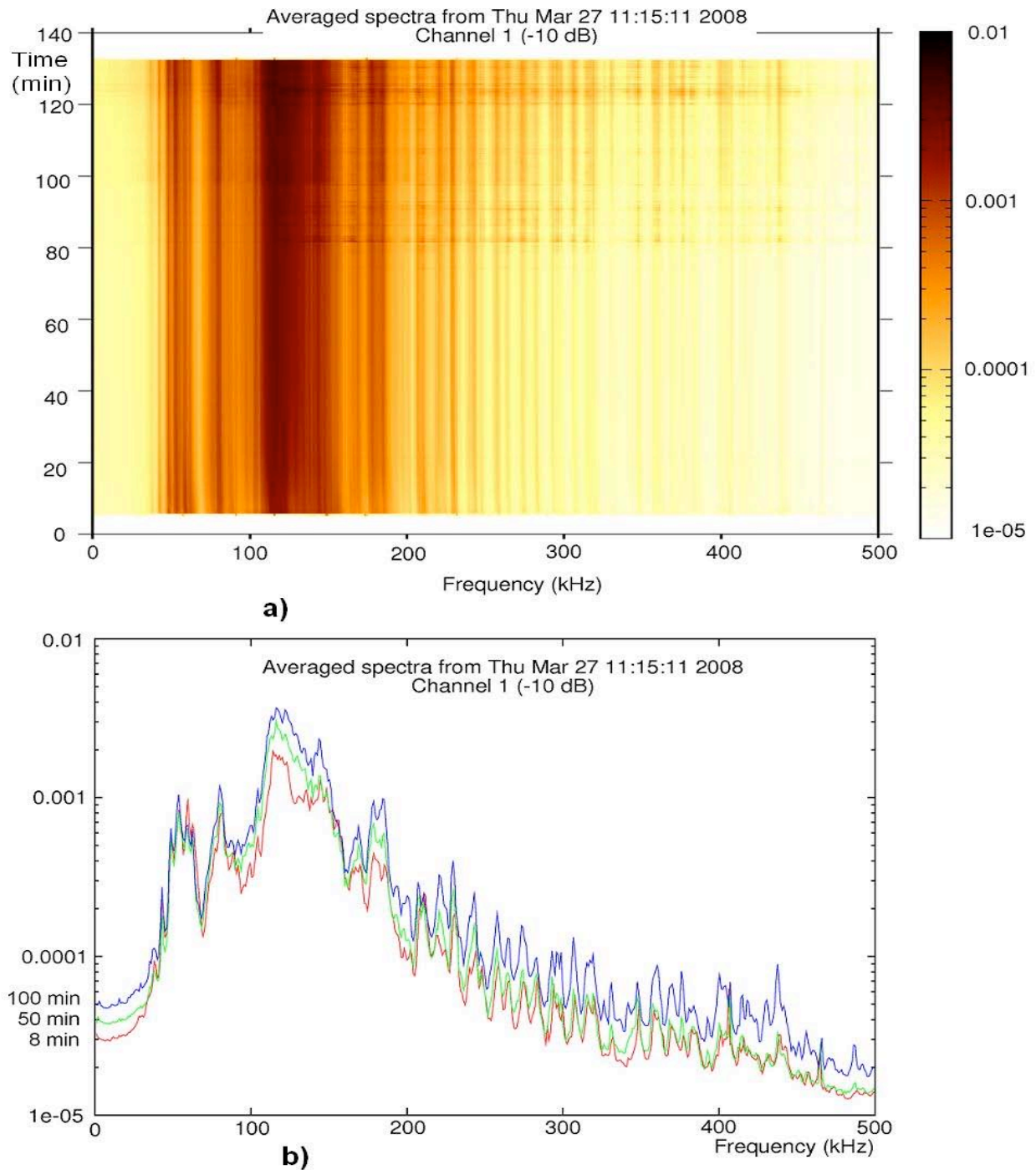


Fig. 6. a) Continuously sampled signal allows us to create a 3D map of continuously evolving averaged spectrograms in time during the whole measurement (or any part of it that we choose). The third dimension on this figure represents the spectral amplitude and is represented by the color according to the displayed scale on the right side of the graph. b) This is a horizontal cut of the 3D spectral map from Fig. 6a at 8 min, 50 min and 100 min in time. This is the common way to display the spectral amplitudes. Testing device Axmat and tested material – carbon steel.

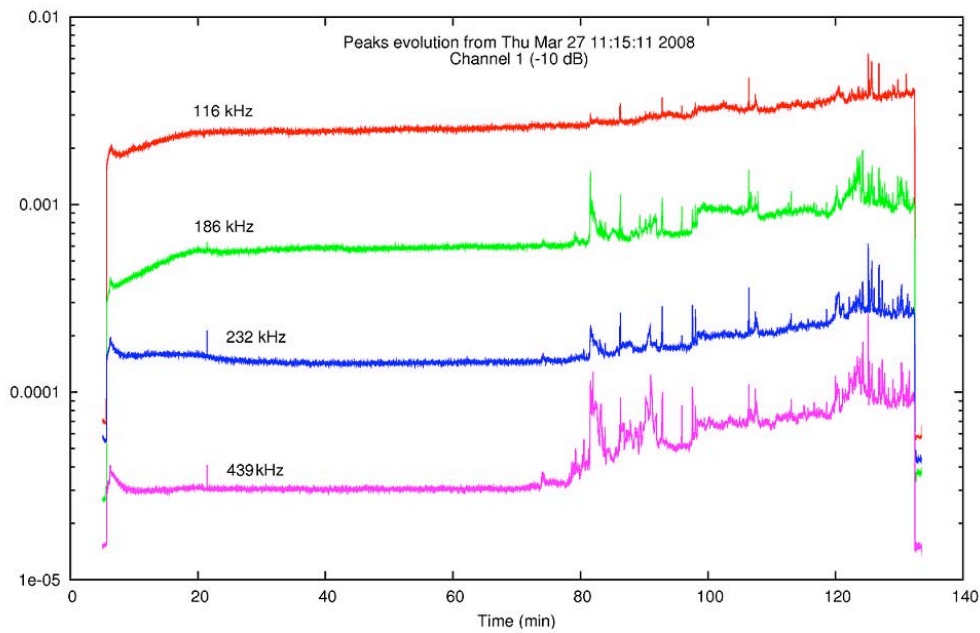


Fig. 7. Displays of a progress of the amplitudes on selected frequencies with time for carbon steel (the vertical cut of the 3D spectral map from Fig. 6a in this case at 116 kHz, 186 kHz, 232 kHz, and 439 kHz frequencies).

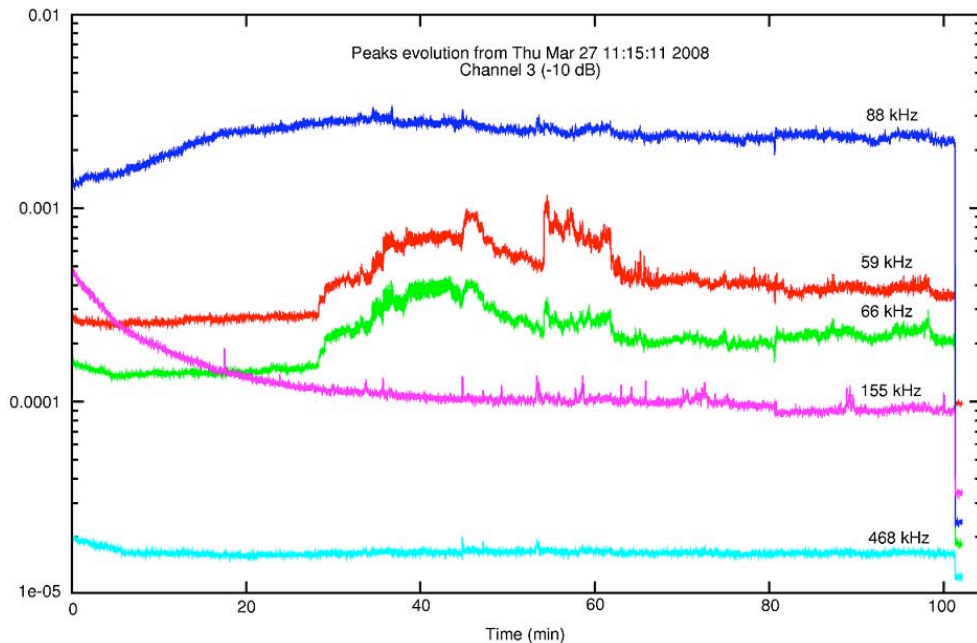


Fig. 8. Record of the amplitudes on selected frequencies with time for grey cast iron is shown for comparison. Frequencies 59 kHz, 66 kHz, 88 kHz, 155kHz and 468 kHz are presented in this case.

3.2 Tests of bearings durability:

Compared to contact fatigue testing, the tests of real bearings present many technical problems. We have conducted a series of successful experiments with axial bearings on a modified Axmat testing station (Fig. 2a). An example of record of the final part of test of a bearing with pitting on both outer and inner ring is presented on Fig. 9. and Fig. 10 shows details of defects.

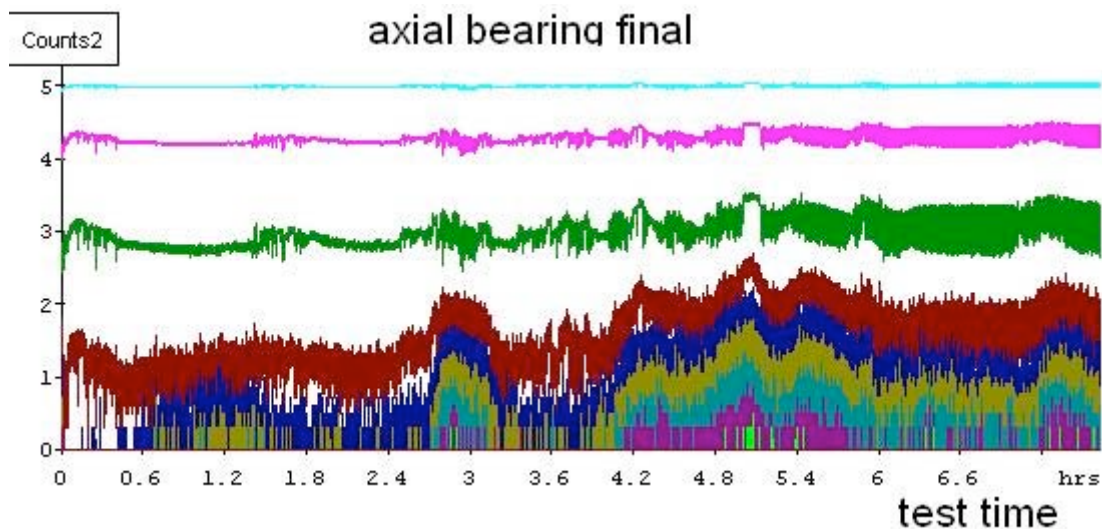


Fig. 9. Example of standard record of AE activity on all levels in the propagation stage of contact damage of axial bearing damage – final part of the test.

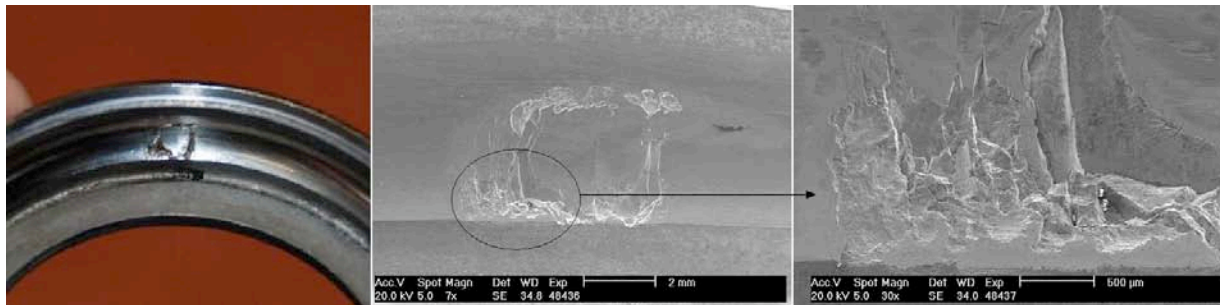


Fig. 10 Overview and more detailed photos of a defect of the outer ring of an axial bearing.

Most recent group of experiments was carried out for durability testing of radial bearings (Fig. 2c). Sensing of AE signal is complicated by position of the tested bearing inside the testing station, so it is not possible to place the AE sensors to its direct vicinity. In this case we use waveguides, whose one end touches the outer ring of the bearing, which is fixed in the testing device and the other end is connected to the sensor. Another sensor is placed on the surface of the testing station.

Despite the mentioned complications with AE signal sensing, we have managed to find optimal setting of the measuring chain and to process some records of high-quality and damaged radial bearings. Example of basic comparison of records from the initial stage of loading of both bearings is depicted on Fig. 11a.

Notably higher level of signal is apparent in the case of the second (damaged) bearing. After disassembly it was found that some balls in this bearing were “low-quality” (Fig. 12) and so it was the cause of high AE activity. After further analysis of AE events, differences in their frequency characteristics were found (Fig. 11b). In the case of the high quality bearing the maximum frequencies were ranged approximately between 45 and 120 kHz, while in the case of the bearing with damaged balls the AE events had maximum on the level at approximately 83-87 kHz.

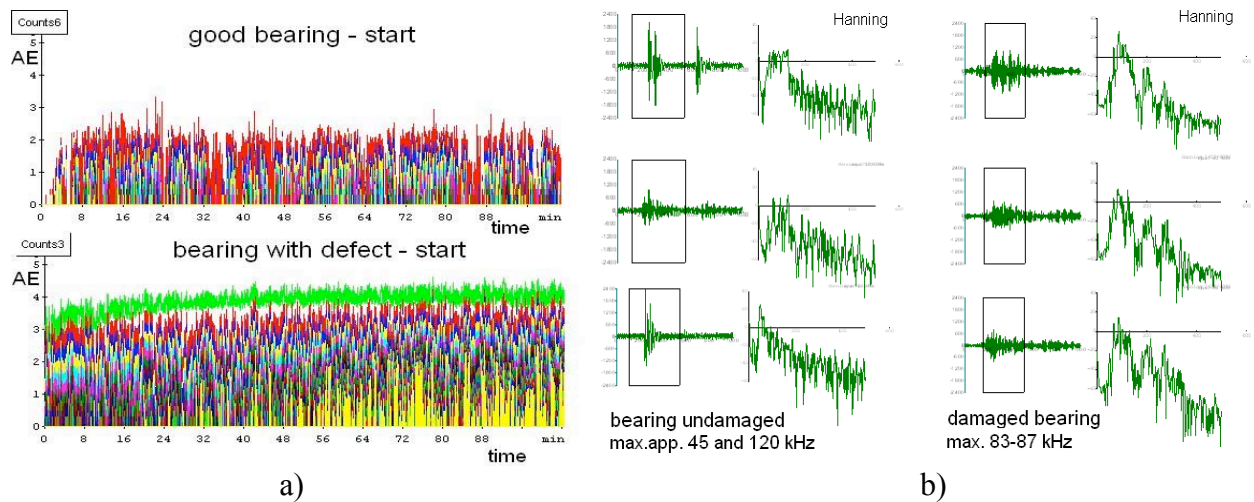


Fig. 11 a) Example of AE signal records from the initial phase of a test of high-quality radial bearing and from a low-quality bearing (with defect), b) typical examples of AE events and their frequency spectra with maximum - Dakel Xedo device and DaeShow software.

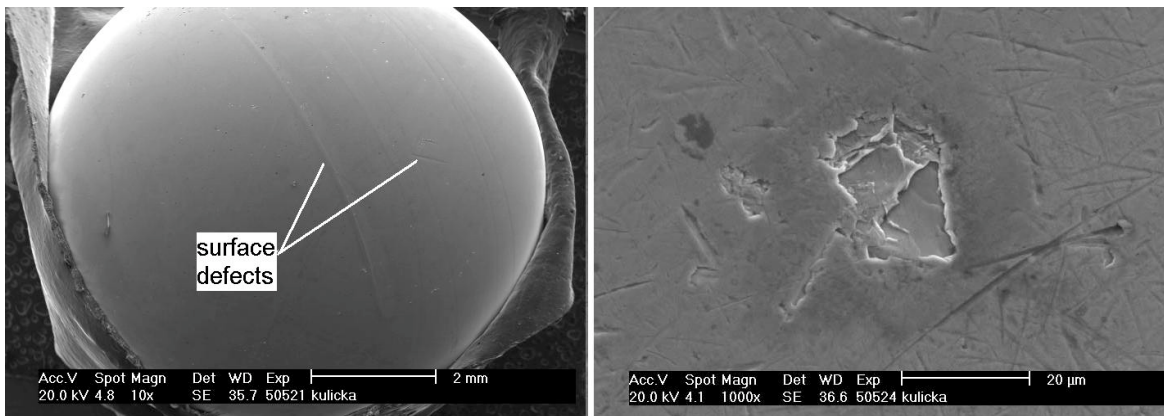


Fig. 12 Damaged ball – the “cause” of high activity of AE signal at damaged bearing from Fig. 11 and other defect on the ball surface.

At the end of 2008, the analyzers with continuous sampling and storage of AE signals (DAKEL IPL) were used also for tests of radial bearings on stations SA 64 (Fig. 2c). Because the tested bearing is located inside the testing station, we have to use sensors placed on waveguides. Here, magnetically held sensors were placed on the surface of the station body. That is why it is necessary to amplify the AE signal more than usual and it can contain undesirable noise. Despite that even in this case it is possible to observe significant changes of signal during the initiation and propagation of bearing damage. The changes are perceptible much earlier than they can be recorded by standard vibro-diagnostics. Examples of the records are shown on Figs. 13 and 14.

4. Conclusions

In our experiments, AE method succeeded in distinguishing the characteristic stages of process of material damage by contact loading, which verified the possibility of improving tests of contact fatigue resistance of materials.

The situation with AE diagnostics of real bearings damage is much more complicated, as the bearings are composed from many parts which are in contact and especially it is usually not possible to place the AE sensors directly on the bearing surface. For this reason, the signal contains

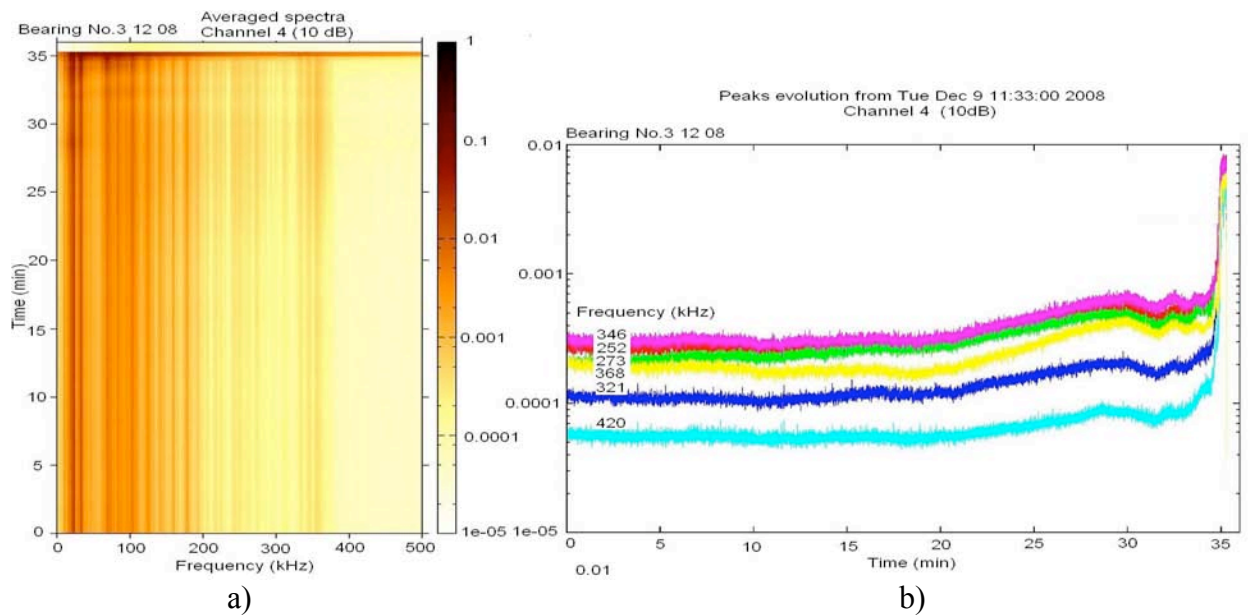


Fig. 13 a) Continuously sampled AE signal (3D map) of spectrograms with time (see also Fig. 6a) during the final part of a real bearing (type 6204) measurement. b) The record of the amplitudes on selected frequencies with time for the same part of the measurement as in a).

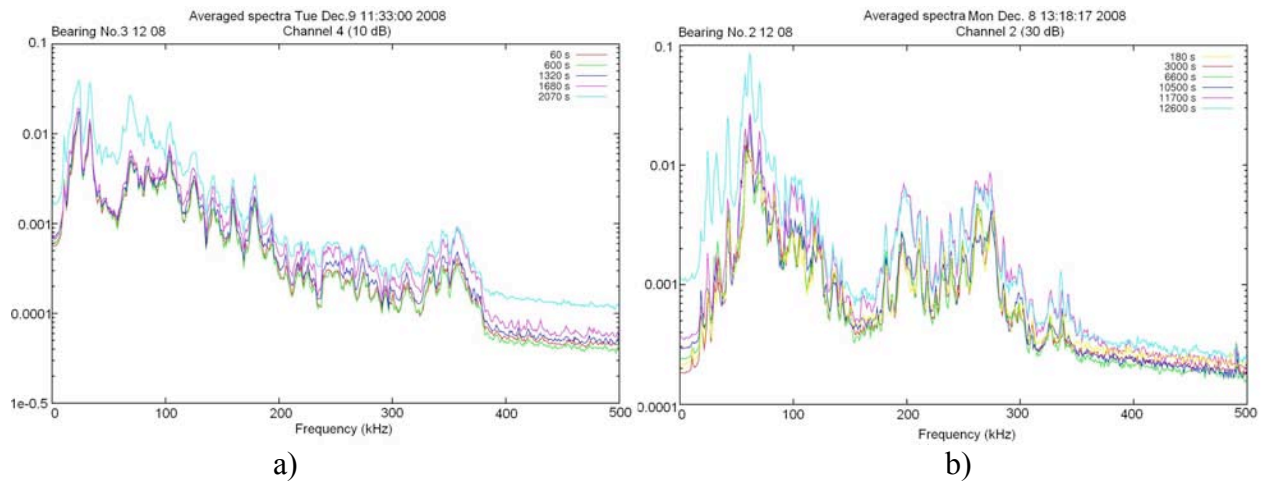


Fig. 14 Examples of horizontal cuts of the 3D spectral maps from various test times of real radial bearings (type 6204): a) bearing No. 3 from Fig. 13. b) bearing No. 2 with different type of damage.

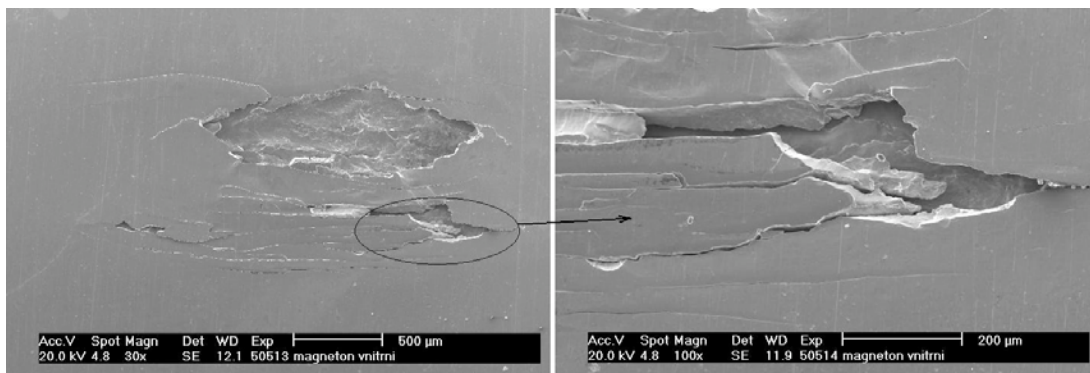


Fig. 15 Examples of contact damage of the inner ring of a radial bearing.

much more undesirable disturbances, which makes adjusting of measuring chain more difficult. Nevertheless the examples shown in this paper suggest that it is possible to identify bearings with damaged parts. After the evaluation of a number of data files, it would be possible to work out simplified way of signal processing of selected signal characteristics that would correspond with real damage of diagnosed bearing. This simplification will result into one-purpose analyzers that will be a part of permanent diagnostic systems used on some important bearings, e.g. in transport technology, in technological lines and energetic devices – in order to optimize intervals of planned maintenance and temporary stoppage of operation connected with it (e.g. turbines mounting, rolling lines, etc.).

Acknowledgement

This work has been carried out in the framework of the project of MPO CR F1-IM3/136 “Research of new methods of measuring and evaluation of acoustic emission signal” (bearings) and as a part of the solution of the project of Grant Agency of CR nr. 106/06/0343 “Research of stages of contact damage using the method of acoustic emission” (contact fatigue of materials).

References

- [1] Yoshioka, T., Takeda, M.: Clarification of Rolling Contact Fatigue Initiation using Acoustic Emission Technique. *Lubrication Engineering*, **51**(1), 1995, 41-44.
- [2] Yoon, D.J. et al.: Early detection of damages in journal bearings by acoustic emission monitoring. *Journal of AE*, **13**(1/2), 1-10, 1995.
- [3] Rowland, C.H. et al.: Condition monitoring using acoustic emission on multiple roller bearings in consignia’s letter sorting machines, In: *Proc. EWGAE 2002*, Vol. 2, p. 131, Prague, 2002.
- [4] Zykova, L., Mazal, P., Pazdera, L.: Identification of Contact Fatigue Stages with Acoustic Emission Method. In: *European conference on NDT*, Poster 4, 8 pages, 2006, DGZfP, Berlin, Germany, CD edition, ISBN 3-931381-86-2.
- [5] Mazal, P.: The comparison of AE data acquisition at Axmat and R-mat contact fatigue stands. In: *Defektoskopia 2007*, pp. 5-11, NDB Bratislava, Tatranska Strba, Slovakia, ISBN 978-80-968724-7-3.

LASER CUTTING AND ACOUSTIC EMISSION SIGNALS

TOMAŽ KEK and JANEZ GRUM

University of Ljubljana, Faculty of Mechanical Engineering, Askerceva 6, 1000 Ljubljana,
Slovenia

Keywords: Burst acoustic emission, laser cutting, PZT sensor, dross

Abstract

The paper presents results of an analysis of acoustic-emission (AE) signals obtained during laser cutting of a steel plates, which are frequently used in the production of automotive body components. In the course of laser cutting, continuous signals, which are related to the quality achieved of the laser cut, are measured. After laser cutting characteristic AE bursts in the specimen material, which are results of a thermal influence, can be detected. The presence of dross is an important indicator of poor quality of laser cutting. The investigation on laser cutting was conducted on an unalloyed steel DC04 sheet and on austenitic stainless steel X5CrNi18-10 sheet of 1.5 mm in thickness. The same physical mechanism in the cut formation at both steels, however, resulted in a considerable different cut quality, which was indicated by the AE signals captured after the cutting process.

Introduction

Laser cutting of unalloyed and stainless steels using oxygen is a well-established cutting process in industrial applications and capable of satisfying requirements of numerous users in terms of production costs and quality [1]. In laser cutting of stainless steel with oxygen, however, the dross formation at the lower edge can hardly be avoided, which results in poorer quality of the cut made. The cutting mechanism is the same as in cutting of unalloyed steel, but during cutting stainless steel oxygen will exothermically react both with iron and chromium, and other alloying elements in steel. The oxidation process, however, is less efficient than in cutting of unalloyed steel.

The melt solidification on the cut face and in the dross, and subsequent cooling, upon the termination of the cutting process, results in various phenomena occurring in the material, which can be sensed as AE bursts. The AE bursts are caused by cracking of the oxide layer due to the difference in the coefficient of thermal expansion of the oxide layer and that of the sheet material [2]. The AE bursts are produced also by crack and microcrack initiation and propagation. Microcrack initiation or propagation shows in momentary energy releases at the microscopic level, which results in elastic waves in the material. A metallographic analysis of the laser-cut surface will confirm that the point of initiation and propagation of microcracks is usually limited to the dross and to the lower edge of the laser cut.

The occurrence of AE signals can be attributed to phase changes, i.e. martensite formation after rapid cooling of austenite [3]. The AE burst signals with lower amplitude values of a voltage signal may result from the events related to the micro-plastic deformation of the material, the nucleation and sliding of dislocations [4]. Acoustic emission may result also from bonding defects during dross cooling, porosity and micro-cavities in the solidified material. An evaluation should also consider reflection of the AE signals from the specimen walls or other obstacles [5].

More information on the influence of the laser cutting conditions on continuous AE signals is given in Refs. [6-8].

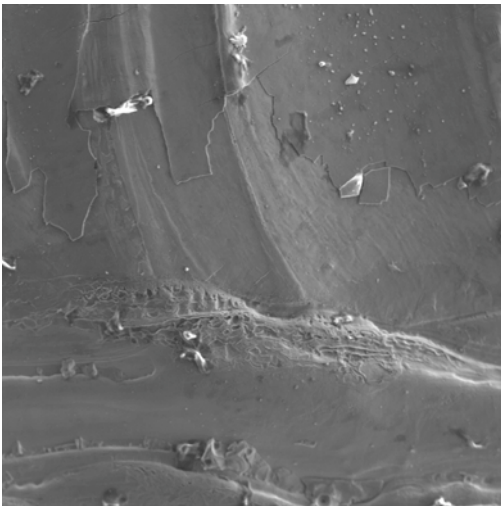


Fig. 2. Cracked and peeled-off oxide film at laser-cut face (DC04).

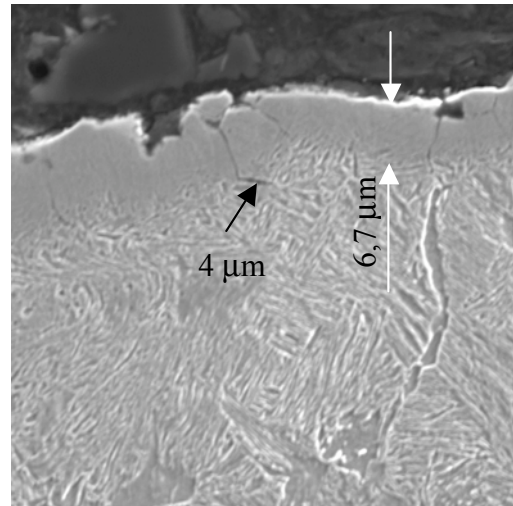


Fig. 3. Crack in oxide film resulting in crack in substrate (DC04).

When cutting is stopped, acoustic emission in the form of bursts with appertaining signal duration can still be captured. The signal duration is a time interval between the first and last transition of the absolute signal voltage value across the amplitude threshold set, i.e. 0.1 mV (40 dB).

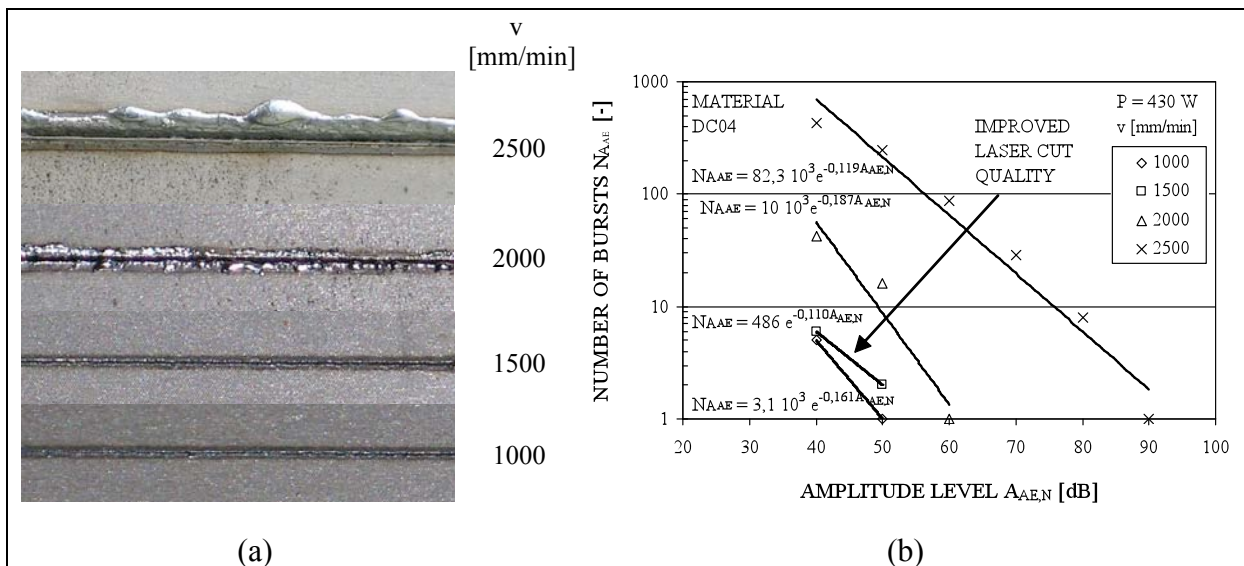


Fig. 4. a) Images of dross at lower cut edge at cutting with different cutting speeds and power $P = 430$ W and b) number of AE bursts N_{AE} above various amplitude levels of AE signals $A_{AE,N}$ immediately after termination of laser cutting of sheet DC04 with power $P = 430$ W.

The presence of dross at the lower cut edge is shown by AE bursts after the termination of laser cutting. Figure 4 shows amplitude distribution of AE burst signals immediately after the termination of cutting of the flat sheet in the duration of 30 s. The number of the bursts exceeding the chosen signal amplitude levels $A_{AE,N}$, i.e. 40 dB, 50 dB, ..., 90 dB, is marked N_{AE} . The number of the bursts N_{AE} at the signal amplitude level of 40 dB is thus equal to the

total number of the bursts $N_{AE,30s}$ in a time period of 30 s immediately after the termination of laser cutting. It was found that the mutual dependence of the number of bursts N_{AAE} and the signal amplitude levels $A_{AE,N}$ can be described with an exponential function. A greater distance of an exponential trend line from the origin of the coordinate system shows the higher AE activity. Higher AE activity is related to the dross formation at the lower laser-cut edge.

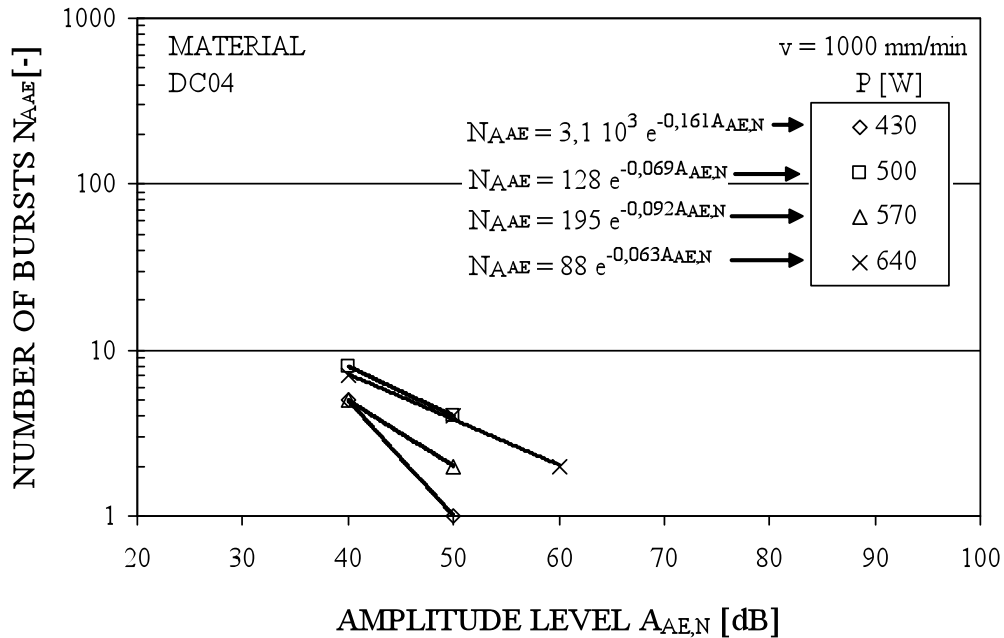


Fig. 5. Number of AE bursts N_{AAE} above various AE signal amplitude levels $A_{AE,N}$ after laser cutting with cutting speed $v = 1000$ mm/min.

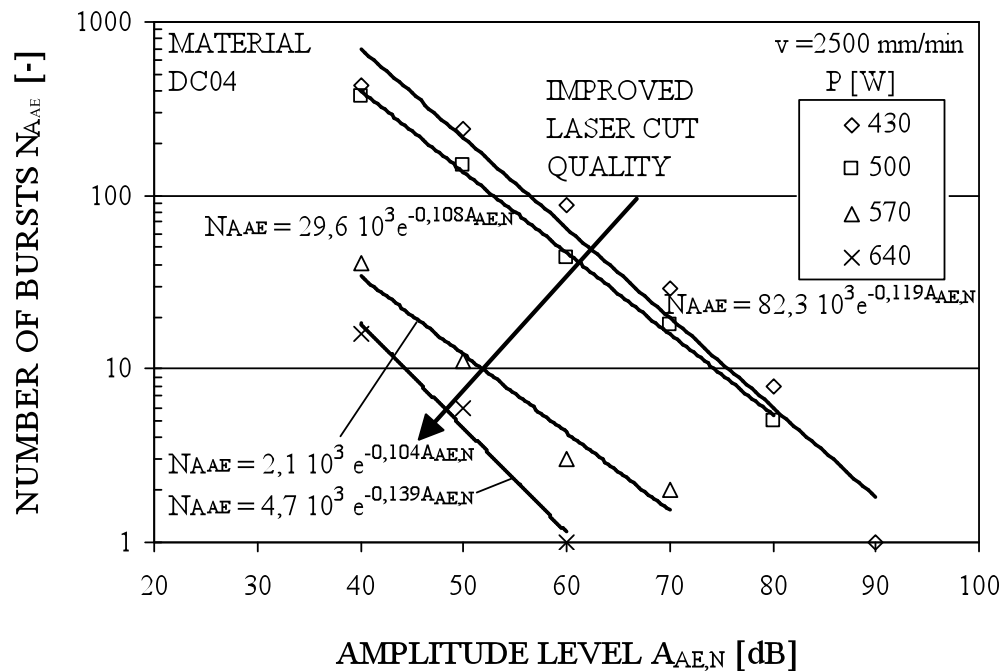


Fig. 6. Number of AE bursts N_{AAE} above various AE signal amplitude levels $A_{AE,N}$ after laser cutting with cutting speed $v = 2500$ mm/min.

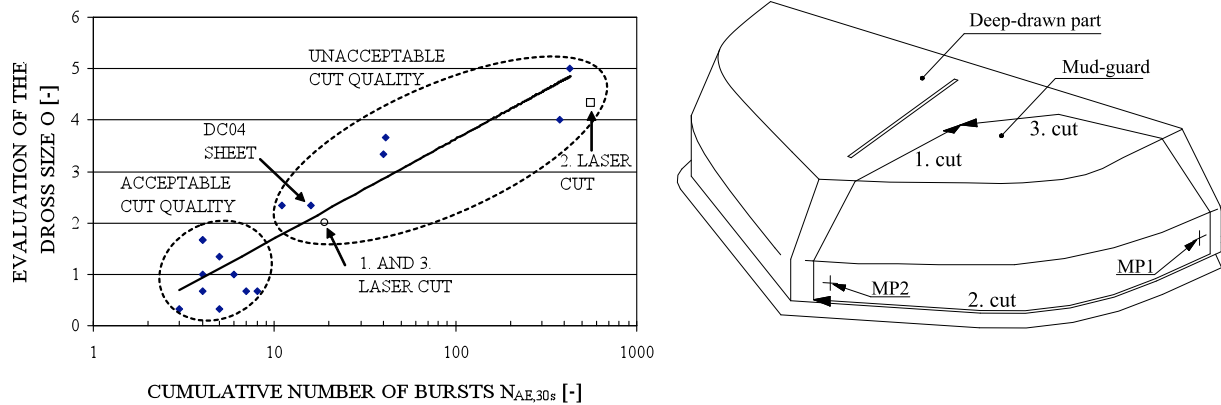


Fig. 7. Dependence between number of AE bursts $N_{AE,30s}$ and evaluation of dross size O .

A statistical analysis of the height and width of the individual characteristic portions of the dross measured at the metallographic specimens shows a strong dissipation of the dimensions measured. Consequently, it was decided to evaluate the dross size at the lower cut edge with the grades ranging between 0 (perfect – no dross) and 5 (poor – large dross). Grade 0 indicates a laser cut without any melt droplets at the lower edge whereas grade 5 indicates explicit dross as shown in Fig. 4 for cutting conditions of $P = 430$ W and $v = 2500$ mm/min.

A distinctive dross enlargement can be detected with smaller energy inputs of a laser-beam to the cutting front. Figures 5 and 6 show the amplitude distributions of AE burst signals in a period of 30 s after the termination of laser cutting taking into account minimum and maximum cutting speed used in experiment. With the lowest cutting speed and with all the laser-beam powers, the dross size and the related laser-cut quality are very similar, which is confirmed also by the closeness of the exponential trend lines. With the highest cutting speed and with the individual powers used, the quality of laser cutting differs strongly, which is confirmed by the number of acoustic-emission bursts sensed and the distance among the exponential trend lines.

Figure 7 shows a mutual dependence of a cumulative number of the bursts in a time period of 30 s after termination of laser cutting $N_{AE,30s}$ and the evaluation of dross size O in cutting of the flat sheet DC04. The enlarged dross will show in a higher cumulative number of bursts $N_{AE,30s}$. A poorer mutual dependence can be noticed only with lower values $N_{AE,30s} < 10$, i.e. in the range of acceptable dross size at the lower laser-cut edge. A circle in Fig. 6 marks number $N_{AE,30s}$ after the 1st and 3rd laser cut, and with a square number $N_{AE,30s}$ after the 2nd laser cut in cutting of a mud-guard from a deep-drawn part. A good agreement with the results of laser cutting of the flat sheet can be stated.

Laser Cutting of Austenitic Stainless Steel X5CrNi18-10

The laser cuts obtained at austenitic stainless steel differ from those obtained at unalloyed steels. With stainless steels a laser-cut surface does not show pronounced striations. Surface roughness of a laser cut at stainless steels results primarily from rapid solidification of a thin film of the melt flowing out during cutting. The laser-cut surface is covered by the oxide layer, consisting of a mixture of iron (Fe_2O_3) and chromium oxides (Cr_2O_3). The portions of the iron and chromium oxides in the oxide layer are approximately equal, which indicates higher affinity of chromium to oxygen atoms in comparison to iron atoms [1]. The ratio of iron to chromium in the substrate is namely $\sim 3.8:1$. The chromium content in the substrate is $\sim 18\%$ and that of iron

~69 %. During laser cutting the hot melt in the cutting front is exposed to the oxygen jet. The iron and chromium atoms enter an oxidation reaction. Greater affinity of chromium results in a higher chromium content at the outer layer of the melt flowing out and lower chromium content below the oxide layer. Below the oxide layer there is a quickly solidified layer of the unoxidized substrate. This results in a re-solidified melt holding to the substrate and the presence of dross at the lower cut edge. Larger amounts of the solidified oxides and of the substrate at the cut surface and in the form of dross at the lower cut edge in comparison with unalloyed steel were confirmed also by the results of the analysis of the AE bursts after the termination of cutting. Figure 8 shows the amplitude distributions of AE burst signals in a period of 30 s after the termination of laser cutting of the flat sheet of steel X5CrNi18-10. The results shown refer to cutting with a power $P = 430$ W and with various cutting speeds. Similarly as with DC04 steel, an exponential trend line can be attributed to the amplitude distributions. In cutting with different cutting speeds but with the same power, i.e. 430 W, different qualities of the cut will be obtained. The latter are indicated also by the appertaining reference images of dross at the lower cut edge. Similarly as with unalloyed steel, poorer cut quality will show in a larger number of bursts after the termination of cutting. A reduced cutting speed with the power chosen permits a higher energy input into the cutting front. This results in scarcer occurrence of dross and a cut of higher quality, which is confirmed by a displacement of the exponential trend line towards the origin of the coordinate system in the diagram of the amplitude distribution of AE signals.

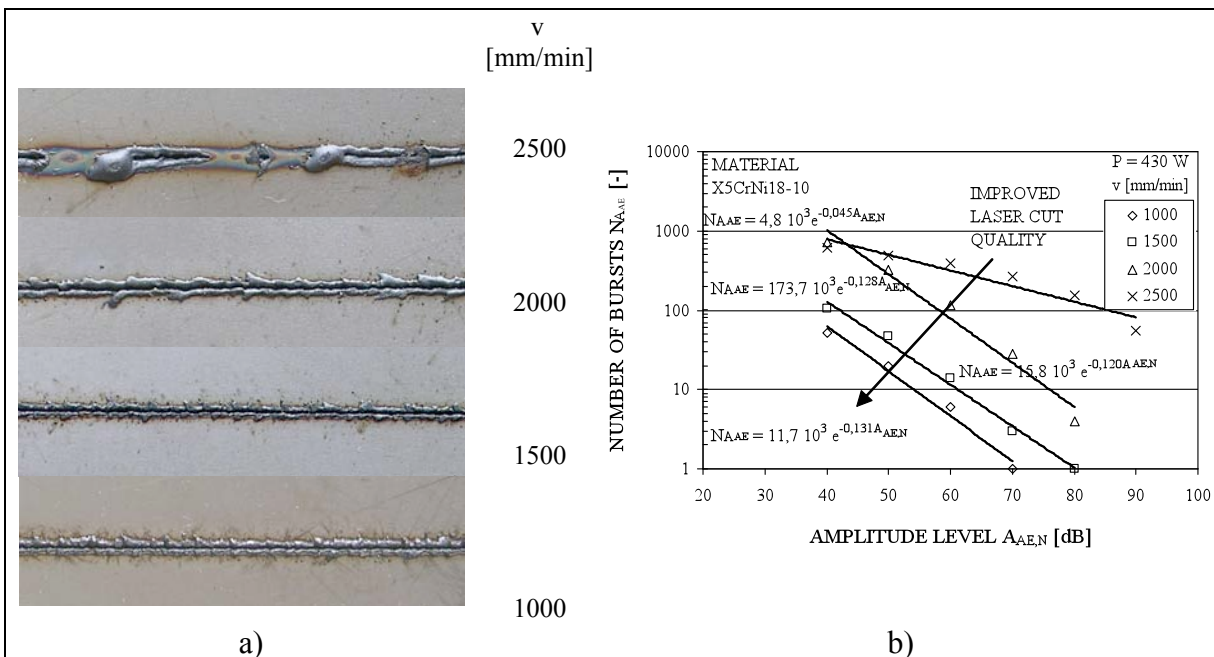


Fig. 8. a) Images of dross at lower cut edge at cutting with different cutting speeds and power $P = 430$ W and b) number of AE bursts N_{AE} above selected amplitude levels of AE signals $A_{AE,N}$ immediately after termination of laser cutting of sheet X5CrNi18-10 with power $P = 430$ W.

Figures 9 and 10 shows the amplitude distributions of AE burst signals in a period of 30 s after the termination of laser cutting taking into account the other cutting speeds. In laser cutting of the sheet X5CrNi18-10 under the cutting conditions chosen within a wide range of energy inputs, the occurrence of dross at the lower edge could not be avoided. Also, smaller differences in the dross size will occur, which is confirmed by the proximity of the exponential trend lines. The difference in the dross size with the chosen conditions of laser cutting of stainless steel

X5CrNi18-10 is less distinctive than in cutting of sheet DC04, which was confirmed also in the analysis of AE bursts.

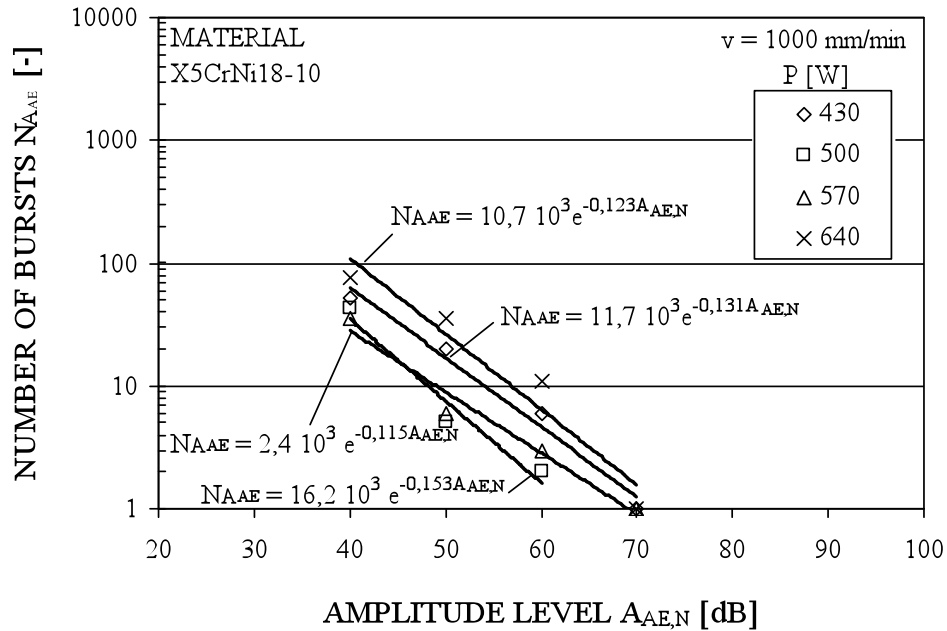


Fig. 9. Amplitude distribution of AE burst signals after laser cutting of austenitic stainless steel with cutting speed $v = 1000$ mm/min.

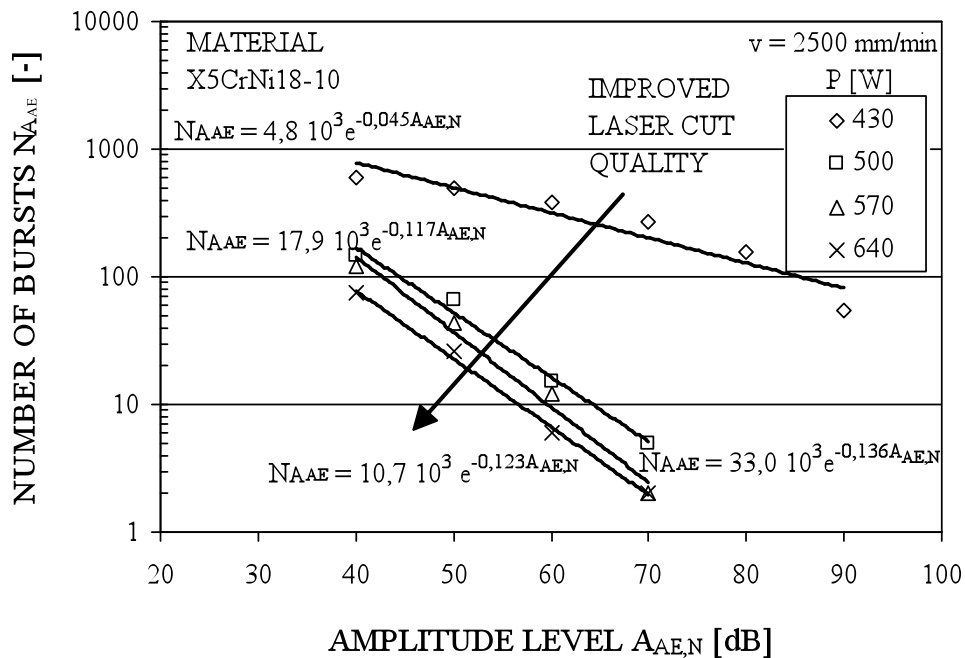


Fig. 10. Amplitude distribution of AE burst signals after laser cutting of austenitic stainless steel with cutting speed $v = 2500$ mm/min.

Laser Cutting of a Deep-drawn Part

With unalloyed steels, the acoustic emission after the termination of laser cutting of a sheet makes it possible to very successfully predict the quality of a laser cut under different cutting

conditions. Poorer quality is noticed with an increased number of AE bursts after the termination of cutting, which is shown in an increased activity n_{AE} . The increased activity n_{AE} is a result of the way the AE signals are treated. In the analysis the continuous signals were divided into defined time intervals of 0.1 s each. This means that the AE activity with the continuous signals does not exceed a value of 10/s. In case the AE bursts occur after the termination of cutting, the signal duration is less than 0.1 s because of which the AE activity can be essentially higher. During and after cutting mud guard out of deep drawn product (Fig. 11) at selected measuring points, i.e. MP1 and MP2, acoustic emission was monitored with the PZT contact sensor. The signals captured showed that the activity mightily increase after the 2nd cut. This indicates a poorer quality of the 2nd cut in comparison to the 1st and 3rd cuts (Fig. 12).



Fig. 11. Two mud guards were cut out of deep drawn product made of DC04 steel.

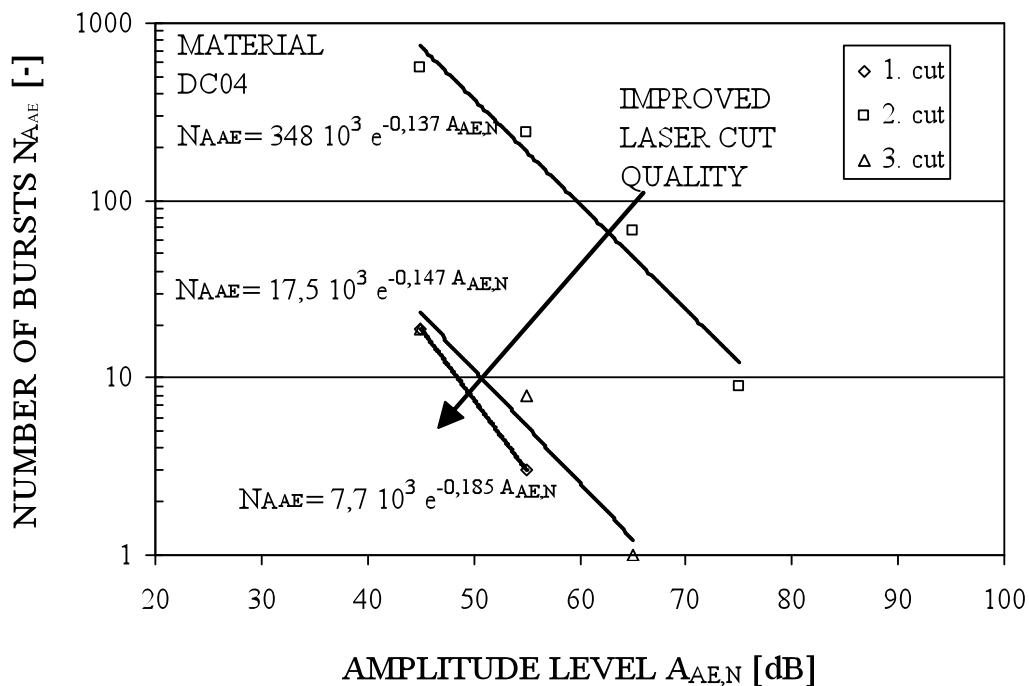


Fig. 12. Amplitude distribution of AE burst signals in laser cutting of mud-guard.

Conclusions

AE monitoring in laser cutting with the PZT contact sensors makes it possible to efficiently control the quality of laser cutting. A good agreement between the quality of a laser cut and the number of bursts after the termination of laser cutting of the sheet made of unalloyed steel DC04 was found. The results of AE measurements confirm that more intense acoustic emission after the termination of laser cutting indicates the presence of larger dross at the lower cut edge. Intense acoustic emission in the form of bursts is mainly attributed to cracking and peeling-off of the oxide layer formed at the surface of the laser cut and dross. The presence of dross increases the amount of the oxide layer.

With a quantitative way of treating AE signals, the determination of quality of the laser cut is more demanding in cutting of the sheet made of austenitic stainless steel X5CrNi18-10 under different conditions than in cutting of unalloyed steel. This is a result of the presence of distinctive dross under different laser-cutting conditions used, which is a result of an increased Cr concentration in the substrate.

References

1. Powell J.: *CO₂ Laser Cutting*; Springer-Verlag, London, 1993, pp. 16 – 22.
2. Beyer E. (edt.), *Schneiden mit CO₂ Lasern*, VDI-Technologiezentrum *Physikalische Technologien*, VDI Verlag GmbH, Düsseldorf, 1993, pp. 83-102.
3. P.O. Moore, R.K. Miller, R.K. Hill (eds), *Nondestructive Testing Handbook*, 3rd Edition, *Volume 6, Acoustic Emission Testing*, American Society for Nondestructive Testing, Inc., 2005, pp. 227-270.
4. Vallen H.: AE Testing Fundamentals, Equipment, Applications, NDT.net, **7** (9), (2002) (<http://www.ndt.net/article/v07n09/05/05.htm>).
5. Esmail E., Grabec I.: Quantitative Analysis of Acoustic Emission During Martensitic Transformation of the β -CuZnAl Alloy, *Journal of Physics D, Applied Physics*, **19**, (1986), 605 – 614.
6. Grum J., Kek T.: Quality assessment of laser cut based on captured acoustic emission signals, *4th International Conference on NDT*, Hellenic Society for NDT, October, 2007, Chania, Greece.
7. Kek T., Grum J.: AE signals as laser cutting quality indicators, *The 5th Int. Conference on Condition Monitoring & Machinery Failure Prevention Technologies*, 2008, Edinburgh, UK.
8. Slabe J.M., Kek T., GRUM J.: Measurement of acoustic emission and deformations in laser cutting of deep-drawn sheet parts, *International Journal of Microstructure and Materials Properties*, **1**, (2006), 383-396.

ONLINE MONITORING OF HOT DIE FORGING PROCESSES USING ACOUSTIC EMISSION (PART I)

ISLAM EL-GALY and BERND-ARNO BEHRENS

Institute for Metal Forming and Metal Forming Machines, Leibniz Universität Hannover,
An der Universität 2, 30823 Garbsen, Germany

Keywords: Hot die forging, online monitoring, forging defects, Mg-alloys

Abstract

Online process monitoring systems have been used on forming machines such as forging hammers or multi-stage presses for a good number of years. These systems typically measure forming forces, punch displacement or frame strains and compare them to learned target values trying to infer about the tooling or the product condition. In spite of the reached measurement accuracy, these methods are not physically capable or not sensitive enough to express many types of the tooling failures or product damage. Over the last few decades, acoustic emission (AE) has proved its strength and reliability as an online monitoring technique, and demonstrated a high degree of confidence in characterizing various phenomena related to material deformation, phase transformation as well as crack initiation and propagation at various scales.

In this paper, the concept of a forging support system, based on AE as an online monitoring and analysis technique, is introduced. The proposed support system relies on a damage and failure diagnosis module. This diagnosis module combines different AE analysis and clustering and pattern recognition methods to infer about different types of damage or failures taking place during the forging operation. AE patterns recorded from error-free forgings produced on faultless undamaged dies serve as a reference for the comparison. In addition, patterns generated by samples with pre-induced damages or artificial defects, or AE patterns collected during the deformation under predefined faulty machine or process settings are used as reference to assist in analyzing the complex patterns, which will be obtained during real forging processes.

Some preliminary results obtained during upsetting of magnesium-alloy specimens are presented. Three different geometries have been machined from AZ31 and AZ80 extruded bars. The specimens were upset at three constant levels of strain rates and at three different temperatures. The results reflect the influences of alloy composition, forming speed, and temperature on the obtained AE signals. In addition, different AE patterns could be correlated to the sequence of deformation and the evolution of damage based on the geometry of the specimen and the induced stress states.

Introduction

The forging industries are characterized by the existence of many medium-scale companies. These companies struggle to withstand in the market of today, while they are faced with the influence of high manufacturing and inspection costs, as well as the demanding requirement of their clients regarding the product quality and safety. Moreover, the current quality concept of “zero defect”, especially in case of safety components, requires 100% inspection in order to avoid defective products. The currently used off-line inspection procedures normally result in a huge percentage of defectives, which are manufactured in the time span that elapses between the

first occurrence of the defect and its detection. Furthermore, unscheduled interventions or stoppages of the automatic manufacturing lines add unexpected service and repair costs.

The incorporation of advanced online monitoring techniques into forging lines enables the integration of quality control/assurance into the production process itself. This helps maintain the required level of product quality, makes it possible to determine defective product and tooling damages as early as possible and at the same time provides a means to plan and schedule maintenance tasks [1, 2].

New technological developments suggest the use of AE to be the decisive step toward zero-defect production when tooling and products are completely online monitored [3-5]. However, there are still several challenges to be overcome to make AE a viable option in mainstream manufacturing facilities.

Acoustic Emission in Metal Forming Applications

During the second half of the 20th century, AE from materials was studied extensively. However, most studies were hardly complete due to the lack of experimental and theoretical resources [6]. Scientific research has shown that tooling failures in the form of cracking, breaking, chipping or wearing emit strong AE signals. These AE signals can be monitored for process deviations as well as for the investigation of dynamic behavior of materials [7]. Most of the published investigations have focused on correlating the recorded AE signals to the progress of some standard mechanical or technological tests such as tension, compression, wear, fatigue, or cupping tests [8-17]. Due to the development in the field of applying AE for monitoring sheet metal working processes, many machine manufacturers offer AE systems. On the other hand, very limited research work e.g. [18] has used AE to monitor real bulk forming processes. Most studies related to bulk forming processes were carried out by the manufacturer of AE equipment themselves, trying to draw the attention of the forming industries to the AE capabilities as an effective monitoring and analysis tool.

In a recent industrial oriented study by Skäre [19] information about the deep drawing process (wear of tool, penetration of lubricant, wrinkling of sheet material and cracking of tool or product) could be obtained with the aid of AE measurements. Adjusting the influence of boundary layer friction based on these measurements, mounting of tools and parts as well as correction of blank holder pressures can be optimized. It is important to mention here that the process parameters and environmental conditions (forming velocity, temperature, noise, etc.) by deep drawing processes cause little disturbances to the AE measurement when compared to those dominating in bulk forming or forging processes.

Monitoring high temperature forming processes using AE presents a further challenge. In spite of the direct influence of temperature on damage or transformation progress and consequently on the AE, this topic was avoided by most researchers due to its experimental difficulties and due to the lack of suitable hardware and software [6].

In different investigations, Hsu, Okajima and Ono [20-22] examined AE during deformation of several materials (austenitic stainless steels, short-range ordering alloys, bcc alloys) at high temperatures and were able to clarify plastic deformation behavior. In the most examined materials, the AE signal recorded at yield has shown higher signal strength proportional to the temperature increase, followed by considerable decrease at a limiting temperature [22, 23].

Through the examination of these studies, it is obvious that most tests were performed under quasi-static strain conditions and to a limited strain (max. 0.5). This means that the results of these investigations, despite their convenience for material characterization purposes, do not consider the most important aspects concerned by most forging specialists. For example, strain rates of more than 10 s^{-1} and strains that exceed unity are the usually experienced ranges in most forging processes. Fundamental studies and investigations, which consider these industrial requirements and which try to build the necessary know-how, are strongly required. Parasad [24] also reported on this requirement in his study about the feasibility of using AE for monitoring forming processes. Undoubtedly, the current development in both control and data acquisition technology enables more accurate experimental investigations at higher forming velocities and temperatures. This will certainly facilitate the AE analysis tasks performed under controlled testing conditions.

Over the past two decades, many studies at the Institute of Metal Forming and Metal Forming Machines (IFUM), Leibniz Universität Hannover, have been concerned with machine health monitoring, product quality control, as well as quality assurance throughout the whole process chains of both bulk and sheet metal forming processes [25-34]. For example, Terzyk [29] has examined the possibility of monitoring die-forging processes through the analysis of force and sound signals in the audible frequency range ($<20 \text{ kHz}$). The investigations showed that some process deviations could be determined through the evaluation of AE signals and guided with 3D-force measurements. For example, mass or position deviation of the pre-form, punch tilting or misalignment of upper and lower die halves could be to some extent detected. Since the deformation action, as well as crack initiation/propagation and phase transformation activities emit no relevant signal in the examined frequency range, only whole body vibration signals resulting from tooling/workpiece interaction or generated by machine element could be recorded. Detection of die or workpiece damage could not be realised in this work.

Strache [34] has used both force and AE sensors to monitor stamping (blanking) processes. The influences of sensor locations and assembly method on the recorded AE signals were examined. Using trend and envelope analysis algorithms, process faults like tooling fractures, sheet doubling, asymmetrical press loads could be accurately detected. In addition, it was possible to recognize the wear of the stamping tool based on the AE analysis.

Aim of Current Research

Based upon the AE state of the art presented, two main research objectives have been defined:

- First, test methods based on AE monitoring techniques have not, until now, been standardized. Therefore, the development (and standardization) of AE test methods to monitor standard mechanical tests under manufacturing-process-related conditions, and the construction of AE reference patterns and maps will present the milestones for the analysis of complex events encountered during the production process.
- Second, using signal analysis to develop AE method into an online monitoring system for forging process.

This presents several challenges in order to discriminate the AE data sets of interest. Moreover, forging processes are susceptible to high dynamic and thermal stress cycles. The distinction between different AE fatigue events and patterns caused by various mechanisms presents a significant and decisive factor for using AE to monitor forging operations.

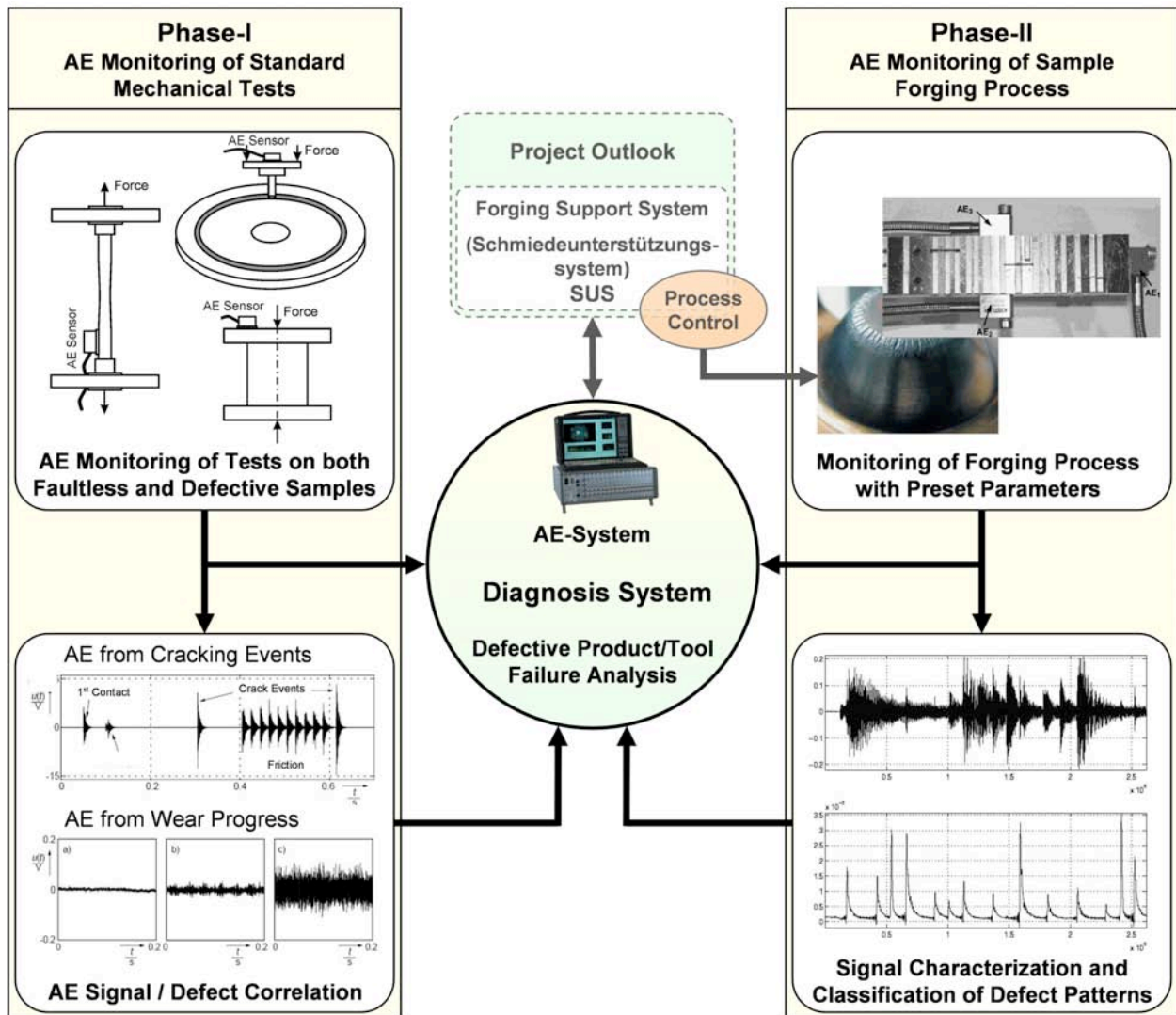


Fig. 1. Proposed online forging support system based on acoustic emission analysis.

The first phase of the current study, as presented in Fig. 1, will focus on conducting a sequence of AE monitored mechanical tests that simulate mechanical and thermal loading conditions prevalent in forging processes. The AE signals recorded during testing are used to build AE maps correlating different test parameters to the recorded AE signal parameters (arrival time, rise time, amplitude, duration, counts, hits, energy as well as their distribution and timing). Moreover, AE time patterns will be also recorded to help provide more accurate description for the progress of the forming process, determination of defect types and locations, as well as the identification of the different damage and failure mechanisms.

In the second phase of the project, and once reference patterns and AE maps are available, analysis of real complex AE patterns generated during forging operations should be analyzed, aiming at a complete online monitoring and fault detection of both tooling and products.

Part of the challenge in this project lies in correlating AE patterns to the corresponding generating defects. Another lies in identifying the meaningful AE events from a wide range of simultaneous events, which result from different external effects (i.e. machine elements and hydraulics, or environmental noise). Applying different time and frequency analysis methods as

well as clustering and pattern analysis techniques to complex processes presents more challenge, because every manufacturing process has its own unique characteristics and variables, which influence the AE patterns as the damages within the tooling or the product initiate and progress.

Experimental Setup

In order to realize the first objective of this study, a series of upsetting tests were performed on two magnesium alloys (AZ31, AZ80) and an aluminium alloy (Al7075) whose chemical composition are shown in Table 1.

Table 1: Chemical composition of the specimen materials.

Material	Mg%	Al%	Zn%	Mn%	Si%	Cu%	Cr%	Fe%	Ti%
AZ31	95.87	3.1	0.8	0.23	0.05	0.02	-	-	-
AZ80	90.84	8.3	0.64	0.22	-	-	-	-	-
Al7075	2.4	89.9	5.8	0.025	0.06	1.45	0.2	0.15	0.015

To study the influence of geometry and the sequence of deformation as well as the damage mechanism on the generated AE, specimens with three different geometries have been used. The dimensions and geometries of the specimens are shown in Fig. 2. All specimens have been upset from 18 to 5 mm in one or two consecutive stages. The cylindrical specimens were used to evaluate the role of standard specimen geometries in characterizing upsetting processes. The modification in the specimen geometry through the introduction of collar or through recessing and drilling was performed to develop stress concentration areas, which are more vulnerable to damage. The specimens were upset at three different temperatures (200, 300 and 400°C). To assure nearly constant temperature during the test, the specimens were heated and compressed within a hardened steel container (Fig. 3c).

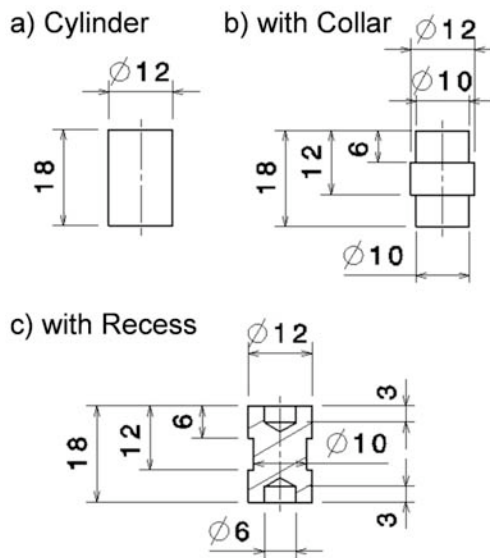


Fig. 2 Geometry and dimension of the specimens used for upsetting test.

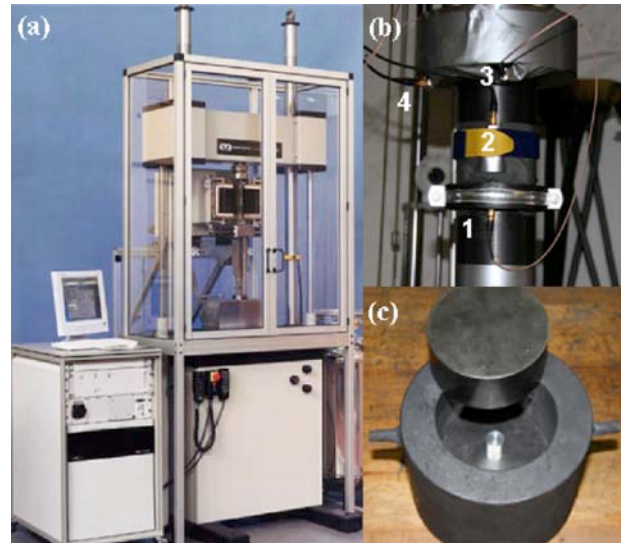


Fig. 3. (a) Instron high-speed upsetting machine. (b) Punch with mounted AE sensors. (c) Specimen in heating/upsetting container.

The upsetting experiments were carried out on a high strain-rate testing machine (Instron VHS 8000, Fig. 3a) to simulate the high strain rates encountered in forging processes. Three

constant levels of strain rates of 1, 10 and 20 s⁻¹ could be achieved through programming of velocity profiles using closed-loop-control facility available on the test machine. The amplified punch displacement and force signals were sampled by a data acquisition card (National Instruments NI-6111) at 10 kHz. The AE signals were acquired by a synchronized (NI-6110) card at 5 MHz. The data acquisition, processing, and signal analysis were programmed with LabView 8.5. Two main modes of operation were used:

- Data acquisition mode: In this mode, minimum amounts of graphical presentation were implemented in order to increase system performance and reduce latency. This module consists mainly of adjustable band-pass filter and a signal parameter computation module. Based on adjustable threshold gate, threshold-crossing count, hits, cumulative hits, burst duration as well as rise and fall time can be calculated. Both filtered signal and derived signal parameters can be stored efficiently to a single file with the corresponding timed displacement and force signals.
- Data processing and presentation module: This module is responsible for further data processing and analysis. All recorded data can be reloaded, processed and represented on different graphs.

Results

In this section, results describing different influences from product geometry or material as well as process parameters including temperature and strain rate will be presented. Due to space limitation, only interesting waveforms that reflect the similarity or dissimilarity of signals (or patterns) will be presented. Note that for the purpose of statistical assurance, every test has been repeated three times under the same test conditions. Only tests with high repeatability are considered. More than 75% of all performed test delivered comparable results with acceptable deviations. To facilitate the comparison, the following abbreviations have been used: Materials (AZ80, AZ31, Al7075), Strain rates (PP1, PP10, PP20), and Temperatures (T200, T300, T400).

One of the difficulties encountered in the current investigations was the influence of background noise level (close to 0.18 volt) caused mainly by the hydraulic drive and generated by the circulating cooling water inside the punch. Due to the elevated noise to signal ratio, linear scales have been preferred in order to distinguish between the different signal levels.

Influence of Investigated Materials

Three different trends could be registered for the different materials investigated. In all performed tests, AZ31 has generated signals of higher strength as compared to AZ80 and Al7075. The registered maximum amplitude has shown a remarkable decrease with the increase of the test temperature. The recorded signals from AZ31 specimens have longer duration than those from AZ80 under all performed test conditions. This difference decreased with increasing the strain rate. On the other hand, Al7075 demonstrated a very long signal as compared to those from Mg-alloys. In the most examined Al7075 samples, an exponentially increasing signal was recorded. For Mg-alloy specimens, deformed without damage development, the signal envelope has shown the usually cited shape of an increasing signal followed by an exponential decay. Examples of the recorded signals are shown in Fig. 4.

Influence of Investigated Geometries

All cylindrical specimens deformed without cracking did not emit any useful signal, which could be used for the specimen evaluation. Signal strength, duration or recorded counts reflect the aforementioned influences arising from material, temperature or strain rate effects.

Due to the small specimen dimensions and the small geometrical modification in the specimens with collar, it was hard to get any analyzable changes in the recorded signal. A recognizing characteristic of the obtained signals from the specimens with collar is that they have a nearly flat envelope ending with a concentrated, slightly higher, pulse. This can be also seen as a set of superimposed and overlapped signals ending with cracking (Fig. 5).

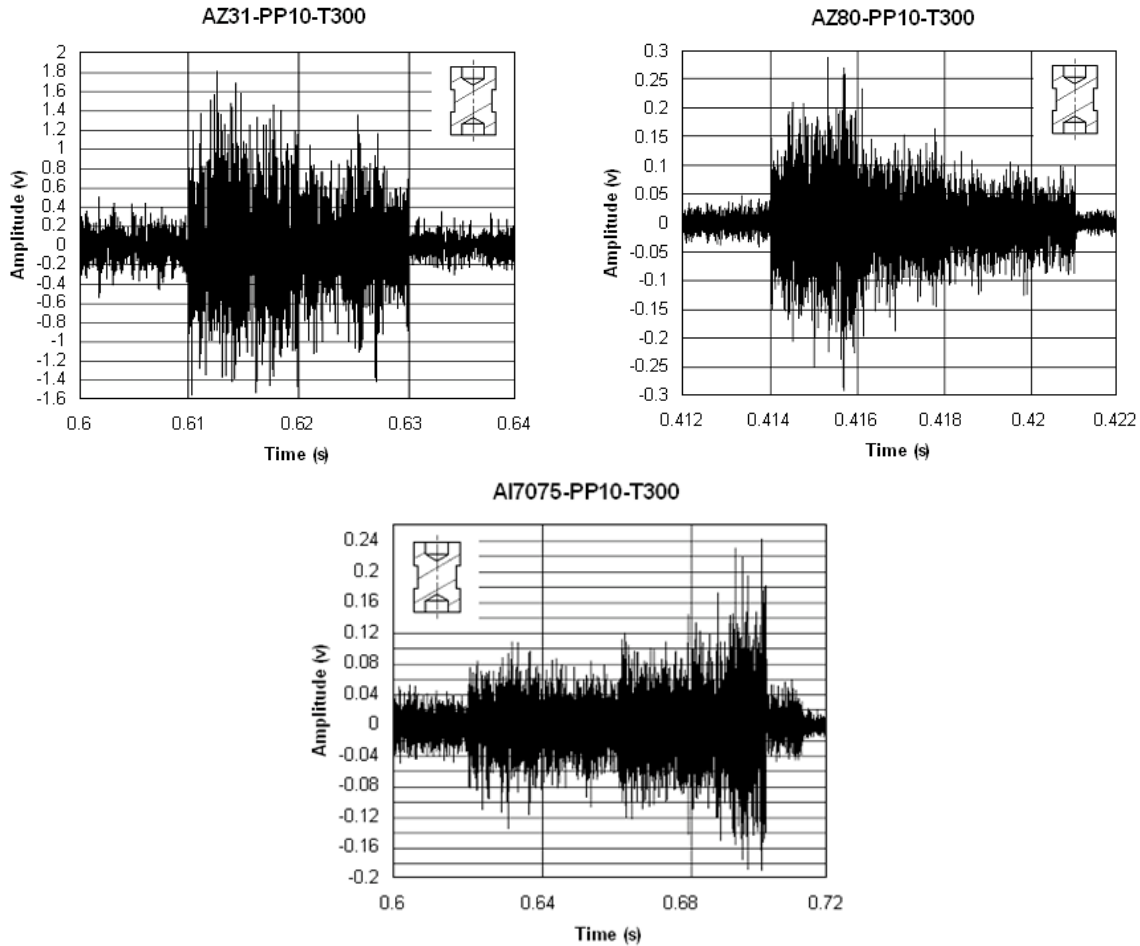


Fig. 4 Influence of examined material on the generated AE signal from undamaged specimens.

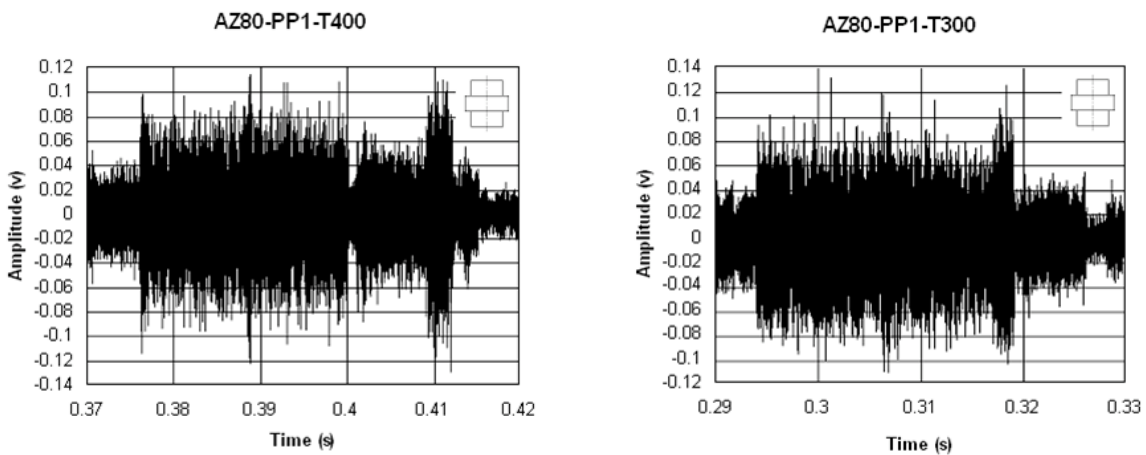


Fig. 5 AE signals from undamaged specimens with collar.

Recessed specimens with drilled holes have shown remarkable patterns as compared to the other types of specimens. Due to variations in the dominating stress states during deformation, the emitted AE signals are consequently changed. The presented example compares a specimen, which has been upset in a single stage (Fig. 6a) with another, which has been deformed first from 18 to 10 mm followed by the second upsetting stage from 10 to 5 mm (Figs. 6b and 6c). It is clear that the developed signal in the single stage experiment (total duration = 5 ms) that ends with a lower frequency of higher amplitude signal (1 ms) is equivalent to the 2-ms signal for the first 8 mm of the punch movement followed by the 4-ms signal from the 5-mm stroke in the second upsetting operation. The relatively higher amplitudes in the second stroke are related to the cooling of the specimen. This was caused by preparation time needed for the second stroke.

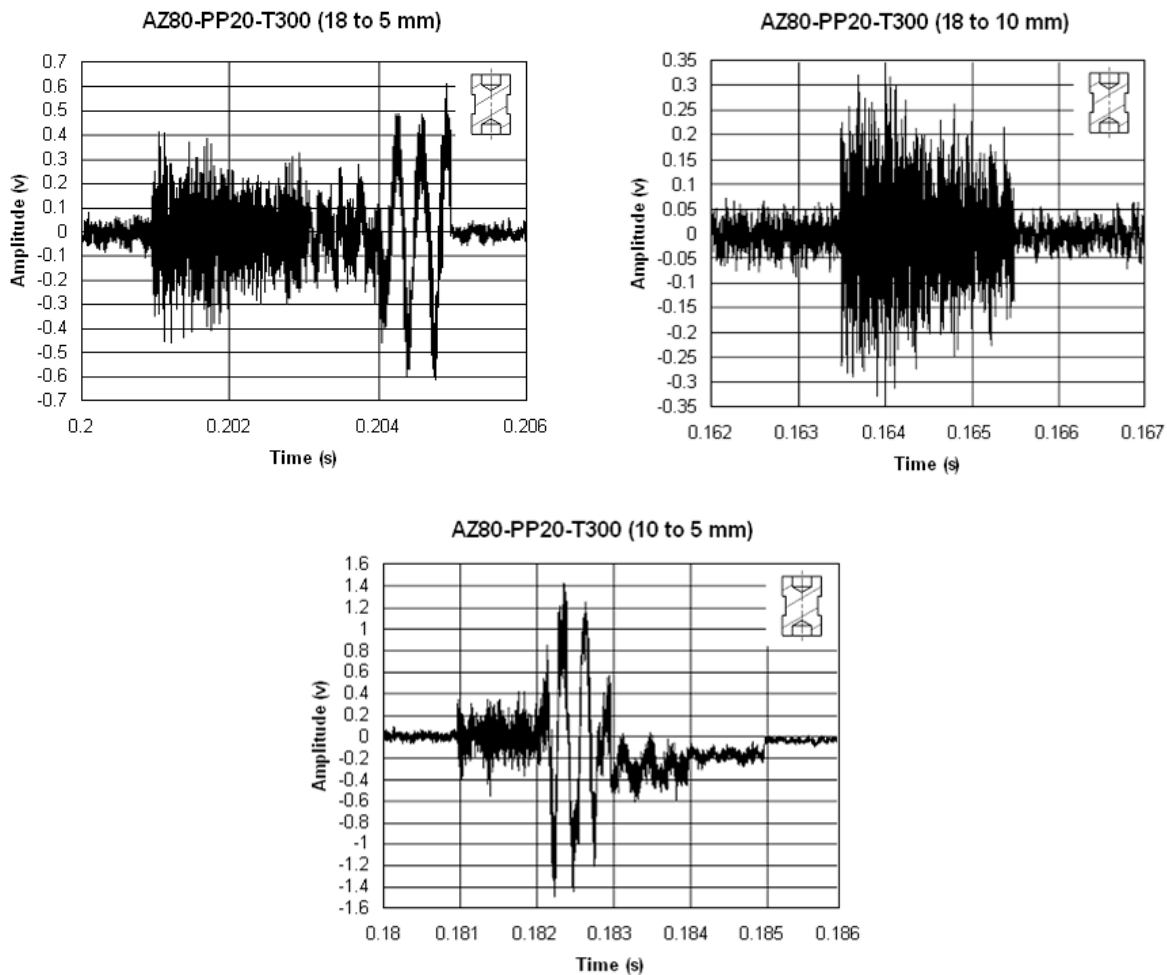


Fig. 6 AE signals from recessed specimens with drilled ends.

Influence of Temperature and Strain Rate

Comparing all the previously presented signals, it is evident that increasing the test temperature causes AE signals to decrease. It is well known that structural changes and formation of new slip planes take place in Mg at about 225°C. Therefore, most of Mg specimens upset at 200°C featured obvious damage. For this test temperature, a limited amount of strain (max. 0.6) has been applied to avoid complete damage of the specimen although a cracking signal has been recorded.

On the other side, increasing the forming speed has proved to increase the emitted AE for the investigated materials under the given test conditions. It is clear that this effect cannot be directly and physically related only to the release of AE from defects, and can be influenced by the impact signals generated by the machine. However, if the generated signals could be classified and analyzed even with these erroneous influences, the main goal of the research could be achieved. In order to consider the impact effect during experiments, the impact signals were measured with the aid of an accelerometer. Results from tests accompanied by impact signals on the body of the testing machine were ignored.

A more detailed examination of the signals recorded during the upsetting of the recessed AZ31 Mg specimens, at strain rate of 1 s^{-1} and temperature of 300°C , shows five consecutive stages (Fig. 7). The development of these stages was verified through finite element simulations, although the separation and the splitting stages were inferred from the developed stress states.

In stage (1) crack initiation signals from both the upper and lower corners of the recess sections can be recognized. With an increased strain, an upper ring is separated by shearing along the cone extending from the outer recess to the inner hole. This shear cracking results in the high cracking signals seen in (2). Further deformation will cause fold-like contact between the upper and lower rings. The resulting friction could be evident from segment (3). As the upsetting progresses, the formed ring expands circumferentially due to the existence of resisting cone in the axial direction and splits up emitting a strong AE signal (4). This signal is characterized by longer rise time nearly equal to its decay time. The emitted friction signals proceed till the lower section of the specimen is separated forming a lower ring. The increased contact area between the surface of the lower hole and the lower upsetting plate generate excessive friction signal as shown in section (5).

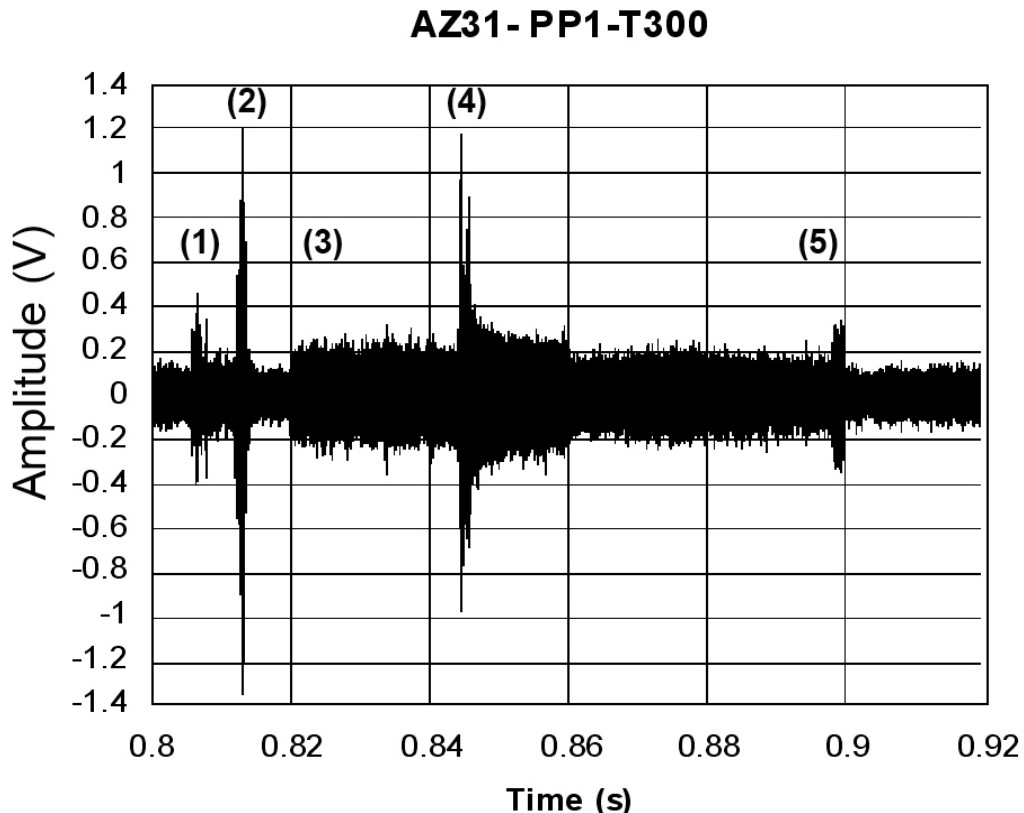


Fig. 7. Consecutive stages of damage induced during upsetting.

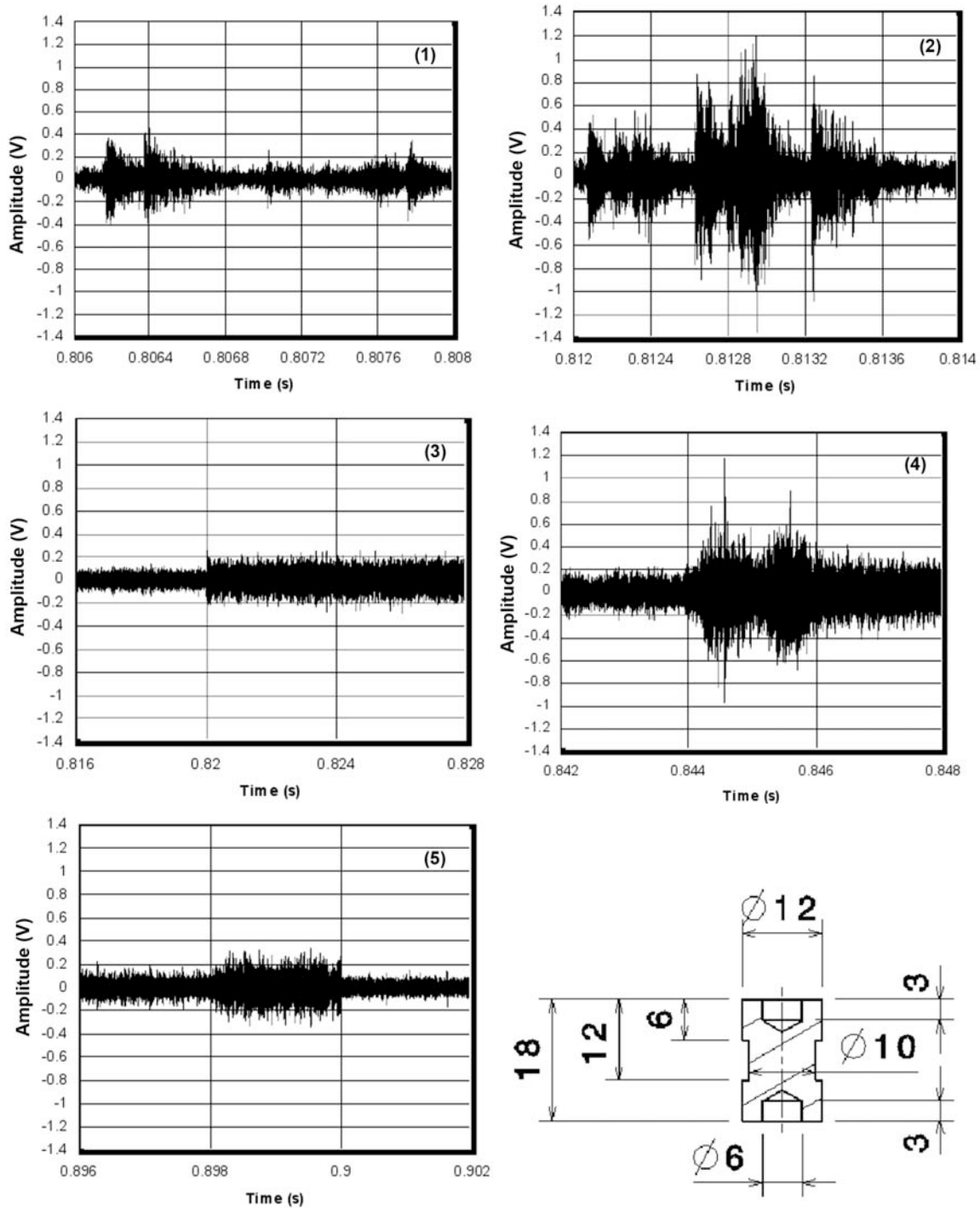


Fig. 7 (continued). Consecutive stages of damage induced AE during upsetting. (1) to (5) show detailed waveforms of 5 stages observed. Specimen details are also given.

Conclusion and Outlook

A series of upsetting tests was carried out in order to correlate the emitted AE signals to different materials and geometries under various temperatures and strain rates. In addition to the reported influences from strain rate and temperature, the geometry of the specimen has proven to exhibit a great influence on the AE pattern. In a more detailed metallographic examination, the developed cracks and their mechanisms should be investigated, and correlation of the signal

parameters to the detected damages should be carried out. More tests should be performed in order to gather enough parameters to feed the proposed AE "Pattern/Parameters/Damage" data bank. During the next series of experiments, the use of an advanced measurement system will facilitate the classification and the analysis of the obtained AE signals. Moreover, an attenuation system will be installed to reduce the hydraulic noise. In addition, the punch will be equipped with un-cooled hardened end. In combination with guard sensors, the influences of background noise can be minimized.

Acknowledgement

The authors would like to thank the German Research Foundation (DFG) for the financial support of this project under the Grant BE-1691/78.

References

1. Schüppstuhl, T.; Kuhlenkötter, B.; Raedt, H.-W.; Steib, S.: Möglichkeiten zur automatisierten Fehlererkennung, -markierung und -nachbearbeitung von Bauteiloberflächen. *Schmiede-Journal*, 9/2004.
2. Geiger, R.: Prozessregelung und Prozessüberwachung in der Kaltumformung. Konferenz-Einzelbericht: Neuere Entwicklungen in der Massivumformung, Stuttgart, 1991, 229-275.
3. Blumenauer, H.; Dehne, G.; Michel, F.; Mook, G.; Pohl, J.: Non-destructive damage evaluation of adaptive materials. *Inter. J. Mat. Prod. Tech.*, **14** (2, 4), 1999, 291-303.
4. Finck, F.; Kurz, J.; Grosse, C.; Reinhardt, H.-W.: Fortschritte in der Datenbearbeitung zur Automatisierung der quantitativen Schallemissionsanalyse. DGZfP Berichtsband 82-CD, 14. Kolloquium Schallemission, Berlin, 2003, 9-16.
5. Herbertz, R.; Hertlin, I.; Pannekamp, J.: Neue Entwicklungen in der Rissprüftechnik für Bauteile der Massivumformung. *Schmiede-Journal*, Mach 2005, 37-39.
6. Ono, K.: New goals for acoustic emission in material research. Keynote lecture, in *Acoustic emission beyond the millennium*, Tokyo, Japan, 11-14 September 2000.
7. Lee, D.E.; Hwang, I.; Valente, C.; Oliveira, J.; Dornfeld, D.: Precision manufacturing process monitoring with acoustic emission. *Machine tools and Manufacturing*, **46**, 2006, 176.
8. Hamstad, M. A.; Mukherjee, A.K.: Comparison of the acoustic emission generated by tensile and compressive testing of 7075 Aluminium. UCID-17787, California University, 1978.
9. Schneider, V.; Kopp, R.; Hirt, G.; Ziegelmayer, O.: Ermittlung der Formänderungsgrenzen für das Freiformschmieden von hochlegierten Stählen. Konferenz-Einzelbericht: MEFORM 2005, 276-287.
10. Wolske, M.; Kopp, R.; Parteder, E.: Untersuchungen der Verformbarkeit von Wolfram-Legierungen mittels Schallemissionsprüfung. 15th Int. Plansee Seminar 2001, Powder Metallurgical High Performance Materials, Proc., **3**: General Topics, 2001.
11. Haupt, H.: Ein auf der Schallemissionsanalyse basierendes Verfahren zur Risserkennung in Umformprozessen. Dissertation, Messtechnische Berichte, **19**, 2003.
12. Sun, J.; Wood, R.; Care, I.; Powrie, H.: Wear monitoring by acoustic emission (AE) and electrostatic (ES) technologies. *Wear - An Int. J. on the Science and Technology of Friction, Lubrication and Wear*, **259** (7), (2005), 1482-1489.
13. Hamstad, M. A.; McColskey, J.D.: Wideband and narrowband acoustic emission waveforms from extraneous sources during fatigue of steel samples. *Journal of acoustic emission*, **15** (1), (1997), S1-18.
14. Huang, M.; Jiang, L.; Liaw, P.; Brooks, C.R.; Seeley, R.; Klarstrom, D.: Using AE in fatigue and fracture material research. *JOM-e*, Bd. **50** (11), (1998).

15. Barschdorff, D.; Haupt, H.: Supervising of metal forming processes by acoustic emission. 9th IMEKO TC-10 Int. Conf. on Technical Diagnostics, In: Scientific papers of the institute of mining of the Wroclaw University of Technology, **86**, (1999), 74-80.
16. Barschdorff, D.; Haupt, H.: Monitoring of deep drawing by means of acoustic emission. *Technisches Messen*, **68** (4), (2001), 166-169.
17. Dornfeld, D. A.; Lee, Y.; Chang, A.: Monitoring of ultra-precision machining processes. *Inter. J. of Advanced Manuf. Tech.*, **21** (8), (2003), 571-578
18. Schneider, V.; Hirt, G.; Brethfeld, A.; Lehmann, G.; Diener, U.: Ermittlung von Umformgrenzen beim Freiformschmieden. *Mat.-wiss u. Werkstofftech*, **38**(4), (2007), 274.
19. Skåre, Th.: Dynamically loaded tribosystems in plastic forming operations. Doctoral dissertation, Lund University, Sweden, June 2001.
20. Hsu, S.; Ono, K.; Hatano, H.: *Material Science Engineering*, **38**, (1979), 187.
21. Hsu, S.Y.S.; Ono, K.: *Proc. 5th Int. AE Symposium, JSNDI, Tokyo*, (1980), 283.
22. Okajima, K.; Ono, K.: *Proc. 5th Int. AE Symposium, JSNDI, Tokyo*, (1980), 270 und 294.
23. Heiple, C.; Carpenter, S.; Armentrout, D.; McManigle, A.: Acoustic emission from single point machining: source mechanisms and signal changes with tool wear: *Material Evaluation*, **52**(5), (1994), 590-596.
24. Prasad, Y.: Research on advanced non-destructive evaluation methods for aerospace structures, Section 6: Special Projects, Air Force Research Laboratory Final Report: AFRL-ML-WP-TR-2004-4237, 2004.
25. Doege, E.; Weber, F.: In-Prozess-Überwachung von Kenngrößen beim Präzisionsschmieden. *VDI-Zeitschrift*, **134** (4), (1992), 95.
26. Doege, E.; Wack, P.: Prozessüberwachung in der Warmmassivumformung durch werkstückspezifische Prozesskennfelder. Universität Hannover, DFG Abschlussbericht, DFG-Do-190-74, 1992.
27. Ecker, W.; Doege, E.; Teryzk, T.; Bode, E.: Möglichkeiten der Prozessüberwachung beim Gesenkschmieden mit Grat. *Umformtechnik*, **27** (6), (1993), 405-410.
28. Doege, E.; Sasse, J.: Verbesserung der Qualität und Produktivität beim Gesenkschmieden durch Prozessüberwachung. *Production Engineering, München*, **2** (2), (1995), 199-202.
29. Terzyk, T.: Prozessüberwachung beim Gesenkschmieden mit Grat durch Auswertung prozessbedingter Signale. Universität Hannover, Dissertation, VDI, Reihe 2, **346**, 1995.
30. Behrens, B.-A.: Entwicklung eines automatisierten Präzisionsschmiedeprozesses mit integrierter Qualitätsprüfung. Universität Hannover, Dissertation, VDI, Reihe 2, **445**, 1997.
31. Brüggemann, K.: Methoden des Qualitätsmanagement beim Gesenkschmieden. Universität Hannover, Dissertation, VDI, Reihe 2, **432**, 1997.
32. Roskam, R.: In-Prozess-Überwachung von Pressen der Blechverarbeitung. Universität Hannover, Dissertation, 1999.
33. Strache, W.: Multisensorielle Überwachung des Stanzprozesses. Universität Hannover, Dissertation, VDI, Reihe 2, **563**, 2000.
34. Wesnigk, T.: Sensorlose Prozessüberwachung beim Gesenkschmieden. Universität Hannover, Dissertation, IFUM, **3**, 2004.

NATURAL FIBER COMPOSITES MONITORED BY ACOUSTIC EMISSION

IGOR MARIA DE ROSA¹, CARLO SANTULLI² and FABRIZIO SARASINI¹

¹ University of Rome “La Sapienza”, Department of Chemical Engineering – Materials – Environment, Via Eudossiana 18, 00184 Rome, Italy; ² University of Rome “La Sapienza”, Department of Electrical Engineering, Via Eudossiana 18, 00184 Rome, Italy

Keywords: AE monitoring, mechanical tests, natural fiber composites

Abstract

During the last decade, ecological concerns have resulted in a renewed interest in natural materials, and issues such as sustainability and eco-efficiency have gained more and more attention, thus controlling the development and introduction of new materials, products and processes. Plant fibers are currently being evaluated as environmentally friendly and low cost alternatives for glass fibers in engineering composites and structures. However, serious concerns are still present on the level of mechanical performance that can be achieved with these materials. In this regard, applying acoustic emission (AE) to monitor monotonic mechanical loading can provide useful information.

In this work, three case studies on AE monitoring of mechanical tests of plant-fiber composites are presented and discussed. The fibers used as reinforcement are jute (case 1), celery (case 2) and phormium (case 3). As a whole, AE data analysis can yield some indications about the effectiveness of reinforcement, the prevalent mode of failure and the selection of different configurations, to obtain the best mechanical performance.

Introduction

Plant-fiber composites and hybrid laminates including plant fibers are increasingly used for semi-structural applications, as they show a better end-of-life profile, being intrinsically carbon-dioxide neutral [1]. However, the mechanical behavior of plant fibers as reinforcement is not easily predicted. In particular, plant fibers are heterogeneous, being cellular structures assembled in nature through a hierarchical procedure, and present a hollow, or lumen, of variable dimensions [2]. The cell wall of a fiber consists of a number of layers: the primary wall, which is the first layer deposited during cell development, and the secondary wall, which in turn is made up of three layers, containing cellulose, hemicellulose and lignin in varying amounts. In addition, the introduction of plant fibers in a polymer matrix may generate compatibility issues, whose consequence may be a large scattering of properties in the final laminate [3].

Real-time monitoring of mechanical tests is a traditional application of AE in composite material studies, which has been hardly ever applied on plant fiber composites, e.g., to contribute in material characterization during post-impact loading [4], or to offer further indications on failure mode during tensile or flexural testing [5]. The results were able, e.g., to confirm concerns about scarce impact resistance of these materials [6] and the difficulty in obtaining predictive indications about materials performance, which suggest that specific tools of analysis of AE data would need to be disposed for these materials [7].

In this paper, three case studies of the application of AE monitoring to the characterization of plant-fiber composites are presented. Post-analysis of AE data according to a traditional approach based on cumulative counts vs. load, event localization, amplitude and duration distributions allowed clarifying the importance of fiber morphology and compatibility in controlling the mechanical behavior of the resulting composites. This can contribute to the selection of fibers and laminates for the development of plant-fiber composites of engineering significance.

Materials and Test Methods

The experimental characterization was carried out on three different natural-fiber-reinforced composites. Tests on these were referred respectively as Case 1, 2 and 3.

Laminates used in Case 1 consisted of hybrid composites reinforced with glass and jute fibers. In particular, jute/glass fiber hybrid laminates were manufactured using an RTM procedure. Plain-woven jute fabric (300 g/m²) and E-glass (Vetrotex VR38, 290 g/m²) were used as reinforcement. The resin was unsaturated polyester (1629 NT from Lonza). Two different configurations (labeled as Q and T) were obtained, whose stacking sequences and characteristics are summarized in Table 1. From the plates, four-point bend specimens were obtained with 150-mm length, 30-mm width, and 5-(±0.2)-mm thickness. Specimens from T and Q laminates were impacted and then subjected to post-impact four-point bending tests. The impact point was located at the centre of the specimens. The impact energy was changed, varying the mass of the hemispherical drop-weight striker ($\phi = 12.7$ mm), which has a constant velocity of 2.5 m/s. Impact tests were performed on an instrumented impact tower fitted with an anti-rebound device. Four different impact energies were considered: 5, 10, 12.5 and 15 J. The flexural tests were carried out in accordance with ASTM D-790 using quarter-point loading configuration. These tests were performed in a universal testing machine (Zwick Roell Z010) with a support span length of 140 mm and a crosshead speed of 5 mm/min. The strain at the mid-span was determined by means of strain gauges. Five specimens were tested for each configuration (T and Q) and for each impact energy value, as well as for non-impacted specimens, which served as reference materials. Post-impact flexural tests were monitored by AE until final fracture occurred using an AMSY-5 AE system by Vallen Systeme GmbH. The AE acquisition settings used throughout were as follows: threshold = 35 dB, RT (rearm time) = 0.4 ms, DDT (duration discrimination time) = 0.2 ms and total gain = 34 dB. Four PZT AE sensors resonant at 150 kHz were used: two sensors were placed on the surface of the specimens at both ends to allow linear localization, while the other two sensors were used as guard sensors in order to discriminate between AE signals and noise.

Table 1. Summary of laminate configurations (case 1).

Sample name	Stacking Sequence (G = Glass; J = Jute)	Number of Jute Layers	Number of Glass Layers	Overall Fiber Content [vol %]
Q	4G/1J/2G/1J/2G/1J/2G/1J/4G	4	14	50±2
T	7G/4J/7G	4	14	50±2

In Case 2, celery-fiber reinforced composites were tested. Natural untreated fibers from local celery (*Apium graveolens*) and P25 epoxy system produced by REA Industries were used. The average length of the fibers was 10 cm and they were randomly arranged like a mat. The composites were manufactured using the hand lay-up process in a closed aluminum mould. The curing cycle was 7 days at room temperature and under slight pressurization followed by 48 h at 40°C. Two fiber fractions were used, corresponding to about 10 and 20 wt%. Five tensile samples having a length of 230 mm, a width of 20 mm and a thickness of 3.5 (±0.2) mm were

obtained and tested. In addition, five tensile samples of neat epoxy resin were manufactured to evaluate the effect of fiber introduction on the composite properties. The mechanical characterization of the composites was conducted by longitudinal tension tests (ASTM D-3039) using an Instron 5584 test machine. The crosshead speed for tensile tests was 0.5 mm/min. All the specimens tested were equipped with strain gauges to determine the Young's modulus. Tensile tests were monitored by AE using the same equipment, set-up and parameters previously described.

In Case 3, untreated *Phormium tenax* (New Zealand flax, harakeke)-reinforced epoxy composites were tested. The matrix was an epoxy resin (Ampreg 26) by SP systems. The fibers were cut to a length of approximately 2 cm and were randomly arranged in the final composite. The specimens were manufactured using the hand lay-up process in a closed aluminum mould. The curing cycle was 20 days at room temperature. Two sets of phormium fiber reinforced laminates were produced with 10- and 20-wt% fiber content, respectively. Five specimens were tested in flexure (200 mm x 30 mm x 4.5±0.2 mm) for each laminate and for comparison five specimens of neat resin were also tested. Flexural tests were performed in accordance with ASTM D-790 using a three-point loading configuration. These tests were performed using an Instron 5584 test machine at a constant crosshead speed of 2.5 mm/min. Span-to-thickness ratio in these three-point bending tests was 20:1. The strain at midpoint was determined by means of strain gauges. Flexural tests were monitored by AE using the same equipment, set-up and parameters previously described.

Results

Case 1: Jute/glass hybrid laminates

Here the idea was to demonstrate which one of the hybrid configurations, T (sandwich hybrid) or Q (intercalated hybrid), both with the same amount of plant fibers and therefore with a similar reduction in weight, would prove more suitable to sustain the application of load. Flexural tests carried out on both configurations demonstrated that T hybrids are superior to Q hybrids at all impact energies by more than 20% both in strength and modulus [8]. Post-impact flexural and AE test results are summarized in Table 2.

Table 2. Post-impact flexural strength and AE cumulative counts "knee" stress for Q and T glass/jute hybrids impacted at different energies.

<i>Specimens</i>	<i>Flexural Strength (MPa)</i>	σ_c (MPa)
Q _{0J}	209.91±0.37	93.66±3.12
Q _{5J}	172.89±7.18	84.92±9.95
Q _{10J}	160.42±8.98	75.40±7.45
Q _{12.5J}	157.08±10.42	71.07±0.99
Q _{15J}	154.57±3.31	72.50±10.34
T _{0J}	269.34±15.47	90.33±6.43
T _{5J}	244.13±0.69	82.64±4.73
T _{10J}	227.43±14.87	79.85±3.11
T _{12.5J}	212.76±14.20	80.61±2.56
T _{15J}	195.04±18.49	54.50±10.13

AE analysis was focused on the measurement of the cumulative counts curve "knee": the stress value associated with the change in slope of the above curve was referred to as σ_c and was supposed to be an acceptable indication of the upper limit for materials service. Values of σ_c were comparable both for T and Q configuration, representing in general about 30-40% of the maximum strength. However, in the specific case of flexural tests after 15-J impact, which was

the highest impact energy applied, T configuration showed a much lower value of σ_c than Q configuration (54.5 ± 10.1 MPa vs. 72.5 ± 10.3 MPa). It is suggested that the intercalated layers of glass-fiber composite in Q hybrids offer more gradual degradation to the material with increasing impact energy. In contrast, on T hybrids, the mechanism of failure is dominated by the breakage of jute-fiber composite core, which takes place by abrupt tearing off of the fibers from the matrix, as noticed elsewhere [9].

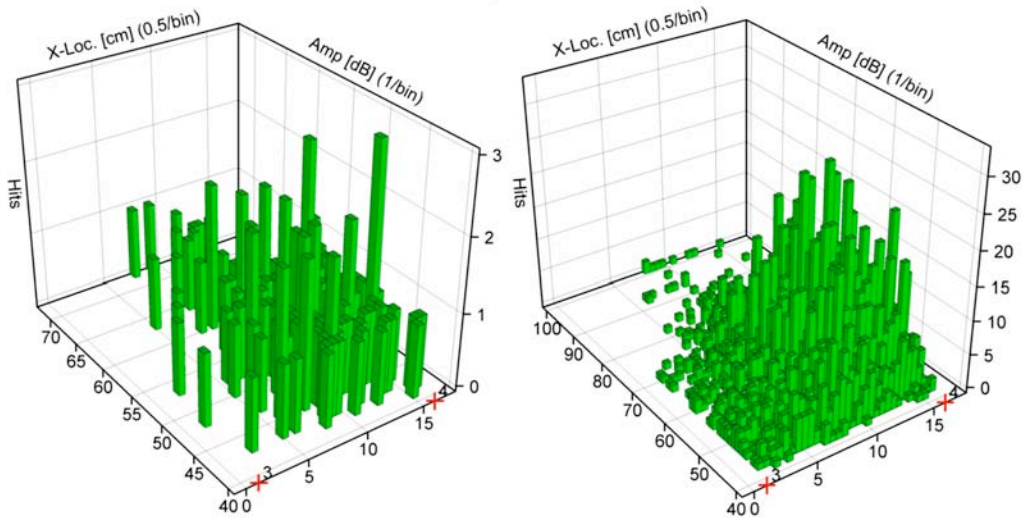


Fig. 1. AE localization plots vs. amplitude for Q hybrids taken at σ_c (left) and at failure (right).

Further characterization on laminates impacted at 15 J, shown in Fig. 1 for Q hybrids and in Fig. 2 for T hybrids, did indicate that AE events are more concentrated in T hybrids than in Q hybrids, although damage appears to be more precocious in Q hybrids, as shown by localization plots taken at σ_c . AE data confirm therefore the effectiveness of intercalated hybrids in dispersing impact damage close to the penetration site.

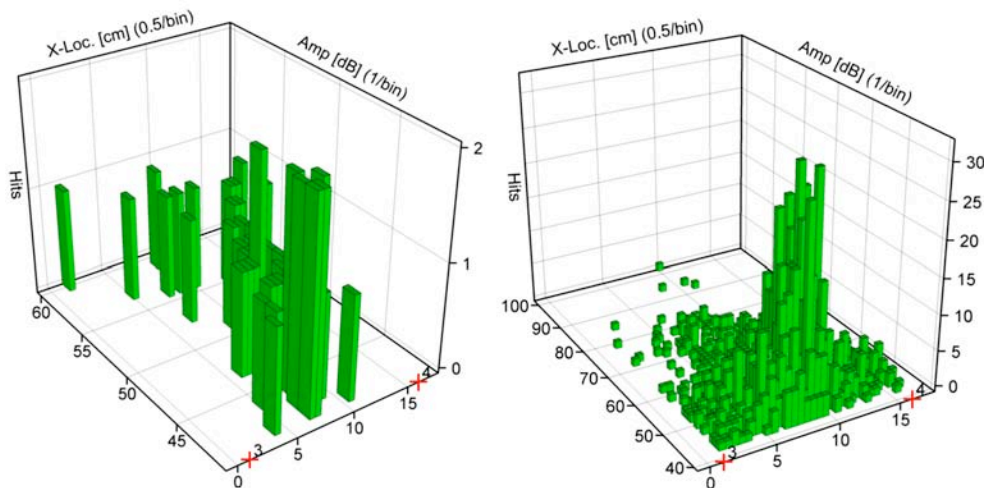


Fig. 2. AE localization plots vs. amplitude for T hybrids taken at σ_c (left) and at failure (right).

Case 2: Celery fiber composites

The introduction of celery fibers in a polymer matrix was attempted, as an example of agro-waste product to be employed in materials. In this case, it could be observed that the largest part

of localized events is connected with the presence of fibers. This can be shown by comparison between Fig. 3a, showing AE events for the neat resin and Fig. 3b, showing AE events for the resin with 10-wt% celery fibers. An issue, which was encountered in fiber introduction due to their variable diameter, is that it was not possible to obtain a balanced random orientation of fibers in the matrix. As a consequence, resin-rich areas and conversely areas with higher fiber content are heavily present, which affected the mechanical properties of the laminate [10]. Increasing the amount of fiber introduced from 10 to 20 wt%, the negative effect of fiber introduction is somehow attenuated. In particular, the tensile strength and modulus of the neat-resin samples were 29.1 ± 3.9 MPa and 3.45 ± 0.1 GPa, respectively, whilst the tensile strength and modulus of the celery/epoxy laminates were 18.67 ± 0.60 MPa and 3.3 ± 0.17 GPa for the 10-wt% laminates and 24.45 ± 3.65 MPa and 3.7 ± 0.2 GPa for the 20-wt% laminates.

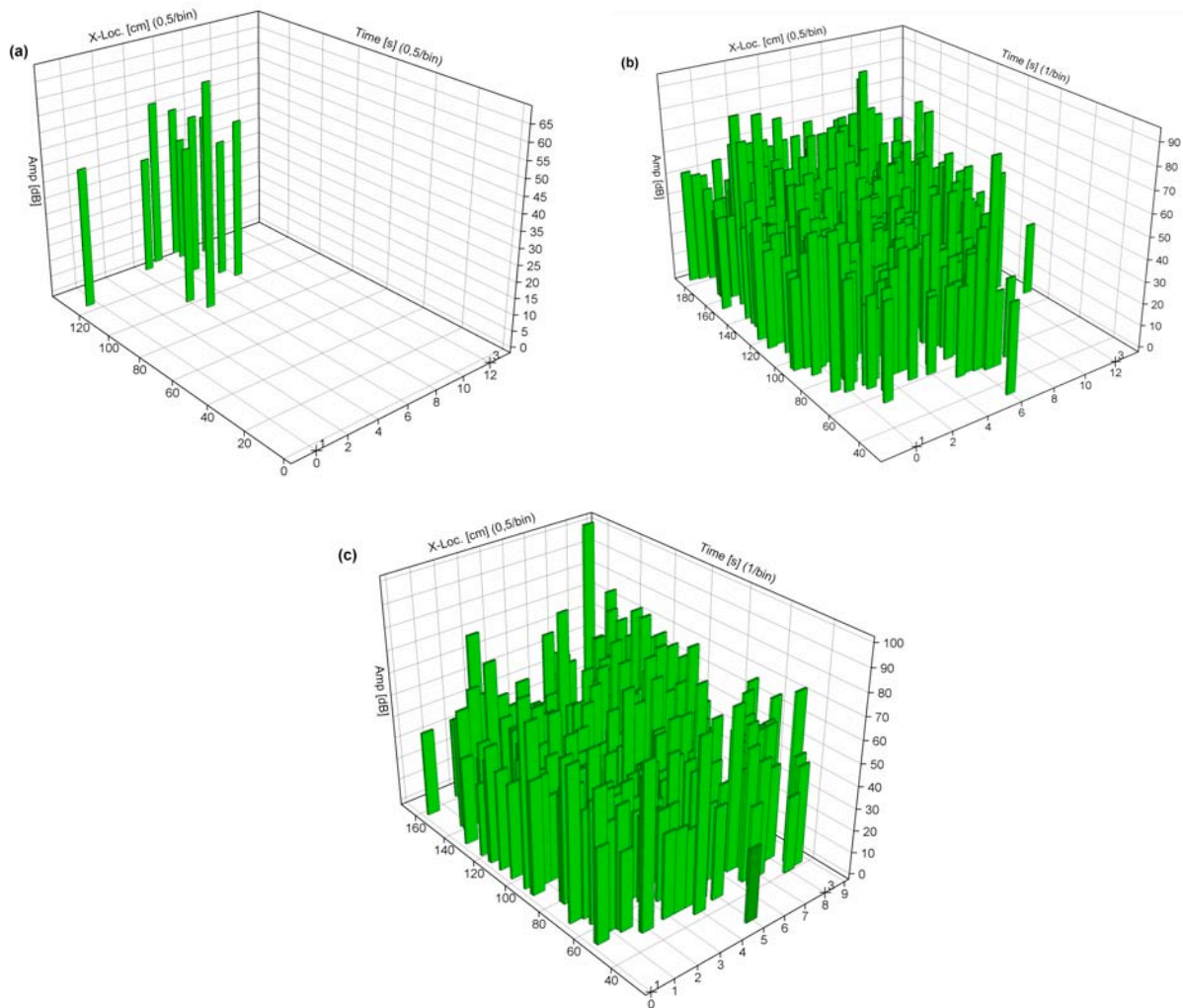


Fig. 3. AE localization plots vs. amplitude at failure for neat epoxy resin (a), for 10-wt% celery/epoxy (b) and 20 wt% (c)

The poor mechanical performance of the composite indicates that the introduction of 10-wt% fibers does not result in effective reinforcement. This would cause the composite to break because of concentration and accumulation of damage in a local region of the sample, ideally situated at the center of the gauge length [11]. In contrast, no preferential localization of AE events and hardly any high amplitude event are revealed from Figs. 3b and 3c, even at stress close to failure: it may be suggested that fibers tend to behave as defects, possible triggers for final failure.

The largest majority of AE events detected in celery fiber composites have low amplitudes (less than 60 dB), as shown in Table 3, both in the 20-wt% laminate and in the 10-wt% one. In general, the introduction of a larger volume of fibers does not result in further composite degradation.

Table 3. Relative distribution (%) of amplitude in neat resin (NR) and celery fiber reinforced epoxy composites at 10 wt% (10) and 20 wt% (20) during tensile loading (I: 0-0.25 F_{max} ; II: 0.25-0.5 F_{max} ; III: 0.50-0.75 F_{max} ; IV: 0.75-1.0 F_{max}).

Specimen	Interval	Amplitude interval (dB)						Avg. Loc. Events
		35-49	50-59	60-69	70-79	80-89	90-99	
10	I	80	20					1.67±2.08
	II	75	11.58	7.32	4.27	0.61	1.22	54.67±15.65
	III	63.02	22.27	6.51	3.78	2.73	1.68	158.67±35.08
	IV	66.94	17.27	7.40	4.93	2.30	1.16	202.67±22.85
20	I	100						1
	II	57.27	20.91	12.73	7.27	1.82		55±13.59
	III	58.15	23.35	11.01	6.61	0.88		113.5±14.84
	IV	68.45	18.18	8.02	3.21	0.54	1.60	93.5±13.43
NR	I	25	25	37.5	12.5			2
	II	33.33	8.33	16.68	25	8.33	8.33	3
	III	58.62	13.79	17.24	6.90	3.45		7.25±3.96
	IV	62.86	20	2.86	5.71		8.57	8.75±2.87

AE data appear to confirm that a reduced number of defects, originated from fiber introduction, are present in the 20-wt% laminate: here, a lower total number of events is detected, of which a higher percent is between 60 and 80 dB. The larger number of higher amplitude events may suggest that, in spite of the fact that most fibers in the composite work at very low stresses (ultimate tensile strength for celery fibers is 100±25 MPa, while modulus is equal to 4±1.5 GPa), some fiber-matrix interaction is perceived. This is also indicated by Fig. 4, where no evidence of fiber-matrix debonding is shown.

Case 3: Phormium fiber composites

Phormium proved to be a particularly strong and elastic fiber for possible use as reinforcement [12]. In the micrograph in Fig. 5, a fiber bundle is shown, which is extracted from the plant leaf, in which also oriented elementary fibers are visible, indicating the high strength of the structure, when subjected to unidirectional loading.

When introduced in a polymer matrix, this fiber showed an elastic behavior up to a stress close to failure. Flexural strength and modulus values obtained for the two laminates, compared with those for neat resin, are reported in Figs. 6a and 6b, respectively. The strength of the 20-wt% laminate appears to be superior to the 10-wt% one, and to the level measured on the resin.

In this sense, the measurement of σ_c , as suggested above, represents in some cases a suitable method to calculate a value for the maximum load in material service, such as for 10 wt%, where σ_c was 23.03±0.89 MPa, which is just above 40% of the ultimate load. In contrast, for 20-wt% laminate, the proximity of the measured σ_c value to the ultimate load value (in practice, around 80% of it) is likely to hamper failure prediction, as will be shown below. This is likely to be due to the scarce deviation from elasticity of the behavior of phormium fibers, which results in most AE activity being concentrated in the last period of loading, indicating a lower rate of premature

fiber failure. This is consistent with the improvement in composite strength and modulus observed in the 20-wt% laminate with respect to the 10-wt% one.

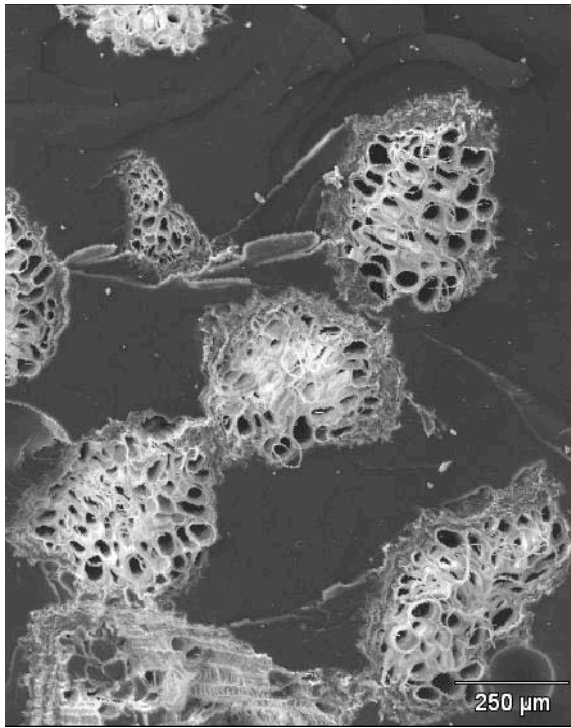


Fig. 4 SEM image of a part of the fracture surface in a celery/epoxy composite (20 wt%).

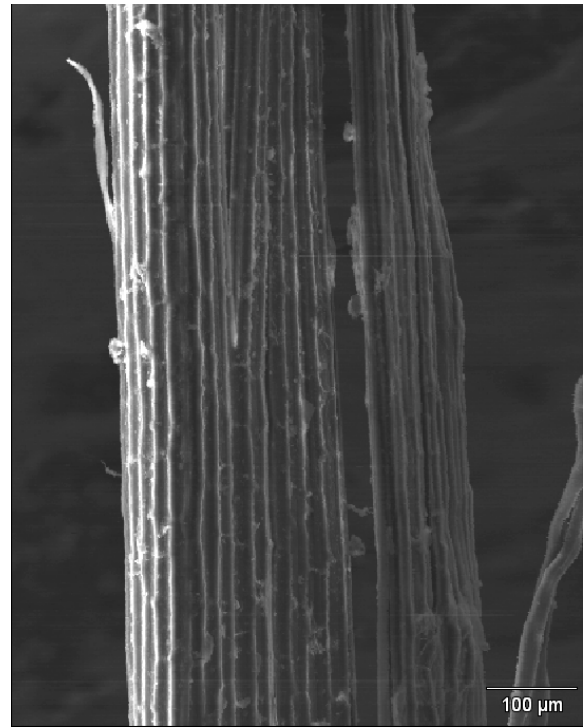


Fig. 5. Typical shape of an untreated phormium fiber (SEM image).

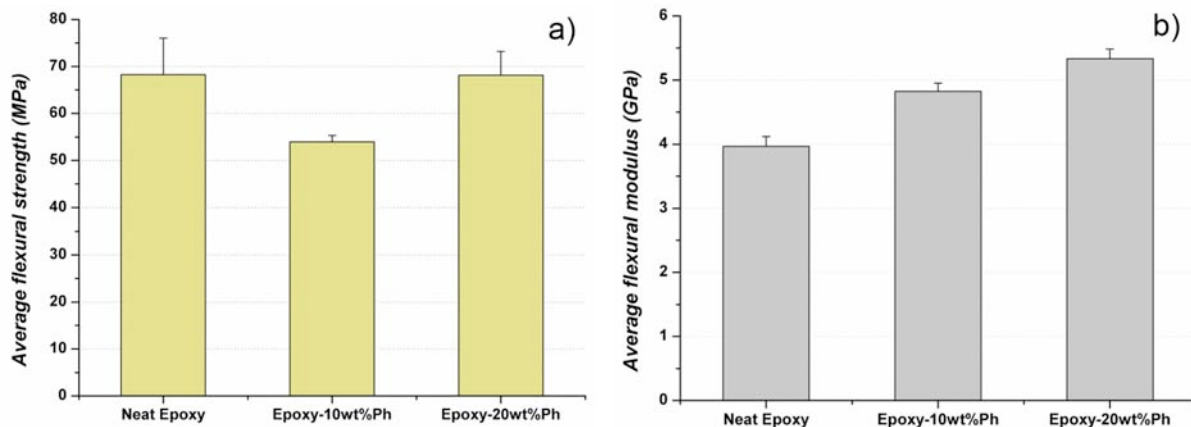


Fig. 6 a) Flexural strength and b) Flexural modulus of phormium fiber composites.

As a consequence, alternative parameters to the cumulative counts “knee”, which could provide indications of critical damage development, were searched for, in order to confirm σ_c as the limit for material use, or suggest a lower value for it. A different parameter, mean-amplitude hit frequency or MAHF, defined as the *average amplitude in a time interval multiplied by the fraction of hits in that interval with respect to the total hits number*, plotted against time, gives in a repeatable way on phormium-fiber composites a limit for material use which is consistently inferior to that given by σ_c , as described in Fig. 7. The perceived advantage of MAHF with respect to σ_c is that it is sensitive to the increase in average amplitude of the hits that may precede the cumulative counts “knee”.

For the particular sample selected in Fig. 7, the ultimate flexural strength was 71.85 MPa, σ_c was 67 MPa, whilst MAHF was only 59.26 MPa, as indicated by the two circles on the curve in Fig. 7. This indicated that, in spite of the perceived macroscopic elasticity of the composite almost up to failure, increasing average amplitude of detected hits appears to indicate the presence of significant damage at a lower stress than σ_c . In our opinion, this suggests that MAHF offers an additional opportunity for AE analysis to characterize the behavior during quasi-static tests in composites not showing appreciable plastic deformation, because of the nature of the reinforcement used.

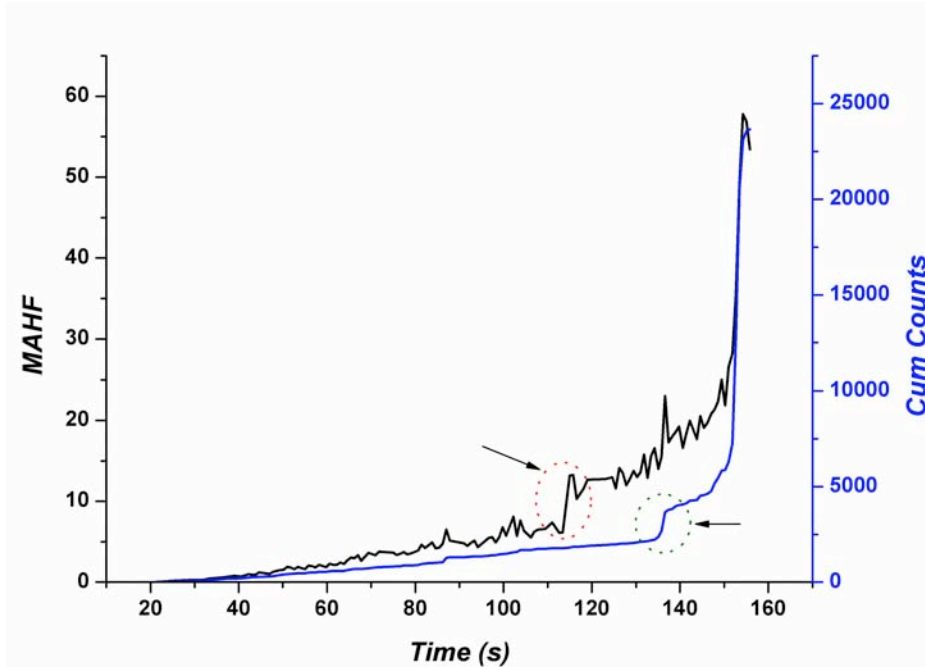


Fig. 7. MAHF and cumulative counts vs. time for phormium-reinforced epoxy composites.

Conclusions

AE proved suitable to analyze the mechanical behavior of plant-fiber-reinforced composites. These materials, which are increasingly used for environmental reasons, are not easily characterized by other methods, because of the inherent variability in fiber properties, and the not always effective fiber/matrix compatibility, which leads to an absence of warnings as regards materials failure. The three case studies reported, pointing to a broad range of plant fiber composites, reinforced with jute (hard bast fiber), celery (elastic stem fiber) and phormium (elastic leaf fiber), were also deemed capable of confirming the versatility of the acoustic emission technique.

The results also indicated that AE analysis centered on amplitude distribution and cumulative count vs. load curves can offer some indications on the mode of failure and the maximum service load for these materials.

References

1. Joshi S.V., Drzal L.T., Mohanty A.K., Arora S. : *Composites Part A*, **35** (3), 2004, 371–376.
2. Madsen B., Lilholt H.: *Composites Science and Technology*, **63** (9), 2003, 1265-1272.
3. Eichhorn SJ, Baillie C.A., Zafeiropoulos N., Mwaikambo L.Y., Ansell M.P., Duffresne A., Entwistle K.M., Herrera-Franco P.J., Escamilla G.C., Groom L., Hughes M., Hill C., Rials T.G., Wild P.M.: *Journal of Materials Science*, **36** (9), 2001, 2107 - 2131.

4. Santulli C.: *Journal of Materials Science*, **41** (4), 2006, 1255 - 1259.
5. Czigány T.: *Journal of Composite Materials*, **38** (9), 2004, 769 – 778.
6. Santulli C.: *NDT & E International*, **34** (8), 2001, 531-536.
7. Park J.M., Quang S.T., Hwang B.S., DeVries K.L.: *Composites Science and Technology*, **66** (15), 2006, 2686-2699.
8. De Rosa I.M., Santulli C., Sarasini F., Valente M.: Accepted for publication in *Composites Science and Technology*, February 2009. doi:10.1016/j.compscitech.2009.02.011.
9. Santulli C., Cantwell W.J.: *Journal of Materials Science Letters*, **20** (5), 2001, 477-479.
10. Caneva C., De Rosa I.M., Santulli C., Sarasini F.: accepted by *International Journal of Materials and Product Technology*, November 2007.
11. Hamstad M.A., *Acoustic Emission Beyond the Millennium*, Elsevier, 2000, pp. 77-91.
12. Newman R.H., Clauss E.C., Carpenter J.E.P., Thumm A.: *Composites Part A: Applied Science and Manufacturing*, **38** (10), 2007, 2164-2170.

ACOUSTIC EMISSION FEATURE FOR EARLY FAILURE WARNING OF CFRP COMPOSITES SUBJECTED TO CYCLIC FATIGUE

RUNAR UNNTHORSSON, THOMAS P. RUNARSSON and MAGNUS T. JONSSON
Department of Mechanical & Industrial Engineering, University of Iceland, Reykjavik, Iceland

Keywords: Feature patterns, Multi-axial fatigue, Failure warning, Fibre reinforced material

Abstract

The purpose of the study presented in this paper is to evaluate whether the probability distribution of AE features can be used to provide a timely warning of impending failure in CFRP composites subjected to multi-axial cyclic loading. The probability distribution of each feature, as a function of lifetime, is estimated from experimental AE data. A warning is given if the value of the AE feature is likely to belong to a distribution close to failure.

The paper presents a new AE feature – a trough-to-peak pattern feature. The trough-to-peak pattern feature is compared against hit-based and frequency-based AE features frequently used in the literature. Of all the AE features studied, only the probability distributions of few trough-to-peak patterns can be separated. Furthermore, the evolution curves of these patterns have a salient slope change at around 60% of the lifetime, but the curves of other AE features have only a significant change in the last 5-10% of the fatigue life. Hence, the results show that valuable information can be extracted from the "rhythm" of AE features.

Introduction

Fatigue in a carbon fiber reinforced polymer (CFRP) composites is a stochastic process influenced by several random factors such as material variations, manufacturing variations and in-service variations. In addition, fatigue is also influenced by the orientations, locations and the type of the damage mechanisms introduced in the composite. The high damage tolerance of composites means that composites are able to meet their in-service requirements for a prolonged period of time while damages accumulate and grow.

Acoustic emission (AE) testing is a non-destructive condition monitoring technique, which can be used for *in situ* monitoring of composite fatigue. Acoustic emissions are transient stress (pressure) waves, which are generated by the energy released when microstructural changes occur in materials [1,2]. The stress waves travel through the composite and when they reach the surface, they cause it to vibrate. AE waves can be measured using sensitive transducers, which respond to surface displacements of several picometers. The AE technique can detect delamination, matrix cracking, debonding, fibre cracking, and fibre pull-out [1, 3-6]. Hence, the high sensitivity of the AE technique may potentially enable early detection of damage.

However, there is no such thing as a free lunch; the high sensitivity of the AE technique means that the measured AE signal may contain a high number of AE transients from sources in both the composite and the environment. The sources in the composite include damage growth, rubbing of crack surfaces and friction between the fibres and the matrix due to their different material properties. The varying material properties will result in an anisotropic speed of propagation [7]. In addition, reflection and attenuation of the AE waves add to the complexity. Attenuation can be caused by geometric spreading, dispersion, internal friction and scattering [8].

Furthermore, the AE waves from damage growth can be buried in the AE generated by the friction and rubbing of crack surfaces [2]. As a result, multiple AE transients with varying amplitude, duration, and frequency can be emitted in each cycle and simultaneously. The values of the AE signal features from cumulated damage usually fall in the same range as those that result from damage growth [9,4]. Hence, a reliable detection of imminent failure while minimizing false alarms is a challenging task.

In this paper it is proposed that a timely warning about imminent failure can be issued by using the probability distribution of a suitable AE feature. In order to investigate this, experimental AE data acquired during cyclic testing of 75 prosthetic feet is used and AE features are extracted from the data. The probability distribution of each AE feature is estimated as a function of lifetime. A failure warning is given if the value of the AE feature is likely to belong to a probability distribution close to failure. The AE features are evaluated by how well the estimated probability distributions at 50% and 95% of the normalized lifetime can be separated. Several well established AE features in the literature are studied and also a trough-to-peak pattern feature. The trough-to-peak pattern, which is presented in this paper, is a combination of two features which were recently proposed by the authors [10] and used for tracking the locations of individual AE sources using a methodology introduced in reference [11].

AE Features

In this study, AE hits are located and determined using a procedure that was described in detail in [12]. Figure 1 shows a flow chart of the procedure. In the first step, the acquired AE signal is processed in order to extract descriptive features for detection. The resulting signal is called a detection function, or novelty function, and can be in any suitable domain of interest, e.g. time and time-scale/time-frequency domains. For detecting and locating hits, the detection function is input to a peak-picking algorithm that automatically detects and locates hits based on the trough-to-peak difference of local troughs and peaks. The peaks and troughs that have trough-to-peak difference below a specified threshold, T_{tp} , are filtered out. In the final step, the detected transients are compared against a threshold, T_{AE} , both to locate the hits more accurately and to filter out weak hits.

In this study, the detection function is the temporal energy of the AE signal in the time-frequency domain. The function is computed using a short-time Fourier transform (STFT). Figure 2 illustrates the procedure. The STFT-based detection function is computed using a segment size of $k = 128$ samples and $d = 120$ sample overlapping. The hits are located by setting the trough-to-peak threshold, T_{tp} , to 304 dB V-s and determined by setting the determination threshold, T_{AE} , to 3 mV. With these settings an AE failure criterion equivalent to the 10% displacement failure criterion was designed in [12]. Once the AE hits are determined, the hit-based features can be determined.

AE Hit Patterns

Hit and ring-down counts have been used extensively for interpreting AE data. Both are pulsations in the signal, but on different time scales. The success that has been achieved using these two features provided an impetus for the authors to investigate whether the information provided by the timing between the pulses could be used to provide valuable additional information.

In “On Using AE Hit Patterns for Monitoring Cyclically Loaded CFRP” [10], the authors introduced two features for this purpose and used them for tracking the locations of multiple AE

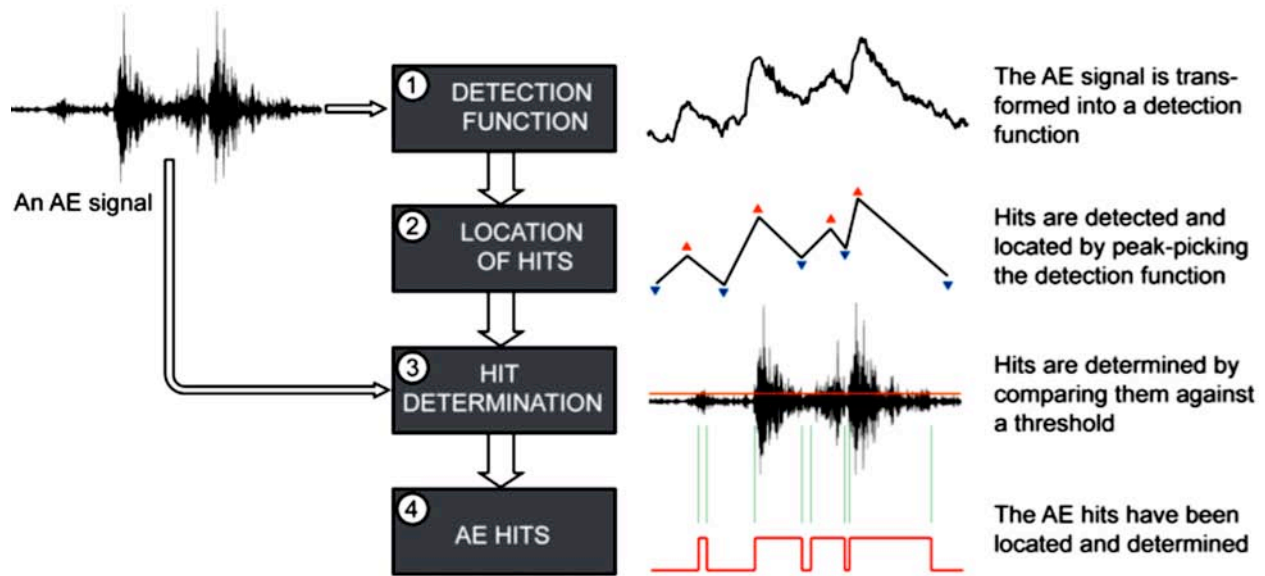


Fig. 1. Flow chart of the AE hit determination procedure.

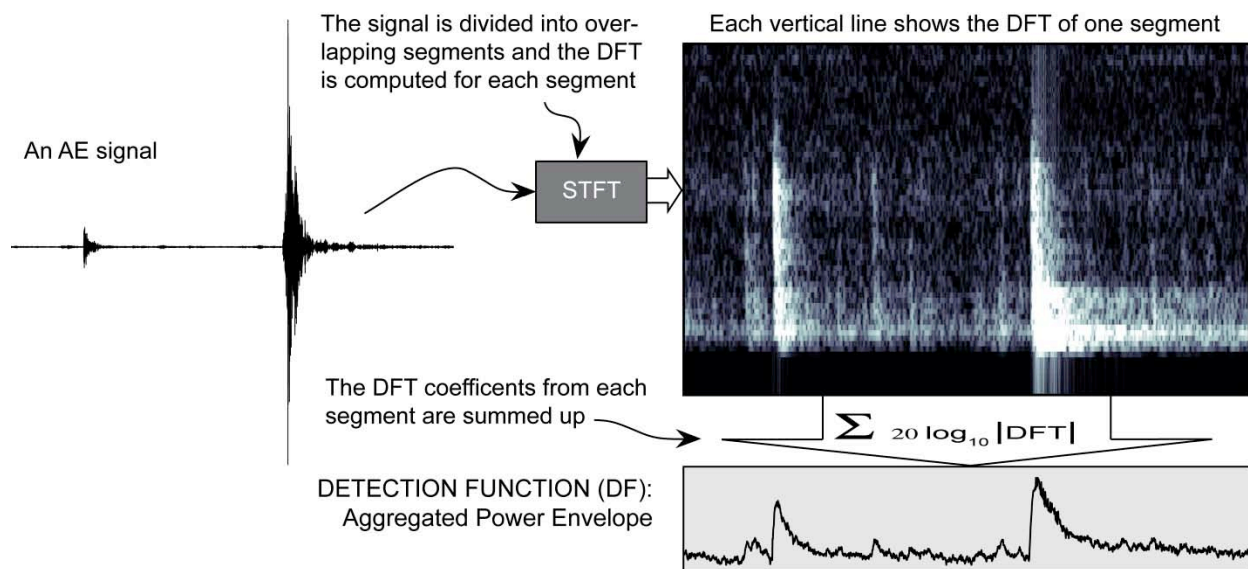


Fig. 2. Illustration of how the STFT-based detection function is generated.

sources relative to the phase of a reference signal. These two features are the inter-spike interval (ISI) feature and the hit pattern feature. The ISI feature is the time between two sequential hits and the hit pattern feature is essentially a technique for fusing AE features, extracted from each AE hit, and for finding and locating patterns which appear within the fused data representation.

In this study, a new feature is made by combining these two features. The new feature is called a through-to-peak pattern feature. It is computed by first determining the time from a trough to a peak (and also from a peak to a trough) for each AE hit, then coding the results and then counting the occurrences of all patterns found in the coded representation. A trough-to-peak interval is a variant of the Inter-spike Interval (ISI). It can also be recognized to include variants of two commonly used AE hit-based features, namely the rise time and the fall time.

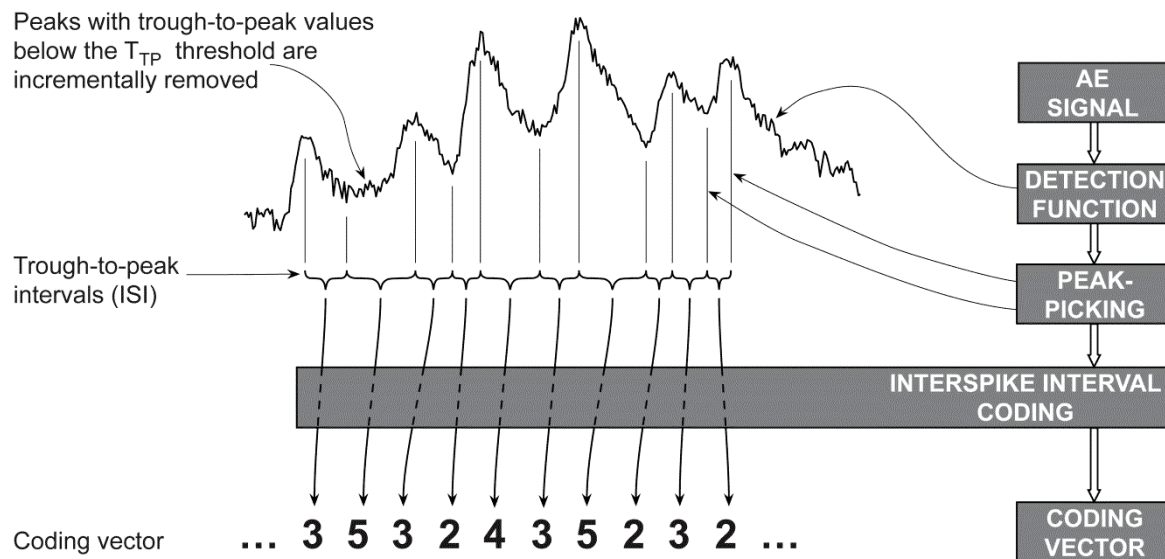


Fig. 3. The first step in computing the hit pattern feature is the generation of the coding vector for the signal segment.

The AE hits are located using the procedure described above, but no determination is performed, i.e. the determination threshold T_{AE} is set to 0 mV. This means that the threshold will not filter out weak hits. Figure 3 illustrates how the trough-to-peak feature is coded into a coding vector. The trough-to-peak intervals, in μs , are quantized by using a natural logarithm and rounding the result to the nearest integer. Figure 4 explains how the hit pattern feature is computed; by counting how often a certain pattern in the coding vector appears.

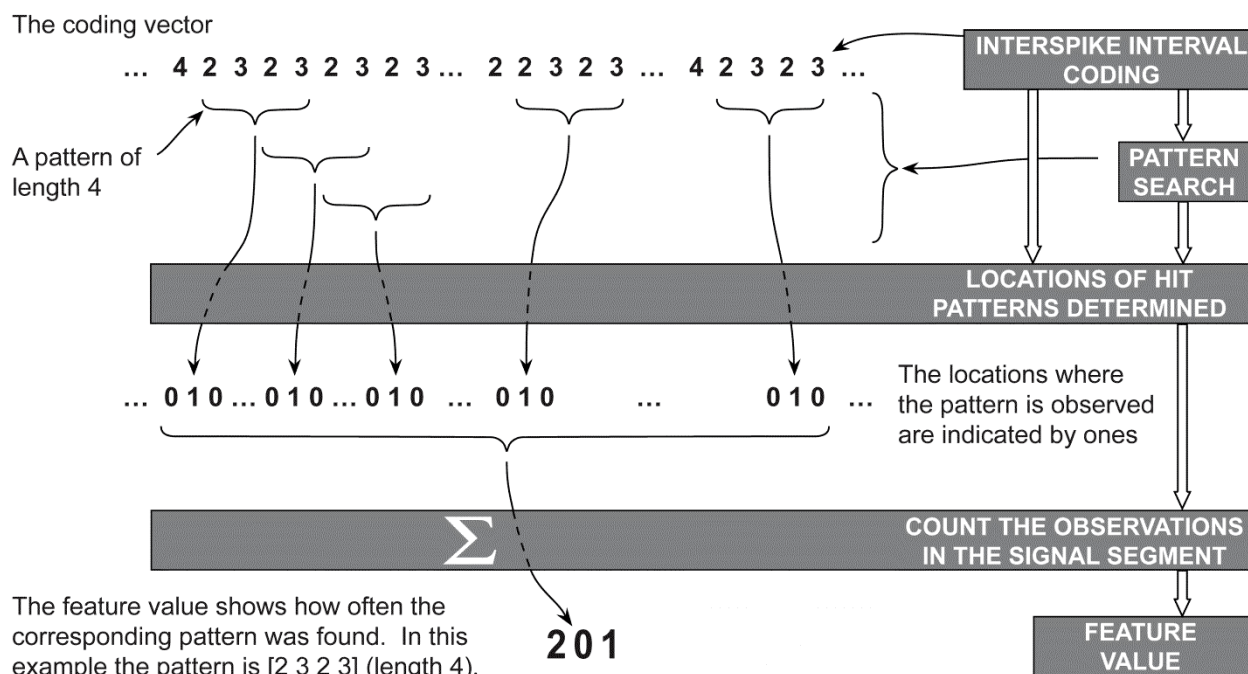


Fig. 4. The second step in computing the hit pattern feature is to find and count the number of occurrences for each hit pattern in the coded representation of the signal segment.

The patterns can be of arbitrary integer length containing an arbitrary combination of coded trough-to-peak (TTP) and peak-to-trough (PTT) intervals from any number of hits. For example, consider the following pattern of length 5: [TTP₁ PTT₁ * * TTP₃]. In order to match this pattern the coded intervals from two hits are required. The asterisk (*) is a wildcard symbol which means that any value is accepted; hence, the required coded intervals are not required to be from adjacent hits.

Results

The AE data used for this study was acquired during fatigue testing of 75 nominally identical samples of a prosthetic foot called Vari-Flex. The foot is made by Össur. In the test, a foot is placed in the test machine where two actuators are used to flex the foot using a 90°-phased sinusoidal loading. One actuator loads the forefoot and the other loads the heel. The feet were tested at 1 Hz with 50% higher maximum load amplitude than is used at Össur. All feet were tested until failure. The failure was defined by a 10% displacement criterion. The failure criterion is a heuristic criterion used in-house at Össur. It defines a failure when a 10% change in the displacement of either actuator, with respect to initial value, is observed. Throughout each test, the AE data was acquired for one full fatigue cycle every 5 minutes. The test specimen, the test setup, and the experimental procedure used in this study, are described in more detail in references [11, 12, 16].

The goal of this study is to find an AE feature, which can be used to provide a timely warning of impending failure in a CFRP composite subjected to multi-axial loading. The failure is defined by the 10% displacement-based failure criterion. In order to achieve this objective, experimental data acquired during cyclic testing of 75 prosthetic feet is used.

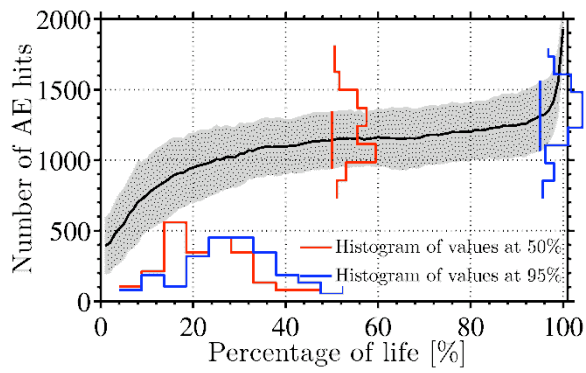
The lifetime of each foot is normalized to 100% according to the 10% displacement failure criterion. The probability distribution, of the feature values at each percentage point is estimated by first computing the feature from all measurements, for each foot tested, and then generating a histogram of the feature values at the given percentage point of lifetime. All figures in this section have a grey area that represents all values that lie within one standard deviation from the mean. Also superimposed on the figures are histograms that show the distributions of the feature values at 50% and 95% of the fatigue life. The AE features are evaluated by how well the two probability histograms at 50% and 95% of the normalized lifetime can be separated using an estimated Bayes optimal decision threshold. The threshold is computed using the corresponding feature computed from all the tested feet. Although the Bayes optimal decision boundary does not guarantee an error free classification, it gives the lowest error rate [13].

AE Features in the Time Domain

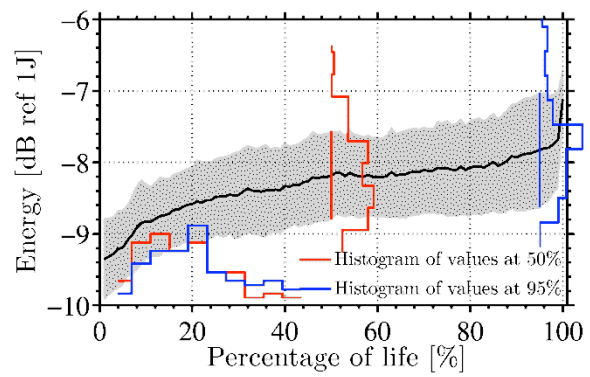
Figures 5a and 5b show the average evolution of the AE hit count and the AE signal's energy for all feet tested respectively. The energy of the AE signal, E, is computed using:

$$E = \frac{1}{R} \sum_{i=1}^N x^2 \Delta t,$$

where x is a vector of length N, containing the discrete values of the AE signal. The sampling interval, Δt, is equal to the reciprocal of the sampling rate, or 1/fs. The reference resistance, R, is 10 kΩ [14]. As a result, the energy unit is joules (equal to Watts-seconds or volts²-seconds per ohm).

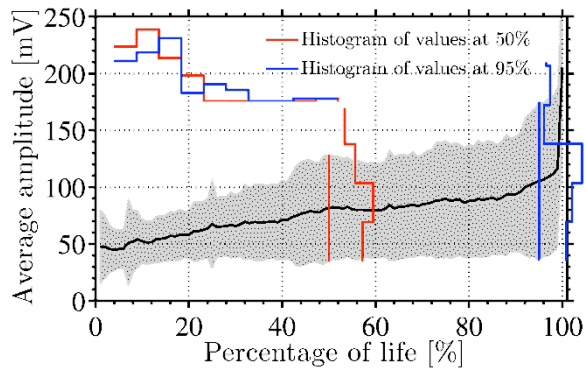


(a) The average evolution of the AE hit count rate.

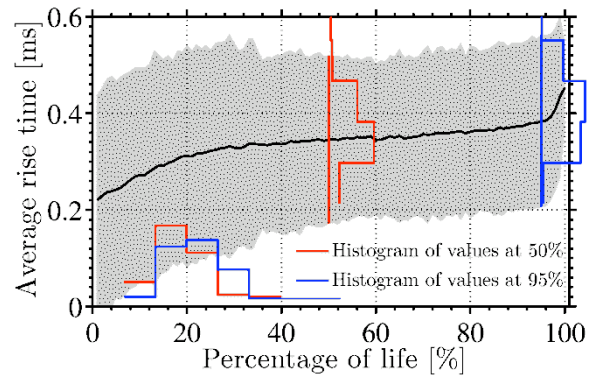


(b) The average evolution of the signal energy.

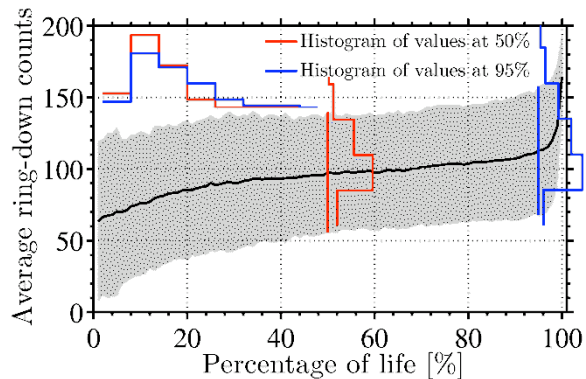
Fig. 5. The average evolution of the AE hit count and the signal's energy. The grey area represents all values that lie within one standard deviation from the mean.



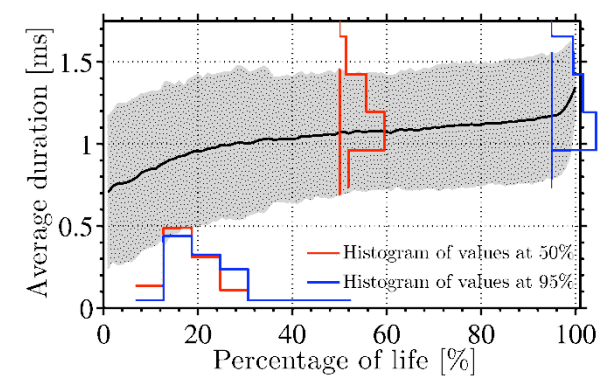
(a) The average evolution curve for the amplitude.



(b) The average evolution curve for the rise time.



(c) The average evolution curve for the ring-down counts.



(d) The average evolution curve for the duration.

Fig. 6. The average evolution of five commonly used AE hit features. The grey area represents all values which lie within one standard deviation from the mean.

Figure 6 shows the evolution of four AE hit-based features. Each curve is generated by averaging the feature evolution curves from all feet. The points on the evolution curve for each foot are computed by extracting the AE hit features from all hits in a segment and then computing their average. By computing the average, extreme AE hit values may pass unnoticed because a few high values will not alter the mean by much. For this reason, it is of interest to study the evolution of the hit features extracted from the hit with the largest amplitude. Figure 7 shows the

evolution of the amplitude, duration, and the rise time of the hit with the largest amplitude from each signal segment. Also depicted in the figure is the amplitude ratio of the two hits with the largest amplitudes.

Spectral Features

Elliptical bandpass filters, each with 25-kHz bandwidth, are used to divide the original bandwidth into subbands. The power in the subbands is computed along with the ratio between the two subbands with the largest powers and the ratio between the subbands with the maximum and minimum power. The evolution of four selected subbands and the ratios is presented in Fig. 8.

The two histograms for each of the features presented in Figs. 5-8 have nearly identical shapes and overlap almost completely. For this reason they cannot be used to separate the feature values at 50% of the lifetime from the values at 95% of the lifetime. Furthermore, from these results it can be deduced that the fall time feature cannot be used for this purpose (in fact, this was verified). This is because the duration of a hit is the sum of the rise time and the fall time.

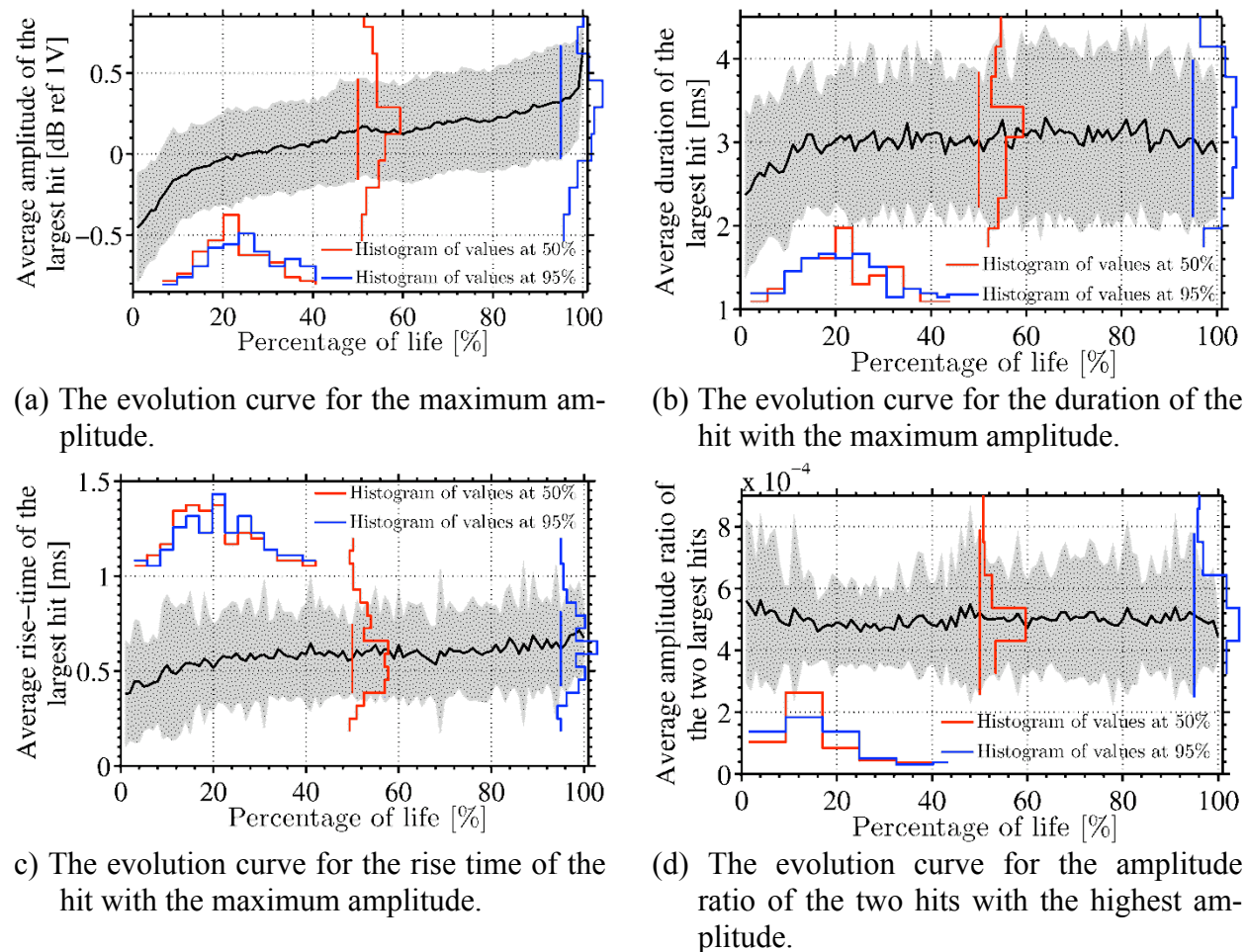


Fig. 7. The average evolution of AE hit features extracted from the hit with the maximum amplitude and the amplitude ratio of the two hits with the largest amplitudes. The grey area represents all values that lie within one standard deviation from the mean.

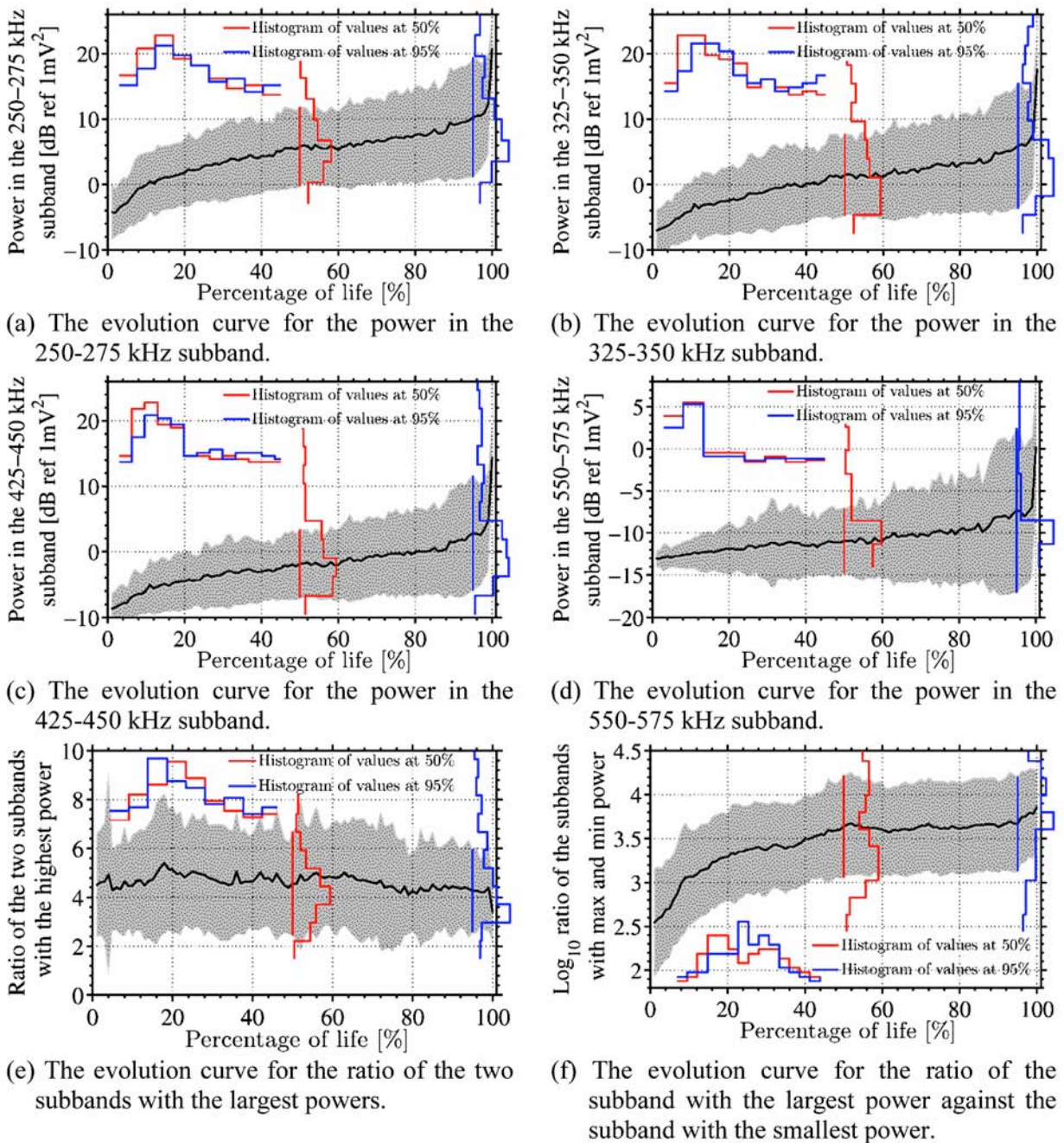
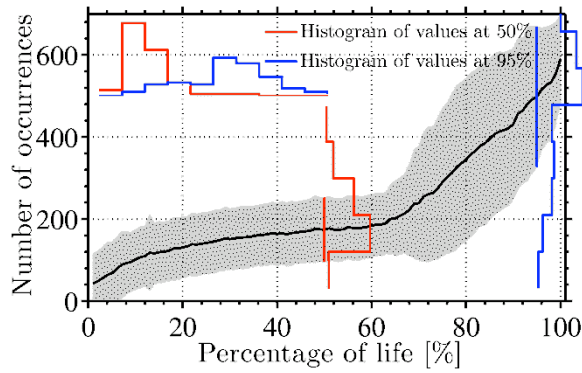


Fig. 8. The average evolution of AE features in the frequency domain. The grey area represents all values that lie within one standard deviation from the mean.

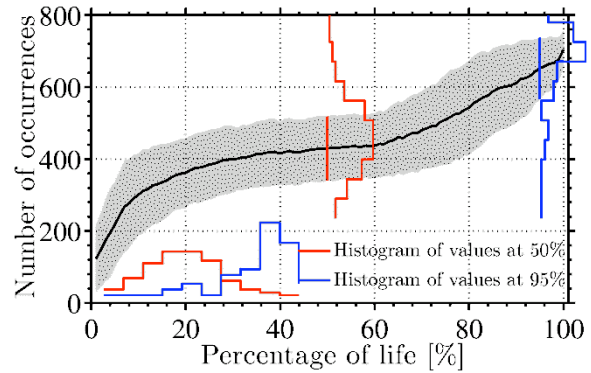
Trough-to-peak Pattern Feature

Figure 9 shows the average evolution of four selected trough-to-peak patterns of length 2 (see Fig. 4 for illustration). These patterns contain the coded values of the fall time of one hit and the rise time of the next adjacent hit.

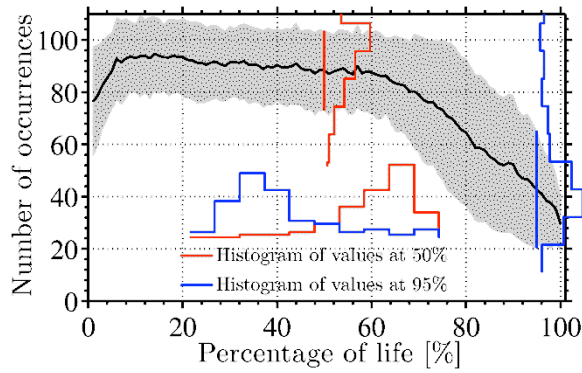
The evolution curves of these four trough-to-peak patterns have a slope change at around 60% of the lifetime. The evolution curves corresponding to the other AE features shown above do not have a slope change at this percentage point of the lifetime. Instead, the evolution curves of most of the features shown above change abruptly during the last 5-10% of the lifetime. This abrupt change, however, is not present in the evolution curves for the trough-to-peak patterns.



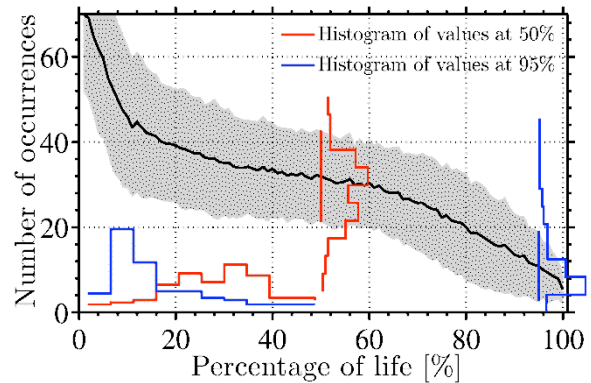
(a) The average evolution of the number of occurrences of trough-to-peak pattern no. 87.



(b) The average evolution of the number of occurrences of trough-to-peak pattern no. 94.



(c) The average evolution of the number of occurrences of trough-to-peak pattern no. 95.



(d) The average evolution of the number of occurrences of trough-to-peak pattern no. 102.

Fig. 9. The average evolution of the number of occurrences of four trough-to-peak patterns computed from the AE segments. The grey area represents all values that lie within one standard deviation from the mean.

Furthermore, as one can observe, the histograms of the number of occurrences at 50% and 95% of the lifetime for these patterns can be separated using thresholds.

Table 1 lists the four patterns and the corresponding estimated Bayes optimal decision thresholds. In order to make the patterns more intuitive for the reader, the patterns are augmented by placing – and + where the troughs and peaks are located respectively.

Table 1. Four trough-to-peak patterns of length 2. The last column contains the estimated Bayes optimal decision threshold.

	The Pattern	Decision Threshold
Pattern 87	[3 – 3 +]	388. 6
Pattern 94	[3 – 2 +]	562
Pattern 95	[4 – 3 +]	64
Pattern 102	[4 – 4 +]	11. 6

Conclusions

In this paper several commonly used AE features have been studied for the purpose of using them to provide a timely warning of impending failure. Furthermore, a trough-to-peak pattern feature was presented and compared against the other AE features. The trough-to-peak pattern feature is a pattern of an arbitrary length, containing a combination of rise times and fall times of one to several AE hits. The authors are not aware of any published research on AE where patterns in the occurrences of these two features have been studied.

The evolution curves of the trough-to-peak patterns have a slope change at around 60% of the lifetime. The slope then remains constant until failure. This slope change is not present in the evolution curves for the other AE features. This suggests that these trough-to-peak pattern features are capturing important information from the AE signal, e. g. the slope change may be caused by the formation of a damage that grows until failure. Intuitively, the salient slope change can be used to provide an early warning about the health of the composite, and the results support this. The trough-to-peak patterns is the only feature, studied here, which probability distributions at 50% and 95% of the lifetime can be reasonably well separated using a Bayes optimal decision boundary.

The evolution curves studied in this section are all normalized according to the lifetime determined by a 10% displacement criterion. Half of the split-toe foot component for some feet, however, delaminates before the criterion is met. This is represented by a minute increase in the standard deviation in the last 10% of the lifetime for the energy, amplitude and the subband powers.

It has been suggested that AE from cumulated damage can provide valuable information about the material health [15]. This type of AE has mainly been regarded as unwanted and many attempts have been made to filter it out. In this study, a few AE features are extracted from the AE signals without any attempt to filter out AE from cumulative damage. These features are the energy, the subband powers and the trough-to-peak patterns that gave the best results.

The promising results obtained using the trough-to-peak patterns strongly encourage further investigations of ISI and hit pattern features. Patterns made using different coding, different pattern lengths and fusing of different features can possibly be used to extract more useful information from the AE signal.

Acknowledgements

The work of the first author was supported by grants from the University of Iceland Research Fund, the Icelandic Research Council (Rannis) Research Fund, and the Icelandic Research Council Graduate Research Fund. Furthermore, the authors wish to acknowledge Össur for both providing prosthetic feet for testing and for providing access to their testing facilities.

References

1. M. Wevers, NDT and E International, **30**, (1997), 99-106.
2. A. P. Mouritz, *Fatigue in Composites*, Woodhead Publishing Ltd., Cambridge, 2003, 242–266.
3. M. Giordano, A. Calabro, C. Esposito, A. D'Amore, and L. Nicolais, *Composites Science and Technology*, **58**, (1998), 1923-1928.

4. D. Tsamtsakis, M. Wevers, P. De Meester, *J. of Reinforced Plastics and Composites* **17**, (1998), 1185–1201.
5. H. Nayeb-Hashemi, P. Kasomino, and N. Saniei, *J. of Nond. Evaluation*, **18**, (1999), 127-137.
6. E. R. Green, *Journal of Nondestructive Evaluation*, **17**, (1998), 117-127.
7. L. A. Duesing, *Reliability and Maintainability Symposium*, 1989, 128–134.
8. W.H. Prosser, *SPIE Conference on NDE Techniques for Aging Infrastructure and Manufacturing: Materials and Composites*, Dec. 1996, pp. 146–153.
9. Y. A. Dzenis and J. Qian, *International Journal of Solids and Structures*, **38**, (2001), 1831-1854.
10. R. Unnthorsson, T. P. Runarsson, M. T. Jonsson, *J. of Acoustic Emission*, **25**, (2007), 260–266.
11. R. Unnthorsson, T. P. Runarsson, M. T. Jonsson, *J. of Acoustic Emission*, **25**, (2007), 253–259.
12. R. Unnthorsson, T. P. Runarsson, and M. T. Jonsson, *International J. of Fatigue*, doi:10.1016/j.ijfatigue.2007.02.024, 2007.
13. R. Duda, P. Hart, D. Stork, *Pattern Classification*, Wiley-Interscience, New York, 2001.
14. M. F. Carlos and H. Vallen, *Nondestructive Testing Handbook*, ASNT, vol. 6, 2005, pp. 153-154
15. J. Awerbuch, S. Ghaffari, *J. of Reinforced Plastics and Composites*, **7**, (1988), 245–264.
16. R. Unnthorsson, University of Iceland, Ph.D. Thesis, 2008

IDENTIFICATION OF DAMAGE INITIATION AND DEVELOPMENT IN TEXTILE COMPOSITE MATERIALS USING ACOUSTIC EMISSION

D.S. IVANOV, S.V. LOMOV, I. VERPOEST and M. WEVERS

Department of Metallurgy and Materials Engineering, Katholieke Universiteit Leuven,
Kasteelpark Arenberg, 44, B-3001 Leuven, Belgium

Keywords: Textile composites, strength, stress/strain curves

Abstract

Damage in textile composites is closely connected with the internal micro- and meso-geometry of the reinforcement, and reveals features different from classical laminates. This paper presents a test sequence to characterise damage in textile composites and its dynamics of initiation and development on different scale levels in order to achieve a deep understanding of the relevant phenomena. The proposed test sequence consists of the following steps: 1) Tensile tests on samples cut in characteristic directions of the textile reinforcement with acoustic emission (AE) and full-field strain measurement on the surface. The test produces stress-strain diagrams and identifies based on the AE characteristic strain levels: Full-field strain measurement highlights relation between strain concentrations (linked with the damage initiation) and the reinforcement structure. 2) Samples loaded are examined with microfocus-X-ray computed tomography and radiography, revealing the damage pattern and allowing a quantitative analysis of the damage development. 3) Microscopic examination of cross-sections through the damage sites, determined with X-ray, identifies the local damage modes. Macro-, meso- and micro-characterisation of damage result in a thorough understanding of the material behaviour. The paper presents and discusses the results of the proposed experimental protocol for carbon/epoxy 3-axial braided and quasi-UD composites.

Introduction

Textile composites are steadily gaining positions in aeronautical, automotive, ground transportation and other applications, offering weight reductions over the metal alternative and cost saving against the lay-up of UD tapes. Whilst the design for stiffness of textile composite parts can use validated predictive modelling, related to the meso-structure of textile reinforcements [1-5], the reliable design for strength with not-that-exaggerated safety factors has to be based mostly on empirical information, with modelling approaches being developed [1, 6-11], but still have not reached a mature state. Validation of the modelling methods asks for adequate experimental characterisation of the damage processes on different scale and hierarchical levels of the composite, as the damage phenomena in textile composites are much more complicated than in UD laminates, and involves processes and parameters on different scale levels: macro (overall strength and strain-to-failure of the sample and stiffness reduction), meso (damage initiation sites inside the textile structure of the reinforcement) and micro (local damage mode inside yarns and fibrous plies).

The aim of the paper is to describe a methodology of a systematic study of the damage phenomena in textile composites during tensile deformation. The proposed experimental protocol is illustrated on two cases of carbon/epoxy textile composites.

Tensile Test, Damage Monitoring and Post-mortem Characterisation

The proposed suite of tests includes: tensile test with AE and full-field strain-mapping (SM); X-ray and ultrasonic C-scan examination of the samples after tension up to certain strain levels, identified by AE and SM results; cross-sectioning and microscopic examination of the samples in the places defined by the X-ray examination. Full-field measurements of strain fields and damage identification in textile composites are reported in detail in [12, 13].

Tensile test: The tensile tests are carried out on a standard testing machine (Instron 4505, test speed 1 mm/min). The samples are cut out of composite plates in the characteristic directions dictated by the textile structure: (1) test in the direction of one of the yarn systems of the textile (warp/weft for woven fabrics; braiding/inlay yarns for braids); (2) test in the direction transversal or bias to the direction of the yarn systems in the textile (bias for woven fabrics, perpendicular to the production direction for braids). In literature, damage in textile composites is often studied only for the fibre direction, which does not give the full picture.

Acoustic emission: In the tensile test setup described here, two AE sensors are used situated at the boundaries of the gauge length region. To calibrate the AE sensors, 2H-pencil lead is broken on the sample surface on the “grip side” of each sensor and signals that occur outside of the sensors are filtered out. The cumulative energy of AE events versus tensile strain is produced. Changes of AE event rates indicate change in damage mechanisms in the sample.

Strain mapping: Strain mapping is a system of measuring strain using digital images taken of a sample during loading. The samples are first painted with a black and white random speckle pattern to give a unique pattern of the examined surface, which can then be identified by the strain mapping software program. Changes in the speckle dot pattern can quantify the deformation of the sample as the tensile test proceeds. For textile composites, the stress and strain values may vary significantly over the pattern of weaving, braiding or knitting. Local strain values can be averaged and global strain levels can be computed, hence the strain mapping system is used also as an optical extensometer, with a precision of about 0.01% strain.

X-ray, ultrasonic C-scan and microscopy: The AE and SM registration during the tensile test allows identifying the characteristic applied strain levels for damage onset or change of the damage mode. In subsequent tests, the tensile test stops at these strain levels, and the sample is examined using X-ray and ultrasonic C-scan. The aim of X-ray investigation is detecting very fine matrix cracks that occur within the yarns. An X-ray opaque penetrant (Diiodomethane) is used to fill the cracks and make the contrast higher (only cracks and defects that are connected in some way to the surface can be seen). Ultrasonic C-scan test is useful for characterisation of the overall damage extent and in revealing overall damage pattern, as previously reported in [15]. Finally, having identified the positions of the cracks in the sample, microscopic study showed a fine structure of the damage inside the sample. The sites and direction for the cuts are determined using X-ray images of the particular sample.

Materials

The materials used as examples of application of the proposed experimental methodology are shown in Fig. 1 and Table 1.

Triaxial braided carbon/epoxy composites: Braiding yarns in the triaxial braided fabric are organised in a so-called diamond pattern 1/1 (Fig. 1a). If the orientation of inlay yarns (“machine” direction) is chosen as 0°, then the braiding yarns are directed as $\pm 45^\circ$. Note the uneven placement of the braiding yarns, which produces large open regions in the fabric. The tensile tests were performed in machine direction (MD), bias direction (BD) and cross direction (CD), as indicated in Fig. 1a. From six to ten tests were performed for each direction.

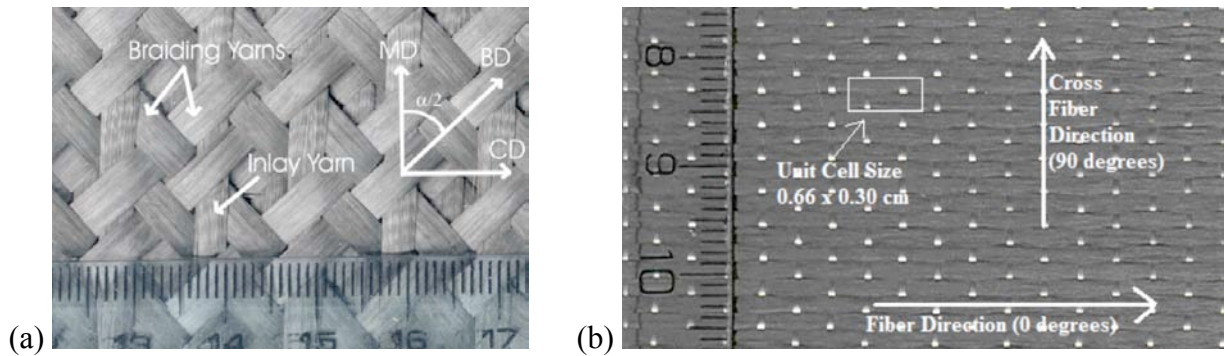


Fig. 1. Textile reinforcements: (a) triaxial braid; (b) quasi-UD woven fabric.

Quasi-UD woven fabric: The textile used for this study is a quasi-UD fabric from Cramer GmbH. It is produced by weaving flat UD carbon yarns (warp) with sparse, flat, thin glass yarns (weft). The result is an unbalanced plain weave material. This procedure reduces crimp as much as possible for the warp, however there is still some crimp of the carbon yarns, which are inclined to the fabric plane in average by an angle of 3.8° . The tensile tests were performed in the directions 0° , 30° , 45° , 60° and 90° , 0° being the direction of the warp carbon yarns (Fig. 1b). From five to seven tests were performed in each direction.

Table 1. Parameters of the textile reinforcements, matrices and the composites.

Fabric type	Triaxial braid	Quasi-UD woven
Fibres	carbon T700	carbon T400 /glass EC5
Yarns	24 K	6K / n.a.
Linear density, tex	1600	400 / 22
Thickness, mm,	variable	0.311 ± 0.011 / 0.058 ± 0.012
Width, mm	4.21 ± 0.21 / 3.75 ± 0.16	1.58 ± 0.12 / 0.62 ± 0.04
Fabric	Fig. 2a	Fig. 2b
Spacing between yarn centre lines, mm	5.03 ± 0.24 ; 9.25 ± 0.03 / 20	1.53 ± 0.10 / 3.27 ± 0.06
Areal density, g/m^2	600	285
Matrix	Epoxy	
Young modulus, GPa	2.7	
Poisson coefficient	0.4	
Strength, MPa	70	
Composite tensile specimens	produced using RTM	
Number of layers	4	10
Thickness, mm	3.09 ± 0.06	3.5
Width x Length between the grips, mm	40 x 250	15 x 200
Fibre volume fraction, %	44 ± 1	46.3

Damage Initiation: Characteristic Strain Levels

When damage is characterised inside a composite by “post-mortem” study of the sample, it is important that the expected damage condition of the sample when the test is stopped, is well

identified. The following stages of the damage development and the correspondent levels of the applied load (strain) can be introduced: (1) onset of transverse cracks (inter-fibre, intra-yarn failure), (2) onset of delamination on the boundaries of the fibre bundles and (3) onset of fibre failure, starting at delamination, and the ultimate failure of the sample.

This classification could be refined [16], but we propose to keep these three levels as reference points of the damage investigation. An important difficulty is definition what exactly “the damage initiation” means. As the inter-fibre transversal cracks may be created by coalescence of the “crescent” debonding on the individual fibres, the definition of “initiation” is rather fuzzy. We consider the damage initiation strain to be an indication of appearance of a crack, which connects several debonded fibres. In reality such a transversal crack develops fast into a crack through the whole thickness of the yarn.

Figure 2 shows stress-strain diagrams of two types of composites together with diagrams of cumulative energy of AE events. At the very beginning of the test, few events of low energy contents occur with low frequency. Then the frequency of events increases sharply and the energy content reaches higher levels. This is reflected by the increase of the slope of the cumulative AE event energy curve, which was negligent before. The corresponding *first transition strain* is calculated by the best fit of the bilinear curve (zero before the transition and linearly increasing after it) to the AE cumulative energy diagram. We will designate this first transition strain ϵ_1 . The AE events “heard” before could be interpreted as micro-debonding events; the onset of steady generation of higher energy AE events – as appearance of transversal inter-fibre cracks (tri-axial braid) or delaminations on the boundaries glass/carbon yarns (quasi-UD woven).

For triaxial braid this interpretation is confirmed by X-ray observation of the samples loaded to a strain just below the first transition strain and after it (Fig. 2a). X-ray images reveal no cracks before the transition and appearance of few cracks just after it, which further multiply with the increase of the strain. For quasi-UD woven fabric X-ray examination does not reveal any crack as they are not connected with the surface of the samples; the damage initiation, detected by AE, was confirmed by microscopic examinations.

For the loading in fibre direction (Fig. 2a) the damage initiation does not affect the slope of the stress-strain diagram, as the resistance to the deformation in fibre direction is provided by the corresponding fibre system (inlay 0° yarns). For the loading in an off-axis direction (Fig. 2b) initiation of damage also corresponds to the transition from the initial linear part of the stress-strain diagram to the non-linear behaviour.

After the initiation strain ϵ_1 the damage behaviour is characterised by constant increase of AE events in the same energy range, giving a steady slope or a “jump” to the cumulative energy curve. This region covers a wide range of strain, until high deformations. At a certain moment a second “knee” on the AE cumulative energy curve may appear. The corresponding *second transition strain* ϵ_2 can be again identified by fitting a bilinear curve to the AE cumulative energy diagram. The second transition strain is not that clearly determined as the first. For the case of tri-axial braid X-ray observations allow identifying it with the onset of local delamination (Fig. 2a).

Finally, fibre breakage (loading in fibre direction, Fig. 2a) is indicated by the appearance of extremely high-energy AE events and sharp rise of the cumulative AE events diagram. This happens very close to the final failure of the specimen.

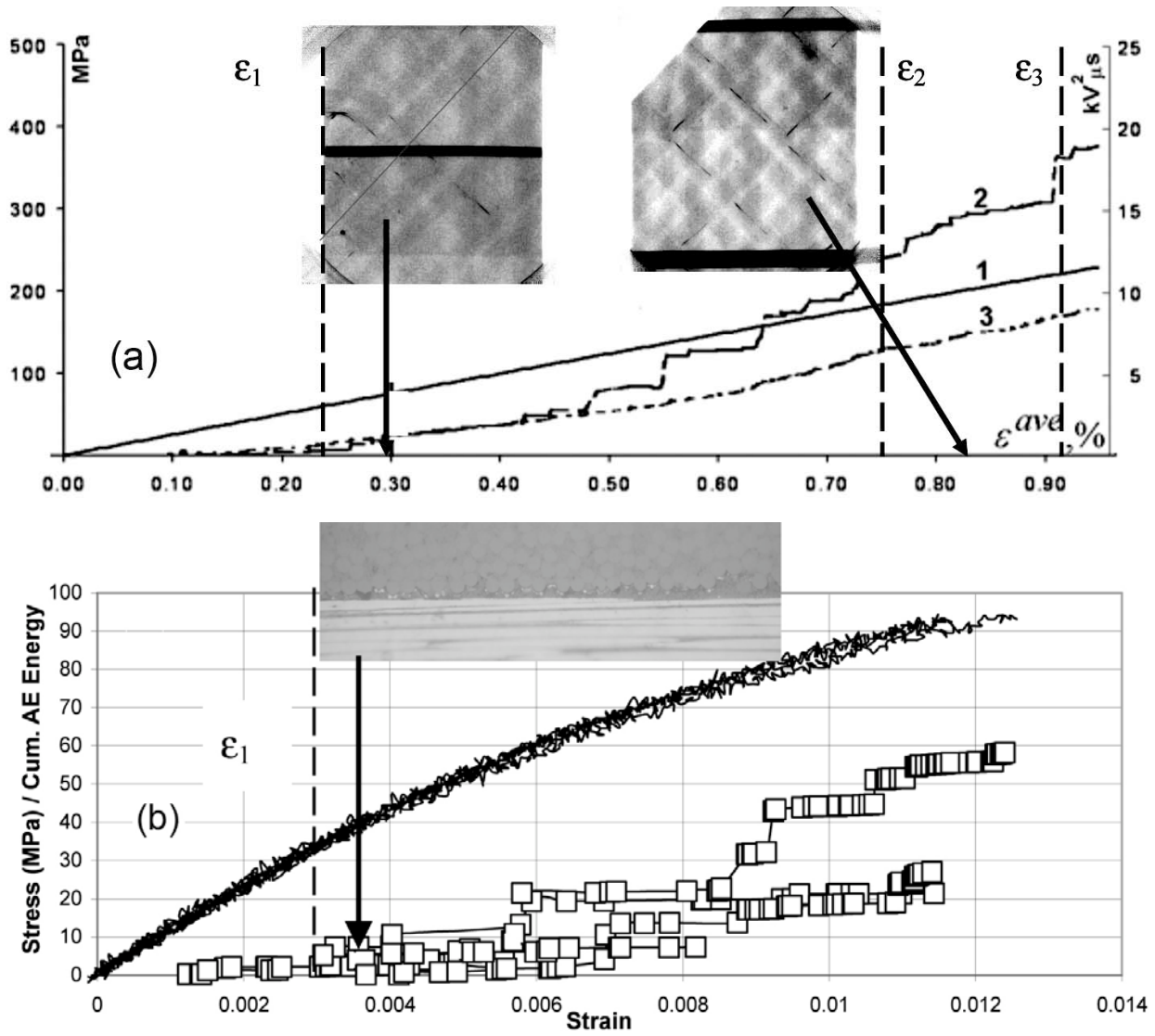


Fig. 2 Stress-strain diagrams and AE registration for carbon/epoxy composites: (a) triaxial braided composite, MD test, 1 – stress-strain diagram, 2 – cumulative AE events energy, 3 – cumulative AE event count; insets – X-ray images; (b) quasi-UD woven composite, 30° test direction, combined results of 5 tests, lines – stress-strain diagrams, points – cumulative AE event energy; inset: micrograph showing early delamination between carbon and glass yarn.

Formal calculation of the transition strains ε_1 and ε_2 (if the second transition on the AE curve exists) is performed by the least-square fit of all the cumulative AE energy (CAE) data points (ε_k , CAE_k) by a bilinear function with fitting parameters $\varepsilon_1, \varepsilon_2, CAE_1, CAE_2$.

$$CAE(\varepsilon; \varepsilon_1, \varepsilon_2, CAE_1, CAE_2) = \begin{cases} 0, & \varepsilon < \varepsilon_1 \\ (\varepsilon - \varepsilon_1) \cdot \frac{CAE_1}{\varepsilon_2 - \varepsilon_1}, & \varepsilon_1 \leq \varepsilon \leq \varepsilon_2 \\ CAE_1 + (\varepsilon - \varepsilon_2) \cdot \frac{CAE_2 - CAE_1}{\varepsilon_{\max} - \varepsilon_2}, & \varepsilon > \varepsilon_2 \end{cases}$$

Table 2 lists the characteristic strain levels for the studied materials and different test directions.

Damage Development

With the characteristic strain levels identified, the damage investigation proceeds further to studying the damage structure under loading up to the characteristic levels. This is done using non-destructive techniques: Ultrasonic C-scan and X-ray investigation, and then doing microscopy at the sections made on the sites identified by the X-ray investigation. The results of this study for the two materials under consideration are only discussed here without illustration.

Table 2. Characteristic strain levels, %.

Material	Test direction	ϵ_1	ϵ_2	ϵ_{ult}
3-axial braid	MD	0.29	0.55	1.45±0.15
	BD	0.36	0.45	1.25±0.18
	CD	0.33	0.43	1.11±0.03
quasi-UD	0°	0.16	n/a	2.25±0.058
	30°	0.4	n/a	1.79±0.28
	45°	0.4	n/a	1.08±0.23
	60°	0.4	n/a	1.00±0.26
	90°	0.15	n/a	0.80±0.25

Triaxial braided composite: The crack structure is clearly revealed by X-ray images and is further investigated by microscopy of the cross-sections. Transversal cracks in the yarns, with the plane oriented in the direction of the yarns, start developing at ϵ_1 . The cracks are confined in one ply/one yarn, being therefore limited in width as well as in length. When two yarns with the same direction of the fibres are in contact, a crack can travel from one yarn to another. FE modelling, reported in detail in [11,17] shows that these cracks are caused either by transversal tension or shear strains. With the increase of strain the cracks multiply and the length increases. Longer cracks are developed in the yarns, which are oriented at 90° to the loading direction, but these cracks still have limited length and do not go from one end of the sample to another. At the strain level ϵ_2 local delaminations start.

The samples final failure for MD and BD tests (in the direction of inlays and braiding yarns correspondingly) is delamination and consecutive fibre breakage. Straightening of highly crimped braiding yarns produce out-of-plane stresses, which create large delamination zones. These delamination zones are smaller for samples tested in MD, as the inlay yarns are less crimped. Off-axis CD loading leads to more localized fracture locus coinciding in the direction and width with the braiding yarns.

Quasi-UD woven composite: In spite of the clear detection of AE events over the ϵ_1 threshold, X-ray examination of samples after tensile test up to this strain level did not show any cracks in the samples, apart from 90° tests, where transversal cracks were revealed. To determine the source of AE activity and stiffness degradation, optical microscopy was used. In the cross-sections of the samples (made in two directions: orthogonal to the carbon warp and glass weft yarns) small cracks have formed between the carbon and glass yarns in only the surface textile layers within the composite in the off-axis samples. These cracks, surprisingly, are parallel to the sample surface. The fact that these cracks are parallel to the force, and are located at or near the carbon-glass interface indicates that these cracks have formed due to shear between the glass and carbon yarns. The crack runs between the carbon and glass yarns when the glass yarn is on the outside (at the edge of the composite), but when the glass yarn moves under the next carbon yarn, the crack is transferred into the second carbon yarn, and continues there until the next carbon yarn

where it resumes its place between the glass and carbon yarns. This transfer of the crack across the glass yarn is accomplished without breaking the glass yarn itself. The glass interlacing yarns are very thin and are sparsely distributed in the textile, and the cracks generated in the material only seem to occur when there is an interaction (overlapping) between the carbon and the glass yarns at the surface. Therefore the size of the defects is small and they are generally not connected to the surface and thus were not readily observable using X-ray. The samples tested in the fibre direction (0°) fail by fibre failure. Other test directions (30°, 45°, 60° and 90°) produce clear shear/transversal failure along the fibres.

Conclusions

We have outlined an experimental methodology for study of initiation and development of damage in textile composites in tension test. The methodology has been applied to different textile composites: carbon/epoxy triaxial braids and quasi-UD woven. The methodology is based on identification of the characteristic levels of the applied load. These levels are further used for investigation of damage modes and crack structure in the material.

References

1. Bogdanovich, A.E. *Journal of Materials Science*, 2006; **41**(20): 6547-6590.
2. Bogdanovich, A.E. and Pastore C.M. *Mechanics of Textile and Laminated Composites*. 1996, London: Chapman and Hall.
3. Bogdanovich, A.E. and Pastore C.M. *Composites Sci. and Tech.*, 1996; **56**: 291-309.
4. Lomov, S.V., Huysmans, G., Luo, Y., Parnas, R., Prodromou, A., Verpoest, I. and Phelan, F.R., *Composites part A*, 2001; **32**(10): 1379-1394.
5. Verpoest, I. and Lomov, S.V. *Composites Sci. and Tech.*, 2005; **65**(15-16): 2563-2574.
6. Zako, M., Uetsuji, Y. and Kurashiki, T. *Composites Sci. and Tech.*, 2003; **63**: 507-516.
7. Fish, J. and Yu, Q. *Composites Sci. and Tech.*, 2001; **61**: 2215-2222.
8. Karkkainen, R.L. and Sankar, B.V. *Composites Sci. and Tech.*, 2006; **66**: 137-150.
9. Tang, X. and Whitcomb, J.D. *Journal of Composite Materials*, 2003; **37**(14): 1239-1259.
10. Greve, L. and Pickett, A.K. *Composites Part a-Applied Science and Manufacturing*, 2006; **37**(11): 1983-2001.
11. Lomov, S.V., Ivanov, D.S., Verpoest, I., Zako, M., Kurashiki, T., Nakai, H. and Hirose, S. *Composites Sci. and Tech.*, 2007; **67**: 1870-1891.
12. Ivanov, D.S., Lomov, S.V., Verpoest, I., Baudry, F. and Xie, H., *Proc of the European Conf. on Composite Materials (ECCM-12)*, 29th August - 1st September. 2006: Biarritz. CD edition.
13. Ivanov, D.S., Baudry, F., Xie, H., Lomov, S.V. and Verpoest, I. *Composites part A*, submitted.
14. Wevers, M. and Surgeon, M., *Acoustic Emission and Composites* (Chapter 5.14), in *Comprehensive Composite Materials*, A. Kelly and C. Zweben, Editors. 2000, Elsevier, pp. 345-357.
15. Truong Chi, T., Vettori, M., Lomov, S.V. and Verpoest, I. *Composites part A*, 2005; **36**: 1207-1221.
16. Benmedakhene, S., Kenane, M. and Benzeggagh, M.L. *Composites Sci. and Tech.*, 1999; **59**: 201-208.
17. Ivanov, D.S., Lomov, S.V., Verpoest, I., Zako, M., Kurashiki, T., Nakai, H. and Hirose, S. *Proc. of the 8th Intl. Conf. on Textile Composites (TexComp-8)*. 2006: Nottingham. CD edition.

WAVELET ENTROPY AND POWER OF AE SIGNALS AS TOOLS TO EVALUATE DAMAGE IN COATINGS SUBMITTED TO SCRATCH TEST

ROSA PIOTRKOWSKI^{1,2}, ENRIQUE CASTRO¹ and ANTOLINO GALLEGO¹

¹Departamento de Física Aplicada, Universidad de Granada, 18071 Granada, Spain;

²ECyT, Universidad Nacional de San Martín, 1650 Pcia. Buenos Aires, Argentina

Keywords: Wavelet power; Wavelet entropy; Damage evaluation; Coatings; Galvanized steel; Corrosion.

Abstract

Wavelet entropy and power were calculated for acoustic emission (AE) signals obtained from scratch tests on hot dip galvanized samples with different corrosion levels. Wavelet power was distributed in different frequency bands, according to damage mechanisms. The frequency bands were automatically obtained by an innovative method that consisted in searching for the relative minima of the wavelet entropy of signals and the subsequent application of a clustering algorithm. The damage evaluation entailed studying the evolution of the wavelet power in a specific frequency band, which corresponded to the fracture of the zeta-phase columns of the galvanized coating. Results showed damage to increase along with the level of corrosion.

1. Introduction

The early detection of corrosion in galvanized steel used as reinforcement in concrete structures is crucial in monitoring the condition of concrete structures in different environments and under different load circumstances. The identification of damage processes by acoustic emission (AE) has proven very effective in many applications [1-4]. AE through signal processing can be applied on-line as a non-destructive technique on remote or inaccessible parts of a structure. This approach is rooted in the broad field of pattern recognition and damage detection in materials and structures.

The present paper is within a program destined to evaluate the adherence of commercial galvanized coatings with varying depth, working under different load and corrosion conditions (see [5, 6] and included references). Wavelet transform (WT) was applied to AE signals coming from scratch test (ST) on corroded galvanized steel. The aim was to identify damage mechanisms through the assignment of a few concise and precise parameters to different coating damage processes, and then use some of them to evaluate damage.

With this purpose in mind, hot-dip galvanized samples were corroded in a salt chamber and then submitted to ST. Damage mechanisms involving deformation, fracture and/or extraction of the different phases that conformed to the corroded coating, briefly denoted in [5] as oxide, chloride, eta phase and zeta phase, were identified. WT results were adequately obtained as time-frequency AE patterns, which revealed that AE power was distributed in five frequency bands. Consequently, the evolution of AE wavelet power in different frequency bands was carefully compared with SEM and EDX observations along scratches, which permitted the assignment of one mechanism to each band. In particular, signals due to corrosion and non-corrosion mechanisms could be easily separated; different mechanisms coexisted along the ST.

In the present paper we present and exhaustively explain a new automated method to assign frequency bands to damage mechanisms based on wavelet entropy considerations. Once the bands are obtained for different scratches, a damage evaluation criterion is applied. We face the problem of adherence evaluation in non-corroded and corroded samples; corrosion levels 1, 2 were considered.

2. Experimental

The preparation of hot-dip galvanized samples (50 mm x 20 mm x 4 mm plates) involved the procedure described in [5]. Samples were hot-dip galvanized at 450°C for 3 min, after which some were submitted to corrosion.

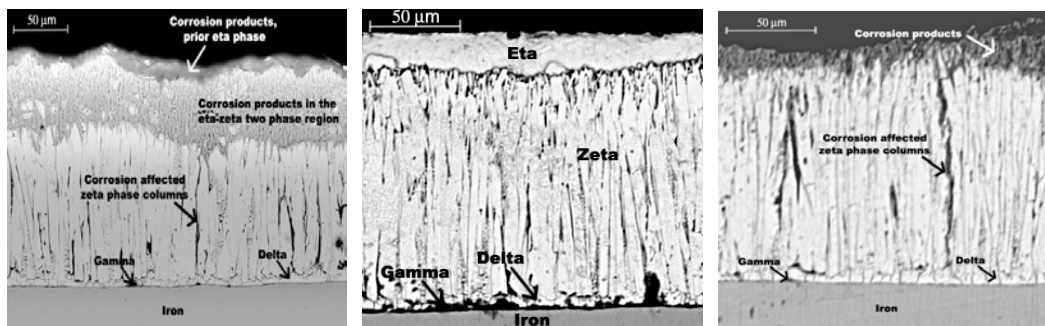


Fig. 1. Transversal cuts of samples. Left: T0; centre: T1; right: T2.

In the present study we compare results for material that was either not corroded (level 0) or corroded up to two corrosion levels (1, 2). Results are given for one sample of each type since general results coincide. According to the corrosion level (0, 1 and 2), samples are respectively named as T0, T1 and T2. The mean coating thicknesses were 152, 158 and 166 μm , in that order. T1 and T2 were respectively corroded for about 900 h and 1800 h in a salt mist chamber to simulate a marine environment, and afterwards they were cleaned with an ammonia hydroxide water solution (150/850 ml). Sample T0 was left as cast and was taken as a reference. Figure 1 shows a transversal cut of each sample. The coating of sample T0 appears quite homogeneous. The Zn-Fe phases, gamma (very thin), delta (well defined and homogeneous), zeta (columnar grains) and eta (almost pure Zn), are observed from steel to Zn (top). The interior part of the coating of sample T1 remained largely unchanged, and only the top of the eta phase was affected by corrosion. Corrosion also affected the eta-zeta two-phase region of the coating of sample T2. As was stated in [5], corrosion products are a mixture of a Zn oxide and a hydrated Zn chloride.

Two scratches were performed on each sample, according to the procedure described in [5]. STs with AE were performed under controlled conditions using a device that consisted of a loaded probe with a diamond indenter moving linearly along the sample at constant speed, and with linearly increasing force (0-150 N) over 180 s; the scratch length was about 1 cm. The piezoelectric sensor was in the 100-1000 kHz range, signals were pre-amplified (60 dB), the threshold was at 25 dB and digitization was at 4 MHz/16 bits. In addition to digitizing the signal, the AE system entails the measurement of pertinent hit parameters, where a hit is defined as each signal that surpasses the threshold.

We denote the n -th AE signal recorded along the test as $s^n(t)$, with $n = 1 \dots N_r$. The total number of registers (N_r) depends on the sample and the scratch that corresponds to each ST. If $\Delta t = 2.5 \cdot 10^{-7}$ s is the sampling period, $s^n(k)$ corresponds to $s^n(k\Delta t)$ with $k = 1 \dots N$; it thus denotes the

k -th sample of the signal $s^n(t)$. In our case, 4000 data were recorded for each AE signal, which means $N = 4000$ for all signals.

The supra-index n is related with the position along the scratch. If T_n is the instant, at which the AE signal $s^n(t)$ was captured, the corresponding position on the scratch is given by $x_n = vT_n$, where v is the speed of the diamond indenter. At the beginning of the ST time is initialized to zero, and at the end it is set at $T_e = 180$ s. We emphasize that two temporal scales are involved. One is designated with lower case t to measure time in each register, which ranges within 0 – 1 ms, and the other is designated with capital T that measures time among registers, ranging within 0 - 180 s.

For practical reasons, we use the relative position in %, $X_n(\%)$, on the scratch instead of the real position x_n . Thus, the relative position where the signal $s^n(t)$ is captured is at $X_n(\%) = 100 (T_n/T_e)$.

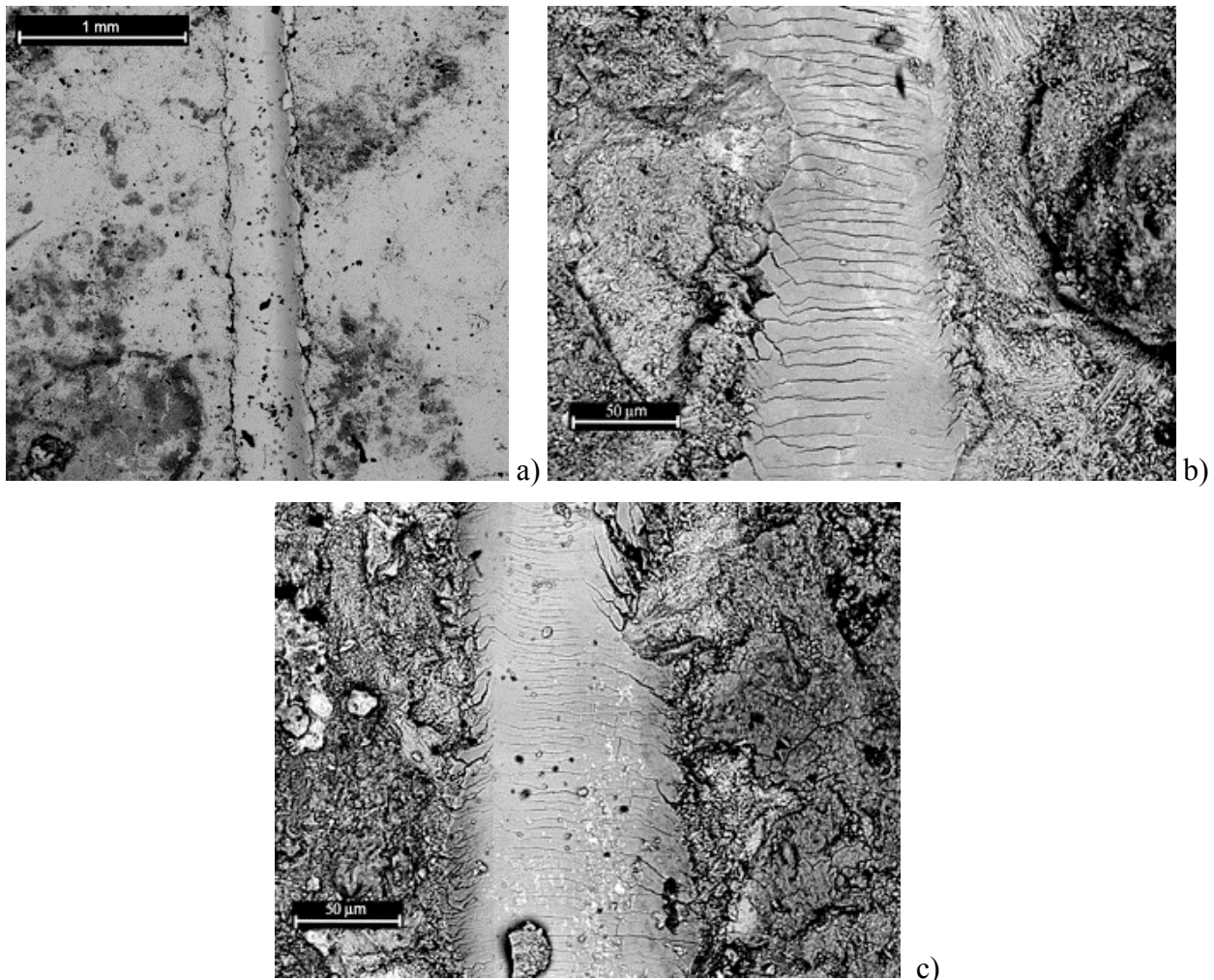


Fig. 2. Details of the central part of scratches. Top left: T0; top right: T1; bottom: T2.

SEM and EDX observations showed in [5] that the failure mechanisms in the non-corroded samples (such as sample T0) were the slippage of the eta phase and the breakage of zeta phase columns with eventual ulterior extraction of the zeta phase cracked particles. Other mechanisms besides the aforementioned appeared when corrosion was considered as for samples T1 and

T2—namely, the transversal cracking of the oxide phase and the interfacial cracking and extraction of the chloride particles. Figure 2 shows the central part of scratches in the three samples. For samples T1 and T2, we can observe transversal oxide cracks in the middle of scratches and extracted chloride particles (white and sized in the order of microns) at the borders. The density of transversal cracks is higher for sample T2.

3. Damage Mechanisms Identified by WT Parameters

3.1. Visual frequency bands obtained by wavelet power

AE is a non-stationary process, i.e. the power spectrum changes with time, where short and long-time phenomena coexist. For this reason a scale-time procedure like the WT [7] is an ideal tool for managing data. The synthesis and analysis formulas are respectively displayed in (1) and (2) for the register n :

$$s^n(t) = \sum_j \sum_k c_{jk}^n \psi_{jk}(t), \quad (1)$$

where

$$c_{jk}^n = \int_{-\infty}^{\infty} s^n(t) \psi_{jk}^*(t) dt \quad (2)$$

are the coefficients that constitute the WT; sub-index k corresponds to time displacement (in our case as previously mentioned $1 \leq k \leq 4000$) and sub-index j corresponds to scale, which is associated with frequency (in our case $50 \leq f \leq 600$ kHz). Moreover, $\psi_{jk}(t)$ is the displaced and dilated version of a wavelet $\psi(t)$. The $\psi_{jk}(t)$ set is an orthonormal basis of functions with finite energy.

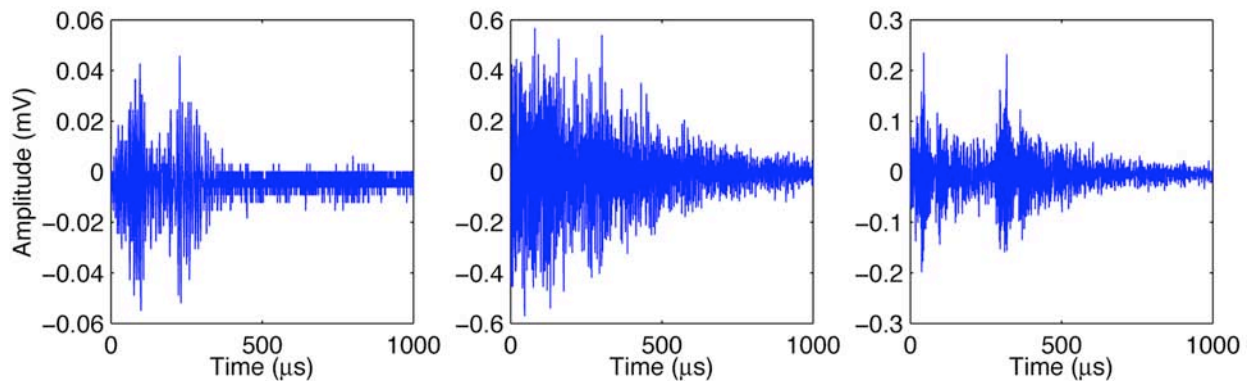


Fig. 3. AE signals coming from scratch 1 of samples: Left (T0; $s^{1432}(t)$); centre (T1; $s^{704}(t)$); right (T2; $s^{1096}(t)$).

Continuous wavelet analysis does not directly provide the time-frequency analysis of the signal; it considers dilation and translation factors for continuous time and time-scale parameters, where the scale can be correlated with frequency (the correspondence depending on the wavelet employed). At the same time, the best wavelet basis depends strongly on the physical process involved. For this reason, we used the AGU-Vallen Wavelet software [8] designed for AE signals and based on Suzuki's work [9], where the mother function is a Gabor (Gaussian) wavelet. The Gabor wavelet choice was made for different reasons: it is suited to the AE phenomena and the scale-frequency correspondence is provided, as is clearly explained in [9]. Furthermore, when WT with different bases (Haar, Gaussian, Symmlet, Daubechies) was applied to signals in

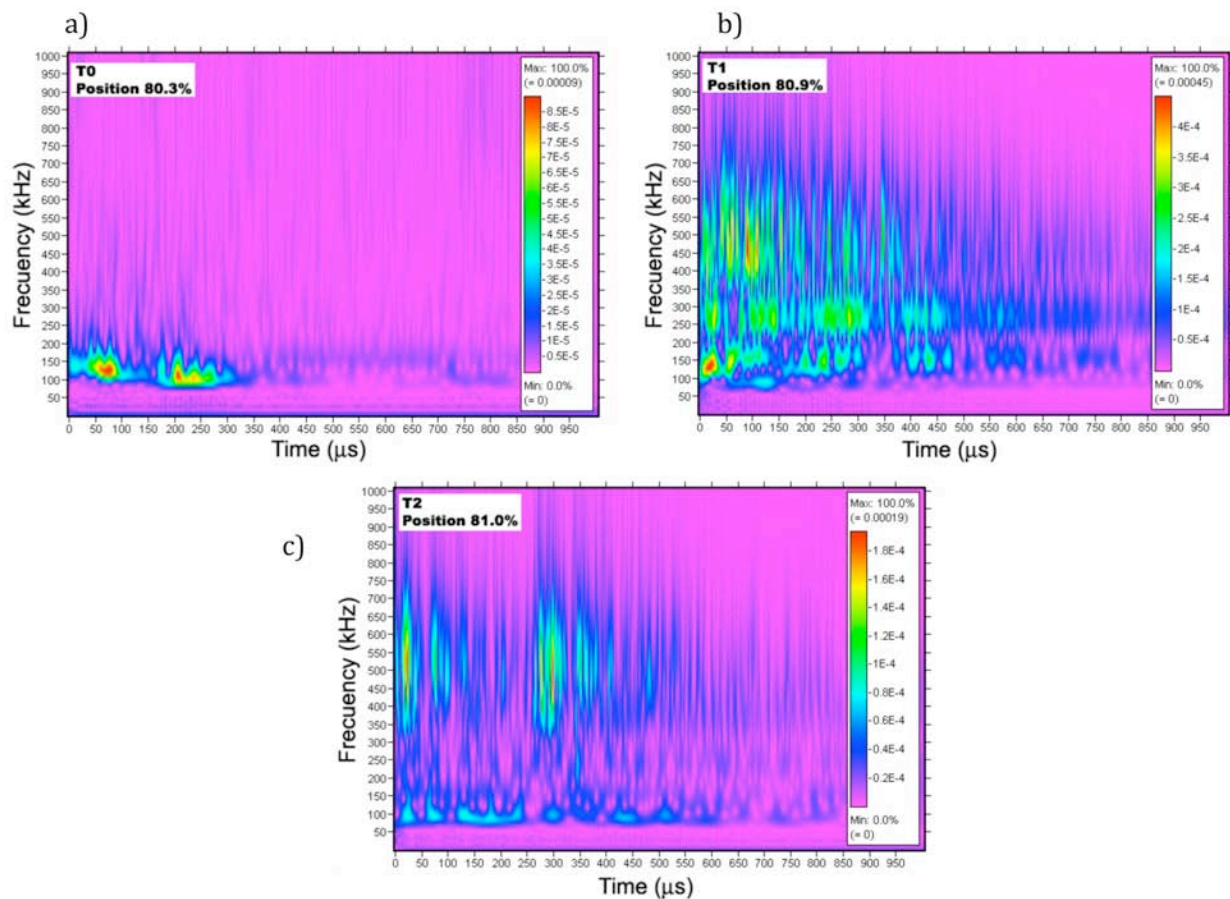


Fig. 4. WT maps from signals of Fig. 3: a) (T0; $X_{1432}=80.3\%$); b) (T1; $X_{704}=80.9\%$); c) (T2; $X_{1096}=81.0\%$).

previous work [6], we found that the scales where information was pertinent were essentially the same.

Continuous wavelet analysis does not directly provide the time-frequency analysis of the signal; it considers dilation and translation factors for continuous time and time-scale parameters, where the scale can be correlated with frequency (the correspondence depending on the wavelet employed). At the same time, the best wavelet basis depends strongly on the physical process involved. For this reason, we used the AGU-Vallen Wavelet software [8] designed for AE signals and based on Suzuki's work [9], where the mother function is a Gabor (Gaussian) wavelet. The Gabor wavelet choice was made for different reasons: it is suited to the AE phenomena and the scale-frequency correspondence is provided, as is clearly explained in [9]. Furthermore, when WT with different bases (Haar, Gaussian, Symmlet, Daubechies) was applied to signals in previous work [6], we found that the scales where information was pertinent were essentially the same.

Our results after applying the software [8] were obtained as time-frequency patterns where different colors were assigned to the different power intensities. Numerically, a matrix of squared absolute values of WT coefficients was assigned to each signal register; the number of rows and columns was determined by the register duration and the sampling frequency. Each matrix is graphically represented by a wavelet map that represents the AE power distribution in a color scale, increasing from blue to red, with one color assigned to each rectangle determined by time-frequency intervals. Figure 3 shows some examples of registers, and their corresponding

wavelet maps are seen in Fig. 4. We observe that AE power is distributed in a number of frequency bands.

On the basis of visual observation of the total wavelet maps like those presented in Fig. 4, the entire frequency range $B_0 = [50-600]$ kHz, was divided into three frequency bands, which were:

$$\begin{aligned} B_1 &= [50-200] \text{ kHz} \\ B_2 &= [200-350] \text{ kHz} \\ B_3 &= [350-600] \text{ kHz}. \end{aligned}$$

Due to results such as those shown in Fig. 4, one of the parameters that proved successful in identifying damage was related with the wavelet power for frequency interval j for each register defined by:

$$WP_j^n = \sum_{k=1}^N |c_{jk}^n|^2. \quad (3)$$

We used the same parameter defined in [5], the frequency location of the wavelet-power maximum. As different mechanisms coexisted, we studied the evolution of primary, secondary and tertiary maxima occurring in the previously defined B_1 , B_2 and B_3 frequency bands. We followed a special procedure in order to determine the position of these maxima: if the first maximum corresponded to one of the bands, the second was the one that fell in one of the other two bands; so that for the third maximum only one band remained as a possibility. Second and third maxima were only considered if their amplitude was higher than 80% of the amplitude of the first maximum. Primary, secondary and tertiary maxima for the n -th register are respectively named as $WP_{j_{max1}}^n$, $WP_{j_{max2}}^n$ and $WP_{j_{max3}}^n$. For the frequency positions of these maxima, it holds that $j_{max1} \in B_{m1}$, $j_{max2} \in B_{m2}$ and $j_{max3} \in B_{m3}$, where $m1$, $m2$ and $m3$ can take the values 1, 2, or 3. Thus, one, two or three maxima can be assigned to each register $s^n(t)$, respectively located at j_{max1} ; j_{max1} and j_{max2} ; or j_{max1} , j_{max2} and j_{max3} . The procedure is summarized in the flow chart displayed in Fig. 5.

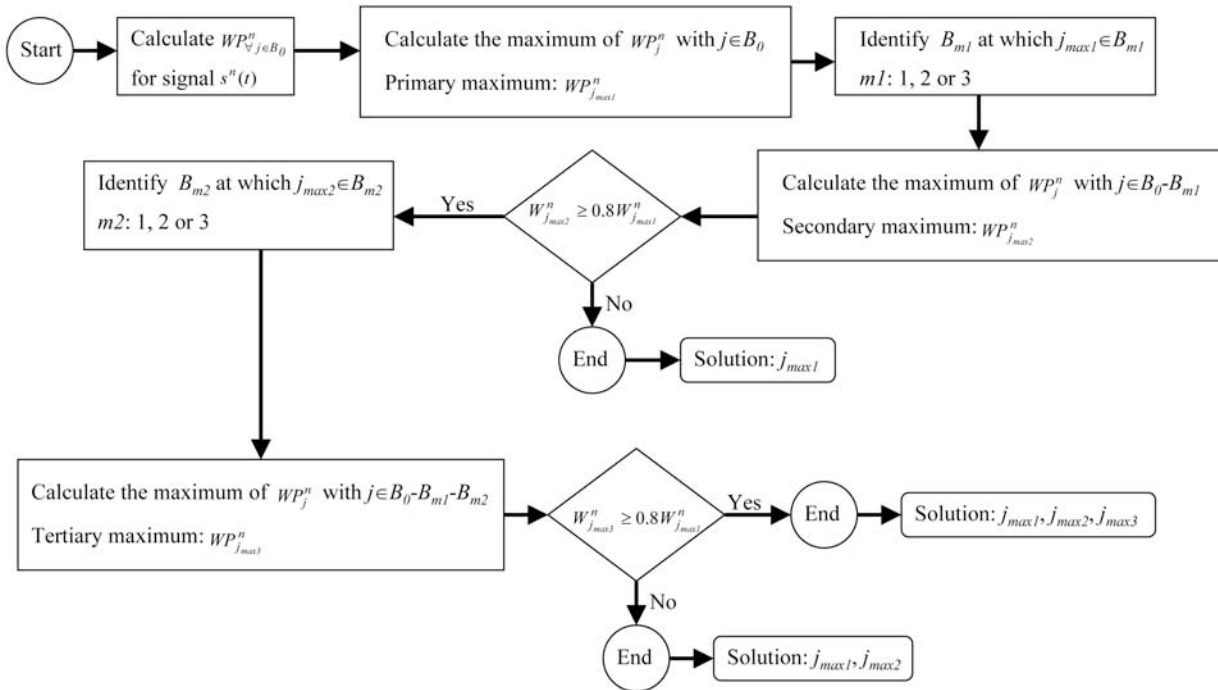


Fig. 5. Flow chart 1, which summarizes the frequency location of WP maxima.

The frequency location of maxima versus the relative position X_n (%) is shown for each register in Fig. 6. The present study includes two levels of corrosion. The important finding is that the procedure was successful for corrosion levels 0, 1 and 2. In all the cases it can be seen that the different maxima were distributed in narrower frequency bands than the three initially proposed B_1 , B_2 and B_3 . A set of five frequency bands was finally obtained, as can be seen in Fig. 6. We denote them in lower case, as $b_1 - b_5$ to distinguish them from the initially defined bands $B_1 - B_3$.

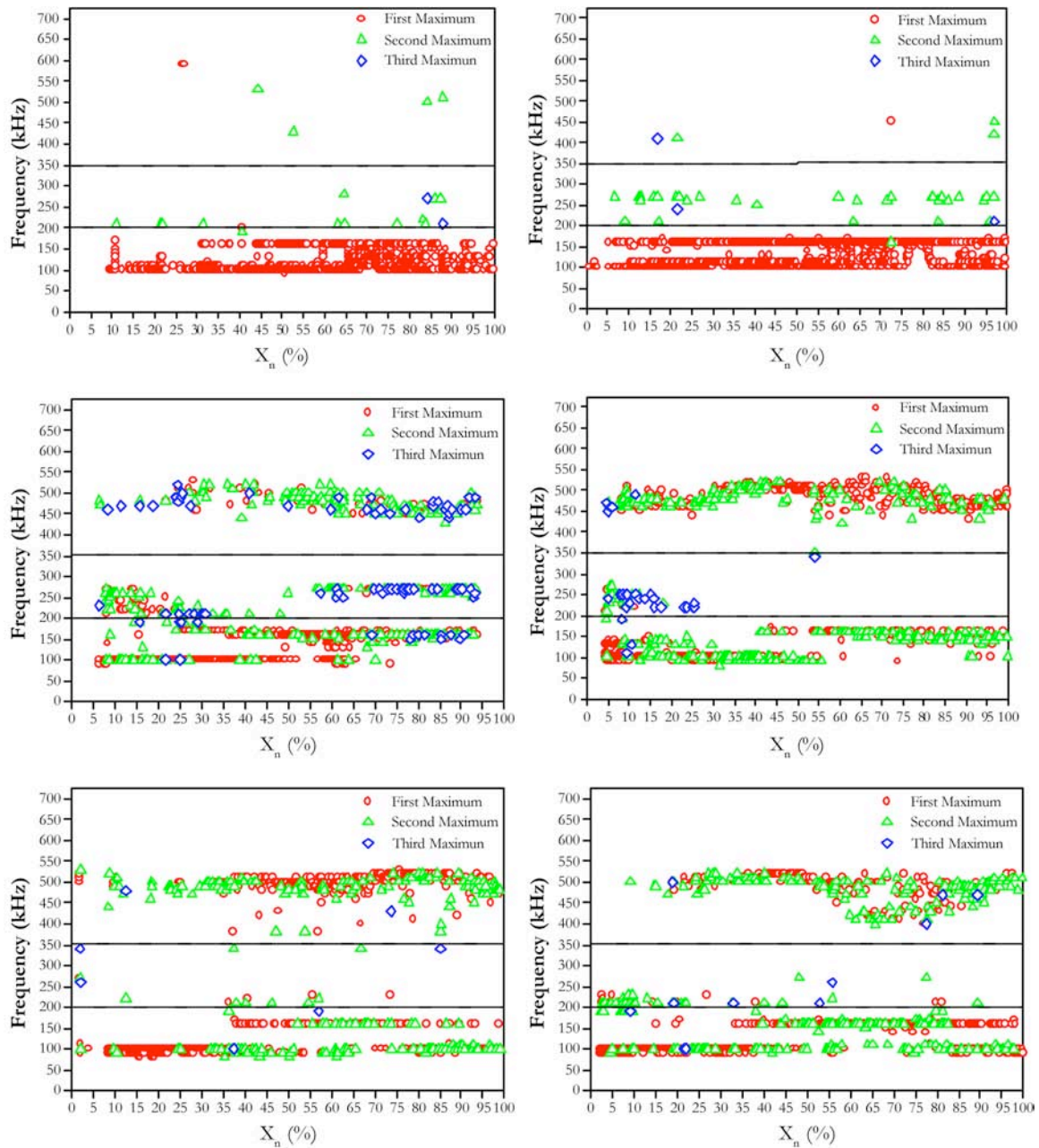


Fig. 6. Position of the primary, secondary and tertiary maxima of WP . Upper: T0 (Left: scratch 1; Right: scratch 2); centre: T1 (left: scratch 1; right: scratch 2); lower: T2 (left: scratch 1; right: scratch 2).

The correlation between the visually obtained $b_1 - b_5$ frequency bands and failure mechanisms established in [5] was based on careful SEM, EDX and XRD observation of the coatings, before and after the STs. In this way the obtained classification was:

- b_1 : [100] kHz: Deformation by slippage of the eta phase (mechanism A).
- b_2 : [100-150] kHz: Extraction of the cracked zeta particles by zeta-eta interfacial sliding (mechanism B).
- b_3 : [150-160] kHz: Cracking of the columnar zeta phase (mechanism C).
- b_4 : [210-270] kHz: Transversal cracking of the oxide phase (mechanism D).
- b_5 : [\approx 500] kHz: Extraction of chloride particles by oxide-chloride interfacial cracking (mechanism E).

3.2. Automated frequency bands obtained by wavelet entropy

The classification of AE signals in frequency bands $b_1 - b_5$, based on wavelet power considerations, is visually noticeable. Nevertheless, it is not suited for introduction in on-line damage detection algorithms. Moreover, the position and the width of the frequency bands that identify the mechanisms varied somewhat among different samples and even among different scratches on the same sample. This has to do with the rheological status of the coatings, i.e. the level of internal stresses. In [10] Reumont et al. have clearly shown that internal cracks form during galvanization following internal stresses, due to the different properties of phases; this also happens in the corroded coatings. So, the specific value of the characteristic frequency could suffer some variation for different samples and also for different scratches of the same sample.

For these reasons, an improved automated clustering method, based on entropy considerations, was applied to each ST. Less explained results were previously presented in [11, 12]. For entropy, we used the Shannon-Weaver definition [13]; (4) is the version adapted for wavelets. Formulas (4) and (5) allow us to obtain the entropy S_j^n for scale j (frequency interval related with j) for each register $s^n(t)$.

$$S_j^n = -\sum_{k=1}^{N_j} p_{jk}^n \log p_{jk}^n \quad (4)$$

where N_j is the number of coefficients involved at level j (in our case N_j is always N) and p_{jk}^n is given by:

$$p_{jk}^n = |c_{jk}|^2 / WP_j^n. \quad (5)$$

The concept of information entropy appears in different fields dealing with complex systems and with different definitions, including the description of the dynamic behavior of complex systems [14], in deconvolution filters [15], or as an estimator for blind source separation [16].

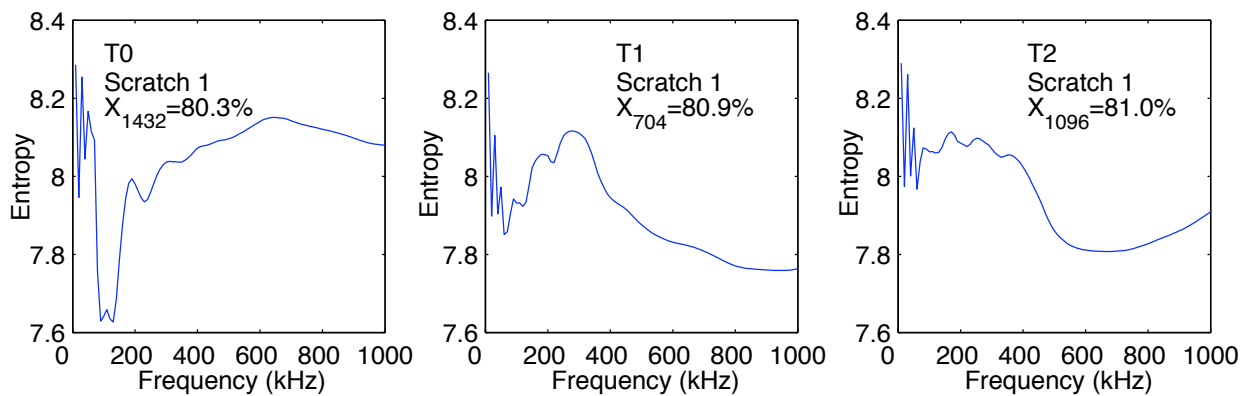


Fig. 7. Entropy versus frequency curves corresponding respectively to the signals of Fig. 4.

In our case, entropy is a parameter that represents the degree of intrinsic order or degree of organization of the signal: a relatively low entropy value indicates the existence of a structure recognizable in the elementary wavelet patterns. Contrarily, a high entropy value indicates the lack of a simple and identifiable structure. We used these concepts to divide the total frequency band into different bands. When we examine different wavelet power maps as those shown in Fig. 4, we observe a structure in certain frequency bands, and a quasi-uniform distribution in others. Entropy takes lower values for the frequencies, for which a structure is found.

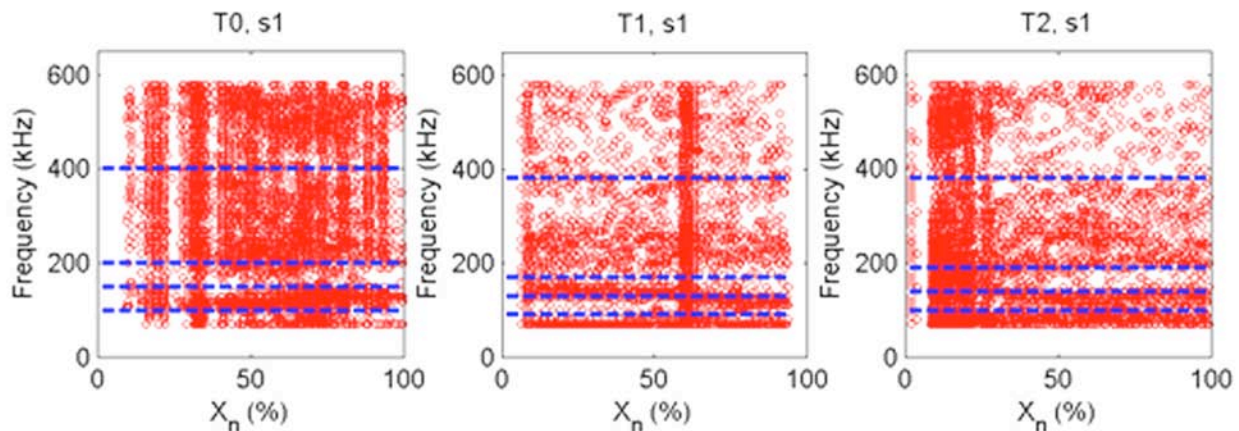


Fig. 8. Map of relative entropy minima in the frequency- X_n (%) plane. From left to right: scratch 1 of samples T0, T1, T2. The limits of bands are shown.

Applying (4), for each register located at relative position $X_n(\%)$, we obtained an entropy-frequency function; this calculation was carried out for all the frequencies of the entire band B_0 . Figure 7 shows as examples the entropy-frequency curves corresponding to the three particular registers shown in Fig. 3. In these curves we notice several relative minima located for each register n at frequencies j_{min}^n . Note that a number of different values of j_{min}^n are obtained for each register. Thus, it is possible to collect a set of relative minima j_{min}^n in a map of points in the frequency- X_n % plane. Figure 8 shows these results for scratch 1 of samples T0, T1 and T2. It can be seen that these points, corresponding to entropy relative minima, are roughly organized in frequency bands for the three samples.

In order to improve the separation in frequency bands, a *K-means* clustering method was applied to the points, using the subroutine “*kmeans*” of the statistics toolbox of MATLAB [17] (which uses a two-phase iterative algorithm to minimize the sum of point-to-centroid distances $[a,b]$). We applied the procedure in two-steps in order to eliminate the high frequency dispersion of the $[>500]$ kHz band. First, we clustered all the points corresponding to the entire band B_0 in three bands, thus obtaining (in an automated form) the bands b_5 , b_4 and b_l , b_l being the lowest frequency band (note that $B_0 = b_5 + b_4 + b_l$). Second, the points in band b_l were clustered in three bands, thus obtaining automatically the bands b_1 , b_2 and b_3 (note that $B_l = b_1 + b_2 + b_3$). The whole procedure is summarized in Fig. 9, which displays flow chart 2.

Table 1 shows the bands $b_1 - b_5$ automatically obtained for both scratches of samples T0, T1 and T2. Note that the automated bands $b_1 - b_5$ are now re-defined with respect to those obtained visually, which were shown in Section 3.1. The values now obtained are seen to be similar, although they vary from one ST to another.

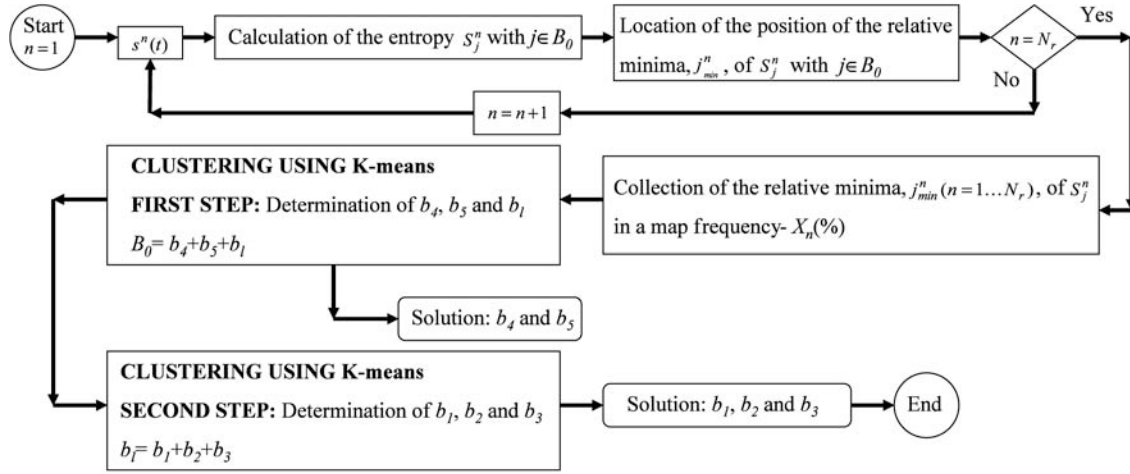


Fig. 9. Flow chart 2, which summarizes the bands b_1 - b_5 automatically obtained by searching the entropy relative minima.

Table 1. Frequency bands obtained by the automated clustering of entropy relative minima for all STs.

ST (sample, scratch) / band (kHz)	T0, s1	T0, s2	T1, s1	T1, s2	T2, s1	T2, s2
b_1	[50-100]	[50-100]	[50-90]	[50-100]	[50-100]	[50-100]
b_2	[100-150]	[100-160]	[90-130]	[100-140]	[100-140]	[100-140]
b_3	[150-200]	[160-210]	[130-170]	[140-190]	[140-190]	[140-190]
b_4	[200-400]	[210-410]	[170-380]	[190-390]	[190-380]	[190-380]
b_5	[400-600]	[410-600]	[380-600]	[390-600]	[380-600]	[380-600]

4. Coating Damage Evaluation

Damage is necessarily related with the number of broken atomic bonds, while AE power is connected with the strength of these bonds, which could be affected by the corrosion level, but in a way not easily elucidated. Below we propose a method for evaluating damage based on the evolution of the number of cracked zeta phase columns over the ST. It was shown in Section 3 that mechanism C, cracking of the columnar zeta phase, which corresponds to band b_3 , is the one affecting the deepest region in the galvanized coating over the ST, both in corroded and non-corroded samples. This encouraged us to seek a method suited to evaluate the number of broken zeta phase columns over STs for different corrosion levels.

Consequently, we calculated the relative wavelet power for each record in band b_3 , $WP_{b_3}^n$, defined as

$$WP_{b_3}^n = \frac{\sum_{j \in b_3} WP_j^n}{\sum_{n=1}^{N_r} \sum_{j \in b_3} WP_j^n} \quad (6)$$

Figure 10 shows this parameter along the two scratches carried out on samples T0, T1 and T2. Note the presence of very different features for corroded and non-corroded samples, with a very different density of maxima in each case. We considered the location of the maxima (i.e.,

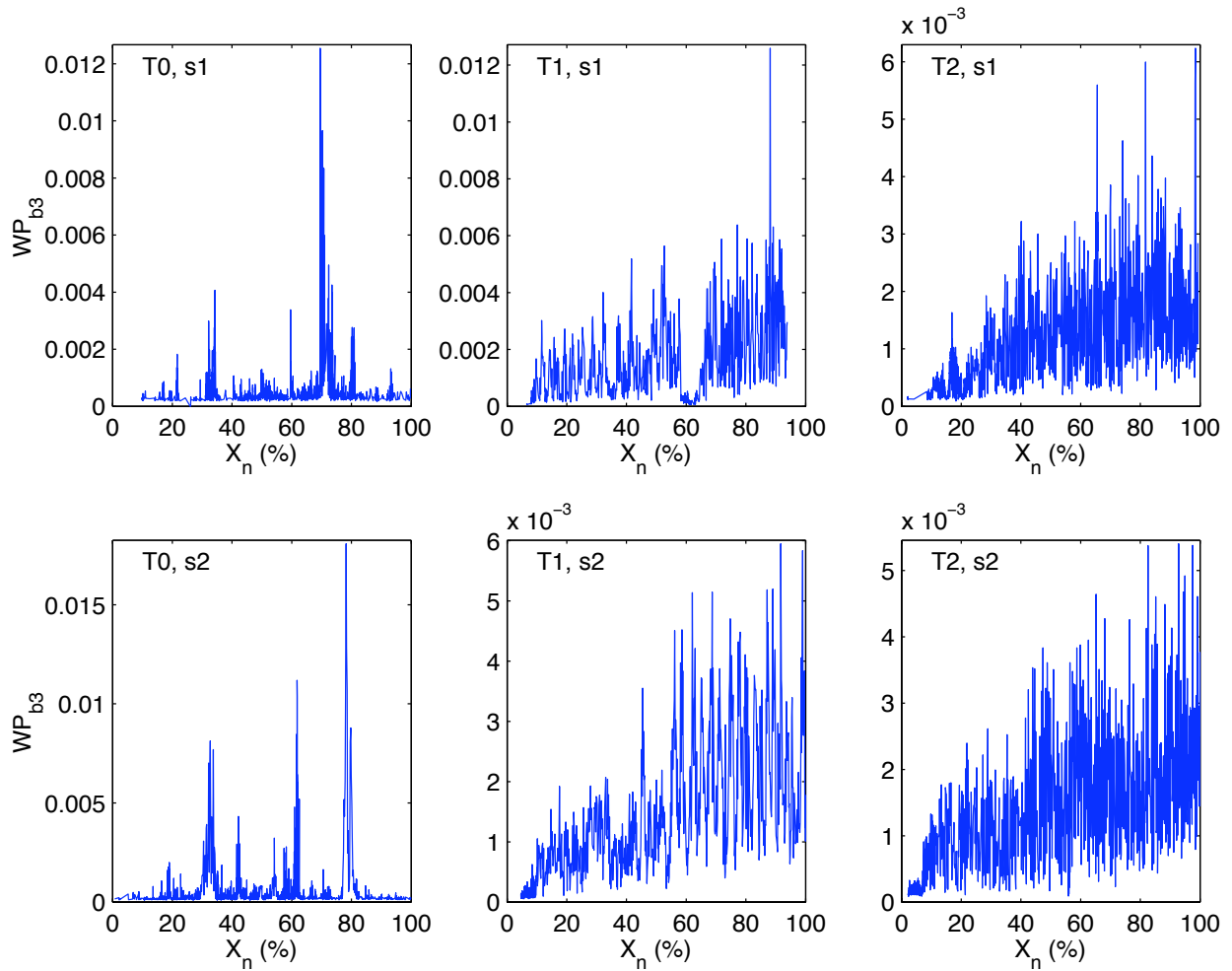


Fig. 10. $WP_{b_3}^n$ for scratch 1 (upper) and scratch 2 (lower). From left to right, samples T0-T2.

the location of peaks) in the curves shown in Fig. 10 to be directly related with the location of damaged zeta phase columns. This is justified by a simple calculation: The width of the columns is about $6 \mu\text{m}$, as can be observed in Fig. 1. Similar values are obtained for the inter-maxima distance, because the total length of scratches was around 1 cm.

For this reason, the density of $WP_{b_3}^n$ maxima was calculated in small and finite intervals of AE registers (i.e., the local density of maxima). To this end we determined the mean number of relative maxima with values surpassing a threshold, set at 0.001, for a given number of AE consecutive registers (we opted for 5). This density was assigned to the five AE registers of the same interval. The results in Fig. 11 illustrate this density of $WP_{b_3}^n$ maxima versus the relative position along the scratch, for the two STs and the three samples. The features are seen to be very different for the corroded and non-corroded samples. Clearly, higher values of density of $WP_{b_3}^n$ maxima are obtained for corroded samples than for non-corroded samples, and values increase along with the level of corrosion.

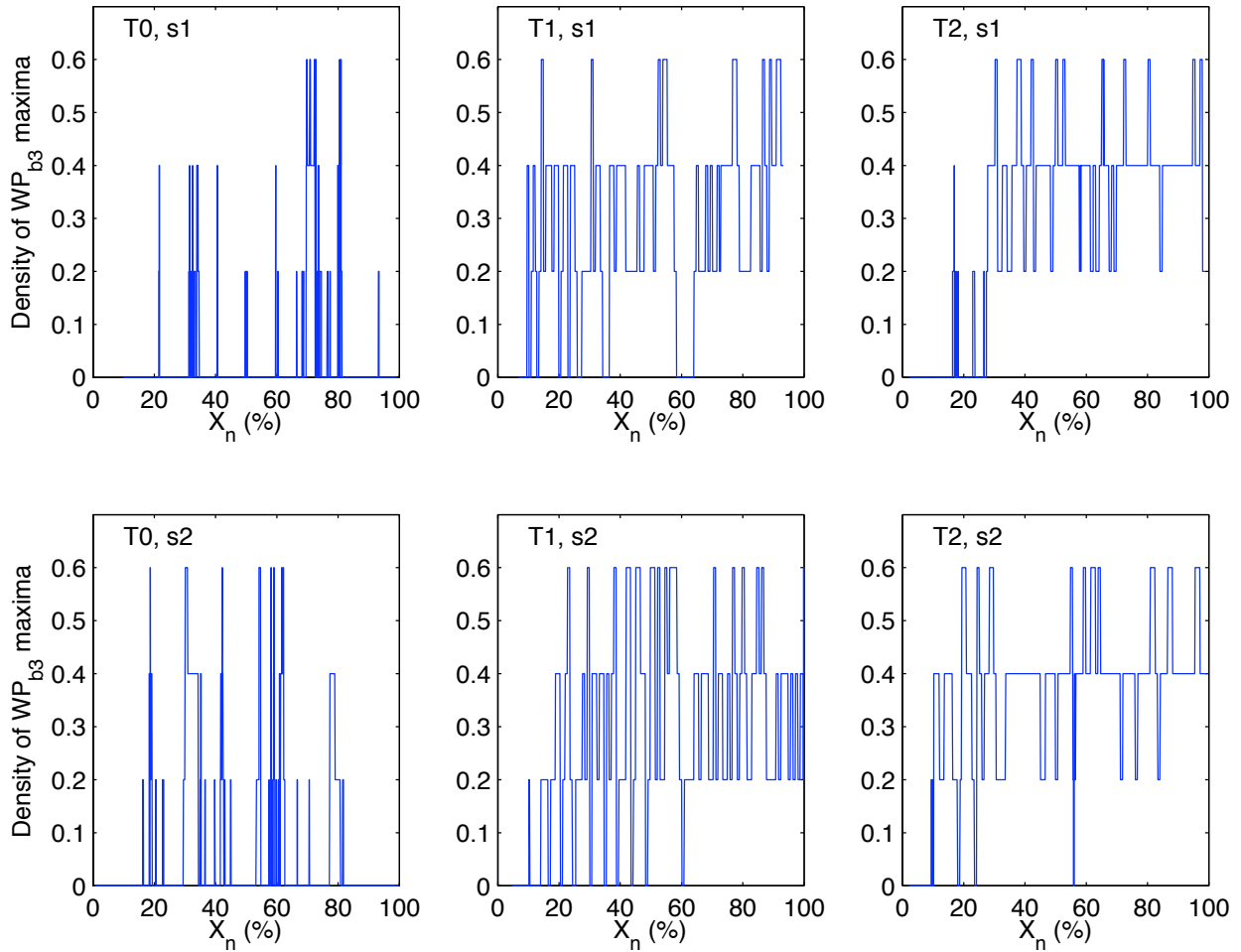


Fig. 11. Density of $WP_{b_3}^n$ maxima for scratch 1 (upper) and scratch 2 (lower). From left to right, samples T0-T2.

However, results were even more significant when we calculated the cumulative number of the $WP_{b_3}^n$ maxima with values higher than the 0.001 threshold. This parameter is plotted versus the relative position along the scratch in Fig. 12. Note that some steps took place at some $X_n(\%)$ values for scratches on sample T0. It can also be seen that both the qualitative and quantitative features in Fig. 12 are certainly very different for corroded and non-corroded samples. The quantitative evaluation of damage can thus be defined straightforward by means of this parameter. The first line in Table 2 shows the total number of the maxima (directly related with the total number of damaged zeta phase columns) in each ST for samples T0, T1 and T2. It clearly increases in conjunction with the corrosion level.

Somewhat arbitrarily, we defined the critical damage point (*CDP*) on each scratch as the point in position %, at which the number of cumulative maxima is 40. Results for all STs and samples are shown in the second line of Table 2. Note that the *CDP* shows a decreasing trend according to corrosion level.

Thus, the correct ascription of frequency bands to different mechanisms, the selection of the frequency band that corresponded to the deepest located damage mechanism, and the definition of an appropriate parameter to quantify damage both permitted the evaluation of damage evolving over STs and allowed us to establish the difference corresponding to corrosion level.

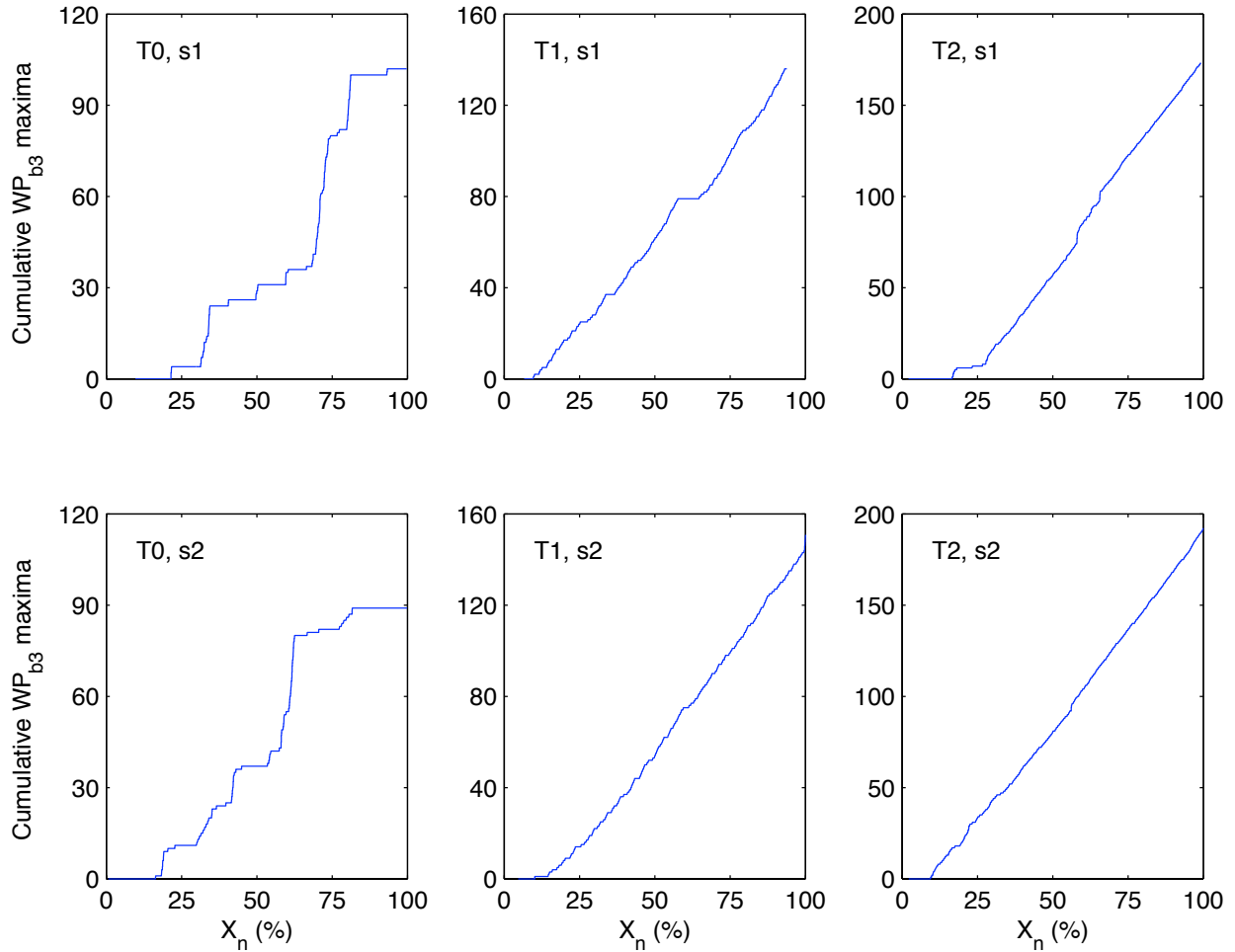


Fig. 12. Cumulative number of $WP_{b_3}^n$ maxima for scratch 1 (upper) and scratch 2 (lower). From left to right, samples T0-T2.

Table 2. Total number of WP maxima in band b_3 and Critical Damage Point (CDP) for scratches 1 and 2 corresponding to samples T0-T2

ST (sample, scratch)	T0, s1	T0, s2	T1, s1	T1, s2	T2, s1	T2, s2
Total number of WP maxima in band b_3	104	90	136	157	171	192
CDP (position %)	61	55	40	42	42	29

Some of the results have been previously summarized in Refs. [11, 12], but some more details and references regarding entropy calculations and the criterion to evaluate damage are given in the present paper. We understand that the supply of these details is important. This is because the present paper renders a twofold purpose. On the one hand it deals in evaluating damage in galvanized steel analysing AE signals. On the other hand it intends to go further in the route of searching for regularities in the evolution of some parameters that connect damage and AE. These regularities could be useful in a future complete theory that is still lacking.

5. Conclusions

In the line of previous work, specific frequency bands were assigned to different failure mechanisms applying the WT to AE signals coming from STs on corroded and non-corroded galvanized coatings. The damage identification procedure was improved by using an entropy criterion and a clustering method.

Damage evaluation was performed defining new parameters related with the transversal fracture of the zeta phase columns. The parameters were connected with the evolution of certain parameters over STs. They were: the wavelet power in the corresponding frequency band, the density of maxima of this function, the cumulative number of maxima, and a critical damage point, defined at the position on the scratch, at which a given number of maxima were cumulated. The *CDP* showed a clearly decreasing trend in relation with the level of corrosion.

Acknowledgements

This work was partially supported by MEC (Spain), through the financial help for the sabbatical year 2006 of R. Piotrkowski, spent at the University of Granada (SAB 2004-0081); and by the Spanish I+D National Plan DPI 2006-02970 Project. Hot-dip galvanization was performed at Galvanizados, S.A., Madrid. Scratch tests were performed at the Elastic Waves Laboratory, ENDE, CNEA, Argentina.

References

- [1] C. Grosse, H. Reinhardt, T. Dahm, Localization and classification of fracture types in concrete with quantitative acoustic emission measurement techniques, *NDT&E International*, **30** (1997) 223-230.
- [2] A. Iturraspe, D. Dornfeld, V. Atxa, J.M. Abete, Bicepstrum based blind identification of the acoustic emission (AE) signal in precision turning, *Mechanical Systems and Signal Processing*, **19** (2005) 447-466.
- [3] Gang Qi, Wavelet-based AE characterization of composite materials, *NDT&E International*, **33** (2000) 133-144.
- [4] Q. Liu, X. Chen, N. Gindy, Investigation of acoustic emission signals under a simulative environment of grinding burn, *Machine Tools & Manufacture*, **46** (2006) 284-292.
- [5] A. Gallego, J.F. Gil, E. Castro, R. Piotrkowski, Identification of coating damage processes in corroded galvanized steel by acoustic emission wavelet analysis, *Surface and Coating Technology*, **201** (2007) 4743-4756.
- [6] A. Gallego, J. F. Gil, J. M. Vico, J. E. Ruzzante, R. Piotrkowski, Coating adherence in galvanized steel assessed by acoustic emission wavelet analysis, *Scripta Materialia*, **52** (2005) 1075-1080.
- [7] Y. Meyer, *Wavelets: Algorithms and Applications*, SIAM, Philadelphia, 1992.
- [8] AGU-Vallen Wavelet, <http://www.vallen.de/wavelet/index.html>, 2002.
- [9] H. Suzuki, T. Kinjo, Y. Hayashi, M. Takemoto, K. Ono, Wavelet Transform of Acoustic Emission signals, *Journal of Acoustic Emission*, **14** (1996) 69-84.
- [10] G. Reumont, J.B. Vogt, A. Iost, J. Foct, The effect of an Fe-Zn intermetallic-containing coating on the stress corrosion cracking behavior of a hot dip galvanized steel, *Surface and Coating Technology*, **139** (2001) 265-271.

- [11] R. Piotrkowski, E. Castro, A. Gallego, Wavelet power, entropy and bispectrum applied to AE signals for damage identification and evaluation of corroded galvanized steel, *Mechanical Systems and Signal Processing*, **23** (2009) 432-445.
- [12] R. Piotrkowski, E. Castro, A. Gallego, J.M. Vico, J.J. González de la Rosa, Damage identification in corroded galvanized and duplex coatings using wavelet power and entropy, *Proceedings of the 28th European Conference on Acoustic Emission Testing*, Krakow, Sept. 17-19, 2008, edited by Kanji Ono, pp. 244-249.
- [13] C.E. Shannon, W. Weaver, *The Mathematical Theory of Communication*, University of Illinois, Urbana, 1964.
- [14] R.M. Yulmetyev, N.A. Emelyanova, F. Gafarov, Dynamical Shannon entropy and information Tsallis entropy in complex systems, *Physica*, **A341** (2004) 649-676.
- [15] H. Endo, R.B. Randall, Enhancement of autoregressive model based gear tooth fault detection technique by the use of minimum entropy deconvolution filter, *Mechanical Systems and Signal Processing*, **21** (2007) 906-919.
- [16] K. E. Hild, D. Erdogmus, J.C. Principe, An analysis of entropy estimators for blind source separation, *Signal Processing*, **86** (2006) 182-194.
- [17] Matlab, version 6.5, The Mathworks Inc, 2002.

AE ENTROPY FOR THE CONDITION MONITORING OF CFRP SUBJECTED TO CYCLIC FATIGUE

RUNAR UNNTHORSSON, THOMAS P. RUNARSSON and MAGNUS T. JONSSON
Department of Mechanical & Industrial Engineering, University of Iceland, Reykjavik, Iceland

Keywords: Entropy, Multi-axial fatigue, Condition monitoring, Fiber reinforced material

Abstract

The purpose of this study is to investigate whether the entropy of acoustic emissions (AE), generated both by cumulated damage and damage growth, can be used for the condition monitoring of carbon fiber reinforced polymers (CFRP) subjected to multi-axial cyclic loading. The average evolution of four entropies is studied; two in the time domain and two in the frequency domain. The AE used for studying the average evolution is acquired during fatigue testing of 75 nominally identical CFRP prosthetic feet. The results show that the evolutions of the two entropies estimated in the time domain correlate well with the evolution of the AE hit count. One of time domain entropies is computationally simpler than the AE hit count procedure and uses the whole AE signal. Further research is needed to answer if it is a better alternative to conventional AE hit counting.

Introduction

During the progressive degradation process of a cyclically loaded CFRP composite material various damage mechanisms are introduced in the material [1, 2]. In each cycle, AE is emitted from both damage progression and from cumulated damage, i.e. rubbing of delaminated surfaces. As a result multiple AE transients, with varying amplitude, duration, and frequencies, can be simultaneously emitted from the numerous AE sources within the material. Depending on both the damage mechanisms and loading, AE from cumulated damage is either separable transients or inseparable, e.g. due to high degree of overlapping. Throughout the cyclic life the number of AE signals increases with increasing cumulated damage. The energy of the AE also increases and for some composites the energy also varies within a cycle.

Features extracted from the AE signal have been used for detection of damage, i.e. delamination, matrix cracking, debonding, fiber cracking, and fiber pull-out [3-7]. AE from cumulated damage has mainly been regarded as unwanted and many attempts have been made to filter it out, e.g. by thresholding the AE features [8], coupling the AE to the load [5], limiting the analysis to a part of the loading cycle [9, 10], and frequency analysis [11]. The AE waves in the material will reflect and undergo attenuation before being picked up by the AE sensor. The attenuation is due to geometric spreading, dispersion, internal friction and scattering. The values of AE features from cumulated damage usually fall in the same range as the ones from damage growth [5, 13] and it can be very difficult to distinguish between the two types. Because important AE events can get buried in the AE signals generated by friction and the rubbing of crack surfaces [11, 12] attempts have been made to filter out AE events from these damage mechanisms [5, 10, 13]. Awerbuch and Ghaffari concluded that frictional AE should not be eliminated as it may provide important information about the condition of a composite [10]. They argued that damage detection could be made easier by using frictional AE, since damage growth, i.e. a material change, produces AE only once, but the resulting rubbing of damage surfaces generates AE many times.

It is reasonable to assume that both environmental and measurement noise can be kept relatively constant during monitoring. Hence, an increase in the randomness of the AE measurements will mainly be due to increased AE activity, from either cumulated damage or damage growth. In this study, it is investigated whether the randomness can be used for condition monitoring, i.e. if it can be used to provide early failure warning. For estimating the randomness of the AE measurements a fundamental concept in Information Theory is used; that is, the entropy.

Entropy and its Estimation

The information entropy was introduced by C. E. Shannon in 1948 [14]. In his paper Shannon developed a method of measuring the randomness of a signal, or its uncertainty. The randomness is information encoded in the signal and the entropy increases with more information. Shannon recognized that the form of the measure was the same as the entropy in statistical mechanics and, for this reason, he called his measure 'entropy'. Shannon's formula for the entropy is

$$H_{SHANNON}(X) = - \sum_{\lambda} Pr(x = \lambda) \log(Pr(x = \lambda)). \quad (1)$$

The signal's values are denoted by x and are considered to be discrete random variables. The possible signal values are denoted by λ , and $Pr(x = \lambda)$ is the probability mass function (PMF) of X . Consequently, the entropy is a function of the signal's probability mass function, but not the values themselves. Without any constraints, the maximum entropy is attained when all values are equally probable, i.e. when the signal is white noise. The entropy is the minimum weighted average number of units, per value, required to encode the signal. The unit of measurement depends on the choice of the logarithm base, i.e. by choosing 2, 10, or e as the base the units will be bits, hartleys, or nats, respectively. The base can be changed by using the law of logarithm, i.e.

$$\log_a(X) = \log_a(b) \log_b(X). \quad (2)$$

In practice, computing the entropy can be challenging because the underlying distribution is often unknown, for instance the AE signal measured during cyclic testing of CFRP. Consequently, the entropy needs to be estimated. This can be done by estimating the probability mass function using statistical methods or by estimating the entropy directly using data compression [15,16]. A normalized histogram of the random variable can be used to estimate the probability mass function. By using a histogram to estimate probabilities, the entropy is estimated with respect to a model that assumes that the frequencies of the signal's values are constant within the signal segment. The histogram can be normalized to sum to one by

$$n_i = \frac{m_i}{\sum_{i=1}^k m_i} \quad \text{for } i = 1, \dots, k \quad (3)$$

where k is the number of bins and m_i is the number of observed signal values that fall in bin i . The normalized values of the histograms represent the proportion, or probability, of the corresponding signal's values. In the frequency domain, the frequency can be considered to be the random variable and the normalized spectrum to be the probability mass function. The spectrum is normalized by

$$x_i = \frac{X_i}{\sum_{i=1}^N X_i} \quad \text{for } i = 1, \dots, N \quad (4)$$

where X_i is the magnitude of the i^{th} frequency component of the spectrum, e.g. the amplitude if

an amplitude spectrum is used. Based on this probability mass function, entropy can be computed using Shannon's formula. By considering the spectral amplitude to be the random variable, a different entropy can also be defined and computed using Shannon's formula; the probability mass function of the amplitude intensities can be estimated using a histogram. When the probabilities are based on discrete Fourier transform, or histograms, the entropy is estimated with respect to a static model. These two entropies will be referred to as the frequency entropy and the spectrum entropy, respectively.

The Shannon entropy is properly defined as the minimum entropy over all possible models, i.e. it is an entropy computed using Shannon's formula and the correct probability mass function. In other words, it is the theoretical upper limit on lossless data compression that can be achieved for a given signal [15, 16]. Consequently, the entropy can be used to evaluate compression algorithms to determine whether there is room for improvement. Conversely, compression algorithms can be used to estimate the entropy of data. The compressed data can be written to a file and the file size then converted from bytes to nats using:

$$H_{COMPRESSION} = \frac{8 \log_e(2) \text{File_Size}}{\text{length_of_signal}}. \quad (5)$$

Where **File_Size**, the size of the compressed file in bytes, is multiplied by 8 to convert to bits. Equation 2 is used to change from bits (base 2 logarithm) to nats (base e logarithm). The results are then averaged over all values (samples) by dividing the results with **length_of_signal**. If the header of the compressed file is included in the file, then the entropy estimate will be higher. If the AE signal length is kept constant then the error due to the header will be approximately same for all computations.

Among the best lossless compression approaches are those based on a scheme known as prediction by partial matching (PPM). The PPM compression scheme is divided into two steps: modeling, from which the scheme takes its name, and coding. Arithmetic coding is used to code the output of the modeler. Arithmetic coding is a highly effective technique, which can code data close to its entropy with respect to the model [16]. The PPM modeler works with the data in a symbol-wise manner and its output is a set of conditional probabilities for the symbols. The probabilities of the symbols are estimated adaptively and used to predict the next unseen symbol. For predicting the modeler uses finite context models of k symbols, which immediately precede the one to be predicted. The number k is also referred to as the model order and is specified by the user before the data compression is initiated.

During the modeling for each symbol, the modeler begins by looking up how many times the current context of length $l_c = k$ has occurred before. If the context has been observed before, followed by the symbol, the symbol can be coded using a probability of n_c/n , where n_c is equal to the number of times the context has been observed followed by the symbol and n is the number of times the context has been observed. If the context hasn't been encountered before, or it has only been followed by different symbols, an escape character is passed to the modeler. When the modeler receives the escape character it switches to a context that is one symbol shorter, i.e. to a context of length $l_c = k - 1$. Again, if the current context has not been observed before, or has only been followed by different symbols, another escape character is passed to the modeler and it starts to look for contexts, which are one symbol shorter. This can be repeated until the context length becomes $l_c = -1$ symbols. When this occurs, all symbols from the alphabet are considered equally probable. Equi-probability is undesirable since it does not provide an accurate model;

however, it poses no problem for accurate coding. The arithmetic coder is able to proceed even though the model is inaccurate; however, a higher number of bits may be required to encode the data. Intuitively, better compression is achieved with more accurate modeling. Fortunately, the context of $l_c = -1$ symbols is only considered at most once for each symbol, and as the modeling proceeds the data statistics improve and lower values of l_c become less and less frequent. Every time an escape character is sent (i.e. whenever the modeler is unable to code a symbol) the probability of observing a novel symbol, when presented with the current context, is updated. By assigning a probability to the escape character the modeling can be improved. For a detailed description of the PPM scheme and examples, the reader is referred to Text Compression [15] and Managing Gigabytes: Compressing and Indexing Documents and Images [16].

Different variants of the PPM compression scheme have been introduced in order to improve the PPM compression and to speed up calculations. One variant suggested by Howard [17] is referred to as method D, or PPMD, and estimates the conditional probability of observing a particular symbol given a specific context to be $(2n_c - 1)/(2n)$, where n_c is the number of times which the modeler has seen the symbol being preceded by the context and n is the total number of symbols preceded by the current context. The escape probabilities are estimated by $n_u/(2n)$, where n_u is the number of unique symbols preceded by the current context and n has the same meaning as before.

Another variant was introduced by Dmitry Shkarin in Improving the Efficiency of the PPM Algorithm [18] (in Russian) under the name PPM with information inheritance, or PPMII. Shkarin presented the PPMII a year later in English [19]. The PPMI uses an additional model in order to get better estimation of the escape probabilities. In order to overcome the lack of statistical information when estimating the escape probabilities of long contexts, the PPMII allows the longer contexts to inherit statistics from shorter contexts. The inheritance reduces the computational cost compared with other approaches to this problem [19]. Starting with a code from Nelson [20], Shkarin implemented his improvements, and several other variations, and made them available in the public domain under the name PPM by Dmitry (PPMd).

Experimental Procedure

The test specimens used in this study are nominally identical prosthetic feet called Vari-Flex. The Vari-Flex is made by Össur hf. A total number of 75 Vari-Flex feet were tested. The cyclic testing was performed in an ISO 10328 Foot/Limb test machine at Össur's testing facilities. In the test, a foot is placed in the test machine where two actuators apply a load to the foot using a 90° phased sinusoidal constant amplitude loading at 1.0 Hz. One actuator loads the forefoot and the other loads the heel. The tests were accelerated by increasing the maximum loading by 50% and placing a 2° plastic wedge between the heel and the toe components. The wedge is used by amputees in order to stiffen the foot. The increased load and the use of the wedge result in considerably shorter fatigue tests. Frequently the damage mechanics change depending on the stress level, however, both preparatory tests and the fatigue test results show that the damage mechanisms leading to final failure are the same as observed under normal fatigue testing conditions.

All feet were tested until failure. The failure was defined by a 10% displacement criterion. The failure criterion is a heuristic criterion used in-house at Össur. It defines a failure when a 10% change in the displacement of either actuator, with respect to initial value, is observed. Throughout each test, the AE data was acquired for one full fatigue cycle every 5 minutes. For a more detailed description of the experimental procedure the reader is referred to references [21-23].

Results

Two entropies are estimated in the time domain, one using Shannon's formula and the other using data compression. In order to apply Shannon's formula the probability mass function of the signal's values from each measurement is estimated from a normalized histogram using 2^{16} bins. In other words, the number of bins is set equal to the number of quantized discrete values from the 16-bit A/D converter used for AE acquisition. In order to estimate the entropy using data compression, the signed 16-bit integer data is written to a file in ASCII form with no spaces in between. The file is then compressed using variant H of the PPMd algorithm (PPMdH), as implemented in an open source software program called 7-Zip. The resulting file size is then converted from bytes to nats (see Eq. 5). The model order is determined manually. The best compression results are obtained using model order $k = 5$, or when the maximum context length is equal to the maximum number of digits used (omitting the sign). In the remaining part of this paper, the entropy computed using Shannon's formula in the time domain will be referred to as the signal's entropy, and the entropy estimated using the PPMdH compression scheme will be referred to as the PPMdH entropy.

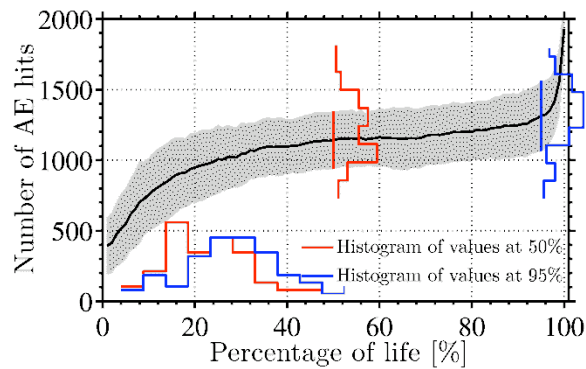
In the frequency domain Shannon's formula for the entropy is used to estimate both the frequency and the spectrum entropies. In order to compute the frequency entropy, the probability mass function of the frequencies is estimated by first transforming the signed 16-bit integer data to the frequency domain and then normalizing the one-sided amplitude spectrum to sum to one. Because of the normalization there is no need to convert the data values to volts. The transformation is made by applying a 221-point discrete Fourier transform (DFT). The number of DFT points is set to the next power of two higher than the length of the data series, for faster computation. This is done by zero-padding the data to make its length a power of two. The computations can also be made faster by using fewer points. If fewer points are used, the resolution of the spectrum decreases and less information is provided. Consequently, the entropy also decreases. If more points are used, the number of frequency bins increases, as does the entropy. This requires zero-padding. Zero-padding the data before applying the DFT results in a frequency interpolation, which means that the added frequency bins will not contain any new information. As a result, the entropy increase will only be a function of the number of added bins and is the same for all measurements.

In order to compute the spectrum entropy, the probability mass function of the spectral amplitudes is estimated from a histogram of the amplitude intensities. Amplitudes below the highest amplitude in the one-sided amplitude spectrum of all measurements are quantized with 16 bits. A 216-bin histogram is used to estimate the probability mass function of the quantized amplitudes.

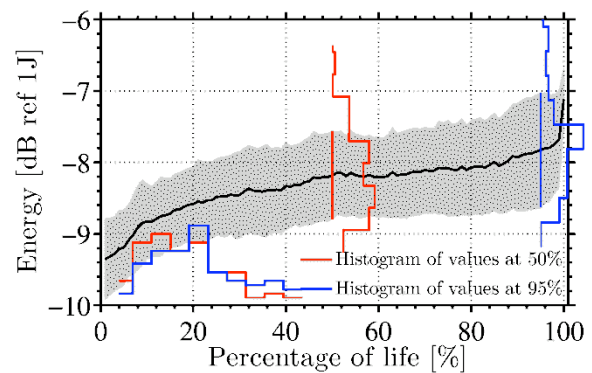
Entropy as a Condition Signature

For evaluating whether the entropies can be used to provide early failure warnings and to compare them against other AE features, the approach in reference [24] is used. The probability distribution, of the entropy values at each percentage point is estimated by first computing the entropy from all measurements, for each foot tested, and then generating a histogram of the entropy values at the given percentage point of lifetime. The lifetime of each foot is normalized to 100% according to the 10% displacement failure criterion. All figures in this section have a grey area that represents all values that lie within one standard deviation from the mean. Also superimposed on the figures are histograms that show the distributions of the corresponding entropy at 50% and 95% of the normalized fatigue life. Figures 1a and 1b show, respectively, the average

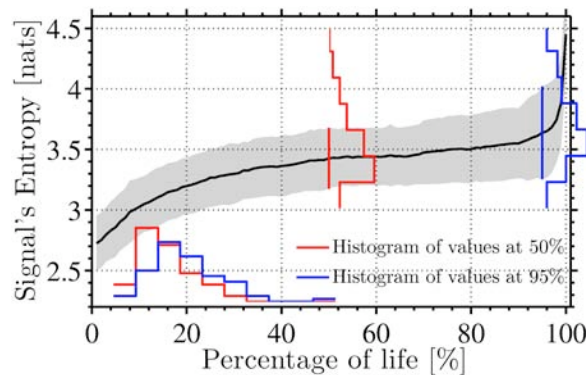
evolution of the AE hit count and the signal's energy for all feet tested. These two figures were presented in reference [24].



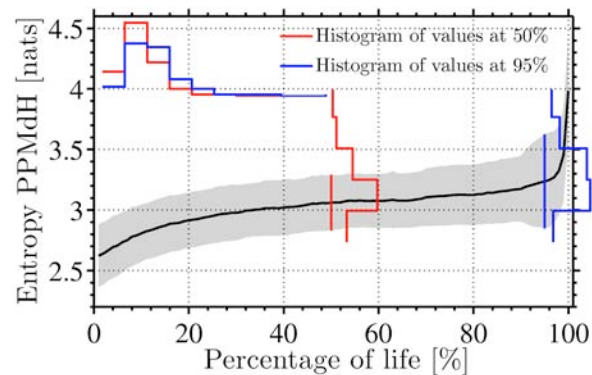
(a) The average evolution of the AE hit count rate.



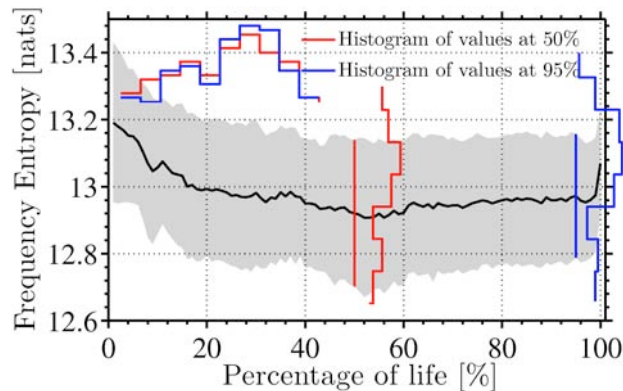
(b) The average evolution of the signal energy.



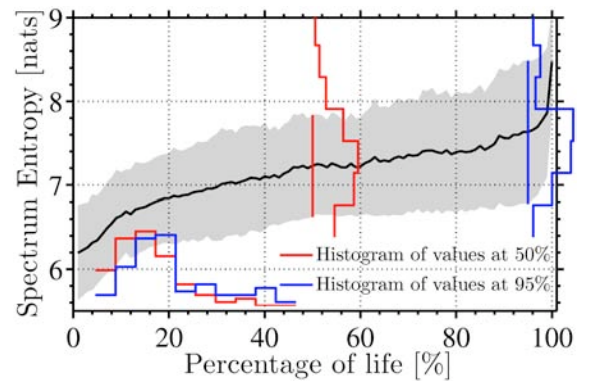
(c) The evolution curve for the signal's entropy.



(d) The evolution curve for the PPMdH entropy.



(e) The evolution curve for the frequency entropy.



(f) The evolution curve for the spectrum entropy.

Fig. 1. The average evolution of the AE hit count rate, energy and four entropies computed from the AE segments. The grey area represents all values that lie within one standard deviation from the mean.

The average evolution of the four entropies for all the feet is shown in Figs. 1c-1f. As one can observe, the curves are relatively flat from approximately 20% to 95% of the normalized lifetime, and the standard deviation is high. The curves are therefore not suitable for issuing early failure alerts. This is verified by the almost perfect overlap of the histograms of the entropy values at 50% and 95% of the lifetime.

It is interesting to note that, of the two entropies computed in the time domain, the PPMdH entropy (shown in Fig. 1d) is lower than the signal's entropy (shown in Fig. 1c). In order to apply Shannon's formula, the probability mass function of the signal's values is estimated using a histogram of the signal's values. This estimates the entropy of the signal with respect to a static model. This is by no means the best model for the data – as can be observed; the PPdH compression scheme produces a better model. Nonetheless, the evolution curve for the PPMdH entropy shows no additional information.

Table 1 presents the median Pearson and Spearman correlation coefficients estimated between the AE hit count, the energy and the four entropies. Each coefficient is estimated by first computing the corresponding coefficient between the curves from each fatigue test and then computing the median of the coefficients obtained from all feet.

Table 1. The median Pearson (left) and Spearman (right) correlation coefficients between the AE hit count, the energy, and the four entropies.

	AE hit count	Energy [dB]	Signal's entropy	PPMdH entropy	Freq. entropy	Spectrum entropy
AE Hit Count	1	0.63 / 0.58	0.93 / 0.89	0.92 / 0.89	-0.24 / -0.19	0.71 / 0.65
Energy[dB]		1	0.74 / 0.72	0.73 / 0.70	-0.44 / -0.52	0.92 / 0.91
Signal's Entropy			1	0.99 / 0.99	-0.28 / -0.31	0.79 / 0.79
PPMdH Entropy				1	-0.24 / -0.29	0.78 / 0.79
Freq. Entropy					1	-0.23 / -0.20
Spectrum Entropy						1

The results presented in the table show that the evolution of the two entropies estimated in the time domain, i.e. the signal's entropy and the PPMdH entropy, correlate well with the evolution of the AE hit count. Furthermore, the calculations also show that there is a significant correlation between the energy and the spectrum entropy. Since the energy requires less computation and its interpretation is more intuitive the spectrum entropy does not seem to offer any advantage. The frequency entropy measures the flatness of the spectrum. It can be used to detect the presence of broadband events that may not be detected from the evolution of the energy. Consequently, the frequency entropy can possibly be used to supplement the energy feature.

Summary

In this study the AE hit count, energy and the entropies were extracted from the AE signals without applying any special filters to filter out any AE, e.g. from cumulative damage. The purpose of the study was to investigate whether the entropies could be used for condition monitoring of CFRP subjected to multi-axial cyclic loading, i.e. for providing early failure warning.

The results show that the entropies studied here cannot be used with the proposed approach for issuing early failure alerts. This is because they have relatively flat evolution curves from 20% to 95% of the normalized lifetime.

The results also showed that the trending results obtained using both the signal's entropy and the PPMdH entropy (file compression) are nearly the same as those obtained using a STFT based AE hit counting. This suggests that the signal's entropy might be a better alternative to the AE hit count for monitoring AE activity because it requires less computational effort, no filtering (the number of hits is reduced by thresholding) and the only tuning required is the choice of the

histogram's bin size. These results suggest that further work should be done to compare the signal's entropy against AE hit counts that based on conventional thresholding.

Acknowledgements

The work of the first author was supported by grants from the University of Iceland Research Fund, the Icelandic Research Council (Rannis) Research Fund, and the Icelandic Research Council Graduate Research Fund. Furthermore, the authors wish to acknowledge Össur for both providing prosthetic feet for testing and for providing access to their testing facilities.

References

1. G. Sims, *Fatigue in Composites*, Woodhead Publishing Ltd., Cambridge, 2003, 36–62.
2. M. Knops and C. Bogle, *Composites Science and Technology*, **66**, 2006, 616–625.
3. M. Giordano, A. Calabro, C. Esposito, A. D'Amore, and L. Nicolais, *Composites Science and Technology*, **58**, 1998, 1923–1928.
4. M. Wevers, *NDT and E International*, **30**, 1997, 99–106.
5. D. Tsamtsakis, M. Wevers, P. De Meester, *J. of Reinforced Plastics and Composites*, **17**, 1998, 1185–1201.
6. H. Nayeb-Hashemi, P. Kasomino, and N. Saniei, *J. of Nond. valuation*, **18**, 1999, 127–137.
7. E. R. Green, *J. of Nondestructive Evaluation*, **17**, 1998, 117–127.
8. N. Ativitavas, T. J. Fowler, T. Pothisiri, *J. of Nondestructive Evaluation*, **23**, 2004, 21–36.
9. Y. A. Dzenis and J. Qian, *International J. of Solids and Structures*, **38**, 2001, 1831–1854.
10. J. Awerbuch, S. Ghaffari, *J. of Reinforced Plastics and Composites*, **7**, 1988, 245–64.
11. G. Kamala, J. Hashemi, A. A. Barhorst, *J. of Reinf. Plastics and Comp.* **20**, 2001, 222–238.
12. A. P. Mouritz, *Fatigue in Composites*, Woodhead Publ. Ltd., Cambridge, 2003, 242–266.
13. Y. A. Dzenis, *International J. of Fatigue*, **25**, 2003, 499–510.
14. C. E. Shannon, *Computational Communication Rev.* **5**, 1948, 3–55.
15. T. Bell, J. Cleary, I. Witten, *Text Compression*, Prentice Hall, 1990.
16. I. Witten, A. Moffat, T. Bell, *Managing Gigabytes: Compressing and Indexing Documents and Images*, Morgan Kaufmann, 1999.
17. P. G. Howard, Ph.D. thesis, Brown University, 1993.
18. D. A. Shkarin, *Problems of Information Transmission*, **37**, 2001, 226–235.
19. D. Shkarin, DCC 2002, IEEE Computer Society, April, Snowbird, Utah, 2002, 202–211.
20. M. Nelson, Arithmetic coding and statistical modeling, *Dr. Dobb's Journal*.
21. R. Unnthorsson, T. P. Runarsson, and M. T. Jonsson, *International J. of Fatigue*, doi:10.1016/j.ijfatigue.2007.02.024, 2007.
22. R. Unnthorsson, T. P. Runarsson, M. T. Jonsson, *J. of Acoustic Emission*, **25**, 2007, 253–259.
23. R. Unnthorsson, University of Iceland, Ph.D. Thesis, 2008
24. R. Unnthorsson, T. P. Runarsson, M. T. Jonsson, *J. of Acoustic Emission*, **26**, 2008, 229–239.

EXPERIMENTAL SIMULATION AND DYNAMIC BEHAVIOR OF THE AE DUE TO MARTENSITIC TRANSFORMATION USING SHEAR WAVE TRANSMISSION SENSOR

TAKESHI YASUDA, SHINYA KONDO, HIDEO NISHINO and KENICHI YOSHIDA
The University of Tokushima, 2-1 Minamijosanjima, Tokushima, 770-8506 Japan

Keywords: Shear AE wave source, martensitic transformation, source rise time

Abstract

We conducted the waveform analysis of acoustic emission (AE) signals to study the dynamic behavior of materials deformed or transformed; namely, two types of martensitic transformation in Cu-Ni-Al shape-memory-alloy (SMA) single crystals during tensile deformation that produce different martensitic structures. The AE source behavior is expected to be of shear. We simulated AE signals due to martensitic transformation using a shear-wave transducer as the artificial source. Results of AE waveform analysis in Cu-Al-Ni SMA single crystals are compared with the simulation results. The martensite with a simpler stacking structure exhibits faster transformation behavior.

Introduction

Acoustic emission is generated by microcracking and phase transformation in materials. AE waveform analysis has the possibility to determine the dynamic behavior of materials under martensitic transformation. We have investigated AE waveforms due to two types of martensitic transformation during tensile deformation of Cu-Al-Ni SMA single crystal [1]. Their detected waveforms were analyzed by the modified Takashima's spectrum-gradient method to calculate source rise time. The different tendency of the source rise time was considered to reflect the dynamic behavior of martensitic transformation. However, this result was not quantitative. It is expected that AE source is of shear nature due to the generation of martensitic habit plane in this material. However, there are few reports on AE source analysis with the shear-type vibration like the martensitic transformation.

In this research, an experiment is conducted using a shear-wave transducer to simulate AE sources of martensitic transformation. A Cu-Al-Ni SMA single crystal plate was used as a wave propagation medium. We changed the rise time of step function voltage to the shear-wave transducer. The induced waves were detected by a wideband AE sensor and recorded with a digital oscilloscope. S_0 -mode (zeroth-order symmetric) Lamb waves were analyzed using FFT, and the relation between the source-wave rise time and the obtained m -value from Takashima's spectrum gradient method was confirmed. Finally, we detected the AE waveforms during two types of martensitic transformation in Cu-Al-Ni SMA single crystals. The results of source rise time during actual martensitic transformation were obtained from the experimental simulation results.

Martensitic Transformations and Habit Plane

The two kinds of martensitic transformation used in this study are $\beta_1 \rightarrow \beta_1'$ phase transformation and $\beta_1 \rightarrow \gamma_1'$ phase transformation. Sample Cu-Al-Ni alloy has the composition of 14.1 wt% Al and 4.1 wt% Ni. It was melted and cast in a high-frequency induction furnace under argon atmosphere. A single crystal of the Cu-Al-Ni alloy was grown with (001) surface and [100] tensile direction, respectively, using the Bridgman method at a pulling rate of 32 mm/hr.

To generate martensitic transformation by tensile deformation, it was solution-treated at 1273 K for 1 hr. One sample was quenched into water at room temperature ($M_s = 250$ K, $A_f = 280$ K) and the other into water at 373 K in order to keep the β_1 matrix phase (M_s and A_f higher than room temperature), respectively. These two specimens were formed to a shape for tensile test (thickness = 1.25 mm) as shown in Fig. 1. The specimens showed the stress relaxation with appearance of habit plane on surface when tensile stress was applied to each specimen. The optical microphotographs of habit plane of two kinds of martensitic transformation taken on the front surface and right-side surface are shown in Fig. 2. The specimen quenched into water at room temperature shows $\beta_1 \rightarrow \beta_1'$ phase transformation and one quenched into water at 373 K shows $\beta_1 \rightarrow \gamma_1'$ phase transformation.

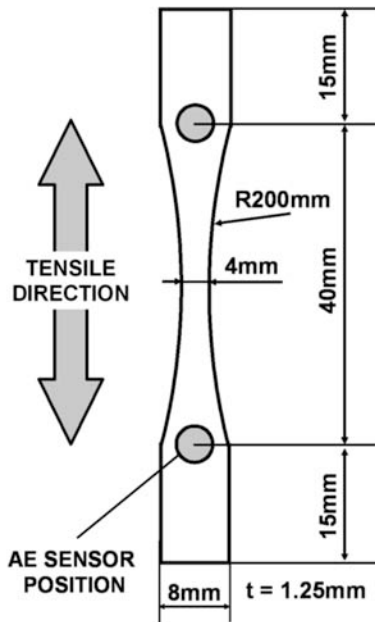


Fig. 1 Shape of specimen used.

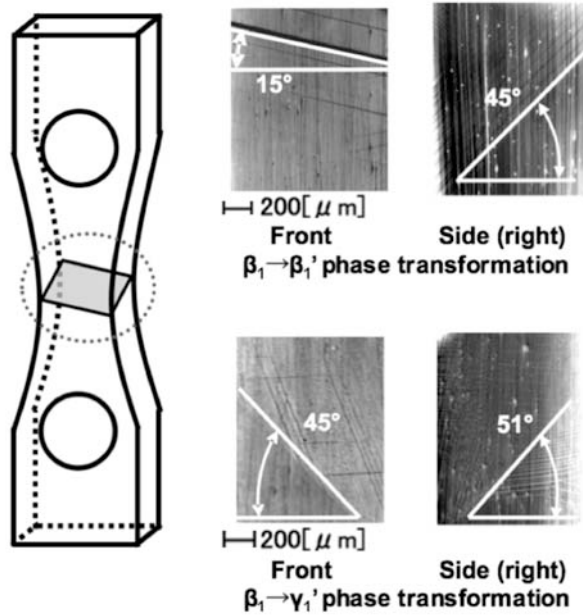


Fig. 2 Habit plane of each martensitic transformation.

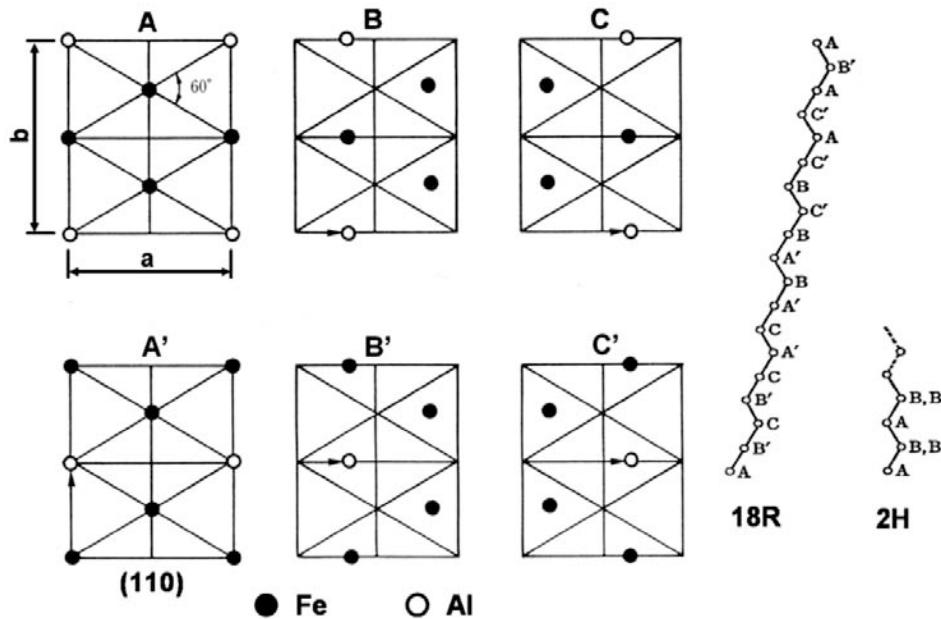


Fig. 3 (110) plane stacking figures of martensitic formations from β_1 phase, and 18R and 2H structure [2].

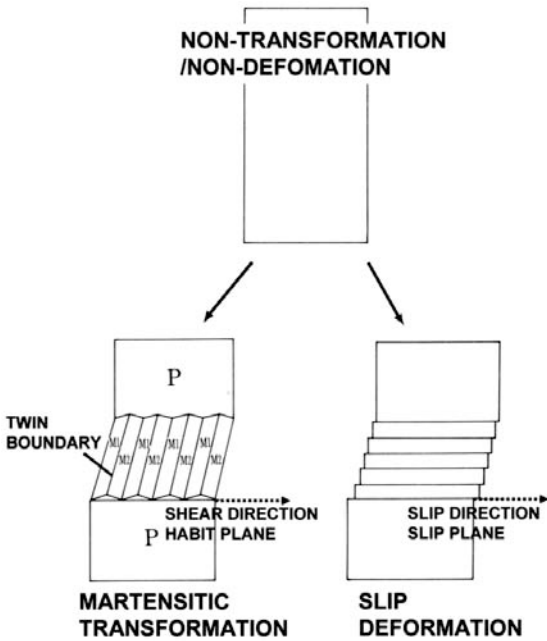


Fig. 4 Deformation state due to habit plane and slip plane [3].

These martensitic transformations were confirmed by surface trace analysis. These martensites have the same matrix phase (β_1 phase) of the DO_3 crystal structure. The transformation was by shear along $\langle 110 \rangle$ directions of the β_1 structure [2]. However, $\beta_1 \rightarrow \beta_1'$ and $\beta_1 \rightarrow \gamma_1'$ phase transformations have different structures when they undergo the martensitic transformation. The accumulating stacking structures are of six kinds of martensitic plane generated in the (110) plane. The β_1' phase has 18R structure and the γ_1' phase has 2H structure. The 2H structure is simpler than the 18R structure as shown in Fig. 3.

Many kinds of martensitic transformation produce the lattice invariant deformation with twin. This combination of twin is called the martensitic variant. We can assume that the slip plane is replaced with the habit plane in the case of the shear deformation as shown in Fig. 4 [3]. Its volume change is extremely small under the martensitic transformation because of the existence of shear direction on the habit plane [3].

AE Simulation of the Martensitic Transformation

We simulated the AE waves generated on the martensite habit plane using a shear-wave transducer (resonance frequency = 2.5 MHz). This experimental setup is shown in Fig. 5. This shear-wave transducer was attached to the oriented plane of a Cu-Al-Ni SMA single crystal. The cross-section of the specimens is the same as that of the tensile specimens, and we attached an AE sensor (M5W) to the surface 20 mm from the shear-wave transducer. Two martensite habit planes were shown in Fig. 2. In $\beta_1 \rightarrow \beta_1'$ transformation, the habit plane is inclined by 15° at the front and 45° at right-side surface. In $\beta_1 \rightarrow \gamma_1'$ transformation, the habit plane is inclined by 45° at the front and 51° at right-side surface. The shear wave transducer was put on the corresponding planes. The voltage was applied to shear-wave transducer using a function generator. We used impulse or step function. The signals detected by the AE sensor were sent to the digital oscilloscope with 50-ns sampling time after amplified 40 dB through a band-pass filter of 100 Hz to 20 MHz (NF9913). A longitudinal-wave transducer (resonance frequency = 2.25 MHz) was also used in this experiment for comparison. The experimental setup is shown in Fig. 5.

We characterized Lamb waves due to a shear-wave transducer. An impulse voltage (5 V, rise time = 1.0 μ s) was applied. The waveforms obtained were analyzed with the wavelet transform

(AGU-Vallen Wavelet software). The waveforms and these wavelet contour maps simulating the $\beta_1 \rightarrow \beta_1'$ and $\beta_1 \rightarrow \gamma_1'$ phase transformations respectively are shown in Fig. 6.

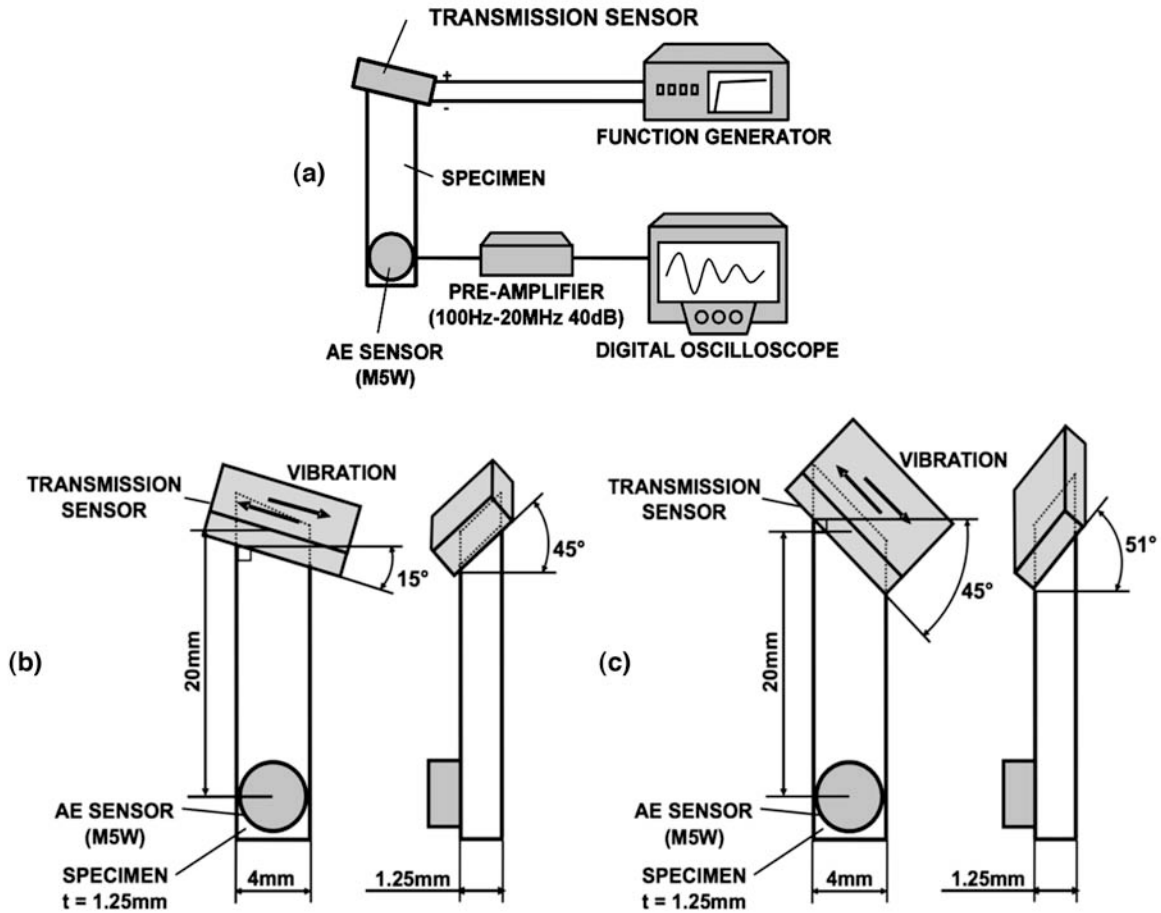


Fig. 5 Experimental set up of the wave transmission sensor to simulate Lamb waves. (a) Experimental setup; (b) $\beta_1 \rightarrow \beta_1'$ simulation; (c) $\beta_1 \rightarrow \gamma_1'$ simulation

The curves in wavelet contour maps are the group-velocity dispersion curves of S_0 -mode Lamb waves calculated with copper velocity (P-wave = 4361 m/s, S-wave = 2322 m/s). The contrasts in the wavelet contour maps and the group velocity dispersion curves of S_0 -mode Lamb waves were almost same, implying that the Lamb waves are generated by shear AE source. Considering the range to 8.5 μ s and 1200 kHz, we find that the only S_0 -mode Lamb waves arrived. Similar results were obtained using a longitudinal-wave transducer as the source in this range. Beyond the initial stage, the two AE simulation sources had different behavior of the AE waveform amplitude increase. Figure 7 shows AE waveforms of the shear and longitudinal source in the $\beta_1 \rightarrow \beta_1'$ simulation. AE amplitude due to the shear source has five-times difference in amplitude between the second and third waves. The corresponding difference in AE amplitude due to the longitudinal source was sixty times. The third wave is thought that A_0 -component starting at 8.5 μ s and this part is similar in both cases. Therefore S_0 -component in the longitudinal case is much weaker than A_0 -component and results in the observed difference.

The existence and starting time of A_0 -component can be explained using Two-surface sensing method [4]. Two same sensors were put on the front and back surfaces of the specimen, respectively. S_0 -component should detect same wave phase at both sensors. Figure 8 shows Two-surface sensing of simulated AE waveform ($\beta_1 \rightarrow \beta_1'$ transformation) due to longitudinal wave transmission sensor as the example. The detected AE waveform at the front and back sensors

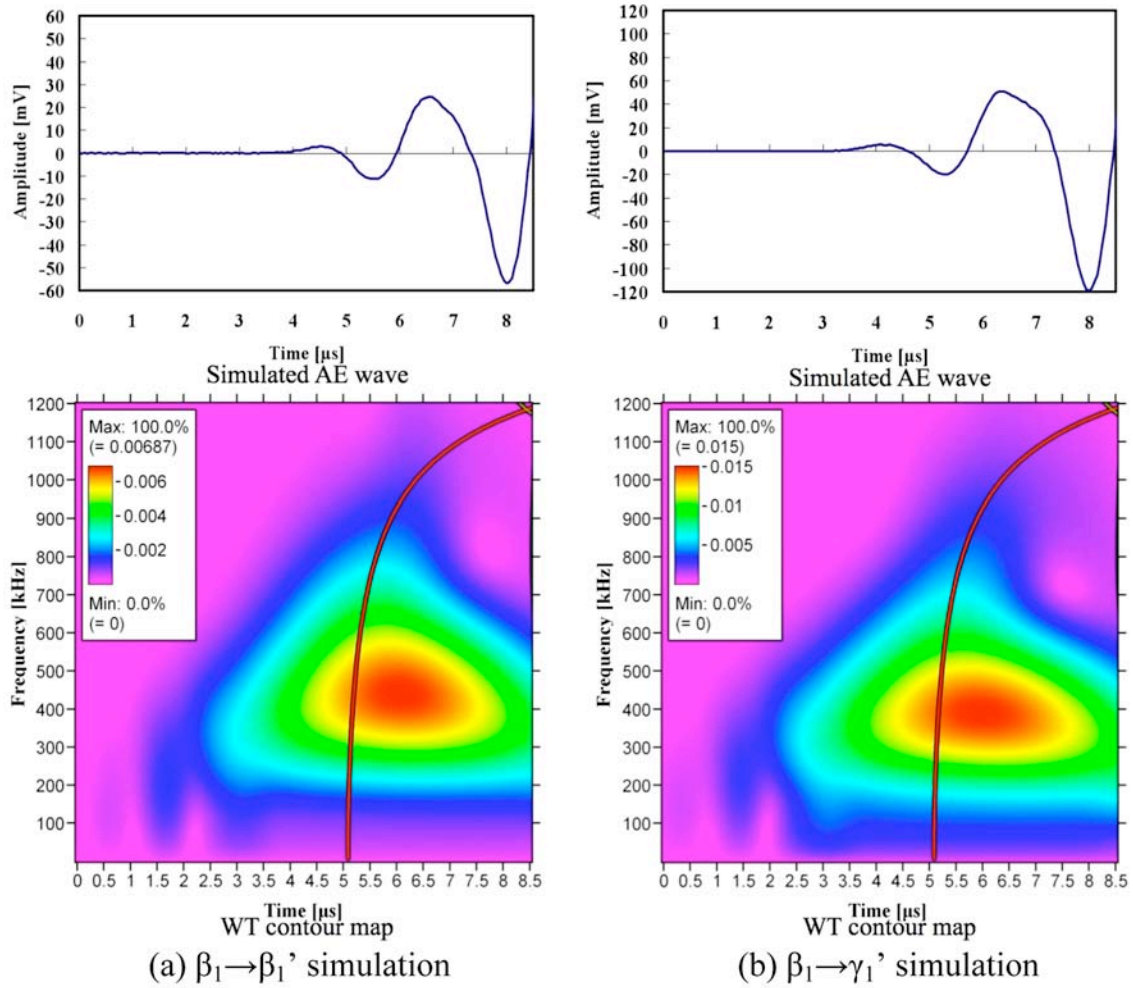


Fig. 6 WT contour map of simulated AE.

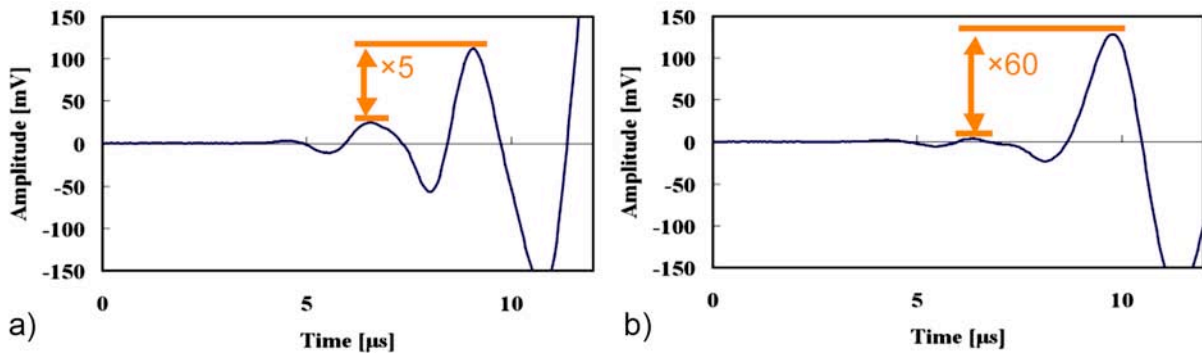


Fig. 7 AE waveform due to simulated source. (a) Shear source. (b) Longitudinal wave source.

showed almost similar wave phase until 8.5 μ s, but after this part these wave phases reversed each other. It is thought that this point indicates border between S_0 -component and A_0 -component.

We need step functions as input applied to the shear-wave transducer to simulate the dynamic behavior. The rise time of step function was changed from 1.0 to 2.0 μ s at 0.1- μ s step. We used “m-value” obtained from Takashima’s method [5] to characterize the AE signals by source rise time changes. The “m-value” is the gradient of frequency spectrum. When the AE waveform includes high frequency spectrum, m-value is lower [5]. FFT analysis with Hanning window was

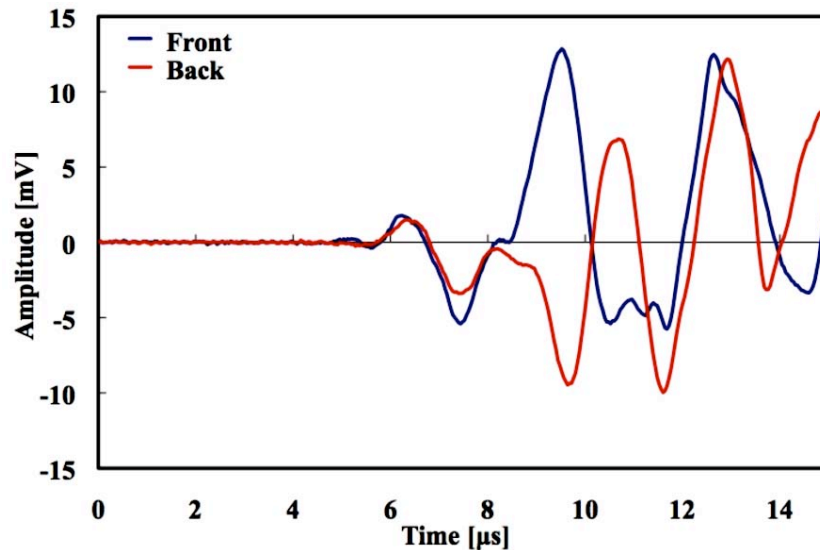
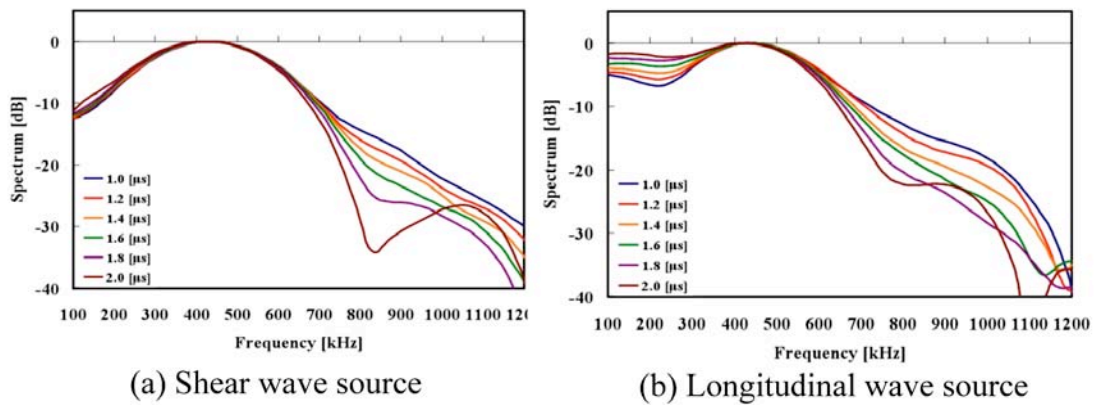


Fig. 8 Two-surface sensing of $\beta_1 \rightarrow \beta_1'$ simulation due to longitudinal wave source.

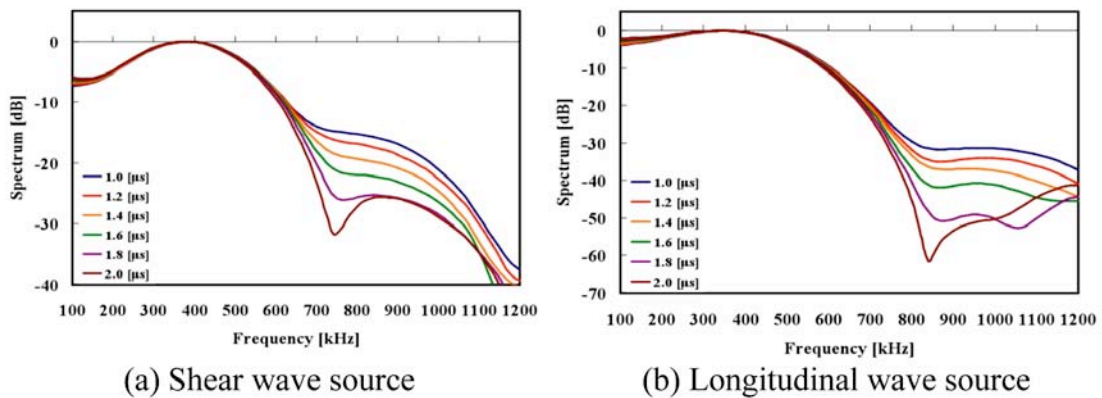
conducted to the simulated AE waveforms in the 0.1~1.2 MHz range until 8.5 μ s that only includes S_0 -mode Lamb waves. Figures 9 and 10 show the frequency spectra in varied conditions.



(a) Shear wave source

(b) Longitudinal wave source

Fig. 9 Frequency response of $\beta_1 \rightarrow \beta_1'$ simulation.



(a) Shear wave source

(b) Longitudinal wave source

Fig. 10 Frequency response of $\beta_1 \rightarrow \gamma_1'$ simulation.

In Figs. 9 and 10, the maximum frequency was constant for each group regardless of the increase in source rise time. As expected, the power spectra decreased beyond the maximum frequency with increasing source rise time.

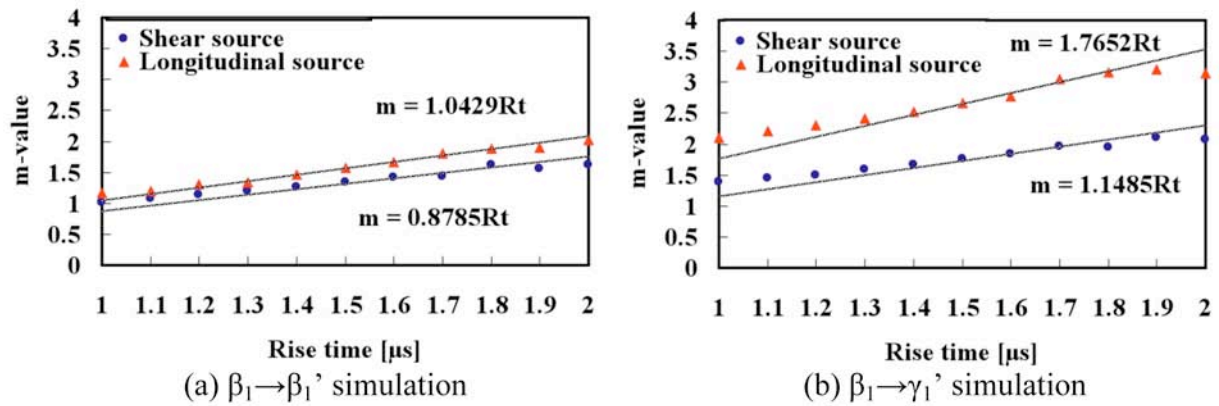


Fig. 11 Relation between rise time and m-value.

Figure 11 shows the obtained m-value vs. source rise time. In each experimental simulation with a given source, the obtained m-value increased gradually. The gradient values of these relations were obtained by linear regression. This result shows that m-values can be used to estimate the source rise time, but one must use a unique relation for the geometry and source type.

Dynamic Behavior of Martensitic Transformation

We detected AE waveforms due to two kinds of martensitic transformations ($\beta_1 \rightarrow \beta_1'$ and $\beta_1 \rightarrow \gamma_1'$) in Cu-Al-Ni SMA single crystals during tensile deformation. The martensitic transformation appeared at the center of the specimen. We attached two AE sensors (M5W) separated by 20 mm from the specimen center. AE measurements used a 2-channel AE monitoring system to discriminate the grip noise. The AE threshold level was 50 dB. Detected AE signals were amplified 40 dB through a band-pass filter of 100 Hz to 20 MHz (NF9913) and recorded at 50 ns sampling time and sampling points of 2500. In this experiment, we detected AE waveforms obtained until the elongation of 0.1 mm after the beginning of stress relaxation from the appearance of martensitic plane on the surface. AE waveform analysis was conducted off-line using the same analysis as in the simulation. Figure 12 shows the load-elongation curve of each specimen. In the case of $\beta_1 \rightarrow \beta_1'$ phase transformation, the martensite plate appeared at about 0.57 mm elongation with stress relaxation. In the case of $\beta_1 \rightarrow \gamma_1'$ phase transformation, martensite plate appeared at about 0.29 mm elongation with stress relaxation. The martensite plates are shown in Fig. 2.

In AE experiments, $\beta_1 \rightarrow \beta_1'$ and $\beta_1 \rightarrow \gamma_1'$ phase transformations generated 401 and 174 AE event counts, respectively. AE signals were classified into two types from the amplitude behavior. This depends on the third-wave amplitude. When this is five-times or less of the second-wave amplitude, the AE is shear type (Event A; circles in Fig. 12). When this is more than five-times of the second-wave amplitude, the AE is apparently longitudinal type (Event B; triangles in Fig. 12). The m-values were obtained by waveform analysis of AE detected by each martensitic transformation. Using the data shown in Fig. 11, we estimated source rise time of each martensitic transformation.

Since martensitic transformation as the AE source is due to shear behavior, we only consider AE Event A (filled circles) in Fig. 12. The average rise times of $\beta_1 \rightarrow \beta_1'$ and $\beta_1 \rightarrow \gamma_1'$ phase transformation were 1.4 μs and 0.82 μs, respectively. The $\beta_1 \rightarrow \gamma_1'$ phase transformation appears to occur at a higher speed in generating the 2H stacking structure, as it is simpler than 18R stacking structure of the $\beta_1 \rightarrow \beta_1'$ phase transformation. With the use of simulation, we can estimate quantitatively the rise time of martensitic transformation.

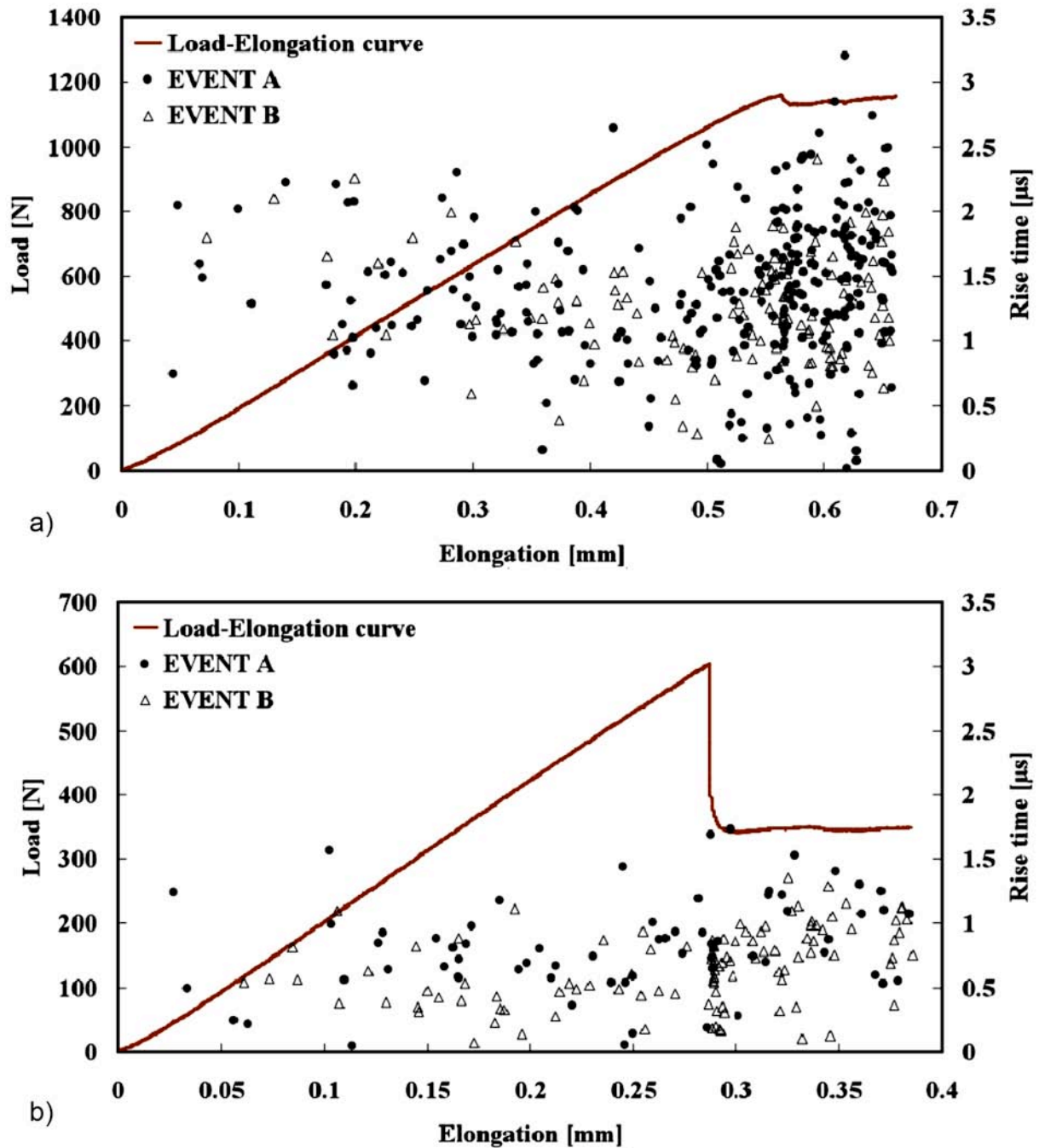


Fig. 12 Rise time distribution of martensitic transformation and load-elongation curves. (a) $\beta_1 \rightarrow \beta_1'$ transformation. (b) $\beta_1 \rightarrow \gamma_1'$ transformation.

About the AE of Event B (triangles in Fig. 12), its source seems to have the longitudinal behavior on the basis of the behavior of increasing AE waveform amplitude. There is a possibility of a combination of shear sources of martensitic transformation producing this mechanism, but we need to examine this further.

Conclusions

We have investigated the relation between source rise time and obtained m-value by AE waveform analysis using shear wave transducer for the quantitative evaluation of two types of martensitic transformations in Cu-Al-Ni shape-memory-alloy single crystal.

1. In the case that the AE source is shear, AE wave propagation in a Cu-Al-Ni SMA single crystal thin plate is due to Lamb waves.
2. The relation between the source rise time and m-value was obtained. The change of AE source rise time appears with decrease of power spectrum in the high frequency range of the S_0 -mode Lamb waves.
3. The source rise times of two kinds of martensitic transformation in Cu-Al-Ni SMA single crystal were estimated by each AE waveform analysis. The source rise time of $\beta_1 \rightarrow \gamma_1'$ phase transformation was shorter than the $\beta_1 \rightarrow \beta_1'$ phase transformation.

References

1. T. Yasuda, D. Tani, H. Nishino, and K. Yoshida: *J. Acoustic Emission*, **24**, 2006, 153-160.
2. T. Hunakubo, ed.: *Shape Memory Alloy* (in Japanese), Sangyou-tosho, 1984, pp. 12-17.
3. K. Tanaka, H. Tobushi, and S. Miyazaki: *Mechanical Properties of Shape Memory Alloy* (in Japanese), Yokendo, 1993, pp. 10-13.
4. K. Ono, Y. Mizutani and M. Takemoto: *Advances in Acoustic Emission-2007*, 2007, pp. 336-341.
5. K. Takashima, Y. Higo, and S. Nunomura: *Philosophical Magazine A*, **49-2**, 1984, 221-229.

IMPLEMENTATION OF ACOUSTIC EMISSION METHOD TO THE CONVENTIONAL NDT STRUCTURE IN OIL REFINERY

V.P. GOMERA, V.L. SOKOLOV and V.P. FEDOROV

Kirishinefteorgsintez, 187110, Kirishi, Russia

Keywords: pressure vessels, complex testing, oil refinery

Abstract

The article is the addition to the article [1] and describes some results of AE laboratory at an oil refinery during the past 17 years. Some problems of AE application for testing industrial pressure vessels and possible solutions of these problems are presented. On the pressure vessel tests, it is shown that AE testing is the essential factor for increasing of the efficiency of complex NDT of dangerous industrial hardware.

Introduction

NDT is the main means of achieving reliable operation of industrial pressure vessels and piping. This information is necessary for industry and environmental safety provision of potentially dangerous processes. Usage of new NDT methods, such as AE method, gives a chance to improve traditional NDT structure of industrial objects in essence. Such improvements could include:

- Considerable growth of testing volume without increasing testing time;
- Testing of previously inaccessible parts of constructions;
- Increased effectiveness of traditional NDT methods;
- Possibility to obtain new diagnostic information, for example, about flaws growth.

In order to realize this, change is possible only in case of successfully passing complicated stages of adaptation to industrial conditions. The first stage considers potential advantages of a new method against other methods in practical inspection, and establishes the scope of correct applications of this method. Factory management should get conclusive proof that the new method is really useful for equipment testing.

Kirishi refinery is the largest one in Russia. It processes 22 billion tons of crude oil per year. More than 70% of production is exported. There are several thousands of pressure vessels at the refinery and they are the main objects for AE testing at the plant.

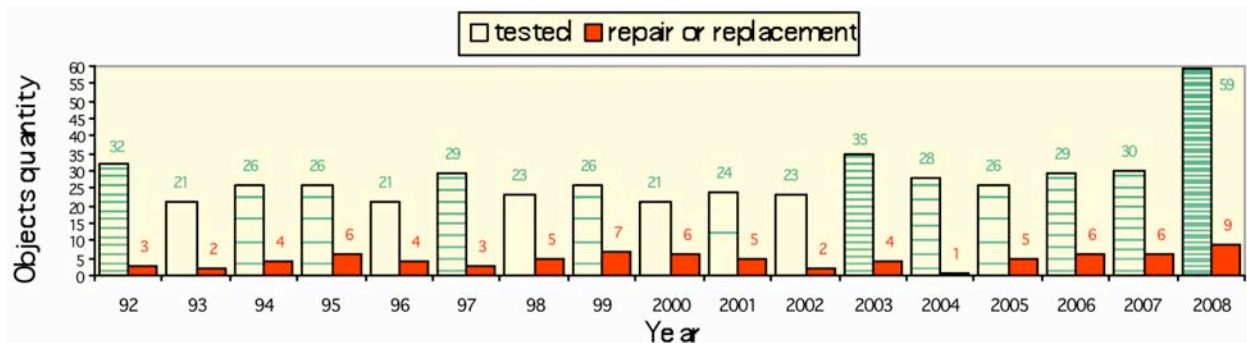


Fig. 1. Results of pressure vessels AE testing at Kirishi oil refinery.

Usage of AE method in Kirishi refinery has not become widespread for piping, though its periodical testing was successful. Possibly piping is thought to be simpler objects compared to vessels. So, their validation used less complicated methods than AE. Moreover, from the point of view of factory management, if there are doubts in quality of some parts of piping, it is more rational to change them at once, rather than assigning their resource by complicated testing methods.

Thus, the complicated testing methods such as AE have the best perspective in solving really difficult tasks, or tasks that can not be solved by other NDT methods.

Problems of AE Applications at the Refinery

1. The feature of AE testing is an opportunity of integral assessment of condition of an industrial object. Meanwhile collected information contains reactions of a large number of control channels to physical processes of different nature; for example, the formation of cracks, fretting or friction of construction elements, noise of turbulent flows, etc. The extraction of the informative characteristics of crack formation from the “interfering” processes is complicated task.

2. AE test procedure is connected with the detection of dynamical processes. The analysis of such processes is more complicated, than one of static processes, which are the base of the most traditional NDT methods. Therefore the serious problem in AE testing of industrial objects is the correctness of usage criteria for assessing the hazard level of defects. These criteria, basically, are derived for the small specimens for laboratory testing, but we believe that AE testing of pressure vessels requires another type of testing including material testing in fracture mechanics. Every industrial object (unlike laboratory specimen) is a complicated system with individual features of AE generation during its loading. Many factors influence on AE features, part of which is impossible to predict *a priori*. Therefore, direct use of formal criteria and automatic algorithms does not yield adequate assessment of defect hazard. Automatic algorithms are advantageous in speed of decision-making, but often unsuitable for solving non-standard tasks.

In the situation described above, the competency of experts is essential. But this practical experience is difficult to be formalized. It accumulates as a result of analyzing a large volume of experimental test data of industrial objects. Unfortunately, in such experience prevails subjective component. The objective component of our practice is the usage of high-quality hardware and software for data collection and analysis. During 16 years we utilized several AE systems, each of which was one of the best in the world at that time. Our experience has been formed as a result of about 500 pressure-vessel tests. Synthesis of objective and subjective components has given the results that may be assessed as successful: in our plant AE method becomes established and included in the system of basic NDT methods, though it was taken as exotic at the beginning [2-4]. Even so the role of subjective experience is still significant.

3. As a rule, in today's Russia, the development of high technology and expensive NDT methods is possible only with direct financial support of large industrial companies. In spite of advantages of AE method, its implementation is possible only where management has progressive thinking for enhancing the safety and is willing to provide financial support until the benefits overcome the cost. For this reason the implementation of AE method does not depends on its advantages but depends more on the attainment level of factory management.

4. The problem of “false-negative rejection”. According to testing results of alternative NDT methods only a small part of active AE sources (15-20%) are considered as indicators of significant defects. As a rule we cannot predict the hierarchy of the relative hazard of defects on the

result of AE testing. All active sources in AE test method are considered to indicate potentially dangerous defects, until the opposite would be proved. For the testing of dangerous objects this strategy is more preferable, than “non-rejection”. Such approach may be compared with inadmissibility of any cracks in pressure vessels, which is declared to be Russian norms [5]. Probably such approach could be compared to the complication and ambiguity of the hazard assessment of cracks that is offered today by fracture mechanics. All the more, it is hard to expect that similar tasks would be solved explicitly by AE method.

5. The previous problem is only the consequence of other problems: the verification of the results of AE testing is not just useful, but necessary. Unfortunately, in our applications, we cannot use AE method as in-depth method. AE results must be confirmed with other NDT methods. On the other hand, AE method is used to assess results obtained with other NDT methods. If any local defects are first detected with a conventional NDT method during vessel inspection, it is a reason for further AE testing. As a result of AE testing, first, AE is used for logging the kinetics of defect's development for danger assessment. Second, AE determines the location of other defects, if they exist in the structure, but undetected due to their locations being out of inspection zone of traditional methods.

Efficiency of AE Method for Integral Testing

Complex testing allows us to compensate disadvantages of different methods and to combine their advantages. Furthermore, combination of test methods increases the probability of detection (POD). Periodic AE testing by loading a vessel by pressure is an example of complex testing due to AE is combined with such classical method, as is hydraulic test. This is a good illustration of the advantages of complex testing. It is obvious that hydraulic test of a vessel, combined with AE test, gives much more information than ordinary hydraulic test.

It is well known that a testing procedure during consecutive applications of several NDT methods is optimal, if methods with maximal speed of getting information are used first. Probably, AE method has no match with this qualitative characteristic. AE method may be used as the basis in complex testing due to its performance and other unique properties, such as the capability to integral testing of large constructions and the detection of defects with potential for growth. It also may be thought as investment to achieve savings in testing of large objects. For example, if AE testing is applied, it is not necessary to test 100% of welds of large pressure vessels by conventional methods. Disadvantages of conventional methods (low productivity, large costs of material and time for metal preparation, etc.) do not allow making the complete testing of large objects within a reasonable period of time. In complex testing, AE method is first applied for localizing zones with potential defects, and then other NDT methods with lower productivity are used in those local zones to find geometry of probable and confirmed defects. In such way realized the conception of economically efficient 100% test of large objects.

This approach is shown in the following example. Test object - spherical vessel for LPG storage with inner diameter 10.5 m, wall thickness 16 mm, volume 600 m³. There are 16 longitudinal steel sheets welded with each other and terminated by the hemi-spherical top and bottom caps. Analysis of AE test data showed local zones of the shell (with pointed coordinates and size), which need additional testing by conventional methods (VT, UT, PT, RT). Also indicated are the possible type of defects and the degree of their possible hazard (according to the features of detected signals). On Figs. 2 and 3 are shown the results of additional testing.

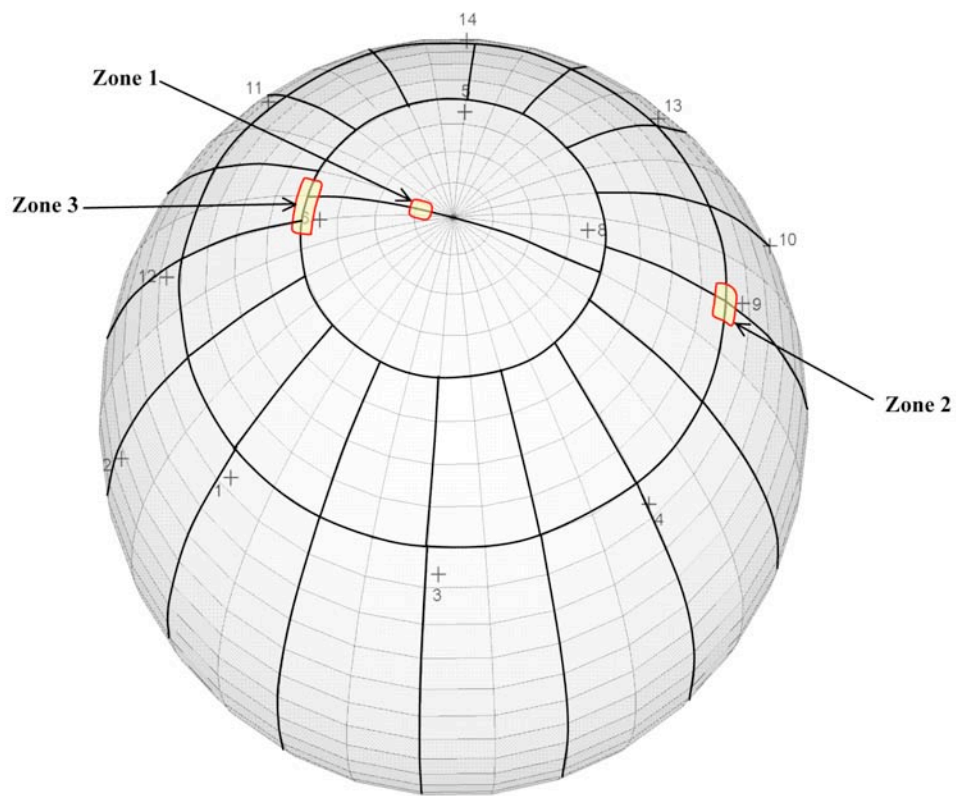


Fig. 2. Drawing of upper part of the sphere tank (10.5-m diameter) with weld marks. Defect zones (1 to 3) are also indicated.

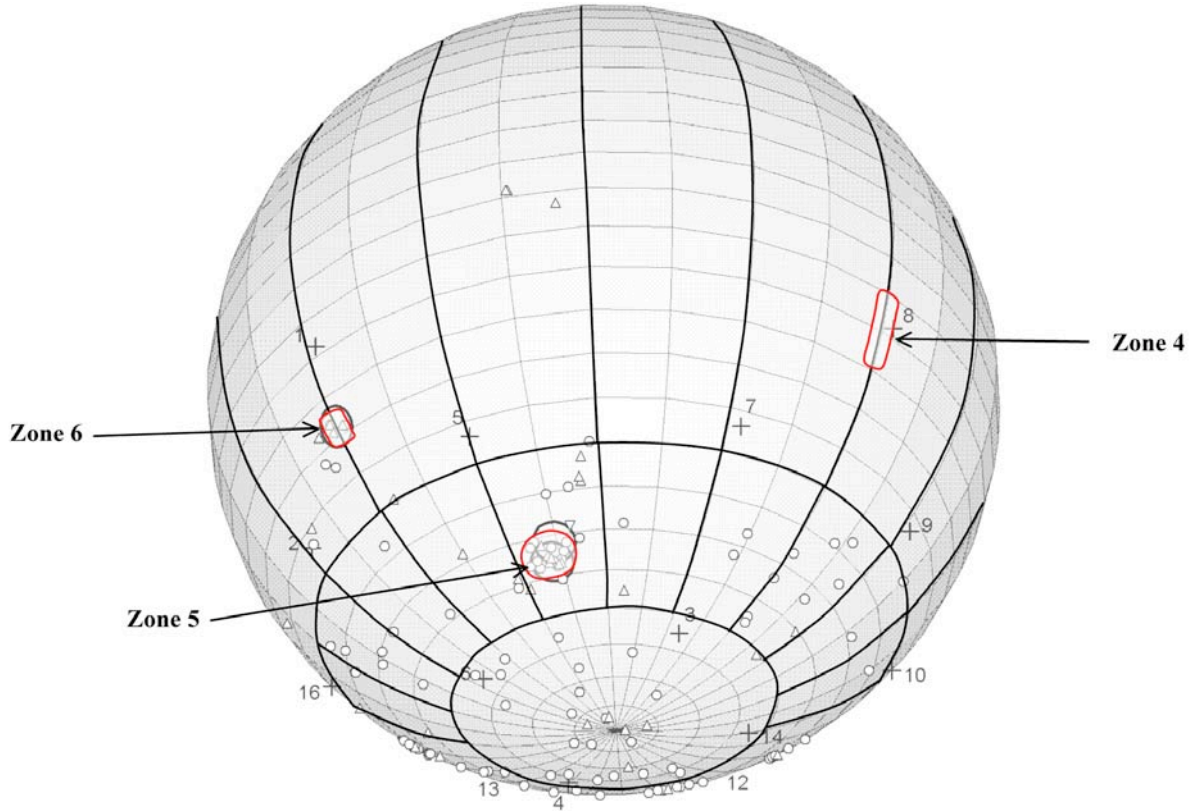


Fig. 3. Drawing of lower part of the sphere tank (10.5-m diameter) with weld marks. Defect zones (4 to 6) are also indicated.

Zones 1 to 3 with defects localized by AE and then verified with conventional NDT methods are shown in Fig. 2:

- Zone 1 – a cross crack of 5-mm depth at the weld of upper cap; verified with VT and PT.
- Zones 2 and 3 – zones with relatively high AE zonal activity. Sources were not localized by location algorithms. This could be explained that these are small defects, which increased their AE activity while load was applied. Probable type of source is the irregularities of metal or small defects, which are located close to sensors. There were small defects below the UT limits, but detected with AE.

In two zones, determined with planar location, and in one zone determined by zonal location, there were no defects verifiable with UT and PT.

To carry out additional inspection for finding the type of active AE sources, it was needed to use the aerial lift, to build scaffoldings and partially dismount service passes (in the upper part of the vessel). After the additional inspection, that constructions were used during repair job of detected defects. It is necessary to notice that the probability to find these defect zones by traditional NDT methods was very low; zones with defects (base metal, welds, located in the upper part of the vessel) are seldom getting in the scope of ordinary testing.

In Fig. 3 are shown zones with defects localized by AE and then verified with conventional NDT methods:

- Zone 4 – a part of weld (900-mm long) in the middle part of the tank: UT was applied and it detected defects of non-allowed dimensions; the defective weld was repaired (shell segment was localized as a zone of high AE activity around channel #8).
- Zone 5 – area of parent metal on the inner part of the surface with crater type defects, which had the mechanical nature (maybe they appeared during the tank assembly); the depth is 2-4 mm., area to 250 mm², defects verified with UT and PT;
- Zone 6 – weld defect in the middle part of the tank, verified with UT, repaired. Zone registered with planar location on the sphere.

In two more zones localized on one of vertical welds, the defects were verified with UT, and weld was repaired. There were also detected two zones of AE activity, but defects were not verified with UT or PT.

Concerning the precision of localization of defect by AE, in real engineering practice, the scraped square for the conventional NDT methods of UT and PT is usually 300 x 300 mm. The test takes place at this square. Let us consider, for example, Zone 5 (Fig. 3), determined by AE. Zone is formed with three closely located clusters. The largest cluster (100-cm diameter) contained 12 events, detected by a minimum of three sensors. The cluster was initiated by integral action of crater defects. They are located, mainly, in the form of three compact groups, localized on squares with dimensions from 10 to 30 cm² (in Fig. 3 the dimensions of location cluster are enlarged for visualization; in real tests, cluster dimensions were smaller). For three compact groups of defects, at a given cluster size of 30-cm diameter, the coordinates of cluster center calculated by the spherical location algorithm differ from the coordinates of cluster centers of real defect groups, measured at the object in the following table.

According to Russian standards [6], the precision of multi-channel location shall be better than greater of two wall thicknesses or 5% of distance between two sensors. According to the first criterion we obtain: $\Delta_1=2h=32$ mm. On the second criterion (the distance between two sensors varied from 2700 to 3400 mm) $\Delta_2=135-170$ mm. So the precision of location is within the limits prescribed in the standards. The minimal size of inspection for NDT used in refinery

Location clusters	Coordinates of AE sources measured directly on object (the centers of defects groups, Degrees)		Spherical location results (coordinates of the location clusters centers, Degrees)		Absolute difference in coordinates value			
	Longitude	Latitude	Longitude	Latitude	Longitude		Latitude	
					Deg	mm	Deg	mm
Cluster №1	131.0	-58.0	130.6	-57.8	0.4	19	0.2	18
Cluster №2	138.5	-58.0	137.0	-59.3	1.5	73	1.3	119
Cluster №3	146.5	-57.0	145.5	-57.6	1.0	49	0.6	55

practice is 300-mm square. Therefore, such precision is satisfactory for engineering applications. In some cases, the size of preparation zone for additional NDT may be increased to 400 or 500-mm square when location uncertainty is suspected.

It can also be used for the planar scheme for locating specific segments of a vessel, because the sphere diameter is large and the square segment is small relative to the whole surface. It is useful for detailed analysis of spherical location and is shown on Fig. 4 for Zone 3.

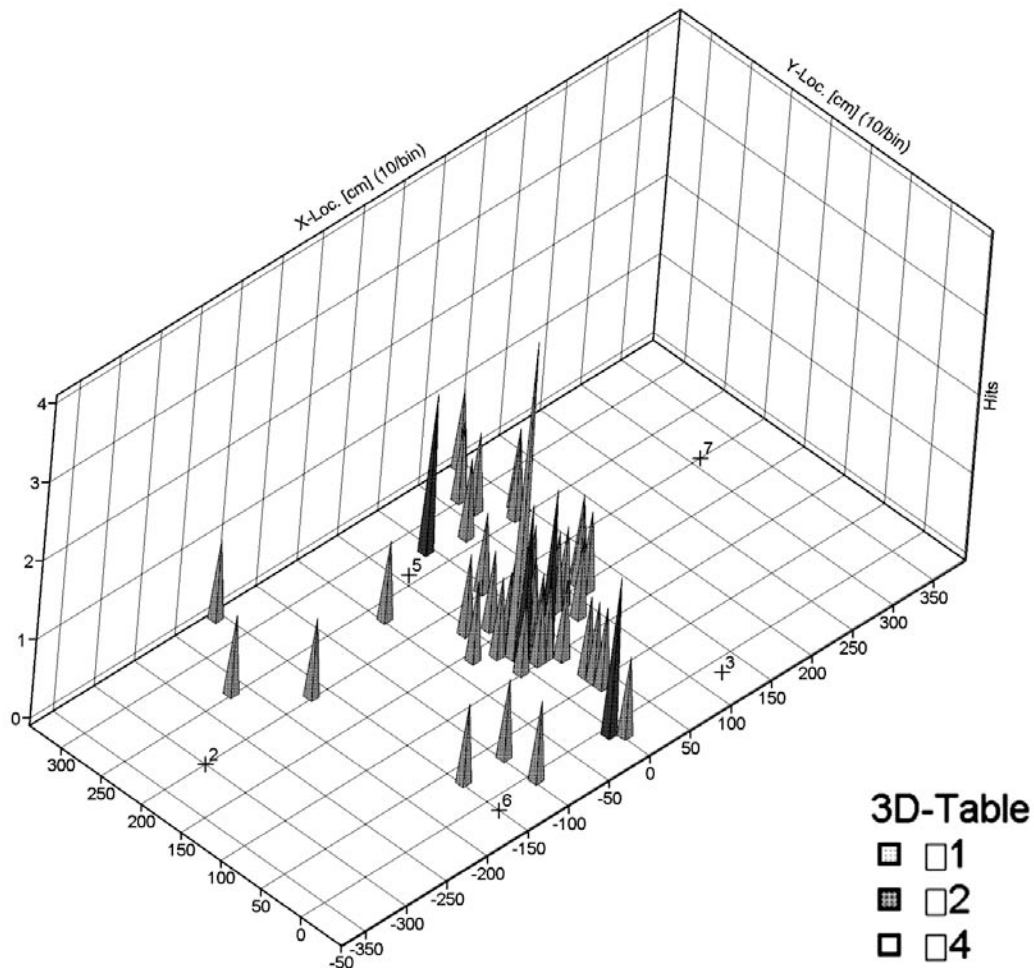


Fig. 4. Results of planar location of AE source activity on the shell segment of LPG storage tank, which was identified as defect group of crater type defect on the inner surface of the vessel.

On the example vessel, it is necessary to test about 490 m of welds. For inspection with PT or UT (under a code clause of 100% welds inspection), we must prepare the metal surface area of

more than 147 m² (covering 150 mm on both sides of the weld). Yet, such methods do not inspect the parent metal of the shell outside the welds. Here lies the effectiveness of AE method for inspection as every part of structure is examined automatically.

By AE testing the whole volume of metal is evaluated with a network of 48 sensors (mesh of the network is determined with test conditions and test purposes). Scraped area for 48 sensors is about: $0.01 \times 48 = 0.48 \text{ m}^2$. Furthermore, for checking AE test results by PT and UT methods, it is necessary also to scrape the surface in the zones, localized with AE method. So in the example considered, the scraped area for NDT was 1.35 m². Total scraped area was 1.83 m². Comparison with previous evaluation shows a high efficiency of AE testing applied as an integral method for diagnostics of large pressure vessels.

So, AE testing is a good tool for NDT resource optimization in condition monitoring, when it is necessary to provide a high level of diagnostics of dangerous industrial objects within limited time available for inspection.

Usage of AE Information Power

One of the advantages of AE method is the ability to collect much information, which contributes to its successful usage. It is especially important in cases where the lack of preliminary information about test object could cause non-optimal usage of testing procedures or possible inaccuracies in measuring flaw locations. Unfortunately, such events sometimes take place during testing of large industrial objects.

Usually, modern AE equipment collects large quantity of information during a test, which may be redundant for our conventional practice of vessel testing. For example, we seldom use waveform analysis. To gain desired results we are often satisfied with other data analysis procedures. However, this redundancy appears as insurance from possible testing imperfections and is a powerful compensatory factor when some parts of information is lost (due to non-optimal sensor arrangement, or their insufficient quantity, or existence of background noise).

These circumstances can be illustrated on example of vertical column testing with following parameters: outer diameter – 3200 mm, wall thickness – 36 mm, volume – 426 m³, height – 53.6 m, insulation layer – 150-200 mm thickness. The column was assembled on site from 3 segments, manufactured at factory. Segments were assembled with two mounting welds, which were made during the column installation. Lower field weld is located at 28.6 m height, upper – at 47.6 m. Lifetime of column - 29 years.

The primary intent of AE testing was the quality control of these welds. AE testing was carried out twice with an interval of 5 years. Before the first testing it was assumed that there were no serious problems in field welds. Therefore we used a less number of sensors than really needed for this column. To place several sensors we needed help of steeplejacks (industrial mountaineers). Their dangerous work could cause inaccuracies in some length measurements. However, these shortcomings in testing arrangement were compensated by information power of AE method. The quantity of information was quite enough to detect serious flaws in field welds with confidence and to localize most of these flaws. The results of AE testing became the reason for 100% test of field welds by other NDT methods and consequent repair of several parts of field welds. The second AE testing, carried out 5 years later, had several differences from the first one, which are shown in table below.

Conditions	First AE testing		Second AE testing (5 year later)	
	Low weld	Upper weld	Low weld	Upper weld
Number of sensors in location map	8	6	17	11
Distance between nearest sensors	170-190 cm	200 cm	120-140 cm	130-160 cm
Possibility of planar location	Problem	Problem	Satisfactorily	Satisfactorily
Basic location algorithms (part of weld's length)	Linear ($\frac{1}{3}$) Planar ($\frac{2}{3}$)	Linear ($\frac{3}{4}$) Planar ($\frac{1}{4}$)	Planar	Planar
Preliminary information about flows	No		Yes	
Type of testing	Hydraulic		Pneumatic	
Internal agent	Water		Nitrogen	
Pressure rise speed	≈ 0.064 MPa/min (+ hold)		≈ 0.009 (without hold)	
Max. Test pressure	2.9 MPa		2.1 MPa	
Number of previous repairs (changes of weld's structure)	0		3	
Interferences from new welding of new internal facilities of column	Yes		No	
Threshold	45 dB		40 dB	

As it could be seen in this table, the outlines of two testing differ considerably. Main advantage of the second testing was using more sensors. Therefore information of flaw coordinates was more accurate. Probably the second testing was more informative than first one.

It should be taken in account that key task of AE laboratory in an oil refinery could be formulated simply:

1. To detect problem part of construction;
2. To localize with sufficient accuracy the most dangerous flaws existing at the time of testing.

On the base of such statements the results of two testing practically coincide. However, the results of these two testing have differences. These differences gave us data going beyond the scope of key task. For example, we obtained data about flaw growth dynamic in this area. Also, we got data about the quality of repair done and about the suitability of further repair. For this it is convenient to use instruments of AE data analysis, which permit us to visualize the structure of problem areas in whole construction (or in big segments of construction).

Two drawings, taken from results of data analysis, show planar locations of AE sources in the lower field weld area. The drawing is matched with drawing of shell reamer, where positions of manholes, welds and repaired areas are shown.

In Figs. 5 and 6 are marked several zones with the following conditions:

- Zone 1.1, 1.2, 1.3 – large clusters of non-metallic inclusions and small discontinuities on different depths in base metal.
- Zone 2.1, 2.2, 2.3 (same positions as zone 1.1, 1.2, 1.3 – 5-year later) discontinuities with areas from 4 to 140 cm² formed. The largest bulge was placed in zone 2-1.
- Zones from 2.4 to 2.8 join to repaired parts of weld. AE activity appeared in these zones after weld repair. UT instrument detected high concentration of small discontinuities there. By analogy with variations in zones 1.1 – 1.3, it could be supposed with great probability that in zones 2.4 – 2.8 are forming discontinuities as a result of small flaws fusion.
- Zone 2.9 – crack in the weld made at a machinery plant (7 mm in depth, 30 mm in length).

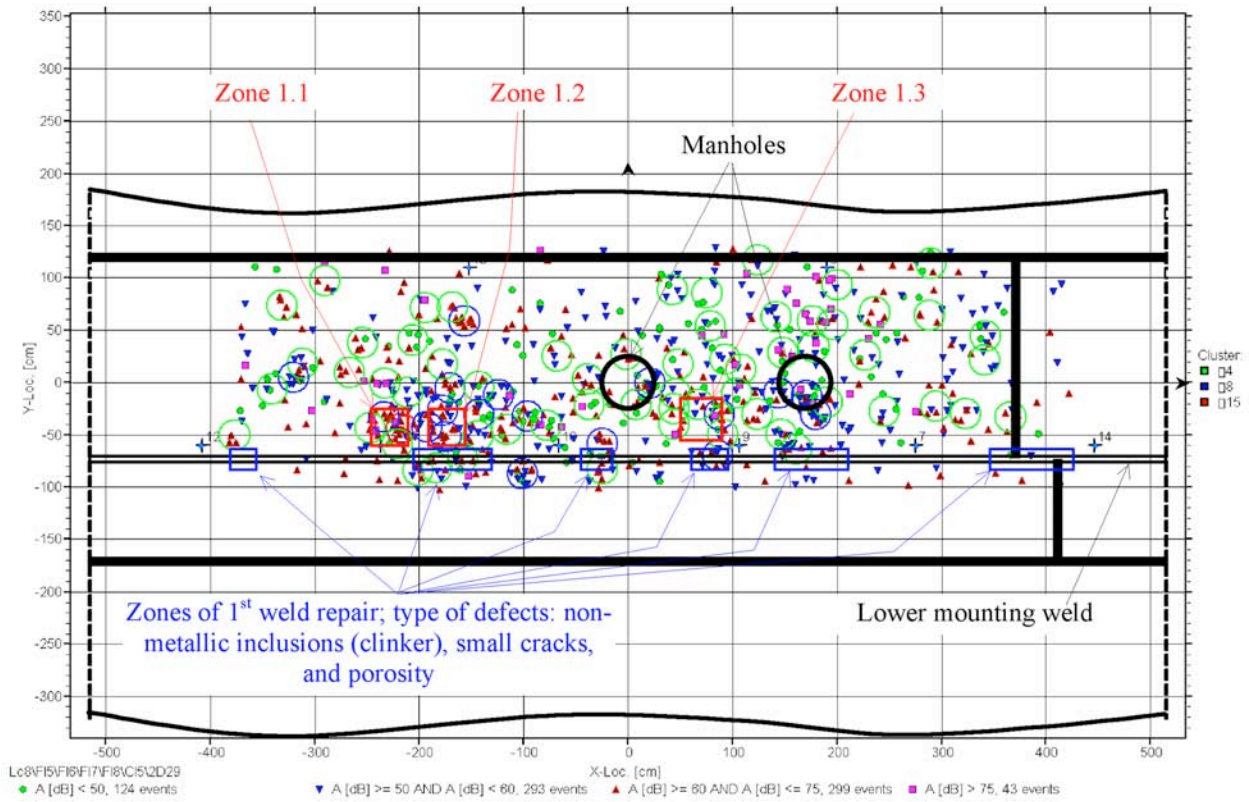


Fig. 5. Results of planar locations of AE sources in lower mounting weld area in first testing.

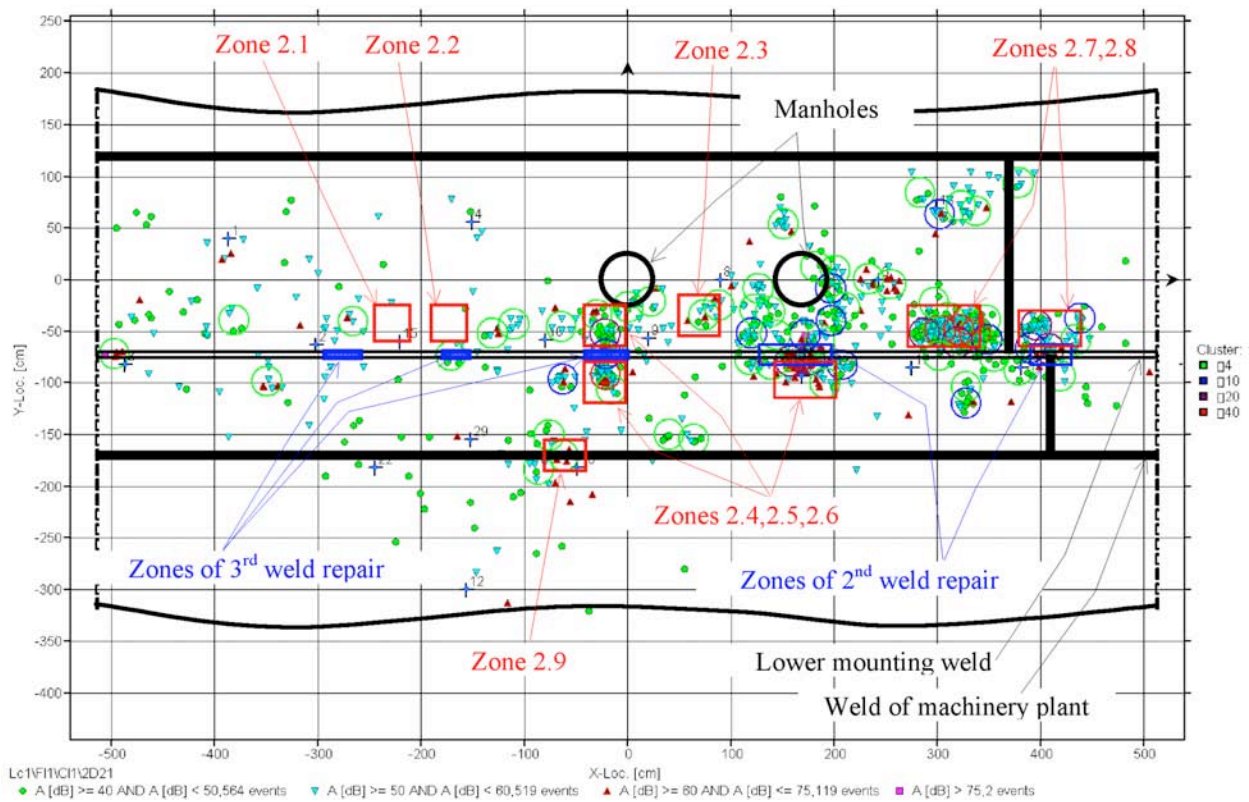


Fig. 6. Results of planar locations of AE sources in lower mounting weld area in second testing.

Analysis of the distribution of active zones on these two drawings and the results of additional NDT in these zones led to several important conclusions:

1. The quality of field welds was considerably worse than that made on a machinery plant. Therefore just the use of field welding limit the safe lifetime of the vessel.

2. As a result of long operation time, the degradation processes of material of welds and of base metal near welds were actively developed over the last 5 years. The second AE testing showed that with time these processes spread to plant-made welds too.

Repair of the weld does not always eliminate the problems. During repair the strain conditions of the metal in repair zone can get worse. It intensifies the degradation process in metal due to hydrogen embrittlement, which is the main damaging factor for this vessel. In fact, it can raise the risk of vessel failure. Therefore, the continuation of repair of local flaw zones is not recommended.

In general, similar results were received during testing of the upper field weld. On the basis of complex results the refinery management made decision to change the column. Whole chain of testing and repairs during the 5 year period is as follows:

(AE-1) → (NDT-1, 100%) → (Repair-1) → (+ 2 year) → (NDT-2, Local) → (Repair-2) → (+ 3 year) → (NDT-3, Local) → (Repair-3) → (AE-2) → (NDT-4, Local) → (Decision of column change).

So, in our practice we are using only a small part of information collected by AE system. For this reason its volume is redundant, but even during solving simple tasks of industrial testing, this AE redundancy can be useful. It can be used:

1. As additional insurance from testing arrangement faults;
2. As a reserve for solving more high-level tasks than we are solving routinely.

Conclusions

1. Phases for implementation, for demonstrating the capabilities and for proving the efficiency of AE method are successfully finished at Kirishi oil refinery.

2. It is now at a stage of determining the optimal utilization schemes of AE method in complex testing, which combines the capabilities of several NDT methods.

3. We have started the implementation of continuous AE-monitoring technology. The results of trial performance will be used for the assessment of implementing AE-monitoring systems at the new production lines. New equipment will operate in more difficult conditions than one of the existing production lines. Therefore, it is necessary to develop new technologies for their safe exploitation.

References

- [1] B.S. Kabanov, V.G. Gomera, V.L. Sokolov, V.P. Fedorov, A.A. Okhotnikov, Some Results of AE Pressure Vessels at Kirishi Oil Refinery In: *Proceeding of the 28th European Conference on Acoustic Emission Testing*, Krakow, 2008, Poland, pp. 298-303.
- [2] Kabanov B., Gomera V., Sokolov V., Fedorov V., Okhotnikov A., AE Testing of Refinery Structures, In: *Proceeding of the 27th European Conference on Acoustic Emission Testing*, Cardiff, 2006, Wales, UK, pp.133-138.
- [3] Gomera V., Forker J., Acoustic Emission for industrial testing – some examples and recent developments, In: *Proceeding of the Conference on Non-destructive Testing Equipment and Devices*, Moscow, 2003, Russia, no.2.21.

- [4] Kabanov B., Gomera V., Sokolov V., Okhotnikov A., Fedorov V., AE technology as a key element of the safe operation system at refinery: Journal of Acoustic Emission, **20**, 2002, 218-228.
- [5] PS 03-576-03. Pressure vessels design regulations and their safe operation, § 4.7 (ПБ 03-576-03. Правила устройства и безопасной эксплуатации сосудов, работающих под давлением, п.4.7).
- [6] PS 03-593-03. Regulations of AE testing of vessels, apparatus, boilers and operation pipelines, § 4.5 (ПБ 03-593-03. Правила организации и проведения акустико-эмиссионного контроля сосудов, аппаратов, котлов и технологических трубопроводов, п.4.5).

AN EXPERIMENTAL ANALYSIS OF FREQUENCY EMISSION AND NOISE DIAGNOSIS OF COMMERCIAL AIRCRAFT ON APPROACH

S. KHARDI

INRETS-LTE, 25, avenue François Mitterrand, 69675 Bron cedex, France

Abstract

Simple noise level monitoring systems, which are currently used around airports to create a noise map in residential areas, are unable to identify source frequencies and their impact on the environment. This article presents dominant frequencies during aircraft approaches of the Saint-Exupéry Lyon International Airport (France), and analyzes the evidence of impact on the environment. The main objective is the characterization of the most dominant frequencies emitted during approach operations, and the diagnosis of frequencies having a negative impact on populations living around the airport. A detailed analysis of signal processing concerns for measuring aircraft flyover noise is presented. A study of the emission angle has been completed and a classification period depending on the noise level has been achieved. Development of a de-Dopplerization scheme for both corrected time history and spectral data is discussed along with an analysis of motion effects on measured spectra. It is shown that correcting for Doppler amplitude and frequency can give some idea about source directivity. The obtained results provide additional information placing the results of theoretical models in their context, and will help validate and extend certain methods of calculating the propagation of aircraft noise. They have the potential to quantify environmental quality around the airports. The precise measured frequencies during the operations can be treated by passive or active control systems developed by aircraft manufacturers.

Introduction

Among environmental concerns, excessive aircraft noise and its control have become a major objective of airport authorities. Assessment of aircraft noise depends upon reliable information including noise measurement. During recent decades, aircraft noise levels have been successively reduced by 20 dB. Nevertheless, the large numbers of people, who live in communities near airports, are affected by aircraft noise, which has increased tremendously in scope. Decisions have been made to enable the choice of possible solutions of aircraft noise control around airports. Several procedures have been used in the worldwide aircraft operation such as low-noise during the take-off and landing flight procedures, optimal route distributions, flight route optimization around airports, etc. Nevertheless, the noise in the vicinity of airports, in particular under the take-off and landing flight paths, remains high disrupting the quality of life of local residents. Complaints are increasing despite the withdrawal of the noisiest aircraft, the fleet renewal, and the international resolutions recommending that airports, faced with the problem of noise, introduce restrictions of operations. These nuisances therefore continue to represent an environmental problem. Technology solutions and the positive measures taken by airport authorities (restrictions on use of land, procedures for takeoff and landing, operating restrictions, compensating residents, etc.) failed to reduce their impact near airports because of the growth in air traffic. The aircraft manufacturers foresee a demand for aircraft to cope with the increased traffic and fleet renewal in the coming years. The proportion of heavy-lift is progressing towards almost half the fleet. This growth will differ by two essential characteristics: 1. mass transport anticipating the scarcity of take-off slots; 2. transport playing on the increasing frequency and flexibility of operations continuing despite the anticipated shortage of oil. All the experts agree that around 2020, taking into

account the known oilfields and the potential extraction, the production of oil will reach a maximum level and then decrease especially with the growing economic power of China and India. Whatever the efforts to conserve energy and promote renewable energy, air transport will continue to grow, even with very expensive oil. This problem can only be solved within the framework of a global vision for sustainable development involving new technology engines and fuselages (Julliard, 2003), breakthrough technologies, the design of new procedures and flight paths (Zaporozhest and Tokarev, 1998; Zaporozhest and Khardi, 2004), airspace management, new regulation rules and certification (ECAC, 1997). It is a major challenge for the future of air transport in the context of economic development linked to compliance with the conditions of people living near airports.

In recent years, increasingly strict regulations on aircraft noise have imposed large economic penalties on aircraft companies and airlines that fail to comply. As engine technology leads to quieter engines, airframe noise – defined as the non-propulsive component of aircraft noise, which is due to unsteady flow around the airframe components – has become a major contributor to the overall aircraft noise levels. The physics behind airframe noise generation is still not fully understood and must be characterized before reduction techniques can be implemented. R&D projects confirmed that research in this field is active, and that current technological developments can help reduce aircraft noise levels. The current challenge is to establish an objective assessment taking account of the evolution of air traffic, and a permanent control of noise. This control is complementary to the actions initiated by the government as the mastering of urban planning in the vicinity of the airport, assistance for soundproofing, optimization and control of operational rules, etc. A compromise should be found between environmental acceptability, the lower cost of design, development, production and exploitation, and increasing the operational capacity of the airspace. Furthermore, the known absence of a clear link between the certified noise levels and noise levels measured on the ground justifies the experimental work undertaken by research and development. Indeed, at the end of each certification, changes have taken place, due to technological leaps facing the aviation industry (Oishi and Nakamura, 2000; Kenzakowski et al., 2002; Hunter and Thomas, 2003; Kannepalli et al., 2003). In flight, commercial jet aircraft sources are active (Smith, 1989; Hubbard, 1994; Michel et al., 1998). Their relative importance depends on the flight segment and the airframe-engine combination. There are many components in aircraft noise - different parts of the air-frame (flaps, under-carriage etc.), engine fan, and engine jet etc. - whose relative importance changes according to which aircraft is considered and with the aircraft's operational configuration and mode of flight. Thus, directivity has a much greater contribution in aircraft noise source characteristics.

This paper describes spectral characteristics of aircraft noise during approaches, indices used to quantify the effects of aircraft noise and cumulative noise levels as a result of aircraft operations. The main objective of this work is the characterization of the dominating frequencies defined by the most raised levels and which could be treated by the aeronautical manufacturers. Protocol for measuring the aircraft noise (ICAO, 1988, 1993, 2004) was strictly respected and used. The work presented in this article makes an additional contribution to a better understanding of the problems of aircraft noise and its control. It gives the results of measurements made for a year concerning the dominant frequencies emitted by aircraft approaching the Saint-Exupéry International Airport (Lyon, France). Analysis of the aircraft passage duration, and statistical indices describing the impact on the environment, in particular during night periods, were studied.

Experimental Setup

This section describes the measurement procedures and conditions under which aircraft noise was recorded. We used approved procedures recommended by the ICAO (1988, 1993, 2004) applied during acoustic tests and analysis of aircraft noise measurements. The measurement campaign of aircraft noise approaching the Saint-Exupéry Lyon International Airport lasted one year. It was used as a reference year because of changes in the airport infrastructure project (two new runways) and the predictable fleet renewal (new certification rules and regulations). During one-year-long measurements, the noise of commercial aircraft of different types was recorded according to annex 16 of the ICAO convention. The noise signals were recorded so that we can assess noise exposure following indices based on A-weighting (L_{Aeq} , SEL, L_{10} , L_{95} , L_{eq} , L_{DN} , L_{DNL} , L_{den} , etc.). Locations for recording aircraft noise in flight are surrounded by flat terrain having no excessive sound absorption characteristics (grass fields cut). No obstructions that could influence the sound field from the aircraft exist within a conical space above the point on the ground vertically below the microphone, the cone being defined by an axis normal to the ground and by a half-angle 80° from this axis. The type of aircraft (engines and their number, fuselage, procedures, loads, thrust changes, etc.) was not recorded. This variable could not be collected in real-time for each flight, since it would require direct access to data from the flight data recorder (FDR).

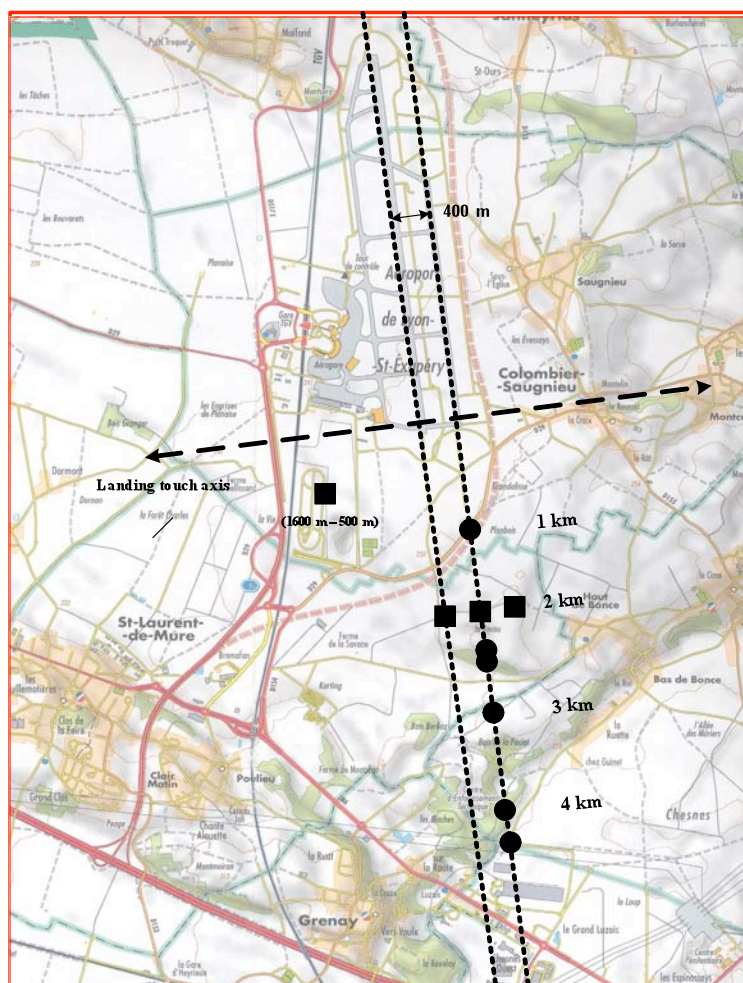


Fig. 1: Measuring points under flight path and at lateral locations. The site elevation is between 251 and 263 m.

The data were recorded at the four observation points designated in Fig. 1: under flight path 2 km \pm 400 m lateral, and lateral to a 1600 meter runway and 500 m from the touch axis. Acoustic data stored under the flight path allows analysis of the frequencies issued without lateral and angular corrections and without the need for multiple systems of expensive measurement stations. The two side points to \pm 400 m are used to make an adjustment on the data especially when the trajectories practiced during the approach deviate from the main axis of the runway due to a change in the runway landing (particular traffic regulation or incident). The last measurement point is used to control the data when weather conditions change slightly and that the air control modifies the direction of the aircraft approach operations. Measurements were performed under the following and stable atmospheric conditions:

- no precipitation;
- ambient air temperature not above 35°C (95°F) and not below -10°C (14°F);
- relative humidity is between 20% and 95% over the whole noise path between a point of 4 m above the ground and the aircraft;
- average wind velocity at 4 m above ground may not exceed 12 knots;
- no anomalous meteorological conditions that would significantly affect the measured noise levels when the noise is recorded.

Ambient air temperature, relative humidity, wind speed, cloudiness and global radiation profiles were recorded during noise measurements. Measurements are performed under the same atmospheric conditions. Their stability was checked and timetabled. Table 1 shows their fluctuations in the intervals where stability criteria are met for the whole noise measurements.

Table 1: Changes of meteorological parameters provided by Meteo France. The influence of humidity on the noise levels of less than 0.5 dB for a relative humidity between 30% and 90% at 40 °C and at 1 kHz.

Meteorological parameters (per hour)	Value intervals
Wind speed (m / s)	1-3
Average temperature (°C)	15-35
Cloudiness (octas)	0-2
Humidity (%)	35-50
Global radiation (J/cm ³)	240-290

A SIP 95 sound level meter, a Symphony (01dB Stell[®]) measurement station, and a DAT FOSTEX PD-4 (44.1 kHz sampling frequency) were used to record the acoustic data. The measurement systems are inspected every two years and approved by the French National Laboratory for testing in accordance with the international standards. The four microphones are positioned to 4 meters above the ground to comply with the requirement of free fields. The ground is flat and consists of grass shorter without brush, wood or obstacles. The calibrations are performed every day. The free-field sensitivity level of the microphone and preamplifier in the reference direction, at frequencies over at least the range of one-third-octave nominal midband frequencies from 50 Hz to 10 kHz inclusive, is within \pm 1.0 dB of that at the calibration check frequency, and within \pm 2.0 dB for nominal midband frequencies of 6.3 kHz, 8 kHz and 10 kHz. The output of the analysis system consists of one-third octave band sound pressure levels as a function of time, obtained by processing the noise signals through an analysis system with the following characteristics:

- A set of 24 one-third-octave bands filters [50 Hz - 10 kHz];
- Response and averaging properties in which the output from any one-third octave filter band is squared, averaged and displayed or stored as time-averaged sound pressure levels;

- The interval between successive sound pressure level samples is $500 \text{ ms} \pm 5 \text{ ms}$ for spectral analysis with or without slow time-weighting;

Analysis system operated in real time from 50 Hz through at least 10 kHz inclusive. Ambient noise, including both an acoustical background and electrical noise of the measurement system was recorded for 5 minutes a day with the system gain set at the levels used for the aircraft noise measurements. The recorded aircraft noise data is acceptable according to international standards, e.g. the ambient noise levels, when analyzed in the same way, are 20 dB below the maximum of the aircraft. The reference interval used for defining noise exposure to the residents of the airport, taking into account human activities, corresponds to the periods of 6h-18h, 18h-22h and 22h-6h. The exclusion criteria of the recorded data are: strike days and special weather conditions (gusty winds, stormy rainfall, atmospheric turbulence...). After each calibration, any level deviation greater than 1 dB lead to the rejection of data for the 24 hours involved. Basic physical properties of sound pressure were measured: level, frequency distribution, time variation, and time of flight duration characterizing aircraft passage.

During the final flight phase, aircraft noise source is located well above the receiver position. Consequences of the atmosphere at high altitudes are less well defined than at low altitudes and their effects have not been reported in this paper. They are well studied by Salomons and de Roo (1999) and by Iserman et al. (2004) using the PE method where their limitations were discussed. Irregularities, which occur in measured spectra due to interference effects caused by reflection of sound from the ground surface or by perturbations during the propagation of aircraft noise to the microphone, have been identified and corrections are applied to spectral characteristics, which are not related to aircraft noise source. No measurements of the reflection coefficient were made. As specified in Appendix 2 of the Annex 16 of the ICAO convention, narrow-band analysis is one recommended procedure for identifying these false tones.

According to the above measurement specifications, we identified and retained 15460 turbo-jet aircraft executing approaches of the airport in the same conditions among 84.5% (+20 T) equipped by turbojet engines, which land at the airport. It should be remembered that 15% of the traffic represents propeller aircraft (3–9 T and +20 T) and 0.5% other (-3 T and 3-9 T). It is because the difficulties appear on all the levels of which analysis of the harmonic frequencies, propeller aircraft were excluded in this analysis. The time and frequency signals are analyzed by DBTrait[®] software and by specific algorithms developed in a MatLab[®]/C++[®] computing environment taking into account the spectral characteristics of the recorded signals. This analysis has been developed for characterizing source frequencies. It required particular evaluation and selection of the data analysis parameters including the data sampling frequency. Those mainly calculated are noise levels, statistical indices, aircraft passage duration (time of flight TOF), and the pure frequencies and frequency bands in the one-third octave characterized by the higher noise levels.

Results and Discussion

Aircraft noise varies both in frequency and level during a flight for three main different reasons. First, individual sound generating mechanism each has a distinct frequency dependent directivity, e.g. for high frequencies, jet noise exhibits a ‘zone of silence’ in downstream direction while for low frequencies the radiation is maximal in this direction. Second, owing to the directivity of the individual sound generating mechanisms, the different sound component contributions dominate the sound radiation in different directions. Furthermore, the relative

importance of the different sources depends on the flight phase and the engine-airframe combination. The basic propagation model describing sound propagation with particular assumptions (homogeneous atmosphere, heuristic corrections, etc) is unable to assess dominant frequencies. Thus, the modelling of the source region and the region outside the immediate vicinity of the source appears to be unfeasible by the most specific methods. Third, the measured noise levels are inclusively affected by Doppler effect that modifies the frequency contents and the cumulated energy. Identifying the origin of frequency annoyances of aircraft noise during approach phases and diagnosis of their source is major. This identification has grown since the 1960s with the development of jets and the expansion of their environmental impact. In spite of the development of new technologies and initiatives to reduce the emergence of generating high noise levels (passive and active control, intelligent materials, new technology use, etc.), and successive improvement of aircraft certification on the basis of the ICAO convention, technological break-through and comprehension of the most emitted frequencies characterized by their high noise levels are needed.

Thus, the study of dominant frequencies emitted during operations is important because it should allow manufacturers to focus their R&D on improving the sound-proofing of active and passive systems that could be implemented in the engine for noticeably achieving a noise reduction. This study also helps to make a diagnosis of frequencies that contribute more to the discomfort or the annoyance of local residents around airports. Frequencies emitted by fan, turbine, compressor, jet noise and aerodynamic noise due to flows around the body of the aircraft (cell, flaps, slats...) cannot be identified under static conditions. They can all be dominant and depend on the mode of operation or the engaged landing procedure. Another advantage of research carried out in this paper characterizing the dominant emitted frequencies is to reduce the computational time of noise propagation models often conducted in a wide frequency band. In the absence of data on specific studies on emitted frequencies in operation and the impact of emerging frequencies on the sound quality around the airport, this research work confirms the interest of dominant frequency bands and pure frequencies characterized by higher noise levels. For a number of reasons, 40 % of the used flight paths do not correspond to the theoretical flight plan published before the take-off. Those changes are generally related to operational conditions (meteorological conditions, power setting, thrust management, etc.) and are confirmed by radar track information, which samples accurately aircraft position each 0.5 s. These arguments support this work.

Because human hearing is not equally sensitive to all frequencies, it is most sensitive to frequencies around 4 kHz. Humans perceive broadband noise by dividing the frequency axis into bands. Different bands describing the human hearing and its functioning have been developed. Third-octave bands describe human hearing rather well and have been used in much published research. When hearing broadband noise without dominant frequencies, the human ear perceives the central frequencies of all covered third-octave bands. Despite the current knowledge about human hearing and aircraft noise annoyance, the perception of sound is still too complex to be understood as adequately as needed for accurate prediction of perceived noise during aircraft operations. To complete the understanding of the impact of aircraft noise, we have also analyzed the pure frequencies.

A further point having an impact on measurements, which has to be highlighted, concerns aircraft directivity. It is asymmetric and it may be expected that asymmetry should be changed in the future due to the effect of modifications such as chevrons, scarfed inlets ... and should become available in coming years. Assessment of the directivity of a moving source is

generally a complex problem because directivity functions may be described in various coordinate systems: fixed to the aircraft, fixed to the flight track or to the ground. Directivity and spectral content measured at a reception point could be particularly altered by the influence of the forward speed. The Doppler effect changing the frequency content of the signal and the distribution of energy in time transforms the true radiated directivity into an apparent directivity as observed at a fixed receiver on the ground. Removing Doppler effects from recorded sound levels is a possible technique but requires very complex procedures. Because of this complexity, it seems more realistic to describe the source by its apparent spectral components measured at a fixed receiver position, as is done for noise certification. Measurement recording under the flight path, avoiding angular corrections, allows access to frequencies at the reception point. Of course, knowing the speed of each aircraft and making adjustments due to the Doppler effect, we obtain the frequencies emitted by the sources. Geometric calculations performed thereafter allow a correction of Doppler effect. Knowing the frequencies recorded at the receiver, we can assess the frequencies emitted by aircraft sources according to the emission angle θ_j (Fig. 2) and the indicated aircraft speed. To remove Doppler effect, we first consider an aircraft as a source in motion where the receiver is placed under the track in X_j position. The aircraft height Z is considered above the reference (X-Y) plane, generally taken to be the ground plane, with the measurement microphone at 4 m above this reference plane.

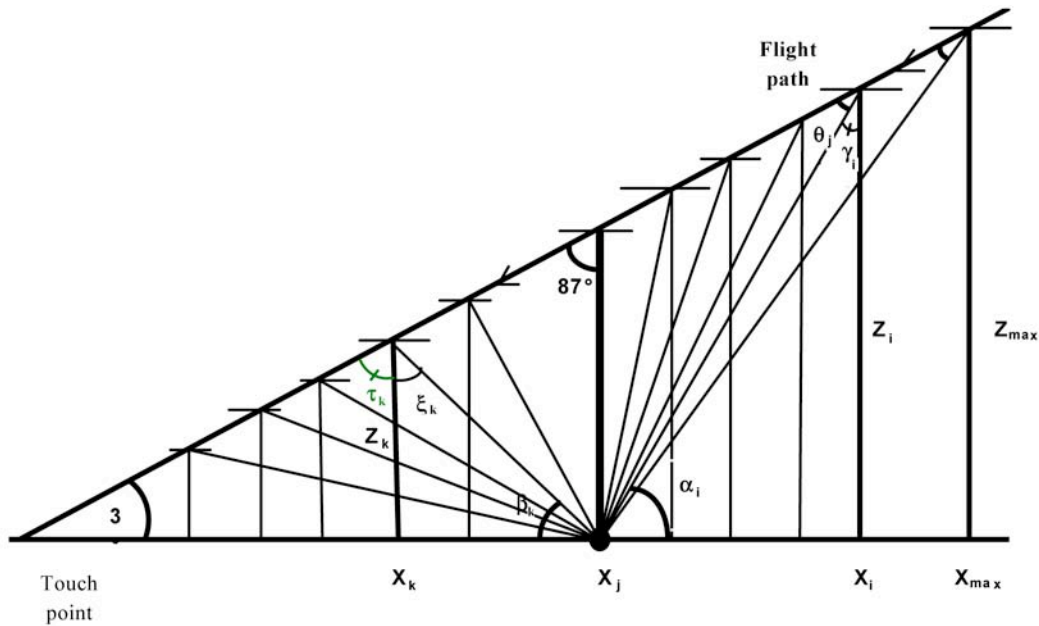


Fig. 2: Illustration of emission angles under flight path. Height of the receiver and the wind speed are neglected.

Because of Doppler effect, the measured sound under the flight path is perceived differently by the receiver because of aircraft speed and angular effects. Analysis by Miyara et al. (2001) gave at the reception point the observed frequency f_d as:

$$f_d = \frac{1 - \frac{V_w}{c} \cos(\theta_j + 3)}{1 - \frac{V_w}{c} \cos(\theta_j + 3) - M \cdot \cos(\theta_j)} f$$

where θ_j is the emission angle between the flight path and the sound direct radius.

$\theta_j + \gamma_i + \alpha = \frac{\pi}{2}$ ($\alpha = 3^\circ$ the aircraft glide slope). Mach number $M = V/c$ (V and c are respectively the speed of the aircraft and the sound). V_w the wind speed supposed to be parallel to the ground. f is the main emitted turbojet engine frequency. Geometrical calculation allows the recovery of the pure frequencies emitted by the source.

For a given time t and X_j , $\alpha_i = \text{artg} \left[\frac{X_i \cdot \text{tg}(3^\circ)}{X_i - X_j} \right]$ where X_i is the relative distance when the

aircraft is at a height Z_i . Then, $\theta_j = 87 - \gamma_i$ and $\gamma_i = 90 - \alpha_i$. For X_j , we have divided the lateral interval into two parts for the purpose of calculation. For $X_i \in [0, X_{\max}]$ (example of $X_{\max} = 8000$ m corresponding roughly to the lateral distance when almost all aircraft are aligned with respect to the axis of the main runway of the Saint-Exupéry Lyon International Airport; $Z_{\max} = 419$ m), we can write:

$$\theta_j = \text{artg} \left[\frac{X_i \cdot \text{tg}(3^\circ)}{X_i - X_j} \right] - 3 \quad \forall X_i \in [X_j, X_{\max}].$$

In addition, $\beta_k = \text{artg} \left[\frac{Z_k}{X_j - X_k} \right]$, $Z_k = X_k \cdot \text{tg}(3^\circ)$, $\theta_k = \xi_k + \tau_k$, $\xi_k = 90 - \beta_k$, then $\theta_k = 177 - \beta_k$

where $\theta_k = 177 - \text{artg} \left[\frac{X_k \cdot \text{tg}(3^\circ)}{X_j - X_k} \right] \quad \forall X_k \in [0, X_j]$. Figure 3 show the emission angle θ_j behavior depending on the lateral distance for four X_j values under the flight path. $\theta_j = \alpha_i - \alpha$,

$$f_d = \frac{c - V_w \cos(\alpha_i)}{c - V_w \cos(\alpha_i) - V \cos(\alpha_i - \alpha)} f.$$

In order to obtain the aircraft speed, two methods can be used. Either the aircraft speed is measured by the on-board instruments or assessed by experimental data. The first solution required a reliable device ensuring a perfect data synchronization between on-board and ground instruments. It was not possible to perform that synchronization with all aircraft landing at the airport. The second could be effective and robust. It is based on the frequency measurements and geometrical calculation. In order to obtain V , two conditions were chosen: x large and positive and x large and negative, yielding α_i close to 0 and π . This results in two equations from which the frequency f could be eliminated and the system solved for V supposed constant and $f_{-\infty}$ is the observed frequency before the aircraft over flight and $f_{+\infty}$ after the over flight.

For $x \sim +\infty$, then the observed frequency $f_{+\infty} = \frac{c - V_w}{c - V_w - V \cos(\alpha)} f_+$

For $x \sim -\infty$, then the observed frequency $f_{-\infty} = \frac{c + V_w}{c + V_w + V \cos(\alpha)} f_-$

with $f_+ \cong f_- \cong f$ the main engine frequency, $V = \frac{c - V_w}{\cos(\alpha)} \left[\frac{f_{+\infty} - f_{-\infty}}{\frac{c - V_w}{c + V_w} f_{-\infty} + f_{+\infty}} \right]$

If we take into account the height of the receiver h_1 (4 m), h_2 , relation between the previous variables and angles (Fig. 4), f and f_d can be easily written using the following θ_j :

$$\theta_j = \frac{\pi}{2} - \alpha - \frac{X_j + \frac{h_1}{\operatorname{tg}(\alpha_i)}}{h_2}$$

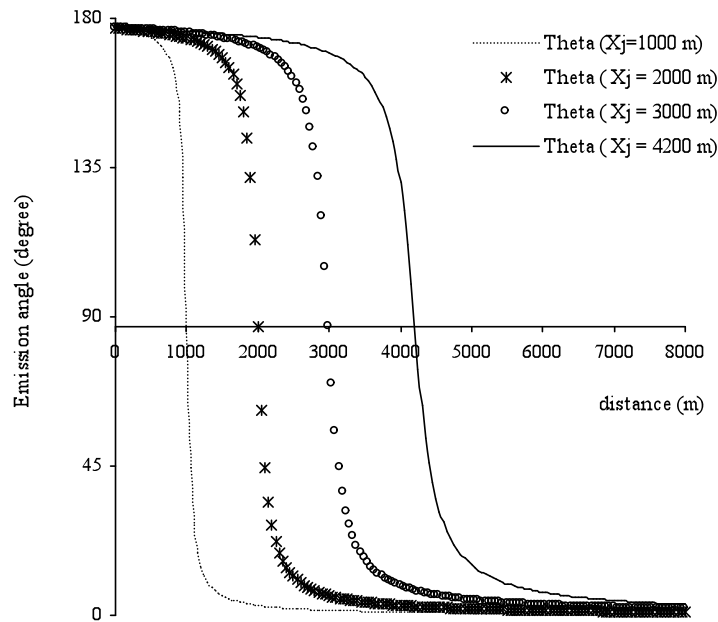


Fig. 3: Emission angle behavior under flight path.

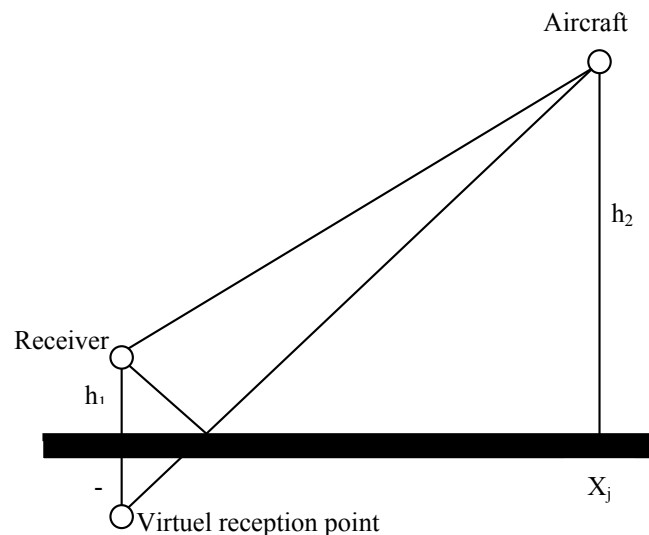


Fig. 4: Interference between direct and reflected sound waves responsible for the so-called “comb-filter” effect (or Lloyd's mirror effect).

The interference arises between two sound waves as a combination of a direct and a reflected wave. Analysis by Smith (1989) showed interference patterns caused by ground reflections, and frequencies shown in the Fig. 5 used the following expressions:

$$f_{cons,j} = (j+1)\frac{c}{\Delta l} \quad \text{and} \quad f_{des,j} = (j+0.5)\frac{c}{\Delta l} \quad \text{with} \quad j = 0, 1, 2, \dots$$

and Δl the path length difference between the direct and the reflected sound wave; c is the sound speed, f_{cons} and f_{des} are respectively the frequency at which a constructive and destructive interference occurs.

As shown in Fig. 5, the main objective was to show that the frequencies, which will be obtained in the following sections, cannot in any case to be confused with those, which correspond to the frequencies resulting from the constructive interference. The effect of destructive interference between the direct and the reflected sound waves at the microphone is not considered in this work because the unvested frequencies are considered destroyed. This is the reason why this well-known effect (comb-filter effect) has not been considered in this paper. Nevertheless, a study by Miyara et al. (2001) shows that effect could be used in the estimation of the aircraft's altitude. For outdoor experiments, without any habitation, this effect does not occur. If we want to take this into account, as part of measures for assessing sound quality, we can use the results of Fergusson et al. (1994), Schulten (1997), and Miyara et al. (2001). They provide the conditions where Doppler patterns and comb filter are superimposed on the spectrogram and must be considered. They particularly show how to obtain a directivity of a single aircraft over-flight. Other research has been carried out by Lo et al. (1999), who developed a model describing the temporal variations of the destructive interference for an aircraft approach. As far as we are concerned, the free field condition is filled and this combined effect neglected.

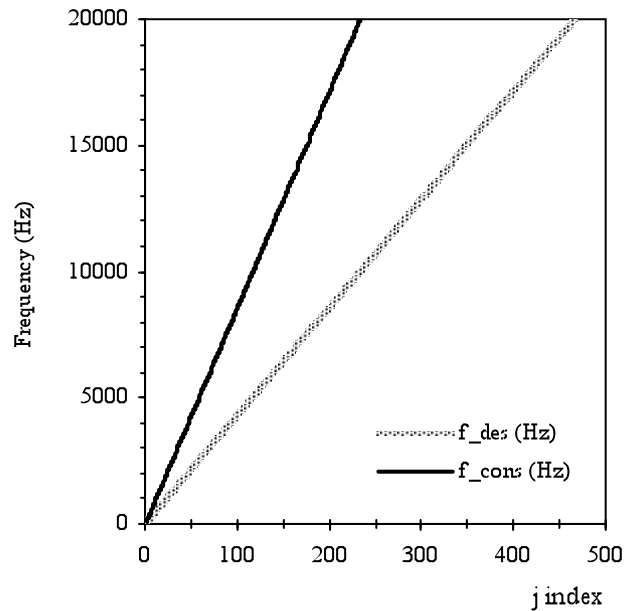


Fig. 5: Model of frequency interference.

Aircraft Sound Spectra

This section describes the method for analyzing the spectral content of recorded aircraft noise of different aircraft, representative for the fleet of passenger aircraft in the year of 2007. Different types of commercial aircraft have been studied, mainly aircraft with jet engines. Approach events are captured and noise recorded according to annex 16 of the ICAO convention.

Over the last two decades, many techniques have been developed for spectrum analysis of discrete time series. It is clear that aircraft noise on approach is considered as unsteady states. Estimation of the power spectral density or the spectrum of discretely sampled deterministic and stochastic processes is often based on procedures employing the fast Fourier transform (FFT). This spectral analysis is computationally efficient and produces acceptable results in the large class of signal processing. The most important limitation is that the frequency resolution is able to distinguish spectral responses of two or more signals. A further limitation is due to the implicit windowing of data that occurs when processing with FFT, which manifests itself as leakage in the spectral domain. Time-frequency distributions (TFD) can be used to study non-stationary signals of aircraft noise. They give a spectral representation of the signal, which is function of time. When the signal dynamics change slowly, and high frequency resolution is not required, TFD are usually obtained by computing the spectrogram. When high time and frequency resolutions are needed, TFD such as the Wigner-Ville or the Choi-Williams distributions are preferred (Griffin, 1991; Papandreou and Boudreaux-Bertels, 1993; Hlawatsch et al., 1995; Li, 1997).

Thus, efficient time-frequency representation analyzing the nature of non-stationary aircraft noise signals is needed (Orfanidis, 1988; Lo et al., 1999). This is performed by mapping a one-dimensional signal in the time domain, into a two-dimensional time-frequency representation of the signal. A variety of methods exist in the open literature, based on the Wigner-Ville distribution (Jones and Baranuik, 1994 and 1995). A separate analysis of a time domain or a frequency response is not sufficient to assess the behavioral aspect of the aircraft noise levels. Time-frequency distribution (Kwok and Jones, 2000; Biscainho, 2001; Boashash, 2003) that associates for each instant a frequency representation of the signal can be effective in assessing aircraft noise frequencies corresponding to the raised levels. The Wigner-Ville distribution (Baraniuk, and Jones, 1993; Czerwinski and Jones, 1994; Cohen, 1995) chosen for this paper is defined as:

$$WV(t, f) = \int_{-\infty}^{\infty} s\left(t + \frac{\tau}{2}\right) s^*\left(t - \frac{\tau}{2}\right) e^{-2j\pi f\tau} d\tau$$

where s is the analytical signal of the signal time measurements and s^* the complex conjugate. In addition to the time-frequency representation as found in the spectrogram, integrating the distribution for a given time (respectively frequency), gives the instantaneous power (respectively the power spectrum). The instantaneous frequency can be assessed by the marginal moment $\frac{\int_{-\infty}^{\infty} f * WV(t, f) df}{\int_{-\infty}^{\infty} WV(t, f) df}$ and its dual the group delay $\frac{\int_{-\infty}^{\infty} t * WV(t, f) dt}{\int_{-\infty}^{\infty} WV(t, f) dt}$. A valuable property of the

Wigner-Ville distribution is that it satisfies the marginal conditions. For time-series $X(n)$ (Oppenheim and Schaffer, 1989; Orfanidis, 1988), the expression of the discrete-time Wigner-Ville distribution, $WV(n, f)$ is:

$$WV(n, f) = 2 \sum_{k=-\infty}^{\infty} h_N^2(k) X(n+k) X^*(n-k) e^{-4j\pi f k}$$

where $h_N(k)$ is a data-window, which performs a frequency smoothing. While Fourier spectra are periodic with period equal to the sampling rate, $WV(n, f)$ is periodic in frequency with period equal to half the sampling rate. This may cause a spectrum disturbance, which can be removed either by over-sampling or by using the corresponding analytic signal. The distribution is negatively affected by important cross-terms, which limit its practical use. Cross-terms may be adequately reduced by smoothing the distribution over time. The resulting smoothed Wigner-Ville, $SWV(n, f)$ is:

$$SWV(n, f) = \sum_{m=-\infty}^{\infty} g_M(m) \sum_{k=-\infty}^{\infty} h_N^2(k) X(n+k+m) X^*(n-k+m) e^{-4j\pi f k}$$

The time-resolution depends on the time-window $g_M(m)$, and it is lower in SWV than in WV. Moreover, SWV does not satisfy the marginal conditions. To reduce the cross-terms satisfying the marginal conditions, a larger class of time-frequency distributions, such as the Choi-Williams distribution, which includes the Wigner-Ville as a special case, could be suggested. When the signal is composed of several components interference occurs between their time-frequency patterns due to the bilinear nature of the distribution. To reduce this effect the transform is smoothed in frequency – in our case by a Hanning window over 512 points. The software toolbox (MatLab[®] and C++[®]) has been used for aircraft-noise signal processing that offers a more informative description of signals such as the predominant frequency emitted during aircraft approach. Figure 6 shows a typical time-frequency spectrum of aircraft noise measured during three approaches. It gives an illustration of a Wigner-Ville distribution used in this paper showing the distribution of energy in the sound across frequency.

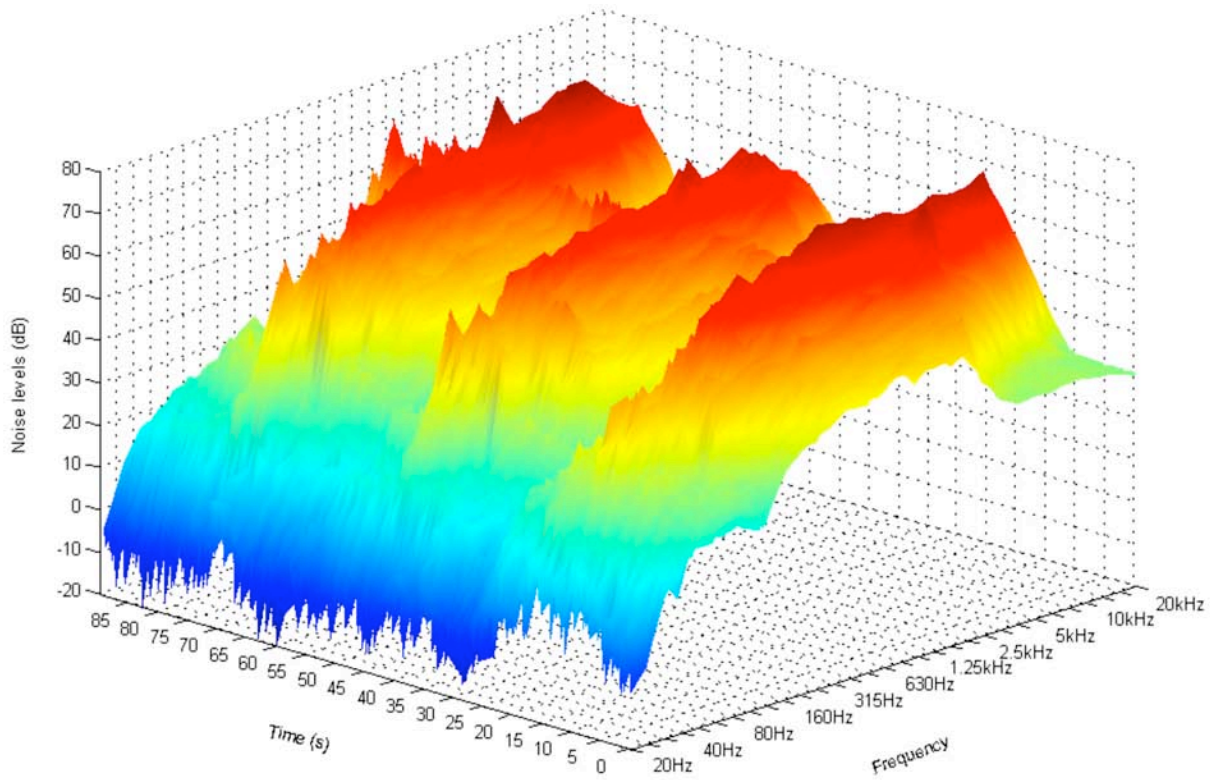


Fig. 6: Time-frequency spectrum of three aircraft approaches.

Figure 7 reveals the two major components in ground-perceived aircraft noise: broadband noise and some tonal components. As previously mentioned, interference pattern resulting from direct and reflected noise is not considered.

The amplitude of the broadband noise in third-octave bands is determined based on the average energy that remains in each band after removing all tonal components from that band. An automatic search of maximum levels was achieved and pure frequencies or frequency bands were made from recording spectra. Identification and counting of frequency bands were made by using specific routines developed under MatLab[®] and C++[®]. After normalization compared to the total number of sound signatures, we obtained the result shown in Figure 8 to show what the

third-octave bands perceived level sensor with the highest levels. The major observed bands are 630 Hz, 800 Hz, 1000 Hz, 1250 Hz and 1600 Hz, whose noise levels are the highest. The third-octave bands 1.25 kHz and 1.6 kHz are dominating. Their origin could be either the airframe of the aircraft (fuselage, wing, drift, landing gear and high lift devices), which upon landing with an engine rpm in slow motion, may have a higher contribution from 10 dB above the noise of the engine; or engines, particularly the combustion chamber and the turbines that are emitting broadband sounds between 1500 Hz and 5000 Hz. At this stage, one cannot attribute these frequency bands to a defined source but to the whole (nacelle - components - engines).

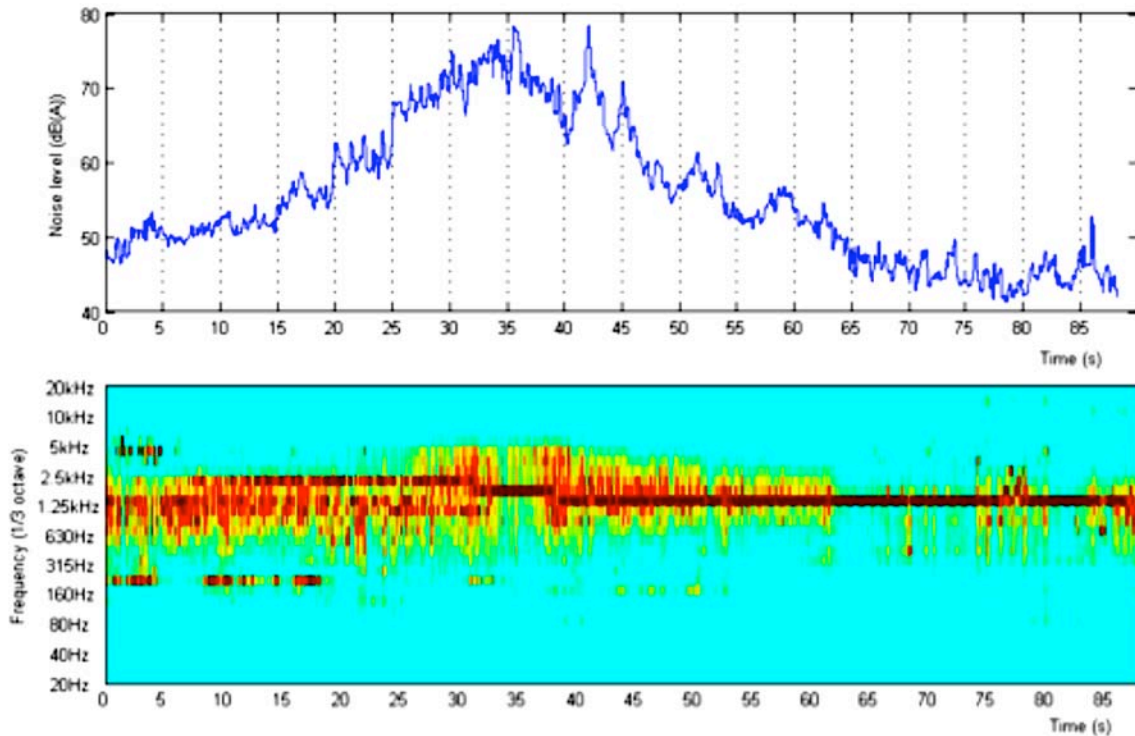


Fig. 7: Cumulate noise levels (1/3-octave bands).

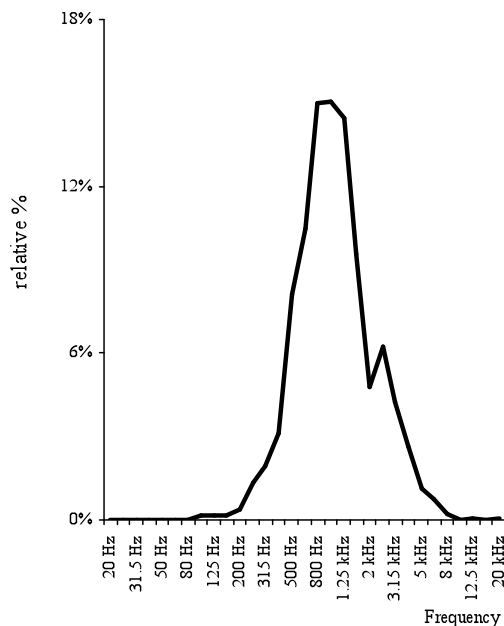


Fig. 8: The dominant frequency bands.

The pure dominant frequencies emitted by sources, corrected for the Doppler effect described above were evaluated for speeds of approaches between 56 m/s to 150 m/s. These are the frequencies 800 Hz, 1000 Hz, 1142 Hz and 3500 Hz. Figure 9 shows these frequencies. It should be noted that the frequencies 800 Hz, 1000 Hz and 1142 Hz are almost equal in energy compared to 3500 Hz. Their maximum intensities and their width at half height are: 800 Hz (77 dB, 32 Hz), 1000 Hz (75 dB, 38 Hz), 1142 Hz (79 Hz, 38 Hz) and 3500 Hz (62 dB, 34 Hz). The 1-kHz frequency observed was highlighted by Cremezi (2000) and Cremezi and Legros (2000) by modeling the propagation of noise emitted by aircraft in a complex and turbulent atmosphere. The study by Miyara et al. (2001) has also highlighted the frequency of 1 kHz during aircraft overflights.

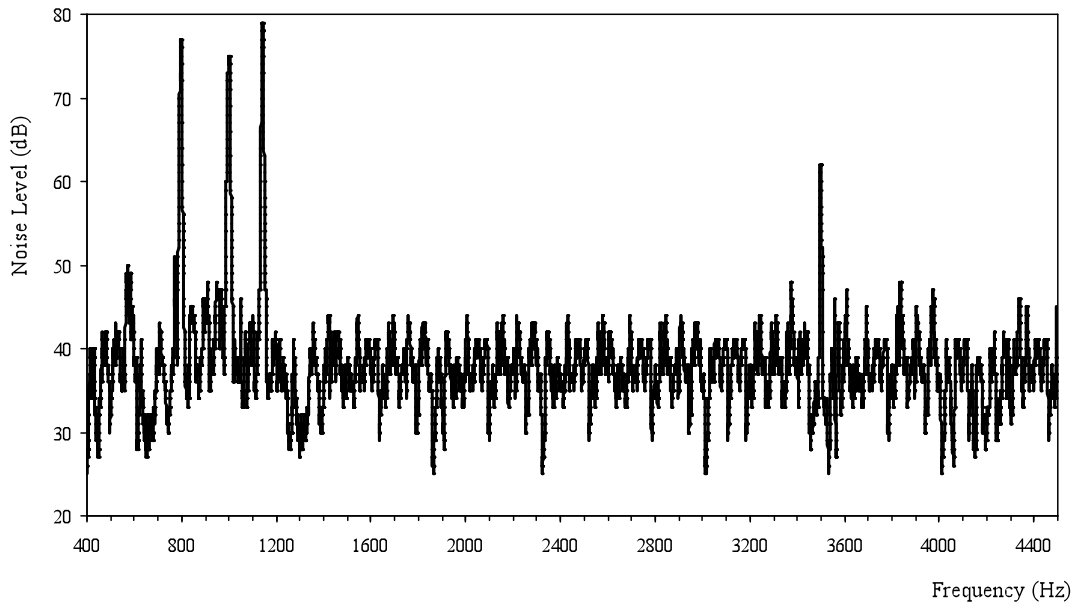


Fig. 9: Spectral analysis showing dominant frequencies.

The observed frequencies in our experiments, not recovered by Cremezi calculations, are due to the fact that the engine was ignored or unknown in its modeling. A method of re-trajectory simulation has subsequently been used by Cremezi to determine noise levels and the associated spectra. Among the difficulties, resolution required a large number of approximations simplifying the overall problem. Cremezi confirmed that the model parameters are still quite sensitive, and interference generated by turbulence may introduce significant differences with the experimental results. Moreover, the absence of the directivity of the source in motion is an additional difficulty when making approximate calculations. The experimental results presented in this article, will certainly provide additional useful information, thus placing the results of theoretical models in context. Theoretical approach has difficulties due, in part, to simplifying approximations. Experimental approach is handicapped by the lack of data from the black box of each aircraft. It can therefore be objectively argued that the combination of the two approaches contributes to a better understanding of emitted frequency problem.

The frequency of 3500 Hz is characteristic of the fan noise. This noise, known to aircraft engine manufacturers, accounts for up to 7% of the noise on approach. However, we have no explanation for the observed frequency of 1142 Hz. It could originate from the engines. Finally, certain frequencies were not observed. They correspond to the low frequency noise (50 Hz - 500 Hz), which may occur under certain weather conditions and engine operation. They result from

the mixing of hot jet at the exit reactors (severe turbulence). The frequency of 63 Hz, observed by Miyara et al. was not found in this study, due to limitations of our system of measurements at frequencies below 200 Hz. Regarding noise in the environment, it is essential to remember that the observed frequency bands 630 Hz, 800 Hz, 1000 Hz, 1250 Hz and 1600 Hz and 800 Hz frequency pure, 1000 Hz, 1142 Hz, and 3500 Hz, are emitted during phases of approach and are characterized by the highest noise levels. This may steer some research on the nuisance of aircraft noise around airports and assesses the relevant areas to be developed taking into account the type of aircraft and flights, while preserving the performance gained for flight safety and useful lives of the engines.

On the one hand, broadband noise arises from the combustion chamber during the combustion process, from the turbulence in the jet of engines and from air flow around the aircraft nacelle. On the other hand, tonal components occurring between 1000 and 7000 Hz are particularly emitted by the turbine and the compressor for the turbojet engines. In addition, the latter can be generated by flows over cavities such as the landing gear box and flows on the level of the flaps. Also, it has been shown that from time to time the tonal components do not appear in a narrow frequency region but in a large interval of the spectrum. It can occur when tonal components have very close values or when the source frequencies have undergone fast changes around an average frequency. This phenomenon is significant for aircraft manufacturers because of active and passive controls implementation. Nevertheless, it has no meaning for the psycho-acoustic community because human hearing is often unable to distinguish close frequencies. In addition, even a clear directivity towards the front of aircraft, time-frequency spectra recorded from aircraft approaches did not show discrete tones due to rotational speed of the engine axis.

Aircraft Time of Flight

The study of aircraft noise in the environment supposes knowledge of the relevant objectives and tools for characterizing its quality. For a long time, a lot of work has been directed towards statistical indicators (Nelson, 1987; CEC, 1999; Koppert, 2000). Many authors continue to suggest indicators even if L_{den} is nowadays considered as a reference. Literature review shows differing visions which confirm the continuation of research in this field. Impact of aircraft noise around airports is often associated with the duration of exposure to noise events. Thus, analysis of the time of flight (TOF) completes those indices in the context of an overall vision, which must implicitly take into account air traffic morphology. For one-year measurements, we therefore determined classes corresponding to the TOF, by time intervals. These classes are divided into five: 1. C1 (TOF is between 20 and 30 sec), 2. C2 (31 - 60 sec), 3. C3 (61 - 90 sec), 4. C4 (91 - 120 sec) and 5. C5 (121 - 125 sec) shown in Figure 10 which TOF varies from 20 s to 125 s for all selected flights. 88% of the TOF are between 31 and 90 sec (51.6% between 31 and 60 s; 36.3% between 61 and 90 s). Raney and Cawthorn (1979) established an average TOF of 60 s, and Cremezi (2000) gave an average time between 40 and 50 s.

Noise levels represented by the index SEL ranged from 54 dB (A) to 109.3 dB (A). 2% of approaches (SEL varying from 62 to 101 dB (A)) have not been accepted (over flight, passages of light vehicles, heavy agricultural or construction sites ...) for social and economic activities around the airport.

We calculated, in turn, the full width at half maximum FWHM as an index of each aircraft acoustic signature to explore future opportunities allowing to progress in the field of the indicators, which objectify the environmental impact of aircraft noise around airports. Thus,

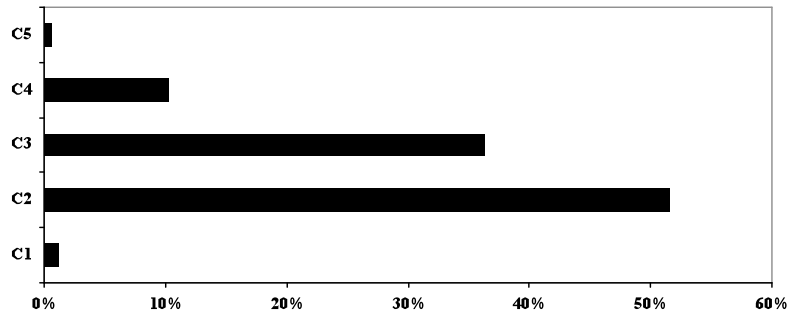


Fig. 10: Percentage of classes related to the aircraft over flight duration.

FWHM is an expression of the extent of a function, given by the difference between the two extreme values of the independent variable, at which the dependent variable is equal to half of its maximum value. It also can be used to estimate the width of a spectral line. A first assumption supposes that the distribution, which makes it possible to model the signal, is of Gaussian type. The scientific literature from the solid state physics through spectroscopy and astrophysics evokes the notion of FWHM. The common thread in all those disciplines is the profile of the distribution (for example, crystallite size, flight time, angular size of stars, etc.) (Warengem et al. (1978), Fried (1994)).

Indeed, a signature must have a theoretical sound profile characterized by its width at half height characterizing its energy. As soon as the constructive interferences mentioned are present, we cannot logically attribute the total signature to one aircraft noise. The study of changes in FWHM gives a clear idea of the energy characteristics for each aircraft passage. FWHM is made according to the following three steps: 1. Calculation of the maximum measured value during the passage of each aircraft divided by two ($I_{\max} / 2$). 2. Identification of the two instants t_1 and t_2 where we find $I_{\max} / 2$ sides of the maximum of this passage; 3. Calculating the width at half height $FWHM-t_2 = t_1$. In our case, the FWHM values are between 7 s and 70 s, with an average of 31 s.

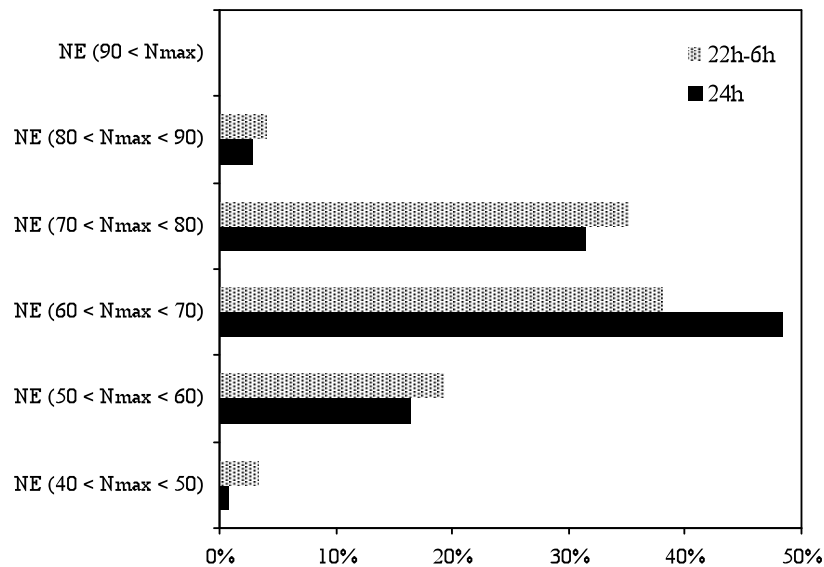


Fig. 11: Comparison between the numbers of events occurring during the night by 24 hour. $NE_{24h}(90 \text{ dB(A)} < N_{\max}) = 0.1 \%$ and $NE_{22h-6h}(90 \text{ dB(A)} < N_{\max}) = 0.05 \%$.

We also analyzed the following noise indices: Leq_{24h} , Leq_{6h-18h} , $Leq_{18h-22h}$, Leq_{22h-6h} , LDN, LDEN, SEL, and DEN LDNL depending on the day of the week. Three groups can be distinguished: SEL whose levels are distributed around 100 dB (A), [DEN, LDNL] around 75 dB (A) and the group [Leq_{24h} , Leq_{6h-18h} , $Leq_{18h-22h}$, Leq_{22h-6h} , LDN, LDEN] whose levels are between 48 and 56 dB (A). The problem is to define the upper and lower limits for each of the indices and their ability to objectify the impact of air traffic on the environment. This result confirms that we must guide the analysis of indices to study each event such as the aircraft passage. It would be necessary to introduce the type of aircraft and flights. Thus, for night flights (22h-6h), we have performed an analysis of events (maximum levels produced by the passage of each aircraft) representing 15.1% of the total number of aircraft because people neighboring the airport are sensitive to those flights. The effect on health has already been demonstrated in the past. In this paper, we classified noise levels and we compared them to their corresponding period of 24 h. Events producing maximum noise levels belonging to a specified interval were recorded. Figure 11 shows the percentages of the numbers of events (NE). 0.1% of events whose maximum levels are above 90 dB (A) for periods of 24h and 0.05% for periods of night (respectively 8 and 1 aircraft) are not represented.

The analysis shows that the majority of NE is situated between 50 and 80 dB(A). Almost every percentages of night are slightly higher than those obtained during the 24 h except for those, which are located in the interval 60-70 dB(A). The differences vary from 1 to 3%.

In conclusion, we have fewer aircraft at night but that generate maximum levels comparable to those of 24 h or even in days. This finding could lead policy makers, managers of airports, airlines ... to recommend that pilots use approach procedures, which generate less noise, in particular, at night.

To broaden the scope of this analysis, we reviewed in the next paragraph quiet and noisy periods. In addition, before examining the quiet and noisy periods, we made an initial separation according to the time and number of aircraft on approach. The traffic distribution providing additional information useful in interpreting the results is: 61% of aircraft approaching between 6h and 18h, 24% between 18h and 22h, and 15% between 22h and 6h. This traffic distribution certainly has an effect on the analysis of the noisy and quiet times of the day. The analysis of the noisiest and quietest periods was carried out every 30 minutes; they are defined in the following manner: first, we define a cumulative duration of one minute corresponding to the time step and calculate levels minute by minute. Then, for each 30 minutes the highest and lowest values are compared to background noise. We show in Fig. 12 periods and percentages corresponding to the lowest observed levels. 60% of the lowest levels are achieved during the period between 0h and 2h, which is followed by the 2h-4h period (26%), then 14% for 4h-6h and 22h-0h periods.

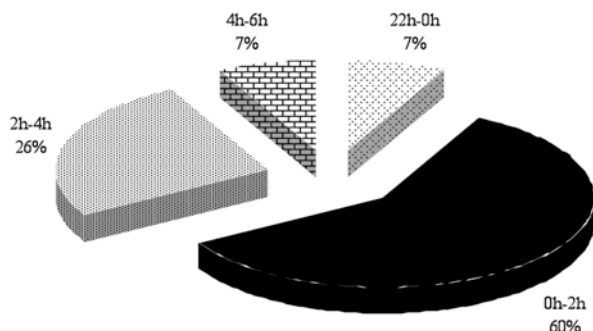


Fig. 12: The quietest periods.

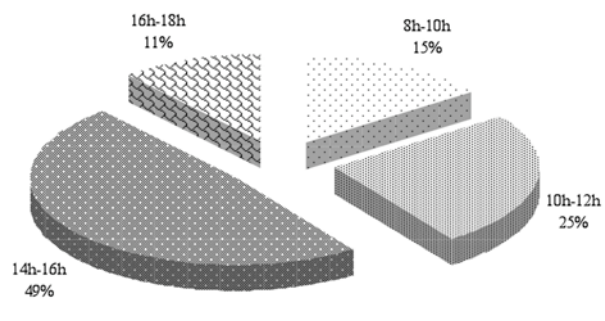


Fig. 13: The noisiest periods.

The silent period is between 0h-2h. The average difference between the levels recorded during this period and L_{95} (~ 41 dB (A)) is 1.7 dB (A). In addition, the period 14h-16h represents 49% of the highest noise levels of the day (Figure 13). It is followed by the period 10h-12h (25%), and then by periods 8h-10h and 16h-18h (respectively 15% and 11%). The average difference between the levels recorded during the noisiest and L_{95} is 36.8 dB (A). This gap is almost 22 times higher than for the quietest period.

The average noise level of the most silent period is 45 dB (A) and 77.3 dB (A) for the most noisy. Periods 6h-8h, 12h-14h and 18h-22h do not appear, according to the definition, among the noisiest or the quietest period of a day. These periods are characterized by intermediate noise levels between the two provided previously. When one counts the number of hours corresponding to the quieter periods (S), intermediate (I), and most noisy (B), there is an equi-partition, i.e. 8 hours for each type of period. Clearly, in terms of sound annoyances, periods (I), or a part, might be confused with periods (B). It is known that the impacted ground surface decreases with the noise level. Thus, it is essential that this information be considered in the analysis of events as it gives objective knowledge of a sound situation.

Conclusion

Time-frequency analysis (Wigner-Ville distribution) has been applied to process experimental data. Computing and interpreting time-frequency distributions of aircraft noise is quite a long operation. A procedure was tested using one-dimensional variables. This work is directed towards the search of the dominant pure frequencies and the aircraft passage times when approaching the Saint-Exupéry Lyon International Airport. This research provides aircraft manufacturers with frequencies emitted during approaches, which should be treated at the source. It also allows the diagnosis of frequencies responsible for the noise annoyances surrounding the airport.

Measurements of aircraft noise in the vicinity of the airport were conducted during one year. They served as a reference year because of changes in the airport infrastructure project including the two new runways, planned for 2015, renewal of fleets conditioned by the evolution of aircraft certification and regulation, etc. A geometric study of frequency emission according to the angles and indicated aircraft speeds on approach has been finalized. Doppler corrections have been made and diagnosis of the effects of destructive interference examined. Dominant pure frequencies were observed and their analysis reveals an agreement with theoretical works. Their origin could come from the airframe of the aircraft (fuselage, wing, drift, landing gear and high lift devices), which upon landing with an engine rpm at idle up to 55% for some aircraft can have a higher contribution from 10 dB above the noise of the engine. Next, we analyzed the noise levels over time and aircraft passage times. We identified the quietest and noisiest periods.

The relative sensitivity of acoustical indices confirms the need for further research including the morphology of air traffic, the type of aircraft and flight configurations. One must take account fleet renewal, introduction of engines and cells' breakthrough technologies, etc. We must focus more on analysis of individual temporal events considering the impacted ground surfaces. This is a result of environmental situations conditioned by the emergence of new aviation technologies. Experimental results presented in this paper could validate and extend calculation methods. They provide additional useful information placing the results of theoretical models in context because of strong approximations for calculation needs. This work has been performed for turbojet aircraft with the aim of analyzing the frequency characterized by higher levels. Nevertheless, it is clear that additional research is needed to achieve this goal by performing noise

analysis of commercial propeller aircraft. Moreover, it is certain that one of the main objectives supplementing this work is the addition of the aircraft typology (type, model, dimensions, engine and their locations, thrust, EPR, fuel consumption, flight configurations, performance, etc.).

References

Baraniuk R.G. and Jones D.L. (1993) A signal-dependent time-frequency representation: optimal kernel design. *IEEE Trans. on Signal Processing*, **41** (4), 1589–1602.

Biscainho L.W.P., Diniz P.S.R. and Esquef P.A.A. (2001). ARMA processes in sub-bands with application to audio restoration, *Proceedings of IEEE International Symposium on Circuits and Systems*, Sidney, **2** (2001), pp. 157–160.

Boashash B. (2003). Heuristic Formulation of TFDs. in *Time Frequency Signal Analysis and Processing: A Comprehensive Reference*, ed. B. Boashash, Elsevier, Oxford, pp. 29-57.

Commission of the European Communities (CEC, 1999). DG XI. Working group on noise indicators. Position paper on EU noise Indicators.

Cohen L. (1995), *Time-Frequency Analysis*, Prentice Hall, New Jersey.

Cremezi C. and Legros C. (2000). Application de la méthode GF-PE à une source élevée en mouvement. In *Actes du 5^{ème} congrès français d'acoustique*, EPFL, Lausanne (Suisse).

Cremezi C. (2000). *Etude de la propagation du son dans l'atmosphère: application au bruit des avions en phase d'approche et de décollage*. Thèse de Doctorat.

Czerwinski R. N. and Jones D. L. (1995). Adaptive cone-kernel time-frequency analysis. *IEEE Transactions on Signal Processing*, **43** (7), 1715–1719.

European Civil Aviation Conference (ECAC, 1997). Doc 29 (2nd edition).

Ferguson B. (1992). “A ground-based narrow-band passive for estimating the altitude and speed of a propeller-driven aircraft”. *Journal of the Acoustical Society of America*, **92** (3), 1403-07.

Ferguson B. and Quinn B. (1994). “Application of the short-time Fourier transform and the Wigner-Ville distribution to the acoustic localization of aircraft”. *Journal of the Acoustical Society of America*, **96** (2), Part 1, 821-827.

Fried D.L. (1994). Atmospheric turbulence optical effects: understanding the adaptive-optics implications. *Adaptive optics for astronomy*. NATO-ASI, ed. D. Alloin and J.-M. Mariotti, Kluwer.

Griffin C. (1991). A comparison study on the Wigner and Choi-Williams distributions for detection. *Proceedings of the Acoustics, Speech, and Signal Processing*, 1991. ICASSP-91, IEEE Computer Society. 1485 – 1488.

Hlawatsch F., Manickam T.G., Urbanke R.L. and Jones W. (1995). Smoothed pseudo-Wigner distribution, Choi-Williams distribution, and cone-kernel representation: ambiguity-domain

analysis and experimental comparison Source. *Signal Processing*. **43** (2), 149 – 168. Elsevier North-Holland, Inc.

Hubbard H. H. (1994). *Aeroacoustics of flight vehicles*, vol. 1: Noise sources, Acoustical society of America, New York

Hunter, C.A. and Thomas, R.H. (2003). Development of a Jet Noise Prediction Method for Installed Jet Configurations. 9th AIAA/CEAS Conf. and exhibit, 12-14. Hilton Head, SC.

ICAO (1988). “Recommended method for the calculation of the noise level contours in the vicinity of airports”. Circular 205-AN/1/25. International Civil Aviation Organization. Montreal, Canada.

ICAO (1993). “Aircraft Noise”. Annex 16 to the Convention on International Civil Aviation. International Civil Aviation Organization. Montreal, Canada.

ICAO (2004). *Environment protection*. Vol. 1: aircraft noise – specifications for aircraft noise certification, noise monitoring, and noise exposure units for landuse planning. Available on <http://www.icao.int/>

Iserman, U., Boguhn, O., Henkel, C., Kowalski, T. Schmid, R. (2004) “Simulationsverfahren zur Fluglärmprognose”, Abschlusspräsentation Project “Leiser Flugverkehr”. Köln-Porz, March 2004.

Jones D.L. and Baranuik (1994). A Simple Scheme for Adapting Time-Frequency Representations. *IEEE Trans. Sig. Proc.*, **42**, 3530-3535.

Jones D.L. and Baraniuk R.G. (1995). An adaptive optimal kernel time-frequency representation. *IEEE Transactions on Signal Processing*, **43** (10), 2361–2371.

Julliard J. (2003). Bruit des turboréacteurs et dispositifs réducteurs. Dans S. Khaldi, Journée Spécialisée « Réduction des bruits des avions commerciaux au voisinage des aéroports civils. Problématique, enjeux et perspectives ». Actes n°88, 53 – 63.

Kannepalli, C., Kenzakowski, D. C. and Dash, S.M. (2003). Evaluation Of Some Recent Jet Noise Reduction Concepts. Paper No. AIAA-2003-3313, 9th AIAA/CEAS Aeroacoustics Conference & Exhibit, Hilton Head, SC.

Kenzakowski, D.C., Papp, J.L., and Dash, S.M. (2002). Modeling Turbulence Anisotropy For Jet Noise Prediction. Paper No. AIAA-2002-0076, 40th AIAA Aerospace Sciences Meeting and Exhibit, Reno, NV, 14-17.

Koppert A.J. (2000). Fact sheets on different European noise calculation methods (RLD).

Kwok H.K. and Jones D.L. (2000). Improved Instantaneous Frequency Estimation Using an Adaptive Short-Time Fourier Transform. *IEEE Trans. Sig. Proc.*, **48** (10), 2964-2972.

Li M., 1997. Experimental research for processing of Choi-Williams distribution and Bessel distribution. *Proceedings of International Conference on Information, Communications and Signal Processing ICICS*. Volume 3, 1593 – 1597.

Lo, K.W.; Perry, S.W. and Ferguson, B.G. (1999). An image processing approach for aircraft flight parameter estimation using the acoustical Lloydapos; mirror effect. *Signal Processing and Its Applications. ISSPA. Proceedings of the Fifth International Symposium on Digital Object Identifier*. Vol. 2, pp. 503-506.

Michel U., Barsikow B., Helbig J., Hellmig M. and Schüttpelz M. (1998). “Flyover noise measurements on landing aircraft with a microphone array”, AIAA Paper 98-2336.

Miyara C., Cabanellas S., Mosconi P., Pasch V., Yanitelli M., Rall J.C. and Vasquez J. (2001). The acoustical geometry of aircraft overflights. *International Congress and Exhibition on Noise Control Engineering*. Hague (NL), 27 – 30.

Nelson P.M. (1987). *Transportation Noise Reference Book*. Part. Aircraft Noise, Butterworth & Co. Ltd.

Oishi T. and Nakamura Y. (2000). Research on exhaust jet noise reduction technology. *Ishikawajima-Harima Giho*. **40** (2), 65-67. ISSN 0578-7904. CODEN ISHGAV.

Oppenheim AV and Schafer RW (1989) *Discrete-time signal processing*, Prentice-Hall, Englewood Cliffs, NJ.

Orfanidis S.J. (1988). *Optimum signal processing*. 2nd ed., McGraw-Hill.

Papandreou, A. and Boudreaux-Bertels, G.F. (1993). Generalization of the Choi-Williams Distribution and the Butterworth Distribution for Time-Frequency Analysis. *IEEE Transactions on Signal Processing*. **41** (1), 463 – 498.

Raney, J.P. and Cawthorn J.M. (1979). Aircraft noise. *Handbook of noise control*. ed. C.M. Harris. McGraw-Hill.

Salomons E. and de Roo F. (1997). “Modelling of Aircraft Noise Propagation”, *Proceedings of NAG symposium*. NAG Journaal **147**, 31-44.

Schulten J.B.H.M. (1997). Computation of aircraft noise propagation through the atmospheric boundary layer. National Aerospace Laboratory NLR, Amsterdam, The Netherlands.

Smith M.J.T. (1989). *Aircraft noise*, Cambridge Univ. Press, Cambridge, UK.

Warenghem M., Cuvelier P. and Billard J. (1978). Plane uniformly heterogeneous wave diffraction. *J. Opt.* **9**, 79-82.

Zaporozhets O. I. and Khardi S. (2004). Optimisation of aircraft trajectories as a basis for noise abatement procedures around the airports. Theoretical considerations and acoustic applications. Les collections de l'INRETS. Rapport INRETS n° 257. 97 pages.

Zaporozhets O. I., Tokarev V. I. (1998). Predicting Flight Procedures for Minimum Noise Impact. *Applied Acoustics*, **55** (2), 129–143.

NEW DEVELOPMENTS OF SOFTWARE FOR A-LINE FAMILY AE SYSTEMS

SERGEY ELIZAROV, ANTON BUKATIN, MIKHAIL ROSTOVTSEV
and DENIS TERENTYEV

Interunis Ltd., bld. 24 corp 3-4, Myasnitskaya str., Moscow, 101000, Russia

Keywords: acoustic emission software, source location, statistical division criterion, wavelet-analysis

Abstract

The universal A-Line software of Interunis is an integral part of acoustic emission (AE) systems and is designed for solving various problems of data processing and visualization, and for full-scale control of the system hardware component. Simultaneously with development of new generations of the A-Line AE systems the software has been improved, is based on the up-to-date information technologies and programming methods, incorporating real AE applications experience of internal and external users of the A-Line family AE systems. This paper briefly describes the significant functional features of program features implemented recently; a method of approximate location of AE sources using a free-form sensor array on surfaces of thin-wall vessels, information statistical criterion for division of AE sources according to the type and method for evaluating the distance from a sensor to an estimated source on the basis of wavelet-analysis of AE impulse taking into account the dispersion dependencies of group velocities of Lamb waves.

Approximate Location by Free-form Sensor Array (ALFS).

One of principal disadvantages of the classical methods of AE source location on thin-wall vessels is their sensitivity to distortions of the wave front formed by several Lamb waves possessing the propagation velocity dispersion. Often, the source coordinates are computed with an error of the difficult-to-define magnitude. The new method attempts to increase confidence level and accuracy of the AE signal source location by taking into account an influence of various factors on the signal propagation velocity and AE wave front distortion.

The backbone of the suggested method is an assignment of a range (or several ranges) of velocities containing the velocities of basic modes of elastic waves on the structure. This velocity range can be additionally extended for taking into account the wave front distortion due to the test object design features (for example, hatches, branch pipes, welds, etc.) and the anisotropic properties of structure material. The AE source location is calculated on the principle that the wave velocity, whose the front arrival time is recorded by each of the sensors, lies within the selected velocity range.

When describing this location method, it is convenient to operate with a concept of wave “packet”: a set of the AE signals recorded by different sensors mounted on the test object. The packet’s critical feature is its duration, i.e. the time interval between the first and last impulse in chronological sequence as its components. If the packet duration is less than the characteristic magnitude dependent on the object geometric parameters and the evaluation velocity of elastic waves propagation in the object material, it can be expected that the whole set of impulses has been emitted during a single AE event. The ALFS method consists in calculating for each such

wave packet the object region comprising all possible points where the event could be capable to generate this wave packet at the given arrangement of sensors and the given velocity range of elastic wave propagation over the object surface. For this purpose the object surface is modeled with a discrete mesh of finite number of points. For each wave packet, the ALFS method calculates all nodes of this mesh, near which the given AE event could theoretically occur. The list of all such nodes is the location region description for the given wave packet.

The location is approximate because for each packet not one point on the object is indicated, but a region. However, the calculation of a single location point is impossible without an error. This approximate method is more accurate than the point location, since the desired source of event is within the obtained region with a high probability. Intersection of the location regions obtained for the different packets allows the source to be located more precisely, provided that the several packets of signals have been received from the same source as a result of the several discrete AE events. When the object regions are displayed in A-Line program the overlay sections of location regions are different in color depending on how many regions are overlapped on this section.

The size of the region thus determined can be reduced and so the accuracy of source locating can be additionally increased by the following several methods:

- Proved reduction of the selected range of elastic wave velocities, for instance, at the cost of the more accurate measurement of velocities of the wave modes used and exclusion of some modes from the consideration due to impossible recording of their arrival to the sensors.
- Research of the intersection of regions computed for different wave packets. If the regions are sufficiently strongly intersected, that is the regions intersection area exceeds the definite percentage of their combination, appropriate wave packets can be assigned presumably to the same source, while the intersection of regions found for wave packets relevant to this source can be assumed as the source location region.
- Selection of the optimum sensor number for calculating each region of the source location, i.e. the usage of data from the optimum sensor number.
- For some sensors the velocity ranges of acoustic waves can be specified individually, taking into account that the certain wave modes can, or on the contrary, cannot arrive to one or other sensor.

To obtain the best results, the operator can change all the above-mentioned parameters of the method on-line. Figure 1 shows results of ALFS implementation compared to the classical triangulation location method on the spherical tank surface.

We summarize the basic advantages of ALFS over the classic point location methods:

- The method does not impose restrictions on the sensors' geometrical order and arrangement on the test object.
- Specified is the velocity range of elastic wave propagation on the test object surface that is more realistic than its assignment with the constant or the selection of scalar values.
- The location is carried out by a random number of any impulses in the wave packet (from one or more), and the maximum number of impulses used for location is specified as an algorithm parameter.
- The location is carried out with regard to the real geometric shape of an object. This minimizes the distortions and errors, but requires the more accurate description of the object geometric shape and assignment of all relevant parameters.

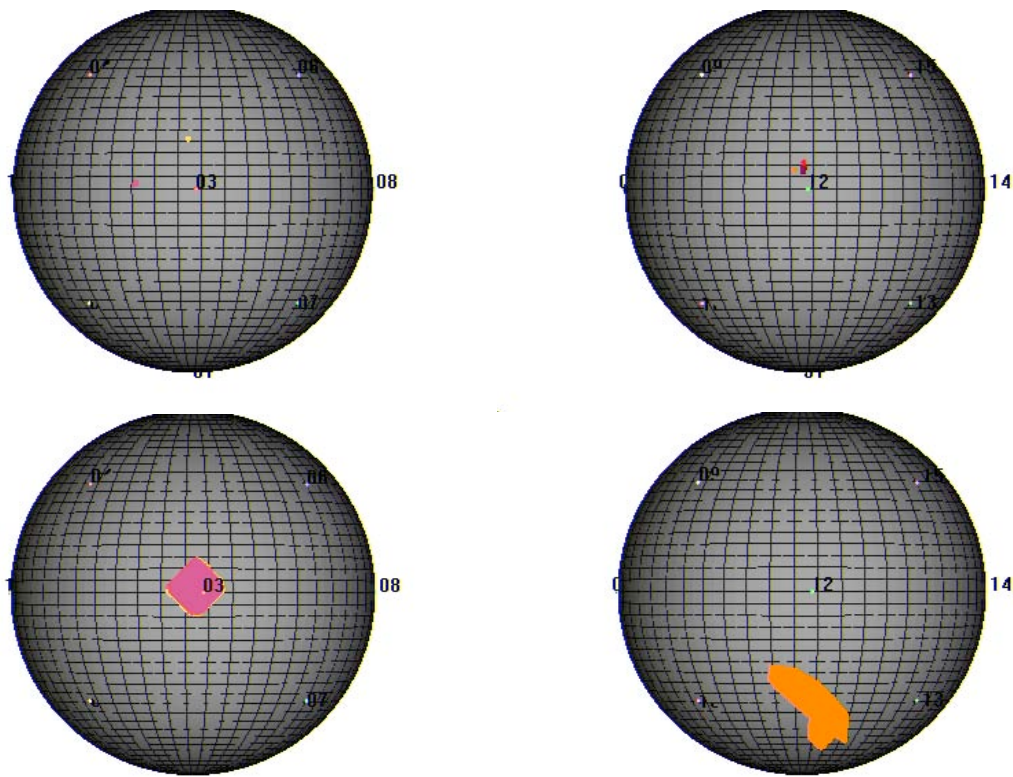


Fig. 1 Results of ALFS implementation (two lower pictures) compared to the classical triangulation location method (two upper pictures) on the spherical tank surface.

- The location result for one AE wave packet is a region on the object wherein the source is positioned with a high probability.
 - The location result for a number of wave packets is a set of the regions. The intersection of such regions with each other makes possible to define a small section on the object wherein the source is positioned with an even higher probability.
- The authors have obtained the Russian Federation patent on the above method.

Information Statistical AE-Criterion

By virtue of a number of the AE characteristic features both of the random process and the irreversible process, the statistical methods of AE information processing appear to be the most acceptable. Such methods can reveal the most typical regularities of process development, on the one hand, and average the influence of statistical spikes, on the other hand. When the behavior of not one attribute of the AE test data is analyzed, but two or three as a whole, we can increase the efficiency of identifying phenomena occurring within the test area. From the classic threshold principle of recording, the AE data are not a continuous signal but a sequence of values of impulse parameters (amplitude A , energy E , duration Dur , etc.), which are obtained directly during the experiment or tests and contain information about a process or a set of processes generating AE. Statistical consideration of these parameters enables to define the criterion of separation of the underlying processes; in particular, we utilize a significant relative change in the statistic characteristics of the impulse parameter distributions. In other words, the moment of transition from one stage of damage development in the test region to another stage can be determined by the moment of violation of AE data flow. To provide access to the information about the set of processes occurring in the test object, the whole sequence of AE impulses

arriving channel-by-channel is divided into samples. In this paper, we have used the sampling with the fixed number of impulses n . The critical characteristic of the histogram obtained is its pattern. Thus, at the stage of dispersed accumulation of micro-cracks the AE impulse flow is usually considered as the Poisson flow, and the main crack growth is accompanied by the deviation from this distribution [1]. One more analysis of the amplitude distribution pattern forms the basis of the widely currently known “*Ib-value*” criterion [2].

Recently, the Scientific & Training Center of Welding and Control and Interunis have applied one more evaluating characteristic, the distribution entropy S^H [3]. This allows for evaluating the degree of disordering in the histogram under consideration. The evaluation of data obtained during the model experiments, and also during the industrial testing has shown that the relationship $F_P = P_{mod}(S^H_P)$ can be selected as an example of the identification parameter. This F_P function is dependence of the histogram distribution characteristic P_{mod} , representing the most probable value of the random parameter P in the sample, on the relative entropy of this distribution S^H_P . The computational results for different recording channels are plotted on a chart in different colors in the indicated coordinates, whereby the diagnosis diagram is formed. The source can be identified by the group position of points in the diagram field. In Fig. 2a, b and c several examples of resultant diagnostic diagrams for the amplitude distribution are presented: for the loading of a defect-free object (Fig. 2a), loading of an object with active AE source (Fig. 2b) and cyclic loading of standard specimen loaded to failure (Fig. 2c). In Fig. 2a, registered AE signals concentrated into zone I. This zone is defined by entropy value S^H_A interval [0.3...0.7], and most probable amplitude value (A_{mod}) increases threshold level on [0...5] dB. Actually, the signals fulfilling this zone appear to be noise of loading object, distributed exponentially. Zone II (Fig. 2b) stands out against a background of zone I by A_{mod} and entropy value, taking place in S^H_A interval [0.5...0.8]. This zone appears because the signals with increased amplitude begin to prevail. Entropy in turn increases because the dispersion of amplitude becomes larger.

Zone III corresponds to the leakage signals, defines by S^H_A interval [0.0...0.3]. In Fig. 2c zone III appearance explains by plastic deformation following by the large number of low amplitude impulses. Besides zone IV, the last one, corresponds to the critical crack appearance before specimen failure. Finally, note that in all cases of the process-type identification (accumulation of dispersed micro-damages, growth of main cracks, leak) by the cumulative attributes (AE signal amplitude mode; entropy of amplitude probability distribution), no preliminary filtration of data has been carried out.

Some Aspects of Wavelet-Analysis Software A-Line OSC Processing

In this part of paper one version of the application of continuous wavelet transform for evaluating the distance to an AE signal source is described. This is implemented in the specialized program for waveform processing. The AE signal in-time smearing caused by the group velocity dispersion which noticeably reduces the accuracy of arrival time determination, and as consequence, the AE sources coordinates, has resulted in the development of various methods for the additional processing of signal waveforms. One of the methods of such analysis is the use of the signal time-frequency transform, and the wavelet-spectrograms rather long-used in AE are the most known and convenient among them [4]. To visualize the wavelet-spectrograms, the use is made of the traditional color diagram on which the X-axis corresponds to time, and Y-axis corresponds to frequency, while the energy density distribution is displayed by the different color (or black-white) tones: violet and dark blue (white) tones – minimum density, red and yellow (black) – maximum.

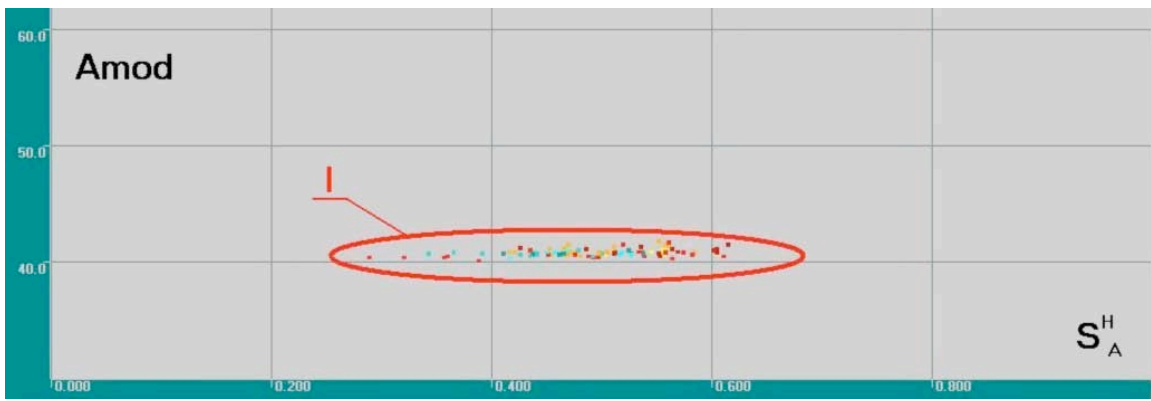


Fig. 2a Diagnostic diagram for the defect-free object loading.

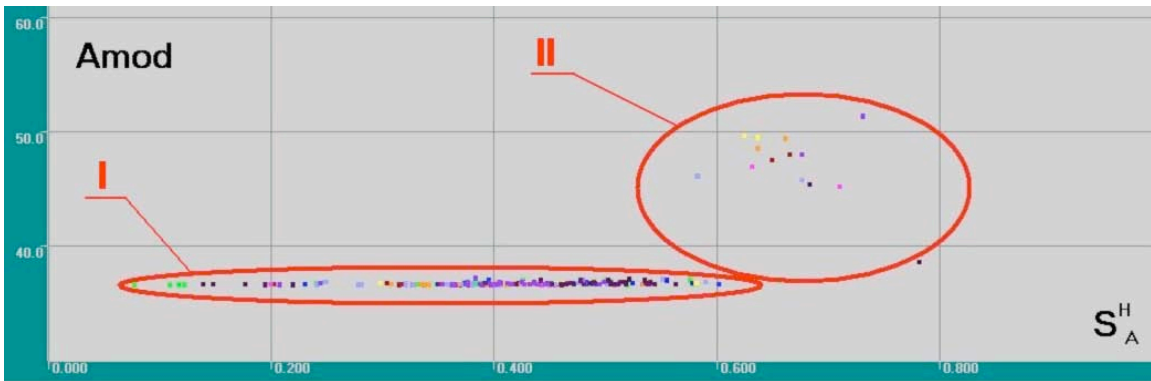


Fig. 2b Diagnostic diagram for loading of an object with active AE source.

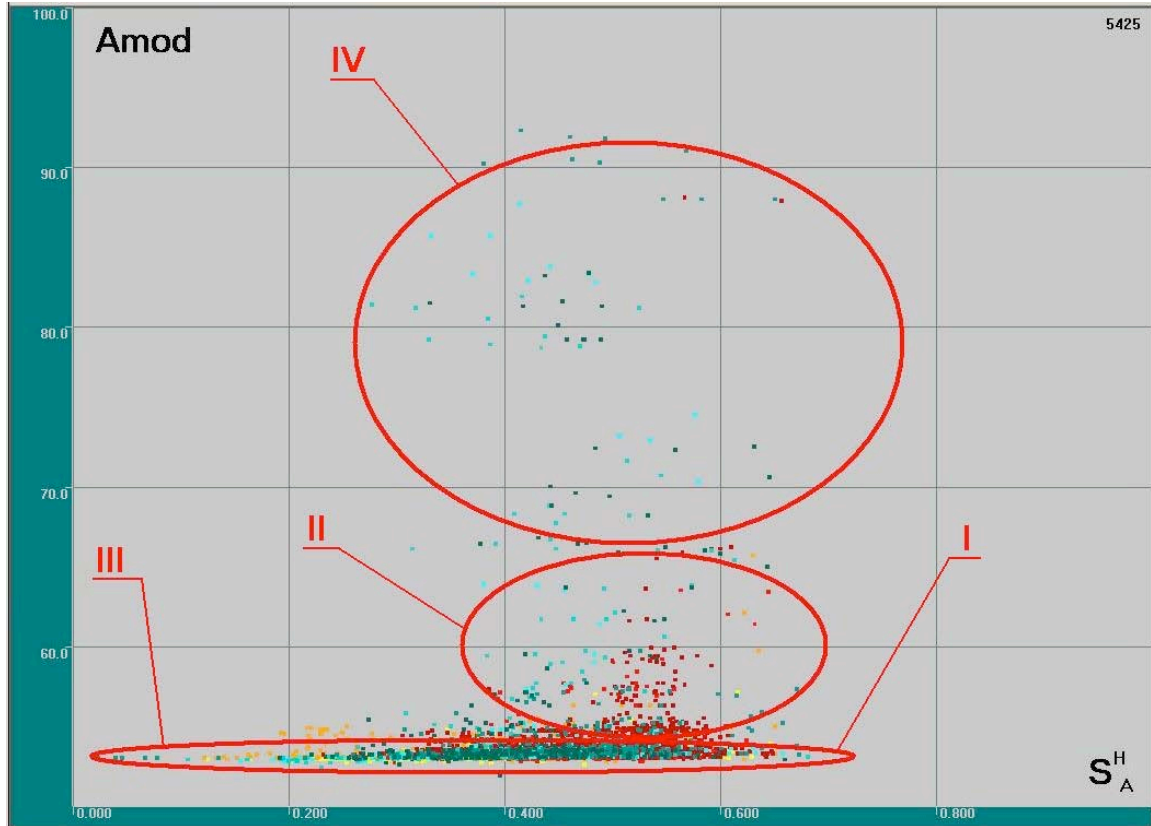


Fig. 2c Diagnosis diagram for cyclic loading of standard specimen loaded to failure.

In a separate window calculated and displayed are the dispersion curves for the specified values of object thickness, and C_L and C_T are velocities of the volume longitudinal and transverse waves in the object material. Just here it is possible to select the desired mode of Lamb waves (usually A0 and S0) for calculating and displaying, and to indicate the magnitudes of sound speed in liquid, possibly filling up the object. To suit user's convenience, the program offers the tabulated velocity values for a number of hard materials and liquids. From the plot containing the dispersion curves $V(f)$, we can obtain the dependences of the arrival times of signal different frequency components to the AE sensor located at the distance L from the source [5].

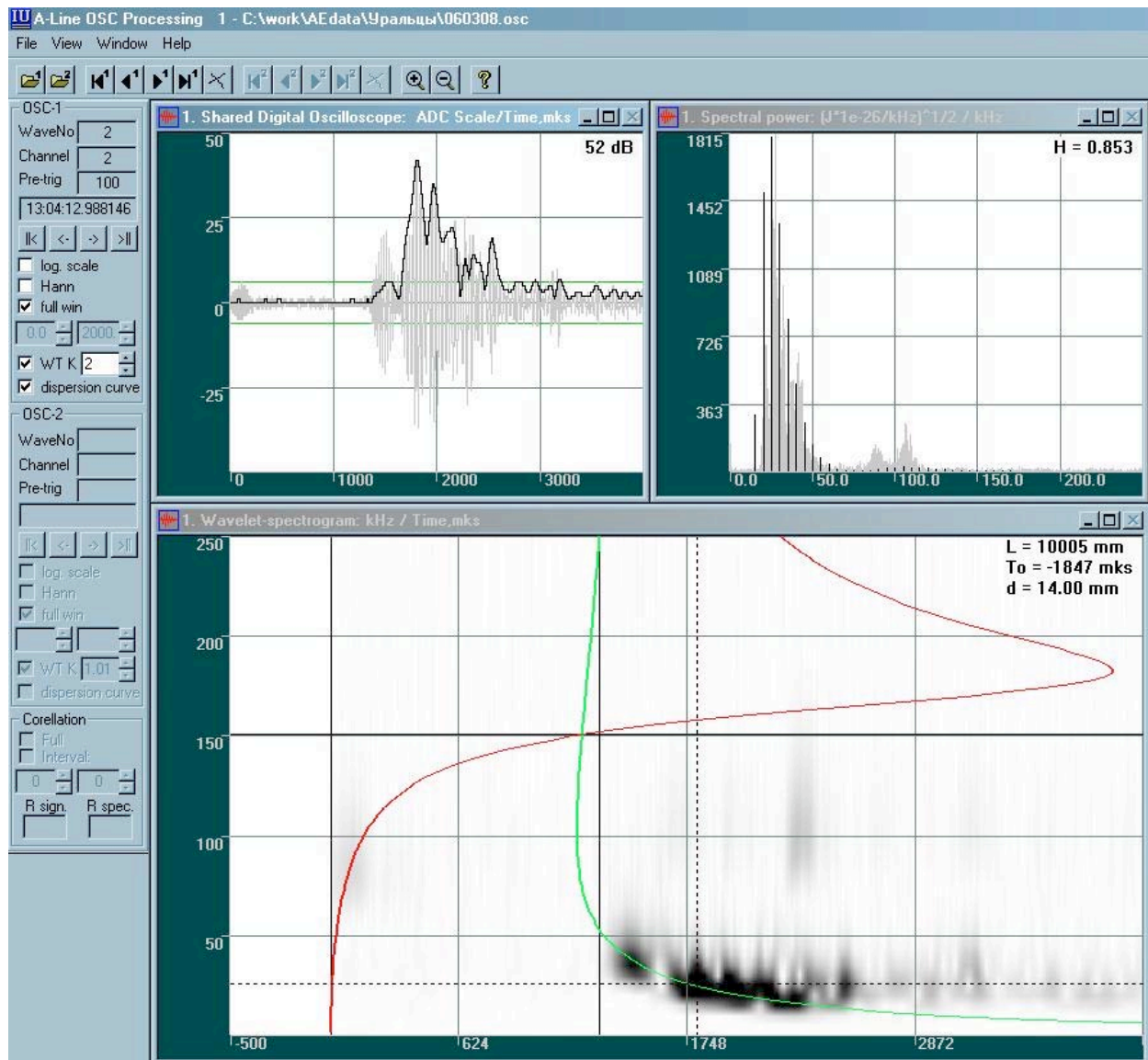


Fig. 3 Wavelet-spectrogram window with evaluation results for L , t_0 and d and results of wavelet-spectrogram section plot.

Figure 3 presents an example of the wavelet-spectrogram window with the superimposed picture of dispersion curves for the detected waveform. The imposition parameter values L and t_0 (t_0 – time of signal emission relative to the time of waveform onset) are selected on-line by moving the scaling markers (two light-gray verticals) with the mouse in the wavelet-spectrogram

window. The left marker corresponds to the fastest Lamb-wave arrival (mode S_0 at $f \rightarrow 0$), and the right one to the arrival of high-frequency components (all modes at $f \rightarrow \infty$). The horizontal scaling marker allows adjusting obtained curves onto frequency scale, so the wall thickness d value may be corrected if it is not known in advance. As a rule, when selecting the parameters, it is convenient to be guided by the characteristic frequency in the wavelet-spectrogram, in which the values of group velocities of modes A_0 , S_0 and A_1 are equal. Under marker movement at the upper right of the appropriate window displayed are: t_0 , L and d , which correspond to the current variant of the dispersion curves superimposed. Moreover, in some instances, it is useful to know the time of wave arrival through the liquid inside the object, and this time is displayed by the appropriately-colored vertical line.

When it is difficult to carry out the correct superimposition of dispersion curves (in case of high noise at the small distance between the source and AE sensor or if a great number of the modes in signal is present [6]), we can apply the wavelet-transform for making more precise the arrival time by determining the energy density maximum in the spectrogram on the preselected frequency. The point of time conforming to this maximum can be applied for AE source location instead of the usually used threshold intersection time or the time of signal amplitude maximum [5, 6]. The A-Line OSC Processing program offers the plotting of the movable wavelet-spectrogram sections by means of the constant frequency and constant time lines, and the appropriate envelope spectra complete the picture in the waveform windows as shown in Fig. 3. The application of the normal wave velocity on the maximum-conformable frequency allows the AE-source coordinates determination error to be reduced.

References

1. Kuksenko V.: Model for the transition from micro- to macro-fracture, *Mechanics of Jointed and Faulted Rock*, 1995, Balkema, Rotterdam. p. 997.
2. Shiotani T., Nakanishi Y., Luo X., Haya H.: Damage Assessment in Railway Sub-Structures Deteriorated Using AE Technique, *Proc. 26th EWGAE Conf.* Berlin. 2004, pp. 225-232.
3. Ship V., Muravin G., Samoilova I., Dorokhova E.: The application of complex information parameter to acoustic emission for diagnostic during the stage of fracture, *Nondestructive Testing Evaluation*, **13**, 1997, 57-71.
4. Suzuki H., Kinjo T., Hayashi Y., Takemoto M., Ono K.: Appendix by Hayashi Y., Wavelet Transform of Acoustic Emission Signals, *Journal of Acoustic Emission*, **14** (2), 1996, 69-84.
5. Hamstad M., O'Gallagher A, Gary J.: Examination of the Application of a Wavelet Transform to Acoustic Emission Signals, *Journal of Acoustic Emission*, **20**, 2002, 39-81.
6. Cole P., Miller S.: Use of Advanced A.E. Analysis for Source Discrimination Using Captured Waveforms, *3rd MENDT - Middle East Nondestructive Testing Conference & Exhibition*, 27-30 Nov. 2005, Bahrain, Manama.
<http://www.ndt.net/article/mendt2005/pdf/30.pdf>.

APPLICATION OF ACOUSTIC EMISSION IN OPTIMIZING THE DESIGN OF NEW GENERATION CASTINGS OF HIGH-VOLTAGE ELECTRIC DEVICES

JAN PŁOWIEC^{1,2}, WOJCIECH L. SPYCHALSKI^{1,2}, HUBERT MATYSIAK¹, and KRZYSZTOF J. KURZYDŁOWSKI¹

¹Warsaw University of Technology, Faculty of Materials Science and Engineering, Materials Design Division, 141 Woloska St, 02-507 Warsaw, Poland;

²Materials Engineers Group Ltd., Warsaw, Poland

Keywords: sand casting, pressure test, Al alloys, optimization, design verification, FEM

Abstract

The technological progress in power systems requires the application of new solutions that will meet higher specifications than the currently used, in all parts of equipment design. This also refers to the external castings of power devices, especially those operating over a long time under high-pressure SF₆ dielectric gas. Increased requirements include a 20% increase of the SF₆ operating pressure and the same increase of the destructive test pressure, and simultaneous reduction of the casting weight. In this paper we present test results of casting materials and strength calculations for the implemented changes in design. The optimization and design verification activities included acoustic emission (AE) measurements performed during a hydraulic pressure test. The results obtained allowed to determine the locations and pressure values, at which the plastic strain began to occur, and the position of the final failure.

Introduction

Technological progress in power engineering has been observed over recent years and requires the implementation of solutions meeting higher requirements than those used at present in all devices and elements in this area, taking into account also the external castings of these devices, which are operated under multi-year influence of high-pressure SF₆ gas as the best available dielectric. Higher requirements consist in 20% increases in working, control and destructive SF₆ pressures, as well as the reduced weight of castings [1]. Increased requirements in relation to castings can be met through the implementation of structural modifications and new manufacturing processes, with simultaneous increase in their strength and tightness adapted to higher pressure. Users of the castings demand also the delivery by manufacturers in ready-to-assemble commercial condition, i.e. as fully machined castings accompanied with the certificate confirming their strength, gas tightness matched to higher pressure, gas permeability checked with helium and resistance to control and destroying pressure checked in hydraulic test. Correct functioning of such castings requires appropriate strength and gas tightness to keep required working pressure of filling medium for 30 years. An example of such a casting is shown in Fig. 1.

To meet such rigorous requirements, a series of examinations was carried out during structural and manufacturing-process optimization, including examination of microstructure, material properties, modeling process and behavior in working conditions [2]. Hydraulic pressure tests with simultaneous recording of AE signals on the basis of the accepted criteria were some of the significant examinations during optimization and checking of the finished products. The AE examination was carried out during increasing and maintaining the pressure until the part was

destroyed. Vallen Systeme AMSY-5 multi-channel signal recording system with R2007.0904 software was used for AE examination. Because of non-magnetic properties of the cast material, the sensors were attached with assembly tapes. Figure 2 shows the arrangement of the sensors on the casting [3]. The examination was aimed at correlating AE results with test pressure value, and also at locating the source locations, where because of the complex shape of the element the crack could develop the earliest.



Fig. 1. Example of an aluminum casting, an element of high-voltage electric device.

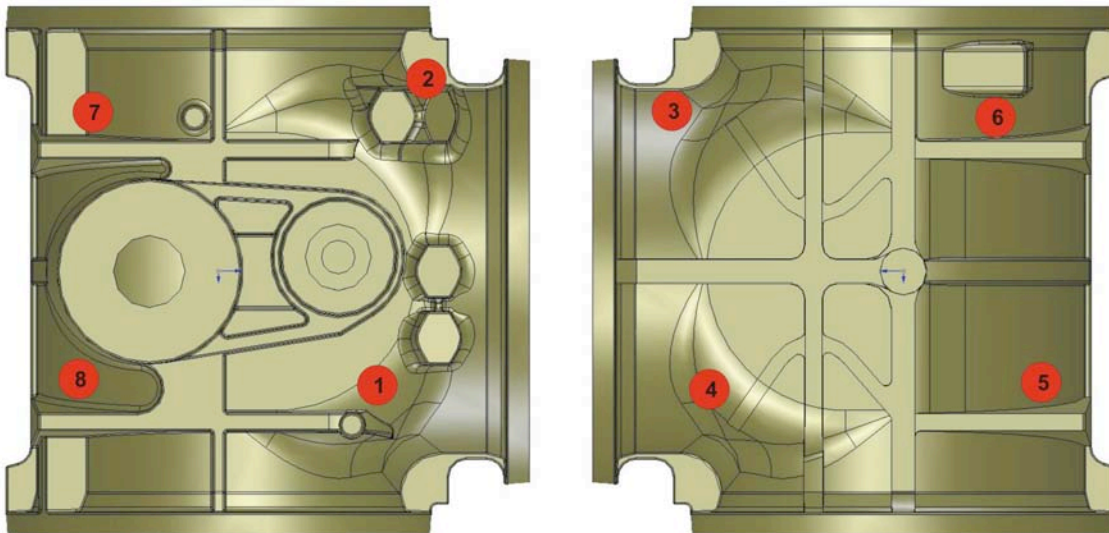


Fig. 2. Example of sensor arrangement on examined T-connection.

Results

Figure 3 shows AE signal amplitude vs. time, and reflects the increasing AE activity with pressure during a pressure test [4, 5]. The locations, at which the AE signal sources occur initially, are the local stress concentrations resulting from the cast geometry. The pressure applied during examination was much higher than the working pressure of 3 bar. The maximum pressure achieved during examination was 38 bar. Thanks to holding the pressure at various levels, the occurrence of Felicity effect was revealed, determining the level of structural damage, at the pressure amounting to 25 bar for one of these casts.

Example of such an effect can be seen on Fig. 3, where the first occurrence of Felicity effect is marked. A large number of the AE counts can be seen within area 2 as compared to area 1. Although the AE signals from both groups were recorded during the same pressure-hold level of 25 bar, higher AE intensity (higher number of counts of higher amplitude, energy or longer duration) and activity (higher number of hits, counts and signals of higher energy) during the second pressure hold at the same level shows the existence of significant structural damage. This example indicates the occurrence of Felicity effect, which determines the presence of localized plastic deformation.

Subsequent analysis fully confirmed the occurrence of the Felicity effect (Fig. 4). Already at 25 bar, significant structural damages were found in the material, determining its possible use.

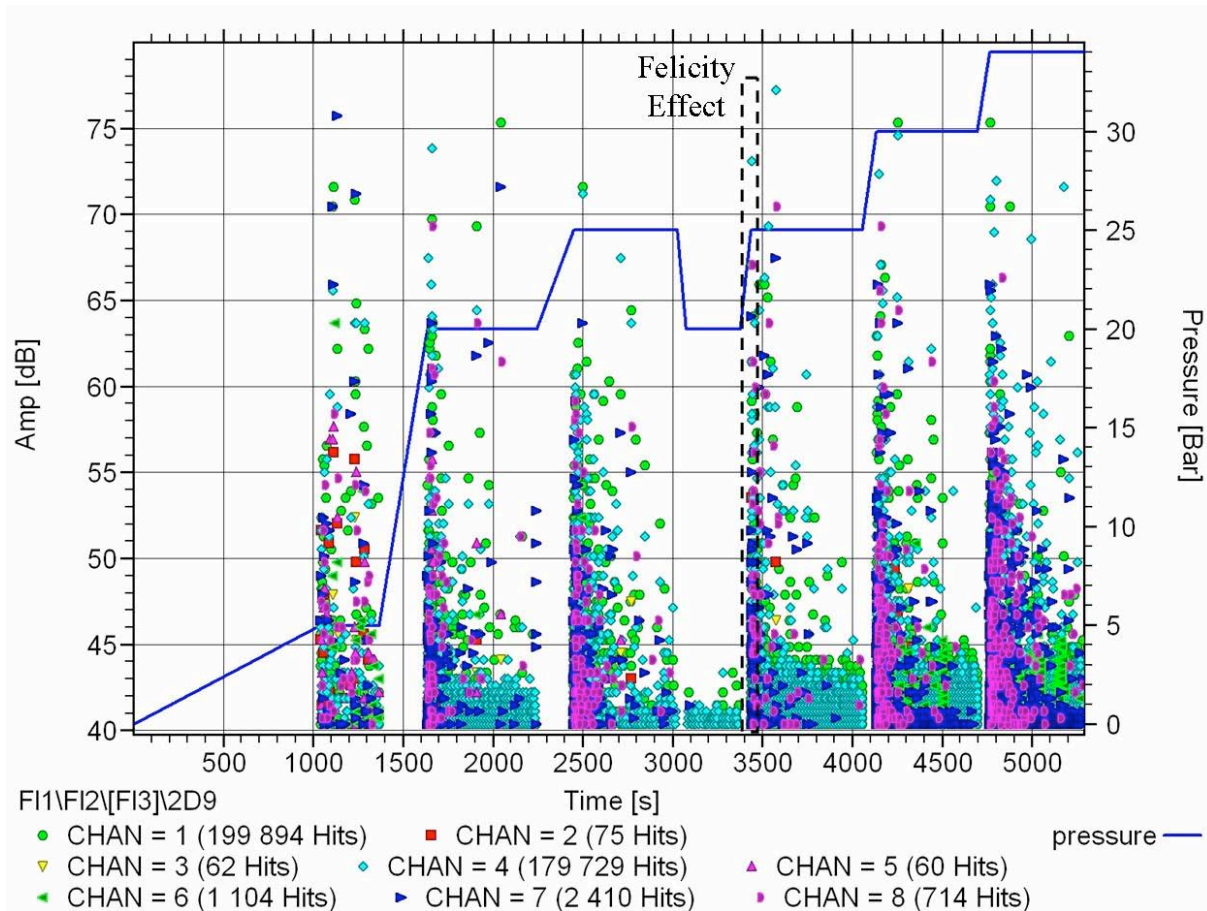


Fig. 3. Amplitudes of the AE signals recorded during the time when the pressure was held during the pressure test performed on a T-connection casting, including the pressure change pattern and the Felicity effect analysis.

Other parameters used to evaluate the damages presented in this article are RA value and the mean frequency for an AE hit, F_a , defined in JCMS-III B5706 [6]. The RA value is the ratio of rise time to amplitude, expressed in ms/V [7]. The F_a value is the ratio of AE counts to the duration. By using these two indices we can determine whether the nature of a crack is a result of tensile or shear forces. Ohtsu and coworkers [8] linked the F_a vs. RA relation to the tensile/shear nature of concrete cracks, but recently Takuma [9] used these indices successfully to evaluate the degree of tool wear, which demonstrates that these parameters can be successfully used for other applications [10].

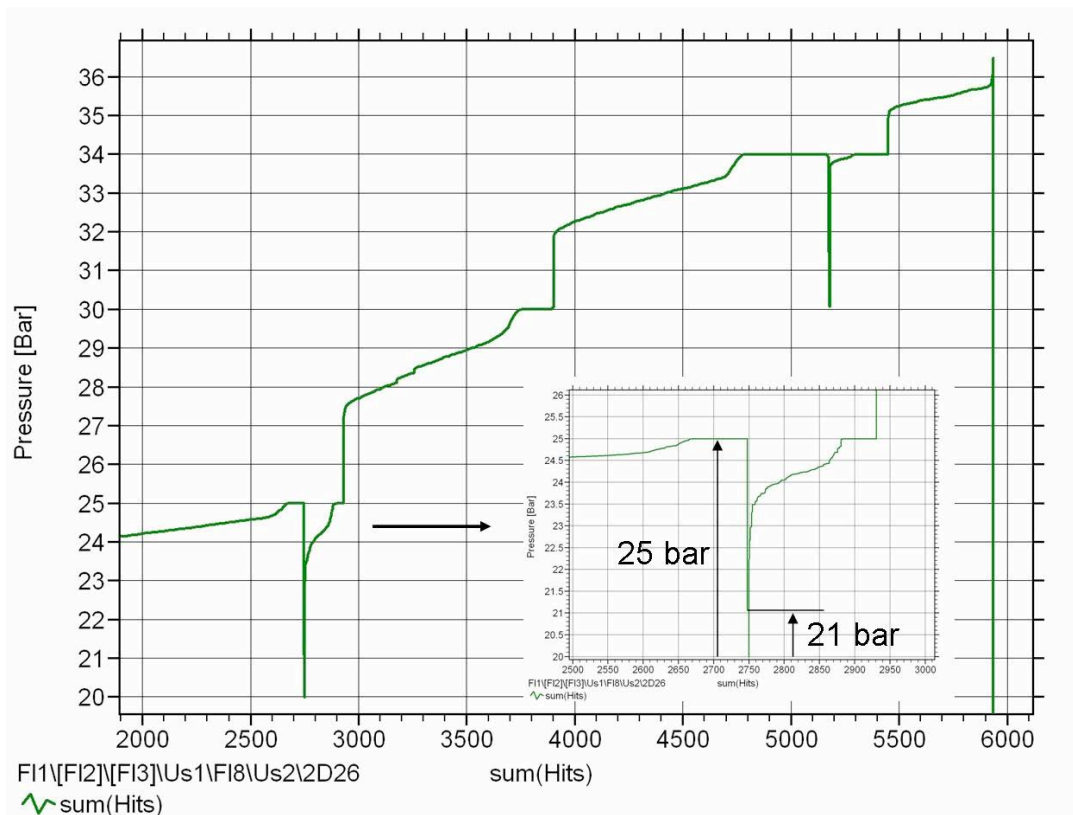


Fig. 4. The pressure during the pressure test performed on a T-connection vs. the AE counts, showing the Felicity effect. Insert shows the start of AE activity at 21 bar (Felicity ratio of 0.84).

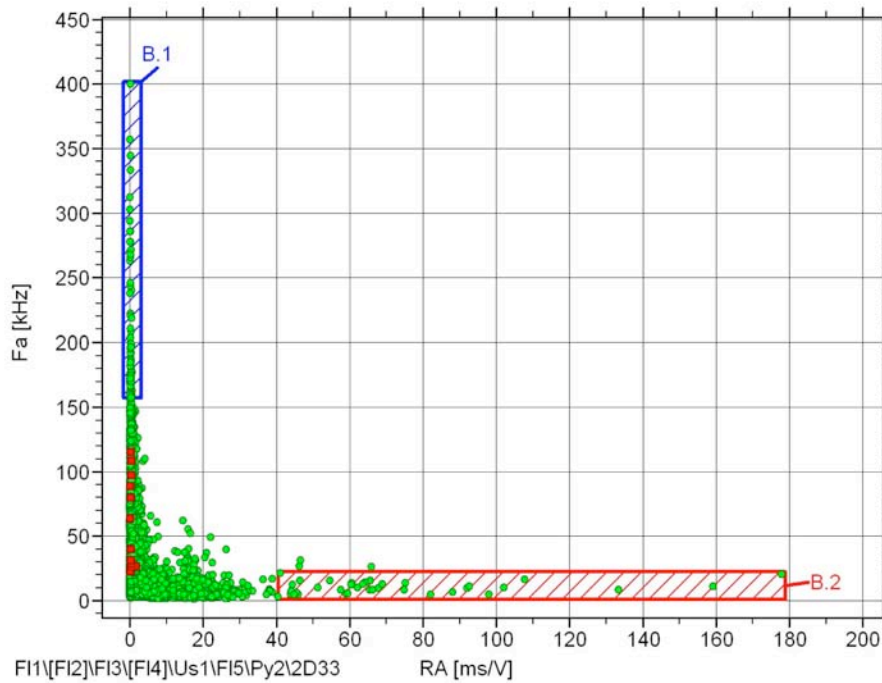


Fig. 5. Relations of Fa frequency indexes and RA values.

In connection with the above, the next analysis was aimed at comparing the relations of the Fa mean frequency and RA values. The relation between these indices is shown in Fig. 5. There

are two areas isolated in the figure. The first area, B1, is characterized by high Fa frequency values, and low RA values. The other, B2, presents low Fa values, and RA values are higher than in B1 area.

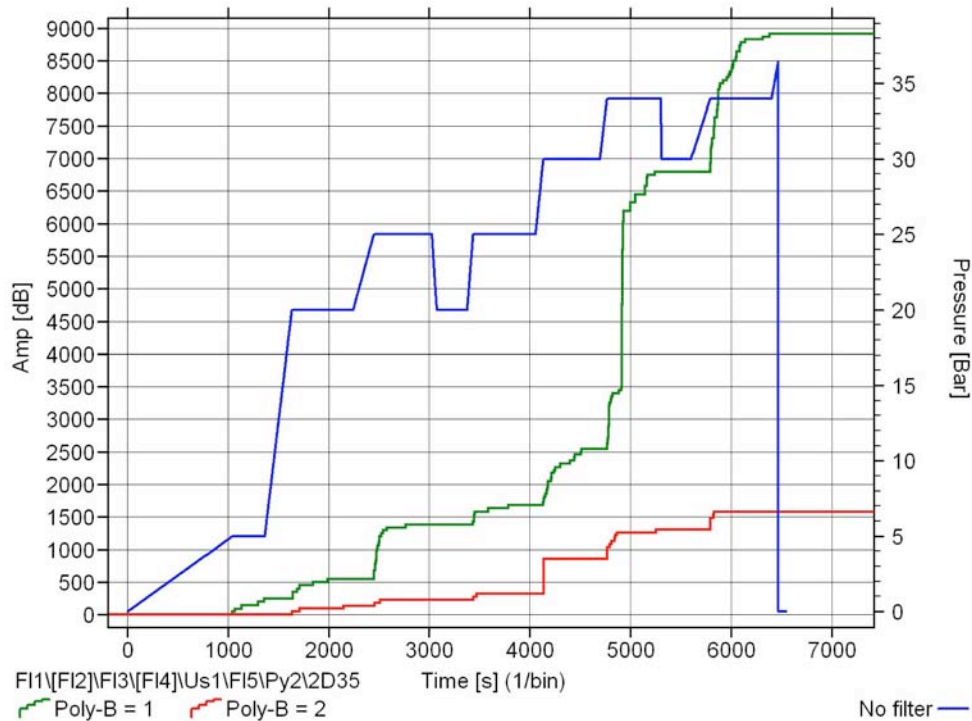


Fig. 6. Total changes of AE signal amplitudes recorded during pressure hold-ups in the course of the pressure test of the tee.

We can assume that the AE signals coming from the cracks have high amplitudes at very low rise time values. B1 area isolated in Fig. 5 is distinguished by such AE signals. While the AE signals that come from crack friction show low amplitude with high values of the rise time. The signals of such parameters are grouped in B2 area.

Figure 6 presents the total AE signal amplitude changes recorded during pressure changes in the course of the pressure test of the tee. The signals of B1 area, resulting from the cracks and featuring high Fa frequency value and low RA value, marked in Fig. 6 by a green line, are the dominant signals during all the pressure holds. B2 signals, coming from the crack friction and featuring low Fa values and higher than B1 area RA values, marked in Fig. 6 by a red line, are not recorded as intensively as the crack signals, and appear in the early part of the pressure hold stages. It is worth noting the sudden rise of B1-type signals (from the cracks) after exceeding the pressure of 30 bar. Note that typically this rise occurs mainly at a fixed pressure at the level of 35 bar. Figure 7a presents localized events recorded in one of the cast areas with a crack drawn (in red). Compare with the crack visible on Fig. 7b. The localized AE events occurred along the crack.

It is noteworthy that the location, at which the plastic deformation was located, and at which the final crack occurred, is only a one of a few locations where stresses determined with the finite elements method [11] are concentrated (Fig. 8). Use of the AE monitoring allowed us to verify the numerical calculations based on assumption of uniform cast material and ideal mapping of the assumed shape.

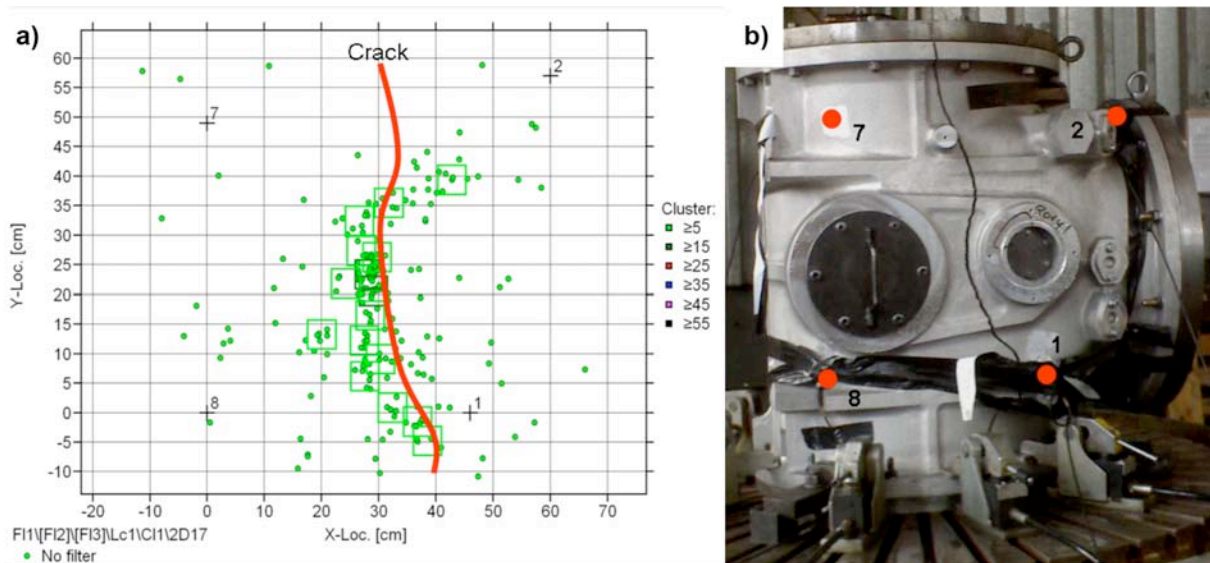


Fig. 7 a) Planar location of the AE events recorded during the entire pressure test of a T-connection in the area of 1, 2, 7 and 8 sensors; b) Picture of the T-connection with attached sensors and a clearly visible crack at center.

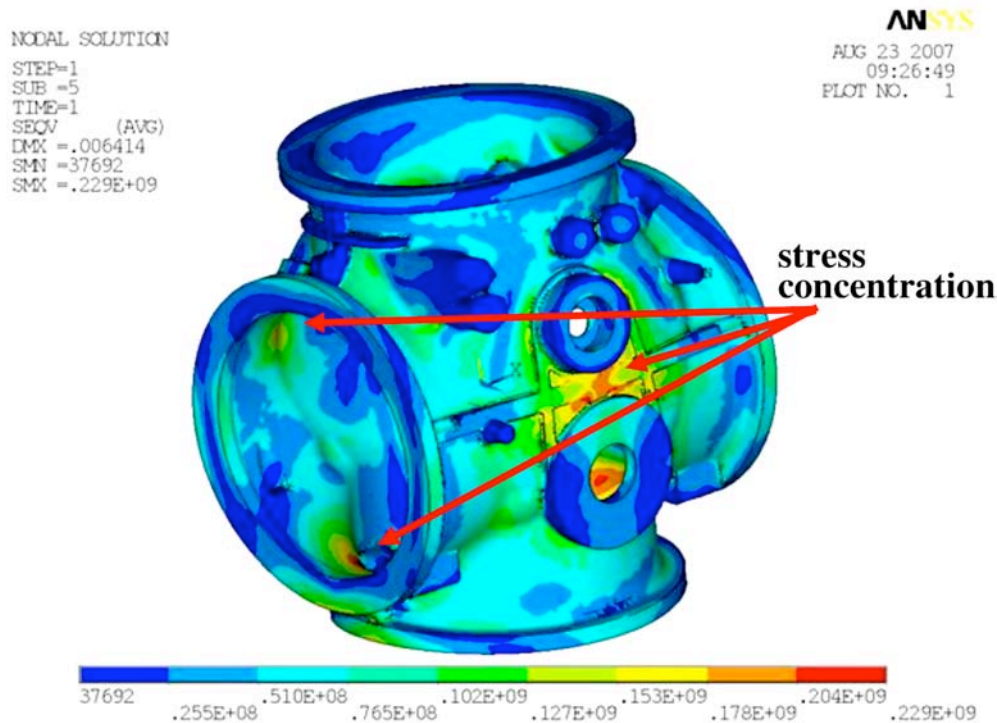


Fig. 8. Reduced stresses at 20-bar pressure with indicated positions of concentrated stresses.

Other examination results, presented on Figs. 9 and 10, show the change of amplitude, signal duration and AE counts for various test pressure ranges. The ranges 5-10 bar, 10-15 bar and 25-30 bar were selected for the presentation. It can be seen that, in initial testing phase within the 5-10 bar range, the recorded signals were of low amplitude, no higher than 50 dB. Analysis of their character showed that they are caused by plastic deformation. Because the source of the signals was not found, plastic deformation in this pressure range was assumed in a significant part of the cast material. An analysis of the AE signals occurring in the subsequent pressure range of 10-15 bar shows a distinct increase of amplitude of the recorded signals. We also observed distinct

localization of signal sources, which in most cases were located at the central part of the casting, at the place where the cracking occurred in the final phase of the test. The last results in the 25–30 bar range (the cracking occurred at 31 bar) showed the further growth of both the signal amplitude and the number of located sources. The amplitude distribution within the 25–30 bar area, as shown in the Figure 10, reveals very high amplitude signals at the level of 100dB, which obviously proves propagation of the crack.

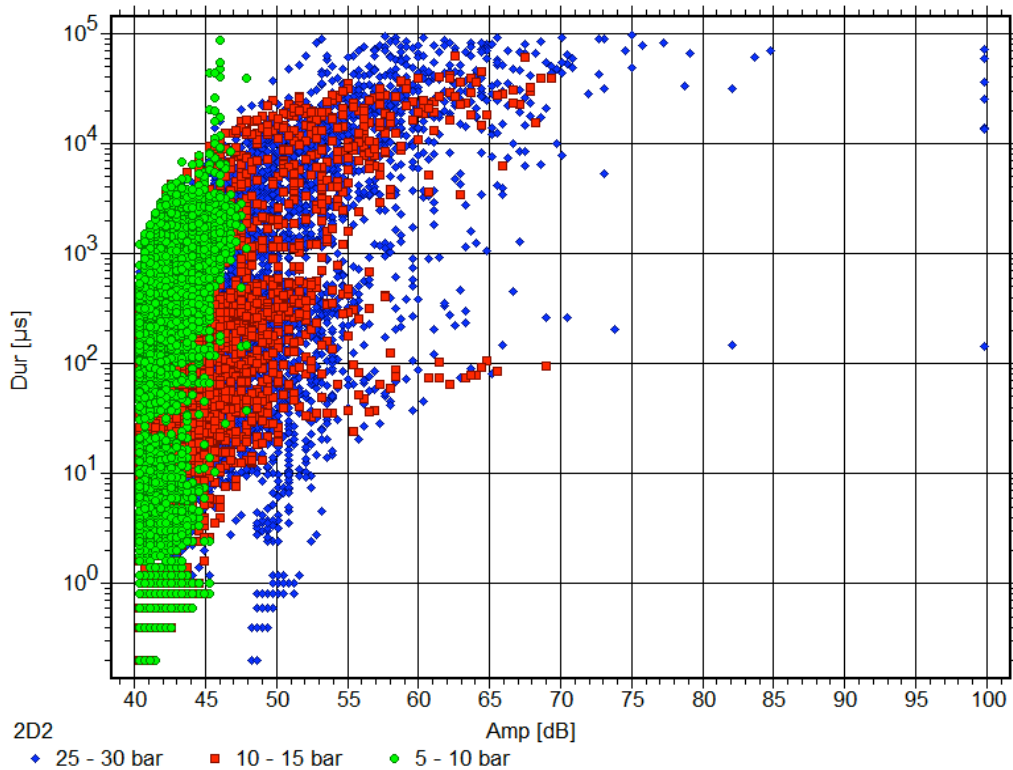


Fig. 9. Signal duration vs. amplitude. Green: 5-10 bar; Red: 10-15 bar; Blue: 25-30 bar.

It has to be noted that just before the cracking, at the 28–31 bar range, a relatively small number of AE signals were recorded. This low AE activity probably results from the relatively low ductility of the material. Along with the pressure rise, resulting from plastic deformation of the material, there is a decrease in the number of mobile dislocations whose movement is the source of the AE signals. Figure 10 also allows one to observe simultaneous rise of the mean amplitude of the AE signals with the rise of the pressure value. In addition, the rise of AE signal amplitude ranges can also be observed.

Conclusions

The presented results show that the AE method can be an efficient tool for optimization of structure and the manufacturing methods of pressure devices. Using the AE measurements during the pressure tests allowed us to determine the particularly strenuous spots and the beginning of plastic deformation in the examined castings. Knowledge of locations and pressure ranges, at which the plastic deformation was initiated allowing us to implement the structural changes aimed at decreasing the stress concentration. No phenomenon of plastic deformation localization was found after optimization was performed. This is significant for achieving the long-term operation without a failure.

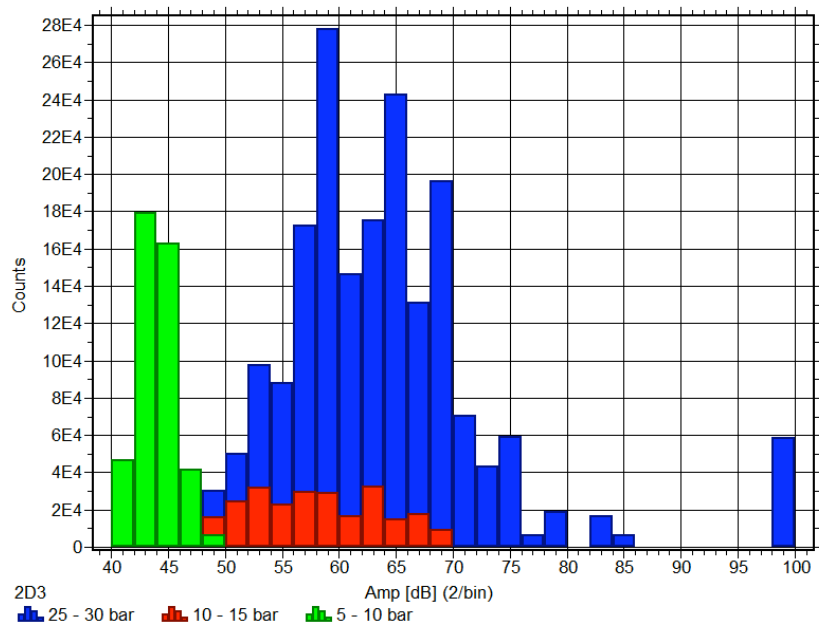


Fig. 10. AE counts vs. amplitude. Green: 5-10 bar; Red: 10-15 bar; Blue: 25-30 bar.

Acknowledgement

This work was supported by the Industrial R&D grant 6ZR92006C/06775 of Polish Ministry of Science and Higher Education.

References

1. Kopejtkova D., Molony T., Kobayashi S., and Welch I.M.: A twenty-five-year Review of Experience with SF₆ Gas Insulated Substations CIGRE Session, Paris 30 Aug.-4 Sept. 1992, paper 23-101.
2. Materials Engineers Group Ltd., Aluminum casts for energetic – Report for WKS Rzeszow, Warsaw 2007.
3. Materials Engineers Group Ltd. Internal Procedure: Guide for Acoustic Emission Examination of Pressure Vessels, Warsaw 2007.
4. Płowiec J., Spychalski W.L., Matysiak H., Michalski J., Proc. 28th European Conference Acoustic Emission Testing, Krakow, Poland, 17-19 Sept. 2008, pp. 274-279.
5. Preparation and implementation of high-voltage chambers casting technology for power application – industrial project, cooperation with ZM WSK Rzeszow (grant 6ZR92006C/06775 of Polish Ministry of Science and Higher Education).
6. JCMS-III B5706 (2003), Monitoring method for active cracks in concrete by acoustic emission. Federation of Construction Materials Industries, Japan
7. Ohtsu, M., Isoda T., Tomoda Y.: Acoustic emission techniques standardized for concrete structures, *J. Acoustic Emission*, **25**, (2007), 21-25.
8. Tsuji N., Uchida M., Okamoto T., Ohstu M.: Application of acoustic emission technique to evaluation of cracking in concrete structures, *Progress in Acoustic Emission X, JSNDI*, 2000, pp. 189-194
9. Takuma, M. Shinke, N., Nishiura, T. and Akamatu, K., *J. Acoustic Emission*, **24** (2006) 52-66.
10. Ono K.: Structural integrity evaluation using acoustic emission, *J. Acoustic Emission*, **25**, (2007), 1-20.
11. Zienkiewicz O., Taylor R., *The finite element method*. 4th ed. McGraw-Hill, London, 1994.

CUMULATIVE CONTENTS

J. of Acoustic Emission, Volumes 1 - 26, 1982 - 2008

Volume 1 (1982)

Number 1

- Page 1 An Acoustic Emission Study of the Intergranular Cracking of AISI 4340 Steel
A. Nozue and T. Kishi
- Page 7 Acoustic Emission Behavior of a Low Alloy Steel R. J. Landy and K. Ono
- Page 21 An Acoustic Measurement of Boiling Instabilities in a Solar Receiver Alan G. Beattie
- Page 29 A Broadband Acoustic Emission Transducer
Mark B. Moffatt, Theodore J. Mapes and Arthur T. Grodotzke
- Page 35 A Simple Tape Recording System for Acoustic Emission P. G. Bentley and A. Plevin
- Page 37 Earthquakes as Acoustic Emission - 1980 Izu Peninsula Earthquake In Particular Kiyoo Mogi
- Page 45 AE Literature T. F. Drouillard
- Conferences and Symposia
- Page 67 The Fifth International Acoustic Emission Symposium K. Ono
- Page 68 Third Conference on AE/Microseismic Activity in Geologic Structures and Materials H. R.
Hardy, Jr.
- Page 69 The Tenth European Working Group on Acoustic Emission K. Ono
- Page 72 Future Meetings
- Number 2
- Page 73 Reciprocity and Other Acoustic Emission Transducer Calibration Techniques Roger Hill
- Page 81 Production Acoustic Emission Testing of Braze Joint T. F. Drouillard and T. G. Glenn
- Page 87 Acoustic Emission Transducer Calibration by Means of the Seismic Surface Pulse F. R.
Breckenridge
- Page 95 Acoustic Emission Testing of Filament-Wound Pipes under Repeated Loading
Leszek Golaski, Maciej Kumosa and Derek Hull
- Page 103 Source Mechanism and Waveform Analysis of Acoustic Emission in Concrete Masayasu Ohtsu
- Page 114 Acoustic Emission in Aircraft Structural Integrity and Maintenance Programs J. M. Rodgers
- Page 121 AE Literature T. F. Drouillard
- Conferences and Symposia
- Page 141 The 23rd Meeting of AEWG K. Ono
- Page 144 The 24th Meeting of AEWG W. F. Hartman and J.W. Whittaker
- Page 145 AEWG AWARDS K. Ono
- Page 146 Third National Conference on Acoustic Emission K. Ono
- Page 147 CARP - Sixth Meeting J. Mitchell

Page 148	The XIth EWGAE Meeting B. Audenard BOOK REVIEW
Page 149	Elastic Waves in Solids Roger Hill
Number 3	
Page 151	Testing Fiber Composites with Acoustic Emission Monitoring Marvin A. Hamstad
Page 165	On the SPI/CARP Recommended Practice for Acoustic Emission Testing of Fiberglass Tanks and Vessels C. Howard Adams
Page 173	Some Details on the NBS Conical Transducer Thomas M. Proctor, Jr.
Page 179	Low Temperature Behavior of Liquid Couplants used in Acoustic Emission Experiments J. Baram and J. Avissar
Page 183	Acoustic Emission Behavior of Nickel during Tensile Deformation S.-Y. S. Hsu and K. Ono
Page 191	Instrumented Impact Testing of Structural Fiber-Reinforced Plastic Sheet Materials and the Simultaneous AE Measurements S. I. Ochiai, K. Q. Lew and J. E. Green
Page 193	On the Sensitivity of the Acoustic Barkhausen/Magnetomechanical Acoustic Emission Effect A. E. Lord, Jr.
Page 195	AE Literature Thomas F. Drouillard Conferences and Symposia
Page 211	1982 ASNT Spring Conference K. Ono
Page 211	Fifth Internatl Conf. on NDE in the Nuclear Industry K. Ono
Page 211	The Institution of Metallurgists Meeting on AE A. P. G. Rose
Page 213	Review of Progress in Quantitative NDE K. Ono
Page 214	The 24th Meeting of AEWG K. Ono
Page 215	The Sixth International Acoustic Emission Symposium
Page 219	Symposium on Structural Faults: Inspection and Repair
Page 220	First International Symposium on AE from Reinforced Composites
Page 220	Sixth Internatl Conf. on NDE in the Nuclear Industry BOOK REVIEW
Page 220	AE in Geotechnical Engineering Practice Robert M. Koerner
Page 221	Acoustic Emission Clinton Heiple New Products and Services AE Events of Interest / Letter from the Editor
Number 4	
Page 223	In-Flight Acoustic Emission Monitoring of a Wing Attachment Component S. L. McBride and J. W. Maclachlan
Page 229	Effect of Crack PreAence on In-Flight Airframe Noises in a Wing Attachment Component S. L. McBride and J. W. Maclachlan
Page 237	Leak Detection Using Acoustic Emission A. A. Pollock and S.-Y. S. Hsu
Page 244	Acoustic Emission from Glass/Polyester Composites; Effect of Fibre Orientation F. J. Guild, B. Harris and A. J. Willis
Page 251	Changes in Acoustic Emission Peaks in Precipitaion Strengthened Alloya with Heat Treatment C. R. Heiple and S. H. Carpenter
Page 263	A Miniature Optical Acoustic Emission Transducer D. C. Emmony, M. W. Godfrey and R. G. White
Page 266	Classification of NDE Waveforms with Autoregressive Models Ronald B. Melton

Page 271	AE Literature Thomas F. Drouillard Conferences and Symposia
Page 294	The 11th Meeting of the European Working Group on Acoustic Emission Roger Hill
Page 300	ASTM Subcommittee E 7.04 on Acoustic Emission Alan G. Beattie
Page 300	Meetings of Japanese Committee on Acoustic Emission
Page 301	The 10th World Conf. on Non-Destructive Testing
Page 302	Conference on Periodic Inspection of Pressurized Components
Page 302	1983 ASNT Spring Conference
Page 302	Symposium; Nondestructive Methods for Material Property Determination
Page 303	First International Symposium on AE from Reinforced Composites
Page 303	Review of Progress in Quantitative NDE
Page 303	25th Meeting of Acoustic Emission Working Group
	BOOK REVIEW
Page 303	Progress in Acoustic Emission Adrian A. Pollock
	ANNOUNCEMENTS
	AE Events of Interest / Letter from the Editor
Page I-1	Index to Volume 1

Volume 2 (1983)

Number 1/2	
Page 1	Rotating Machinery Diagnosis With Acoustic Emission Techniques Ichiya Sato, Takao Yoneyama, Soji Sasaki, Toshitaka Suzuki, Tomoaki Inoue, Tsuguaki Koga and Takashi Watanabe
Page 11	In-Field Experience in Condition Monitoring of Rotating Machinery by Demodulated Resonance Analysis G. Buzzacchi, M. Cartoceti, C. De Michelis and C. Sala
Page 19	Acoustic Emission from Environmental Cracking of a High Strength Titanium Alloy S. Yuyama, T. Kishi, Y. Hisamatsu and T. Kakimi
Page 29	Detection of Corrosion Fatigue by Acoustic Emission P. Jax and B. Richter
Page 39	Effect of Overaging on Acoustic Emission Behaviour of 7075-T651 Aluminum During Crack Growth S.L. McBride and J.W. Maclachlan
Page 47	AE Source Identification by Frequency Spectral Analysis for an Aircraft Monitoring Application L. J. Graham and R. K. Elsley
Page 57	A User's Perspective of Small Computer-Based Acoustic Emission Equipment M.A. Hamstad
Page 64	Magnetomechanical Acoustic Emission: A Non-Destructive Characterization Technique of Precipitation Hardened Steels I. Roman, S. Maharshak and G. Amir
Page 67	Acoustic Emission Couplants I: The ASTM Survey A.G. Beattie
Page 69	Acoustic Emission Couplants II: Coupling Efficiencies of Assorted Materials A. G. Beattie, J. A. Baron, R. S. Algera and C. C. Feng
Page 71	AE Analysis During Corrosion, Stress Corrosion Cracking and Corrosion Fatigue Processes S. Yuyama, T. Kishi and Y. Hisamatsu
Page 96	Acoustic Emission, Principles and Instrumentation A.G. Beattie
Page 129	AE Literature Thomas F. Drouillard
Page 143	Conference and Symposia

Page 143	The 25th MEETING OF AEWG	A.G. Beattie
Page 146	AEWG Awards	
Page i	AEWG XXV	
Page ii	Editorial	S.L. McBride
	A Note from the Editor	Kanji Ono
Number 3		
Page 151	Acoustic Emission Source Kinematics Based on the Moving Dislocation Theory	Masayasu Ohtsu
Page 159	Characterization of Concrete Damages by Acoustic Emission Analysis	Marie-Christine Reymond and Andre Raharinaivo
Page 169	Effects of Solute Distribution on Acoustic Emission Behavior of Solid Solution Alloys	S.-Y. S. Hsu and Kanji Ono
Page 179	Acoustic Emission During Fatigue Crack Growth in 7075-T6 Aluminum at 20°C and 120°C	S.L. McBride and J.W. Maclachlan
Page 187	An Acoustic Pressuremeter to Determine In-Situ Soil Properties	Arthur E. Lord, Jr., and Robert M. Koerner
Page 191	An Acoustic Emission Data Acquisition and Analysis System Using an Apple II Microcomputer	P.E. Wilson and S.H. Carpenter
Page 195	Acoustic Emissions in Geological Materials	Arthur E. Lord, Jr. and Robert M. Koerner
Page 221	AE Literature	Thomas F. Drouillard
Page 239	Conferences and Symposia	
Page i	AE Event of Interest	M.A. Hamstad
Page ii	Editorial	Davis M. Egle/ERRATUM
Number 4		
Page 247	Resonance Analysis of Piezoelectric Transducer Elements	M. Ohtsu and K. Ono
Page 261	Acoustic Emission Evaluation of Metal-Elastomer Junctions	M. Sorel and C. Schepacz
Page 267	Partial Discharge Detection in Bushings by an Acoustic Emission Method	J. Skubis
Page 272	Acoustic Emission as a Measure of Material Damage under Thermal Cycling	Ryszard Zuchowski and Leszek Korusiewicz
Page 275	Acoustic Emission Sensors	C.M. Scala
Page 281	Mechanical Properties and Acoustic Emission in Laser Welded HSLA Steel	G. Dionoro and R. Teti
Page 289	Acoustic Emission Detection of Crack Initiation during Dynamic Fracture Testing of High Strength Materials	S. I. Ochiai, M. C. Cheresh and J. E. Green
Page 292	AE Literature	T.F. Drouillard
Page 319	Conferences and Symposia	
Page 319	12th EWGAE Meeting	L.M. Rogers
Page 327	Cover Photos	
Page I-1	Index to Volume 2	

Volume 3 (1984)

Number 1	
Page 1	Acoustic Emission Due to Crack Growth, Crack Face Rubbing and Structural Noise in the CC-130 Hercules Aircraft S. L. McBride and J. W. Maclachlan
Page 11	Determination of the Source of Acoustic Emission Generated during the Deformation of Magnesium Mark Friesel and Steve H. Carpenter
Page 19	Thermal Restoration of Burst Emissions in A533B Steel I. Roman, H. B. Teoh and Kanji Ono
Page 27	A Generalized Theory of Acoustic Emission and Green's Functions in a Half Space Masayasu Ohtsu and Kanji Ono
Page 41	Acoustic Emission Characterization of the Mechanical Strength of Sintered SAE-316 Stainless Steel I. Roman, M. Watad and A. Mittelman
Page 46	AE Literature Thomas F. Drouillard
Page I	Editorial S. Vahaviolos
Page ii	Meeting Calendar
Number 2	
Page 51	Description of Compound Parameters of Particle-Filled Thermoplastic Materials by Acoustic Emission Techniques Jorg Wolters
Page 59	A New Method of Acoustic Emission Transducer Calibration Masayasu Ohtsu and Kanji Ono With Appendix By F.R. Breckenridge and T. Watanabe
Page 69	Pattern Recognition Analysis of Magneto-Mechanical Acoustic Emission Signals Masayasu Ohtsu and Kanji Ono
Page 81	An Investigation of the Acoustic Emission Generated during The Deformation of Carbon Steel Fabricated by Powder Metallurgy Techniques Yue-Huang Xu, Steve H. Carpenter and Bruce Campbell
Page 90	AE Literature Thomas F. Drouillard
Page 100	Conferences and Symposia
Page 100	AEWG-26 (Abstracts)
Page 104	AEWG-27/AEWG AWARDS
Page 104	AEWG Chairman's Letter Davis M. Egle
Page 105	CARP-8/JCAE/ASNT Methods Committee
Page 106	Other Conferences
Page 107	Book Review Arthur E. Lord, Jr.
Page i	AE Events Of Interest
Page ii	2nd Internat'l AE Conf/EWGAE-13/7th AE Symp.
Page ii	Ultrasonics 85/ASME Symposium
Number 3	
Page 108	Monitoring of Metal Cutting and Grinding Processes by Acoustic Emission Y. Kakino
Page 118	Classification of Acoustic Emission Signals from Deformation Mechanisms in Aluminum Alloys D. Robert Hay, Roger W.Y. Chan, Douglas Sharp and Khalid J. Siddiqui
Page 130	Effects of Interfacial Segregation on Acoustic Emission Behavior of A533B Steel H.B. Teoh, Kanji Ono, E. Kobayashi and I. Roman

Page 144	Magnetomechanical Acoustic Emission of Ferromagnetic Materials at Low Magnetization Levels (Type I Behavior) May Man Kwan, Kanji Ono and M. Shibata
	Technical Note
Page 158	Acoustic Emission during Nickel Electroplating of Copper I. De Iorio, F. Langella and R. Teti
Page 164	AE Literature Thomas F. Drouillard
Page 172	Conferences and Symposia
Page 172	EWGAE-13
Page 173	5th Colloquium on AE D. Schumann and W. Morgner
Page 174	Book Review Kanji Ono
Page 117	Meeting Calendar
Page 157	Available Books on AE
Page 175	Cover Photograph
Number 4	
Page 176	Measurement, Detection and Analysis of Longitudinal and Transverse AE Waves Emitted Near A Crack C. Duytsche, P. Fleischmann and D. Rouby
Page 182	Three-Dimensional Crack Location by Acoustic Emission C. B. Scruby and G. R. Baldwin
Page 190	Magnetomechanical Acoustic Emission of Ferromagnetic Materials At High Magnetization Levels (Type II Behavior) May Man Kwan, Kanji Ono and M. Shibata
	Technical Note
Page 204	A Report on the Pulsed Acoustic Emission Technique Applied to Masonry James D. Leaird
Page 212	AE Literature Thomas F. Drouillard
Page 224	Conferences and Symposia
Page 224	AEWG-27 A. G. Beattie
Page 226	EWGAE-13 (Abstracts)
Page 233	7th Int'l Ae Symposium Kanji Ono
Page 239	ASTM A. G. Beattie/PROC. AE Workshop R. H. Jones et al.
Page 242	ASME Symposium D. A. Dornfeld/4th Conf on AE/MA H. R. Hardy, Jr.
Page 243	Cover Photograph/Announcements
Page 181	Meeting Calendar
Page 189	Available Books On AE
Page i	Ae Events Of Interest
Page ii	Editorial Kanji Ono
Page ii	Thomas/Hochwald Award for Dr. Tim Fowler
Page I-1	Index to Volume 3

Volume 4 (1985)

Number 1	
Page 1	Acoustic Emission Monitoring of Flaw Growth in A Graphite-Epoxy Experimental Wing Segment John Rodgers
Page 9	Acoustic Emission Measurements Using Point-Contact Transducers C. B. Scruby
Page 19	Relationship of Acoustic Emission to Internal Bond Strength of Wood-Based Composite Panel Materials F. C. Beall
Page 31	Laboratory Leak Detection in Gas and Liquid Storage Tanks Using Continuous Wave Acoustic Emission A. E. Lord, Jr., R. M. Koerner and R. N. Sands

Page 41	AE Literature Thomas F. Drouillard
Page 61	Conferences And Symposia
Page 61	AEWG-27 (Abstracts) Kanji Ono
Page 65	ASTM E-7.04 Alan G. Beattie
Page 66	EWGAE-14 (Provisional Programme)
Page 67	WCNDT-11/ Other Conferences
Page 68	AE in Brazil
Page 40	Call for Papers (2nd Int'l Symp AE from RP/8th Int'l AE Symp)
Page 69	EWGAE-14
Page 70	2nd Internat'l AE Conf
Page i	AE Events of Interest
Page ii	ASME Boiler and Pressure Vessel Code/Activities at AEWG-27

Numbers 2 and 3

Pages S1-S332

Proceedings of the Second International Conference on Acoustic Emission, Oct. 28 - Nov. 1, 1985

S1	Characterizing Fracture Types in Rock/Coal Subjected to Quasi-Static Indentation Using Acoustic Emission Technique, A. Wahab Khair
S7	Applications of Statistical Inference to Improve an Evaluation of Rockburst Danger in Underground Coal Mines, Stanislaw Lasocki
S11	Field Determination of Prestress (Existing Stress) in Soil and Rock Masses Using Acoustic Emission, A. E. Lord, Jr. and R. M. Koerner
S17	Directional Acoustic Emission Activity in Response to Borehole Deformation in Rock Masses, Robert J. Watters and Amir Soltani
S19	Acoustic Emission during Dissolution of Salt, H. Reginald Hardy, Jr.
S21	Kaiser Experiment in sawcut Rock, J. D. Leaird, J. Dunning and M.E. Miller
S26	Acoustic Emission Technique for Solid Propellant Burn Rate Control, V. Lalitha, S. K. Athithan and V. N. Krishnamurthy
S30	AE Monitoring of Jet Engine Breech Chambers, Nitin Dhond and Davis M. Egle
S32	Acoustic Emission Studies for Detection and Monitoring Incipient Cracks in a Simulated Aero Engine Mount under Fatigue, S. C. Pathak and C. R. L. Murthy
S35	Post-Test Selective Screening of Acoustic Emission Data - How Helpful Is It?, B.C. Dykes
S38	Comparison between Experimentally Detected Surface Motions Due to a Disbonding and Simulated Waveforms, Shigenori Yuyama, Takuichi Imanaka and Masayasu Ohtsu
S42	Attenuation and Dispersion in AE Waveforms: a Comparison of Theory and Experiment, R. A. Kline and S. S. Ali
S46	The Effects of Transducers on the Decay of a Diffuse Energy Field, H. A. L. Dempsey and Davis M. Egle
S50	The Generalized Theory and Source Representations of Acoustic Emission, Masayasu Ohtsu and Kanji Ono
S54	Experimental Studies of Diffuse Waves for Source Characterization, Richard L. Weaver

- S58 Effect on Flaw Location by the Wave Shape of Acoustic Emission Propogating in a Limited Medium,
Yukuan Ma
- S62 Applications of Quantitative AE Method; Dynamic Fracture, Materials and Transducer Characterization,
Wolfgang Sachse and K. Y. Kim
- S64 A Case for Acoustic Emission Surveilence of Operating Reactors, William F. Hartman
- S69 Characterization of Acoustic Emission Signals Generated by Water Flow Through Intergranular Stress Corrosion Cracks, T. N. Claytor and D. S. Kupperman
- S74 On-Line Acoustic Emission Monitoring of Nuclear Reactor Systems - Status and Future,
P. H. Hutton
- S77 Acoustic Leak Detection in Nuclear Power Plants, John W. McElroy
- S78 On the Application of Acoustic Emission Analysis to Evaluate the Integrity of Protective Oxide Coatings,
H. Jonas, D. Stover and R. Hecker
- S82 Utilization of Acoustic Emission for Detection, Measurement and Location of Partial Discharges,
Jerzy Skubis, Jerzy Ranachowski and Boguslaw Gronowski
- S86 Acoustic Emission Examination of Power Plant Components, G. Tonolini, G. Villa and S. Ghia
- S90 Acoustic Emission from Aluminum Alloy 6061 Strengthened by Whisker and Particulate Silicon Carbide,
James R. Kennedy
- S94 Acoustic Emission during Phase Transformation in Alloys GCr15 and Fe-32Ni,
B. Q. Zhang, C. K. Yao and R. M. Tian
- S98 Acoustic Emission Studies of Structural Relaxation in a Metallic Glass,
G. L. Goswami, P. K. K. Nair, P. Raj and G. P. Tiwari
- S102 Effects of Secondary Phases on Acoustic Emission in 316 Stainless Steel and a Nimonic Alloy PE-16 during Tensile Deformation and Fracture,
Baldev Raj, T. Jayakumar, D. K. Bhattacharya and P. Rodriguez
- S106 Burst-Type Behavior of Structural Steels, O. Y. Kwon, I. Roman and Kanji Ono
- S111 Acoustic Emission Behavior of an Advanced Aluminum Alloy,
I. Roman, Kanji Ono and C. H. Johnson
- S116 Acoustic Emission Produced by the Deformation of Uranium, C. R. Heiple and S. S. Christian
- S119 An Investigation of the Acoustic Emission Generated during the Deformation and Fracture of Molybdenum, J. B. James and S. H. Carpenter
- S123 Manufacturing Process Monitoring and Analysis using Acoustic Emission, David A. Dornfeld
- S127 Acoustic Emission of Flexible Disk Magnetic Media Systems,
Ming-Kai Tse and Armand F. Lewis
- S131 Acoustic Emission Monitoring of Drilling, M. W. Hawman
- S132 Vibro-Acoustic Emission - A Conventional Means of Inspection using AE Technology,

J. R. Webster and T. J. Holroyd

- S134 Weld Penetration Monitoring Using Acoustic Emission, J. Maram and J. Collins
- S135 Using Acoustic Emission Measurements to Establish the Quality of Bonding of Fine Wires to Microchips, S. H. Carpenter, D. R. Smith and J. H. Armstrong
- S137 Real-Time Aircraft Structural Monitoring by Acoustic Emission, S. Y. Chuang
- S138 Aircraft Structure Surveillance in-Flight Using Acoustic Emission, P. H. Hutton
- S142 In-Flight AE Monitoring, G. G. Martin and I. G. Scott
- S147 In-Flight Monitoring for Incipient Cracks in An Aero Engine Mount: An Approach Through Pattern Recognition, C. R. L. Murthy, M. A. Majeed, S. C. Pathak and A. K. Rao
- S151 Acoustic Emission Monitoring of Aircraft Structures, S. L. McBride and J. W. Maclachlan
- S155 Real-Time Acoustic Emission Monitoring Requirements For Cold Proof Testing of the USAF F-111 Aircraft, J. M. Rodgers
- S157 Leakage Test by Acoustic Emission Testing (AET) on Flat Bottom Tanks, Peter Tscheliesnig and Heinrich Theiretzbacher
- S161 Acoustic Emission of Offshore Structures; Attenuation - Noise - Crack Monitoring, Steinar Løvaas
- S165 Acoustic Emission Monitoring of a Node in An Off-Shore Platform, A. B. M. Hoff and M. Arrington
- S166 Acoustic Emission Monitoring of a Bellows and Wye Section on a Fluidized Catalytic Cracking Unit, Thomas Gandy, Martin Peacock and Bobby Wright
- S170 Acoustic Emission Modulus Determination and Source Location in Unidirectional Fibre Reinforced Polymer Composites, A. M. G. Glennie, T. J. Gulley and J. Summerscales
- S174 Acoustic Emission Monitoring of Iosipescu Shear Test On Glass Fibre-Epoxy Composites, M. K. Sridhar, Iyer Subramaniam, Chandra Ajay and A. K. Singh
- S178 Fracture Mechanisms Characterization in Discontinuous Fibre Composites using Acoustic Emission Amplitudes, J-M. Berthelot
- S182 Testing Stress Corrosion of Glass Reinforced Plastic With Acoustic Emission Monitoring, Leszek Golaski and Andrzej Figiel
- S186 Analysis of Fatigue Damage in CFR Epoxy Composites by Means of Acoustic Emission: Setting up a Damage Accumulation Theory, M. Wevers, I. Verpoest, E. Aernoudt and P. De Meester
- S191 Characteristics of Acoustic Emission Generated from GFRP during Tensile Test, Kusuo Yamaguchi, Hirotada Oyaizu, Yasuaki Nagata and Teruo Kishi
- S195 Acoustic Emission during Load-Holding and Unload-Reload in Fiberglass-Epoxy Composites, M. Shiwa, M. Enoki and T. Kishi
- S199 Acoustic Emission Monitoring of Composite Damage Occurring under Static and Impact Loading, D. S. Gardiner and L. H. Pearson
- S203 Fatigue Crack Closure Study, Guozhi Lu

- S207 Amplitude Distribution Analysis of Acoustic Emission during Fatigue Testing of Steels Used in Offshore Structures, R. Visweswaren, M. Manoharan, G. Jothinathan and O. Prabhakar
- S211 AE Monitoring of Corrosion Fatigue Growth; Secondary AE Sources, Christian Thaulow
- S215 Slow Strain Rate Stress Corrosion Cracking of Compact Tension Specimen and Measurement with Acoustic Emission, X. Q. Zhu and J. Z. Xiao
- S220 Temperature Dependence of Inclusion-Fracture-Related Acoustic Emissions in 7075-T651 Aluminum,
S. L. McBride and J. Harvey
- S224 Assessment of Fatigue Damage with Acoustic Emission, M. Nabil Bassim
- S228 Monitoring the Wood Cutting Process with Acoustic Emission, Richard L. Lemaster and David A. Dornfeld
- S232 Acoustic Emission Characterization of Wood Fiber Hardboard, Henrique L. M. dos Reis
- S236 Detection of Western Hemlock Wood in Very Early Stages of Decay using Acoustic Emissions, Masami Noguchi and Koichi Nishimoto
- S240 Application of AE to Mechanical Testing of Wood, Keiichi Sato, Takeshi Okano, Ikuo Asano and Masami Fushitani
- S244 Effect of Moisture Conditioning on AE from Particleboard, Frank C. Beall
- S247 In-Process Acoustic Emission Monitoring of Laser Welds,
J. W. Whittaker, T. M. Mustaleski and K. D. Nicklas
- S251 Monitoring of Thin Welds by Acoustic Emission, G. L. Goswami and P. R. Roy
- S255 Defect Detection in Stainless Steel *Uranus 45* Tig Welded Joints by Acoustic Emission, Vincenzo Dal Re, B. Birolo and F. Cipri
- S259 Classification of Acoustic Emission Signals Generated during Welding,
Roger W. Y. Chan, D. Robert Hay, Khalid J. Siddiqui and Douglas R. Sharp
- S263 Acoustic Emission Behavior of Metal Matrix Composites,
C. Johnson, Kanji Ono and D. Chellman
- S269 Detection of Crack Initiation and Propagation Using Acoustic Emission, W. G. Reuter
- S270 Fracture Toughness Measurement of a NiCrMoV Steel by Acoustic Emission, Vincenzo Dal Re
- S274 Microcrack Initiation and Acoustic Emission of A533B Steel in Fracture Toughness Tests,
Takanori Ohira and Yih-Hsing Pao
- S278 Quantitative Evaluation of Microcrackings during Fracture Toughness Testing of Al₂O₃ by AE Source Characterization, S. Wakayama and T. Kishi
- S282 Three Dimensional Location and Quantitative Evaluation of Cracking Size in Ti Alloy by Acoustic Emission Source Characterization, T. Kishi, H. Ohyama and K. H. Kim
- S286 The Features and the Mechanism of AE Generation from Fatigue Cracks of SUS304 Piping Components, Kusuo Yamaguchi, Hirotsada Oyaizu and Akio Yamashita

S290	Acoustic Emission Study in Arctic Sea Ice in a Field Laboratory, N. K. Sinha
S294	Acoustic Emission Monitoring of the Main Shaft in the Hydroelectric Power Plant, H. Imaeda, H. Kimura and A. Yasuo
S296	Acoustic Emission Applied to Reinforced Concrete Wall, M. C. Reymond and M. Diez
S300	Damage Process Characterization in Concrete by Acoustic Emission, J-M. Berthelot and J-L. Robert
S304	Detection of Fatigue Cracks in Highway Bridges with Acoustic Emission, David W. Prine and Theodore Hopwood II
S307	Laboratory Acoustic Emission Investigation of Full Size ASTM A-588 Bridge Beams, Al Ghorbanpoor and Donald W. Vannoy
S311	Acoustic Emission Made Audible by Time Dilation of Digitally-Recorded AE Signals, Nelson N. Hsu and Steven E. Fick
S312	Magnetoelastic Resonance Spectroscopy, Wolfgang Stengel
S316	Discrimination of Fracture Mechanisms via Pattern Recognition Analysis of AE Signals during Fracture Testing, Kanji Ono and Masayasu Ohtsu
S321	Some Design Concepts for an Accurate, High Speed AE Signal Acquisition Module, T. Kevin Bierney
S325 the	Advanced Acoustic Emission Monitoring System by Distributed Processing Waveform Microdata and System Configuration, Kusuo Yamaguchi, Takashi Hamada, Hatsuo Ichikawa, Hirotsada Oyaizu, Teruo Kishi and Hisashi Ishitani
S329	Advanced AE Instrumentation Concepts With Real Time Source Identification Through Correlation Plots and Soft Ware Filtering, S. J. Vahaviolos and John M. Carlyle
S330	Authors Index
Number 4	
Page 71	Evaluation of Pattern Recognition Analysis of Acoustic Emission from Stressed Polymers and Composites R. M. Belchamber, D. Betteridge, Y. T. Chow, T. Lilley, M. E. A. Cudby and D. G. M. Wood
Page 85	The Use of Acoustic Emission to Measure the Ductility of Hardened Surface Layers J. Roget and D.P. Souquet
Page 93	The Detection of Longitudinal Rail Force via Magnetomechanical Acoustic Emission M. Shibata, E. Kobayashi and K. Ono
Page 103	Application of Acoustic Emission on Railroad Car Cushioning Devices V. Godinez and W.D. Jolly
Page 107	Methods of Calculating Attenuation and Dispersion Effects on Acoustic Emission Signals R. A. Kline and S. S. Ali
Page 115	Classification of Acoustic Emission Signals Generated during Welding Roger W.Y. Chan, D. Robert Hay, Victor Caron, Michel Hone and R. Douglas Sharp
Page 124	Conferences and Symposia
Page 124	The 2nd International Conference on AE/28th AEWG Meeting
Page 124	29th AEWG Meeting/AE Primer/The 8th International AE Symposium
Page 125	AE Training Course Announced
Page S333	Extended Abstracts from The Second International Conference on AE

Volume 5 (1986)

Number 1

- Page 1 Nondestructive Monitoring of Installed Refractories by Acoustic Emission David A. Bell
- Page 7 Improving the Reliability of Critical Parts by Acoustic Emission Surveillance during Proof Testing Edward Goliti
- Page 15 On the Applicability of Amplitude Distribution Analysis to the Fracture Process of Composite Materials Luis Lorenzo and H. Thomas Hahn
- Page 25 Detection, Measurements and Location of Partial Discharges in High Power Transformers using Acoustic Emission Method Jerzy Skubis, Jerzy Ranachowski and Boguslaw Gronowski
- Page 31 Is it Time for Acoustic Emission Surveillance of Operating Nuclear Reactors? W. F. Hartman
- Page 39 Fracture Toughness Measurement of a NiCrMoV Steel by Acoustic Emission V. Dal Re
- Page 45 Uncommon Cries of Cast Iron Elucidated by Acoustic Emission Analysis
Winfred Morgner and Hartmut Heyse
- Page 51 The XVth and XIVth EWGAE Meetings Roger Hill
- Page 53 ASTM E7.04 Meeting A. G. Beattie / French AE Codes / E. German AE Colloquium
- Page 54 The Second International Conference on AE from Reinforced Plastics
- Page ii 29th AEWG Meeting / AE Primer
- Page 50 Meeting Calendar
- Page i Appreciation K. Ono / European Perspective Roger Hill
- Page 6 Available Books on AE
- Page 14 EWGAE Provisional Form
- Page 59 Montreal Conference Information / Cover Photo
- Page 60 AE Training Courses

Number 2

- Page 61 Prediction of Lumber Checking during Drying by Means of Acoustic Emission Technique
Shigeru Ogino, Koji Kaino and Masahiko Suzuki
- Page 67 On the Acousto-Ultrasonic Characterization of Wood Fiber Hardboard
Henrique L. M. dos Reis and D. Michael McFarland
- Page 71 Effect of Moisture Conditioning on Acoustic Emission from Particleboard Frank C. Beall
- Page 77 Acoustic Emission During the Deformation and Fracture of Molybdenum at Low Temperatures
Jay B. James and Steve H. Carpenter
- Page 85 Acoustic Emission Produced by the Deformation of Uranium
C. R. Heiple and S. S. Christiansen
- Page 95 A Discussion of the Basic Understanding of the Felicity Effect in Fiber Composites
M. A. Hamstad
- Page 103 AE Literature - Concrete Thomas F. Drouillard
- Page 110 Book Review M. A. Hamstad
- Page 111 The 29th Meeting of Acoustic Emission Working Group
The Second International Symposium on Acoustic Emission from Reinforced Composites
XVth Meeting of The European Working Group of Acoustic Emission (EWGAE)
The 8th Int'l AE Symposium / The 30th Meeting of AEWG

Page 66	Acousto-Ultrasonics: Theory and Application
Page 94	Meeting Calendar
Page 102	The Second CARP Symposium
Page i	Cover Photograph
	AE Events of Interest
Number 3	
	A SPECIAL ISSUE ON AEWG AND EWGAE MEETINGS - EXTENDED ABSTRACTS
Page S1	The 29th Meeting of Acoustic Emission Working Group
Page S42	XVth Meeting of The European Working Group of Acoustic Emission (EWGAE)
Page 113	The 29th Meeting of Acoustic Emission Working Group (AEWG) XVth Meeting of The European Working Group of Acoustic Emission (EWGAE) The 8th International AE Symposium/ The 30th Meeting of AEWG Acousto-Ultrasonics: Theory and Application
Page 114	Program of The 29th Meeting of Acoustic Emission Working Group
Page 116	Abstracts of The 29th Meeting of Acoustic Emission Working Group
Page 121	Program of XVth Meeting of The EWGAE
Page 122	Program of The 8th International AE Symposium
Page 123	The 2nd International Symposium on AE from Reinforced Composites M. A. Hamstad
Number 4	
Page 124	The Generalized Theory and Source Representations of Acoustic Emission Masayasu Ohtsu and Kanji Ono
Page 134	More Recent Improvements on the NBS Conical Transducer Thomas M. Proctor, Jr.
Page 144	Nondestructive Evaluation of Adhesive Bond Strength Using the Stress Wave Factor Technique Henrique L. M. dos Reis and Harold E. Kautz
Page 148	A Note on the Prediction of Fatigue Life of Metal Structures by Use of the Felicity Effect J. W. Whittaker
Page 152	Vibro-Acoustic Emission in Plastic Bars A. E. Lord, Jr.
Page 156	Acoustic Emission Testing of Glass Fiber Reinforced Plastic Components R. Teti
Page 162	Correlation of Acoustic Emission to Microstructural Sources James Mohr and Amiya K. Mukherjee
Page 172	Acoustic Emission Characterization of Pinch Welds A. G. Beattie and C. W. Pretzel
Page 184	XVth EWGAE Meeting/ 8th Int'l AE Symp. DGM Symp. on AE/ 16th Symp. on NDE/ Prog. QNDE/ AE in Sci. & Tech. 30th AEWG Meeting/ Acousto-Ultrasonics/ XVIth EWGAE Meeting
Page 185	9th Int'l AE Symp./ 3rd Int'l AE Conf./ 3rd Int'l Symp. on AE - Composites
Page 186	Instruction for AEWG-EWGAE Extended Abstracts
Page S69	Abstract; XVth EWGAE Meeting
Page 155	Meeting Calendar
Page 143	Call for Papers - 30th AEWG Meeting and AEWG Short Course
Page 171	Registration Forms for 30th AEWG Meeting and AEWG Short Course
Page 185	Call for Papers/ Announcements/ AE Training Courses
Page 151	Available Books on AE
Page 161	Progress in Acoustic Emission III
Page i	AE Events of Interest
Page ii	Acoustic Emission of a Kouros Kanji Ono
Page I - 1	Index to Volume 5

Volume 6 (1987)

Number 1	
Page 1	Fracture-Induced Acoustic Emission during Slow Bend Tests of A533B Steel H.B. Teoh and Kanji Ono
Page 13	Real-Time Monitoring of Multi-Pass Welding by Acoustic Emission K. Ishihara and K. Yamada
Page 19	Application of Pattern Recognition Concepts to Acoustic Emission Signals Analysis C.R.L. Murthy, B. Dattaguru and A.K. Rao
Page 29	Punch Stretching Process Monitoring Using Acoustic Emission Signal Analysis--Part 1: Basic Characteristics Steven Y. Liang and David A. Dornfeld
Page 37	Punch Stretching Process Monitoring Using Acoustic Emission Signal Analysis - Part 2: Application of Frequency Domain Deconvolution Steven Y. Liang, David A. Dornfeld and Jackson A. Nickerson
Page 43	Modeling Concrete Damage by Acoustic Emission J.M. Berthelot and J.L. Robert
Page 61	Pattern Recognition Analysis of Acoustic Emission from Unidirectional Carbon Fiber-Epoxy Composites by using Autoregressive Modeling Masayasu Ohtsu and Kanji Ono
Page 73	A New Approach to the Use of Acoustic Emission Peak Amplitude Distribution as a Tool of Characterizing Failure Mechanisms in Composite Materials A. Mittelman and I. Roman
Page 84	Waveform Digitizers Kanji Ono
Page 79	30th AEWG Meeting/8th Int'l AE Symp. M. Ohtsu
Page 80	Int'l Conf. of NDE with AE Technology
Page 81	Letter to Editor/An Erratum/ AE Training Courses
Page 83	31st AEWG Meeting and AEWG Short Course
Page 83	Progress in Acoustic Emission III
Number 2	
Page 85	Acoustic Emission Wave Characterization: A Numerical Simulation of the Experiments on Cracked and Uncracked Specimens T. Aizawa, T. Kishi and F. Mudry
Page 93	Flaw Growth in Alumina Studied by Acoustic Emission M.A. Hamstad, P.M. Thompson and R.D. Young
Page 99	Acoustic Emission Characteristics in Concrete and Diagnostic Applications Masayasu Ohtsu
Page 109	Measurement of the Maximum Applied Loads to Automobile Components by Acoustic Emission Technique Tatsuhiko Yoshimura and Shigeto Kano
Page 115	Effects of Heat Treatment on the Acoustic Emission Generated During the Deformation of 7075- T651 Aluminum Alloy Zu-Ming Zhu and S.H. Carpenter
Page 121	An Overview of Acoustic Emission Codes and Standards J.C. Spanner, Sr.
Page 125	Acoustic Emission Applied to Pressure Vessels Brian R.A. Wood
Page 133	Third Symposium on AE W. Morgner
Page 133	Fourth European Conf. on NDT and 16th EWGAE
Page 135	AE Codes/Standards Activity within ASME and ASNT J. R. Mitchell
Page 136	Prof. S.H. Carpenter, 1987 University Lecturer
Number 3	
Page 137	Application of Acoustic Emission to the Field of Concrete Engineering Taketo Uomoto

Page 145	A Method of Rapidly Estimating the Fatigue Limits by Acoustic Emission Tatsuhiko Yoshimura and Shigeto Kano
Page 151	Preliminary Investigation of Acoustic Emission from Wood During Pyrolysis and Combustion Frank C. Beall
Page 157	Preliminary Investigation of the Feasibility of Using Acousto-Ultrasonics to Measure Defects in Lumber R.L. Lemaster and D.A. Dornfeld
Page 167	Development and Application of Acoustic Emission Methods in the United States - A Status Review P.H. Hutton
Page 177	Acoustic Emission Produced by Deformation of Metals and Alloys - A Review: Part I C. R. Heiple and S.H. Carpenter
Page 205	30th Meeting of AEWG D.M. Egle and R.A. Kline
Page 205	A Brief Note on the Kaiser and Felicity Effects R.A. Kline and D.M. Egle
Page 206	The Third Int'l Workshop on Composite Materials / The Sixth (Japanese) Conference on AE
Page 166	31st Meeting of AEWG
Page 156	Available Books on AE
Page 176	Cover Photograph
Page 208	AE Training Courses/Announcements
Number 4	
Page 209	The Application of Acoustic Emission Techniques in High-Temperature Oxidation Studies A. S. Khanna, B. B. Jha and Baldev Raj
Page 215	Acoustic Emission Produced by Deformation of Metals and Alloys - A Review: Part II C. R. Heiple and S.H. Carpenter
Page 239	Acoustic Emission During Deformation and Crack Initiation of Pipeline Steels M. W. Drew, B. R. A. Wood and R. W. Harris
Page 249	Acoustic Emission Waveform Analysis to Identify Fatigue Crack Propagation in a Mirage Aircraft C. M. Scala and R. A. Coyle
Page 257	The Detection of Hydrogen-Assisted-Crack Formation in U - 0.8% Ti Alloy Electron-Beam Weldments J. W. Whittaker and M. W. Richey
Page 261 by	The Detection of the Fracture of Autoclaved Aerated Concrete during Autoclave Curing Process Acoustic Emission Satoshi Teramura, Koichi Tsukiyama and Hideaki Takahashi
Page 267	31st Meeting of AEWG - Abstracts
Page 273	Meetings on AE and related topics
Page 238	9th Int'l AE Symp/World Meeting on AE
Page 256	Cover Photograph
Page 273	INDEX to Volume 6

Volume 7 (1988)

Number 1	
Page 1	Evaluation of Fracture Toughness of Autoclaved Lightweight Concrete by Means of Acoustic Emission Technique, Satoshi Teramura, Koichi Tsukiyama and Hideaki Takahashi
Page 9	Identification of Crack Propagation Modes in 304 Stainless Steel by Analysis of Their Acoustic Emission Signatures Daniel R. Smith Jr. and Steve H. Carpenter

Page 21	A New Sensor for Quantitative Acoustic Emission Measurement Chung Chang and C. T. Sun
Page 31	Acoustic Emission Propagation and Source Location in Small, Spherical Composite Test Specimens J. W. Whittaker, W. D. Brosey, O. Burenko and D. A. Waldrop
Page 41	A High Fidelity Piezoelectric Tangential Displacement Transducer for Acoustic Emission Thomas M. Proctor, Jr.
Page 49	Acoustic Emission from Fatigue Cracks in Chrome-Molybdenum Steel Cylinders P.R. Blackburn
Page 57	31st Meeting of AEWG
Page 20	Meeting Schedule
Page 40A	World Meeting on AE
Page 48	Instructions to Authors - World Meeting on AE
Page 30	Books Available
Number 2	
Page 59	Acoustic Emission Measurements on PWR Weld Material with Inserted Defects using Advanced Instrumentation P. G. Bentley and M. J. Beesley
Page 81	Acoustic Emission Measurements on PWR Weld Material with Inserted Defects C. B. Scruby and K. A. Stacey
Page 95	Characterization of Acoustic Emission from Thermally-Cycled Lithium Hydride J. W. Whittaker and D. G. Morris
Page 103	Apparatus for Coupling an Acoustic Emission Transducer to a Rotating Circular Saw Richard L. Lemaster and David A. Dornfeld
Page 111	Measurement of Density Profiles in Wood Composites Using Acoustic Emission Richard L. Lemaster, Michael F. Gasick and David A. Dornfeld
Page 119	Acoustic Emission during Intergranular Stress Corrosion Cracking of Iron M. A. Friesel and R. H. Jones
Page 129	XVIIth Meeting of EWGAE - Program
Page 129	The 9th International Symposium on AE - Program
Page 80	Meeting Schedule
Page 94	World Meeting on AE
Page 102	Books Available/Training Courses
Number 3	
Page 135	Acoustic Emission from Porous Films of Aluminum Oxide during the Application of Electrical Voltage J. Sampath Kumar and S.P. Mallikarjun Rao
Page 139	Third Domestic Conf. on Subsurface Acoustic Emission (Sendai, Japan) - Program
Page 140	Acoustic Emission (UK) - Abstracts
Page 141	Seminar on Acoustic Emission (India) - Abstracts
Page S1	Extended Abstracts of Presentations at AEWG(I) Seminar on ACOUSTIC EMISSION Acoustic Emission during Tensile Deformation and Fracture in Austenitic Stainless Steels Baldev Raj and T. Jayakumar
Page S13	Detection of Breakaway Oxidation of Zircaloy-2 by Acoustic Emission Technique B. K. Gaur, A. K. Sinha, B. K. Shah, P. G. Kulkarni and R. Vijayaraghavan
Page S18	Magnetomechanical Acoustic Emission Behaviour of Some Structural Steels

	S. G. Savanur and C. R. L. Murthy
Page S29	A Study of Acoustic Emission Activity in Granites during Stress Cycling Experiments M.V.M.S. Rao
Page S35	Acoustic Emission Studies on Adhesive Potted Inserts of Honeycomb Sandwich Panels T.S. Sriranga and R. Samuel
Page S40	Location of Weld Defects by Acoustic Emission G.L. Goswami and P.R. Roy
Page S43	Thermally Induced Relaxation Behaviour in a Metallic Glass G. L. Goswami, S. K. Jha and G. P. Tiwari
Page S47	Meeting Schedule/Training Courses
Page S48	Announcements
Number 4	
Page 145	Acoustic Emission During Quasi-Static Loading/Hold /Unloading in Notched Reinforced Fiber Composite Materials S. V. Hoa and L. Li
Page 161	The Acoustic Emission Generated during the Plastic Deformation of High Purity Zinc S. H. Carpenter and Chung-Mei Chen
Page 167	Evaluation of Concrete Structure Deterioration via AE Observation of Core Tests Masayasu Ohtsu, Tatsuro Sakimoto, Yutaka Kawai and Syuro Yuji
Page 173	Diagnosis of Rotating Slides in Rotary Compressors using Acoustic Emission Technique Ichiya Sato, Takao Yoneyama, Kouichi Sato, Toshiyuki Tanaka and Hiroaki Hata
Page 179	AE-Monitoring Systems for the Detection of Single-Point and Multipoint Cutting Tool Failures Thomas Blum, Ippei Suzuki and Ichiro Inasaki
Page 185	Direct Measurement of Water Hammer Pressure by AE Source Wave Analysis Mikio Takemoto and Yasuhisa Hayashi
Page 193	Acoustic Emission from an Industrial Applications Viewpoint Trevor J. Holroyd
Page 201	Downhole AE Measurement Technique and Its Application to Geothermal Fields Hiroaki Niitsuma
Page 211	Acoustic Emission Source Location in Fiber Reinforced Plastic Composites D. J. Buttle and C. B. Scruby
Page 225	The Acoustic Emission Source Mechanism for Fatigue Crack Propagation in 7075 Aluminum S. L. McBride, P. Bowman and K. I. McRae
Page 231	Conferences and Symposia
Page 231	Third International Symposium on AE from Composite Materials/EWGAE Meeting
Page 192	Meeting Schedule
Page 200	Books Available
Page 210	Progress in AE IV, Proc. The 9th International AE Symposium
Page 224	The World Meeting on AE/ASNT Recognition/Codes and Standards Committee
Page I-1	Index to Volume 7

Volume 8 (1989)

Numbers 1 and 2

Pages S1-S338 **Proceedings of the World Meeting on Acoustic Emission, March 20-23, 1989**

- S1 "Acoustic Emission Technology using Multi-parameter Analysis of Waveform and the Applications to Fracture Modes and Growth Recognition in Composites", K. Yamaguchi, H. Oyaizu, J. Johkaji and Y. Kobayashi
- S4 "Acoustic Emission Detection of Crack Presence and Crack Advance During Flight", S. L. McBride, M. D. Pollard, J. D. MacPhail, P. S. Bowman and D. T. Peters
- S8 "Time-frequency domain (3-D) Analysis of AE Signals using Simple Instrumentation Techniques", S. V. Subba Rao, K. V. Srincivasan and M. Annamalai
- S12 "Improving Acoustic Emission Crack/Leak Detection in Pressurized Piping by Pattern Recognition Techniques", R. W. Y. Chan, D. R. Hay, J. R. Hay and H. B. Patel
- S16 "An Efficient Unsupervised Pattern Recognition Procedure for Acoustic Emission Signal Analysis", M. A. Majeed and C. R. L. Murthy
- S20 "Solving AE Problems by a Neural Network", I. Grabec and W. Sachse
- S24 "The General Problems of AE Sensors", Y. Higo and H. Inaba
- S28 "Acoustic Emission Transducer Modelling Using System Identification Techniques", S. Kallara, P. K. Rajan and J. R. Houghton
- S32 "Design of 3-Dimensional AE/MS Transducer Arrays", M. Ge and H. R. Hardy
- S38 "Simultaneous Velocity Tomography and Source Location of Synthetic Acoustic Emission Data", S. C. Maxwell, R. P. Young, and D. A. Hutchins
- S42 "Use of Mechanical Waveguides and Acoustic Antennae in Geotechnical AE/MS Studies", H. R. Hardy, Jr., F. Taioli and M. E. Hager
- S49 "Linear Location of AE Simulated Sources on Steel Pipelines with Waveguides", B. Q. Zhang
- S53 "AE Application and Recent Results on Nuclear Components", P. Jax and V. Streicher
- S57 "Acoustic Emission from Steel Structures", A. Nielsen
- S62 "AE Role in the Diagnosis and Prognosis of Defects in Industrial Plant Steel Components", F. Tonolini
- S66 "Structural Integrity Evaluation Using Acoustic Emission Techniques", B. R. A. Wood and R. W. Harris
- S70 "On-line Application of Acoustic Emission Analysis", W. Morgner
- S71 "AE - For when you absolutely cannot afford a Failure of a Critical Pressure Boundary", H. L. Dunegan
- S75 "Periodic Inspection of Compressed Gas Cylinders and Transport Vessels by Using Acoustic Emission Testing", H. Barthelemy
- S79 "Locating Fatigue Cracks by Acoustic Emission Testing", P. M. Horrigan, J. F. Finn, F. R. Tuler and J. H. Smith
- S84 "A New Acoustic Emission Measurement System and its Application to the Local Monitoring of a Crack in a Pressure Vessel", B. Tirbonod and L. Hanacek
- S88 "An Approach for the Integrity Assessment of M250 Maraging Steel Pressurized Systems", T. Chelladurai, R. Krishnamurthy and A. R. Acharya

- S93 "Detectability of Defects in Reactor Pressure Components by Location and Interpretation of AE-Sources", C. Sklarczyk and E. Waschkies,
- S97 "Application of Acoustic Emission Technique during In-service Pressure Vessel Inspection", S. Liu, G. Shen, Y. Wan and Q. Duan
- S101 "Acoustic Emission Leak Monitoring in Pressurized Piping", H. B. Patel and A. W. Cook
- S103 "Application of Acoustic Emission Technique in the High-temperature Oxidation Studies – A Review", A. S. Khanna
- S105 "Acoustic Emission during Phase Transformation in Cr12MoV Steel and Fe-33Ni-4Ti-10Co Alloy", B. Q. Zhang, C. K. Yao and C. G. Jiao
- S109 "Effect of Pre-exposure to Water on the Acoustic Emission Behavior of 2091-T3 Al-Li Alloy", F. M. Zeides and I. Roman
- S114 "Acoustic Emission from Weld-seam of 16MnR Steel during Stress Corrosion", B. Q. Zhang and J. Q. Sun
- S118 "The Influence of Crack Front Geometry on Acoustic Emission During Fatigue of Al2024-T351", F. A. Veer and J. Zuidema
- S122 "Acoustic Emission Monitoring of Incipient Crack Propagation and its Growth Rate in EN-24 Steel under Fatigue", S. C. Pathak and C. R. L. Murthy
- S126 "Acoustic Emission during Tensile Deformation and Fracture in Austenitic Alloys", B. Raj and T. Jayakumar
- S131 "Relationship between Acoustic Emission and Flaw Size in Si₃N₄ Ceramics", Y. Mori, M. Nishino, K.-I. Aoki, T. Kishi and K. Kitadate
- S135 "A Comparison of the Acoustic Emission Generated from the Fracture and Decohesion of Graphite Nodules with Theoretical Predictions", S. H. Carpenter and Z. Zhu
- S140 "Influence of Grain Size on Frequency Spectra of AE Signal Generated during Tensile Deformation in an AISI Type 316 Stainless Steel", B. Raj, P. Kalyanasundaram, T. Jayakumar, P. Barat and P. Rodriguez
- S145 "Evaluation of Fatigue Crack Growth Rate of Carburized Gear by Acoustic Emission Technique", Y. Obata, H. Kobayashi, K. Aoki, T. Yamaguchi and K. Shibata
- S149 "Acoustic Emission Investigations in Poland", J. Ranachowski, Poland "Comparative Studies on Acoustic Emission Generated During Lüder's Deformation in Mild Steel and Portevin-Le Chatelier Effect in Austenitic Stainless Steel", B. Raj, T. Jayakumar, P. Kalyanasundaram, P. Barat, B. B. Jha, D. K. Bhattacharya, P. Rodriguez
- S154 "Development and Future Aspects in AE Source Characterization", M. Enoki and T. Kishi
- S158 "AE Source Modelling-Comparison of Inversion and Forward Techniques", D. J. Buttle and C. B. Scruby
- S162 "Source Inversion of Acoustic Emission for the Determination of Crack Kinematics and Kinetics", M. Ohtsu
- S166 "Acoustic Emission Analysis and Ultrasonic Velocity Imaging in the Study of Rock Failure", S. D. Falls, T. Chow, R. P. Young and D. A. Hutchins

- S170 "Thin-Film Acoustics: Line and Point Sources Generation and the Testing of thin Films", K. Y. Kim and W. Sachse
- S175 "Acousto-Ultrasonics: An Update", A. Vary
- S179 "Theoretical Basis of Acousto-Ultrasonics", M. T. Kiernan and J. C. Duke
- S184 "Fracture of Boron Particles in 2219 Aluminum as a Known Acoustic Emission Source", C. R. Heiple, S. H. Carpenter and S. S. Christiansen
- S188 "Surface Analysis by Tribo-acoustic Emission", M.-K. Tse and P.-Y. Gu
- S192 "Acoustic Emission Measurements of Rubbing Surfaces", S. L. McBride, R. J. Boness, M. Sobczyk and M. R. Viner
- S197 "Vibro-Acoustic Emission Rubbing Sources", J. R. Webster
- S201 "Acoustic Characterisation of Small Particle Impact", D. J. Buttle and C. B. Scruby
- S205 "Estimation of Impact Force between Rough Surfaces by Means of Acoustic Emission", I. Kukman and I. Grabec
- S209 "Acoustic Emission Monitoring of Magnetic Hard Disks during Accelerated Wear Testing", J. C. Briggs, M. M. Besen and M.-K. Tse
- S213 "Applications of Acoustic Emission Techniques for Diagnosis of Large Rotating Machinery and Mass Products", I. Sato, T. Yoneyama, K. Sato, T. Tanaka, M. Yanagibashi and K. Takigawa
- S217 "Quality Inspection of Rolling Element Bearings using Acoustic Emission Technique", V. Bansal, A. Prakash, V. A. Eshwar and B. C. Gupta
- S219 "Stress Wave Sensing - Affordable AE for Industry", T. J. Holroyd
- S223 "Cavitation Monitoring of Hydroturbines with True-RMS Acoustic Emission Measurement", O. Derakhshan, J. R. Houghton, R. K. Jones and P. A. March
- S227 "Monitoring of the Cutting Process by Means of AE Sensor", D. A. Dornfeld
- S231 "Tool Monitoring by Acoustic Emission", J. Roget, P. Souquet, M. Deschamps and N. Gsib
- S236 "MONPAC - An Acoustic Emission based System for Evaluating the Structural Integrity of Metal Vessels", T. J. Fowler, J. A. Blessing and T. L. Swanson
- S238 "ICI's Perspective on Acoustic Emission Monitoring", S. Hewerdine
- S239 "MONPAC - Condition Monitoring for Static Plant - Case Histories", P. T. Cole
- S240 "Acoustic Emission Monitoring of a Large Pressure Vessel during a Pneumatic Re-Qualification Test", M. Peacock
- S241 "Summary of Experiences with MONPAC Testing by MQS/Dunegan Testing Group", R. K. Miller
- S242 "Microseismics and Geotechnical Applications", M. Ohtsu
- S246 "Acoustic Emission Phenomena in Geological Media", R. A. Kline, A. S. Khan, Y. Xiang, J. Shlyapobersky and F. Irani

- S250 "Acoustic Emission/Microseismic Activity at very low Strain Levels", B. H. Armstrong
- S254 "Focal Mechanism Determinations for a Sequence of Mining-Induced Seismic Events Recorded at a Hard Rock Mine", T. I. Urbancic, S. Talebi and R. P. Young,
- S258 "Effects of Porosity on Acoustic Emission Signatures", R. J. Watters and D. M. Chuck
- S262 "Acoustic Emission Monitoring and Analysis Procedures Utilized during Deformation Studies on Geologic Materials", X. Sun, H. R. Hardy, Jr. and M. V. M. S. Rao
- S266 "PDP 11/34 Based Microseismic Monitoring System for Kolar Gold Fields, India", G. Jayachandran Nair
- S268 "Fracture Mechanism Studies of Carbon/PMR-15 Composites by Acoustic Emission", J. S. Jeng, K. Ono and J. M. Yang
- S272 "Assessment of Fatigue Damage in Carbon Fibre Reinforced Epoxy Laminates with the Energy Discriminating Acoustic Emission Method", M. Wevers, I. Verpoest, P. De Meester and E. Aernoudt,
- S276 "NDE Procedure for Predicting the Fatigue Life of Composite Structural Members", M. J. Sundaresan, E. G. HennekeII and A. Gavens
- S280 "Detection of Impact Damage in Composite Structures by Use of Thermally-activated Acoustic Emission", J. W. Whittaker and W. D. Brosey
- S284 "Characterization of Failure Modes in Glass Fibre Reinforced Plastic Composites", M. N. Raghavendra Rao and C. R. L. Murthy
- S288 "Spectrum Analysis of Acoustic Emission Signals from Carbon-Glass Hybrid Composites", M. R. Madhava and H. N. Sudheendra
- S292 "Analysis of AE Signals in Time and Frequency Domains Coupled to Pattern Recognition to Identify Fracture Mechanisms in CFRP", A. Maslouhi and C. Roy
- S297 "Some New Results in the Damage Identification in Kevlar-Epoxy Composites", D. S. Rajan, N. Kishore and B. D. Agarwal
- S301 "Monitoring Initiation and Growth of Matrix Splitting in a Uni-directional Graphite/Epoxy Composite", S. Ghaffari and J. Awerbuch
- S306 "Correlation of Internal Bond Strength of Particleboard with Acousto-Ultrasonics", A. T. Green
- S311 "Acoustic Emission during Contact Drying of Southern Pine Veneer", F. C. Beall
- S314 "Nondestructive Evaluation of Adhesively Bonded Joints using Acousto-Ultrasonics", S. Tanary, A. Fahr and Y. Haddad
- S317 "AE Research on Adhesion in Composite Materials", H. G. Moslé
- S318 "Acoustic Emission Testing of Flexed Concrete Beams Reinforced with Bonded Surface Plates", D. P. Henkel and J. D. Wood
- S322 "Acoustic Emission Investigation into some Concrete Construction Problems", J. D. Leaird and M. A. Taylor
- S326 "Correlation of AE and Fracture Intensity during Impact Indentation of Coal Block", S. J. Jung and A. W. Khair

S330	"Acoustic Emission Monitoring of Pressure Vessel Preventing Catastrophic Failure", S. F. Botten
S334	Limiting State Prediction from AE Signals for Large-size Structures under Static, Cyclic and Thermocyclic Loads, V.A. Strizhalo and V.A. Strelchenko
S337	Authors Index
Number 3	
Page 1	The MONPAC System Timothy J. Fowler, James A. Blessing, Peter J. Conlisk and Terry L. Swanson
Page 11	Acoustic Emission Monitoring of a Large Pressure Vessel during a Pneumatic Re-qualification Test M. J. Peacock
Page 21	ICI's Perspective on Acoustic Emission Monitoring S. Hewerdine
Page 25	A Summary of Experiences with MONPAC™ Testing by the MQS/Dunegan Testing Group R.K. Miller, R.G. Tobin, D.J. Gross and D.T. Tran
Page 31	MONPAC - Condition Monitoring for Static Plant - Case Histories Phillip T. Cole
Page 35	Detection of an Impulse Force in Head-Disk Media Contact using Small Piezoelectric Transducer Kenji Mochizuki, Isamu Sato and Takefumi Hayashi
Page 41	Investigations of Sensor Placement for Monitoring Acoustic Emission in Machining David V. Hutton and Qing Huan Yu
Page 47	Use of Plane-Strain Compression for the Diagnosis of Acoustic Emission Source during Plastic Deformation F. Zeides and I. Roman
Page 51	Transverse Cracking and Longitudinal Splitting in Graphite/Epoxy Tensile Coupons as Determined by Acoustic Emission Steven M. Ziola and Michael R. Gorman
Page 8	Cover Photographs
Page 9	Meeting Calendar -- 33rd AEWG Meeting, 10th IAES, Kumamoto Workshops
Page 61	Third International Symposium on AE from Composite Materials (AECM-3)
Page 61	EWGAE Meeting/Future Meetings/Errata
Page 34	The Status of EWGAE Panel on Standards J. Roget /Codes and Standards Committee
Page 20, 30, 40	Abstracts of Third International Symposium on AE from Composite Materials (AECM-3)
Page 50, 50, 62	Selected Abstracts of AECM-3 (continued)
Number 4	
Page 65	A Review of International Research Relative to the Geotechnical Field Application of Acoustic Emission/ Microseismic Techniques H. Reginald Hardy, Jr.
Page 93	A Review of Acoustic Emission in Civil Engineering with Emphasis on Concrete Masayasu Ohtsu
Page 99	Application of Acoustic Emission for the Evaluation of Microseismic Source Location Techniques M. Kat and F. P. Hassani
Page 107	Acoustic Emission Characteristics of Unstable Slopes A. Chichibu, K. Jo, M. Nakamura, T. Goto and M. Kamata
Page 113	Experimental Studies on the Effect of Stress History on Acoustic Emission Activity – A Possibility for Estimation of Rock Stress Sumio Yoshikawa and Kiyoo Mogi

Page 125	Acoustic Emission from Phase Transformations in Au - 47.5 at. % Cd C. R. Heiple and S. H. Carpenter
Page 135 Wood	The Effect of Same-side and Through-Thickness Transmission Modes on Signal Propagation in Richard L. Lemaster and Stephen L. Quarles
Page 92	Meeting Schedule
Page 143	Abstracts of Third International Symposium on AE from Composite Materials
Page 200	EWGAE Meeting/AEWG -33 Books Available
Page 210	Progress in Acoustic Emission IV, Proc. The 9th International AE Symposium
Page I-1	Index to Volume 8

Volume 9 (1990)

Number 1

Page 1	Origin of Acoustic Emission Produced during Deformation of Beryllium C. R. Heiple and S. H. Carpenter
Page 9	Optimal Waveform Feature Selection Using a Pseudo-Similarity Method K. J. Siddiqui, Y.-H. Liu, D. R. Hay and C. Y. Suen
Page 17	The Effect of Same-Side and Through-Thickness Transmission Modes on Signal Propagation in Wood Richard L. Lemaster and Stephen L. Quarles
Page 25	Defect Detection in Rolling Element Bearings by Acoustic Emission Method N. Tandon and B. C. Nakra
Page 29	Monitoring of a Pressure Vessel (ZB2) by means of Acoustic Emission H.-A. Crostack and P. Böhm
Page 37	A Procedure for Acceptance Testing of FRP Balsa Wood Core Pressure Vessels P. Ouellette, S.V. Hoa and L. Li
Page 45	AE Literature A Comprehensive Guide to the Literature on Acoustic Emission from Composites, Supplement II Thomas F. Drouillard
Page 69	Conferences and Symposia Abstracts of 33rd Acoustic Emission Work Group Meeting
Page 72	ASNT Spring Conference
Page 73	1st International Conf. on AE in Manufacturing, AECM-4
Page 8	Available Books on AE
Page 31	Cover Photograph
Page ii	Meeting Calendar
Number 2	Composites
Page 75	Felicity Ratio Behavior of Pneumatically and Hydraulically Loaded Spherical Composite Test Specimens J. W. Whittaker, W. D. Brosey and M. A. Hamstad
Page 84	Correlation of Felicity Ratio and Strength Behavior of Impact-Damaged Spherical Composite Test Specimens J. W. Whittaker, W. D. Brosey and M. A. Hamstad
Page 91	Delayed Acoustic Emission: A Rheological Approach N. Rochat, R. Fougères and P. Fleischmann
Page 97	Acoustic Emission Analysis of the Accumulation of Cracks in CFRP Cross-ply Laminates under

	Tensile Loading	J.-P. Favre and J.-C. Laizet
Page 103	Analysis of Acoustic Emission Events from Single Fiber Pullout Experiments	W. Mielke, A. Hampe, O. Hoyer and K. Schumacher
Page 109	Digital Signal Analysis of Acoustic Emission from Carbon Fiber/ Epoxy Composites	Kanji Ono and Kenji Kawamoto
Page 117	Acoustic Emission: A Micro-Investigation Technique for Interface Mechanisms in Fiber Composites	D. Rouby
Page 123	Acoustic Emission Characterization of the Deformation and Fracture of an SiC-Reinforced, Aluminum Matrix Composite	Oh-Yang Kwon and Kanji Ono
Page 131	Burst Prediction by Acoustic Emission in Filament-Wound Pressure Vessels	Michael R. Gorman
Page 140	Critical AE Problems for the Researcher	Adrian A. Pollock
Page 142	Quality Inspection of Rolling Element Bearing using Acoustic Emission Technique	Vibha Bansal, B.C. Gupta, Arun Prakash and V.A. Eshwar
	Conferences and Symposia	
Page 147	XIX Meeting of EWGAE, 10th International Acoustic Emission Symposium	
Page 152	1st Symp. Evaluation of Adv. Materials by AE	
Page 153	Intl Joint Meeting at Kumamoto	
Page 154	Korean Working Group on Acoustic Emission (KWGAE), AE Training Courses	
Page 122	Meeting Schedule	
Page 130	34th AEWG Meeting	
Page 154	Cover Photograph	
Number 3		
	Wood	Frank C. Beall, Topical Editor
Page 155	Anecdotal History of Acoustic Emission from Wood	Thomas F. Drouillard
Page 177	An Experiment on the Progression of Fracture (A Preliminary Report)	Fuyuhiko Kishinouye (Translated by Kanji Ono)
Page 181	Acoustic Emission from Drought-Stressed Red Pine (Pinus resinosa)	Robert A. Haack and Richard W. Blank
Page 189	The Effect of Moisture Content and Ring Angle on the Propagation of Acoustic Signals in Wood	Stephen L. Quarles
Page 197	Nondestructive Evaluation of Adhesive Bond Strength of Finger Joints in Structural Lumber Using the Acousto-Ultrasonic Approach	Henrique L. M. dos Reis, Frank C. Beall, Michael J. Chica and Dick W. Caster
Page 203	Determining the Abrasiveness to Tools of Wood-Based Composites with Acoustic Emission	Richard L. Lemaster
Page 209	Lumber Stress Grading utilizing the Acoustic Emission Technique	Keiichi Sato, Hajime Takeuchi, Katsuya Yamaguchi, Naoto Ando and Masami Fushitani
Page 215	AE Literature - Wood	Thomas F. Drouillard and Frank C. Beall
	Conferences and Symposia	
196, 214, 223	10th International Acoustic Emission Symposium (abstracts)	
Page 226	Intl Joint Meeting at Kumamoto/ KWGAE/ 34th AEWG Meeting, AE Training Courses	
Page 188	Meeting Schedule	

Page 180	Fuyuhiko Kishinouye (biography) / Cover Photograph
Number 4 Page 227	Detection of Irradiation Effects on Reactor Vessel Steels by Magneto-Acoustic Emission Oh-Yang Kwon and Kanji Ono
Page 237	New Algorithm for Acoustic Emission Source Location in Cylindrical Structures Dong-Jin Yoon, Young H. Kim and Oh-Yang Kwon
Page 243	Characterization of Fatigue of Aluminum Alloys by Acoustic Emission, Part I - Identification of Source Mechanism D. J. Buttle and C. B. Scruby
Page 255	Characterization of Fatigue of Aluminum Alloys by Acoustic Emission, Part II - Discrimination Between Primary and Other Emissions D. J. Buttle and C. B. Scruby
Page 271	Acoustic Emission Source Location Using Simplex Optimization M. P. Collins and R. M. Belchamber
Page 277	Acoustic Emission during Lumber Drying S. Ogino, K. Kaino and M. Suzuki
Page 283	AE Source Orientation by Plate Wave Analysis Michael R. Gorman and William H. Prosser
Page 289	Conferences and Symposia 10th International AE Symp.
Page 270	Cover Photograph AE Inspection of Monorail Trains
Page 276A	Meeting Calendar
I-i	Index to Volume 9

Volume 10 (1991/92)

Number 1/2 Page i	Current Research and Future Trend of AE Applications to Civil Engineering and Geological Technology Masayasu Ohtsu, Topical Editor
S1-S12	Variety of Acoustic Emission Waveforms Produced by Discrete Crack Growth in Rock Steven D. Glaser and Priscilla P. Nelson
S13-S17 Signals	Estimation of Maximum Stress in Old Railway Riveted I-Girder Bridges using Acoustic Emission Hisanori Otsuka, Hiroshi Hikosaka, Hiroyuki Miyatake and Syouzou Nakamura
S18-S21	Another Look at Booming Sand Marcel F. Leach and Gottfried A. Rubin
S22-S28	Expected Acoustic Emission from Around a Shaft in Intact Rock B.J.S. Wilkins and G.L. Rigby
S29-S34	Acoustic Emission Monitoring during Microseismic Activity Caused by Mine Subsidence Brian R. A. Wood and Robert W. Harris
S35-S41	Acoustic Emission/Microseismic Activity Monitoring of Salt Crystallization for Stone Conservation M. Montoto, R.M. Esbert, L.M. Suárez del Río, V.G. Ruiz de Argandoña and C.M. Grossi
S42-S48	Acoustic Emission Monitoring during In-situ Heater Test of Granite T. Ishida, K. Kitano, N. Kinoshita and N. Wakabayashi
S49-S54	Using Acoustic Emission Testing in Seepage Investigations Andrew R. Blystra

S55-S58	Acoustic Emission of Penetration Experiments to Judge Soil Condition S. Naemura, M. Tanaka, S. Nishikawa, M. Nakamura, K. Jo and T. Kishishita
S59-S62	A Laboratory Investigation of AE from Coal R. W. Harris, B. R. A. Wood and T. Flynn
S63-S76	Determination of the Initial Stresses on Rock Mass using Acoustic Emission Method K. Michihiro, K. Hata, H. Yoshioka and T. Fujiwara
S77-S89	U.S. Bureau of Mines Research on the Kaiser Effect for Determining Stress in Rock Michael J. Friedel and Richard E. Thill
S90-S96	Evaluation of Joint Properties of Anti-washout Underwater Concrete by Acoustic Emission Measurement Kazuya Miyano, Tatsuo Kita, Yuji Murakami and Takako Inaba
S97-S103	Automated Determination of First P-Wave Arrival and Acoustic Emission Source Location E. Landis, C. Ouyang and S. P. Shah
S104-S109	Application of Acoustic Emission Techniques in the Evaluation of Frost Damage in Mortar Hisatoshi Shimada and Koji Sakai
Number 3/4 Pages 1-11	Acoustic Emission of the 45HNMF A Structural Steel during Low-Cycle Fatigue J. Siedlaczek, S. Pilecki and F. Dusek
Pages 13-17	Parameter Estimation in Acoustic Emission Signals C. E. D'Attellis, L. V. Perez, D. Rubio and J. E. Ruzzante
Pages 19-23	Acoustic Emission Technique at Proof Tests of Nuclear Pressure Vessels in Hungary Peter Pellionisz and János Geréb
Pages 25-29	Effects of Wave Velocity Change on Magnetomechanical AE in Sintered Iron Noboru Shinke and Yoshitugu Ohigashi
Pages 31-33	Origin of Acoustic Emission in Naturally Aged Aluminum-Lithium Alloys F. Zeides and I. Roman
Pages 35-41	Analysis of Artificial Acoustic Emission Waveforms Using a Neural Network Hironobu Yuki and Kyoji Homma
Pages 43-48	Source Force Waveforms: The Use of a Calibrated Transducer in Obtaining an Accurate Waveform of a Source Thomas M. Proctor, Jr. and Franklin R. Breckenridge
Pages 49-60	Acoustic Emission Monitoring of a Fatigue Test of an F/A-18 Bulkhead C. M. Scala, J. F. McCardle and S. J. Bowles
Pages 61-65	Maximum Curvature Method: A Technique to Estimate Kaiser-Effect Load from Acoustic Emission Data M. Momayez, F. P. Hassani and H. R. Hardy, Jr.
Pages 67-70	Acoustic Emission Measurements on Bridges H. Hick, H. Willer, E. Winter and F. Simacek
Pages 71-82	Acoustic Emission Monitoring of the Sensitivity of Chemicals to Impact Timothy G. Crowther, Adrian P. Wade and Nancy Brown
Pages 83-89	Study of Acoustic Emission Generation in Sliding Motion Musa K. Jouaneh, Richard Lemaster and Frank C. Beall
Pages 91-95	The Role of Acoustic Monitoring as a Diagnostic Tools in Nuclear Reactors

Shahla Keyvan and Ron King

Pages 97-101	Acoustic Emission Produced by Sliding Friction and its Relationship to AE from Machining S. H. Carpenter, C. R. Heiple, D. L. Armentrout, F. M. Kustas and J. S. Schwartzberg	
Pages 103-106	Comments on the Origin of Acoustic Emission in Fatigue Testing of Aluminum Alloys C. R. Heiple, S. H. Carpenter and D. L. Armentrout	
Pages 107-111	Acoustic Emission of Wood during Swelling in Water Stefan Poliszko, Waldemar Molinski and Jan Raczkowski	
Pages 113-116	Characterization of the ASL Parameter J. W. Whittaker	
Pages 117-121	Acoustic Emission from Bubbles in a Water Column, Mark A. Friesel and Jack F. Dawson	
Pages 122-124	In Memoriam, Dr. Raymond W. B. Stephens (1902-1990)	
	Conferences and Symposia	
12, 18, 24, 30, 34	Progress in Acoustic Emission VI, Proceedings of The 11th International AE Symposium	
42, 66, 90, 96, 102	36th Meeting of Acoustic Emission Working Group	
Page I-i	Index to Volume 10	

Volume 21, 2003

21-001	Identifying Acoustic Emission Sources In Aging Bridge Steel Takao Kobayashi And Donald A. Shockey	1
21-014	Analysis Of Source Location Algorithms, Part I: Overview And Non-Iterative Methods Maochen Ge	14
21-029	Analysis Of Source Location Algorithms, Part Ii: Iterative Methods Maochen Ge	29
21-052	Wavelet Transform Signal Processing To Distinguish Different Acoustic Emission Sources K. S. Downs, M. A. Hamstad And A. O’Gallagher	52
21-070	Practical Aspects Of Acoustic Emission Source Location By A Wavelet Transform M. A. Hamstad, K. S. Downs And A. O’Gallagher	70
21-A01	Appendices: Practical Aspects Of Acoustic Emission Source Location By A Wavelet Transform M. A. Hamstad, K. S. Downs And A. O’Gallagher	A1
21-095	Acoustic Emission Monitoring Of A High Pressure Test Of A Steel Reactor Containment Vessel Model A. G. Beattie	95
21-112	Micro-Cracking And Breakdown Of Kaiser Effect In Ultra High Strength Steels Hideo Cho, Kenzo Fukaura And Kanji Ono	112
21-120	Acoustic Emission From The Fracture Of Atmospheric Rust M. Takemoto, T. Sogabe, K. Matsuura And K. Ono	120
21-131	Acoustic Property Of Cvd-Diamond Film And Acoustic Emission Analysis For Integrity Evaluation R. Ikeda, Y. Hayashi And M. Takemoto	131

21-142	Evaluation Of Coated Film By Laser-Based Ae-Ut Technique M. Enoki And T. Kusu	142
21-149	Acoustic Emission From Micro-Fracture Processes Of Bio-Ceramics In Simulated Body Environment Shuichi Wakayama, Teppei Kawakami, Satoshi Kobayashi, Mamoru Aizawa And Akira Nozue	149
21-157	Corrosion Monitoring In Reinforced Concrete By Acoustic Emission Masayasu Ohtsu And Yuichi Tomoda	157
21-166	Evaluation Of Bond Behavior Of Reinforcing Bars In Concrete Structures By Acoustic Emission K. Iwaki, O. Makishima, H. Tanaka, T. Shiotani And K. Ozawa	166
21-176	Development Of A Novel Optical Fiber Sensor For Ae Detection In Composites Isamu Ohsawa, Kazuro Kageyama, Yukiya Tsuchida And Makoto Kanai	176
21-187	Acoustic Emission Evaluation Of Corrosion Damages In Buried Pipes Of Refinery S. Yuyama And T. Nishida	187
21-197	New Concept Of Ae Standard: Jis Z 2342-2002 “Method For Acoustic Emission Testing Of Pressure Vessels During Pressure Tests And Classification Of Test Results” Y. Mori, M. Shiwa, M. Nakano And K. Iwai	197
21-206	Acoustic Emission Caused By Environmental Embrittlement Of An Al-Mg-Si Alloy Keitaro Horikawa, Kenichi Yoshida, A. Ohmori And Kiyoshi Sakamaki	206
21-213	Quantitative Study Of Acoustic Emission Due To Leaks From Water Tanks K. Morofuji, N. Tsui, M. Yamada, A. Maie, S. Yuyama And Z. W. Li	213
21-223	Effect Of Pinhole Shape With Divergent Exit On Ae Characteristics During Gas Leak K. Yoshida, Y. Akematsu, K. Sakamaki And K. Horikawa	223
21-230	Operation Monitoring Of Roll Cover By Acoustic Emission Juha Miettinen And Pekka Salmenperä	230
Contents21.Pdf	Contents Of Volume 21 (2003)	I-1 - I-3
Auindex21.Pdf	Authors Index Of Volume 21	I-4
Ausnotes.Pdf	Policy/Author’s Notes/Meeting Calendar/Subscription Information	I-5 - I-7
Iaes16.Pdf	Iaes16, 16-th International Acoustic Emission Symposium	
Appendices (Available On Cd-Rom Only)		
AGU-Vallen	Wavelet Transform Freeware And Introduction By M. Hamstad	

Volume 22, 2004

22-S01	The Kaiser-Effect And Its Scientific Background Hans Maria Tensi	S1
22-001	Modal-Based Identification Of Acoustic Emission Sources In The Presence Of Electronic Noise M. A. Hamstad And A. O’gallagher	1
22-A01*	Appendix A: Details Of The Application Of The Source Identification Scheme M. A. Hamstad And A. O’gallagher	A1
22-022	Experience With Acoustic Emission Monitoring Of New Vessels During Initial Proof Test	

	Phillip Cole And Stephen Gautrey	22
22-030	Quantitative Damage Estimation Of Concrete Core Based On Ae Rate Process Analysis Masayasu Ohtsu And Tetsuya Suzuki	30
22-039	Damage Assessment In Deteriorated Railway Sub-Structures Using Ae Technique Tomoki Shiotani, Yasuhiro Nakanishi, Xiu Luo And Hiroshi Haya	39
22-049	Defect Detection By Acoustic Emission Examination Of Metallic Pressure Vessels Franz Rauscher	49
22-059	Evaluation Of Acoustic Emission Signals During Monitoring Of Thick-Wall Vessels Operating At Elevated Temperatures. Athanasios Anastasopoulos And Apostolos Tsimogiannis	59
22-071	Acoustic Emission Technique And Potential Difference Method For Detecting The Different Stages Of Crack Propagation In Carbon And Stainless Steels C. Ennaceur, A. Laksimi, C. Hervé, M. Mediouni And M. Cherfaoui	71
22-077	Detection Of Incipient Cavitation And Best Efficiency Point In A 2.2mw Centrifugal Pump Using Acoustic Emission L. Alfayez And D. Mba	77
22-083	Investigation Of Fracture Processes Using Moment Tensor Inversion Technique F. Finck, C. U. Grosse And H.-W. Reinhardt	83
22-091	AE Kaiser Effect And Electromagnetic Emission In The Deformation Of Rock Sample Yasuhiko Mori, Yoshihiko Obata, Jan Pavelka, Josef Sikula And Thomas Lokajicek	91
22-102	Acoustic Emissions From Transpiring Plants– New Results And Conclusions Ralf Laschimke, Maria Burger And Hartmut Vallen	102
22-110	Acoustic Detection Of Cavitation Events In Water Conducting Elements Of Norway Spruce Sapwood Sabine Rosner	110
22-119	AE Monitoring From Cvd-Diamond Film Subjected To Micro-Indentation And Pulse Laser Spallation R. Ikeda, H. Cho, M. Takemoto And Kanji Ono	119
22-127	Composites From Piezoelectric Fibers As Sensors And Emitters For Acoustic Applications Andreas J. Brunner, Michel Barbezat, Peter Flüeler And Christian Huber	127
22-138	Processing Of Ae Signals In Dispersive Media Michal Blahacek, Zdenek Prevorovsky, And Michal Landa	138
22-147	Basic Principles Of Acoustic Emission Tomography Frank Schubert	147
22-159	Acoustic Emission Behavior Of Martensitic Transformation During Deformation Of Cu-Al-Ni Shape-Memory Alloy Single Crystals Kenichi Yoshida, Kotaro Hanabusa And Takuo Nagamachi	159
22-166	Acoustic Emission Monitoring Of Concrete Hinge Joint Models K. M. Holford, R. Pullin And R. J. Lark	166
22-173	Characterization Of Acoustic Emission Sources In A Rock Salt Specimen Under Triaxial Load Gerd Manthei	173

22-190	Testing Of Diamond-Like Carbon Coatings Under Slip-Rolling Friction Monitored By Acoustic Emission Manuel Löhr	190
22-201	Field Testing Of Flat Bottomed Storage Tanks With Acoustic Emission – A Review On The Gained Experience Gerald Lackner And Peter Tscheliesnig	201
22-208	Acoustic Emission Examination Of Polymer-Matrix Composites Jürgen Bohse	208
22-224	Acoustic Emission From Rust In Stress Corrosion Cracking Hideo Cho And Mikio Takemoto	224
22-236	Acoustic Emission Measurement System For The Orthopedic Diagnostics Of The Human Femur And Knee Joint R.P. Franke, P. Dörner, H.-J. Schwalbe And B. Ziegler	236
22-243	Rods And Tubes As Ae Waveguides Kanji Ono And Hideo Cho	243
22-253	Acoustic Emission For On-Line Monitoring Of Damage In Various Application Fields Martine Wevers, Gert Van Dijck, Wendy Desadeleer, Mark Winkelmans And Koen Van Den Abeele	253
22-264	The Effect Of Waveguide Material And Shape On Acoustic Emission Transmission Characteristics - Part 1: Traditional Features Joanna Sikorska And Jie Pan	264
22-274	The Effect Of Waveguide Material And Shape On Ae Transmission Characteristics - Part 2: Frequency And Joint-Time-Frequency Characteristics Joanna Sikorska And Jie Pan	274
Contents22.Pdf	Contents Of Volume 22 (2004)	I-1 - I-4
Auindex22.Pdf	Authors Index Of Volume 22	I-5
Ausnotes.Pdf	Policy/Author's Notes/Meeting Calendar/Subscription Information	I-6 - I-8
Berlin2004.Pdf	Activities At 2004 Ewgae Meeting;	I-9
Inmemorium.Pdf	Dick Blackburn (T.F. Drouillard)	I-10
Tensi.Pdf	Professor H.M. Tensi	I-12
Ewgae Folder*	2004 And 2006 Ewgae Meetings, 2004 Program, 2006 Local Information	
Jae Index Folder*	Cumulative Indices Of J. Of Acoustic Emission, 1982 - 2004	

* Indicates The Availability In CD-Rom Only.

Volume 23, 2005

23-001	Effects Of Noise On Lamb-Mode Acoustic-Emission Arrival Times Determined By Wavelet Transform <i>M. A. Hamstad And A. O'gallagher</i>	I
23-025	Acoustic Emission Technique For Detecting Damage And Mechanisms Of Fracture In A Knitted Fabric Reinforced Composite Carlos R. Rios, Steve L. Ogin, Constantina Lekakou And K. H. Leong	25
23-037	Quantitative Damage Estimation Of Concrete Core Based On Ae Rate Process Analysis <i>William Prosser, Eric Madaras, George Studor, And Michael Gorman</i>	37

23-047	Moment Tensors Of In-Plane Waves Analyzed By Sigma-2D <i>Masayasu Ohtsu, Kentaro Ohno And Marvin A. Hamstad</i>	47
23-064	Development Of An Optical Micro AE Sensor With An Automatic Tuning System <i>Hiroshi Asanuma, Hironobu Ohishi, And Hiroaki Niitsuma</i>	64
23-072	Development Of Stabilized And High Sensitive Optical Fiber Acoustic Emission System And Its Application <i>Hideo Cho, Ryouhei Arai And Mikio Takemoto</i>	72
23-081	High Precision Geophone Calibration Masahiro Kamata	81
23-091	Development Of Heat-Resistant Optical Fiber Ae Sensor <i>Pornthep Chivavibul, Hiroyuki Fukutomi, Shin Takahashi And Yuichi Machijima</i>	91
23-096	Damage Detection System For Structures With Smart Ae Sensors Takahito Yanase And Sei Ikegaya	96
23-102	Hierarchical Fracture Process In Brittle Rocks By Means Of High-Speed Monitoring Of Ae Hypocenter Xinglin Lei, Osamu Nishizawa, Andre Moura And Takashi Satoh	102
23-113	Measurement Of Hydraulically Activated Subsurface Fracture System In Geothermal Reservoir By Using Acoustic Emission Multiplet-Clustering Analysis Hirokazu Moriya, Hiroaki Niitsuma And Roy Baria	113
23-119	A Modeling Method On Fractal Distribution Of Cracks In Rocks Using Ae Monitoring Yoshinori Watanabe, Ken-Ichi Itakura, Kazuhiko Sato, Yoshiaki Fujii, Rao Balusu, Hua Guo And Xun Luo	119
23-129	Interpretation Of Reservoir Creation Process At Cooper Basin, Australia By Acoustic Emission Yusuke Kumano, Hirokazu Moriya, Hiroshi Asanuma, Nobukazu Soma, Hideshi Kaieda, Kazuhiko Tezuka, Doone Wyborn And Hiroaki Niitsuma	129
23-136	Micromechanics Of Corrosion Cracking In Concrete By Ae-Sigma Farid A. K. M. Uddin And Masayasu Ohtsu	136
23-142	Evaluation Of Parameter Dependencies Of Ae Accompanying Sliding Along A Rough Simulated Fracture <i>Katsumi Nemoto, Hirokazu Moriya And Hiroaki Niitsuma</i>	142
23-150	Ae Characterization Of Thermal Shock Crack Growth Behavior In Alumina Ceramics By Disc- On-Rod Test Huichi Wakayama, Satoshi Kobayashi And Toshiya Wada	150
23-156	Fatigue Damage Progression In Plastics During Cyclic Ball Indentation Akio Yonezu, Takayasu Hirakawa, Takeshi Ogawa And Mikio Takemoto	156
23-164	Evaluation Of Fatigue Damage For Frm With Ae Method <i>Masanori Takuma And Noboru Shinke</i>	164

23-173	Acoustic Emission Behavior Of Failure Processes Of Glass-Fiber Laminates Under Complex State Of Loading <i>Jerzy Schmidt, Ireneusz Baran And Kanji Ono</i>	173
23-181	Rolling Contact Fatigue Damage Of WC-Co Cermet Sprayed Coating And Its Ae Analysis <i>Junichi Uchida, Takeshi Ogawa, Mikio Takemoto Yoshifumi Kobayashi And Yoshio Harada</i>	181
23-189	Boron Effects On Ae Event Rate Peaks During Tensile Deformation Of Ni ₃ Al Intermetallic Compound <i>K. Yoshida, Y. Masui, T. Nagamachi And H. Nishino</i>	189
23-196	Ae And Electrochemical Noise Analysis For Fracture Study Of Hard Surface Film <i>Akio Yonezu, Hideo Cho, Takeshi Ogawa And Mikio Takemoto</i>	196
23-206	The Origin Of Continuous Emissions Kanji Ono, Hideo Cho And M. Takuma	206
23-215	Precursor Of Hydrogen Induced Glass Lining Chipping By Ae Monitoring Kohei Murakami And Mikio Takemoto	215
23-224	Real-Time Executing Source Location System Applicable To Anisotropic Thin Structures <i>Yu Kurokawa, Yoshihiro Mizutani And Masami Mayuzumi</i>	224
23-233	Investigation On Ae Signal/Noise Processing In Corrosion Damage Evaluation Of Tank Bottom Zhengwang Li , Shigenori Yuyama, Minoru Yamada, Kazuyoshi Sekine, Shigeo Kitsukawa, Hiroaki Maruyama And Shigeo Konno	233
23-243	Examination of AE Wave Propagation Routes In A Small Model Tank <i>Hideyuki Nakamura, Takahiro Arakawa, Minoru Yamada</i>	243
23-249	Integrity Evaluation Of Glass-Fiber Reinforced Plastic Vessels By Lamb Wave Ae Analysis <i>Takashi Futatsugi</i>	249
23-260	Evaluation Of Reinforcement In Damaged Railway Concrete Piers By Means Of Acoustic Emission <i>Tomoki Shiotani, Yasuhiro Nakanishi, Keisuke Iwaki, Xiu Luo Hiroshi Haya</i>	260
23-272	Water-Leak Evaluation Of Existing Pipeline By Acoustic Emission Tetsuya Suzuki, Yukifumi Ikeda, Yuichi Tomoda And Masayasu Ohtsu	272
23-277	Acoustic Emission For Fatigue Damage Detection Of Stainless Steel Bellows Koji Kagayama, Akio Yonezu, Hideo Cho, Takeshi Ogawa, And Mikio Takemoto	277
23-285	Plastic Region Bolt Tightening Controlled By Acoustic Emission Monitoring <i>Tadashi Onishi, Yoshihiro Mizutani And Masami Mayuzumi</i>	285

23-292	Acoustic Emission Behaviors Of Recovery For Mg Alloy At Room Temperature <i>Y. P. Li And M. Enoki</i>	292
23-299	An Acoustic Emission Test System For Airline Steel Oxygen Cylinders: System Design And Test Program <i>Alan G. Beattie</i>	299
23-310	Development Of In-Situ Monitoring System For Sintering Of Ceramics Using Laser Ae Technique <i>S. Nishinoiri And M. Enoki</i>	310
23-318	Pattern Recognition Techniques For Acoustic Emission Based Condition Assessment Of Unfired Pressure Vessels <i>Athanasios Anastasopoulos</i>	318
23-331	The Acoustic Emission Halon 1301 Fire Extinguisher Bottle Tester: Results Of Tests On 649 Bottles Alan G. Beattie And D. D. Thornton	331
Contents23.Pdf	Contents Of Volume 23 (2005)	I-1 - I-4
Auindex23.Pdf	Authors Index Of Volume 23	I-5
Aueaddress.Pdf	Authors E-Mail Addresses	I-6
Ausnotes.Pdf	Policy/Author's Notes/Meeting Calendar/ Subscription Information	I-7 - I-9

Jae Index Folder* Cumulative Indices Of J. Of Acoustic Emission, 1982 - 2005

* Indicates The Availability In CD-Rom Only.

Volume 24, 2006

24-001	A Variable Velocity Approach To Locate Fatigue-Induced Microcracks Occurred In Structures With Multiple Material Layers <i>Jihui Li And Gang Qi</i>	1
24-012	Lamb-Wave Acoustic Emission For Condition Monitoring Of Tank Bottom Plates <i>Mikio Takemoto, Hideo Cho And Hiroaki Suzuki</i>	12
24-022	Wavelet Transform Analysis Of Experimental Ae Waveforms On Steel Pressure Vessel <i>Mulu Bayray And Franz Rauscher</i>	22
24-044	Acoustic Emission Pattern Recognition Analysis Applied To The Over-Strained Pipes In A Polyethylene Reactor <i>Ireneusz Baran, Marek Nowak And Kanji Ono</i>	44
24-052	Acoustic Emission Evaluation Systems Of Tool Life Forshearing Of Piano And Stainless Steel Wires <i>Masanori Takuma, Noboru Shinke, Takako Nishiura And Kensuke Akamatu</i>	52
24-067	Optical Fiber System For Ae Monitoring Of High Temperature Damage Of Stainless Steel Tubing <i>Tomoharu Hayano, Takuma Matsuo, Hideo Cho And Mikio Takemoto</i>	67
24-076	Development Of Measurement System Using Optical Fiber Ae Sensors For Actual Piping <i>Satoshi Nishinoiri, Pornthep Chivavibul, Hiroyuki Fukutomi And Takashi Ogata</i>	76
24-084	Utilization Of Cascade Optical Fiber Ae System For Source Location Of Lamb Waves Through A Cross-Ply Cfrp Plate	

	<i>Takuma Matsuo, Hideo Cho And Mikio Takemoto</i>	84
24-097	Elastic Waves From Fast Heavy-Ion Irradiation On Solids <i>Tadashi Kambara, Yasuyuki Kanai, Takao M. Kojima, Yoichi Nakai, Akira Yoneda, Yasunori Yamazaki And Kensuke Kageyama</i>	97
24-104	Acoustic Emission Rate Behavior Of Laminated Wood Specimens Under Tensile Loading <i>Andreas J. Brunner, Martin T. Howald And Peter Niemz</i>	104
24-111	Ae Measurements For Superconducting Devices <i>Kazuaki Arai, Katsuyuki Kaiho, Hiroshi Yamaguchi, Hirofumi Yamasaki, Akira Ninomiya, Takeshi Ishigohka, Katsutoshi Takano, Hideo Nakajima And Kiyoshi Okuno</i>	111
24-119	Acoustic Emission Of Sensitized 304 Stainless Steel With Simultaneous Hydrogen Charging <i>S. H. Carpenter, Kanji Ono And D. Armentrout</i>	119
24-127	Ae And Corrosion Potential Fluctuation (Cpf) For Environmental Assisted Fracture <i>Koji Kagayama, Takeshi Ogawa, Akio Yonezu, Hideo Cho And Mikio Takemoto</i>	127
24-139	Damage Evaluation By Frequency Analysis Of Continuous Recorded Ae Waveform <i>Kaita Ito And Manabu Enoki</i>	139
24-145	Frequency Filtering Algorithms Of Plate Wave Ae For Source Location <i>Yu Kurokawa, Yoshihiro Mizutani And Masami Mayuzumi</i>	145
24-153	Evaluation Of Two Types Of Martensitic Transformation In Cu-Al-Ni Shape Memory Alloy Single Crystal By Acoustic Emission Waveform Analysis <i>Takeshi Yasuda, Daiki Tani, Hideo Nishino And Kenichi Yoshida</i>	153
24-161	Fatigue Fracture Dynamics Of High Strength Steel Studied By Acoustic Emission Technique <i>Akio Yonezu, Takeshi Ogawa And Mikio Takemoto</i>	161
24-173	Quantitative Detection Of Microcracks In Bioceramics By Acoustic Emission Source Characterization <i>Shuichi Wakayama, Takehiko Jibiki And Junji Ikeda</i>	173
24-179	Determination Of Wave Attenuation In Rock Salt In The Frequency Range 1 - 100 Khz Using Located Acoustic Emission Events <i>Gerd Manthei, Jürgen Eisenblätter And Thomas Spies</i>	179
24-187	Acoustic Emission Behavior Of Prestressed Concrete Girder During Proof Loading <i>Leszek Golaski, Grzegorz Swit, Małgorzata Kalicka And Kanji Ono</i>	187
24-196	Multipler Analysis For Estimation Of Structures Inside An Ae Cloud Associated With A Compression Test Of A Salt Rock Specimen <i>Hirokazu Moriya, Gerd Manthei, Hiroaki Niitsuma And Jürgen Eisenblätter</i>	196
24-205	Damage Diagnosis Of Railway Concrete Structures By Means Of One-Dimensional Ae Sources <i>Tomoki Shiotani, Xiu Luo And Hiroshi Haya</i>	205
24-215	Characteristics Of Damage And Fracture Process Of Solid Oxide Fuel Cells Under Simulated Operating Conditions By Using Ae Method <i>Kazuhiisa Sato, Toshiyuki Hashida, Hiroo Yugami, Keiji Yashiro, Tatsuya Kawada And Junichiro Mizusaki</i>	215

24-222	Acoustic Emission Detection Of Damage Evolution In Short-Fiber Composites <i>Jerzy Schmidt, Ireneusz Baran, Marek Nowak And Kanji Ono</i>	222
24-228	Ae Monitoring Of Microdamage During Proof Test Of Bioceramics For Artificial Joints <i>Shuichi Wakayama, Chikako Ikeda And Junji Ikeda</i>	228
24-234	Small Diameter Waveguide For Wideband Acoustic Emission <i>M. A. Hamstad</i>	234
Contents24.pdf	Contents of Volume 24 (2006)I-1, -2, -3	
AUindex24.pdf	Authors Index of Volume 24 I-4, -5	
AusNotes.pdf	Policy/Author's Notes/Meeting Calendar/Subscription Information	I-6 - I-8
JAE Index Folder*	Cumulative Indices of J. of Acoustic Emission, 1982 - 2006	

* indicates the availability in CD-ROM only.

Volume 25, 2007

25-001	STRUCTURAL INTEGRITY EVALUATION USING ACOUSTIC EMISSION <i>KANJI ONO</i>
25-021	ACOUSTIC EMISSION TECHNIQUES STANDARDIZED FOR CONCRETE STRUCTURES <i>MASAYASU OHTSU, TOSHIRO ISODA and YUICHI TOMODA</i>
25-033	ACOUSTIC EMISSION MONITORING OF REINFORCED CONCRETE FRAME DURING SEISMIC LOADING <i>A. ANASTASOPOULOS, S. BOUSIAS and T. TOUTOUNTZAKIS</i>
25-042	ACOUSTIC EMISSION LEAK TESTING OF PIPES FOR PRESSURIZED GAS USING ACTIVE FIBER COMPOSITE ELEMENTS AS SENSORS <i>ANDREAS J. BRUNNER and MICHEL BARBEZAT</i>
25-051	ACOUSTIC EMISSION TECHNIQUE APPLIED FOR MONITORING AND INSPECTION OF CEMENTITIOUS STRUCTURES ENCAPSULATING ALUMINIUM <i>L. M. SPASOVA, M. I. OJOVAN and C. R. SCALES</i>
25-069	EVALUATION OF REPAIR EFFECT FOR DETERIORATED CONCRETE PIERS OF INTAKE DAM USING AE ACTIVITY <i>TOMOKI SHIOTANI and DIMITRIOS G. AGGELIS</i>
25-080	ACOUSTIC EMISSION MONITORING OF FLEXURALLY LOADED ARAMID/EPOXY COMPOSITES BY EMBEDDED PVDF SENSORS <i>CLAUDIO CANEVA, IGOR MARIA DE ROSA and FABRIZIO SARASINI</i>
25-092	ACOUSTIC EMISSION SIGNALS GENERATED BY MONOPOLE (PENCIL-LEAD BREAK) VERSUS DIPOLE SOURCES: FINITE ELEMENT MODELING AND EXPERIMENTS <i>M. A. HAMSTAD</i>
25-107	HIGH-TEMPERATURE ACOUSTIC EMISSION SENSING USING ALUMINUM NITRIDE SENSOR <i>HIROAKI NOMA, TATSUO TABARU, MORITO AKIYAMA, NORIKO MIYOSHI, TOMOHARU HAYANO and HIDEO CHO</i>

- 25-115 DAMPING, NOISE, AND IN-PLANE RESPONSE OF MEMS ACOUSTIC EMISSION SENSORS
AMELIA P. WRIGHT, WEI WU, IRVING J. OPPENHEIM and DAVID W. GREVE
- 25-124 IMMERSION-TYPE QUADRIDIRECTIONAL OPTICAL FIBER AE SENSOR FOR LIQUID-BORNE AE
TAKUMA MATSUO, HIDEO CHO, TAKESHI OGAWA and MIKIO TAKEMOTO
- 25-132 A SIMPLE METHOD TO COMPARE THE SENSITIVITY OF DIFFERENT AE SENSORS FOR TANK FLOOR TESTING
HARTMUT VALLEN, JOCHEN VALLEN and JENS FORKER
- 25-140 DAMAGE IN CARBON FIBRE COMPOSITES: THE DISCRIMINATION OF ACOUSTIC EMISSION SIGNALS USING FREQUENCY
MARK EATON, KAREN HOLFORD, CAROL FEATHERSTON and RHYS PULLIN
- 25-149 CHARACTERISTICS OF ACOUSTIC EMISSIONS FROM DEHYDRATING WOOD RELATED TO SHRINKAGE PROCESSES
SABINE ROSNER
- 25-157 CHARACTERIZATION OF TITANIUM HYDRIDES USING A HYBRID TECHNIQUE OF AE AND FEM DURING INDENTATION TEST
YOSHIHIRO TANIYAMA, HIDEO CHO, MIKIO TAKEMOTO and GEN NAKAYAMA
- 25-166 ANALYSIS OF THE HYDROGEN DEGRADATION OF LOW-ALLOY STEEL BY ACOUSTIC EMISSION
KRYSTIAN PARADOWSKI, WOJCIECH SPYCHALSKI, KRYSTYNA LUBLINSKA and KRZYSZTOF J. KURZYDLOWSKI
- 25-172 HYDROGEN RELATED BRITTLE CRACKING OF METASTABLE TYPE-304 STAINLESS STEEL
HIDEO CHO and MIKIO TAKEMOTO
- 25-179 ANALYSIS OF ACOUSTIC EMISSION FROM IMPACT AND FRACTURE OF CFRP LAMINATES
KANJI ONO, YOSHIHIRO MIZUTANI AND MIKIO TAKEMOTO
- 25-187 NEURAL NETWORK BURST PRESSURE PREDICTION IN COMPOSITE OVERWRAPPED PRESSURE VESSELS
ERIC v. K. HILL, SETH-ANDREW T. DION, JUSTIN O. KARL, NICHOLAS S. SPIVEY and JAMES L. WALKER II
- 25-194 ACOUSTIC EMISSION SOURCE LOCATION IN A THICK STEEL PLATE BY LAMB MODES
M. A. HAMSTAD
- 25-215 NOVEL ACOUSTIC EMISSION SOURCE LOCATION
RHYS PULLIN, MATTHEW BAXTER, MARK EATON, KAREN HOLFORD and SAM EVANS
- 25-224 ACOUSTIC EMISSION SOURCE LOCATION ON AN ARBITRARY SURFACE BY GEODESIC CURVE EVOLUTION
G. PRASANNA, M. R. BHAT and C. R. L. MURTHY

- 25-231 PROBABILITY OF DETECTION FOR ACOUSTIC EMISSION
ADRIAN POLLOCK
- 25-238 PLASTIC-REGION TIGHTENING OF BOLTS CONTROLLED BY
ACOUSTIC EMISSION METHOD
YOSHIHIRO MIZUTANI, TADASHI ONISHI and MASAMI MAYUZUMI
- 25-247 REAL-TIME DENOISING OF AE SIGNALS BY SHORT TIME FOURIER
TRANSFORM AND WAVELET TRANSFORM
KAITA ITO and MANABU ENOKI
- 25-252 MONITORING THE EVOLUTION OF INDIVIDUAL AE SOURCES IN
CYCLICALLY LOADED FRP COMPOSITES *RUNAR UNNTHORSSON,
THOMAS P. RUNARSSON AND MAGNUS T. JONSSON*
- 25-260 ON USING AE-HIT PATTERNS FOR MONITORING CYCLICALLY
LOADED CFRP *RUNAR UNNTHORSSON, THOMAS P. RUNARSSON
and MAGNUS T. JONSSON*
- 25-267 AE MONITORING OF SOIL CORROSION OF BURIED PIPE
HIDEO CHO and MIKIO TAKEMOTO
- 25-276 THIRTY YEARS EXPERIENCE OF INDUSTRIAL APPLICATIONS OF
ACOUSTIC EMISSION TESTING AT TÜV AUSTRIA
PETER TSCHELIESNIG
- 25-286 ACOUSTIC EMISSION TESTING OF SEAM-WELDED HIGH ENERGY PIPING
SYSTEMS IN FOSSIL POWER PLANTS
JOHN M. RODGERS
- 25-294 ACOUSTIC EMISSION AND X-RAY TOMOGRAPHY IMAGING OF SHEAR
FRACTURE FORMATION IN CONCRETE
TATYANA KATSAGA and R. PAUL YOUNG
- 25-308 GLOBAL MONITORING OF CONCRETE BRIDGE USING ACOUSTIC
EMISSION
T. SHIOTANI, D. G. AGGELIS and O. MAKISHIMA
- 25-316 DEMAND ON FLEXURAL TENSION STEEL REINFORCEMENT
ANCHORAGE ZONES IN FULL-SCALE BRIDGE BENT CAPS
QUANTIFIED BY MEANS OF ACOUSTIC EMISSION
*THOMAS SCHUMACHER, CHRISTOPHER HIGGINS, STEVEN GLASER
and CHRISTIAN GROSSE*
- 25-324 DAMAGE EVALUATION OF POST-TENSIONED CONCRETE VIADUCT
BY AE DURING PROOF LOADING *EDOARDO PROVERBIO,
GIUSEPPE CAMPANELLA and VINCENZO VENTURI*
- 25-331 EARLY FAULT DETECTION AT GEAR UNITS BY ACOUSTIC EMISSION
AND WAVELET ANALYSIS *CHRISTIAN SCHEER, WILFRIED REIMCHE
and FRIEDRICH-WILHELM BACH*
- 25-341 APPLICATION OF ACOUSTIC EMISSION IN MONITORING OF FAILURE
IN SLIDE BEARINGS
IRENEUSZ BARAN, MAREK NOWAK and WOJCIECH DARSKI
- 25-348 MAPPING OF WHEEL FLANGE RUBBING ON RAIL USING AE:
LABORATORY TEST

N. A. THAKKAR, R. L. REUBEN and J. A. STEEL

25-355	DAMAGE ASSESSMENT OF GEARBOX OPERATING IN HIGH NOISY ENVIRONMENT USING WAVEFORM STREAMING APPROACH <i>DIDEM OZEVIN, JASON DONG, VALERY GODINEZ and MARK CARLOS</i>	
25-364	CLUSTERING ANALYSIS OF AE IN ROCK <i>N. IVERSON, C-S. KAO and J.F. LABUZ</i>	
25-373	IMPACT IMAGING METHOD TO MAP DAMAGE IN CONCRETE BRIDGE DECK SLABS <i>STEPHEN D. BUTT, VIDYADHAR LIMAYE and JOHN P. NEWHOOK</i>	
Contents25	Contents of Volume 25 (2007)I-1 – I-4	
AUindex25	Authors Index of Volume 25 I-5 – I-7	
AusNotes	Policy/Author’s Notes/Meeting Calendar/Subscription Information	I-8 – I-10
In Memoriam	Professor Reginald Hardy, Jr. I-11	
EWGAE27	Note on expanded contributions from Cardiff Conference.	I-12
JAE Index Folder*	Cumulative Indices of J. of Acoustic Emission, 1982 - 2007	

* indicates the availability in CD-ROM only.

Cover photograph is from 25-294 by *TATYANA KATSAGA and R. PAUL YOUNG*.

Volume 26 (2008)

26-001	Acoustic Emission Investigation of Coating Fracture and Delamination in Hybrid Carbon Fiber Reinforced Plastic Structures <i>Markus G. R. Sause, Daniel Schultheiß and Siegfried Horn</i>	1-13
26-014	Acoustic Emissions Related to the Dehydration Stress Behavior of Green Norway Spruce Wood <i>Sabine Rosner, Bo Karlsson, Johannes Konnerth and Christian Hansmann</i>	14-22
26-023	Investigation of the Z-Direction Strength Properties of Paper by Use of Acoustic Emission Monitoring <i>S. Norgren, P. A. Gradin, S. Nyström and M. Gullikson</i>	23-31
26-032	Assessment of Stress Corrosion Cracking in Prestressing Strands Using AE Technique <i>Marianne Perrin, Laurent Gaillet, Christian Tessier and Hassane Idrissi</i>	32-39
26-040	Comparison of Wavelet Transform and Choi-Williams Distribution to Determine Group Velocities for Different Acoustic Emission Sensors <i>M. A. Hamstad</i>	40-59
26-060	A Comparison of AE Sensor Calibration Methods <i>Jiri Kepert and Petr Benes</i>	60-71
26-072	Experimental Transfer Functions of Acoustic Emission Sensors <i>Kanji Ono, Hideo Cho and Takuma Matsuo</i>	72-90
26-091	Couplants and Their Influence on AE Sensor Sensitivity <i>Pete Theobald, Bajram Zeqiri and Janine Avison</i>	91-97
26-098	Laboratory Experiments for Assessing the Detectability of Specific Defects by Acoustic Emission Testing <i>Franz Rauscher</i>	98-108
26-109	Integrity Evaluation of COPVs by Means of Acoustic Emission Testing	

	Yoshihiro Mizutani, Kouki Saiga, Hideyuki Nakamura, Nobuhito Takizawa, Takahiro Arakawa and Akira Todoroki	109-119
26-120	Structural Integrity Evaluation of CNG Composite Cylinders by Acoustic Emission Monitoring Olivier Skawinski, Patrice Hulot, Christophe Binétruy and Christian Rasche	120-131
26-132	Automated Method for Statistical Processing of AE Testing Data V. A. Barat and A. L. Alyakritskiy	132-141
26-142	Termites Detection via Spectral Kurtosis and Wavelet De-Noising of Acoustic Emission Signals Juan-José G. De La Rosa, Antolino Gallego, Rosa Piotrkowski, Enrique Castro and Antonio Moreno-Muñoz	142-151
26-152	Acousto-Ultrasonic Signal Analysis for Damage Detection in GFRP Adhesive Joints Andreas J. Brunner and Giovanni P. Terrasi	152-159
26-160	Bending Fracture Behavior of 3D-Woven SiC/SiC Composites with Transpiration Cooling Structure Characterized by AE Wavelet Analysis Toshimitsu Hayashi and Shuichi Wakayama	160-171
26-172	Acoustic Emission Monitoring of Bridge Structures in the Field and Laboratory Rhys Pullin, Karen M. Holford, Robert J. Lark and Mark J. Eaton	172-181
26-182	Arrival Time Detection in Thin Multilayer Plates on the Basis of Akaike Information Criterion Petr Sedlak, Yuichiro Hirose, Manabu Enoki and Josef Sikula	182-188
26-189	Some Possibilities of AE Signal Treatment at Contact Damage Tests of Materials and Bearings Pavel Mazal, Filip Hort, Martin Drab and Tomas Sluneko	189-198
26-199	Laser Cutting and Acoustic Emission Signals Tomaž Kek and Janez Grum	199-207
26-208	Online Monitoring of Hot Die Forging Processes Using Acoustic Emission (Part I) Islam El-Galy and Bernd-Arno Behrens	208-219
26-220	Natural Fiber Composites Monitored by Acoustic Emission Igor Maria De Rosa, Carlo Santulli and Fabrizio Sarasini	220-228
26-229	Acoustic Emission Feature for Early Failure Warning of CFRP Composites Subjected to Cyclic Fatigue Runar Unnthorsson, Thomas P. Runarsson and Magnus T. Jonsson	229-239
26-240	Identification of Damage Initiation and Development in Textile Composite Materials Using Acoustic Emission D.S. Ivanov, S.V. Lomov, I. Verpoest and M. Wevers	240-246
26-247	Damage Identification in Corroded Galvanized and Duplex Coatings Using Wavelet Power and Entropy Rosa Piotrkowski, Antolino Gallego and Enrique Castro	247-261
26-262	AE Entropy for the Condition Monitoring of CFRP Subjected to Cyclic Fatigue Runar Unnthorsson, Thomas P. Runarsson and Magnus T. Jonsson	262-269
26-270	Experimental Simulation and Dynamic Behavior of the AE due to Martensitic Transformation Using Shear Wave Transmission Sensor Takeshi Yasuda, Shinya Kondo, Hideo Nishino and Kenichi Yoshida	270-278
26-279	Implementation of Acoustic Emission Method to the Conventional NDT Structure in Oil Refinery V.P. Gomera, V.L. Sokolov and V.P. Fedorov	279-289
26-290	An Experimental Analysis of Frequency Emission and Noise Diagnosis of Commercial Aircraft on Approach	

	on Approach S. Khardi	290-310
26-311	New Developments of Software for A-line Family AE Systems Sergey Elizarov, Anton Bukatin, Mikhail Rostovtsev and Denis Terentyev	311-317
26-317	Application of Acoustic Emission in Optimizing the Design of New Generation castings of High-Voltage Electric Devices Jan Płowiec, Wojciech L. Spsychalski, Huber Matysiak and Jakub Michalski	318-325
Contents26	Contents of Volume 26 (2008)	I-1 – I-3
AUindex26	Authors Index of Volume 26	I-4
AusNotes	Policy/Author's Notes/Meeting Calendar/DVD/Subscription Information	I-5 – I-7
JAE Index Folder*	Cumulative Indices of J. of Acoustic Emission, 1982 - 2008	
	PhD Thesis of Runar Unnthorsson, University of Iceland*	

* indicates the availability in CD-ROM only.

Cover illustration is from 26-160 by Toshimitsu Hayashi and Shuichi Wakayama.

This figure shows the WT diagram, AE signal, projected WT-frequency curve and FFT spectrum. While WT identifies the first major frequency at 0.56 MHz and the second major frequency at 0.32 MHz, FFT shows the 1st and 2nd major frequencies of ~0.3 MHz as these frequency components have long duration. This clearly shows that FFT analysis failed to detect the highest characteristic frequency at 0.56 MHz.

In using FFT, it is essential to be cognizant of this shortcoming.

Authors Index, Volumes 1-26 (1982-2008)

Satoshi Abe	19-045
A. R. Acharya	8-S88
C. Howard Adams	1-165
E. Aernoudt	4-S186
B. D. Agarwal	8-S297
Dimitrios G. Aggelis,	25-069, 25-308
Mamoru Aizawa	21-149
T. Aizawa	6-85
Chandra Ajay	4-S174
Kensuke Akamatu	24-052
Y. Akematsu	21-223
M. Akiyama	16-S150
Morito Akiyama,	25-107
L. Alfayez	22-077
R.S. Algera	2-69
S. S. Ali	4-S42, 4-107
Bernhard Allemann	14-119
A.F. Almeida	15-S107, 15-S108
A. L. Alyakritskiy	26-132
Masashi Amaya,	13-S35
J. F. R. Ambler	5-S16
G. Amir	2-64
A. A. Anastassopoulos,	13-011, 18-021, 18-217, 18-224, 20-229, 22-059, 23-318, 25-033
Naoto Ando	9-209
E. Andres,	18-155
M. Annamalai	8-S8
K.-I. Aoki	8-S131
K. Aoki	8-S145
Kazuaki Arai	24-111
Ryouhei Arai	23-072
Takahiro Arakawa	23-243, 26-109
D. Armentrout	10-97, 10-103, 15-43, 16-S10, 24-119
Baxter H. Armstrong,	8-S250, 12-117
J. H. Armstrong	4-S135
M. Arrington	4-S165
Ikuo Asano	4-S240
M. Asano,	19-134
Hiroshi Asanuma	23-064, 23-129
J. Asquith,	18-211
S. K. Athithan	4-S26
Y.H.J. Au,	18-196
B. Audenard	1-148
J. Aviassar	1-179
Janine Avison	26-091

J. Awerbuch	8-S301
Friedrich-Wilhelm Bach, Baldev Raj	25-331 4-S102, 6-209, 7-S1, 8-S126, 8-S140, 8-S149, 11-43
G. R. Baldwin	3-182
Rao Balusu	23-119
R.H. Bannister	19-209
V. Bansal	8-S217, 9-142
J. Baram	1-179
Ireneusz Baran,	17-S37, 23-173, 24-044, 24-222, 25-341
P. Barat	8-S140, 8-S149
V. A. Barat	26-132
Michel Barbezat,	22-127, 25-042
Roy Baria	23-113
A. Barron,	18-87
J.A. Baron	2-69
M.W. Barsoum,	18-61
H. Barthelemy	8-S75
B. L. Baskin,	12-149
M. Nabil Bassim	4-S224
Matthew Baxter,	25-215
M. Bayray,	18-131, 19-241, 20-188
Mulu Bayray	24-022
Frank C. Beall,	4-S244, 4-19, 5-71, 6-151, 8-S311, 9-197, 9-215, 10-83, 12-i (1/2), 12-55
Alan G. Beattie	1-21, 1-300, 2-67, 2-69, 2-95, 2-143, 3-224, 3-239, 4-65, 5-53, 5-172, 15-63, 15-S111, 21-095, 23-299, 23-331
M. J. Beesley	7-59
Bernd-Arno Behrens	26-208
S. Béland,	12-45
R. M. Belchamber	4-71, 9-271
David A. Bell	5-1
S. H. Benabdallah	15-S117
Petr Benes	26-060
P. G. Bentley	1-35, 7-59
Avraham Berkovits	11-85
C. C. Berndt	15-S117
J. M. Berthelot,	4-S178, 4-S300, 6-43, 11-11
Yves H. Berthelot,	12-27
M. M. Besen	8-S209
D. Betteridge	4-71
M. R. Bhat,	25-224
D. K. Bhattacharya,	4-S102, 8-S149, 11-43
Frank S. Biancaniello	5-S69
Thomas Bidlingmaier	14-S47
Jacek M. Biernacki,	12-55
T. Kevin Bierney	4-S321
Christophe Binétruy	26-120

B. Birolo	4-S255	
Jan Bisschop	20-153	
Michal Blaháček	18-279, 20-163, 20-274, 22-138	
P.R. Blackburn	7-49	
M. J. Blanch	20-229	
Richard W. Blank	9-181	
J. A. Blessing	8-S236, 8-1	
Thomas Blum	7-179	
Andrew R. Blystra	10-S49	
T. Boczar	17-S7	
P. Böhm	9-29	
Jurgen Bohse	15-S108, 16-S233, 16-S343, 19-001, 22-208	
Yasuyuki Bokoi	16-S196	
R. J. Boness	8-S192, 15-S117	
R.W. Bosch,	18-293	
S. F. Botten	8-S330	
S. Bousias,	25-033	
P. Bowen,	13-S08	
S. J. Bowles	10-49	
P. Bowman	7-225, 8-S4	
Marcelle Brachet	2-159	
John Brandon	17-49	
Franklin R. Breckenridge	1-87, 3-59, 10-43	
J. C. Briggs	8-S209	
W. D. Brosey	7-31, 8-S280, 9-75, 9-84	
Nancy Brown	10-71	
C. Brun,	18-155	
A.J. Brunner	15-S108,	
Andreas J. Brunner,	22-127, 24-104, 25-042	
G. Budenkov	17-S13, 17-S51	
R. Budzier	20-172	
C. Buelens,	18-34	
Anton Bukatin	26-311	
E. Bulatova	17-S13	
O. Burenko	7-31	
Maria Burger	22-102	
Stephen D. Butt,	25-373	
D. J. Buttle	7-211, 8-S158, 8-S201, 9-243, 9-255	
G. Buzzacchi	2-11	
CARP Aerospace/Advanced Composites Subcommittee		11-C1
Giuseppe Campanella,	25-324	
Bruce Campbell	3-81	
Claudio Caneva,	25-080	
Nicholas J. Carino	5-S24	
Mark Carlos	15-S104, 15-S107, 15-S109, 18-189, 18-248, 18-272, 25-355	
John M. Carlyle	4-S329	
Victor Caron	4-S259, 4-115	
Steve H. Carpenter,	1-251, 2-191, 3-11, 3-81, 4-S119, 4-S135, 5-77, 6-115,	

	6-136, 6-177, 6-215, 7-9, 7-161, 8-S135, 8-S184, 8-125, 9-1, 10-97, 10-103, 11-5, 12-141, 13-S01, 15-43, 16-S10, 24-119
Damian Carter	17-49
M. Cartoceti	2-11
Dick W. Caster	9-197
Enrique Castro	26-142, 26-247
J. Catty,	18-205
M. Cerny	17-S20
J. Cerv	20-025
Roger W.Y. Chan	3-118, 4-S259, 4-115, 8-S12
C. Chang	4-S62
Chung Chang	7-21
C. Chapelier	5-S52
T. Chelladurai	8-S88
D. Chellman	4-S263
Chung-Mei Chen	7-161
Jihua Chen	19-001
M.C.Cheresh	2-289
M. Cherfaoui	5-S66, 22-071
Michael J. Chica	9-197
A. Chichibu	8-107
Chang-Sheng Chien,	15-S118
Y. S. Chin	11-71
Pornthep Chivavibul	23-091, 24-076
Robert Chivers	10-123
T. Chow	8-S166
Y. T. Chow	4-71
Min-Hwa Chung,	13-1
T. Chelladurai,	12-111
M. Cherfaoui	11-1, 18-144
Akiyoshi Chichibu,	11-S47, 12-S1
Milan Chlada	17-S57, 20-134
Frantisek Chmelík	17-S29, 20-108
Hideo Cho	16-S115, 21-112, 22-119, 22-224, 22-243, 23-072, 23-196, 23-206, 23-277, 24-012, 24-067, 24-084, 24-127, 24-161, 25-107, 25-124, 25-157, 25-172, 25-267, 26-072
N. S. Choi	16-S324
A-A. R. Choudhury	16-S125
S. Y. Chuang	4-S137
S. S. Christiansen	4-S116, 5-85, 8-S184
F. Cipri	4-S255
M.A. Clark	15-S107
T. N. Claytor	4-S69
Roger B. Clough	5-S69
D. M. Chuck	8-S258
P. Cole	15-S109
Phillip T. Cole	8-S239, 8-31, 18-61, 18-180, 18-232, 19-191, 22-022
C. E. Coleman	5-S16

J. Collins	4-S134
M. P. Collins	9-271
Peter J. Conlisk	8-1
A. W. Cook	8-S101
David B. Cook	17-83
R. Daniel Costley, Jr.,	12-27
R. A. Coyle	6-249
J. Crha	17-S45
H.-A. Crostack	9-29
Timothy G. Crowther	10-71
M. E. A. Cudby	4-71
C. E. D'Attellis	10-13
V. Dal Re	4-S255, 4-S270, 5-39
Wojciech Darski,	25-341
B. Dattaguru	6-19
A.W. Davies,	18-232
Jack F. Dawson	10-117
V. G. Ruiz de Argandoña	10-S35
Igor Maria De Rosa,	25-080, 26-220
Juan-José G. De La Rosa	26-142
S. De Bondt,	11-95
I. De Iorio	3-158
P. De Meester	4-S186, 8-S272, 13-79, 15-S105, 18-34
C. De Michelis	2-11
L. M. Suárez del Río	10-S35
L. Delaey	11-95
H. A. L. Dempsey	4-S46
O. Derakhshan	8-S223
J. Derenne,	18-299
A. Deruyttere	11-95
Wendy Desadeleer,	22-253
M. Diez	4-S296
Seth-Andrew T. Dion,	25-187
John J. Ditri,	12-23
Nitin Dhond	4-S30
G. Dionoro	2-281
Jason W.P. Dong	16-S1
Jason Dong,	25-355
P. Dörner,	22-236
David A. Dornfeld	3-242, 4-S123, 4-S228, 7-103, 7-111, 8-S227, 6-29, 6-37, 6-157
Henrique L. M. dos Reis,	see Reis
R.D. Douglas,	18-96
Karyn S. Downs,	13-31, 13-45, 13-56, 14-S61, 15-S109, 16-iv, 16-S333, 21-052, 21-070, 21-A01
Martin Drab	26-189
M. W. Drew	6-239
T.F. Drouillard,	1-45, 1-81, 1-121, 1-195, 1-271, 2-129, 2-221, 2-292, 3-46,

	3-90, 3-164, 3-212, 4-41, 5-103, 9-45, 9-155, 9-215, 11-53, 12-71, 12-79, 13-42, 14-1, 16-v
Q. Duan	8-S97
Qingru Duan	16-S243
R. Dubiel,	18-15
J. C. Duke	8-S179
H.L. Dunegan	8-S71, 15-53, 15-S106, 16-v
J. Dunning	4-S22
C. Divaker Durairaj	17-15
F. Dusek	10-1
A. G. Dutton	20-229
C. Duytsche	3-176
J. Dvoracek,	18-81
B.C. Dykes	4-S35
Yuris A. Dzenis	15-S112, 20-016, 20-099
Mark Eaton,	25-140, 25-215, 26-172
J. Eberlein	20-172
Davis M. Egle	2-ii (3), 3-104, 4-S30, 4-S46, 6-205
Gernot Eilers	19-100
J. Eisenblätter	15-S119, 16-S85, 19-100, 19-153, 24-179, 24-196
Islam El-Galy	26-208
T. El-Raghy,	18-61
Sergey Elizarov	26-311
R.K. Elsley	2-47
T. Ely	16-S10
D. C. Emmony	1-263
C. Ennaceur,	22-071
Manabu Enoki,	4-S195, 8-S154, 13-S29, 15-S90, 15-S120, 16-S269, 21-142, 23-292, 23-310, 24-139, 25-247, 26-182
R. M. Esbert	10-S35
V. A. Eshwar	8-S217, 9-142
Sam Evans,	25-215
W. T. Evans	11-71
A. Fahr,	8-S314, 12-39, 15-S122
S. D. Falls	8-S166
Daining Fang	11-85
Ahmed M. Farahat	11-S37
J.-P. Favre	9-97
Carol Featherston,	25-140
V. P. Fedorov	20-218, 26-279
G. Fernando	20-229
F. Ferrer,	18-155
Steven E. Fick	4-S311
Andrzej Figiel	4-S182
Chantal Filion	16-S186
F. Finck,	22-083
P. Finkel,	18-61

R.D. Finlayson,	18-61, 18-189, 18-272
J. F. Finn	8-S79
P. Fleischmann	3-176, 5-S42, 9-91, 19-229
Peter Flüeler	22-127
T. Flynn	10-S59
Jens Forker,	18-258, 25-132
D. S. Forsyth	15-S122
R. Fougères	5-S42, 9-91
Timothy J. Fowler	8-S236, 8-1
H. Frackiewicz,	12-149
R.P. Franke,	22-236
Michael J. Friedel	10-S77
M.A. Friesel,	3-11, 3-239, 7-119, 10-117, 18-61, 18-189
L. Froyen,	11-95
Yoshiaki Fujii	23-119
Taisaku Fujioka	15-S31
Tetsuro Fujiwara	10-S63, 11-S65, 15-S40, 15-S113
T. Fuketa,	11-21
Hiroyuki Fukutomi	23-091, 24-076
Roy D. Fultineer, Jr.	15-S103
Masami Fushitani,	4-S240, 9-209, 13-S42
Takashi Futatsugi	23-249
Laurent Gaillet	26-032
M. Gakumazawa	16-S150
Antolino Gallego	26-142, 26-247
Thomas Gandy	4-S166
D. S. Gardiner	4-S199
John Gary,	12-157, 14-103, 15-S115, 16-S251, 17-37, 17-97, 19-258, 20-039, 20-062
Michael F. Gasick	7-111
Ludwig Gauckler	14-119
B. K. Gaur	7-S13
Stephen N. Gautrey	18-180, 19-191, 22-022
A. Gavens	8-S277
Maochen Ge	15-S105, 8-S32, 21-014, 21-029
P. Gebiski	17-S37, 19-285, 20-083
D. Geisse,	12-171
B. Georgali,	18-21
János Geréb	10-19
S. Ghaffari	8-S301
S. Ghia	4-S86
Al Ghorbanpoor	4-S307
J.D. Gill,	18-96, 18-211
Steven D. Glaser	10-S1, 25-316
T. G. Glenn	1-81
A. M. G. Glennie	4-S170
M. W. Godfrey	1-263,
Valery Godinez,	4-103, 18-272, 25-355

L. Golaski	1-95, 4-S182, 17-S37, 19-285, 20-083, 24-187
Douglas E. Goldsack	16-S186
Edward Goliti	5-7
V.P. Gomera,	18-111, 20-218, 26-279
Javier Gomez,	13-S21
Carlos M. Valdes-Gonzalez,	12-117
M. Gori,	18-167
Michael R. Gorman	8-51, 9-131, 9-283, 13-S01, 14-i (3/4), 17-29, 23-037
G.L. Goswami	4-S98, 4-S251, 7-S40, 7-S43
J. Goudiakas,	18-155
Per A Gradin,	13-97, 26-023
Igor Grabec	8-S20, 8-S205, 11-79
L. J. Graham	2-47
A. T. Green	4-124, 8-S306
J. E. Green	1-191, 2-289
P. Gregson,	18-239
David W. Greve,	25-115
Arthur T. Grodotzke	1-29
Boguslaw Gronowski	4-S82, 5-25
D.J. Gross	8-25
S. Gross,	18-239
C. U. Grosse	14-S74, 22-083
Christian Grosse,	25-316
C. M. Grossi	10-S35
Janez Grum	26-199
N. Gsib	5-S60
P.-Y. Gu	8-S188
F. J. Guild	1-244
T. J. Gulley	4-S170
M. Gullikson	26-023
Dawei Guo	14-S19, 16-S222
Hua Guo	23-119
Yanfeng Guo	16-S317
B.C. Gupta	8-S217, 9-142
Robert A. Haack	9-181
Y. Haddad	8-S314
M. E. Hager	8-S42
H. Thomas Hahn	5-15
P. Hähner	20-265
Shigenori Hamada	15-S40
Takashi Hamada	4-S325
A. Hampe	9-103
M. A. Hamstad	2-57, 2-i(3), 5-95, 5-110, 5-123, 6-93, 9-75, 9-84, 11-33, 12-157, 13-31, 13-45, 13-56, 14-103, 14-S61, 15-1, 15-S108, 15-S109, 15-S115, 16-S222, 16-S251, 16-S333, 17-37, 17-97, 19-258, 20-039, 20-062, 21-052, 21-070, 21-A01, 22-001, 22-A01, 23-001, 23-047, 24-234, 25-092, 25-194, 26-040

L. Hanacek	8-S84
Kotaro Hanabusa	22-159
Mineyuki Hanano	11-S75
L. D. Hall,	19-209
V. Hänel	14-115
J. J. Hanley	11-27
Christian Hansmann	26-014
Yoshio Harada	23-181
H.R. Hardy, Jr.	3-242, 4-S19, 8-S32, 8-S42, 8-S262, 8-65, 10-61, 15-S105, 15-S118, 16-S277
Robert W. Harris	6-239, 8-S14, 8-S66, 10-S29, 10-S59, 15-S113, 17-121
W. F. Hartman	1-144, 4-S64, 5-31
J. Harvey	4-S220
H. Nayeb-Hashemi,	12-1
Toshiyuki Hashida,	13-S68, 24-215
F. P. Hassani	8-99, 10-61
Hiroaki Hata	7-173, 10-S63
Hajime Hatano	15-S115
D. Robert Hay	3-118, 4-S259, 4-115, 8-S12, 9-9
J. R. Hay	8-S12
Hiroshi Haya	22-039, 23-260, 24-205
Tomoharu Hayano	24-067, 25-107
F. Havlíček	17-S45
M. W. Hawman	4-S131
Takefumi Hayashi	8-35
Toshimitsu Hayashi	26-160
Yoshie Hayashi,	19-035
Y. Hayashi	21-131
Yasuhisa Hayashi	7-185, 14-69, 15-S108
Jianmei He	20-194
R. Hecker	4-S78
C. R. Heiple	1-221, 1-251, 4-S116, 5-85, 6-177, 6-215, 8-S184, 8-125, 9-1, 10-97, 10-103
D. P. Henkel,	8-S318
Edmund G. Henneke II	8-S277, 14-53
B. Herrmann,	18-167
C. Hervé,	18-125, 22-071
Stefan Heusermann	16-S85
S. Hewerdine	8-S238, 8-21
Hartmut Heyse	5-45
H. Hick	10-67
Kazuo Hiekata	19-045
Christopher Higgins,	25-316
Y. Higo	8-S24, 16-S150, 16-S196, 19-085
Hiroshi Hikosaka	10-S13
Eric v. K. Hill,	25-187
Roger Hill	1-73, 1-149, 1-294, 5-51, 5-i(1), 10-124, 16-S125
Takayasu Hirakawa	23-156
Yuichiro Hirose	26-182

Y. Hisamatsu	2-19, 2-71
Koji Hisamatsu	11-S1
S.V. Hoa	7-145, 9-37, 11-65
A. B. M. Hoff	4-S165
Karen Holford	17-49, 18-232, 22-166, 25-140, 25-215, 26-172
T. J. Holroyd	4-S132, 7-193, 8-S219
Kyoji Homma	10-35
Michel Hone	4-S259, 4-115
K1-Jung Hong,	13-S61
Theodore Hopwood II	4-S304
K. Horikawa,	19-022
Keitaro Horikawa	21-206, 21-223
Siegfried Horn	26-001
P. M. Horrigan	8-S79
Filip Hort	26-189
J.R. Houghton	8-S28, 8-S223, 14-61
Martin T. Howald	24-104
O. Hoyer	9-103
Nelson N. Hsu,	4-S311, 5-S24, 5-S28, 5-S29, 13-23
S.-Y. S. Hsu	1-183, 1-237, 2-169
J. Hu	16-S150
Christian Huber	22-127
J. H. Huh	15-S80
Derek Hull	1-95
Patrice Hulot	26-120
Donald H. Humes	17-29
Wolfgang Hundt	14-119
U.-D. Hünicke	20-172
David A. Hutchins	5-S29, 5-S34, 8-S38, 8-S166
David V. Hutton	8-41
H. Hutton	3-239, 4-S74, 4-S138, 6-167
Hatsuo Ichikawa	4-S325
Y. Ichimura	19-142
Makoto Ichinose	20-001
Hassane Idrissi,	18-299, 18-307, 26-032
Chikako Ikeda	24-228
Junji Ikeda	24-173, 24-228
R. Ikeda	21-131, 22-119
Yukifumi Ikeda	23-272
Sei Ikegaya	23-096
H. Imaeda	4-S294
Takuichi Imanaka	4-S38
Hidehiro Inaba,	8-S24, 19-196
Takako Inaba	10-S90
T. Inamura,	19-085
Ichiro Inasaki	7-179
Tomoaki Inoue	2-1
Yoshiki Inoue	11-S89

Akichika Ishibashi	11-S65, 15-S40, 15-S113
T. Ishida	10-S42
Takeshi Ishigohka	24-111
K. Ishihara	6-13
Hisashi Ishitani	4-S325
C. Ishiyama	16-S150, 16-S196
Toshiro Isoda,	25-021
Ken-Ichi Itakura,	13-S54, 13-S75, 19-109, 23-119
Kaita Ito	24-139, 25-247
D.S. Ivanov	26-240
V.I. Ivanov,	18-144
N. Iverson,	25-364
K. Iwai	21-197
K. Iwaki	21-166
Keisuke Iwaki	23-260
Y. Iwata	16-S142
S. Iyer,	18-189
Takeshi Izuta,	13-S42
Laurence J. Jacobs,	12-27
Jay B. James	4-S119, 5-77
P. Jax	2-29, 8-S53
T. Jayakumar	4-S102, 7-S1, 8-S126, 8-S140, 8-S149, 11-43
J. S. Jeng	8-S268
Hee-Don Jeong,	13-S61
B. B. Jha	6-209, 8-S149
S. K. Jha	7-S43
Kyung-Young Jhang	16-S261
C.Y. Jian,	13-S68
C. G. Jiao	8-S105
Takehiko Jibiki	24-173
K. Jo	8-107, 10-S55
J. Johkaji	8-S1
C. H. Johnson	4-S111, 4-S263
Malcolm J. S. Johnston,	12-117
W.D. Jolly	4-103
H. Jonas	4-S78
L. E. Jones	20-229
R. H. Jones	3-239
R. K. Jones	7-119, 8-S223
Magnus T. Jonsson,	25-252, 25-260, 26-229, 26-262
Young-Chan Joo	15-S1, 16-S212
P. A. Joosse,	20-229
G. Jothinathan	4-S207
Musa K. Jouaneh	10-83
S. J. Jung,	8-S326
B.S. Kabanov,	18-111, 20-218
Koji Kagayama	23-277, 24-127

Kazuro Kageyama,	13-S89, 19-045, 21-176
Kensuke Kageyama	24-097
Hideshi Kaieda	23-129
Katsuyuki Kaiho	24-111
Karl-Ulrich Kainer	20-108
Koji Kaino	5-61, 9-277
K. Kajiyama	19-022
T. Kakimi	2-19
Y. Kakino	3-108
Małgorzata Kalicka	24-187
S. Kallara	8-S28
P. Kalyanasundaram	8-S140, 8-S149
T. Kamada,	19-134
M. Kamata	8-107
Masahiro Kamata	23-081
Tadashi Kambara	24-097
Peter Kamlot	16-S85
Makoto Kanai	21-176
Yasuyuki Kanai	24-097
Yasuhiro Kanemoto	15-S40
Elijah Kannatey-Asibu, Jr.	15-S118
Shigeto Kano	6-109, 6-145
C-S. Kao,	25-364
Justin O. Karl,	25-187
Bo Karlsson	26-014
M. Kat	8-99
Chiaki Kato	19-053
Tatyana Katsaga,	25-294
K. Katsuyama	11-S19
Kunihisa Katsuyama	11-S27
Harold E. Kautz,	5-144, 12-65
Tatsuya Kawada	24-215
Yoshiaki Kawaguchi,	12-127
Yutaka Kawai,	7-167
Teppei Kawakami	21-149
Kenji Kawamoto	9-109
Tomaž Kek	26-199
James R. Kennedy	4-S90
Jiri Keprt	26-060
Shahla Keyvan	10-91, 14-97, 15-79
A. Wahab Khair	4-S1, 8-S326, 15-S105, 16-S53
A. S. Khan,	8-S246
A. S. Khanna	6-209, 8-S103
S. Khardi	26-290
E. W. Khokhlova,	12-149
Jens Kiehn	20-108
M. T. Kiernan	8-S176
S. Kihara,	18-68
Tadashi Kikuchi	11-S47

Cindi Kilkenny	16-S186
Byoung-Geuk Kim	15-S120
Byung-Nam Kim	12-S24, 15-S90, 16-S269
Dal-Jung Kim	16-S261
K. H. Kim	4-S282
K. Y. Kim	4-S62, 8-S170
Kyung-Woong Kim,	13-1
Sang-Hyo Kim	15-S11
Isao Kimpara,	13-S89, 19-045
H. Kimura	4-S294
Ron King	10-91
Tetsuo Kinjo	15-19, 14-69
N. Kinoshita	10-S42
Teruo Kishi	1-1, 2-19, 2-71, 4-S191, 4-S195, 4-S278, 4-S282, 4-S325, 6-85, 8-S131, 8-S154, 12-127, 13-S29, 15-S90, 15-S120, 16-S269
Fuyuhiko Kishinouye	9-177, 9-180
Takahiro Kishishita	10-S55, 11-S47
N. N. Kishore	8-S297
P. Kisnomo	15-33
Tatsuo Kita	10-S90
K. Kitadate	8-S131
K. Kitano	10-S42
Shigeo Kitsukawa	23-233
Kiyoshi Kiuchi	19-053
R. A. Kline	4-S42, 4-107, 6-205, 8-S246
W. Knabl	20-257
Markku Knuuttila	19-162
E. Kobayashi	3-130, 4-93
H. Kobayashi	8-S145
Satoshi Kobayashi	21-149, 23-150
Takao Kobayashi	21-001
Yoshifumi Kobayashi	23-181
Y. Kobayashi	8-S1
Miroslav Koberna	11-61
R. M. Koerner	1-220, 2-187, 2-195, 4-S11, 4-31
Tsuguaki Koga	2-1
Takao Koide,	13-S47
Masami Koike,	19-202
Takao M. Kojima	24-097
B. Koktavy,	17-S100
J. G. Kolaxis	17-69
V. Kolovos,	18-217
Hidemichi Komura	19-196
Shinya Kondo	26-270
Johannes Konnerth	26-014
Shigeo Konno	23-233
Ja-Ho Koo	15-S90, 16-S269
T. M. Kooistra	20-238

Atsushi Korenaga,	19-196
M. Korenska,	18-29
Leszek Korusiewicz	2-272
I. Kosiková	17-S100
T. Kossivas	20-229
V. Kostopoulos	20-265
A. Kotolomov	17-S51
D. A. Kouroussis,	18-217, 18-224, 20-229
Torsten Krietsch	16-S233, 16-S343
R. Krishnamurthy	4-S26, 8-S88
Vladimir Krivobodrov,	13-87
J. Krofta,	18-279, 20-274
J. Królikowski,	12-149
D.A. Kronemeijer,	18-174
Joseph Krynicki	15-S116
Takafumi Kubo,	13-S42
I. Kukman	8-S205
P. G. Kulkarni,	7-S13
Yusuke Kumano	23-129
J. Sampath Kumar	7-135
M. Kumosa	1-95, 16-S10
M. Kunieda	19-134
D. S. Kupperman	4-S69
Yu Kurokawa	23-224, 24-145
Krzysztof J. Kurzydłowski	25-166
Yasufumi Kusano,	13-S75
F. M. Kustas	10-97
T. Kusu	21-142
May Man Kwan	3-144, 3-190
Oh-Yang Kwon	4-S106, 9-123, 9-227, 9-237, 13-1, 13-S83, 15-S1, 15-S19, 16-S212
H. Kwun,	11-27
J.F. Labuz,	25-364
G. Lackner,	18-167, 20-179, 22-201
J.-C. Laizet	9-97
A. Laksimi,	18-125, 22-071
V. Lalitha	4-S26
Michal Landa	17-S57, 20-025, 20-163, 22-138
E. Landis	10-S97, 15-S104
R. J. Landy	1-7
Terence G. Langdon	20-108
F. Langella	3-158
Stanislaw Lasocki	4-S7
Robert J. Lark	22-166, 26-172
Ralf Laschimke,	22-102
A. Lavrov	20-292
Marcel F. Leach	10-S18, 11-19, 16-S186
James D. Leaird,	3-204, 4-S22, 8-S322, 12-117

R. D. Leblanc	15-S122
Chong Soo Lee,	13-S61, 15-S80
Joon-Hyun Lee,	13-S83
K. A. Lee	15-S80
P. Y. Lee	15-S117
Sang-Ho Lee	15-S11
Seung-Hwan Lee	15-S19
Sekyung Lee	15-S120
Seung-Seok Lee	15-S11
Weon-Heum Lee	16-S261
L. Legin	18-144
Xinglin Lei	23-102
Jack Leifer	4-S127
Constantina Lekakou	23-025
D. J. Lekou	20-229
A. M. Leksowskij,	12-149
A. Lemascon	5-S66
Richard L. Lemaster,	4-S228, 6-157, 7-103, 7-111, 8-135, 9-17, 9-203, 10-83, 12-55
J. C. Lenain,	18-161
K. H. Leong	23-025
Armand F. Lewis	4-S127
Luidmila Lezvinsky	16-S35
Steinar Lfvaas	4-S161
Bang xian Li	16-S243
Jihui Li	24-001
L. Li	7-145, 9-37
Y. P. Li	23-292
Zhengwang (Z. W.) Li	21-213, 23-233
Z. W. Li	19-118
Steven Y. Liang	6-29, 6-37
T. Lilley	4-71
S. Lim,	19-134
Jae-Kyoo Lim	16-S309
R. Lima	15-S117
A. Limam,	18-307
Vidyadhar Limaye,	25-373
C. K. Lin	15-S117
Dan Lindahl	19-162
J. Liöka	17-S108
S. Liu	8-S97
Shifeng Liu	15-S124
T. Liu	15-S117
X1-qiang Liu	15-S123
Y.-H. Liu	9-9
David A. Lockner	14-S88
Manuel Löhr,	22-190
T. Lokajícek	17-S100
Thomas Lokajícek	22-091

S.V. Lomov	26-240
M. I. López Pumarega	17-61
Arthur E. Lord, Jr.	2-187, 2-195, 3-107, 4-S11, 4-31, 5-152
Luis Lorenzo	5-15
E. Lowenhar	15-S109
M.G. Lozev	15-S104
Guozhi Lu	4-S203
Krystyna Lublinska,	25-166
P. Lukác	17-S29, 20-108
K. Lundgren	5-S29
Xiu Luo	22-039, 23-260, 24-205
Xun Luo	23-119
D. Lupascu	17-S78
Yukuan Ma	4-S58
J. D. MacPhail	8-S4
Yuichi Machijima	23-091
A. Machová	20-025
J. W. Maclachlan	1-223, 1-229, 2-39, 2-179, 3-1, 4-S151
Eric Madaras	23-037
M. R. Madhava	8-S288
Morihiko Maeda,	19-202
S. Maharshak	2-64
A. Maie	21-213
Ian Main,	13-S21
M. A. Majeed,	4-S147, 8-S16, 12-107
Z. J. Majewska,	12-S7
Zofia Majewska	16-S105, 18-1
S.A. Majewski,	12-S7
Arup Maji	15-S116
O. Makishima	21-166, 25-308
Ajit Mal	14-S19, 16-S222
M. Manoharan	4-S207
Ll. Mañosa	5-S49
Gerd Manthei	15-S119, 16-S85, 19-100, 22-173, 24-179, 24-196
Theodore J. Mapes	1-29
J. Maram	4-S134
H. Marcak,	12-S7
P. A. March	8-S223
K. Marsh	15-S104
G. G. Martin	4-S142
Hiroaki Maruyama	23-233
A. Maslouhi,	8-S292, 12-45, 15-S122, 16-S299
Y. Masui	23-189
S. Mata	17-23
O. Matal	17-S65
Kristian Mathis	20-108
Takuma Matsuo	24-067, 24-084, 25-124, 26-072

K. Matsuura	21-120
Kimitoshi Matsuyama	11-S65, 15-S40
Huber Matysiak	26-317
S. C. Maxwell	8-S38
Masami Mayuzumi	23-224, 23-285, 24-145, 25-238
P. Mazal	17-S2, 17-S20, 17-S70, 18-75, 26-189
H. Mazille,	18-299, 19-229
D. Mba	19-209, 22-077
Stuart L. McBride	1-223, 1-229, 2-39, 2-179, 3-1, 4-S151, 4-S220, 7-225, 8-S4, 8-S192
J. F. McCardle	10-49
J.D. McColskey	15-1, 15-S108, 15-S111, 15-S119
John W. McElroy	4-S77
D. Michael McFarland	5-67
K. I. McRae	7-225
M. Mediouni	22-071
Ronald B. Melton	1-266
P. G. Meredith,	12-S12
Philip Meredith,	13-S21
Jakub Michalski	26-317
K. Michihiro	10-S63
W. Mielke	9-103
Juha Miettinen	21-230
Hamish D. S. Miller	5-S1
M. E. Miller	4-S22
R. (K.) Miller	8-S241, 8-25, 15-S104, 15-S107, 15-S108, 18-61, 18-189, 18-272
O. Minemura	16-S75
J. R. Mitchell	6-135
J. Mitchell	15-S109
A. Mittelman	3-41, 6-73
S. Miwa,	19-142
Makoto Miwa,	13-S42
Kouitsu Miyachika,	13-S47
Kazuya Miyano	10-S90
Hiroyuki Miyatake	10-S13
Noriko Miyoshi,	25-107
Junichiro Mizusaki	24-215
Souichi Mizutani	20-194
Yoshihiro Mizutani	16-S115, 18-51, 18-286, 19-035, 20-194, 23-224, 23-285, 24-145, 25-179, 25-238, 26-109
Kenji Mochizuki	8-35
Mark B. Moffatt	1-29
K. Mogi	1-37, 8-113, 16-S45
James Mohr	5-162
Waldemar Molinski	10-107
Florian Moll	20-108
M. Momayez	10-61
Keiichi Monma	15-S113

M. Montoto	10-S35
Antonio Moreno-Muñoz	26-142
Bryan C. Morgan	15-69, 15-S103
L. Morgan	16-S125
Winfred Morgner	3-172, 5-45, 6-133, 8-S70
Y. Mori	8-S131, 16-S45, 20-248, 21-197, 22-091
Yoshiki Morino	20-194
Hiroyuki Morishima	20-145
Hirokazu Moriya	23-113, 23-129, 23-142, 24-196
D. G. Morris	7-95
K. Morofuji	21-213
Zofia Mortimer	16-S105, 18-1
W. J. Moś cicki,	12-S7
H. G. Moslé	8-S317
F. Mostert	18-189
Andre Moura	23-102
F. Mudry	6-85
Amiya K. Mukherjee	5-162
M. C. Mumwam	16-S65
Kohei Murakami	23-215
Yuji Murakami	10-S90
K. Murayama	16-S75
Boris Muravin	16-S35
Gregory Muravin	16-S35
S. A. F. Murrell,	12-S12
C. R. L. Murthy,	4-S30, 4-S147, 6-19, 7-S18, 8-S16, 8-S122, 8-S284, 12-107, 25-224
T. M. Mustaleski	4-S247
S. Naemura	10-S55
T. Nagamachi	23-189
Takuo Nagamachi	22-159
Koji Nagano,	11-S1, 13-S54, 13-S75
S. Nagano,	19-085
Jyothi Nagaraj	14-97
Kenji Nagashima,	19-011
Yasuaki Nagata	4-S191
M. M. Nagl,	11-71
G. Jayachandran Nair	8-S266
P. K. K. Nair	4-S98
Hidehumi Naito,	12-S24
Yoichi Nakai	24-097
Hideo Nakajima	24-111
Hideyuki Nakamura	23-243, 26-109
M. Nakamura	10-S55, 8-107
Syouzou Nakamura	10-S13
Yasuhiro Nakanishi	20-145, 22-039, 23-260
Hiroyasu Nakasa	16-S25
Eisaku Nakashima,	19-202

M. Nakano	21-197
Noritaka Nakaso,	13-23
Gen Nakayama,	25-157
B. C. Nakra	9-25
H. Nayeb-Hashemi,	12-1, 14-85, 15-33
O. Nedzvetskaya	17-S13, 17-S51
Priscilla P. Nelson	10-S1
Katsumi Nemoto	23-142
Y.S. Neo,	18-96
K. P. Nerz	5-S56
John P. Newhook	25-373
Eng T. Ng	19-275
K. D. Nicklas	4-S247
Jackson A. Nickerson	6-37
A. Nielsen	8-S57
Peter Niemz	24-104
Hiroaki Niitsuma	7-201, 11-i(4), 11-S1, 23-064, 23-113, 23-129, 23-142, 24-196
Akira Ninomiya	24-111
T. Nishida	21-187
S. Nishikawa	10-S55
Koichi Nishimoto	4-S236
Shigeto Nishimoto	19-202
Hideo Nishino	23-189, 24-153, 26-270
M. Nishino	8-S131
Satoshi Nishinoiri	23-310, 24-076
V. N. Nikolaidis,	17-69, 20-229
Minoru Nishida,	12-S18
H. Nishino,	18-51, 18-102, 18-286, 19-011, 19-035, 19-075
Takako Nishiura	24-052
Osamu Nishizawa	11-S27, 23-102
Masami Noguchi	4-S236
M. Noguchi	11-21
C. Nojiri	16-S150
Hiroaki Noma,	25-107
Richard Nordstrom	15-S108, 16-S204
S. Norgren	26-023
Václav Novák	20-163
Marek Nowak	24-044, 24-222, 25-341
A. Nozue	1-1
Akira Nozue	21-149
J. Nuffer	17-S78
Staffan Nyström,	13-97, 26-023
Y. Obata	8-S145, 16-S45, 20-248, 22-091
S. I. Ochiai	2-289
Satoshi Oda,	13-S47
A. O’Gallagher	14-103, 15-S115, 16-S251, 17-37, 17-97, 19-258, 20-039, 20-062, 21-052, 21-070, 21-A01, 22-001, 22-A01, 23-001

Takashi Ogata	24-076
Takeshi Ogawa	23-156, 23-196, 23-181, 23-277, 24-127, 24-161, 25-124
Steve L. Ogin	23-025
S. Ogino	5-61, 9-277
Eu Seok Oh	16-S277
Yoshitugu Ohigashi	10-25
Takanori Ohira	4-S274
Hironobu Ohishi	23-064
A. Ohmori	21-206
Tatsuma Ohnishi	19-109
Tadashi Onishi,	25-238
Kentaro Ohno	23-047
Isamu Ohsawa,	13-S89, 19-045
Shiro Ohta	15-S40
M. Ohtsu	1-103, 2-151, 2-247, 3-27, 3-59, 3-69, 4-S38, 4-S50, 4-S316, 5-124, 6-43, 6-79, 6-99, 7-167, 8-S162, 8-S242, 8-93, 10-i (1/2), 11-i(4), 11-S37, 11-S57, 11-S65, 11-S89, 13-S14, 15-S31, 15-S40, 15-S50, 15-S60, 15-S70 16-S65, 16-S95, 18-S1, 18-S7, 19-118, 19-142, 19-184, 20-001, 21-157, 22-030, 23-047, 23-136, 23-272, 25-021
H. Ohyama	4-S282
M. I. Ojovan,	25-051
Takahisa Okamoto,	13-S14
T. Okamoto	16-S75
Takeshi Okano	4-S240
A.A. Okhotnikov,	18-111, 20-218
S. Okumura	11-21
L. Okushima	17-15
Kanji Ono,	1-7, 1-67, 1-69, 1-141, 1-145, 1-146, 1-183, 1-211, 1-213, 1-214, 2-169, 2-247, 2-ii(1/2), 3-19, 3-27, 3-59, 3-69, 3-130, 3-144, 3-174, 3-190, 3-233, 3-ii(4), 4-S50, 4-S106, 4-S111, 4-S263, 4-S316, 4-61, 4-93, 5-124, 5-i(1), 5-ii(4), 6-1, 6-43, 6-84, 8-S268, 9-109, 9-123, 9-177, 9-227, 9-270, 11-117, 12-177, 14-35, 14-69, 14-S19, 15-19, 15-S95, 15-S105, 15-S108, 16-S115, 16-S134, 16-S289, 17-S37, 18-51, 18-102, 18-286, 19-011, 19-035, 19-063, 19-075, 19-091, 19-285, 20-083, 21-112, 21-120, 22-119, 22-243, 23-173, 23-206, 24-044, 24-119, 24-187, 24-222, 25-001, 25-179, 26-072
M. Onoe	5-i(4)
Irving J. Oppenheim,	25-115
Hisanori Otsuka	10-S13
P. Ouellette	9-37, 11-65
C. Ouyang	10-S97
H. Oyaizu	8-S1
K. Ozawa	21-166
Didem Ozevin,	25-355

Jie Pan	22-264, 22-274
Yih-Hsing Pao	4-S274
Krystian Paradowski,	25-166
Philip Park	15-S11
Young-Jin Park	15-S11
H. B. Patel	8-S12, 8-S101
S. C. Pathak	4-S32, 4-S147, 8-S122
J. Pavelka	17-S100, 22-091
J. Pazdera,	18-81
L. Pazdera,	18-29
Martin Peacock	4-S166, 8-S240, 8-11
L. H. Pearson	4-S199
Peter Pellionisz	10-19
R. Pensec,	18-125
L. V. Perez	10-13
Marianne Perrin	26-032
D. T. Peters,	8-S4
S. Peteves	20-265
J. Petras,	18-75
L. Petras,	18-81
J. Petrsek	17-S83
Christian Pfleiderer,	12-141
T. P. Philippidis,	13-11, 17-69, 20-229
Rodney G. Pickard	15-79
C. Picornell	5-S49
Aleksander Pilarski,	12-23
S. Pilecki,	10-1, 12-149
J. Pininska,	18-8
Rosa Piotrkowski	17-61, 26-142, 26-247
A. Plevin	1-35
Jan Płowiec	26-317
T. Pochecho	14-85
Stefan Poliszko	10-107
M. D. Pollard,	8-S4
Adrian A. Pollock	1-237, 1-303, 9-140, 10-122, 15-S107, 15-S108, 25-231
Elizabeth L. Porter	17-121
O. Prabhakar	4-S207
Arun Prakash	9-142, 8-S217
A. Prateepasen,	18-196
C. W. Pretzel	5-172
D. Prevorovsky	20-285
Zdenek Prevorovsky	17-S57, 18-279, 20-134, 20-274, 20-285, 22-138
David W. Prine	4-S304, 15-S106
Thomas M. Proctor, Jr.	1-173, 5-134, 7-41, 10-43
William H. Prosser	9-283, 14-S1, 15-S106, 15-S115, 17-29, 17-37, 23-037
A. Proust	17-S83, 18-161, 19-229, 20-229
Jose Pujol	17-111
R. Pullin	22-166, 26-172
M. I. López Pumarega	17-61

K. K. Purushothaman,	12-111
Gang Qi	17-111, 19-275, 24-001
Jie Qian	20-016, 20-099
Stephen L. Quarles	8-134, 9-17, 9-189
M. Raab	20-274
Amani Raad	20-300
Jan Raczkowski	10-107
Andre Raharinaivo	2-159
Baldev Raj,	4-S102, 6-209, 7-S1, 8-S126, 8-S140, 8-S149, 11-43
P. Raj	4-S98
D. S. Rajan	8-S297
P. K. Rajan	8-S28
Jerzy Ranachowski	4-S82, 5-25
A.K. Rao	4-S147, 6-19
M. V. M. S. Rao	7-S29, 8-S262
S. P. Mallikarjun Rao	7-135, 11-101
M. N. Raghavendra Rao	8-S284
Christian Rasche	26-120
Franz Rauscher	17-S92, 18-118, 20-188, 22-049, 24-022, 26-098
Henrique L. M. dos Reis,	4-S232, 5-67, 5-144, 9-197, 11-107, 12-15, 17-83
F. Rehsteiner	14-119
Wilfried Reimche,	25-331
H. W. Reinhardt	14-S74, 22-083
R.L. Reuben,	18-96, 18-211, 25-348
W. G. Reuter	4-S269
L.E. Rewerts	15-S107
Marie-Christine Reymond	2-159, 4-S296, 5-S63
M. W. Richey	6-257
J. Richter	17-S70
B. Richtor	2-29
G. L. Rigby	10-S22
Carlos R. Rios	23-025
L. Rippert,	18-41
Steffen Ritter	14-S47
J. L. Robert	4-S300, 6-43, 11-11
R.A. Roberts	15-S107
N. Rochat	9-91
J. Rödel	17-S78
John M. Rodgers	1-114, 4-S155, 4-1, 25-286
P. Rödhammer	20-257
P. Rodriguez	4-S102, 8-S140, 8-S149, 11-43
L. M. Rogers	2-319
J. Roget	4-85, 5-S60, 5-S66, 8-S231, 8-34
K. Rokugo	19-134
I. Roman	2-64, 3-19, 3-41, 3-130, 4-S106, 4-S111, 6-73, 8- S109, 8-47, 10-31

Igor Maria De Rosa,	25-080
A. P. G. Rose	1-213
Joseph L. Rose,	12-23
Z. Rosecky	20-025
Sabine Rosner	22-110, 25-149, 26-014
J. N. Rossettos,	12-1
Mikhail Rostovtsev	26-311
R. Rothea	19-229
D. Rouby	3-176, 9-117
C. Rowland,	18-87, 18-239
C. Roy	8-S292, 12-45
P. R. Roy	7-S40, 4-S251
Gottfried A. Rubin	10-S18, 11-19
D. Rubio	10-13
Thomas P. Runarsson,	25-252, 25-260, 26-229, 26-262
J. E. Ruzzante	10-13, 17-61
H. Saadaoui,	12-45
Wolfgang Sachse	4-S62, 8-S20, 8-S170, 11-79
S. Sagat	5-S16
Kouki Saiga	26-109
Masahiro Saito,	13-S68
Naoya Saito	15-19, 16-S289
Koji Sakai	10-S104
Norio Sakaino	15-S50
K. Sakamaki	16-S134, 18-68
Kiyoshi Sakamaki	21-206, 21-223
N. Sakata	16-S75
Yasunori Sakata	15-S70
Tatsuro Sakimoto	7-167
Takumi Sakuma	16-S196
C. Sala	2-11
H. M. Sallam	14-85
Pekka Salmenperä	21-230
Peter Sammonds,	13-S21
A. Sampath	5-S12
R. Samuel	7-S35
R. N. Sands	4-31
A. S. Sankaranarayanan,	12-111
N. Saniei	15-33
Mary Sansalone	5-S24
Carlo Santulli	26-220
Fabrizio Sarasini,	25-080
Hiroaki Sasaki	16-S25
Soji Sasaki	2-1
S. Sase	17-15
L. Hanumantha Sastry	11-101
Akihiro Sato,	19-202
Ichiya Sato	2-1, 7-173, 8-S213

Isamu Sato	8-35
Kazuhiko Sato,	13-S54, 13-S75, 19-109, 23-119
Kazuhisa Sato	24-215
K. Sato	16-S45
Keiichi Sato,	4-S240, 8-S213, 9-209, 13-S42
Kouichi Sato	7-173
Takashi Satoh	23-102
Markus G. R. Sause	26-001
S. G. Savanur	7-S18
M.W. Scaife,	18-211
C. M. Scala	2-261, 6-249, 10-49
C. R. Scales,	25-051
G. Schauritsch,	18-138
Christian Scheer,	25-331
R. Schelling	20-238
C. Schepacz	2-267
Jerzy Schmidt	23-173, 24-222
H.J. Schoorlemmer,	18-180, 20-238
Frank Schubert	22-147
M. Schulz	20-172
Daniel Schultheiß	26-001
K. Schumacher	9-103
Thomas Schumacher,	25-316
D. Schumann	3-172
H.-J. Schwalbe	22-236
J. S. Schwartzberg	10-97
Ian G. Scott	4-S142
C. B. Scruby	3-182, 4-9, 7-81, 7-211, 8-S158, 8-S201, 9-243, 9-255
Petr Sedlak	26-182
C. Seguf	5-S49
Kazuyoshi Sekine	23-233
G. P. Sendeckyj	11-33
Hirofumi Sentoku	16-S19
U. Senturk	15-S117
M. Seto	11-S19
Masahiro Seto,	11-S27
B. K. Shah	7-S13
S. P. Shah	10-S97
R. Douglas Sharp	3-118, 4-S259, 4-115
V.V. Shemyakin,	19-172
G. Shen,	8-S97
Gongtian Shen	16-S243
H.W. Shen	15-S105, 18-189
Ping Shen	15-S123
Nanling Shi	16-S317
K. Shibata	8-S145
M. Shibata	3-144, 3-190, 4-93,
Mitsuhiro Shigeishi,	11-S57, 13-S14, 15-S50, 15-S60, 16-S65
Hisatoshi Shimada	10-S104

Shigeo Shimizu,	19-196
Tatsuya Shimizu,	13-S68
Takayuki Shimoda	20-194
J. Sikula	17-S100
T. Simo	17-S65
Masayuki Shimojo	16-S196, 19-085
Noboru Shinke	10-25, 16-S134 , 23-164, 24-052
Takuo Shinomiya	20-145
Tomoki Shiotani	15-S50, 16-S95, 18-248, 19-118, 19-142, 20-145, 20-153. 21-166, 22-039, 23-260, 24-205, 25-069, 25-308
M. Shiwa	4-S195, 21-197
Donald A. Shockey	21-001
Ménad Sidahmed	20-300
Khalid J. Siddiqui	3-118, 9-9
J. Siedlaczek	10-1
Joanna Sikorska	22-264, 22-274
Josef Sikula	22-091, 26-182
F. Simacek	10-67
A. K. Singh	4-S174
A. K. Sinha	7-S13
N. K. Sinha	4-S290
Petr Sittner	20-163
Olivier Skawinski	26-120
C. Sklarczyk	8-S93
A. Skraber,	18-144
Jerzy Skubis	2-261, 4-S82, 5-25
A. Slimani	5-S42
Daniel R. Smith Jr.	4-S135, 7-9
J. H. Smith	8-S79
M. Sobczyk	8-S192
T. Sogabe	21-120
V.L. Sokolov,	18-111, 20-218, 26-279
Amir Soltani	4-S17
Nobukazu Soma	23-129
Jun-Hee Song	16-S309
M. Sorel	2-261
M. Ben Souda	11-11
P. Souquet	4-85, 5-S60, 8-S231
J.C. Spanner, Sr.	6-121
L. M. Spasova,	25-051
Th. Spies	15-S119, 19-100, 19-153, 24-179
Nicholas S. Spivey,	25-187
Wojciech Spsychalski,	25-166, 26-317
M. K. Sridhar	4-S174
K. V. Srincivasan,	8-S8
T.S. Sriranga	7-S35
K. A. Stacey	7-81
J.A. Steel,	18-96, 18-211, 25-348
Wolfgang Stengel	4-S312

D. Stöver	4-S78
H. Strauven,	13-79
V. Streicher	8-S53
V. A. Strelchenko	8-S334
V. A. Strizhalo	8-S334
S.A. Strizkov	19-172
C. E. Stuart,	12-S12
George Studor	23-037
V. Suba	17-S20
S. V. Subba Rao	8-S8
Iyer Subramaniam	4-S174
H. N. Sudheendra	8-S288
C. Y. Suen	9-9
Katsuhiko Sugawara,	13-S54
J. Summerscales	4-S170
C. T. Sun	7-21
X. Sun	8-S262
J. Q. Sun	8-S114
M. J. Sundaresan	8-S277
M. Surgeon	15-S105, 18-34
Hiroaki Suzuki	11-117, 14-35, 14-69, 15-19, 15-S108, 16-S178, 16-S289, 24-012
Ippei Suzuki	7-179
M. Suzuki	9-277
Masahiko Suzuki	5-61
Tetsuya Suzuki	22-030, 23-272
Toshio Suzuki,	13-S89
Toshitaka Suzuki	2-1
P. Svadbik,	18-29
V. Svoboda	17-S2, 17-S83
Terry L. Swanson	8-1, 8-S236
Grzegorz Swit	24-187
Tatsuo Tabaru,	25-107
A.N. Tafuri	15-S104
V.L. Tahiri	16-S299
F. Taioli,	8-S42
H. Takagi	16-S142
Hideaki Takahashi,	6-261, 7-1, 13-S68
K. Takahashi	16-S324
Shin Takahashi	23-091
Katsutoshi Takano	24-111
Atsushi Takashima,	19-109
Kazuki Takashima,	12-S18, 13-S08, 16-S150, 19-085
S. Takashina,	18-102
Nobuo Takeda,	12-127
Mikio Takemoto	7-185, 11-117, 14-35, 14-69, 15-19, 15-S108, 16-S115, 16-S178, 16-S289, 18-51, 18-102, 18-286, 19-011, 19-035, 19-063, 19-075, 21-120, 21-131, 22-119,

	21-120, 21-131, 22-119, 22-224, 23-072, 23-156, 23-196, 23-181, 23-215, 23-277, 24-012, 24-067, 24-084, 24-127, 24-161, 25-124, 25-157, 25-172, 25-179, 25-267
Hajime Takeuchi	9-209
K. Takigawa	8-S213
Masanori Takuma	16-S134, 23-164, 23-206, 24-052
S. Talebi	8-S254
Okiharu Tamura	16-S178
H. Tanaka	21-166
M. Tanaka	10-S55
T. Tanaka	8-S213
Toshiyuki Tanaka	7-173
S. Tanary,	8-S314, 12-39
N. Tandon	9-25, 17-23
Daiki Tani	24-153
Yoshihiro Taniyama,	25-157
O.B. Tarutin	15-S120
Masayuki Tateno,	11-S75
A. Taylor,	18-239
M. A. Taylor	8-S322
C. M. Teller	11-27
Hans Maria Tensi	22-S01
H.B. Teoh	3-19, 3-130, 6-1
Satoshi Teramura	6-261, 7-1
Giovanni P. Terrasi	26-152
Christian Tessier	26-032
R. Teti	3-158, 5-156
Lawrence W. Teufel	15-S124
Kazuhiko Tezuka	23-129
N. A. Thakkar,	25-348
Christian Thaulow	4-S211
Heinrich Theiretzbacher	4-S157
W. Thelen	14-115
Pete Theobald	26-091
Richard E. Thill	10-S77
P.M. Thompson	6-93
D. D. Thornton	23-331
Peter G. Thwaite	14-vi (3/4)
R. M. Tian	4-S94
B. Tirbonod	8-S84
Anil Tiwari	14-53
G. P. Tiwari	4-S102, 7-S43
R.G. Tobin	8-25
Akira Todoroki	26-109
S. Tomecka-Suchoń ,	12-S7
Yuichi Tomoda	15-S31, 21-157, 23-272, 25-021
H. Tonda,	13-S08
F. Tonolini	8-S62
G. Tonolini	4-S86

V. Torra	5-S49
T. Toutountzakis,	25-033
D.T. Tran	8-25
H. Traxler	20-257
D. Tsamtsakis,	13-79
P. Tscheliesnig	4-S157, 17-S108, 18-138, 18-167, 20-129, 20-179, 22-201, 25-276
Ming-Kai Tse	4-S127, 8-S188, 8-S209
A. Tsimogiannis,	18-21, 18-224, 22-059
Yukiya Tsuchida	21-176
N. Tsui	21-213
Nobuyuki Tsuji	15-S60
Yusuke Tsukahara,	13-23
Koichi Tsukiyama	6-261, 7-1
F. R. Tuler	8-S79
F. Uchida,	18-102, 19-075
Junichi Uchida	23-181
Atsushi Uchiyama,	13-S42
Farid A. K. M. Uddin	23-136
Toshiyuki Uenoya,	13-S95, 15-S112
Takateru Umeda	20-248
Runar Unnthorsson,	25-252, 25-260, 26-229, 26-262
Taketo Uomoto	6-137
T. I. Urbancic	8-S254
E. Uria,	13-79
S.J. Vahaviolos	3-i(1), 4-S329, 15-S109, 18-189, 18-248, 18-272, 19-172
S. Vajpayee	5-S12
Carlos M. Valdes-Gonzalez,	12-117
H. Vallen,	18-167, 18-258, 18-265, 22-102, 25-132
J. Vallen,	18-265, 25-132
P.J. Van De Loo,	18-174, 20-238
D. R. V. Van Delft	20-229
Koen Van Den Abeele	22-253
Gert Van Dijck,	22-253
S. Van Huffel,	18-41
J. G. M. Van Mier	20-153
R. Van Nieuwenhove,	18-293
Donald W. Vannoy	4-S307
D. Varchon	20-285
Alex Vary,	8-S175, 12-i (1/2), 12-71, 12-79, 14-53
F. A. Veer	8-S118
Vasisht Venkatesh	14-61
Vincenzo Venturi,	25-324
E. Verbrugghe	11-1
I. Verpoest	4-S186, 8-S272, 26-240
A. Vervoort	20-292
R. Vijayaraghavan,	7-S13

G. Villa	4-S86
M. R. Viner	8-S192
A. Vinogradov	17-1
A. Yu. Vinogradov	16-S158
P. Vionis	18-217, 20-229
R. Visweswaren	4-S207
L.E. Vlasov,	18-150
Aaron C. Voegele	17-83
J. von Stebut,	18-258
Y. Vougiouklakis	20-265
Toshiya Wada	23-150
Adrian P. Wade	10-71
Haydn N.G. Wadley	5-S69
N. Wakabayashi	10-S42
Shuichi Wakayama,	4-S278, 12-S24, 16-S170, 21-149, 23-150, 24-173, 24-228, 26-160
Teruyuki Waki,	12-S1
Akimasa Waku,	12-S1
D. A. Waldrop	7-31
James L. Walker II,	25-187
Y. Wan,	8-S97
Y. Wang,	19-022
Alexander Wanner	14-i, 14-v, 14-vi (3/4), 14-S47
Kris A. Warmann	11-107
E. Waschkie,	8-S93
G. Washer	15-S104
M. Watad	3-41
Hiroshi Watanabe	20-001
Naoaki Watanabe,	13-S42
T. Watanabe	3-59
Takashi Watanabe	2-1
Yoshinori Watanabe	23-119
J.R. Watson,	18-232
Robert J. Watters	4-S17, 8-S258
D.J. Watts	15-S104, 19-172
Richard L. Weaver	4-S54, 5-S40
Z. Weber,	18-29
J. R. Webster	4-S132, 8-S197
Qiang Wei	11-S75
B. Weiler	14-S74
M. Wevers,	4-S186, 8-S272, 13-79, 15-S105, 18-34, 18-41, 20-206, 20-292, 22-253, 26-240
R. G. White	1-263
J. W. Whittaker	1-147, 4-S247, 5-148, 6-257, 7-31, 7-95, 8-S280, 9-75, 9-84, 10-113
B. J. S. Wilkins	10-S22
H. Willer	10-67
A. J. Willis	1-244

P. E. Wilson	2-191
Leo Windecker	ICAE Banquet
M. Winkelmanns	20-206, 22-253
E. Winter	10-67
S. M. Wolf	3-239
A. Wolfert	20-238
Jörg Wolters	3-51
Brian R. A. Wood	6-125, 6-239, 8-S14, 8-S66, 10-S29, 10-S59, 15-S113, 17-121
J. D. Wood	8-S318
D. G. M. Wood	4-71
G. Wormser	5-S52
Amelia P. Wright,	25-115
Bobby Wright	4-S166
Min Wu	11-5
Wei Wu,	25-115
Doone Wyborn	23-129
Y. Xiang,	8-S246
J. Z. Xiao	4-S215
Yue-Huang Xu	3-81
H. Yamada,	18-51
K. Yamada	6-13
M. Yamada	21-213
Minoru Yamada	23-233, 23-243
Yoshiaki Yamade,	12-127
Hiroshi Yamaguchi	24-111
Katsuya Yamaguchi	9-209
Kusuo Yamaguchi	4-S191, 4-S286, 4-S325, 8-S1
T. Yamaguchi	8-S145
Koji Yamamoto	19-196
Hirofumi Yamasaki	24-111
Akihiko Yamashita,	13-S89
Akio Yamashita	4-S286
T. Yamauchi	11-21
Yasunori Yamazaki	24-097
Tinghu Yan	17-49
W. Yan	15-S109
M. Yanagibashi	8-S213
Masa-aki Yanaka,	13-23
Takahito Yanase	23-096
J. M. Yang	8-S268
Xuanhui Yang	15-S123
C. K. Yao	4-S94, 8-S105
Takeshi Yasuda	24-153, 26-270
A. Yasuo	4-S294
Daisuke Yasuoka	15-S60
J.J. Yezzi, Jr.	15-S104

Akira Yoneda	24-097
Takao Yoneyama	2-1, 7-173, 8-S213
Akio Yonezu	23-156, 23-196, 23-277, 24-127, 24-161
Dong-Jin Yoon,	9-237, 13-S83, 15-S11
Kenichi Yoshida	16-S142, 18-68, 19-022, 21-206, 21-223, 22-159, 23-189, 24-153, 26-270
Toshikatsu Yoshiara	19-202
Sumio Yoshikawa	8-113
Tatsuhiko Yoshimura	6-109, 6-145
Hiroshi Yoshino,	12-S1
H. Yoshioka	10-S63
Takeo Yoshioka,	19-196
R.D. Young	6-93
R. P. Young	8-S38, 8-S166, 8-S254
R. Paul Young	5-S29, 5-S34, 25-294
Y. Youssef,	12-39
Qing Huan Yu	8-41
Hiroo Yugami	24-215
Syuro Yuji,	7-167
Hironobu Yuki	10-35
Kunihiro Yuno	11-S89
Shigenori Yuyama,	2-19, 2-71, 4-S38, 13-S14, 15-S107, 16-S75, 18-248, 19-118, 19-184, 21-187, 21-213, 23-233
J. Zaloudek	17-S65
F. Zeides	8-S109, 8-47, 10-31
Bajram Zeqiri	26-091
Kornelija Zgonc,	11-79
B. Q. Zhang	4-S94, 8-S49, 8-S105, 8-S114
Fan Zhang	18-144, 20-300
Zhizhen Zheng	15-S123
X. Q. Zhu	4-S215
Z. Zhu	8-S135
Zu-Ming Zhu	6-115
Zuming Zhu	16-S317
B. Ziegler	22-236
J. Zietek,	12-S7
Steve Ziola	8-51, 14-S12
B. Zogala,	18-15
Daihua Zou	5-S1
Ryszard Zuchowski	2-272
J. Zuidema	8-S118